

Cumhuriyet Science Journal
Faculty of Science, Cumhuriyet University
58140 - Sivas - Türkiye
Phone: +90(346) 487 13 72
Fax: +90(346) 219 11 86
e-mail: csj@cumhuriyet.edu.tr
<http://csj.cumhuriyet.edu.tr/en>
<http://dergipark.org.tr/en/pub/csaj>

Cumhuriyet Science Journal Vol: 43 No: 4 Year 2022

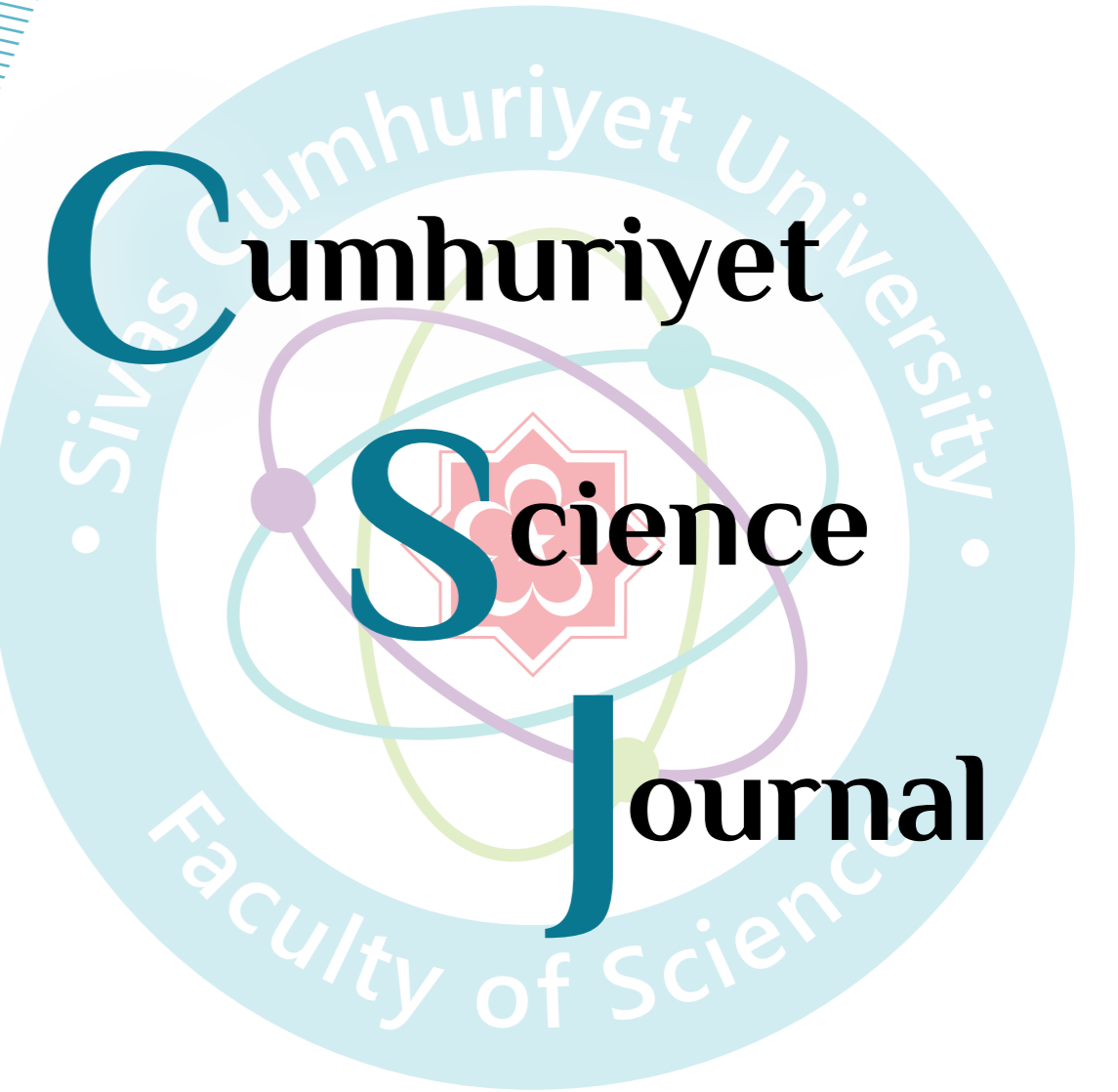


Sivas Cumhuriyet University

ISSN : 2680-2587

e-ISSN : 246-2587X

dergipark.org.tr/tr/pub/csaj
e-mail: csj@cumhuriyet.edu.tr



Cumhuriyet Science Journal (CSJ) is an official publication of Sivas Cumhuriyet University, Science Faculty. The high quality research papers related to the natural sciences are published as online four times a year. CSJ is an open access, free of charge journal and all articles in CSJ have undergone peer review and upon acceptance are immediately and permanently free for everyone to read and download.

Volume: 43

Number: 4

Year: 2022



ISSN: 2587-2680
e-ISSN: 2587-246X
Period: Quarterly
Founded: 2002

Publisher: Sivas Cumhuriyet University

Cumhuriyet Science Journal (CSJ)

Journal Previous Name: Cumhuriyet Üniversitesi Fen-Edebiyat Fakültesi Fen Bilimleri Dergisi

Old ISSN: 1300-1949

Owner on behalf of the Sivas Cumhuriyet University, Faculty of Science

Prof. Dr. İdris ZORLUTUNA (Sivas Cumhuriyet University)

Editor in Chief

Prof. Dr. İdris ZORLUTUNA (Sivas Cumhuriyet University)

Managing Editor

Assoc. Prof. Dr. Adil ELİK (Sivas Cumhuriyet University)

Editors

Prof. Dr. Baki KESKİN

bkeskin@cumhuriyet.edu.tr

Subjects: Mathematics and Statistics

Institution: Sivas Cumhuriyet University

Assoc. Prof. Dr. Adil ELİK

elik@cumhuriyet.edu.tr

Subjects: Chemistry and Chemical Engineering,
Environmental Sciences, Basic Sciences (General)

Institution: Sivas Cumhuriyet University

Prof. Dr. Nilüfer TOPSAKAL

ntopsakal@cumhuriyet.edu.tr

Subjects: Applied Mathematics

Institution: Sivas Cumhuriyet University

Prof. Dr. Serkan AKKOYUN

sakkoyun@cumhuriyet.edu.tr

Subjects: Physics and Physical Engineering

Institution: Sivas Cumhuriyet University

Prof. Dr. Halil İbrahim ULUSOY

hiulusoy@cumhuriyet.edu.tr

Subjects: Chemistry, Analytical Chemistry, Drug Analysis, Pharmacy

Institution: Sivas Cumhuriyet University

Prof. Dr. Fatih UNGAN

funghan@cumhuriyet.edu.tr

Subjects: Optics, Phonotics and Fiber optics

Institution: Sivas Cumhuriyet University

Assoc. Prof. Dr. Nail ALTUNAY

naltunay@cumhuriyet.edu.tr

Subjects: Bioanalytical Chemistry, Chemometric Analysis

Institution: Sivas Cumhuriyet University

Section Editors

Prof. Dr. Natalia BONDARENKO

bondarenkonp@info.sgu.ru

Subjects: Applied Mathematics and Physics

Institution: Samara University

Prof. Dr. Marcello LOCATELLI

marcello.locatelli@unich.it

Subjects: Analytical Chemistry

Institution: University "G. d'Annunzio" of Chieti-Pescara

Prof. Dr. Konstantin P. KATIN

kpkatin@yandex.ru

Subjects: Theoretical Chemistry, Computational design of nanostructures,
nanodevices and nanotechnologies

Institution: National Research Nuclear University

Assoc. Prof. Dr. Duran KARAKAŞ

dkarakas@cumhuriyet.edu.tr

Subjects: Inorganic Chemistry, Theoretical Chemistry

Institution: Sivas Cumhuriyet University

Assoc. Prof. Dr. Yaşar ÇAKMAK

ycakmak@cumhuriyet.edu.tr

Subjects: Applied Mathematics

Institution: Sivas Cumhuriyet University

Assoc. Prof. Dr. Sevgi DURNA DAŞTAN

sdurna@cumhuriyet.edu.tr

Subjects: Molecular Biology

Institution: Sivas Cumhuriyet University

Assist. Prof. Dr. Yener ÜNAL

uyener@cumhuriyet.edu.tr

Subjects: Statistics

Institution: Sivas Cumhuriyet University

Abstracted&Indexing

ULAKBİM TR-Dizin

Index Copernicus (ICI Journals Master List)

Clarivate Analytics Zoological Record

Crossref

WorldCat

Akademik Dizin

Arastirmax Bilimsel Yayın İndeksi

Bielefeld Academic Search Engine (BASE)

Directory of Research Journal Indexing (DRJI)

Google Scholar

Research Gate

Idealonline

Editorial Board

Prof. Dr. Sezai ELAGÖZ (ASELSAN)
Prof. Dr. Mustafa SOYLAK (Erciyes University)
Prof. Dr. Chuan Fu Yang (Nanjing University of Science and Technology)
Prof. Dr. Münevver SÖKMEN (KGTU)
Prof. Dr. Hüseyin MERDAN (TOBB ETU)
Prof. Dr. Mehmet AKKURT (Erciyes University)
Prof. Dr. Mustafa KAVUTÇU (Gazi University)
Prof. Dr. Francois VOS (The University of Queensland)
Prof. Dr. Abuzar KABIR (International Forensic Research Institute)
Prof. Dr. Mustafa TÜZEN (GOP University)
Prof. Dr. Songül KAYA MERDAN (METU)
Prof. Dr. Jose Javier Valiente-Dobon (INFN-LNL, Padova University)
Prof. Dr. Yeşim SAĞ AÇIKEL (Hacettepe University)
Prof. Dr. Mehmet ŞİMŞİR (Sivas Cumhuriyet University)
Prof. Dr. Atalay SÖKMEN (KGTU)
Prof. Dr. Ricardo I. JELDRES (Universitat de Antofagasta)
Prof. Dr. Mustafa YILDIRIM (Sivas Cumhuriyet University)
Prof. Dr. Ali DELİCEOĞLU (Erciyes University)
Prof. Dr. Tuncay BAYRAM (Karadeniz Technical University)
Prof. Dr. Gökhan KOÇAK (Erciyes University)
Prof. Dr. Nadjet Laouet (Freres Mentouri Constantine-1 University)
Assoc. Prof. Dr. Savaş KAYA (Sivas Cumhuriyet University)

Layout Editors:

Lecturer Aykut HASBEK

Copyeditors:

Assist. Prof. Dr. Doğa Can SERTBAŞ
Assist. Prof. Dr. Hacı Ahmet KARADAŞ
Research Assistant Özgür İNCE

Proofreader:

Assist. Prof. Dr. Yener ÜNAL
Lecturer Aykut HASBEK

Publication Type: Peer Reviewed Journal

Cite Type: Cumhuriyet Sci. J.

Contact Information

Faculty of Science Cumhuriyet University
58140 Sivas- TURKEY
Phone: +90 (346) 487 13 72
Fax: +90 (346) 219 11 86
e-mail: csj@cumhuriyet.edu.tr
<http://dergipark.gov.tr/csj>

	CONTENTS		PAGES
1	Ahmet CEYLAN, Gökçe ŞEKER KARATOPRAK, Zekiye KOCAKAYA, Mustafa KOCAKAYA <i>Evaluation of DNA Protective and Antimicrobial Properties of some Cladonia Species</i>	Research Article	550-555
2	Çağlar YILDIZ, Zeki ÖZSOY, Turgut KACAN, Hatice ÖZER <i>The Effects of Lapatinib and Trastuzumab in a Rat Model of Endometriosis</i>	Research Article	556-563
3	Gülizar ÖZER, Çağlar YILDIZ, Hatice ÖZER Ali ÇETİN <i>The Effect of Low Molecular Weight Heparins on Placentation: A Rat Model Study</i>	Research Article	564-568
4	Ayşegül ÖZTÜRK, Vedat SABANCIOĞULLAR, I Yaşar TAŞTEMUR, İbrahim ÖZTOPRAK <i>Evaluation of Thalamus Volumes in Patients with Diabetic Polyneuropathy Using Magnetic Resonance Imaging Method</i>	Research Article	569-576
5	Ertan Mahir KORKMAZ <i>The Complete Mitogenome of Redheaded Pine Sawfly, Neodiprion lecontei (Hymenoptera: Diprionidae): Duplication of trnR Gene and Rearrangement in the ARNS1EF Gene Cluster</i>	Research Article	577-583
6	Demokrat NUHA, Asaf Evrim EVREN, Zennure Şevval ÇİYANCI, Halide Edip TEMEL, Gülşen AKALIN ÇİFTÇİ, Leyla YURTTAŞ <i>Acetylcholinesterase Inhibitor Activity of Some 5-Nitrothiophene-Thiazole Derivatives</i>	Research Article	584-589
7	Hayrani Eren BOSTANCI Ulviye ACAR ÇEVİK <i>Design and Synthesis of Imidazole Derivatives as Anticancer Agents and Potential Aromatase Inhibitors</i>	Research Article	590-593
8	Eda SÖNMEZ GÜRER, Tutku TUNC <i>Investigation of Antimicrobial and Cytotoxic Activities of Palmarosa (Cymbopogon martinii) Essential Oil</i>	Research Article	594-599
9	Beyzanur ÖZDEMİR, Halil İbrahim ULUSOY, Ümmügülsüm MORGÜL, Marcello LOCATELLI, Abuzar KABİR <i>Sensitive Determination of Venlafaxine in Urine Samples by Using HPLC-DAD System After Fabric Phase Sorptive Extraction</i>	Research Article	600-605
10	Merve VURUCUEL, Ali DURAN, Abdullah İNCİ, Erkan YILMAZ <i>Green Synthesis of C-quantum Dots Modified ZnO Nanophotocatalyst: The Effect of Different Solvents Used in Production of C-quantum Dots Modified ZnO Nanophotocatalyst on Photocatalytic Performance</i>	Research Article	606-612
11	Ayşegül KÖSE <i>Synthesis, Structural Characterization and Investigation of DNA/BSA Binding Properties of a Homo-disulphide Schiff Base Compound Carrying Oxo Propargyl Group</i>	Research Article	613-620
12	Sema BİLGİN, Nazan GÖKŞEN TOSUN, Cemil ALKAN, Esra KOÇ, Seçil ERDEN TAYHAN <i>Activity Improvement and Thermal Stability Enhancement of D-Aminoacylase Using Protein-Polymer Conjugates</i>	Research Article	621-628
13	Ayşen IŞIK, Kezban UÇAR ÇİFTÇİ, Hayrani Eren BOSTANCI, Yusuf TUTAR, Ahmet KOÇAK, Mustafa YILMAZ <i>Synthesis and Characterization of Novel Calix[4]arene Schiff Base Derivatives and Cytotoxicity Effect Evaluation on Cancer Cell Lines</i>	Research Article	629-633
14	Ahmet KATI, Sevde ALTUNTAS <i>Proliferative and Antimicrobial Evaluation of the Benzalkonium Chloride Loaded Walnut Shell-Rich Chitosan Gels</i>	Research Article	634-637
15	Nuket KARTAL TEMEL, Esra BAĞDA <i>Decolourization of Methylene Blue in Aqueous Solution by Photocatalytic Oxidation, Fenton Oxidation and Biosorption</i>	Research Article	638-644
16	Emrah EROĞLU <i>Simultaneous Manipulation and Imaging of Chemogenetically Induced Hydrogen Peroxide in Hardly Transfectable Endothelial Cells</i>	Research Article	645-651
17	Mehmet Ali ÖZTÜRK <i>Exactness of Proximal Group Homomorphisms</i>	Research Article	652-655

18	Mehmet MERDAN, Şeyma ŞİŞMAN <i>A Mathematical Model of Susceptible Diabetes Complication (SDC) Model in Discrete Time Fuzzy and Crisp Environment</i>	Research Article	656-664
19	Hasan GÖKBAŞ <i>Dual-Gaussian Pell and Pell-Lucas numbers</i>	Research Article	665-671
20	Betül COŞGUN, Ummahan Merdinaz ACAR <i>On Hyperideals of Multiplicative Hyperrings</i>	Research Article	672-675
21	Mithun PAUL, Krishnadhan SARKAR, Kalishankar TĪWARY <i>Fixed Point Theorems In 2-Banach Spaces For Non-expansive Type Conditions</i>	Research Article	676-683
22	Enes ATA, İ. Onur KIYMAZ <i>Generalized Gamma, Beta and Hypergeometric Functions Defined by Wright Function and Applications to Fractional Differential Equations</i>	Research Article	684-695
23	Neşe ÖMÜR, Kübra Nur SÜDEMEN, Sibel KOPARAL <i>Some Identities with Special Numbers</i>	Research Article	696-702
24	Yusuf GÜREFE, Yusuf PANDIR, Tolga AKTÜRK <i>Analysis of Exact Solutions of a Mathematical Model by New Function Method</i>	Research Article	703-707
25	İbrahim Etem GÜL, Sinan KUDAY <i>Retinoblastoma Radiotherapy Treatment Optimizations Through GATE Simulations</i>	Research Article	708-715
26	Şevki ŞENTÜRK, Tuncay BAYRAM, Serkan AKKOYUN <i>Chemical and Radiological Characterizations of the Desert Dust Coming from Northern Africa to Batman (Southeastern Turkey)</i>	Research Article	716-720
27	Ercan ŞAHİN <i>Calculation of One- and Two-Center Overlap Like Quantum Similarity Integrals over $\psi^{(\alpha)}$ Exponential Type Functions</i>	Research Article	721-725
28	R. Gökhan TÜRECI <i>Machine Learning Applications to the One-speed Neutron Transport Problems</i>	Research Article	726-738
29	Bilge BIÇAK, Serda Kecel GUNDUZ <i>Molecular Docking and ADME Analysis of L-Phe -L-Tyr Dipeptide</i>	Research Article	739-745
30	Deniz ERKAL, Sinan KUDAY <i>Carbon Radiotherapy For Head and Neck Cancer: Dosimetric Comparison with Photon Plans</i>	Research Article	746-751
31	Mert ŞEKERCİ, Abdullah KAPLAN <i>Effects of Deuteron and Alpha Optical Model Potentials on the Production Cross-Section Calculations of Some Radiobromine Isotopes</i>	Research Article	752-759
32	Elif BEKLEN <i>Searching for New Supernova Remnant Candidates from the VTSS Survey</i>	Research Article	760-768
33	Idris DEMİRSOY <i>Testing Complete Spatial Randomness on Linear Networks: Leon County Traffic Accident Example</i>	Research Article	769-776

Evaluation of DNA Protective and Antimicrobial Properties of some *Cladonia* Species

Ahmet Ceylan ^{1,a,*}, Gökçe Şeker Karatoprak ^{2,b}, Zekiye Kocakaya ^{3,c}, Mustafa Kocakaya ^{4,d}

¹ Department of Pharmaceutical Biotechnology, Faculty of Pharmacy, Erciyes University, Kayseri, Türkiye.

² Department of Pharmacognosy, Faculty of Pharmacy, Erciyes University, Kayseri, Türkiye.

³ Department of Crop and Animal Production, Safiye Cikrikcioglu Vocational College, Kayseri University, Kayseri, Türkiye.

⁴ Department of Plant and Animal Production, Boğazlıyan Vocational School, Yozgat Bozok University, Yozgat, Türkiye.

*Corresponding author

Research Article

History

Received: 07/07/2022

Accepted: 02/10/2022

Copyright



©2022 Faculty of Science,
Sivas Cumhuriyet University

ABSTRACT

The present study evaluated the DNA protective properties and antimicrobial activities of the methanol extracts of nine *Cladonia* species, namely *C. pocillum*, *C. subulata*, *C. pyxidata*, *C. coniocraea*, *C. foliacea*, *C. firma*, *C. furcata*, *C. fimbriata* and *C. rangiformis* collected in Turkey. DNA protection properties efficiency of *Cladonia* extracts was evaluated using pBR322 plasmid DNA. In vitro antimicrobial activities of methanol extracts against two Gram-negative bacteria (*Escherichia coli* and *Proteus mirabilis*), three Gram-positive bacteria (*Staphylococcus aureus*, *Micrococcus luteus* and *Bacillus subtilis*) and two fungal strains (*Candida glabrata* and *Candida albicans*) were examined using the disc diffusion method and through the determination of minimal inhibitory concentrations (MIC). DNA protective studies, all *Cladonia* extracts protected pBR322 plasmid DNA against damage caused by the hydrogen peroxide (H₂O₂) with ultraviolet (UV). The results demonstrated that the inhibition zones in the disc diffusion method ranged from 6.5 to 19.0 mm. MIC results were ranged from 3.12 to 6.25 mg/mL. *Cladonia* extracts show a better antimicrobial effect against bacterial strains than fungal strains. The highest antimicrobial effect among lichen species was demonstrated by *Cladonia pocillum*. Our results demonstrated that tested *Cladonia* extracts had strong antibacterial and DNA protective effects. This is the first comprehensive study to evaluate the DNA protective properties activity of *Cladonia* extracts.

Keywords: Antimicrobial activity, *Cladonia*, DNA protective properties, Lichen

^a aceylan@erciyes.edu.tr

^b <https://orcid.org/0000-0002-3087-066X>

^c zekiyekocakaya@kayseri.edu.tr

^d <https://orcid.org/0000-0001-5248-0462>

^e gskaratoprak@erciyes.edu.tr

^f <https://orcid.org/0000-0001-5829-6914>

^g mustafa.kocakaya@yobu.edu.tr

^h <https://orcid.org/0000-0003-2306-8094>

Introduction

Lichens are natural resources used in the treatment of various diseases since ancient times. They are among the most fascinating organisms on earth and formed from the symbiotic relationship between the fungus ascomycetes and green algae or blue-green algae [1-3]. More than 1050 secondary metabolites have been isolated from lichens and have been found to have antibacterial, antiviral, anti-analgesic, antipyretic, and antiproliferative activities [4]. Lichens are of great interest to researchers as new important sources of bioactive substances due to the pronounced antimicrobial activity of secondary metabolites [5, 6]. Natural products are recommended as a therapeutic alternative to traditional antimicrobial therapy. Bacterial and fungal infection diseases remain the major causes of death worldwide [7]. Antibiotics are widely used to prevent and treat microbial infectious diseases, but new antibiotics and drugs are needed due to the emergence of antibiotic-resistant pathogens strains. The growing population of antibiotic-resistant microorganisms motivated the investigation of lichens as an alternative antimicrobial drug [8-10]. Several studies have shown that some lichen species have antibacterial activity against micro-organisms [11-14].

The genus *Cladonia* is classified in the *Cladoniaceae* family (Ascomycota and Lecanorales) [15, 16]. The genus

contains many secondary metabolites [17]. In previous studies, it has been determined that extracts of some *Cladonia* species have strong antioxidant, antimicrobial and anticancer activity in vitro [18-20].

This study aimed to determine the in vitro antimicrobial activities of extracts of *Cladonia* species (*C. pocillum* (Ach) O. J. Rich., *C. subulata* (L.) Weber ex F. H. Wigg., *C. pyxidata* (L.) Hoffm., *C. coniocraea* (Flörke) Spreng, *C. foliacea* (Huds.) Willd., *C. firma* (Nyl.) Nyl., *C. furcata* (Huds) Schrad, *C. fimbriata* (L.) Fr. and *C. rangiformis* Hoffm). All the species used in the study contain fumarprotocetraric acid. This acid has biological properties such as expectorant, antioxidant, antibacterial, antifungal, and anticancer [18, 21-24].

Oxidative stress-related DNA damage is associated with varied diseases. Numerous investigations have found that natural plant components have genotoxicity-protective action against oxidative stress and UV radiation [25]. As a result, the efficiency of *Cladonia* methanol extracts in protecting DNA from UV and oxidative stress was also investigated.

Materials and Methods

Lichen Samples

Lichen species were collected in field studies in different regions of Turkey. The morphological and anatomical features of the specimens were determined

under the microscope, and their diagnosis was made using diagnostic keys [26, 27]. The species are preserved in Yozgat Bozok University, Boğazlıyan Vocational School Lichen Herbarium. The location information and herbarium numbers of the samples are given in Table 1.

Table 1. The Locality Information of Species and Herbarium Numbers

Species	Locality	Voucher
<i>C. coniocraea</i> →	Istanbul, Belgrad forests, Turkey, 28°55'683"E, 41°08'857"N, 20 m, 13 Eylül 2013	CLAD 77, 109
<i>C. fimbriata</i> →	Çankırı, Ilgaz, Turkey, 33°42'495"E, 41°00'848"N, 1200 m, 07 Temmuz 2014	CLAD 712, 713
<i>C. firma</i> →	Turkey, Çanakkale, Bayramiç, 26°45'634"E, 39°55'320"N, 220 m, 16 Eylül 2013	CLAD 52
<i>C. foliacea</i> →	Ankara, Gündül, Turkey, 32°09'54"E, 40°12'55"N, 750 m, 21 Temmuz 2014	CLAD 640
<i>C. furcata</i> →	Rize, Kackar Mountains National Park, Turkey, 41°08'801"E, 40°55'592"N, 1750 m, 16 Augustos 2014	CLAD 488
<i>C. pocillum</i> →	Mersin, Anamur, Turkey, 33°04'345"E, 36°05'592"N, 31 m, 19 Mayıs 2013 and Mersin, Çamlıyayla, 34°37'579"E 37°11'185"N, , 1350 m, 20 Mayıs 2013	CLAD 1, 55
<i>C. pyxidata</i> →	Çorum, Turkey, 34°49'277"E, 40°41'486"N, 1325 m, 25 Mayıs 2013	CLAD 135, 137
<i>C. rangiformis</i> →	Çorum, Turkey, 35°04'103"E, 40°31'855"N, 1186 m, 24 Mayıs 2013	CLAD 53
<i>C. subulata</i> →	Ordu, Çambaşı Plateau, Turkey, 37°56' 9"E, 40°44'06"N, 1560 m, 24 Eylül 2014	CLAD 998

Preparation of Lichen Extracts

Air-dried *C. pocillum* (5 g), *C. coniocraea* (4 g), *C. pxyidata* (3.5 g), *C. rangiformis* (30g), *C. foliacea* (10 g), *C. firma* (5 g), *C. furcata* (11 g), *C. subulata* (15 g), *C. fimbriata* (7g) thalli were pulverized and extracted three times in 70 percent methanol (MeOH) for 24 hours with periodic stirring. The extracts were removed from their solvents under vacuum (37 °C) after filtration. Before analysis, the extracts were lyophilized and kept at -18 °C.

Antimicrobial Assay

Antimicrobial activity of the *Cladonia* methanol extracts against bacterial strains (Gram-negative and Gram-positive), and fungal strains were examined by disc diffusion assay, MIC (Minimum inhibitory concentration), and MMC (Minimum microbicidal concentration). The test indicator bacteria included two Gram-negative bacteria (*Escherichia coli* ATCC25922, *Proteus mirabilis* ATCC25933), three Gram-positive bacteria (*Staphylococcus aureus* ATCT25923, *Micrococcus luteus* ATCC10240, and *Bacillus subtilis* ATCC6633) and two fungal strains (*Candida glabrata* ATCC90030, *Candida albicans* ATCC10231) were obtained from the culture collection of the Laboratory of Biotechnology, Faculty of Pharmacy, Erciyes University, Turkey. The bacterial strains were grown on Mueller Hinton Agar (MHA) medium and incubated at 37°C for 18-24h, and the fungal strains were grown on Sabouraud Dextrose Agar (SDA) medium and incubated 30°C for 36-48 h. A single colony was obtained from overnight strains using a sterile loop and inoculated into 5 mL of Mueller Hinton Broth (MHB) for tested bacterial strains and Sabouraud Dextrose Broth (SDB) for

tested fungal strains. The inoculum strains were adjusted to the 0.5 McFarland standard turbidity. Then 100 µL micro-organisms (approximately 5 x10⁵ CFU/mL) of the dilution was spread onto the agar plates containing MHA and SDA.

Sterile commercial paper discs (Oxoid; 6 mm) were placed on the above-inoculated media and impregnated with 20 µL of the methanol extract and incubated at 37 °C for 18-24 h (for bacteria) and 30°C for 36-48 h (for fungi). DMSO was used as a negative control, while Ampicillin: AMP and Nystatin: NS (10 µg/disc) were used as a positive control. All experiments were performed in duplicate, and the antibacterial/antifungal activities were assayed as the mean of a clear zone of inhibition diameter (mm) produced by the *Cladonia* extracts.

The Microdilution Method Determined the MIC values and minimum microbicidal concentration (MMC) (minimum bactericidal-fungicidal concentration (MBC-MFC)) values of the *Cladonia* methanol extracts in 96 multi-well microplates CLSI guidelines. The serial dilutions of *Cladonia* extracts were prepared with MHB for bacterial strains and SDB for fungal strains at a volume of 90 µL each well in microplates. A 100 µL of a stock solution (200 µg/mL) of all extract was added into the first well of the microplate. Then, serial dilutions were performed among the first and last wells. After, 10 µL of the diluted micro-organism suspension was added to all well to give a final concentration of 5 x 10⁵ CFU/mL, making approximately 200 µL in each well. The obtained concentration range of the extracts was from 0.78 to 100 µg/mL. The added microplates were incubated at 37°C for 18-24 h for bacteria, 30°C for 36-48 h for fungi. Streptomycin and

ketoconazole were used as positive controls, and 10% DMSO solution was used as a negative control. The lowest concentration of the antimicrobial agent that did not produce visible growth (no turbidity observed) was defined as MIC. The MBC/MFC was determined on the agar medium by plating 10 µL of solution from each well where no visible growth was determined. After incubating at 37°C for 18-24h for bacteria and 30°C for 24-48h for bacteria. At the end of the incubation, the lowest concentration without growth was determined as MBC/MFC. All experiments were performed in duplicate.

DNA Cleavage Assay

The DNA cleavage activities of the *Cladonia* methanol extracts were shown by photolyzing hydrogen peroxide (H₂O₂) with ultraviolet (UV) in the presence of plasmid DNA (pBR322) and performing agarose gel electrophoresis. To prepare a 5% stock solution of extracts, 20 mg *Cladonia* extracts were weighed and dissolved in 400 µL dH₂O. Up to 5 µL of the extract was added to each tube except for the control and 3 µL plasmid DNA (pBR322), and then 1 µL hydrogen peroxide (H₂O₂) in microcentrifuge tubes was added. All components with the *Cladonia* extracts, including tubes 2 and 4, were exposed to ultraviolet radiations for five mins. All tubes were incubated at 37°C for 1h. After irradiation, 5 µL of loading dye was added. They were loaded with Ethidium bromide (EtBr) staining 1% agarose gel at 90 V for 1.5-2 h in TAE (Tris base, acetic acid, and EDTA) buffer. The DNA fragments were visualized using ultraviolet illumination with a Bio-Rad Molecular Imager ChemiDoc XRS system (BioRad).

Statistical Analysis

The data are provided as mean values with a 95% confidence interval. ANOVA techniques were used for variance analysis. Tukey's pairwise comparison test was used to evaluate if there were significant differences between means at a threshold of $p < 0.05$.

Results and Discussion

The antimicrobial activity of *Cladonia* methanol extracts was evaluated against microorganisms, and their potential effects were assessed qualitatively/quantitatively against the bacteria and fungi by the presence/ absence of inhibition zones MIC values. The *Cladonia* extracts inhibition zones obtained using disc diffusion assay are shown in Table 2. According to the results, the *Cladonia* extracts had great potential of antibacterial activity against all bacteria but did not have antifungal activity, except only the *C. pocillum* extract. The antimicrobial activity was checked with ampicillin and nystatin. These antibiotics had a more substantial effect than all extracts, as presented in Table 2. No inhibitory effect of DMSO, the negative control, was observed on the extracts. *Cladonia* extracts inhibited the bacterial strains produced a zone diameter of inhibition from 7.0 to 19 mm for Gram (-) and Gram (+) bacteria. In contrast, there was no antifungal activity for fungal strains of *Cladonia* extracts, except only *C. pocillum* extract. Antimicrobial activity analysis showed *C. pocillum* as the most potent extract and *C. pyxidata* as the weakest one. The methanol extract of *C. pocillum* was found to have the same significance ($p > 0.05$) as the standard against Gram-negative *P. mirabilis*. It was also more effective against Gram-positive *B. subtilis* than the standard.

Table 2. Antimicrobial activity of extracts of *Cladonia* species(20 mg/mL) against tested bacteria and fungi using disc diffusion methods.

Micro-organisms	Inhibition zone (mm)										
	<i>Cladonia pocillum</i>	<i>Cladonia subulata</i>	<i>Cladonia pyxidata</i>	<i>Cladonia coniocraea</i>	<i>Cladonia foliacea</i>	<i>Cladonia firma</i>	<i>Cladonia furcata</i>	<i>Cladonia fimbriata</i>	<i>Cladonia rangiformis</i>	Control (-)	Control (+)
<i>E. coli</i>	14.96 ±0.60 ^a	NI*	NI	NI	6.93 ±0.45 ^b	NI	7.5 ±0.20 ^b	6.86 ±0.05 ^b	NI	NI	12.3 ±0.25 ^c
<i>P. mirabilis</i>	19.0 ±0.52 ^a	7.16 ±0.15 ^b	7.1 ±0.26 ^b	7.1 ±0.00 ^b	7.1 ±0.01 ^b	NI	NI	7.56 ±0.11 ^b	7.2 ±0.00 ^b	NI	20.02 ±0.2 ^a
<i>S. aureus</i>	14.13 ±0.06 ^a	7.53 ±0.4 ^d	NI	8.5 ±0.26 ^b	10.10 ±0.52 ^c	6.77 ±0.15 ^d	7.53 ±0.21 ^d	7.10 ±0.1 ^d	6.83 ±0.05 ^d	NI	21.03 ±0.25 ^e
<i>B. subtilis</i>	15.9 ±0.17 ^a	7.5 ±0.26 ^b	6.86 ±0.05 ^b	6.76 ±0.15 ^b	7.13 ±0.15 ^b	6.5 ±0.26 ^b	7.5 ±0.00 ^b	6.76 ±0.05 ^b	8.0 ±0.17 ^b	NI	13.86 ±0.15 ^c
<i>M. luteus</i>	15.06 ±0.77 ^a	NI	NI	12.86 ±0.35 ^b	12.93 ±0.11 ^b	11.2 ±0.26 ^c	7.5 ±0.25 ^d	8.5 ±0.17 ^e	9.5 ±0.32 ^e	NI	22.06 ±0.31 ^f
<i>C. albicans</i>	NI	NI	NI	NI	NI	NI	NI	NI	NI	NI	15.16 ±0.15
<i>C. glabrata</i>	8.0 ±0.43 ^a	NI	NI	NI	NI	NI	NI	NI	NI	NI	14.86 ±0.21 ^b

Values with the same lower case letter (a–f) are not significantly ($p > 0.05$) different, $n=3$.

The MIC values of the tested *Cladonia* methanol extracts against the tested microorganisms ranged from 3.12 to 50 µg/mL (Table 3). The strongest antimicrobial activity was shown in the extract of the *C. pocillum*, which inhibited the tested bacteria and fungi species in a relatively low amount (3.12 to 25 µg/mL). The lowest activity was manifested by *C. pyxidata*, which inhibited the tested bacteria and fungi species at a concentration of 25

to 50 µg/mL. The most sensitive among the microorganisms was *S. aureus*, and the highest resistance was shown in *B. subtilis* and fungal strains. The MIC and MBC/MFC that resulted in the same value for *Cladonia* extracts were observed against all micro-organisms. The strongest MBC and MFC were obtained with *C. pocillum* extract against *S. aureus* and *C. glabrata* (3.12 and 6.25 µg/mL), respectively.

Table 3. MIC and MMC of extracts of *Cladonia* species

Micro-organism	MIC(Minimum inhibitory Concentration)(µg mL ⁻¹)/ *MBC/MFC(Minimum Bactericidal/Fungicidal Concentration)(µg mL ⁻¹)									
	<i>Cladonia pocillum</i>	<i>Cladonia subulata</i>	<i>Cladonia pyxidata</i>	<i>Cladonia coniocraea</i>	<i>Cladonia foliacea</i>	<i>Cladonia firma</i>	<i>Cladonia furcata</i>	<i>Cladonia fimbriata</i>	<i>Cladonia rangiformis</i>	
<i>E. coli</i>	3.12	12.5	25	6.25	6.25	6.25	12.5	6.25	12.5	
	*12.5	*25	*50	*25	*25	*25	*25	*25	*25	
<i>P. mirabilis</i>	3.12	25	25	25	25	25	25	25	25	
	*12.5	*50	*50	*50	*50	*50	*50	*50	*50	
<i>S. aureus</i>	3.12	25	25	3.12	3.12	6.25	12.5	6.25	6.25	
	*12.5	*25	*50	*6.25	*6.25	*12.5	*12.5	*6.25	*6.25	
<i>B. subtilis</i>	3.12	50	50	25	25	12.5	25	50	50	
	*12.5	*50	*50	*50	*50	*50	*50	*50	*50	
<i>M. luteus</i>	3.12	12.5	12.5	3.12	6.25	12.5	12.5	6.25	6.25	
	*12.5	*25	*25	*12.5	*12.5	*12.5	*25	*12.5	*12.5	
<i>C. albicans</i>	25	25	50	25	25	25	25	25	25	
	*50	*50	*100	*50	*50	*50	*50	*50	*50	
<i>C. glabrata</i>	6.25	50	50	50	100	50	50	25	25	
	*25	*100	*100	*100	*100	*100	*100	*50	*50	

DNA cleavage assay has been investigated by inducing plasmid DNA damage by H₂O₂ and UV. The cleavage effect of *Cladonia* methanol extracts was assessed by the conversion of the plasmid DNA in the supercoiled (Form I) to its open circular (Form II) and the linear (Form III). The plasmid DNA (pBR322) damage results are shown in Fig. 1. The pBR322 ladder is clear in lane:1, while the pBR322 treated with UV and H₂O₂ revealed that plasmid DNA was damaged in lanes: 4. The H₂O₂ and UV together also induced pBR322 in lane:4. pBR322 treated with *Cladonia* extracts in the exposure of H₂O₂, and UV irritation results are demonstrated in lanes: 5–13. In lane: 4, as a result of the interaction of the pBR322 with H₂O₂/UV, Form III is formed.

The antibacterial and antifungal properties of methanol extracts from *Cladonia* species (*C. pocillum*, *C. subulata*, *C. pyxidata*, *C. coniocraea*, *C. foliacea*, *C. firma*, *C. furcata*, *C. fimbriata*, and *C. rangiformis*) were investigated in this work. It is known that various *Cladonia* species exhibit different antimicrobial activities. The presence of diverse components is most likely responsible for the variances in antibacterial activity displayed by distinct *Cladonia* species [28]. In our experiments, *Cladonia* extracts demonstrated rather significant antibacterial activity but no antifungal activity. The severity of the antimicrobial effect depends on the lichen species, the concentration of their extracts, the contents of the extracts, and the tested microorganism. In our previous study, total phenol and flavonoid contents of

Cladonia species were determined spectrophotometrically and fumarprotocetraric acid content was determined chromatographically (HPLC).

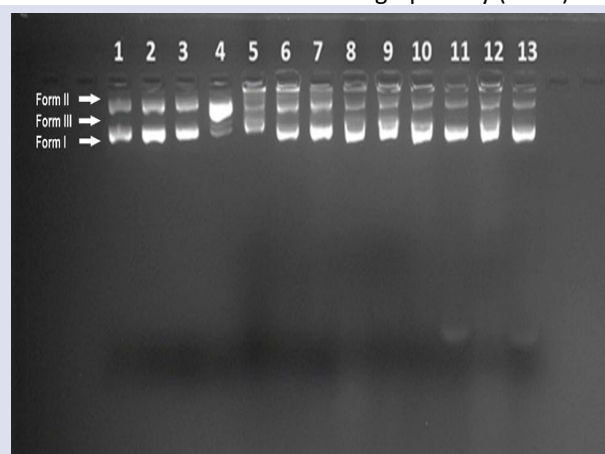


Figure 1. Line 1) PBR322 ladder, line 2) pBR322 / UV, line 3) pBR322 / H₂O₂, line 4) pBR322 / UV + H₂O₂, line 5) pBR322 and *C. pocillum* extract/ UV + H₂O₂, line 6) pBR322 and *C. subulata* extract/ UV + H₂O₂, line 7) pBR322 and *C. pyxidata* extract/ UV + H₂O₂, line 8) pBR322 and *C. coniocraea* extract/ UV + H₂O₂, line 9) pBR322 and *C. foliacea* extract/ UV + H₂O₂, line 10) pBR322 and *C. firma* extract/ UV + H₂O₂, line 11) pBR322 and *C. furcata* extract/ UV + H₂O₂, line 12) pBR322 and *C. fimbriata* extract/ UV + H₂O₂, line 13) pBR322 and *C. rangiformis* extract/ UV + H₂O₂

The amount of fumarprotocetraric acid was found to be between 1.89-23.82 mg g extract⁻¹ by HPLC analysis. The highest total phenol content was found in *C. pocillum* with a value of 124 mg GAE g extract⁻¹. *C. fimbriata* has the highest fumarprotocetraric acid concentration (23.82±1.98 mg g extract⁻¹) [29]. *C. pocillum* showed the strongest antibacterial effect among lichens studied at the same concentrations. This study demonstrated that the antibacterial action was mediated not just by fumarprotocetraric acid, but also by other phenolic compounds. Besides, these results proved that bacteria were more sensitive to antimicrobial agents than fungi in other studies. This difference is due to the cell wall structures of bacteria and fungi. The bacteria cell walls are composed of polysaccharide peptidoglycan, and fungal cell walls consist of chitin. It is thought that fungi are more resistant than bacteria because of the complex structure of the cell wall [19, 30]. *Cladonia* extracts were searched for antimicrobial effects in developing novel antimicrobial agents [31, 32]. Studzińska-Sroka et al. (2019) reported that an acetone extract of *C. uncialis* is active against *S. epidermidis* and *E. faecium* but did not display any activity against fungi. Kosanić et al. (2018) found that the five *Cladonia* lichens have strong antimicrobial activity against five bacteria and ten fungi strains. Mitrovic et al. (2015) investigated the antimicrobial activities of *C. foliacea* extract [13]. As a result of the study, *C. foliacea* extract had strong antimicrobial activity in all used tests. In addition, Açıkgöz et al. (2013) reported that acetone and chloroform extracts of two fruticose soil lichens, *C. rangiformis*, and *C. convoluta*, were active against two Gram-negative bacteria, two Gram-positive bacteria, and one fungal strain [33]. Our study of the antimicrobial effect of the extracts of *Cladonia* species showed a different degree of antimicrobial activity depending on the tested lichen species and the tested species of microorganisms. This is the first study of the antimicrobial activity of different *Cladonia* species originating from our region. In general, the tested lichen extracts showed good antibacterial activity.

Cladonia extracts were shown to have a significant protective effect, resulting in the formation of Form I and Form II fragments. These results demonstrated that UV/H₂O₂ induced plasmid DNA damage was protected. ROS (reactive oxygen species) may be produced by UV radiation and any oxygen factors. These destroy DNA or other cell components through oxidative stress [34]. It has been shown in some studies that free radicals induced DNA damage can be protected by using lichen extracts [35]. Recent research also supported the DNA damage protection efficacy of extracts of *Bryoria fuscescens*, *Umbilicaria decussata*, and *Parmelia tiliacea* lichens [36]. In another study, it has been shown that extracts of *Ganoderma lucidum* have significant radioprotective activity [37]. This is the first study of the DNA damage protective effect of *Cladonia* species. Although it is not feasible to directly compare the results since no studies with *Cladonia* species have been undertaken, this study

has demonstrated that the biological activity potential of lichens is substantial.

Conclusion

The antimicrobial activity of the nine lichen species from the familia *Cladoniaceae* (*C. pocillum*, *C. subulata*, *C. pyxidata*, *C. coniocraea*, *C. foliacea*, *C. firma*, *C. furcata*, *C. fimbriata*, and *C. rangiformis*) were demonstrated. *C. pocillum* methanol extract has the best antimicrobial activity against all bacterial strains. *Cladonia* methanol extracts also protected plasmid DNA (pBR322) from H₂O₂ and UV damage. It also demonstrated the potential of the extract to prevent DNA damage, which could be used in cancer research.

Further work will be done on the isolation and purification of components in the studied *Cladonia* species. Lichen compounds promise great potential for pharmaceutical applications as antimicrobial agents and in the development of novel formulations or molecules for the benefit of humanity.

Acknowledgments

We would like to thank the research councils of Erciyes University and Bozok University for the financial support.

Conflicts of interest

The authors declare that they have no conflict of interest.

References

- [1] Honegger R., Functional aspects of the lichen symbiosis, *Annu. Rev. Plant Physiol.*, 42(1) (1991) 553-578.
- [2] Bates S. T., Cropsey G. W., Caporaso J. G., Knight R., Fierer N., Bacterial communities associated with the lichen symbiosis, *Appl Environ Microbiol.*, 77 (2011) 1309–1314.
- [3] Selbmann L., Zucconi L., Ruisi S., Grube M., Cardinale M., Onofri S., Culturable bacteria associated with Antarctic lichens: affiliation and psychrotolerance, *Polar Biol.*, 33(1) (2010) 71–83.
- [4] Molnár K., Farkas E., Current results on biological activities of lichen secondary metabolites: a review, *Z Naturforsch C.*, 65(3–4) (2010) 157–173.
- [5] Mitscher L. A., Drake S., Gollapudi S. R., Okwute S. K., A modern look at folkloric use of anti-infective agents, *J. Nat. Prod.*, 50 (6) (1987) 1025–1040.
- [6] Hostettman K., Wolfender J. L., The search for biologically active secondary metabolites, *Pestic. Sci.*, 51 (1997) 471–482.
- [7] Bate P. N. N., Orock A. E., Nyongbela K. D., Babiaka S. B., Kukwah A., Ngemenya M. N., In vitro activity against multi-drug resistant bacteria and cytotoxicity of lichens collected from Mount Cameroon, *J. King Saud Univ. Sci.*, 32 (1) (2020) 614–619.
- [8] Nishanth K. S., Sreerag R. S., Deepa I., Mohandas C., Nambisan B., Protocetraric acid: an excellent broad-spectrum compound from the lichen *Usnea albopunctata* against medically important microbes, *Nat. Prod. Res.*, 29(6) (2015) 574–577.

- [9] Timbreza L. P., De los Reyes J. L., Flores C. H., Perez R. J. L. A., Stockel M. A., Santiago K. A., Antibacterial activities of the lichen *Ramalina* and *Usnea* collected from Mt. Banoi, Batangas and Dahilayan, Bukidnon, against multi-drug resistant (MDR) bacteria, *Aust J Mycol*, 26 (2017) 27–42.
- [10] Kilavuz E., Turac E., Ilk S., Sahmetlioglu, E. Electropolymerizations of two novel EDOT-BODIPY zinc oxide nanocomposites and evaluation of their in vitro antibacterial activities, *Polym. Adv. Technol.*, 32(3) (2021) 1086-1100.
- [11] Shukla V., Joshi G. P., Rawat M. S. M., Lichens as a potential natural source of bioactive compounds: a review, *Phytochem Rev.*, 9(2) (2010) 303–314.
- [12] Perry N. B., Benn M. H., Brennan N. J., Burgess E. J., Ellis G., Galloway D. J., Tangney R. S., Antimicrobial, antiviral and cytotoxic activity of New Zealand lichens, *The Lichenologist*, 31(6) (1999) 627–636.
- [13] Mitrović T., Stamenković S., Cvetković V., Tošić S., Stanković M., Radojević I., Marković S. Antioxidant, antimicrobial and antiproliferative activities of five lichen species. *Int. J. Mol. Sci.*, 12(8) (2011) 5428–5448.
- [14] Manojlović N., Ranković B., Kosanić M., Vasiljević P., Stanojković T., Chemical composition of three *Parmelia* lichens and antioxidant, antimicrobial and cytotoxic activities of some their major metabolites, *Phytomedicine*, 19(13) (2012) 1166–1172.
- [15] Lumbsch H. T., Huhndorf S. M., Part One. Outline of Ascomycota-2009. Part Two. Notes on Ascomycete Systematics, *Fieldiana: life and earth sciences 1* (2010) 4751–5113.
- [16] Miadlikowska J., Kauff F., Hofstetter V., Fraker E., Grube M., Hafellner J., Lutzoni F., New insights into classification and evolution of the Lecanoromycetes (Pezizomycotina, Ascomycota) from phylogenetic analyses of three ribosomal RNA-and two protein-coding genes, *Mycologia*, 98(6) (2006) 1088-1103.
- [17] Huovinen K., Ahti T., Biosequential patterns for the formation of depsides, depsidones and dibenzofurans in the genus *Cladonia* (lichen-forming ascomycetes), *In Annales Botanici Fennici* (1982) 225–234.
- [18] Kosanić M., Ranković B., Stanojković T., Rančić A., Manojlović N., *Cladonia* lichens and their major metabolites as possible natural antioxidant, antimicrobial and anticancer agents. *LWT - Food Sci. Technol.*, 59(1) (2014) 518–525.
- [19] Kosanić M., Ristić S., Stanojković T., Manojlović N., Ranković B., Extracts of five *Cladonia* lichens as sources of biologically active compounds, *Farmacia*, 66 (2018) 644–651.
- [20] Mitrovic T. L., Stamenkovic S. M., Cvetkovic V. J., Radulovic N. S., Mladenovic M. Z., Stankovic M. S., Markovic S. D., Contribution to the knowledge of the chemical composition and biological activity of the lichens *Cladonia foliacea* hud s.(wild.) and *Hypogymnia physodes* (L.), *Oxid. Commun.*, 38(4A) (2015) 2016–2032.
- [21] Yano Melo A. M., Vicente C., Xavier Filho L., Allelopathic effect of the *Cladonia verticillaris* lichen extracts and fumarprotocetraric acid on the early growth of germinated seedlings in *Allium cepa* L. *Trop Bryol*, 17 (1999) 133–139.
- [22] Yılmaz M., Türk A. Ö., Tay T., Kivanç M., The antimicrobial activity of extracts of the lichen *Cladonia foliacea* and its (–)-usnic acid, atranorin, and fumarprotocetraric acid constituents, *Z. Naturforsch., C*, 59(3-4) (2004) 249-254.
- [23] Ranković B., Mišić M., The antimicrobial activity of the lichen substances of the lichens *Cladonia furcata*, *Ochrolechia androgyna*, *Parmelia caperata* and *Parmelia conspessa*, *Biotechnol. Biotechnol. Equip.*, 22(4) (2008) 1013–1016.
- [24] Alves de Barros G. M., de Sousa Maia M. B., de Souza Franco E., Galvão A. M., da Silva T. G., Gomes R. M., da Silva N. H., Expectorant and antioxidant activities of purified fumarprotocetraric acid from *Cladonia verticillaris* lichen in mice, *Pulm Pharmacol Ther*, 27(2) (2013) 139–143.
- [25] Sinha S., Biswas D., Mukherjee A., Antigenotoxic and antioxidant activities of palmarosa and citronella essential oils, *J Ethnopharmacol*, 137(3) (2011) 1521–1527.
- [26] Ahti T., Stenroos S., Moberg R., Nordic lichen flora, (Vol 5, Cladoniaceae). Museum of Evolution, Uppsala University, Uppsala, (2013)
- [27] Ahti T., Hammer S., *Cladonia*. In: Nash III T.H., Ryan B.D., Gries C., Bungartz F (ed, Lichen flora of the greater sonoran desert region, Arizona State University, Tempe, (2002).
- [28] Ranković B. R., Kosanić M. M., Stanojković T. P., Antioxidant, antimicrobial and anticancer activity of the lichens *Cladonia furcata*, *Lecanora atra* and *Lecanora muralis*, *BMC Complement Altern. Med.*, 11(1) (2011) 1–8.
- [29] Kocakaya Z., Kocakaya M., Şeker Karatoprak G., Comparative analyses of antioxidant, cytotoxic, and anti-inflammatory activities of different *Cladonia* species and determination of fumarprotocetraric acid amounts. *KSÜ Tarım ve Doğa Dergisi Tarım*, 24(6) (2021) 1196–1207.
- [30] Brakni R., Ali Ahmed M., Burger P., Schwing A., Michel G., Pomares C., Michel T., UHPLC-HRMS/MS Based Profiling of Algerian Lichens and Their Antimicrobial Activities. *Chem Biodivers.*, 15(4) (2018) 1-17.
- [31] Plaza C. M., de Salazar C. P., Vizcaya M., Rodríguez-Castillo C. G., Ramírez G. E. M., Plaza R. E., Potential antifungal activity of *Cladonia* aff. *rappii* A. Evans. *J. Pharm. Pharmacogn. Res.* 5(5) (2017) 301–309.
- [32] Studzińska-Sroka E., Tomczak H., Malińska N., Wrońska M., Kleszcz R., Galanty A., Paluszczak J., *Cladonia uncialis* as a valuable raw material of biosynthetic compounds against clinical strains of bacteria and fungi. *Acta Biochim. Pol.*, 66(4) (2019) 597–603.
- [33] Açıkgoz B., Karaltı İ., Ersöz M., Coşkun Z. M., Çobanoğlu G., Sesal C., Screening of antimicrobial activity and cytotoxic effects of two *Cladonia* species. *Z Naturforsch C*, 68(5–6) (2013) 191–197.
- [34] Russo A., Piovano M., Lombardo L., Garbarino J., Cardile V. Lichen metabolites prevent UV light and nitric oxide-mediated plasmid DNA damage and induce apoptosis in human melanoma cells. *Life Sci.*, 83(13–14) (2008) 468–474.
- [35] Abbas M., Ali A., Arshad M., Atta A., Mehmood Z., Tahir I. M., Iqbal M., Mutagenicity, cytotoxic and antioxidant activities of *Ricinus communis* different parts, *Chem. Cent. J.* 12(3) (2018) 1–9.
- [36] Korkmaz A. I., Akgul H., Sevindik M., Selamoglu Z., Study on determination of bioactive potentials of certain lichens, *Acta Aliment*, 47(1) (2018) 80–87.
- [37] Pillai T. G., Salvi V. P., Maurya D. K., Nair C. K. K., Janardhanan K. K., Prevention of radiation-induced damages by aqueous extract of *Ganoderma lucidum* occurring in southern parts of India, *Curr. Sci.*, (2006) 341–344.

The Effects of Lapatinib and Trastuzumab in a Rat Model of Endometriosis

Çağlar Yıldız ^{1,a,*}, Asker Zeki Özsoy ^{1,b}, Turgut Kacan ^{3,c}, Hatice Ozer ^{4,d}

¹Department of Obstetrics and Gynecology, Cumhuriyet University School of Medicine, 58140, Sivas, Türkiye

²Departments of Obstetrics and Gynecology, Gaziosmanpaşa University School of Medicine, 60010, Tokat, Türkiye

³Department of Medical Oncology, Cumhuriyet University School of Medicine, 58140, Sivas, Türkiye

⁴Department of Pathology, Cumhuriyet University School of Medicine, 58140, Sivas, Türkiye

*Corresponding author

Research Article

History

Received: 30/08/2022

Accepted: 24/11/2022

Copyright



©2022 Faculty of Science,
Sivas Cumhuriyet University

ABSTRACT

Trastuzumab and lapatinib are drugs belonging to tyrosine kinase inhibitors family that are used in cancer treatment to prevent cell proliferation. Trastuzumab is an inhibitor of human epidermal growth factor receptor-2 (HER2) tyrosine kinase, and lapatinib is an inhibitor of epidermal growth factor receptor (EGFR). Tyrosine kinase inhibitors have also been investigated for treatment of endometriosis. In the present study, we aimed to investigate the effects of lapatinib and trastuzumab on rat endometriosis model. Endometriosis was surgically induced by the autologous transplantation of endometrial tissue and formation of endometriosis was confirmed via secondary laparotomy in 32 rats. Initially, 4 mg/kg dose of trastuzumab was applied intraperitoneally, and two additional doses of 2 mg/kg were applied 7 days and 14 days after the initial dose. Lapatinib was administered as 100 mg/kg daily doses for 14 days. Rats were randomly divided into four groups and were subjected to lapatinib, trastuzumab, anastrozole (0.004 mg/day, p.o.) and normal saline (0.1 ml, i.p.) treatments for 14 days. Then, endometriosis foci were excised, and endometriosis scores were calculated in a semi-quantitative manner. Immunohistochemical (IHC) examinations were also performed using VEGF, CD117 and Bax antibodies. Both anastrozole and tyrosine kinase inhibitors lowered endometriosis scores. Significant decreases in ovarian follicle numbers were observed in lapatinib and anastrozole groups but not trastuzumab group. Lapatinib and trastuzumab decreased endometriotic foci through suppressing cell proliferation and promoting programmed cell death.

Keywords: Endometriosis, Lapatinib, Trastuzumab, Anastrozole, Tyrosine kinase inhibitors.

^a dr_caglyildiz@yahoo.com
^c kacanturgut@gmail.com

^b <https://orcid.org/0000-0003-3150-3340>
^d <https://orcid.org/0000-0002-2067-1560>

^b drzekiozsoy@hotmail.com
^d haticeozer@gmail.com

^b <https://orcid.org/0000-0003-0749-4157>
^d <https://orcid.org/0000-0001-6479-3626>

Introduction

Endometriosis is a progressive, chronic disease characterized by the growth of endometrial tissues out of the endometrial cavity, especially on ovarian visceral and pelvic peritoneal surface [1]. It is a common disease with an estimated prevalence of 6-10% of reproductive-aged women, and patients with endometriosis may have chronic pelvic pain and impaired fecundity [2]. Endometriosis poses a significant and costly public health problem because of the expense of medical care including the need for surgical procedure and recurrence after surgical treatment [3].

Although multiple theories exist to explain the pathophysiology of endometriosis, Sampson's retrograde menstruation/transplantation theory suggesting the attachment and adhesion of endometrial fragments in peritoneal surfaces is the most widely accepted one [4]. According to Sampson's theory, for endometrial tissues implantation in peritoneal and subperitoneal surfaces, neoangiogenesis, blood supply and endometrial cell proliferation are absolute necessities [5].

Angiogenesis plays a key role in the formation of endometriosis. [6]. Vascular endothelial growth factor (VEGF) and its receptor VEGFR-1, and epidermal growth factor (EGF) and its receptor EGFR are involved in the

process of neovascularization in endometrial tissue formation [6]. EGF and EGFR have roles in cell proliferation in ectopic endometriotic foci and it has been reported that gene expressions of EGF and EGFR are different from those in eutopic endometrium tissues and they are associated with the severity of the disease [7].

Although endometriosis is a benign, sex hormone-dependent gynecological disease, its pathogenesis is similar to that of malignant tumoural tissues. Therefore the efficacy of multi-targeted tyrosine kinase inhibitors that may inhibit angiogenesis and cell proliferation and commonly studied in current cancer trials, for the treatment of endometriosis have been investigated [8].

Unlike trastuzumab (Herceptin®), a humanized monoclonal antibody that targets the tyrosine kinase receptor, human EGFR-2 (HER2), lapatinib is an oral dual tyrosine kinase inhibitor of both EGFR and HER2 [9]. Lapatinib reversibly binds to intracellular domains of tyrosine kinase domains EGFR and HER2 causing phosphorylation of tyrosine kinases and drives cells to apoptosis and prevents cell proliferation through inhibition of activation of mitogen-activated protein kinase (MAPK) and phosphoinositide 3-kinases (PI3Ks) [10]. The aim of this study was to investigate the role of

anastrozole, a drug used as standard hormonal treatment of endometriosis and tyrosine kinase inhibitors lapatinib and trastuzumab on angiogenesis, apoptosis and endometrial cell proliferation in an experimentally established rat endometriosis model.

Materials and methods

Wistar-Albino adult female rats weighing 220-240 g were obtained from Laboratory Animal Centre of Cumhuriyet University (Sivas, Turkey). Rats were kept in a light-and temperature-controlled (22°C) room with diurnal lighting without limitation for food and water. There was no difference in the weights of the rats before and after the study. Procedures were performed according to the scientific guidelines for Institutional Care and Use of Laboratory Animals. The study was approved by AnimalResearch Ethics Committee of the Cumhuriyet University (Approval No: 394). Minimal numbers of animals were used in the experiments and every efforts were made to minimize their suffering.

Induction of Endometriosis

To induce endometriosis, uterine tissue was autotransplanted into anterior abdominal wall using the technic suggested by Vernon and Wilson [11]. Ketamine and xylazine were administered intraperitoneally for anesthesia (60 mg/kg and 7 mg/kg, Ketalar 1; Eczacıbaşı Warner-Lambert, Istanbul, Turkey and Rompun 1, Bayer, Istanbul, Turkey, respectively). The left uterine horns of the rats were ligated and excised via laparotomy, placed in normal saline, then opened longitudinally and dissected into 5 mm squares. The endometrial tissue containing the myometrium was sutured into the peritoneal cavity. The study groups were allowed to recover for 3 weeks, without any medications.

Evaluation of Endometriosis

Twenty-one days after the day endometriosis was induced, a second exploratory laparotomy was performed to observe the growth of endometriosis. Thirty-two rats having confirmed endometriosis were randomly divided into four groups of eight rats each to receive lapatinib (100 mg/kg/day, p.o.), trastuzumab (after the initial 4mg/kg dose of trastuzumab applied intraperitoneally, two additional doses of 2 mg/kg were applied 7 days and 14 days after the initial dose), anastrozole (0.004 mg/d, p.o.) or normal saline (0.1 ml, intraperitoneally). The treatments were applied for fourteen days.

Collection of Tissue Samples

Twenty-one days after the day the development of endometriosis was confirmed, endometriotic and ovarian tissue samples were excised via a third laparotomy. All the rats were euthanized using pentobarbital sodium after completion of the procedures. One of the authors (C.Y.) performed all of the surgical procedures.

Histopathology

Formalin 10% was used for fixation the ovaries and the ectopic endometriotic tissues, and then histopathological and immunohistochemical examination (IHC) has done. One of the authors (H.O) who is blinded for the groups made all evaluations.

Histopathology of Endometriotic Implants

Endometriosis scoring was performed according to the description of Keenan et al. [12] The epithelial lining of the endometrial implants were classified using the following scale: No epithelium, Score 0; Poorly preserved epithelium (occasional epithelial cells only), Score 1; Moderately preserved epithelium with leukocyte infiltrate, Score 2; Well preserved epithelial lining, Score 3 [12].

Immunohistochemistry of Endometriotic Foci

Immunohistochemical staining was performed on the BenchMark XT system (Ventana Medical Systems, Roche) with antibodies against VEGF (Ab-4, Clone BFD31, Lab Vision, USA), CD117 (K69, Lab Vision, USA), and Bax (Ab-2, Clone 5B7, LabVision, USA).

For VEGF immunohistochemical staining, a semi-quantitative method suggested by Donnez et al. [13] was used. VEGF histologic scores (H) were calculated according to the following formula: $H = \Sigma P_i$, i (intensity) varied between 0 (negative cells) and 3 (intensely stained cells), P (percentage of stained cells) for each given i, and P values of staining of <15% of the cells as 1, staining of 15-50% of the cells as 2, staining of 50-85% of the cells as 3, staining of >85% of the cells as 4 and staining of 100% of the cells as 5. For Bax and CD117 immunohistochemical staining, an immunoreactivity score (IRS) obtained by multiplication of the the P (0-4) and i (0-3) was used [14]. The IRSs were as follows: 0, no staining; 1-4, weak staining; 6, 8, 9 or 12, strong staining.

Histopathology of Ovaries

Formalin 10% solution was used for fixation of the rat ovaries. For dehydration and clearing, ethanol and xylene were used. Sections of 6 mm thickness were taken from the tissues for H&E staining. The follicles were classified according to stage into primordial, primary, secondary, and antral and the numbers of each follicles were counted in five sections for each ovary, with a distance of 120 µm between them in order to ensure counting one follicle once.

Statistical Analysis

SPSS version 20.0 for Windows (SPSS, Chicago, IL, USA) was used for statistical analysis. Post Hoc test in ANOVA was used for analyzing the treatment groups. Tukey's Post Hoc test was used to compare the treatment groups for endometriosis scores, ovarian follicle numbers and VEGF, Bax and CD117 immunostaining scores. The scores are

shown as mean ± standard error of the mean and a p-value less than 0.05 (≤ 0.05) was considered as significant.

Results

The experimental procedures were completed without any apparent side effects. The average weights of the rats before the study entry did not change significantly after the procedures. Evaluation during the second exploratory laparotomy showed that vascularization and cystic appearance of the endometriotic implants were sufficient. Also, the histological examinations confirmed the development of ectopic endometriotic tissue. The histopathological images showing the effect of normal saline, anastrozole, lapatinib and trastuzumab on endometriotic tissues are shown in Figure 1.

The average endometriosis scores, ovarian follicle numbers, and immunostaining scores of VEGF, CD117 and Bax of the normal saline, anastrozole, lapatinib and the trastuzumab groups are shown in Table 1.

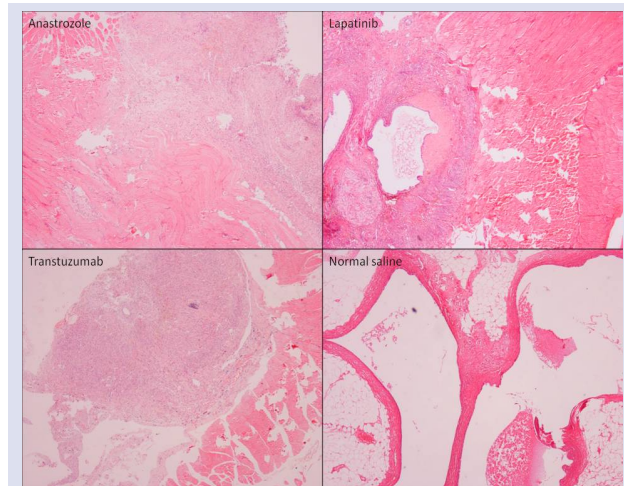


Figure 1. Representative histopathological images (hematoxylin and eosin, 40) of endometriotic tissues obtained from rats administered Anastrozole, Lapatinib, Trastuzumab, and normal saline. Endometriotic tissue shows poorly preserved epithelium in Anastrozole group but moderately preserved epithelium in Lapatinib and Trastuzumab groups, compared to normal saline group.

Table 1. Comparison of histopathologic and immunohistochemical levels of the endometriotic implants

	SF Mean±SEM	Anastrozole Mean±SEM	Lapatinib Mean±SEM	trastuzumab Mean±SEM	ANOVA	Comparison group	Post hoc p
Endometriosis score	2.750±0.13	0.500±0.189	1.625±0.33	1.250±0.366	0.0001	1 vs. 2	0.0001
						1 vs. 3	0.008
						1 vs. 4	0.003
						2 vs. 3	0.005
						2 vs. 4	0.009
						3 vs. 4	0.770
Ovarian follicle number	7.375±0.55	4.000±1.210	4.000±0.77	7.000±0.906	0.012	1 vs. 2	0.005
						1 vs. 3	0.005
						1 vs. 4	0.993
						2 vs. 3	0.991
						2 vs. 4	0.099
						3 vs. 4	0.009
Apoptosis (Bax)	3.500±2.00	4.000±0.755	4.500±1.72	4.125±2.295	0.000	1 vs. 2	0.003
						1 vs. 3	0.001
						1 vs. 4	0.002
						2 vs. 3	0.596
						2 vs. 4	0.114
						3 vs. 4	0.976
Endometriotic proliferation (CD117)	7.250±1.51	6.750±1.752	3.925±1.92	4.325±2.031	0.005	1 vs. 2	0.119
						1 vs. 3	0.0001
						1 vs. 4	0.005
						2 vs. 3	0.006
						2 vs. 4	0.014
						3 vs. 4	0.374
VEGF	6.375±1.86	1.750±0.462	6.000±1.51	5.250±2.439	0.0001	1 vs. 2	0.000
						1 vs. 3	0.972
						1 vs. 4	0.566
						2 vs. 3	0.001
						2 vs. 4	0.002
						3 vs. 4	0.819

Data are expressed as means ± standard error of the mean.

ANOVA: analysis of variance; SEM: standard error of the mean VEGF: vascular endothelial growth factor; NS: normal saline

The average endometriosis scores in the anastrozole, lapatinib and the trastuzumab groups were significantly lower than those in the normal saline group (P=0.000). The endometriosis score of the anastrozole group was significantly lower compared to those of the lapatinib and the trastuzumab groups (p=0.003 and p=0.008, respectively). The endometriosis score did not significantly differ between the the lapatinib and the trastuzumab groups (P=0.770, Figure 2.).

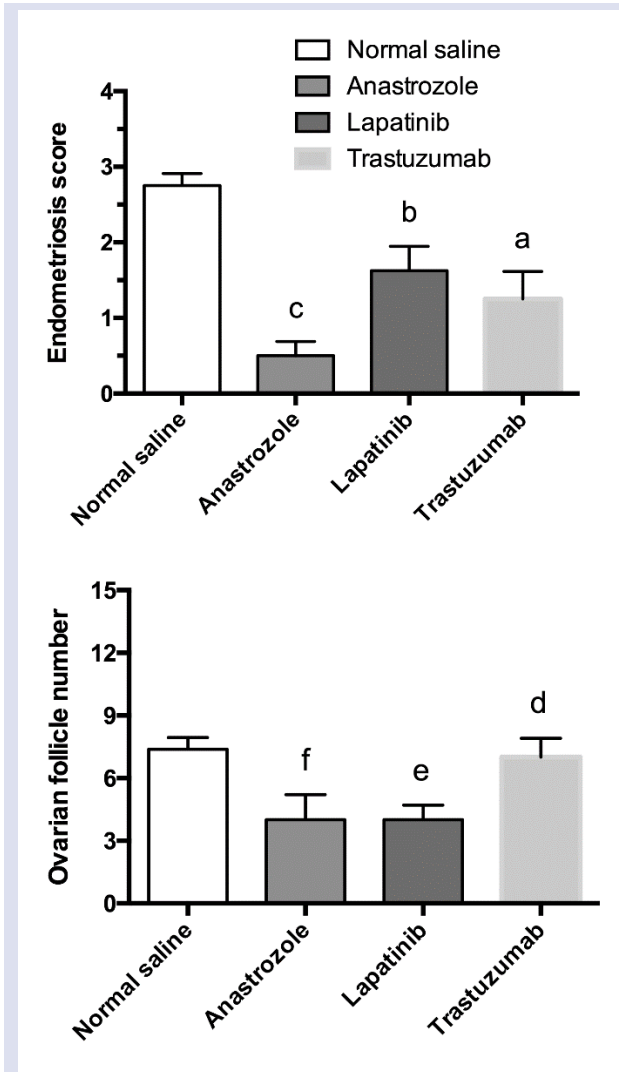


Figure 2. Endometriosis score and ovarian follicle number of normal saline, anastrozole, lapatinib, and trastuzumab groups (n = 8). Data were expressed as mean+SEM(standard error of the mean).aP< 0.05; trastuzumab vs. anastrozole and normal saline. bP< 0.05; lapatinib vs. anastrozole and normal saline. c,fP< 0.05; anastrozole vs. normal saline.dP< 0.05; trastuzumab vs. lapatinib. eP< 0.05; lapatinib vs. normal saline.

Both the anastrozole and the lapatinib groups had significantly lower ovarian follicle numbers than the normal saline group (P=0.005 for both), the trastuzumab group did not differ from the normal saline group regarding the ovarian follicle number (P=0.991, Figure 2).

The anastrozole group had significantly lower VEGF staging scores than the normal saline group (P=0.000), there were no significant differences for VEGF staging

scores between the saline group and the trastuzumab or the lapatinib groups (p=0.972 and p=0.566, respectively, Figure 3.).

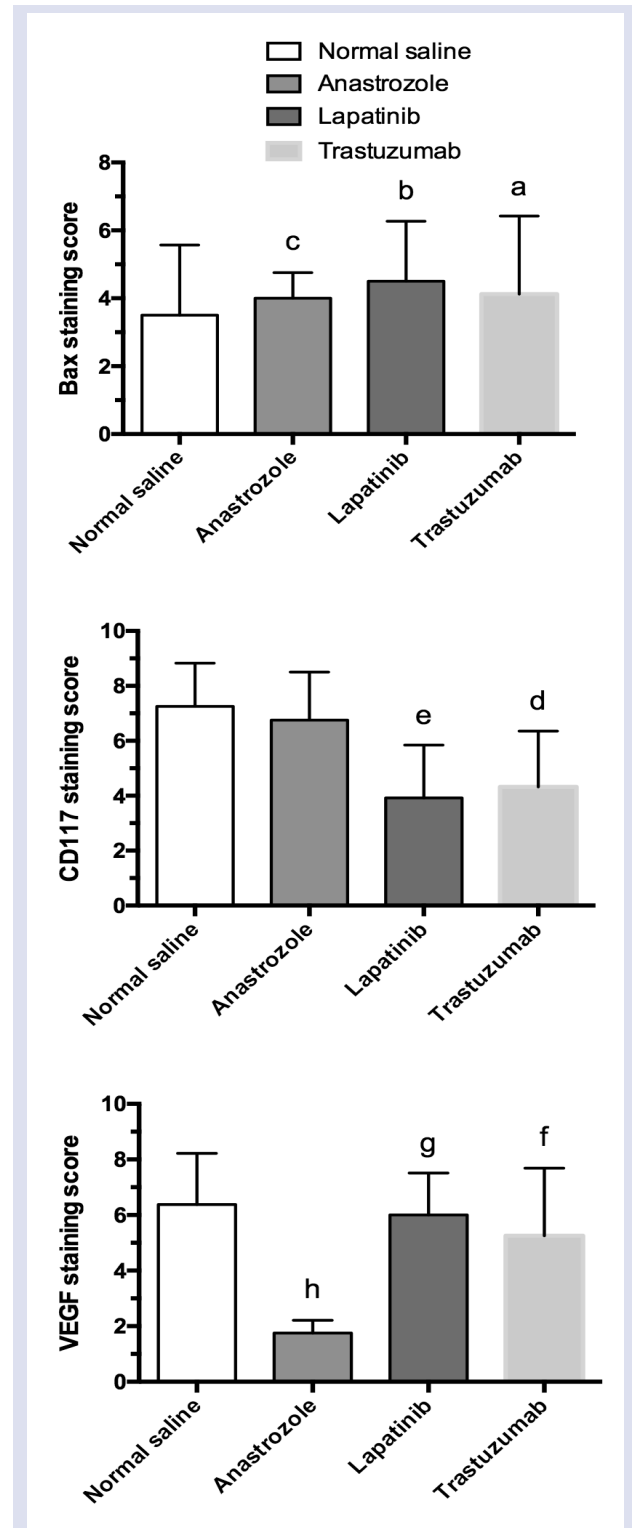


Figure 3. VEGF, CD117, and Bax staining scores of rats administered normal saline, anastrozole, lapatinib, and trastuzumab (n = 8 for each drug). Data were expressed as mean + SEM. a,b,cP< 0.05; trastuzumab, lapatinib, and anastrozole vs. normal saline. dP< 0.05; trastuzumab vs. normal saline. eP< 0.05; lapatinib vs. anastrozole and normal saline. fP< 0.05; trastuzumab vs. anastrozole. gP< 0.05; lapatinib vs. anastrozole.hP< 0.05; anastrozole vs. normal saline.

CD117 staging scores of the anastrozole and the normal saline groups were similar ($p=0.119$), but the lapatinib and the trastuzumab groups had lower CD117 scores than the normal saline group ($p=0.000$ and $p=0.005$, respectively). The difference between the lapatinib and the trastuzumab groups was not significant ($P=0.374$, Figure 3).

Bax staging scores showed that apoptosis significantly increased in all drug groups compared to the normal saline group ($P=0.000$), but the differences among the drug groups were not significant (Figure 3.).

Discussion

Although it may show the characteristics of cancer cells such as spreading to distant organs and surrounding organs, endometriosis is actually considered a benign disease. It can cause chronic pelvic pain, dyspareunia, dysmenorrhea and sometimes infertility. However, it can also cause comorbidities such as adenomyosis, urinary system diseases, gastrointestinal system fasts. For these reasons, it is a disease that both complicates and restricts women's lives and imposes a serious financial burden on the health system. [15]. Despite all these known effects and numerous studies, there are still many question marks about its etiology and treatment options are limited. In the treatment of women with endometriosis, hormonal therapy and surgical treatment or combinations of these are performed. Especially the side effects of long-term hormonal treatment on patients and the inability to always achieve sufficient success in surgical treatment bring along recurrences [16]. Because of these question marks in diagnosis and treatment, endometriosis is still an important disease on which many studies should be done.

With the important developments in molecular biology, targeted therapies have entered clinical use and are increasingly used in treatments. In these new generation therapies, unlike the classical cancer treatment, the targeted therapeutic agents used are directed to the tumor cells, killing the cancer cell while ensuring that the normal cells are not affected [17]. In this process, monoclonal antibodies specific to the epidermal growth factor receptor (EGFR) and tyrosine kinase inhibitors have begun to be used in clinical practice. Blocking the ligand binding to EGFR, blocking the receptor with monoclonal antibodies or inhibiting it with tyrosine kinase activation constitutes an important treatment approach. Trastuzumab is the first targeted drug used in human epidermal growth factor receptor 2 (HER2) positive breast cancer. Lapatinib, on the other hand, is a tyrosine kinase inhibitor that effectively inhibits signaling pathways in cancer cells [18]. Since monoclonal antibodies cannot pass through the cell membrane, they can only act through molecules that are expressed or secreted on the cell surface. Tyrosine kinase inhibitors such as lapatinib interact with the cytoplasmic parts of cell receptors and intracellular signaling molecules. Epidermal growth factor (EGF) initiates a series of intracellular events by binding to specific receptors on cell membranes, and EGFR activation

stimulates tumor growth and progression, increases proliferation, and inhibits angiogenesis, invasion, metastasis, and apoptosis [19]. Especially angiogenesis and cell proliferation play an important role in the development of endometriosis. EGFR is found in the corpus luteum as well as granulosa and theca cells in the follicle in the ovaries [20]. It has been reported that EGFR and HER2 are expressed in the endometrial tissue in the menstrual cycle of humans. It has also been suggested that HER2 (c-erbB2 or neu) is expressed in primordial germ cells, granulosa cells, luteal cells, and oocyte in the ovary and plays a role in primordial follicle growth, regulation of granulosa cell function, and oocyte maturation [21].

In our study, histological observations of endometriotic implants in experimentally established rat endometriosis model showed that lapatinib, trastuzumab and anastrozole decreased the development of endometriosis and suppressed the foci. Anastrozole was the drug that most effectively suppressed endometriosis, whereas the efficacy of lapatinib and trastuzumab was similar. Anastrozole and lapatinib administration decreased ovarian follicle number but such an effect was not observed with trastuzumab. Effects of anastrozole, lapatinib and trastuzumab on angiogenesis were evaluated through VEGF immunostaining and it was shown that anastrozole administration significantly lowered VEGF staining. Although lapatinib and trastuzumab administration seemed to lower VEGF scores, the effects were not statistically significant compared to normal saline administration. Cell proliferation, evaluated by CD117 immunostaining, was significantly decreased by lapatinib and trastuzumab administration. On the other hand, anastrozole did not have an effect on cell proliferation. In terms of efficacy on apoptosis evaluated by Bax immunostaining, all drugs were found to increase apoptosis compared to normal saline. In summary, anastrozole lowered endometriosis scores and ovarian follicle number through promoting apoptosis and suppressing angiogenesis, lapatinib and trastuzumab also lowered endometriosis scores, led to a decrease in cell proliferation and an increase in programmed cell death. Lapatinib lowered ovarian follicle number, whereas trastuzumab did not have such an effect.

Anastrozole is widely used in current endometriosis treatment [22]. The drug inhibits the formation of estrogen from androgens in peripheral tissue and decreases cell proliferation [23]. In line with our findings, anastrozole has an apoptosis-enhancing effect on endometrial implants. [24].

Both benign and malignant endometrial diseases are associated with angiogenesis [25]. Angiogenesis process can be defined as formation of new blood veins ensuring blood supply in which VEGF is the key mediator [26]. Patients with endometriosis have higher VEGF levels in both eutopic and the ectopic endometrium tissues than those in healthy women [27].

Anastrozole has been shown to inhibit the development of new vessels in endometriotic tissue via

decreasing VEGF release [28]. Our findings also showed that anastrozole significantly decreased VEGF release in endometriotic foci. On the other hand, trastuzumab, a HER2 tyrosine kinases inhibitor, and lapatinib, an inhibitor of both EGFR and HER2 tyrosine kinases did not have an effect on VEGF staining in our study. These drugs have been shown to suppress angiogenesis in malignant cells and that this effect was principally due to their suppression of HER2 over-expression [29]. The lack of HER2 over-expression in endometriotic tissue may be the reason why lapatinib and trastuzumab did not suppress angiogenesis in endometriosis.

The presence of abnormal cell proliferation has been shown in endometriosis [30]. C-kit receptor CD117, a trans-membrane protein, is a tyrosine kinase growth factor receptor, playing role in cell proliferation and growth. C-kit expression has been shown to increase in endometriotic foci compared to eutopic endometrium tissue [31]. Yildiz et al. [32] reported that tyrosine kinase inhibitors pazopanib and sunitinib decreased CD117 level and a restoration of endometriosis score was observed due to the decrease in cell proliferation. In the present study, the effect of tyrosine kinase inhibitors lapatinib and trastuzumab on cell proliferation was evaluated by CD117 immunostaining and it was observed that they decreased cell proliferation in endometriotic foci. Anastrozole, on the other hand, did not have an effect on cell proliferation.

Endometriotic tissue differs from healthy endometrium tissue regarding apoptosis mechanisms, including abnormal expressions of major signal proteins associated with apoptosis such as Fas, Fas ligand, BCL2 and BAX, and decreased programmed cell deaths of endometrial cells [33]. Programmed cell death as a result elevated Bax expression in endometriotic foci is one of the action mechanisms of treatments for endometriosis [34, 35]. Tyrosine kinase inhibitors such as lapatinib and trastuzumab have been shown to increase apoptosis in malignant cells along with the inhibition of HER2 in endometrium, breast and stomach cancers [36, 37]. In our study, lapatinib and trastuzumab promoted apoptosis in endometriotic foci.

The mechanisms of action of current medical treatments with endometriosis include the suppression of ovarian hormones and decreasing the secretion and efficiency of peripheral estrogen [38]. This anti-estrogenic activity causes a decline in ovarian follicle numbers [39]. In accordance with the literature, we observed a significant decrease of follicle number in anastrozole treatment group. We also showed that lapatinib decreased ovarian follicle number in rats, but trastuzumab did not.

As far as we know, the present study is the first study using dual tyrosine kinase inhibitor lapatinib in endometriosis model. There are several limitations of the study that should be noted. We did not evaluate the impact of lapatinib on the eutopic endometrium. In addition, we did not evaluate the effect of lapatinib on ovarian functioning through the regular estrous cycle and/or estrogen levels. Finally, we used only a single

standard lapatinib dose and did not evaluate varying doses of the drug on endometriosis regression.

Our study showed that lapatinib and trastuzumab treatments suppress cell proliferation, promote apoptosis process and suppress endometriosis development without a significant effect on angiogenesis. Suppression of endometriotic foci by trastuzumab without any decrease of ovarian follicle number should be further investigated.

Acknowledgement

A.Z.O., C.Y., and T.K. designed the research study. C.Y. and T.K. performed the research. H.O. performed the histopathological examination. A.Z.O, C.Y. and H.O. analyzed the data. A.Z.O. and C.Y. wrote the manuscript. All authors contributed to editorial changes in the manuscript. All authors read and approved the final manuscript.

Conflict of interest

The authors declare no competing interests.

References

- [1] Giudice L.C., Endometriosis, Clinical practice, *N. Engl. J. Med.*, 362 (25) (2010) 2389-98.
- [2] Harel Z., Dysmenorrhea in adolescents and young adults: an update on pharmacological treatments and management strategies, *Expert Opin Pharmacother.*, 13 (15) (2012) 2157-70.
- [3] Simoens S., Dunselman G., Dirksen C., Hummelshoj L., Bokor A., Brandes I, et al., The burden of endometriosis: costs and quality of life of women with endometriosis and treated in referral centres, *Hum. Reprod.*, 27 (5) (2012) 1292-9.
- [4] Jiang Q.Y., Wu R.J., Growth mechanisms of endometriotic cells in implanted places: a review, *Gynecol Endocrinol.*, 28 (7) (2012) 562-7.
- [5] Nisolle M., Donnez J., Peritoneal endometriosis, ovarian endometriosis, and adenomyotic nodules of the rectovaginal septum are three different entities, *Fertil Steril.*, 68 (4) (1997) 585-96.
- [6] Möller B., Rasmussen C., Lindblom B., Olovsson M., Expression of the angiogenic growth factors VEGF, FGF-2, EGF and their receptors in normal human endometrium during the menstrual cycle, *Mol Hum Reprod.*, 7 (1) (2001) 65-72.
- [7] Huang J.C., Papasakelariou C., Dawood M.Y., Epidermal growth factor and basic fibroblast growth factor in peritoneal fluid of women with endometriosis, *Fertil Steril.*, 65 (5) (1996) 931-4.
- [8] Abe W., Nasu K., Tsuno A., Kawano Y., Narahara H., Phosphatidylinositol-3 kinase-Akt-mammalian target of rapamycin signaling pathway mediates contractility of human endometriotic stromal cells: A promising new target for the treatment of endometriosis-associated fibrosis, *Gynecol Minim Invasive Ther.*, 3 (4) (2014) 115-8.

- [9] Melcher C.A., Janni J.W., Schneeweiss A., Fasching PA., Hagenbeck CD., Aktas B., et al. Abstract OT1-1-10: DETECT III - A multicenter, randomized, phase III study to compare standard therapy alone versus standard therapy plus lapatinib in patients with initially HER2-negative metastatic breast cancer but with HER2-positive circulating tumor cells, *Cancer Res.*, 72 (2012) 1-10.
- [10] Blackwell K.L., Burstein HJ., Storniolo A.M., Rugo H., Sledge G., Koehler M., et al. Randomized study of Lapatinib alone or in combination with trastuzumab in women with ErbB2-positive, trastuzumab-refractory metastatic breast cancer, *J Clin Oncol.*, 28 (7) (2010) 1124-30.
- [11] Vernon M.W., Wilson E.A., Studies on the surgical induction of endometriosis in the rat, *Fertil Steril.*, 44 (5) (1985) 684-94.
- [12] Keenan J.A., Williams-Boyce P.K., Massey P.J., Chen T.T., Caudle M.R., Bukovsky A., Regression of endometrial explants in a rat model of endometriosis treated with the immune modulators loxoribine and levamisole, *Fertil Steril.*, 72 (1) (1999) 135-41.
- [13] Donnez J., Smoes P., Gillerot S., Casanas-Roux F., Nisolle M., Vascular endothelial growth factor (VEGF) in endometriosis, *Hum Reprod.*, 13 (6) (1998) 1686-90.
- [14] Remmele W., Stegner H.E., Vorschlag zur einheitlichen Definition eines Immunreaktiven Score (IRS) für den immunhistochemischen Östrogenrezeptor-Nachweis (ER-ICA) im Mammakarzinomgewebe [Recommendation for uniform definition of an immunoreactive score (IRS) for immunohistochemical estrogen receptor detection (ER-ICA) in breast cancer tissue], *Pathologe.*, 8 (3) (1987) 138-40.
- [15] Struble J., Reid S., Bedaiwy M.A. Adenomyosis: A clinical review of a challenging gynecologic condition. *J. Minim. Invasive Gynecol.* 23 (2) (2016) 164–185.
- [16] Bruner-Tran K.L., Mokshagundam S., Herington J.L., Ding T., Osteen K.G., Rodent Models of Experimental Endometriosis: Identifying Mechanisms of Disease and Therapeutic Targets, *Curr Womens Health Rev.*, 14 (2) (2018) 173-188.
- [17] Kansu E., Hedeflenmiş tedavilerde "hedef" moleküller, *ANKEM Derg.*, 19 (2005) 112-6.
- [18] Tokgönül H., Kuyucu Y., Mete U., Lapatinib'in sıçan over ve uterus dokuları üzerine olan etkilerinin ışık ve elektron mikroskopik düzeyde araştırılması, *Cukurova Medical Journal*, 45 (2020) 921-932.
- [19] Chen H.X., Cleck J.N., Coelho R., Dancey J.E., Epidermal growth factor receptor inhibitors: current status and future directions, *Curr Probl Cancer.*, 33 (4) (2009) 245-94.
- [20] Li-Ping Z., Da-Lei Z., Jian H., Liang-Quan X., Ai-Xia X., Xiao-Yu D. et al., Proto-oncogene c-erbB2 initiates rat primordial follicle growth via PKC and MAPK pathways, *Reprod. Biol. Endocrinol.*, 8 (66) (2010) 1-9.
- [21] Sağsöz H., Ketani M.A., Saruhan B.G., Expression of the erbB/HER receptor family in the bovine uterus during the sexual cycle and the relation of this family to serum sex steroids, *Biotech Histochem.*, 87 (2) (2012) 105-16.
- [22] Imai A., Takagi A., Tamaya T., Gonadotropin-releasing hormone analog repairs reduced endometrial cell apoptosis in endometriosis in vitro, *Am. J. Obstet. Gynecol.*, 182 (5) (2000) 1142-6.
- [23] Meresman G.F., Augé L., Barañao R.I., Lombardi E., Tesone M., Sueldo C., Oral contraceptives suppress cell proliferation and enhance apoptosis of eutopic endometrial tissue from patients with endometriosis, *Fertil Steril.*, 77 (6) (2002) 1141-7.
- [24] Meresman G.F., Bilotas M., Abello V., Buquet R., Tesone M., Sueldo C., Effects of aromatase inhibitors on proliferation and apoptosis in eutopic endometrial cell cultures from patients with endometriosis, *Fertil Steril.*, 84 (2) (2005) 459-63.
- [25] Carmeliet P., Jain R.K., Angiogenesis in cancer and other diseases, *Nature.*, 407 (6801) (2000) 249-57.
- [26] Risau W., Mechanisms of angiogenesis, *Nature.*, 386 (6626) (1997) 671-4.
- [27] Xu H., Zhang T., Man G.C., May K.E., Becker C.M., Davis T.N., et. al., Vascular endothelial growth factor C is increased in endometrium and promotes endothelial functions, vascular permeability and angiogenesis and growth of endometriosis, *Angiogenesis.*, 16 (3) (2013) 541-51.
- [28] Bilotas M., Meresman G., Stella I., Sueldo C., Barañao R.I., Effect of aromatase inhibitors on ectopic endometrial growth and peritoneal environment in a mouse model of endometriosis, *Fertil Steril.*, 93 (8) (2010) 2513-8.
- [29] Spector N.L., Blackwell K.L., Understanding the mechanisms behind trastuzumab therapy for human epidermal growth factor receptor 2-positive breast cancer, *J Clin Oncol.*, 27 (34) (2009) 5838-47.
- [30] Wingfield M., Macpherson A., Healy D.L., Rogers P.A., Cell proliferation is increased in the endometrium of women with endometriosis, *Fertil Steril.*, 64 (2) (1995) 340-6.
- [31] Pacchiarotti A., Caserta D., Sbracia M., Moscarini M., Expression of oct-4 and c-kit antigens in endometriosis, *Fertil Steril.*, 95 (3) (2011) 1171-3.
- [32] Yıldız C., Kacan T., Akkar O.B., Karakus S., Kacan S.B., Ozer H., et al. Effects of Pazopanib, Sunitinib, and Sorafenib, Anti-VEGF Agents, on the Growth of Experimental Endometriosis in Rats, *Reprod Sci.*, 22 (11) (2015) 1445-51.
- [33] Harada T., Kaponis A., Iwabe T., Taniguchi F., Makrydimas G., Sofikitis N., et al. Apoptosis in human endometrium and endometriosis, *Hum Reprod Update.*, 10 (1) (2004) 29-38.
- [34] Dmowski W.P., Ding J., Shen J., Rana N., Fernandez B.B., Braun D.P., Apoptosis in endometrial glandular and stromal cells in women with and without endometriosis, *Hum Reprod.*, 16 (9) (2001) 1802-8.
- [35] Konecny G.E., Venkatesan N., Yang G., Dering J., Ginther C., Finn R., et al. Activity of lapatinib a novel HER2 and EGFR dual kinase inhibitor in human endometrial cancer cells, *Br J Cancer.*, 98 (6) (2008) 1076-84.
- [36] Wainberg Z.A., Anghel A., Desai A.J., Ayala R., Luo T., Safran B., et al., Lapatinib, a dual EGFR and HER2 kinase inhibitor, selectively inhibits HER2-amplified human gastric cancer cells and is synergistic with trastuzumab in vitro and in vivo, *Clin Cancer Res.*, 16 (5) (2010) 1509-19.

- [37] Geyer C.E., Forster J., Lindquist D., Chan S., Romieu C.G., Pienkowski T., et al. Lapatinib plus capecitabine for HER2-positive advanced breast cancer, *N Engl J Med.*, 355 (26) (2006) 2733-43.
- [38] Barbieri R.L., Hormone treatment of endometriosis: the estrogen threshold hypothesis, *Am J Obstet Gynecol.*, 166 (2) (1992) 740-5.
- [39] Oral E., Demir B., Inceboz U., Endometriosis and ovarian reserve, *Womens Health.*, 11 (5) (2015) 671-5.

The Effect of Low Molecular Weight Heparins on Placentation: A Rat Model Study

Gülizar Özer ^{1,a,*}, Çağlar Yıldız ^{1,b}, Hatice Özer ^{2,c}, Ali Çetin ^{1,d}¹ Department of Obstetrics and Gynecology, Faculty of Medicine, Sivas Cumhuriyet University, Sivas, Türkiye² Department of Pathology, Faculty of Medicine, Sivas Cumhuriyet University, Sivas, Türkiye

*Corresponding author

Research Article

History

Received: 31/08/2022

Accepted: 27/11/2022

Copyright

©2022 Faculty of Science,
Sivas Cumhuriyet University^a gulizaresikozar@gmail.com
^c haticozar@gmail.com^b <https://orcid.org/0000-0002-3107-2475>
^d <https://orcid.org/0000-0001-6479-3626>^b dr_caglaryildiz@yahoo.com
^d dralicetin@yahoo.com^b <https://orcid.org/0000-0003-3150-3340>
^d <https://orcid.org/0000-0002-5767-7894>

ABSTRACT

Low molecular weight heparins (LMWHs) have been used for the treatment for recurrent pregnancy loss (RPL) for a long time. We aimed to investigate the efficacy of the LMWHs on angiogenesis and apoptosis during placentation. A total of twenty-four rats were randomly divided into three groups each containing 8 rats: normal saline; enoxaparine sodium 0.4 ml, and enoxaparine sodium 0.8 ml were given to the Group 1, 2 and 3, respectively. Normal saline and enoxaparine sodium 0.4 ml or 0.8 ml were given to the rats beginning on the day the pregnancy was detected and continued until the 15th day of the pregnancy. The tissues containing placental decidual zone were immunostained for vascular endothelial growth factor A (VEGF-A) and caspase 7. The decidual and placental VEGF-A and the decidual caspase 7 immunostaining scores of all of the groups were high, however, there were no statistically significant differences among the groups ($p > 0.05$). On the other hand, the placental caspase 7 immunostaining scores of the normal saline group were significantly lower than those of the enoxaparine sodium 0.4 and the enoxaparine sodium 0.8 groups ($p < 0.05$). LMWHs seem to have effects on placental angiogenesis and apoptosis.

Keywords: Low molecular weight heparin, Placenta, Angiogenesis, Apoptosis.

Introduction

Recurrent pregnancy loss (RPL) is an important obstetric health issue. Although there are several etiological factors for RPL, no identifiable underlying cause could be found in approximately half of the couples [1]. Certain hereditary thrombophilias, which are responsible for half of the thromboembolic conditions occurred during pregnancy, thought to be the cause in the idiopathic RPL cases [2, 3]. In these cases, thrombogenic predisposition during pregnancy further contributes to hypercoagulability and may cause uteroplacental blood flow decline, placental thrombosis and pregnancy loss, because placental perfusion should be sufficient for a healthy pregnancy [4, 5].

The appropriate formation and maturation of vascular bed is of paramount importance for healthy placental development [6]. Two basic mechanisms responsible for the development of placental vascular bed are vasculogenesis and angiogenesis [7]. Also, apoptosis and cell proliferation should be appropriately balanced for placentation and remodelling during pregnancy [8]. Therefore, apoptosis related changes in the embryonic and the extra-embryonic tissues may cause congenital structural abnormalities and pregnancy loss [9]. It has been recently shown that trophoblast invasion abnormalities occurred during early pregnancy may cause pregnancy loss [10]. The management of thrombophilic asymptomatic pregnant women is controversial and empiric. Antithrombotic treatment before conception and/or during early pregnancy is usually recommended [11]. The most widely used antithrombotics during

pregnancy are the unfractionated heparin (UFH) and the low molecular weight heparins (LMWHs) [12]. LMWHs have replaced UFH and have been widely used for years because of their ease of use and safety profile [13]. Enoxaparine sodium is one of the most preferred LMWHs because of its safety profile, tolerability and availability [14].

In this study, we aimed to investigate the effect of LMWHs on angiogenesis and apoptosis during placentation to clarify the mechanisms of the efficacy of the LMWHs on live birth rates in RPL cases.

Materials and Methods

Materials

The rats used in the experiments were obtained from Cumhuriyet University Experimental Animal Unit. Four months-old, 200-220 gram weighted Wistar albino female rats were used in the experiments. Clexane sterile solution (Aventis Pharma, İstanbul, Türkiye) containing 100 mg enoxaparine sodium, equivalent to 10,000 anti-Xa IU was given to the rats in either 0.4 ml or 0.8 ml doses. Immunostaining was performed by using Ventana Benchmark XT automated slide-staining system (BenchMark XT Staining Module, Ventana Medical Systems) for VEGF-A antibodies (Rabbit Polyclonal Antibody Thermo Scientific, US) and caspase 7 antibodies (Rabbit Polyclonal Antibody Thermo Scientific, US).

Methods

This study was approved by Cumhuriyet University Faculty of Medicine, Animal Trials Ethics Committee (01.15.2015, approval number: 6). For conception, adult male rats were placed into the cages during 05:00 pm and 09:00 am for five consecutive days (throughout a menstrual cycle). Every next day, vaginal examination with a pediatric otoscope (HEINE mini 2000, Heine Optotechnik, Herrsching, Germany) was performed to detect copulatory plug, which is an indicator of mating. The day copulatory plug detected was considered as the first day of the pregnancy. Twenty-four rats were randomly divided into the three groups each containing 8 rats: normal saline, enoxaparine sodium 0.4 ml, and enoxaparine sodium 0.8 ml were given to the Group 1, 2 and 3, respectively. 1 mg (0.01 ml) enoxaparine sodium is equivalent to 100 anti-Xa IU. Human equivalent doses were given to the rats. The rats were given 1 mg/kg body weight enoxaparine sodium subcutaneously.

The groups were treated as follows:

1. Normal saline group: 0.1 ml/day saline, subcutaneously
2. Enoxaparin sodium 0.4 group: 0.1 ml/day enoxaparine sodium (Clexane, Aventis Pharma, İstanbul, Türkiye), subcutaneously
3. Enoxaparin sodium 0.8 group: 0.1 ml/day enoxaparine sodium (Clexane, Aventis Pharma, İstanbul, Türkiye), subcutaneously

On the 15th day of the pregnancy, the rats were anesthetized with intramuscular ketamine 90 mg/kg body weight and Xylazine 3 mg/kg body weight. After cervical dislocation, rats underwent a laparotomy and their uteri containing pregnancy material were removed.

Histopathology

Placental tissues were carefully separated from embryos and cuts containing placenta-decidual zone were obtained. The tissues were then stained with haematoxylin and eosin and examined with light microscopy by a pathologist (H. Ö.) blinded for the groups.

Immunohistochemistry

For immunohistochemistry analyses, tissue sections at 3 µm thickness were obtained from paraffin-embedded blocks containing placental-decidual zone and transferred onto positively charged surface. Renal tissue for VEGF-A and duodenal tissue for caspase 7 were used as positive controls. Cytoplasmic staining pattern was considered positive for VEGF-A and caspase 7. Immunostaining was scored with regard to quantity and intensity of positively stained cells as follows: for intensity of staining: negative (no staining), 1+ (weak staining), 2+ (moderate staining), 3+ (strong staining); for quantity of staining: the percentage of stained areas: <10%, 1; 10-50%, 2; 51-80%, 3; and >80%, 4. The final immunostaining score was obtained by multiplying the quantity score and the

intensity score. Scores 0-1 was considered as negative or low; 2-6 as moderate; and 8-12 as high expression. Statistical analyses were performed for each antibody used.

Statistical Analysis

A statistical software package program (SPSS, ver. 14.0) was used for statistical analyses. Kruskal Wallis test, Mann Whitney U test and Chi-Square test were used as appropriate. A p value of <0.05 was considered statistically significant.

Results

The mean (±SD) decidual VEGF-A staining scores were 8.75 ± 2.12, 9.62 ± 1.99 and 10.62 ± 1.92 in the normal saline, enoxaparine sodium 0.4 and the enoxaparine sodium 0.8 groups, respectively. The mean (±SD) placental VEGF-A staining scores were 10.75 ± 2.37, 11.50 ± 1.41 and 12.00 ± 0.00 in the normal saline, enoxaparine sodium 0.4 and the enoxaparine sodium 0.8 groups, respectively. There were no statistically significant differences among the groups regarding the decidual and the placental VEGF-A staining scores (p>0.05, Table 1).

Table 1: Decidual and Placental VEGF-A Staining Scores

	Normal saline (n=8)	Enoxaparine sodium 0.4 (n=8)	Enoxaparine sodium 0.8 (n=8)	Results
VEGF-A Decidua				
Mean ± SD	8.75 ± 2.12	9.62 ± 1.99	10.62 ± 1.92	KW=3.75
Median	8.00	8.50	12.00	P=0.153
VEGF-A Placenta				
Mean ± SD	10.75± 2.37	11.50± 1.41	12.00 ± 0.00	KW=2.27
Median	12.00	12.00	12.00	P=0.320

SD=standard deviation

The mean (±SD) decidual caspase 7 staining scores were 11.00 ± 1.85, 11.12 ± 1.64 and 11.25 ± 1.38 in the normal saline, enoxaparine sodium 0.4 and the enoxaparine sodium 0.8 groups, respectively. There were no statistically significant differences among the groups regarding the decidual caspase 7 staining scores (p>0.05, Table 2)

Table 2: Decidual and Placental Caspase 7 Staining Scores

	Normal saline (n=8)	Enoxaparine sodium 0.4 (n=8)	Enoxaparine sodium 0.8 (n=8)	Result
Caspase 7 Decidua				
Mean ± SD	11.00 ± 1.85	11.12 ± 1.64	11.25 ± 1.38	KW=0.07
Median	12.00	12.00	12.00	P=0.096
Caspase 7 Placenta				
Mean ± SD	8.50 ± 0.53	9.37 ± 1.06	9.37 ± 1.06	KW=8.46
Median	8.50	9.00	9.00	P=0.0014*

SD=standard deviation, *p<0,05 statistically significant

The mean (±SD) placental caspase 7 staining scores were 8.50 ± 0.53, 9.37 ± 1.06 and 9.37 ± 1.06 in the normal

saline, enoxaparine sodium 0.4 and the enoxaparine sodium 0.8 groups, respectively. The difference among the groups was found statistically significant, the normal saline group had lower placental caspase 7 staining scores than those of the enoxaparine sodium groups, whereas the enoxaparine sodium 0.4 and the enoxaparine sodium 0.8 groups did not differ from each other ($p < 0.05$ for normal saline vs. enoxaparine sodium 0.4 and normal saline vs. enoxaparine sodium 0.8; $p > 0.05$ for enoxaparine sodium 0.4 and enoxaparine sodium 0.8) (Table 2).

Light microscopy examination of H-E stained tissues revealed that chorioamnionitis were present in the enoxaparine sodium groups and widespread perivillous fibrine deposition was present in the normal saline group.

Discussion

In this study, we aimed to investigate the effect of LMWHs on angiogenesis and apoptosis during placentation and thus understand their reported efficacy of increasing live birth rates in patients with RPL, an obstetric condition with controversial issues regarding its etiology and management. We preferred to use enoxaparine sodium in our experiment because of its safety, tolerability and availability [14]. The reason we used rats in our experiment is that human and rat placenta have many structural and developmental similarities such as hemochorial placentation and rat placenta model is widely used in placental developmental studies [15].

It is known that disorders and deficiencies in placental development cause pregnancy complications [16]. For ethical reasons, it is not possible to carry out studies on the human placenta to understand the potential underlying mechanisms. For this reason, although there are limitations, placenta studies are carried out on animal models. Correct placental development is essential for embryonal and fetal development. The placenta is composed of trophoblast and endothelial cells, and it is a structure where complex molecular interactions of maternal and fetal factors occur. It also provides nutrient and gas exchange between mother and baby, helps the adaptation of the mother's body to pregnancy and acts as a protective barrier for the fetus [17]. The outer layer of the placenta consists of two parts, the inner layer called cytotrophoblast and the outer layer called syncytiotrophoblast. In a normal placental development, cytotrophoblasts settle in the uterus and invade the spiral arteries from the uterine wall. Spiral arteries lose their musculoelastic layer as a result of invasion of cytotrophoblasts, and peripheral resistance and blood pressure decrease in spiral arteries, resulting in the physiological properties required for adequate perfusion of the placenta [18, 19].

Angiogenesis is a vital process in placental development and therefore in embryonal and fetal life. A balance of pro- and anti-angiogenic factors is essential for successful placentation. VEGF has a critical role in the maintenance of blood vessel endothelium and structure as well as in angiogenesis [20].

Pregnancy related thrombogenic changes contribute to underlying hypercoagulopathy in patients with RPL and cause uteroplacental blood flow decline, placental thrombosis and pregnancy loss [4]. Sufficient placental perfusion is fundamental for a healthy pregnancy [5]. Multiple factors controlling vasculogenesis, angiogenesis and trophoblast functions play role in the process of placentation [21].

Antithrombotic treatment before conception or early pregnancy is recommended in women with thrombophilia [11]. The antithrombotic medications of choice during pregnancy are UFH and LMWHs. Currently, LMWHs are the antithrombotic medications most widely used [12]. It has been suggested that LMWHs also have effects on placental function and invasion in addition to their anticoagulant and antiinflammatory properties [22-24]. Thrombosis and infarctions causing placental insufficiency have been reported in patients with thrombophilia and unfavorable obstetric history [25]. Sarto et al. [26] have reported that LMWHs increased live birth rates from 15% to 85% in patients with hereditary thrombophilia and RPL.

UFH and LMWHs have been reported to promote angiogenesis in in vitro healthy first and second trimester placental material [27]. In our study we found that the decidual and the placental VEGF-A scores of the enoxaparine sodium groups were higher than those of the saline group and these scores of the enoxaparine sodium 0.8 group were also higher than those of the enoxaparine sodium 0.4 group, however, these differences did not reach statistical significance. These findings may be due to small sample size in our study. Further studies are warranted.

The presence of apoptotic cells in placental tissue is controversial. Apoptotic cells have been reported in the rat endometrial stromal cells at the fifth day of the pregnancy [28]. On the other hand, Perez et al. [29] have reported the absence of apoptotic cells in the normal placental tissue at the 14th day of the pregnancy. We have found increased apoptosis in the placental tissue at the 15th day of the pregnancy in all of the experimental groups including the normal saline group. However, placental caspase 7 immunostaining scores were higher in enoxaparine groups than those of the normal saline group. Our findings indicate that apoptosis is present in rat placental tissue at the 15th day of the pregnancy and enoxaparine sodium may increase the apoptotic activity. LMWHs have been reported to decrease apoptosis via Bcl-2 activation and Bax suppression in rat placenta [30]. These findings are contradictory to ours. More information is needed to clarify the effect of LMWHs on apoptosis in placental tissue. LMWHs may act differently in pathological conditions such as RPL.

Fibrine accumulation surrounding villi is a frequent finding, it can be seen in one fourth of uncomplicated term pregnancies. However, true massive perivillous fibrine accumulation involving 80-90% of the villous parenchyma can cause fetal death [31]. Diffuse perivillous and intervillous fibrine accumulation possibly caused by perfusion problems in the terminal villi, have been

reported in preeclampsia patients [32, 33]. In our study, only normal saline group had diffuse perivillous fibrine accumulation. This findings indicate that LMWHs can have beneficial effects on placental perfusion.

In conclusion, LMWHs seem to have effects on placental angiogenesis and apoptosis. The small sample size of our study may preclude to detect statistically significance. Further studies with larger sample sizes and molecular analyses are warranted.

Acknowledgments

The work was supported by grants from Cumhuriyet University Scientific Research Projects Coordination Unit (CUBAP, T-648).

Conflicts of Interest

The authors declare that they have no conflict of interest.

References

- [1] Bick R.L., Recurrent miscarriage syndrome due to blood coagulation protein/platelet defects: prevalence, treatment and outcome results. DRW Metroplex Recurrent Miscarriage Syndrome Cooperative Group, *Clin. Appl. Thromb. Hemost.*, 6 (3) (2000) 115-125.
- [2] Ford H. B., Schust D. J., Recurrent pregnancy loss: etiology, diagnosis, and therapy, *Rev. Obstet. Gynecol.*, 2 (2) (2009) 76-83.
- [3] Greer I.A., Inherited thrombophilia and venous thromboembolism. *Best Pract. Res. Clin. Obstet. Gynaecol.*, 17 (3) (2003) 413-425.
- [4] Robertson L., Wu O., Langhorne P., Twaddle S., Clark P., Lowe G.D.O., Walker I.D., Greaves M., Brenkel I., Regan L., Greer I. A., for TheThrombosis: Risk and Economic Assessment of Thrombophilia Screening (TREATS) Study, Thrombophilia in pregnancy: a systematic review, *Br. J. Haematol.*, 132 (2) (2006) 171-196.
- [5] Blumenfeld Z., Brenner B., Thrombophilia-associated pregnancy wastage, *Fertil. Steril.*, 72 (5) (1999) 765-774.
- [6] Ingman K., Cookson V.J.K.W., Jones C.J.P., Aplin J.D., Characterisation of Hofbauer cells in first and second trimester placenta: incidence, phenotype, survival in vitro and motility, *Placenta*, 31 (6) (2010) 535-544.
- [7] Poole, T.J., Coffin, J. D., Vasculogenesis and angiogenesis: two distinct morphogenetic mechanisms establish embryonic vascular pattern, *J. Exp. Zool.*, 251 (2) (1989) 224-231.
- [8] Speroff L., Fritz M.A., In: Taylor, H.S. (Ed). *Klinik Jinekolojik Endokrinoloji ve İnfertilite*. 7th ed. İstanbul: Güneş Kitabevi (2007).
- [9] Toder V., Carp H., Fein A. Torchinsky A., The role of pro- and antiapoptotic molecular interactions in embryonic maldevelopment, *Am J Reprod Immunol.*, 48 (4) (2002) 235-244.
- [10] Pierangeli S.S., Pojen P.C., Raschi E., Scurati S., Grossi C., Borghi M.O., Palomo I., Harris E.N., Meroni P.L., Antiphospholipid antibodies and the antiphospholipid syndrome: pathogenic mechanisms, *Semin. Thromb. Hemost.*, 34 (3) (2008) 236-250.
- [11] Berker B., Cengiz L., Gestasyonel Trombofil, *Maternal Fetal Tıp & Perinatoloji*, (13) (2001) 725-729.
- [12] Brenner B., Hoffman R., Blumenfeld Z., Weiner Z., Younis J.S., Gestational outcome in thrombophilic women with recurrent pregnancy loss treated by enoxaparin, *Thromb. Haemost.*, 83 (05) (2000) 693-697.
- [13] Price G.C., Thompson S.A., Kam P.C.A., Tissue factor and tissue factor pathway inhibitor, *Anaesthesia*, 59 (5) (2004) 483-492.
- [14] Mätzsch T., Bergqvist D., Hedne U., Ostergaard P., Effects of an enzymatically depolymerized heparin as compared with conventional heparin in healthy volunteers, *Thromb. Haemost.*, 57 (01) (1987) 97-101.
- [15] Watson E.D., Cross J.C., Development of structures and transport functions in the mouse placenta, *Physiology*, 20 (3) (2005) 180-193.
- [16] Brosens I., Pijnenborg, R., Vercruyse L., Romero R., The "Great Obstetrical Syndromes" are associated with disorders of deep placentation, *Am. J. Obstet. Gynecol.*, 204 (2011) 193-201.
- [17] Creeth H.D.J., John R.M., The placental programming hypothesis: placental endocrine insufficiency and the co-occurrence of low birth weight and maternal mood disorders, *Placenta*, 98 (2020) 52-59.
- [18] Davies J.E., Pollheimer J., Yong H.E.J., et al., Epithelial-mesenchymal transition during extravillous trophoblast differentiation, *Cell Adh. Migr.*, 10 (3) (2016) 310-321.
- [19] İrtegün S., Ağaçayak E., Devci E., Preeklampsik ve normotansif plasentalarda VEGF ve Vimentin ekspresyon düzeylerinin immunohistokimya ve Western Blot yöntemleri ile incelenmesi, *Dicle Tıp Derg.*, 43 (3) (2016) 400-405.
- [20] Flint E.J., Cerdeira A.S., Redman C.W., Vatish M., The role of angiogenic factors in the management of preeclampsia, *Acta Obstet Gynecol Scand*, 98 (6) (2019) 700-707.
- [21] Lunghi L., Ferretti M. E., Medici S., Biondi C., Vesce F., Control of human trophoblast function, *Reprod. Biol. Endocrinol.*, 5 (6) (2007) 1-14.
- [22] Deruelle P., Coulon C., The use of low molecular weight heparins in pregnancy, how safe are they? *Curr. Opin. Obstet. Gynecol.*, 19 (6) (2007) 573-577.
- [23] De Carolis S., Ferrazzani S., De Stefano V., Garofalo S., Fatigante G., Rossi E., Leone G., Caruso A., Inherited thrombophilia: treatment during pregnancy, *Fetal. Diagn. Ther.*, (21) (2006) 281-286.
- [24] Di Simone N., Di Nicuolo F., Sanguinetti M., Ferrazzani S., D'Alessio M. C., Castellani R., Bompiani A., Caruso A., Low-molecular weight heparin induces in vitro trophoblast invasiveness: role of matrix metalloproteinases and tissue inhibitors, *Placenta*, 28 (4) (2007) 298-304.
- [25] Monien S., Kadecki O., Baumgarten S., Salama A., Dörner T., Kiesewetter H., Use of heparin in women with early and late miscarriages with and without thrombophilia, *Clin. Appl. Thromb. Hemost.*, 15 (6) (2009) 636-644.
- [26] Sarto A., Rocha M., Geller M., Capmany C., Martinez M., Quintans C., Donaldson M., Pasqualini R. S., Treatment with enoxaparin adapted to the fertility programs in women with recurrent abortion and thrombophilia, *Medicina*, 61 (4) (2001) 406-412.
- [27] Sobel M.L., Kingdom J., Drewlo S., Angiogenic response of placental villi to heparin, *Obstet. Gynecol.*, 117 (6) (2011) 1375-1383.
- [28] Xia H.F., Sun J., Sun Q. H., Yang Y., Peng J.P., Implantation-associated gene-1 (Iag-1): a novel gene involved in the

- early process of embryonic implantation in rat, *Hum. Reprod.*, 23 (7) (2008) 1581-1593.
- [29] Perez M.J., Macias R.I.R., Marin J.J.G., Maternal cholestasis induces placental oxidative stress and apoptosis. Protective effect of ursodeoxycholic acid, *Placenta*, 27 (1) (2006) 34-41.
- [30] Yuan Z., Mei Z., Fengyan Liu., Low molecular weight heparin inhibits cell apoptosis in the placenta of rats with preeclampsia-like symptoms. *Nan Fang Yi Ke Da Xue Xue Bao*, 32 (6) (2012) 862-6.
- [31] Fox H., Wells M., Haines and Taylor, *Obstetrical and Gynaecological Pathology*. 4 th ed. Churchill Livingstone; (1995).
- [32] Battistelli M., Burattini S., Pomini F., Scavo M., Caruso A., Falcieri E., Ultrastructural study on human placenta from intrauterin growth retardation cases, *Micros. Res. Tech.*, 65 (2004) 150-158.
- [33] Altshuler G., A conceptual approach to placental pathology and pregnancy outcome, *Semin. Diagn. Pathol.*, 10 (3) (1993) 204-221.

Evaluation of Thalamus Volumes in Patients with Diabetic Polyneuropathy Using Magnetic Resonance Imaging Method

Aysegul Ozturk^{1,a,*}, Vedat Sabanciogullari^{2,b}, Yasar Tastemur^{2,c}, Ibrahim Oztoprak^{3,d}

¹Departments of Medical Services and Techniques, Sivas Cumhuriyet University, Vocational School of Health Services, Sivas, Türkiye

²Departments of Anatomy, Sivas Cumhuriyet University, School of Medicine, Sivas, Türkiye

³Departments of Radiology, Canakkale On Sekiz Mart University, School of Medicine, Canakkale, Türkiye

*Corresponding author

Research Article

History

Received: 15/07/2022

Accepted: 09/12/2022

Copyright



©2022 Faculty of Science,
Sivas Cumhuriyet University

ABSTRACT

The neurological process in diabetes is not limited to peripheral nerves but also affects the central nervous system (CNS). In addition, magnetic resonance images (MRI) showing that this condition can occur early in the neuropathic process are also available. This study was conducted to investigate whether peripheral sensory nerve dysfunction causes changes in thalamus volume in patients with diabetic polyneuropathy (DPNP) who experience sensory loss. Our study is a retrospective study consisting of diabetes mellitus (DM), DPNP and a healthy control group, where brain MRI of 204 individuals aged between 20-90 with no neurological disorder that might affect thalamus. Morphometric measurements for thalamus and cerebrum volumetry were performed in conventional MRI. In order to measure the microstructural changes of thalamus, the apparent diffusion coefficient (ADC) was calculated by the diffusion-weighted imaging method. In conclusion of our measurements, it was found that individuals with DM and DPNP had a decrease in volume of both thalami ($p < 0.05$) and cerebrum ($p < 0.05$). However, no significant difference was found in ADC values ($p > 0.05$). According to the results of research, DM and DPNP affect not only the peripheral nervous system but also the CNS. This effect caused atrophy of thalamus and cerebrum in patients of all age groups.

Keywords: Diabetes mellitus, Diabetic polyneuropathy, Thalamus, Magnetic resonance imaging.

^a fztaysegul@yahoo.com

^c dryasar58@hotmail.com

^b <https://orcid.org/0000-0001-8130-7968>

^d <https://orcid.org/0000-0002-2016-0592>

^b vsabanci@yahoo.com.tr

^d ibrahimoztoprak@comu.edu.tr

^b <https://orcid.org/0000-0001-9059-6554>

^d <https://orcid.org/0000-0002-4334-0350>

Introduction

Diabetes Mellitus (DM) is a very common disease in the world and it is estimated that 629 million people will be affected by this disease by 2045 [1]. DM prevalence is constantly increasing with factors such as a rapidly rising population, aging, urbanization, increasing obesity, and sedentary life. One of the most important complications in patients with diabetes is diabetic neuropathy. 50% of patients with diabetic neuropathy have diabetic polyneuropathy [2-4].

Diabetic polyneuropathy is caused by an imbalance between destruction and repair of nerve fibers. Damage to the nerves affects autonomic and distal sensory fibers more. After the disease affects the nerve endings, symptoms first begin in the distal of the lower extremities, and then progress to the proximal. After exceeding knee level, it first affects the distal of the upper extremities, then the proximal and the distal sensory nerve fibers of the intercostal nerves. In rare cases, with the influence of the trigeminal nerve, there are complaints with regard to head region as well. Almost all sensory messages, such as heat and pain, are lost if the progression of the disease is not prevented [5-7].

The afferents of all these sensory messages end up in nuc. ventralis posterolateralis (VPL) core of thalamus before being transmitted to the cortex. Thalamus organizes the information to be transmitted and sends it to the relevant parts of the cortex [8].

Scientific studies in the literature on the effects of sensory nerve dysfunction on thalamus volume in adult diabetes and diabetic polyneuropathy population are quite limited. In this regard, our purpose is mainly to detect thalamus volumes belonging to diabetes, diabetic polyneuropathy and healthy adult population and to investigate whether sensory nerve dysfunction causes changes in thalamus volume, especially in patients with diabetic polyneuropathy who experience sensory loss.

Material and Method

Ethics Committee Approval

Prior to starting the study, permission was obtained from Sivas Cumhuriyet University Non-invasive Clinical Research Ethics Committee with decision No. 02/30 dated 20th February 2019.

Study Group

The patient group in the study is composed of 74 (45 females, 29 males) adult individuals with diabetes and 57 (29 females, 28 males) adult individuals with diabetic polyneuropathy, aged between 20 and 90, diagnosed with diabetes mellitus and diabetic polyneuropathy at Sivas Cumhuriyet University Faculty of Medicine between January 2013 and April 2019, who applied to Radiology Department of our hospital to have brain MRI.

The control group in the study is composed of 73 (44 females, 29 males) adult individuals aged between 20 and 90, not diagnosed with diabetes mellitus and diabetic polyneuropathy, whose MRI images are archived in the hospital and who do not have any psychological or neurological disorders.

Four hundred patient files were screened in order to form groups of the study we conducted retrospectively.

Patients with a diagnosis of infarction, lesions that occupy space in the brain, bleeding, etc. other than microinfarcts contained in MRI reports in screened files, were excluded from the study. Images of patients who did not have any pathology other than microinfarcts in MRI reports or were considered normal were included in the study. Similarly, patients with psychological disorders, neurological deficits, or neurological examination positives were not included in the study.

MRI Protocol

The same imaging protocol was applied to all individuals included in the study. Morphometric MRI analysis; Routine brain MRI analysis was performed using 20 channel coils in 1.5 Tesla MRI devices

(Magnetom Aera, Siemens, Germany). Parameters in MRI images; T1 SE axial images; Slice thickness: 5 mm, TE: 5.6, TR: 402, FOV: 220, FA: 150, Matrix: 300x512, NSA: 3 T2 SE axial images; Slice thickness: 5 mm, TE: 102, TR: 4350, FOV:220, FA: 150, Matrix: 320x1024, NSA: 2 FLAIR axial images; Slice thickness: 5 mm, TE: 92, TR: 9000, FOV: 230, FA: 150, Matrix: 320x1024, NSA: 1

DAG was performed using an echo-planar (EP) imaging sequence (TR: 5000ms; TE: 130 ms; FA: 90/180; NEX: 1; FOV: 270 x 320 mm; matrix: 128 x 128; slice thickness: 5 mm; slice spacing: 2 mm; b value: 0 and 1000 s/mm²) To measure diffusion on three axes (x, y and z), diffusion gradients were applied in three orthogonal plans.

Image Analysis

T2-weighted MRI sequences were used for morphometric measurements of thalamus. In Coronal sections, measurements were performed on T2-weighted images passing through ventriculus lateralis and tertius. The vertical length of the thalamus was measured in Coronal sections, while the transverse length was obtained from sections in the axial plane [9]. The upper limit of thalamus in the coronal section was determined as the lateral ventricle and the lower limit was determined as the substantia nigra (Figure 1) [10]. For measurements in the axial section, the largest diameter image of the cranium containing the cornu anterior and cornu posterior of the ventriculus lateralis was used. The anterior border of the thalamus in the axial section was determined as the posterior of the foramen interventricularen, the posterior border was determined as the pulvinar thalami, the medial border was determined as the 3rd ventricle, the lateral border was determined as the crus posterior of the capsula interna [11]. Thalamus volume was obtained by multiplying the anteroposterior diameter, transverse diameter, vertical

diameter of the thalamus, and the number $\pi/6$ ($T1 \times T3 \times T5 \times \pi/6$).

As for thalamus morphometry, the following measurements were made on T2-weighted axial and coronal MRI images (Figure 1).

- T1: anteroposterior length of the left thalamus
- T2: anteroposterior length of the right thalamus
- T3: transverse length of the left thalamus
- T4: transverse length of the right thalamus
- T5: vertical length of the left thalamus
- T6: vertical length of the right thalamus
- Tl: volume of the left thalamus
- Tr: volume of the right thalamus
- Tt: total volume of the thalamus

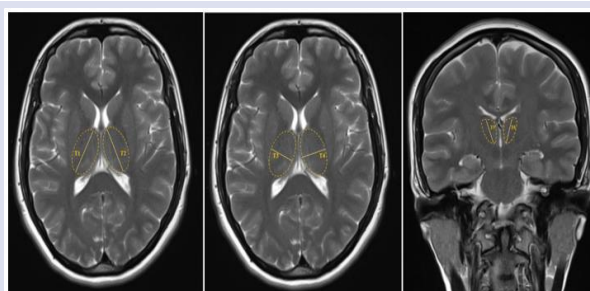


Figure 1. Measurement reference points for thalamus diameters in axial and coronal section

In T1 midsagittal sections, anteroposterior diameter of cerebrum (C1) was found by measuring the distance between polus frontalis and polus occipitalis, cerebrum height (C3) was found by measuring the distance between corpus mamillare and the peak point of cerebrum for cerebrum morphometry. In T2 axial sections, cerebrum transverse diameter (C2) was determined by measuring the distance between the two furthest points of the cerebral hemispheres [12]. Cerebrum volume was calculated by multiplying anteroposterior diameter, transverse diameter, height of cerebrum and the number $\pi/6$ ($C1 \times C2 \times C3 \times \pi/6$).

As for cerebrum morphometry, the following measurements were made on T2 axial and T1 sagittal MRI images (Figure 2).

- C1: anteroposterior diameter of cerebrum
- C2: transverse diameter of cerebrum
- C3: cerebrum height
- Ct: volume of cerebrum

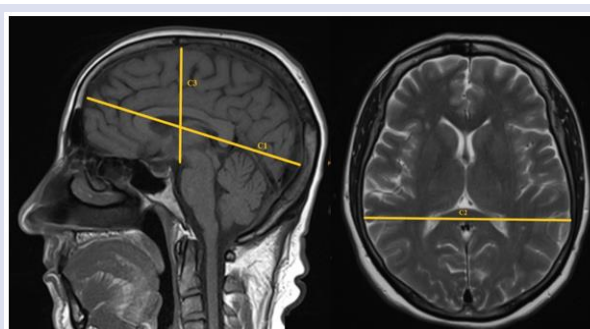


Figure 2. Measurement reference points for cerebrum in axial and coronal section

ADC maps were used to measure mean ADC value of thalamus quantitatively. In order to prevent contamination of other tissues with ADC value of thalamus, the capsula located in the lateral of both thalami were taken far enough from the interna and from the ventriculus tertius in medial, and in the central part, as wide a size as possible of the thalamus was selected. Standardized ROIs (ROI: region of interest) were placed in thalami by considering circular area of analysis 0.5 cm² in order to determine mean ADC values of thalamus (Figure 3).

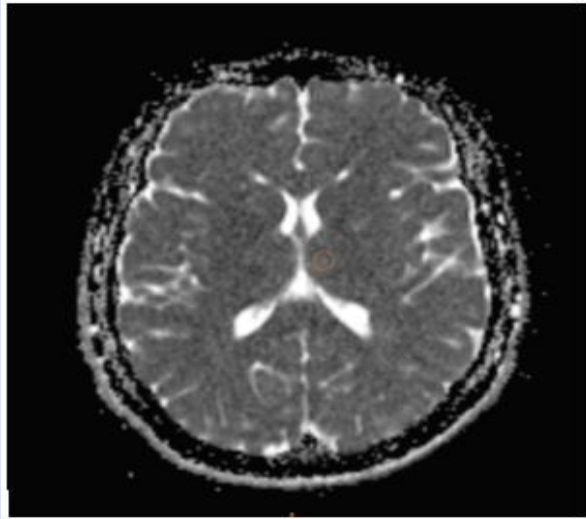


Figure 3. ADC map on thalamus in axial section

Statistical Analysis

The data obtained from our study were evaluated using SPSS 23.0 program. The normality of the data was evaluated using the Kolmogorov-Smirnov test. If the data

met parametric conditions, it was analyzed using the independent sample t test for two independent groups and the F test (ANOVA) for more than two groups. Whereas ANOVA was used for comparison of more than two groups, Tukey test was used in those providing homogeneity hypothesis, and Tamhane's T2 tests were used in those, not providing homogeneity hypothesis, to determine which group was different from the others. Mann Whitney U test was used for two independent groups and Kruskal Wallis test was used for more than two independent groups, in groups not providing parametric test hypotheses. Level of significance was considered 0.05.

Results

A total of 204 individuals between the ages of 20 and 90 were included in the study, 118 (57.3%) of whom were female and 86 (42.3%) were male. Mean age of females was found to be 58.32±15.29; mean age of males was found to be 58.63±17.01; and total mean age was found to be 58.45±16.00.

Of the individuals included in the study, 73 were in healthy control group, 74 had DM, and 57 had diabetic polyneuropathy. The mean age was 60.89 in individuals with diabetic polyneuropathy, 59.00 in individuals with DM and 55.93 in healthy controls.

In our study, the size and volume of thalamus of DPNP, DM and healthy control group were divided into age groups and compared. According to the results obtained from the study, patients with DM and DPNP in all age groups had a decrease in left, right and total thalamus volume compared to healthy individuals ($p < 0.05$) (Figure 4).

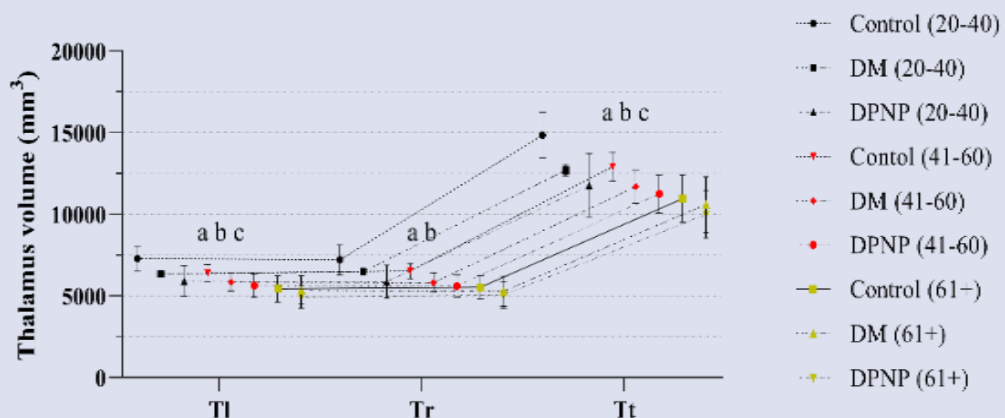


Figure 4. Thalamus volumes of all age groups in the Diabetic Polyneuropathy, Diabetes Mellitus and control; data were expressed as mean ±SD. In all groups; a comparison of thalamus volumes (mm³) in individuals age 20-40, 41-60, 61 plus. a; $p < 0.05$ 20-40 age (DPNP, DM, Control), b; $p < 0.05$ 41-60 age (DPNP, DM, Control), c; $p < 0.05$ 61 plus (DPNP, DM, Control) (Tl; volume of the left thalamus, Tr; volume of the right thalamus, Tt; total volume of the thalamus, DM; diabetes mellitus, DPNP; Diabetic polyneuropathy).

In our study, it was found that thalamus anteroposterior and transverse lengths in all age groups were smaller in individuals with DM and DPNP ($p < 0.05$) (Figure 5). The fact that diseases caused neuronal and axonal loss in thalamus resulted in atrophy in thalamus volume.

Size and volume of thalamus of DM, DPNP and healthy individuals were compared by gender. Left, right, and total thalamus volumes in males and females of all ages were

negatively affected by DPNP and DM ($p < 0.05$). DM and DPNP similarly affected both genders, causing a decrease in thalamus volume.

Morphometric measurements of thalamus of DPNP, DM and healthy individuals were compared by age groups. According to these results, the size and volume of thalamus of each patient and healthy person decreased with the effect of aging ($p < 0.05$).

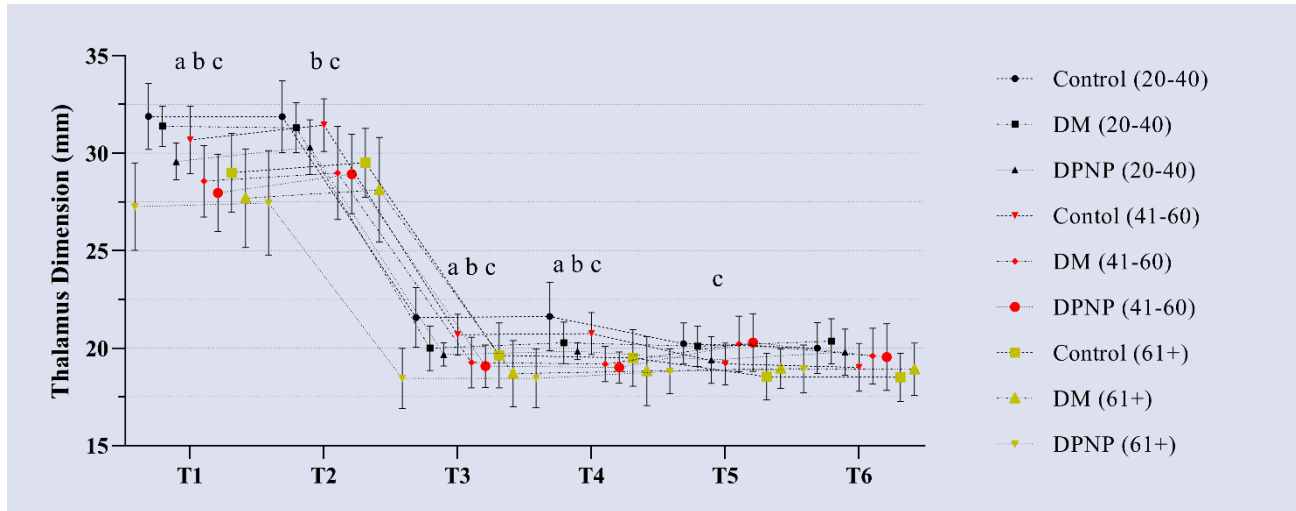


Figure 5. Thalamus dimensions of all age groups in the Diabetic Polyneuropathy, Diabetes Mellitus and control; data were expressed as mean±SD. In all groups; Comparison of thalamus dimensions (mm) in individuals age 20-40,41-60,61 plus. a; $p < 0.05$ 20-40 age (DPNP, DM, Control), b; $p < 0.05$ 41-60 age (DPNP, DM, Control), c; $p < 0.05$ 61 plus (DPNP, DM, Control)(T1; anteroposterior length of the left thalamus, T2; anteroposterior length of the right thalamus, T3; transverse length of the left thalamus, T4; transverse length of the right thalamus, T5; vertical length of the left thalamus, T6; vertical length of the right thalamus, DM; diabetes mellitus, DPNP; Diabetic polyneuropathy).

In our study, size and volume of cerebrum of DM, DPNP and healthy individuals were analyzed based on ages. In our results, volume, anteroposterior and transverse diameter of cerebrum of individuals aged 2 to 40 years are smaller in patients compared to the healthy individuals ($p < 0.05$). There is a significant difference in C3 and Ct parameters in 41-60 age group and C2, C3 and Ct parameters in individuals 61 and above age group ($p < 0.05$). According to these results, it was concluded that

patients with DM and DPNP in the all age groups had a loss in cerebrum size and volume (Figure 6, Figure 7).

When we examined cerebrum sizes of individuals with DM and DPNP based on age groups, it was found that there was a decrease in C3 and Ct parameters of individuals with DPNP and all parameters of individuals with DM, as age increases ($p < 0.05$). Similarly, a decrease in cerebrum volume was found in healthy individuals, as age increases ($p < 0.05$).

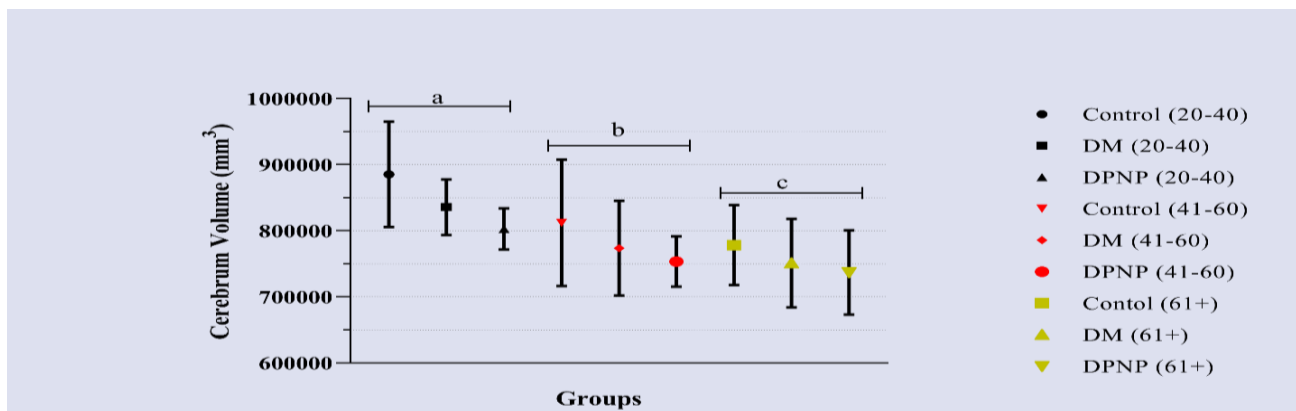


Figure 6. Cerebrum volumes of all age groups in the Diabetic Polyneuropathy, Diabetes Mellitus and control; data were expressed as mean±SD. In all groups; Comparison of cerebrum volumes (mm³) in individuals age 20-40,41-60,61 plus. a; $p < 0.05$ 20-40 age (DPNP, DM, Control), b; $p < 0.05$ 41-60 age (DPNP, DM, Control), c; $p < 0.05$ 61 plus (DPNP, DM, Control). (DM; diabetes mellitus, DPNP; Diabetic polyneuropathy).

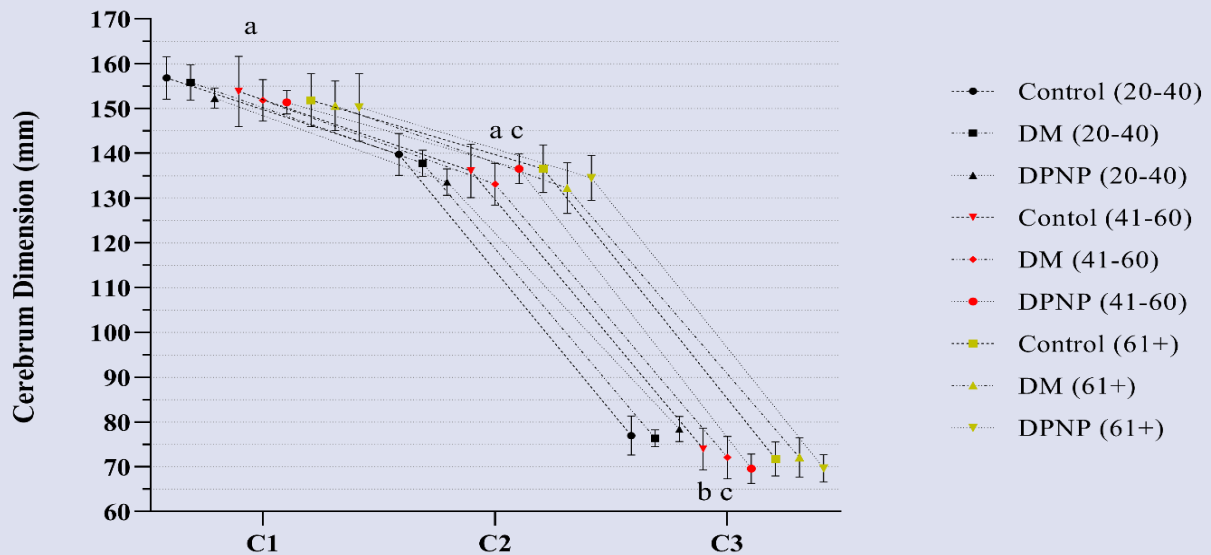


Figure 7. Cerebrum dimensions of all age groups in the Diabetic Polyneuropathy, Diabetes Mellitus and control; data were expressed as mean±SD. In all groups; Comparison of cerebrum dimensions (mm) in individuals age 20-40,41-60,61 plus. a; p < 0.05 20-40 age (DPNP, DM, Control), b; p < 0.05 41-60 age (DPNP, DM, Control), c; p < 0.05 61 plus (DPNP, DM, Control).(C1; anteroposterior diameter of cerebrum, C2; transverse diameter of cerebrum, C3; cerebrum height, DM; diabetes mellitus, DPNP; Diabetic polyneuropathy).

In our study, mean ADC values of thalamus of DPNP, DM and healthy individuals were examined using the DAG method, which reflects the structural and dynamic properties of brain tissue. In conclusion of our results, it

was found that the mean ADC value of thalamus in all age groups was higher in DPNP and DM compared to healthy ones, but was not statistically significant (p>0.05) (Figure 8).

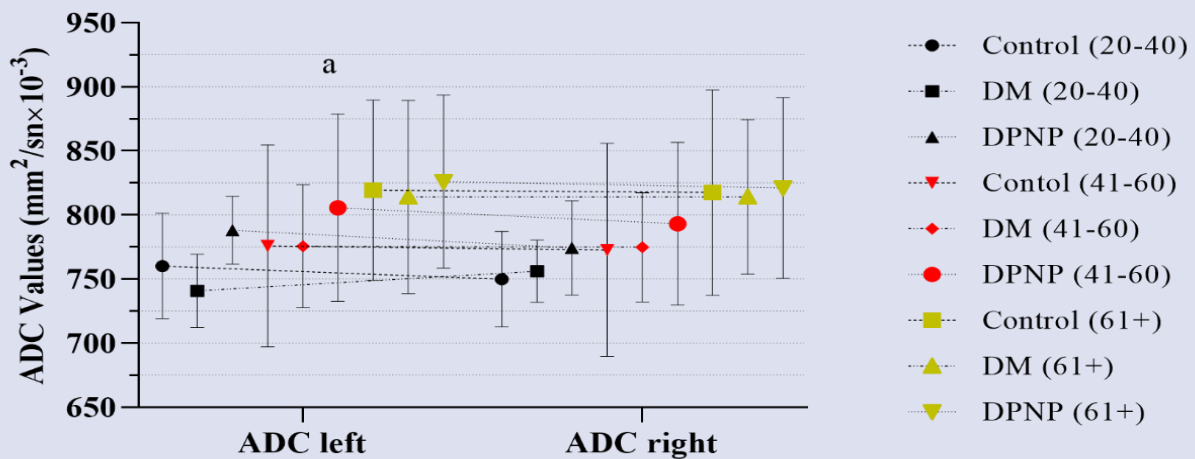


Figure 8. Thalamus ADC values of all age groups in the Diabetic Polyneuropathy, Diabetes Mellitus and control; data were expressed as mean±SD. In all groups; Comparison of thalamus ADC values (mm²/sn×10⁻³) cerebrum dimensions (mm) in individuals age 20-40,41-60,61 plus. a; p < 0.05 20-40 age (DPNP, DM, Control), b; p < 0.05 41-60 age (DPNP, DM, Control), c; p < 0.05 61 plus (DPNP, DM, Control) (DM; diabetes mellitus, DPNP; Diabetic polyneuropathy).

Discussion

Diabetic neuropathy, one of the most common complications in diabetes, is observed in almost half of diabetic patients [2, 13].

Recent studies have shown that the neurological process in diabetes is not limited to peripheral nerves but also affects the central nervous system. In addition, MRI images showing that this condition can occur early in the neuropathic process are also available [14]. Therefore,

researching whether cerebral structures are affected by neuropathic process, assists to have more comprehensive information about the disease.

Selvereajah et al. found grey matter volume of patients with painful diabetic peripheral neuropathy (DPN) to be 585.4 cm³ and grey matter volume pf patients with painless diabetic peripheral neuropathy (DPN) to be 599.6 cm³ and peripheral grey matter volume of healthy

control individuals to be 626.5 cm³ in the study that they examined cerebral volume. In this study, it was found that the gray matter volume of both the painful and painless DPN group decreased at similar rates compared to the healthy control individuals. [15].

As for thalamus, grey matter structure of cerebrum, they stated that volume of thalamus of individuals with painful and painless distal symmetric polyneuropathy (DSP) is less than that of healthy individuals [15].

In their study, Gustin et al. [16] stated that neuropathic pain leads to changes in brain structures. In this study, individuals with trigeminal neuropathic pain (TNP) were compared with individuals with temporomandibular pain (TMP) and healthy volunteers. In conclusion of the study, they found significant volume loss in the nucleus accumbens and thalamus of individuals with TNP, while they reported no volume loss in individuals with TMPD.

Our results are also similar to those in the literature. Accordingly, DM and DPNP lead to atrophy in volume of thalamus. Unlike other studies, these diseases were found to be effective in all age groups.

In their thalamic morphometric measurements, compared with regards to age factor of healthy individuals, Mohammadi et al. [9] stated that anteroposterior, transverse, and vertical length of thalamus of individuals aged 31 to 40 was the highest, while individuals aged 51 and above had the shortest thalamic length. In conclusion of their study, they showed that thalamic sizes slowly increase until the age of 31 to 40 and increasingly decrease after the age of 51.

In their study with regard to age groups in healthy individuals, Sen et al. found no difference in terms of thalamic size and volume [11].

According to the conclusion of our study, thalamic morphometric measurements of DPNP, DM, and healthy individuals were found to decrease as age increases.

In their study with regards to gender, Mohammadi et al. found anteroposterior, transverse, and vertical lengths of thalamus of males to be longer than those of females [9].

In their study that they compared thalamic sizes by gender, Sen et al. [11], reported that transverse diameter of thalamus was longer in males, however vertical and anteroposterior diameters were similar in both genders.

In our study, anteroposterior and vertical diameters of thalamus in individuals with DM aged 20-40 years, transverse and vertical diameter sizes of thalamus in individuals with DPNP were longer in males compared to females, while in individuals aged 41-60 and 61 years and older, there were no significant differences between the genders. In healthy individuals in all age groups, the thalamus transverse diameter and volume were statistically greater in males than females.

Cerebral volumetric measurements cannot identify tissue properties, i.e. cellular components, but help to measure the extent and magnitude of disease effects. Volumetric measurements of cerebral structures provide valuable information about the pathological mechanisms of diseases. In this context, MRI measurements of volume

of cerebrum provide reliable and strong inferences about the disease, providing information about clinical status and progress [17].

In their study, Musen et al. [18] stated that grey matter volume in the cerebellar region and occipital and temporal lobe of patients with Type 1 diabetes was reduced by 4.5%.

In their study, Selverajah et al. [15] found brain volume in painful DPN to be 1470 cm³, in painless DPN to be 1470 cm³ and in healthy individuals to be 1510 cm³. In general, cerebral grey matter volume of patients with DPN decreased by 5.4% compared to healthy controls. This study also showed that the regions first affected by the neuropathic process were the primary somatosensory cortex, supramarginal gyrus, and cingulate cortex.

Ge et al. [19] examined the effects of aging on cerebral grey matter, white matter, and total volume in healthy individuals. In their results, it was stated that the loss of grey matter volume began at the age of 20 and decreased at a constant rate, while the volume of white matter increased until the age of 40, and then decreased rapidly. As a result of changes in the volume of white and grey matter, they reported that the total cerebral volume did not change until the age of 40-50, and the loss of volume began after this age.

In their study, in which they compared the cerebral volume of females and males associated with aging, Gut et al. [20], compared the age group below and above the age of 55. According to these results, they stated that there was a negative correlation between aging and cerebral volume ($r = -0.2$) and cerebral volume loss occurs as a result of neuronal atrophy.

In their study, in which they examined the white matter volume of healthy individuals, Liu et al. [21] found that there was a significant difference ($p < 0.05$) between young (20-40 ages), middle-aged (41-59), and old individuals (60-78). In conclusion of the study, they reported that the volume of white matter gradually increased until the age of 40, was at its highest level around the age of 50, and decreased rapidly after the age of 60.

In our results, it was concluded that size and volume of cerebrum of healthy individuals aged 20-40, 41-60, 61 years and older decreased depending on age. A decrease in cerebral volume can be caused by structural changes such as myelin loss and axonal destruction [22, 23, 24], increased perivascular spaces [25, 26], and dilatation of gliosis [27,28].

Conventional MRI cannot provide sufficient information about local perfusion changes in structures, and biochemical and microstructural differences. Therefore, various MRI methods (Diffusion Weighted Imaging (DWI), perfusion MRI, magnetization transfer imaging, and MRI spectroscopy) are used to obtain quantitative information about the data.

In their study, in which they used MRI spectroscopy to measure the change of cerebrum metabolites in diabetic neuropathic pain, Sorensen et al., found the amount of thalamic NAA (N-Acetylaspartate) in healthy individuals to

be higher than that of patients with diabetic neuropathy [29]. The decrease in NAA resonance is thought to be associated with neuronal/axonal loss, neuron viability, and dysfunction [30].

In their study they conducted with MRI spectroscopy in individuals with type 1 diabetes, diabetic neuropathy, and healthy individuals, Selvarajah et al. found the same voxel in two different TE (echo time) (short TE, long TE). Decreased NAA signal obtained in short TE indicates irreversible neuronal loss/contraction, and a decrease in the NAA/creatine ratio in long TE indicates a state of reversible neuronal damage/dysfunction. According to the study's conclusion, the NAA/creatine ratio in long TE decreased in Type 1 diabetes and diabetic neuropathy compared to healthy individuals however, there was no significant difference in NAA resonance in short TE. They reported that this condition reflected thalamic neuronal dysfunction in patients with DPN rather than neuron death [31].

In their MRI perfusion study, Selvarajah et al. [32], measured cerebral blood volume (rCBV), one of the markers of cerebral microvascular perfusion, in individuals with painful and painless diabetic peripheral neuropathy (DPN) and healthy individuals. According to the conclusion of the study, amount of rCBV of individuals with painful and painless DPN is higher compared to the healthy individuals. They stated that this situation might be caused by high thalamic neuronal activity. In another study conducted on experimental diabetes, it was similarly reported that increased neuronal activity caused neuropathic pain [33]. Studies conducted have shown that thalamic neurons can act as central generators or amplifiers of pain in diabetes.

Detection and evaluation of differentiation in brain tissue that occurs in the aging process is possible by the DAG method [34].

Karasu et al. [35] reported that the mean ADC values of corpus callosum, a white matter mass in the brain, increased significantly with the effect of aging. Mean ADC value of individuals aged 60 and below was found to be $730 \pm 44 \text{ mm}^2/\text{sn} \times 10^{-3}$, and that of individuals aged 60 and above was found to be $758 \pm 26 \text{ mm}^2/\text{sn} \times 10^{-3}$.

Chun et al. [36] stated that the increase in diffusion with aging may be caused by the decrease in myelin fibrils in white matter. Therefore, the decrease in the myelin layer facilitates the diffusion ability of water [37].

Engelter et al. [37], in their study in which they examined the ADC values of the thalamus, found that the mean ADC value of the thalamus of individuals aged 60 and above increased significantly compared to the mean value of the thalamus of individuals aged 60 and below. According to this result, mean ADC values of thalamus increase as age increases.

In our study, the mean ADC values of thalamus of individuals were compared based on the age variable. While the mean ADC value of thalamus increased due to aging in individuals with DM and healthy individuals, no difference was found in individuals with DPNP.

Differences in the structural properties of tissues are suggestive that they might also cause diffusibility of water.

Conclusion

In conclusion the results obtained from our study, it was shown that diabetes mellitus and diabetic polyneuropathy are not limited to peripheral nervous system involvement, but also affect the central nervous system. Besides, DM and DPNP can negatively affect volume of thalamus and cerebrum in individuals of all age groups, leading to atrophy. In this direction, we believe that clinical and laboratory results as well as MRI results can be useful in determining DM and DPNP diseases.

Besides thalamic nuclei are associated with motor activity, limbic system, pain, and visceral activity. A decrease in size volume of the thalamus in diabetes mellitus and diabetic polyneuropathy might cause dysfunctions in these activities. Therefore, we believe that regular patient follow-up is necessary to prevent complications that will negatively affect the lives of individuals with these diseases.

Acknowledgments

The authors would like to thank the Sivas Cumhuriyet University, Sivas, Turkey, for providing the necessary facilities to conduct this study. We would like to thank Research Assistant Handan Gunes for helpful critique and Assistant Professor Ahmet Sevki Taskiran for his critical suggestion and article editing.

Conflict of Interest

The authors declare that they have no conflict of interest.

References

- [1] International Diabetes Federation. International diabetes federation: IDF Atlas. Brussels: Belgium (2017).
- [2] Dyck P. J., Kratz K. M., Karnes J. L., Litchy W. J., Klein R., Pach J. M., Wilson D. M., O'Brien P. C., Melton L. J., 3rd & Service F. J. The prevalence by staged severity of various types of diabetic neuropathy, retinopathy, and nephropathy in a population-based cohort: the Rochester Diabetic Neuropathy Study, *Neurology*, 43 (1993) 817–24.
- [3] Pop-Busui, R., Boulton, A. J., Feldman, E. L., Bril, V., Freeman, R., Malik, R. A., Sosenko, J. M., & Ziegler, D. (2017). Diabetic Neuropathy: A Position Statement by the American Diabetes Association, *Diabetes Care*, 40(1) (2017) 136–154.
- [4] Tesfaye, S., Chaturvedi, N., Eaton, S. E., Ward, J. D., Manes, C., Ionescu-Tirgoviste, C., Witte, D. R., Fuller, J. H. Vascular risk factors and diabetic neuropathy. Prospective epidemiological study showing that, apart from glycaemic control, incident neuropathy is associated with modifiable cardiovascular risk factors, *N. Engl. J. Med.*, 352 (2005) 341–50.
- [5] Said G., Diabetic neuropathy-A Review, *Nat. Clin. Prac. Neurol.*, 3 (2007) 331-340.

- [6] Albers JW., Diabetic Neuropathy: Mechanisms, Emerging Treatments and Subtypes, *Curr. Neurol. Neurosci. Rep.*, 14 (2014) 473.
- [7] Charnogursky G., Emanuele N.V., Emanuele M.A., Neurological Complications of diabetes, *Curr. Neuro. Neurosci. Rep.*, 14 (2014) 457.
- [8] McCormick D.A., Bal T., Sensory gating mechanisms of the thalamus, *Curr. Opin. Neurobiol.*, 4 (1994) 550–556.
- [9] Mohammadi M.R., Hosseini S.H., Ghalipour M.J., Morphometric measurements of the thalamus and interthalamic adhesion by MRI in the South-East of the Caspian Sea border, *Neurosciences*, 13(3) (2008) 272-275.
- [10] Caetano S.C., Sassi R., Brambilla P., Harenski K., Nicoletti M., Mallinger A.G., Frank E., Kupfer D.J., Keshavan M.S., Soares J.C., MRI study of thalamic volumes in bipolar and unipolar patients and healthy individuals, *Psychiatry Res.*, 108 (2001) 161–168.
- [11] Sen F., Ulubay H., Ozeksi P., Sargon M.F., Tascioglu A.B. Morphometric measurements of the thalamus and interthalamic adhesion by MR imaging, *Neuroanatomy.*, 4 (2005) 10-12.
- [12] Tastemur Y., Sabanciogullari V., Salk I., Cimen M. The Relationship of the Posterior Cranial Fossa, the Cerebrum, and Cerebellum Morphometry with Tonsillar Herniation, *Iran J. Radiol.*, 14(1) (2017) e24436.
- [13] Yasuda S., Miyazaki S., Kanda M., Goto Y., Suzuki M., Harano Y., Nonogi H., Intensive treatment of risk factors in patients with type-2 diabetes mellitus is associated with improvement of endothelial function coupled with a reduction in the levels of plasma asymmetric dimethylarginine and endogenous inhibitor of nitric oxide synthase, *Eur. Heart J.*, 27(10) (2006) 1159-65.
- [14] Selvarajah D., Wilkinson I. D., Emery, C. J., Harris, N. D., Shaw, P. J., Witte, D. R., Griffiths, P. D., & Tesfaye, S. Early involvement of the spinal cord in diabetic peripheral neuropathy, *Diabetes Care.*, 29 (2006) 2664–2669.
- [15] Selvarajah D., Wilkinson I. D., Maxwell M., Davies J., Sankar A., Boland E., Gandhi R., Tracey I., Tesfaye S., Magnetic resonance neuroimaging study of brain structural differences in diabetic peripheral neuropathy, *Diabetes Care*, 37 (2014) 1681–8.
- [16] Gustin S.M., Peck C.C., Wilcox S.L., Nash P.G., Murray G.M., Henderson L.A., Different pain, different brain: thalamic anatomy in neuropathic and non-neuropathic chronic pain syndromes, *J. Neurosci.*, 31 (2011) 5956–5964.
- [17] Giorgio A., De Stefano N. Clinical use of brain volumetry, *J. Magn. Reson Imaging*, 37 (2013) 1–14
- [18] Musen G., Lyoo I. K., Sparks C. R., Weinger K., Hwang J., Ryan C. M., Jimerson D. C., Hennen J., Renshaw P. F., Jacobson, A. M., Effects of type 1 diabetes on gray matter density as measured by voxel-based morphometry, *Diabetes*, 55 (2006) 326–333.
- [19] Ge Y., Grossman R.I., Babb J.S., Rabin M.L., Mannon L.J., Kolson D.L., Age-related total gray matter and white matter changes in normal adult brain. Part I: Volumetric MR imaging analysis, *Am. J. Neuroradiol.*, 23 (2002) 1327-1333.
- [20] Gur R. C., Mozley P. D., Resnick S. M., Gottlieb G. L., Kohn M., Zimmerman R., Herman G., Atlas S., Grossman R., Berretta, D., Gender differences in age effect on brain atrophy measured by magnetic resonance imaging, *Proc. Natl. Acad. Sci. USA.*, 88 (1991) 2845–2849.
- [21] Liu H., Wang L., Geng Z., Zhu Q., Song Z., Chang R., Lv H., A voxel-based morphometric study of age- and sex-related changes in white matter volume in the normal aging brain, *Neuropsychiatric Disease and Treatment*, 12 (2016) 453–465
- [22] Salat D.H., Kaye J.A., Janowsky J.S., Prefrontal gray and white matter volumes in healthy aging and Alzheimer disease, *Arch Neurol.*, 56 (1999) 338–344.
- [23] Swieten J.C., Den Hout J.H.W., Ketel B.A., Hydra A., Wokke J.H.J., van Gijn J., Periventricular lesions in the white matter on magnetic resonance imaging in the elderly, *Brain*, 114 (1991) 761–774.
- [24] Sze G., DeArmond S., Brant-Zawadski M., Davis R.L., Norman D., Newton T.H., Foci of MRI signal (pseudo lesions) anterior to the frontal horns: histologic correlations of a normal finding, *Am. J. Neuroradiol.*, 7 (1986) 381–387.
- [25] Fazekas F., Kleinert R., Offenbacher H., Schmidt R., Kleinert G., Payer F., Radner H., Lechner H. Pathologic correlates of incidental MRI white matter signal hyperintensities, *Neurology*, 43 (1993) 1683–1689.
- [26] Awad I.A., Johnson P.C., Spetzler R.F., Hodak J.A., Incidental subcortical lesions identified on magnetic resonance imaging in the elderly, II: postmortem pathological correlations, *Stroke*, 17 (1986) 1090–1097.
- [27] Fazekas F., Kleinert R., Offenbacher H., Payer F., Schmidt R., Kleinert G., Radner H., Lechner H., The morphologic correlate of incidental white matter hyperintensities on MR images, *Am. J. Neuroradiol.*, 12 (1991) 915–921.
- [28] Grafton S.T., Sumi S.M., Stimac G.K., Alvord E.C Jr., Shaw C.M., Nochlin D., Comparison of postmortem magnetic resonance imaging and neuropathologic findings in the cerebral white matter, *Arch Neurol.*, 48 (1991) 293–298.
- [29] Sorensen L., Siddall P.J., Trenell M.I., Yue D.K., Differences in metabolites in pain-processing brain regions in patients with diabetes and painful neuropathy, *Diabetes Care*, 31 (2008) 980–981.
- [30] Nakano M., Ueda H., Li J.Y., Matsumoto M., Yanagihara T., Measurement of regional N-acetylaspartate after transient global ischemia in gerbils with and without ischemic tolerance: an index of neuronal survival, *Ann Neurol.*, 44 (1998) 334–340.
- [31] Selvarajah D., Wilkinson I. D., Emery C. J., Shaw P. J., Griffiths P. D., Gandhi R., Tesfaye S., Thalamic neuronal dysfunction and chronic sensorimotor distal symmetrical polyneuropathy in patients with type 1 diabetes mellitus, *Diabetologia*, 51 (2008) 2088-2092.
- [32] Selvarajah D., Wilkinson I.D., Gandhi R., Griffiths P.D., Tesfaye S., Microvascular perfusion abnormalities of the thalamus in painful but not painless diabetic polyneuropathy: a clue to the pathogenesis of pain in type 1 diabetes, *Diabetes Care.*, 34(3) (2011) 718–720.
- [33] Fischer T.Z., Waxman S.G., Neuropathic pain in diabetes evidence for a central mechanism, *Nat. Rev. Neurol.*, 6(8) (2010) 462–466.
- [34] Bilgili Y., Ünal B., Kendi T., Simsir İ., Erdal H., Huvaj S., Simay K., Bademci G., MRG ile normal görünümü beyaz ve gri cevherde yaşlanmanın etkilerinin ADC değerleri ile saptanabilirliği, *Tanisa ve Girişimsel Radyoloji*, 10(1) (2004) 4-7.
- [35] Karasu R., Bilgili Y., Korpus kallosumun difüzyon ağırlıklı ve konvansiyonel manyetik rezonans görüntüleme ile yaşa göre değerlendirilmesi, *Kırıkkale Üniversitesi Tıp Fakültesi Dergisi*, 20(1) (2018) 51-61.
- [36] Chun T., Filippi C.G., Zimmerman R.D., Ulug A.M., Diffusion changes in the aging human brain, *AJNR*, 21 (2000) 1078-83.
- [37] Engelter S.T., Provenzale J.M., Petrella J.R., DeLong D.M., MacFall JR., The effect of aging on the apparent diffusion coefficient of normal-appearing white matter, *AJR*, 175 (2000) 425-30.

The Complete Mitogenome of Redheaded Pine Sawfly, *Neodiprion lecontei* (Hymenoptera: Diprionidae): Duplication of *trnR* Gene and Rearrangement in the ARNS1EF Gene Cluster

Ertan Mahir Korkmaz^{1,a,*}

¹ Department of Molecular Biology and Genetics, Faculty of Science, Sivas Cumhuriyet University, Sivas, 58140, Türkiye

*Corresponding author

Research Article

History

Received: 26/10/2022

Accepted: 20/12/2022

Copyright



©2022 Faculty of Science,
Sivas Cumhuriyet University

ABSTRACT

Neodiprion is a genus belonging to the small sawfly family Diprionidae, feeding the plant family Pinaceae entirely. Here, the complete mitogenome of the redheaded pine sawfly *Neodiprion lecontei* (Hymenoptera: Diprionidae) was assembled, annotated as third party annotation from the raw genome dataset of *N. lecontei* and comparatively characterised. The length of *N. lecontei* mitogenome was 16,067 bp in size, with an AT content of 81.32%. The initiation codons of protein coding genes (PCGs) are ATN (except for *nad6* (TTA-Phe), while termination codons are TAA or T-. tRNA genes favoured usual anticodons except for *trnS1* which preferred an unusual anticodon GCU. Compared with the *Neodiprion sertifer* mitogenome, the ARNS1EF gene cluster was rearranged as RAS1RNEF and *trnR* gene has a duplicated copy, revealing a new event not formerly reported in Symphyta. The phylogeny confirms the position of *N. lecontei* within the family of Diprionidae and supports the monophyly of included genera and families in Tenthredinoidea.

Keywords: Mitochondrial genome, Rearrangement, Sawflies; Tenthredinoidea, Symphyta

^a ekorkmaz@cumhuriyet.edu.tr

^{id} <https://orcid.org/0000-0003-0699-1354>

Introduction

Mitochondria have a central role in the production of metabolic energy in nearly all living eukaryotic organisms [1]. In addition to its vital functional importance involved in maintaining an accurate energy balance and cellular lifecycle, this organelle has also been extensively used in terms of mitogenome information to investigate genome features and to infer evolutionary relationships from populations to species or higher level of taxa [2–4]. A typical insect mitogenome consists of 14–25 kb with a quite conserved gene content, containing 22 transfer RNAs (tRNAs), 13 protein coding genes (PCGs), two ribosomal RNAs (rRNAs) and one large control region (A + T-rich region) [2,5]. In the last decade, revolutionary advances in next-generation sequencing technology and bioinformatics have also increased the number of insect mitogenomes. In the last release of organelle section of database of NCBI (September 2022) using the “Insecta, mitochondrion” as keywords and filtering the sequence length >10,000 bp, there are complete or nearly complete mitogenomes of more than 9,000 insect species. These contain the mitogenomes from only 978 hymenopteran species, one of the “big four (Coleoptera, Hymenoptera, Diptera and Lepidoptera)” of insect orders including over 150,000 species with remarkable different life strategies [6,7].

The suborder Symphyta (also known as sawflies) is the paraphyletic lineage of Hymenoptera with eight extant phytophagous superfamilies and more than 8900 extant described species [8]. The great majority of this suborder are considered as pest in agriculture and forestry, largely due to their plant-eating lifestyles during larval stage, however, to date, complete or nearly complete mitogenomes of 88 symphytan species have been reported (NCBI, September 2022), with only approximately 9 % of the sequenced hymenopteran mitogenomes. Due to the limited available mitogenome data of sawflies, gene rearrangements are considered to be relatively conserved, but substitution rate is high [9–11], indicating the necessity of more representative mitogenome from Symphyta to infer mitogenome architecture and features.

Here, the complete mitogenome of the redheaded pine sawfly *Neodiprion lecontei* (Fitch, 1859) (Hymenoptera: Diprionidae) was assembled and annotated for the first time. This pest species feeds multiple pine (*Pinus*) tree species throughout its native range in North America [12]. So far, only two mitogenomes from *Neodiprion sertifer* and *N. fabricii*, have been reported for Diprionidae [3]. The mitogenome of *N. lecontei* was also compared with the previously reported mitogenomes of *Neodiprion* for investigating of the mitogenome architectures and features of the Diprionidae.

Materials and Methods

Mitogenome Assembly, Annotation and Analyses

The raw sequencing data of *N. lecontei* was downloaded from the NCBI Sequence Read Archive (SRA) database under the SRA accession numbers of SRR1955932, SRR1956520 and SRR1956730. Quality control steps were performed to get clean reads from the raw sequencing datasets. The adapter sequences, low quality and possible contaminated reads were removed from raw reads by using Fastp v0.20.0 [13] and Lighter v1.0.7 [14]. The obtained clean reads from three datasets were merged into a single fastq file and then the reads were assembled into contigs using both a reference assembly using the mitogenome of *N. sertifer* (MK994526, [3]) from the same genus under the 'iterate up to five times' and 'medium-low sensitivity' parameters in Geneious R9 [15] and *de novo* assembly using SPAdes v3.15.3 [16] in DOE Systems Biology Knowledgebase (KBase) platform [17]. The obtained *de novo* contigs were then mapped with the mitogenome produced under the first approach. The sets of selected assemblies generated by these approaches were finally aligned, compared as manual and gathered into a single contig.

The identification of tRNA genes were performed based on their accepted secondary structure and

anticodon sequence by MITOS web server [18] with the invertebrate genetic code option and ARWEN v1.2 [19] with the default search options and the genetic code as mito/chloroplast. The boundaries and locations of rRNA genes and PCGs were manually designated comparing with the known symphytan homologous gene sequences using ORF Finder (<http://www.ncbi.nlm.nih.gov/gorf/gorf.html>) and BLAST searches in GenBank. The boundaries of the rRNA genes were predicted from location of the adjacent tRNA genes or comparison with homologous symphytan rRNA genes. Overlapping regions and intergenic spacers between genes were estimated manually. The complete mitogenome was graphically mapped by Geneious R9 [15]. Finally, the mitogenome sequence of the redheaded pine sawfly *N. lecontei* was submitted to GenBank under the accession number of TPA: BK062819. Basic statistics on this third party annotated mitogenome nucleotide composition were calculated by MEGA v6.0 [20]. The formulae: AT-skew=[A-T] / [A+T] and GC-skew=[G-C] / [G+C] [21] were used to calculate the base compositional differences between different strands, degenerated codon positions and the genes coded on the alternative strands. The relative synonymous codon usage (RSCU) was also computed for all protein-coding genes by MEGA v6.0.

Table 1. List of sawfly mitogenomes used in phylogenetic analyses.

Family	Species	Accession Number	Family	Species	Accession Number
Diprionidae	<i>Neodiprion lecontei</i>		Tenthredinidae	<i>Allantus luctifer</i>	KJ713152
	<i>Neodiprion sertifer</i>	MK994526		<i>Allantus togatus</i>	MW464859
	<i>Nesodiprion biremis</i>	ON964465		<i>Analcellicampa xanthosoma</i>	MH992752
	<i>Nesodiprion japonicus</i>	ON964464		<i>Asiemphytus rufocephalus</i>	KR703582
Argidae	<i>Arge aurora</i>	MN913350		<i>Birmella discoidalis</i>	MF197548
	<i>Arge bella</i>	MF287761		<i>Colochela zhongi</i>	MT702984
	<i>Arge similis</i>	MG923484		<i>Conaspidia wangi</i>	MW415019
Athaliidae	<i>Athalia birmanica</i>	ON840085		<i>Eutomostethus vegetus</i>	MT663219
	<i>Athalia japonica</i>	ON964466		<i>Hemathlophorus</i> sp.	MW632125
	<i>Athalia proxima</i>	MN527306		<i>Macrophya dolichogaster</i>	MW544890
	<i>Cimbex luteus</i>	MW136447		<i>Metallus mai</i>	MW255941
	<i>Corynis lateralis</i>	KY063728		<i>Monocelicampa pruni</i>	JX566509
Cimbicidae	<i>Labriocimbex sinicus</i>	MH136623		<i>Moricella rufonota</i>	MW487926
	<i>Leptocimbex clavicornis</i>	MT478109		<i>Neostromboceros nipponicus</i>	MW632127
	<i>Leptocimbex praiiformis</i>	MT478110		<i>Sinopoppia nigroflagella</i>	MW487927
	<i>Leptocimbex yanniae</i>	MT478111		<i>Siobla xizangensis</i>	MN562486
	<i>Praia tianmunica</i>	MT665975	<i>Strongylogaster xanthocera</i>	MW324676	
	<i>Trichiosoma anthracinum</i>	KT921411	<i>Taxoblenus sinicus</i>	MW632126	
Pergidae	<i>Trichiosoma vitellina</i>	MN853777	<i>Taxonus zhangi</i>	MZ461490	
	<i>Perga condei</i>	AY787816	<i>Tenthredo tienmushana</i>	KR703581	
Xyelidae	<i>Macroxyela ferruginea</i>	MK270536	<i>Xenapatidea procincta</i>	MW487928	
	<i>Xyela</i> sp.	MG923517			

Phylogenetic analyses were carried out using the dataset of 41 species from Tenthredinoidea, representing six families and of two species from the family Xyelidae as outgroup (Table 1). Nucleotide sequences of each PCG were aligned individually under codon-based alignments using ClustalW as implemented in MEGA v6.0. The alignment of RNA genes was performed using MAFFT algorithm [22] as implemented in Geneious R9. The obtained alignments were concatenated with SequenceMatrix v1.7.8 [23]. The best-fitting partitioning

scheme and model of each partition were selected by PartitionFinder v1.1.1 [24] using Bayesian information criterion (BIC) and the "greedy" algorithm based on branch lengths estimated as "unlinked". The data blocks were stated by codons and genes to create an input configuration partition file with 63 (with all codon positions) and 50 (without 3rd codon positions). All subsequent phylogenetic analyses were performed using the best partitioning schemes and related models (Table 2). The genetic saturation

levels of genes and different codon positions were measured by correlation test implemented in R core packages [25] comparing the distances measured by applying the best-fitting model evolution GTR + G + I proposed by PartitionFinder v1.1.1 with the uncorrected p-distances. The distance values were estimated with PAUP v4.0b10 [26]. The phylogenetic analyses were performed with the dataset of nine PCGs with the first two codon positions plus two rRNAs and 22 tRNAs (9P12RNA). In the preference of this dataset, the result of the test of substitution saturation was considered, which exhibited lower degrees of correlation between 3rd codon positions of all PCGs and the all codon positions of *atp8*, *nad4l*, *nad6* and *nad2*. Maximum

Likelihood (ML) analyses were performed in IQ-TREE v2.1.4 [27] using default parameters under the proposed substitution model (GTR + G + I) with 1000 bootstrap replicates using the fast bootstrapping option implemented in IQTree. Bayesian Inference (BI) analyses were carried out in MrBayes v3.2.2 [28] under the unlinked branch lengths of each partition scheme with two independent runs of five million generations, sampling every 5000 generations. Each run was assessed for stationary using Tracer v1.6 [29]. After the assessment, the first 20% of trees were excluded as burn-in. The generated majority-rule consensus tree (BI tree) from the remaining trees was visualised by FigTree v1.4.2 [30].

Table 2. The best partition scheme selected by PartitionFinder for each dataset used in phylogenetic analyses.

Subsets	Partition scheme	Model
1	<i>atp6</i> 1st + <i>cox1</i> 1st + <i>cox2</i> 1st + <i>cox3</i> 1st + <i>cytb</i> 1st + <i>trnK</i> + <i>trnM</i> + <i>trnS2</i>	GTR + G + I
2	<i>atp6</i> 2nd + <i>cox1</i> 2nd + <i>cox2</i> 2nd + <i>cox3</i> 2nd + <i>cytb</i> 2nd + <i>nad1</i> 2nd + <i>nad2</i> 2nd + <i>nad3</i> 2nd + <i>nad4</i> 2nd + <i>nad4l</i> 2nd + <i>nad5</i> 2nd + <i>nad6</i> 2nd	GTR + G + I
3	<i>atp6</i> 3rd + <i>atp8</i> 3rd + <i>cox1</i> 3rd + <i>cox2</i> 3rd + <i>cox3</i> 3rd + <i>cytb</i> 3rd + <i>nad2</i> 3rd + <i>nad3</i> 3rd + <i>nad6</i> 3rd	GTR + G + I
4	<i>nad1</i> 1st + <i>nad4</i> 1st + <i>nad4l</i> 1st + <i>nad5</i> 1st + <i>rrnL</i> + <i>rrnS</i> + <i>trnF</i> + <i>trnH</i> + <i>trnL1</i> + <i>trnQ</i> + <i>trnV</i>	GTR + G + I
5	<i>nad1</i> 3rd + <i>nad4</i> 3rd + <i>nad4l</i> 3rd + <i>nad5</i> 3rd	GTR + G + I
6	<i>atp8</i> 1st + <i>atp8</i> 2nd + <i>nad2</i> 1st + <i>nad3</i> 1st + <i>nad6</i> 1st + <i>trnA</i> + <i>trnC</i> + <i>trnD</i> + <i>trnE</i> + <i>trnG</i> + <i>trnI</i> + <i>trnL2</i> + <i>trnN</i> + <i>trnP</i> + <i>trnR</i> + <i>trnS1</i> + <i>trnT</i> + <i>trnW</i> + <i>trnY</i>	GTR + G + I

Results and Discussion

Genome architecture and nucleotide composition

The complete mitogenome of the redheaded pine sawfly *N. lecontei* was characterised and comparatively analysed with the mitogenome of *N. sertifer* [3] (Fig. 1 and Table 3). The complete mitogenome of *N. lecontei* was 16,067 bp in length, including 13 PCGs, 23 tRNAs, two rRNAs and A+T rich region (Fig. 1 and Table 3). Fourteen genes are located on the minority N strand, while 24 are

encoded by the majority J strand (Table 3). Mitogenome architecture closely matched all previously reported symphytan mitogenomes [10,11,31] and was nearly consistent with that of the inferred insect ancestral mitogenome. The orientation and position of the predicted genes of *N. lecontei* mitogenome were almost identical with *N. sertifer* [3], except for *trnR* gene duplication and rearrangement of ARNS1EF gene cluster (Fig. 1).

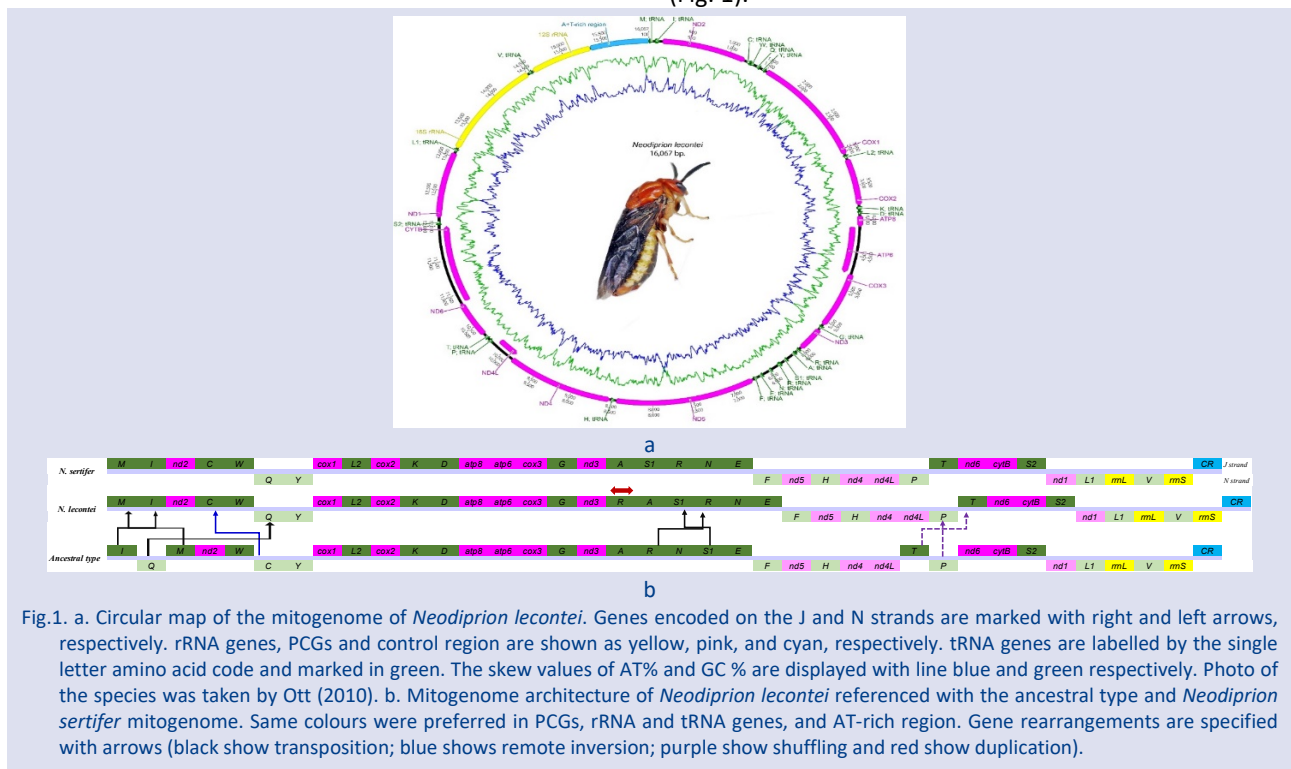


Fig.1. a. Circular map of the mitogenome of *Neodiprion lecontei*. Genes encoded on the J and N strands are marked with right and left arrows, respectively. rRNA genes, PCGs and control region are shown as yellow, pink, and cyan, respectively. tRNA genes are labelled by the single letter amino acid code and marked in green. The skew values of AT% and GC % are displayed with line blue and green respectively. Photo of the species was taken by Ott (2010). b. Mitogenome architecture of *Neodiprion lecontei* referenced with the ancestral type and *Neodiprion sertifer* mitogenome. Same colours were preferred in PCGs, rRNA and tRNA genes, and AT-rich region. Gene rearrangements are specified with arrows (black show transposition; blue shows remote inversion; purple show shuffling and red show duplication).

The duplicated copy of this tRNA was inserted upstream of *trnA* (arranged as RAS1RNEF, Fig. 1), representing a new pattern for Symphyta. The presence of long intergenic regions among the rearranged and/or duplicated genes might be explained by tandem duplication and random loss (TDRL) mechanism proposed as most widely accepted mechanism for gene rearrangements in insect mitogenomes [2,3,31]. The total length of the intergenic regions was 443 bp in 23 locations with a size ranging from 1 to 74 bp (Table 3). These were mainly found in the ARNS1EF gene cluster, with a 55.76% (247 bp) of total length of the intergenic regions. In spite of the commonly observed pattern in hymenopteran mitogenomes [10,32], only three overlapping regions were detected between *atp8* and *atp6* (7 bp), *nd4* and *nd4L* (1 bp), and *nd6* and *cytB* (1 bp) (Table 3).

Table 3. Mitogenome summary of *Neodiprion lecontei* (16,067 bp)

Gene	Strand	Size (bp)	Start codon	Stop codon	Anticodon	IGN
<i>trnM</i>	J	69			CAT	0
<i>trnI</i>	J	70			GAT	28
<i>nd2</i>	J	1050	ATG	TAA		6
<i>trnC</i>	N	64			GCA	0
<i>trnW</i>	J	66			TCA	2
<i>trnQ</i>	N	69			TTG	15
<i>trnY</i>	N	66			GTA	9
<i>cox1</i>	J	1540	ATA	T--		0
<i>trnL2</i>	J	66			TAA	1
<i>cox2</i>	J	675	ATG	TAA		2
<i>trnK</i>	J	72			CTT	0
<i>trnD</i>	J	67			GTC	0
<i>atp8</i>	J	162	ATT	TAA		-7
<i>atp6</i>	J	681	ATG	TAA		3
<i>cox3</i>	J	804	ATG	TAA		3
<i>trnG</i>	J	69			TCC	0
<i>nd3</i>	J	351	ATT	TAA		6
<i>trnR</i>	J	69			TCG	1
<i>trnA</i>	J	67			TGC	74
<i>trnS1</i>	J	61			TCT	30
<i>trnR</i>	J	69			TCG	73
<i>trnN</i>	J	65			GTT	64
<i>trnE</i>	J	65			TTC	3
<i>trnF</i>	N	69			GAA	2
<i>nd5</i>	N	1728	ATT	TAA		0
<i>trnH</i>	N	66			GTG	4
<i>nd4</i>	N	1341	ATG	TAA		-1
<i>nd4L</i>	N	291	ATT	TAA		31
<i>trnP</i>	N	67			TGG	20
<i>trnT</i>	J	63			TGT	26
<i>nd6</i>	J	513	TTA	TAA		-1
<i>cytB</i>	J	1134	ATG	TAA		12
<i>trnS2</i>	J	69			TGA	28
<i>nd1</i>	N	951	ATT	TAA		0
<i>trnL1</i>	N	67			TAG	0
<i>rrnL</i>	N	1374				0
<i>trnV</i>	N	67			TAC	0
<i>rrnS</i>	N	780				0
A + T-rich region		716				

As similar to the reported hymenopteran mitogenomes [11,31,33–35], a bias to A and T nucleotides was observed in the mitogenome of *N. lecontei*, with an average 81.32% AT content (Table 4). Similar to the mitogenome of *N. sertifer* [3], the AT content was high in tRNA genes (84.11%), while low in PCGs (79.48%). AT bias was also strong in N strand (82.00% AT content on average) than in J strand (77.91%), with G strand being richer in G (11.51%) than C (6.50%), and the J strand showing an opposite skew for C (13.37%) and G (9.71%) (Table 4). The AT content of 3rd codon position (91.04%) was higher than those of the 1st (75.62%) and 2nd codon positions (71.79%), indicating the robust effect of mutational pressure and the reduced effect of selection acting on the third codon position. The presence of T bias in the second codon position (50.05% T content) might be explained by the pressure of mutation on mitochondrial proteins in favour of hydrophobic amino acids with codons having a T at the second codon position as phenylalanine, leucine, isoleucine, and methionine [3,10]. A positive AT skew (0.066) and a negative GC skew (-0.182) were counted in the whole mitogenome (Table 4), which is widely reported pattern in the mitogenome of sawflies. However, a deviation out of strand asymmetries is observed in the PCGs: T- and G-skewed (-0.133 and 0.014). The PCGs encoded on the J strand are T- (-0.049) and C-skewed (-0.120), while those of the N strand are T- (-0.260) and G-skewed (0.278) (Table 4). This deviation is most probably related with the effect of the mutational pressures on the mitogenome such as exposure to more DNA damage during replication [37].

Protein Coding Genes

In comparison with the *N. sertifer* mitogenome, the lengths of PCGs were same, except for *nad2*, *cox1*, *cox3* and *nad4L* (Table 3). The *cox1* gene of *N. lecontei* is six codons shorter than that of *N. sertifer*. As widely reported for animal mitogenomes [37], the initiation codons were found as isoleucine (ATY) or methionine (ATR), except for *nad6* (TTA-Phe) (Table 3). The termination codon was found as TAA, except for *cox1* which has truncated termination codon (T-) and its product was probably completed after posttranscriptional polyadenylation of mature mRNA [38]. The RSCU values of *N. lecontei* and *N. sertifer* exhibited a similarity for codon usage bias and pictured an important relation between codon preference and nucleotide composition (Fig. 2). Similar to that of other known symphytan mitogenomes, AUU-Ile, UUA-Leu, AUA-Met and UUU-Phe are the most commonly used codons, consisting 40.08% of total content [3,11,34]. The codons with RSCU greater than 2.00 had T or A in the third codon position (Fig. 2).

Table 4. Nucleotide composition of the *Neodiprion lecontei* and *N. sertifer* mitogenomes

Feature	Species	T%	C%	A%	G%	A+T%	AT-skew	GC-skew
Whole genome	<i>N. lecontei</i>	37.99	11.04	43.33	7.64	81.32	0.066	-0.182
	<i>N. sertifer</i>	38.30	11.03	43.14	7.53	81.44	0.059	-0.189
Protein-coding genes	<i>N. lecontei</i>	45.01	10.11	34.47	10.40	79.48	-0.133	0.014
	<i>N. sertifer</i>	44.57	10.57	34.45	10.42	79.02	-0.128	-0.007
First codon position	<i>N. lecontei</i>	37.96	9.60	37.66	14.78	75.62	-0.004	0.212
	<i>N. sertifer</i>	37.62	10.01	37.81	14.57	75.43	0.003	0.186
Second codon position	<i>N. lecontei</i>	50.05	16.18	21.74	12.03	71.79	-0.394	-0.147
	<i>N. sertifer</i>	50.31	16.12	21.70	11.88	72.01	-0.397	-0.151
Third codon position	<i>N. lecontei</i>	47.03	4.57	44.01	4.39	91.04	-0.033	-0.020
	<i>N. sertifer</i>	45.77	5.58	43.85	4.80	89.62	-0.021	-0.075
Protein-coding genes-J	<i>N. lecontei</i>	40.88	12.37	37.03	9.71	77.91	-0.049	-0.120
	<i>N. sertifer</i>	40.88	12.71	36.81	9.59	77.69	-0.052	-0.140
First codon position	<i>N. lecontei</i>	33.33	11.68	40.58	14.41	73.91	0.098	0.105
	<i>N. sertifer</i>	32.93	12.31	40.55	14.21	73.48	0.104	0.072
Second codon position	<i>N. lecontei</i>	47.37	18.45	22.41	11.77	69.78	-0.358	-0.221
	<i>N. sertifer</i>	47.72	18.25	22.54	11.49	70.26	-0.358	-0.227
Third codon position	<i>N. lecontei</i>	41.95	6.99	48.11	2.95	90.06	0.068	-0.406
	<i>N. sertifer</i>	42.00	7.59	47.33	3.08	89.33	0.060	-0.423
Protein-coding genes-N	<i>N. lecontei</i>	51.64	6.50	30.36	11.51	82.00	-0.260	0.278
	<i>N. sertifer</i>	50.46	7.13	30.67	11.74	81.13	-0.244	0.244
First codon position	<i>N. lecontei</i>	45.37	6.26	32.99	15.38	78.36	-0.158	0.421
	<i>N. sertifer</i>	45.14	6.32	33.40	15.14	78.54	-0.149	0.411
Second codon position	<i>N. lecontei</i>	54.35	12.53	20.67	12.46	75.02	-0.449	-0.003
	<i>N. sertifer</i>	54.44	12.71	20.35	12.50	74.79	-0.456	-0.008
Third codon position	<i>N. lecontei</i>	55.18	0.70	37.44	6.68	92.62	-0.192	0.810
	<i>N. sertifer</i>	51.81	2.36	38.26	7.57	90.07	-0.150	0.525
tRNA genes	<i>N. lecontei</i>	41.63	6.87	42.48	9.01	84.11	0.010	0.135
	<i>N. sertifer</i>	41.56	6.87	42.65	8.91	84.21	0.013	0.129
rRNA genes	<i>N. lecontei</i>	44.96	5.62	39.11	10.31	84.07	-0.070	0.294
	<i>N. sertifer</i>	45.07	5.58	38.89	10.46	83.96	-0.074	0.304

Transfer RNA and Ribosomal RNA Genes

The predicted tRNAs of *N. lecontei* mitogenome were almost same position and orientation with *N. sertifer* (Fig. 1). Their length ranged in size from 63 bp (*trnT*) to 72 bp (*trnK*) (Table 3), with 84.11% of AT content. These tRNAs also folded into a conserved clover-leaf structure, except for *trnS1* with a dihydrouridine (DHU) arm as expected. The anticodons of the tRNAs were identical with the reported symphytan mitogenomes, excepting *trnS1* which prefers GCU as an anticodon (Table 3). The *rrnL* gene was between *trnL1* and *trnV* (Fig. 1) and its length was 1374 bp, with an 84.3% AT content (Tables 3, 4). This was similar to homolog genes of *N. sertifer* and other reported hymenopteran species [3,10,11]. The conservation level of the nucleotide positions is relatively high with an average of 72.01%. The length of the *rrnS* gene was 780 bp with an 83.4% AT content (Tables 3, 4).

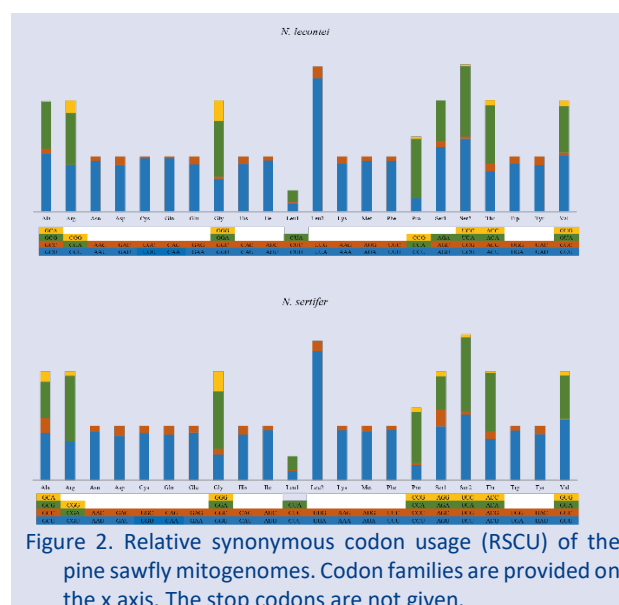


Figure 2. Relative synonymous codon usage (RSCU) of the pine sawfly mitogenomes. Codon families are provided on the x axis. The stop codons are not given.

Phylogeny of Tenthredinoidea

The same and well supported phylogenetic tree topologies were recovered in both analyses (Fig. 3). The recovered trees confirmed the taxonomic position of *N. lecontei* within Diprionidae and supported a relationship of (Pergidae + Argidae) + (Athaliidae + ((Diprionidae + Cimbicidae) + Tenthredinidae)) in the Tenthredinoidea and this is reliable with the most of the reported phylogenies [33,39–40]. The monophyly of included genera and families were also highly supported (Fig. 3). These results highlight that the mitogenome dataset verifies useful in the built of the phylogeny of Tenthredinoidea as well as of Symphyta.

Conclusion

The annotation and characterisation of the complete mitogenome of redheaded pine sawfly *N. lecontei* and the phylogenetic replacements of tenthredinoid families allow us to designate several conclusions: (i) the mitogenome architecture and orientation are mostly reliable with the reported symphytan mitogenomes; (ii) *trnR* gene duplication and rearrangement of ARNS1EF gene cluster seem to be unique to this species; (iii) the phylogenetic analyses confirm the position of *N. lecontei* and also support the monophyly of the tenthredinoid families.

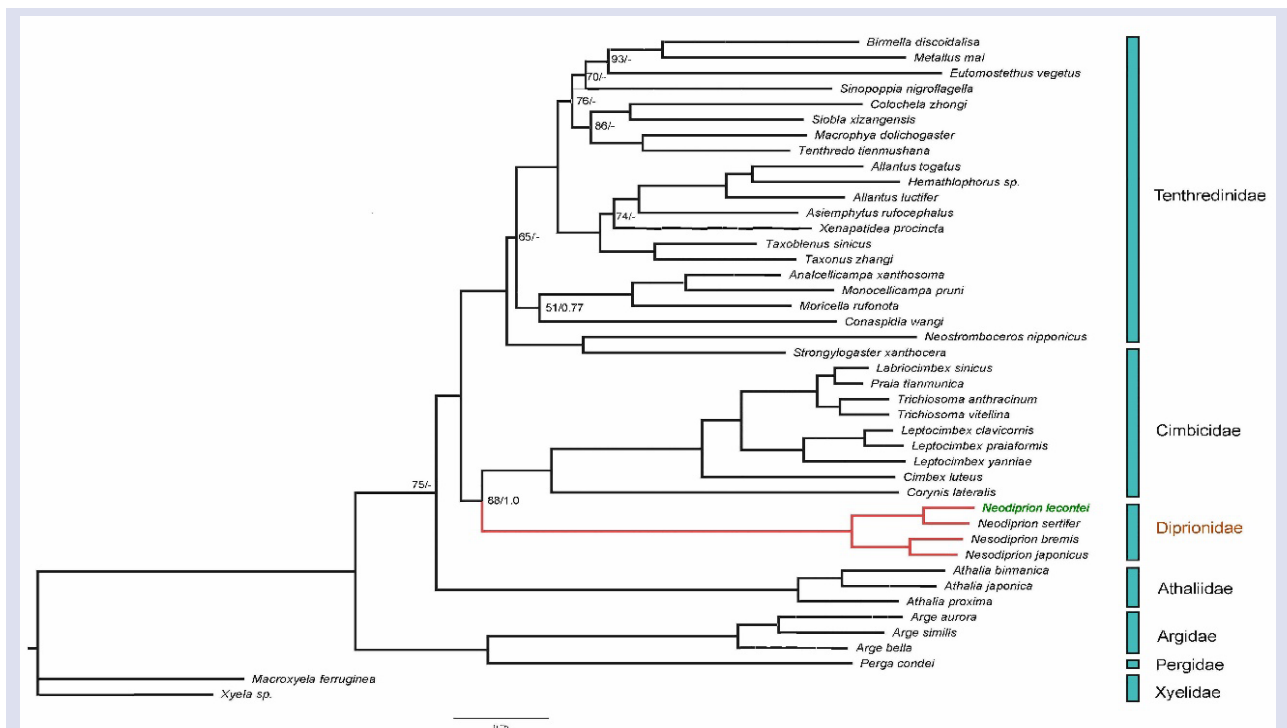


Fig. 3. Phylogenetic tree of the superfamily of Tenthredinoidea. The trees were constructed applying BI and ML methods under a concatenated 9P12RNA dataset (9 PCGs, two rRNAs and 22 tRNAs); both analyses generated the same tree topology. The outgroups were selected from the members of Xyelidae. Support values $\geq 95\%$ in ML and 0.95 in BI were shown.

Acknowledgments

This research did not receive any specific grant from funding agencies in the public, commercial, or not-for-profit sectors. I thank Dr. Özgül DOĞAN for her help in the analysis stages. The members of Evolutionary Bioinformatics Research Group (EBRG) at Sivas Cumhuriyet University are thanked for their contributions in visualising and drawing some of the figures.

Conflicts of interest

The author declares no conflicts of interest.

References

- [1] Carlucci A., Lignitto L., Feliciello A., Control of mitochondria dynamics and oxidative metabolism by cAMP, AKAPs and the proteasome, *Trends Cell Biol.*, 18 (2008) 604–613.
- [2] Cameron S.L., Insect mitochondrial genomics: implications for evolution and phylogeny, *Annu. Rev. Entomol.*, 59 (2014) 95–117.
- [3] Aydemir, M. N., Korkmaz, E. M., Comparative mitogenomics of Hymenoptera reveals evolutionary differences in structure and composition, *International journal of biological macromolecules.*, 144 (2020) 460–472.
- [4] Ballard J.W.O., Pichaud N., Mitochondrial DNA: more than an evolutionary bystander, *Funct. Ecol.*, 28 (2014) 218–231.
- [5] Boore J.L., Animal mitochondrial genomes, *Nucleic Acids Res.*, 27 (1999) 1767–80.
- [6] Grimaldi D., Engel M.S., Evolution of the insects., Cambridge University Press, New York, (2005).
- [7] Klopstein S., Vilhelmsen L., Heraty J.M., Sharkey M., Ronquist F., The hymenopteran tree of life: Evidence from

- protein-coding genes and objectively aligned ribosomal data, *PLoS One.*, 8 (2013).
- [8] Taeger A., Liston A.D., Prous M., Groll E.K., Gehroldt T., Blank S.M. ECatSym – Electronic World Catalog of Symphyta (Insecta, Hymenoptera). Program version 5.0 (19 Dec 2018), data version 40 (23 Sep 2018). – Senckenberg Deutsches Entomologisches Institut (SDEI), Müncheberg. <https://sdei.de/ecatsym/> Access: 15 Oct 2022
- [9] Cheng Y., Yan Y., Wei M., Niu G., Characterization of mitochondrial genomes of three new species: *Leptocimbex praiiformis*, *L. clavicornis*, and *L. yanniae* (Hymenoptera: Cimbicidae), *Entomol. Res.*, 51 (2021) 287–304.
- [10] Doğan Ö., Korkmaz E.M., Nearly complete mitogenome of hairy sawfly, *Corynis lateralis* (Brullé, 1832) (Hymenoptera: Cimbicidae): Rearrangements in the IQM and ARNS1EF gene clusters, *Genetica.*, 145 (2017) 341–350.
- [11] Song S.N., Tang P., Wei S.J., Chen X.X., Comparative and phylogenetic analysis of the mitochondrial genomes in basal hymenopterans, *Sci. Rep.*, 6 (2016).
- [12] Bagley R.K., Sousa V.C., Niemiller M.L., Linnen C.R., History, geography and host use shape genomewide patterns of genetic variation in the redheaded pine sawfly (*Neodiprion lecontei*), *Mol. Ecol.*, 26 (2017) 1022–1044.
- [13] Chen, S., Zhou, Y., Chen, Y., Gu, J., fastp: an ultra-fast all-in-one FASTQ preprocessor, *Bioinformatics.*, 34(17) (2018) i884-i890.
- [14] Song, L., Florea, L., Langmead, B., Lighter: fast and memory-efficient sequencing error correction without counting, *Genome biology.*, 15(11) (2014) 1-13.
- [15] Kearse M., Moir R., Wilson A., Stones-Havas S., Cheung M., Sturrock S., Buxton S., Cooper A., Markowitz S., Duran C., Thierer T., Ashton B., Meintjes P., Drummond A., Geneious Basic: An integrated and extendable desktop software platform for the organization and analysis of sequence data, *Bioinformatics.*, 28 (2012) 1647–9.
- [16] Prjibelski, A., Antipov, D., Meleshko, D., Lapidus, A., Korobeynikov, A., Using SPAdes de novo assembler, *Current protocols in bioinformatics.*, 70(1) (2020) e102.
- [17] Arkin AP., Cottingham RW., Henry CS., Harris NL., Stevens RL., Maslov S., Dehal P., Ware D., Perez F., Canon S., KBase: the United States department of energy systems biology knowledgebase, *Nat Biotechnol.*, 36(7) (2018) 566–9.
- [18] Bernt, M., Donath, A., Jühling, F., Externbrink, F., Florentz, C., Fritzsch, G., Pütz, F., Middendorf. M., Stadler, P. F., MITOS: improved de novo metazoan mitochondrial genome annotation, *Molecular phylogenetics and evolution.*, 69(2) (2013) 313-319.
- [19] Wyman, S. K., Jansen, R. K., Boore, J. L., Automatic annotation of organellar genomes with DOGMA, *Bioinformatics.*, 20(17) (2004) 3252-3255.
- [20] Tamura K., Stecher G., Peterson D., Filipski A., Kumar S., MEGA6: Molecular evolutionary genetics analysis version 6.0, *Mol. Biol. Evol.*, 30 (2013) 2725–2729.
- [21] Perna N.T., Kocher T.D., Patterns of nucleotide composition at fourfold degenerate sites of animal mitochondrial genomes, *J. Mol. Evol.*, 41 (1995) 353–358.
- [22] Katoh K., Standley D.M., MAFFT multiple sequence alignment software version 7: Improvements in performance and usability, *Mol. Biol. Evol.*, 30 (2013) 772–780.
- [23] Vaidya G., Lohman D.J., Meier R., SequenceMatrix: Concatenation software for the fast assembly of multi-gene datasets with character set and codon information, *Cladistics.*, 27 (2011) 171–180.
- [24] Lanfear R., Calcott B., Ho S.Y.W., Guindon S., PartitionFinder: Combined selection of partitioning schemes and substitution models for phylogenetic analyses, *Mol. Biol. Evol.*, 29 (2012) 1695–1701.
- [25] R Core Team, R: A language and environment for statistical computing, Vienna, Austria, 2020.
- [26] Swofford D.L., PAUP. Phylogenetic analysis using parsimony (and other methods), version 4, Sinauer Assoc., Sunderland, Massachusetts. (2002) 294–307.
- [27] Minh B.Q., Schmidt H.A., Chernomor O., Schrempf D., Woodhams M.D., von Haeseler A., Lanfear R., IQ-TREE 2: New models and efficient methods for phylogenetic inference in the genomic era, *Mol. Biol. Evol.*, 37 (2020) 1530–1534.
- [28] Ronquist F., Teslenko M., Van Der Mark P., Ayres D.L., Darling A., Höhna S., Larget B., Liu L., Suchard M.A., Huelsenbeck J.P., MrBayes 3.2: Efficient bayesian phylogenetic inference and model choice across a large model space, *Syst. Biol.*, 61 (2012) 539–542.
- [29] Rambaut A., Suchard M.A., Xie D., Drummond A.J., Tracer v1.6., (2014).
- [30] Rambaut A., FigTree v1.4.2, a graphical viewer of phylogenetic trees, Available from left angle bracket. <http://tree.bio.ed.ac.uk/software/figtree/> (2014).
- [31] Downton M., Cameron S.L., Dowavac J.I., Austin A.D., Whiting M.F., Characterization of 67 mitochondrial tRNA gene rearrangements in the Hymenoptera suggests that mitochondrial tRNA gene position is selectively neutral, *Mol. Biol. Evol.*, 26 (2009) 1607–17.
- [32] Castro L.R., Downton M., The position of the Hymenoptera within the Holometabola as inferred from the mitochondrial genome of *Perga condei* (Hymenoptera: Symphyta: Pergidae), *Mol. Phylogenet. Evol.*, 34 (2005) 469–79.
- [33] Niu G., Jiang S., Doğan Ö., Korkmaz E.M., Budak M., Wu D., Wei M., Mitochondrial phylogenomics of Tenthredinidae (Hymenoptera:Tenthredinoidea) supports the monophyly of Megabelesesinae as a subfamily, *Insects.*, 12 (2021) 495.
- [34] Wu R., Wei M., Liu M., Niu G., Advancement in sequencing the mitochondrial genome of *Birmella discoidalis* Wei, 1994 (Hymenoptera: Tenthredinidae) and the phylogenetic classification of *Fenusini*, *Mitochondrial DNA Part B.*, 4 (2019) 4100–4101.
- [35] Wei S.J., Shi M., He J., Sharkey M., Chen X., The complete mitochondrial genome of *Diadegma semiclausum* (Hymenoptera: Ichneumonidae) indicates extensive independent evolutionary events, *Genome.*, 52 (2009) 308–319.
- [36] Wei S.J., Shi M., Sharkey M.J., van Achterberg C., Chen X., Comparative mitogenomics of Braconidae (Insecta: Hymenoptera) and the phylogenetic utility of mitochondrial genomes with special reference to Holometabolous insects, *BMC Genomics.*, 11 (2010) 371.
- [37] Crozier R.H., Crozier Y.C., The mitochondrial genome of the honeybee *Apis mellifera*: Complete sequence and genome organization, *Genetics.*, 133 (1993) 97–117.
- [38] Ojala D., Montoya J., Attardi G., tRNA punctuation model of RNA processing in human mitochondria, *Nature*, 290 (1981) 470–474.
- [39] Malm T., Nyman T., Phylogeny of the symphytan grade of Hymenoptera: New pieces into the old jigsaw(fly) puzzle, *Cladistics.*, 31 (2015) 1–17.
- [40] Niu G., Budak M., Korkmaz E.M., Doğan Ö., Nel A., Wan S., Cai C., Jouault C., Li M., Wei M., Phylogenomic analyses of the Tenthredinoidea support the familial rank of Athaliidae (Insecta, Tenthredinoidea), *Insects.*, 13 (2022) 858

Acetylcholinesterase Inhibitor Activity of Some 5-Nitrothiophene-Thiazole Derivatives

Demokrat Nuha ^{1,2,3,a,*}, Asaf Evrim Evren ^{1,4,b}, Zennure Şevval Çiyancı ^{5,c}, Halide Edip Temel ^{5,d}, Gülşen Akalin Çiftçi ^{5,e}, Leyla Yurttaş ^{1,f}

¹ Department of Pharmaceutical Chemistry, Faculty of Pharmacy, Anadolu University, 26470, Eskişehir, Turkey.

² Department of Chemistry, Faculty of Science, Eskişehir Technical University, 26555, Eskişehir, Turkey.

³ Faculty of Pharmacy, University of Business and Technology, Prishtina, Kosovo.

⁴ Department of Pharmacy Services, Vocational School of Health Services, Bilecik Seyh Edebali University, 11000, Bilecik, Turkey.

⁵ Department of Biochemistry, Faculty of Pharmacy, Anadolu University, 26470, Eskişehir, Turkey.

*Corresponding author

Research Article

History

Received: 10/06/2022

Accepted: 28/09/2022

Copyright



©2022 Faculty of Science,
Sivas Cumhuriyet University

ABSTRACT

The potential anticholinesterase characteristics of some thiazole derivatives (2a–2j), including the 5-nitrothiophene moiety, were examined in this work. ¹H-NMR, ¹³C-NMR, and HRMS spectral data were used to determine the structure of the compounds. Using a modified Ellman's spectrophotometric approach, each compound was tested for its ability to inhibit acetylcholinesterase (AChE) and butyrylcholinesterase (BuChE) enzymes. It was determined that the compounds exhibited inhibition of between 33.66–47.96 % against AChE and 13.03–63.29 % against BuChE at 80 µg/mL concentration.

Keywords: Thiazole, Thiophene, Achetylcolinesteras inhibition, Galantamine.

^a demokratnuha@gmail.com

^b <https://orcid.org/0000-0002-7271-6791>

^c zsciyanci@anadolu.edu.tr

^d <https://orcid.org/0000-0002-2511-6689>

^e gakalin@anadolu.edu.tr

^f <https://orcid.org/0000-0001-9535-2508>

^b asafevrimvren@anadolu.edu.tr

^g <https://orcid.org/0000-0002-8651-826X>

^d heincedal@anadolu.edu.tr

^h <https://orcid.org/0000-0002-5233-1165>

^f lyurttas@anadolu.edu.tr

ⁱ <https://orcid.org/0000-0002-0957-6044>

Introduction

Alzheimer's Disease (AD), which belongs to the category of degenerative nervous system disorders, refers to the different difficulties that arise in the central nervous system, such as various behavioral abnormalities and cognitive regression problems [1]. Neurotransmitters are strongly linked to neurodegenerative illness, with cholinergic pathway dysfunction being one of the acknowledged causes of AD [2]. The number of people with Alzheimer's disease is expected to exceed 131 million by 2050 [3]. As a result, Alzheimer's disease has become one of the most pressing public health problems we face. Increasing cholinergic neurotransmission while decreasing ACh hydrolysis is the most effective therapy available right now for Alzheimer's disease [4]. Acetylcholinesterase (AChE) and butyryl cholinesterase (BuChE) are the cholinesterases that hydrolyze ACh, with AChE having a 10-fold higher hydrolytic activity than BuChE [5].

However, BuChE inhibitors may produce peripheral side effects since they are mostly found in peripheral systems such as plasma, liver, and muscle tissue [6]. Tacrine, for example, displayed significant hepatotoxicity and other peripheral adverse effects as a dual inhibitor of AChE and BuChE [7]. Accordingly, efficient and selective AChE inhibitors with low side effects are beneficial in the treatment of Alzheimer's disease and diminish peripheral cholinergic adverse effects [8]. Three medications have been licensed for usage in the United States (by the FDA): galantamine, donepezil, and rivastigmine, the mechanism

of which is to raise the quantity of acetylcholine at synapses by blocking acetylcholinesterase while they promote neurotransmission. Despite the fact that AChE inhibitors only provide symptomatic relief, they are still the first-line treatment for cognitive impairment, Alzheimer's disease, and Parkinson's disease [9]. As a result, researchers are still looking for AChE inhibitors to use in drug development [7].

The unique structure of the thiazole derivatives makes these compounds with high potential for biological activities. Thiazole derivatives shows numerous biological activities such as MAO inhibition [10], anticancer [11, 12], anticonvulsant [13], antidiabetic [14], antimicrobial [15–17], anti-inflammatory [18], analgesic [19]. The thiazole ring also has been reported to have anticholinesterase activity in many studies [10, 20–23]. Acotiamide hydrochloride is a thiazole-primarily based totally selective AChEI for the remedy of functional dyspepsia that was recently discovered (as a prokinetic drug) and has been applied therapeutically in Japan. Moreover, previous research has identified thiazolyldiazone derivatives as having potential for the therapy of neurodegenerative diseases. All of these factors suggest that the final compounds may have potential against AD. In fact, it was found that acetylcholinesterase (AChE) enzyme inhibition decreased cell growth in lung tumor cell lines in the literature [24–28]. Thus, it can be concluded that for antiproliferation activity, there is a link between mitochondrial potential loss and apoptosis.

According to the above information, we have designed and synthesized thiazole derivatives originated from 5-nitrothiophene and determined anticancer activity on lung cancer cell lines in our previous study [29]. This study is a continuation of our aforementioned study in which the anticholinesterase activities of the compounds were investigated.

Materials and Methods

Chemistry

Merck Chemicals (Merck KGaA, Darmstadt, Germany) and Sigma-Aldrich Chemicals provided all of the chemicals utilized in the syntheses (Sigma-Aldrich Corp., St. Louis, MO, USA). The reactions and thus the purity of the compounds was determined using thin-layer chromatography (TLC) on Merck's silica gel 60 F254 aluminum sheets (Darmstadt, Germany). The MP90 digital melting point equipment was used to get the uncorrected melting points of the produced compounds (Mettler Toledo, Ohio, USA). The $^1\text{H-NMR}$ and $^{13}\text{C-NMR}$ spectra in DMSO-*d*₆ were recorded using Bruker 300 MHz and 75 MHz digital FT-NMR spectrometers (Bruker Bioscience, Billerica, MA, USA). The following cleavage patterns were identified in the NMR spectra: s: singlet; d: doublet; t: triplet; m: multiplet. The coupling constants (*J*) are expressed in Hertz. An LC/MS-IT-TOF system was used to undertake high resolution mass spectrometric (HRMS) experiments (Shimadzu, Kyoto, Japan).

Synthesis of 2-[(5-nitrothiophen-2-yl)methylene]hydrazinecarbothioamide (1)

At room temperature, a solution of 4-nitrothiophene-2-carbaldehyde (4.17 g, 0.03 mol) in ethanol (50 mL) was treated with thiosemicarbazide (2.52 g, 0.03 mol). The reaction mixture was swirled for 2 hours at 80 °C. TLC was used to monitor the reaction. The precipitate was filtered out and rinsed with cold ethanol once the reaction was done.

m. p. 255–258 °C [30], yield 75%.

General synthesis of 2-thiazole derivatives (2a-2j)

In a solution of 2-[(5-nitrothiophen-2-yl)methylene]hydrazinecarbothioamide (1) (0.3 g, 1.30 mmol), 2-Bromo-1-phenylethanone derivatives (1.30 mmol) were added in ethanol (30 mL). At 80 °C, the mixture was stirred. TLC was used to monitor the reaction. The product was filtered when the reaction was finished. The final compounds were obtained by recrystallizing ethanol.

2-{2-[(5-Nitrothiophen-2-yl)methylene]hydrazinyl}-4-(*p*-tolyl)thiazole (2a)

m. p. 221–222 °C, yield 79 %, $^1\text{H-NMR}$ (300 MHz, DMSO-*d*₆, ppm) δ = 3.42 (s, 3H, -CH₃), 7.22 (d, *J* = 8.08 Hz, 1H, Ar-H), 7.40 (m, H, Ar-H), 7.54 (d, *J* = 4.41 Hz, H, Ar-H), 7.74 (d, *J* = 8.12 Hz, 1H, Ar-H), 8.06–8.10 (m, 2H, thiophene-H), 8.19 (s, 1H, thiazole-H), 8.47 (s, 1H, H-C=N), and 11.83 (brs, 1H, N-N-H). $^{13}\text{C-NMR}$ (75 MHz, DMSO-*d*₆, ppm) δ 21.27 (CH₃), 125.93, 128.19, 129.70, 130.92, 131.40, 135.71,

137.52, 147.23, 151.20, and 178.59 (S-C=N). HRMS (m/z): [M+H]⁺ calculated for C₁₅H₁₂N₄O₂S₂: 345.0474; found 345.0460.

4-(4-Nitrophenyl)-2-{2-[(5-nitrothiophen-2-yl)methylene]hydrazinyl}thiazole (2b)

m. p. 252–254 °C, yield 82%, $^1\text{H-NMR}$ (300 MHz, DMSO-*d*₆, ppm) δ = 7.42 (d, *J* = 4.34 Hz, 1H, Ar-H), 7.78 (s, 1H, thiazole-H), 8.05–8.09 (m, 3H, Ar-H), 8.18 (s, 1H, H-C=N), 8.25 (d, *J* = 8.83 Hz, 2H, thiophene-H), and 12.82 (brs, 1H, N-N-H). $^{13}\text{C-NMR}$ (75 MHz, DMSO-*d*₆, ppm) δ 110.22, 124.62, 126.83 (-CH=N), 128.49, 131.32, 135.24, 140.81, 146.76, 147.46, 149.21, 150.23, and 168.05 (S-C=N). HRMS (m/z): [M+H]⁺ calculated for C₁₄H₉N₅O₄S₂: 376.0169; found 376.0172.

2-{2-[(5-Nitrothiophen-2-yl)methylene]hydrazinyl}-4-phenylthiazole (2c)

m. p. 209–210 °C, yield 75%, $^1\text{H-NMR}$ (300 MHz, DMSO-*d*₆, ppm) δ = 7.31 (d, *J* = 7.19 Hz, 1H, Ar-H), 7.37–7.40 (m, 3H, Ar-H), 7.42 (s, 1H, thiazole-H) 7.84 (d, *J* = 8.17Hz, 2H, thiophene-H), 8.03 (dd, *J*₁ = 1.44Hz, *J*₂ = 4.32 Hz, 1H, Ar-H), 8.16 (s, 1H, H-C=N), and 12.75 (brs, 1H, N-N-H). $^{13}\text{C-NMR}$ (75 MHz, DMSO-*d*₆, ppm) δ 105.29, 125.97 (-CH=N), 128.05, 128.15, 129.09, 131.23, 134.68, 147.80, 150.02, 151.01, and 167.69 (S-C=N). HRMS (m/z): [M+1]⁺ calculated for C₁₄H₁₀N₄O₂S₂: 331.0318; found 331.0310.

4-{2-2-[(5-Nitrothiophen-2-yl)methylene]hydrazinyl}thiazol-4-yl} benzonitrile (2d)

m. p. 249–251 °C, yield 81%, $^1\text{H-NMR}$ (300 MHz, DMSO-*d*₆, ppm) δ = 7.47 (d, *J* = 4.43 Hz, 1H, Ar-H), 7.76 (s, 1H, thiazole-H), 7.88 (d, *J* = 8.54 Hz, 2H, Ar-H), 8.03 (d, *J* = 8.50Hz, 2H, thiophene-H), 8.10 (d, *J* = 4.37 Hz, 1H, Ar-H), 8.22 (s, 1H, H-C=N), and 12.83 (brs, 1H, N-N-H). $^{13}\text{C-NMR}$ (75 MHz, DMSO-*d*₆, ppm) δ 109.29, 110.24, 119.42 (-CN), 126.60 (-CH=N), 128.49, 131.36, 133.24, 135.19, 138.94, 147.49, and 167.95 (S-C=N). HRMS (m/z): [M+1]⁺ calculated for C₁₅H₉N₅O₂S₂: 356.0270; found 356.0272.

4-(4-Fluorophenyl)-2-{2-[(5-nitrothiophen-2-yl)methylene]hydrazinyl}thiazole (2e)

m. p. 218–221 °C, yield 76 %, $^1\text{H-NMR}$ (300 MHz, DMSO-*d*₆, ppm) δ = 7.25 (t, *J* = 8.91 Hz, 2H, Ar-H), 7.42–7.46 (m, 2H, Ar-H), 7.87–7.91 (m, 2H, Ar-H), 8.10 (d, *J* = 4.86 Hz, 1H, Ar-H), 8.20 (s, 1H, H-C=N), and 12.77 (brs, 1H, N-N-H). $^{13}\text{C-NMR}$ (75 MHz, DMSO-*d*₆, ppm) 105.21, 115.85, 116.14, 127.94 (-CH=N), 128.05, 128.27, 131.37, 134.84, 147.70, 150.08, 160.53, and 163.77 (S-C=N). HRMS (m/z): [M+1]⁺ calculated for C₁₄H₉FN₄O₂S₂: 349.0224; found 349.0229.

2-{2-[(5-Nitrothiophen-2-yl)methylene]hydrazinyl}-4-(pyridin-4-yl)thiazole (2f)

m. p. 278–279 °C, yield 84 %, $^1\text{H-NMR}$ (300 MHz, DMSO-*d*₆, ppm) δ = 7.50 (d, *J* = 4.44 Hz, 1H, Pyridine-H), 8.11 (d, *J* = 4.35 Hz, 1H, pyridine-H), 8.27 (s, 1H, thiazole-H), 8.34 (d, *J* = 6.76 Hz, 2H, thiophene-H), 8.37 (s, 1H, H-C=N), 8.90 (d, *J* = 6.80 Hz, 2H, pyridine-H), and 12.99 (brs, 1H, N-N-H). $^{13}\text{C-NMR}$ (75 MHz, DMSO-*d*₆, ppm) δ 117.12, 122.45, 128.93 (-CH=N), 131.34, 136.09, 143.32, 146.64, 147.10, 148.74, 150.46, and 168.67 (S-C=N). HRMS (m/z): [M+1]⁺ calculated for C₁₃H₉N₅O₂S₂: 332.0270; found 332.0272.

4-(Naphthalen-2-yl)-2-{2-[(5-nitrothiophen-2-yl)methylene]hydrazinyl}thiazole (2g)

m. p. 216–217 °C, yield 80%, ¹HNMR (300 MHz, DMSO-d₆, ppm) δ = 7.43–7.56 (m, 4H, Ar-H), 7.92–8.06 (m, 6H, Ar-H), 8.21 (s, 1H, H-C=N), and 8.37 (brs, 1H, N-N-H). ¹³C-NMR (75 MHz, DMSO-d₆, ppm) δ 106.01, 124.29, 124.62, 126.49 (-CH=N), 126.88, 128, 128.59, 131.09, 132.12, 132.91, 133.54, 134.72, 147.75, 150.01, 150.79, and 167.74 (S-C=N). HRMS (m/z): [M+1]⁺ calculated for C₁₈H₁₂N₄O₂S₂: 381.0474; found 381.0471.

4-(Naphthalen-1-yl)-2-{2-[(5-nitrothiophen-2-yl)methylene]hydrazinyl}thiazole (2h)

m. p. 226–227 °C, yield 77%, ¹HNMR (300 MHz, DMSO-d₆, ppm) δ = 7.20 (s, 1H, thiazole-H), 7.45 (d, *J* = 4.42 Hz, 1H, thiophene-H), 7.52–7.57 (m, 3H, naphthalene-H), 7.68–7.71 (m, 1H, naphthalene-H), 7.94–7.99 (m, 2H, naphthalene-H), 8.09 (d, *J* = 4.36 Hz, 1H, thiophene-H), 8.22 (s, 1H, H-C=N), 8.39–8.42 (m, 1H, naphthalene-H), and 12.81 (brs, 1H, N-N-H). ¹³C-NMR (75 MHz, DMSO-d₆, ppm) δ 108.95, 125.94 (-CH=N), 126.43, 126.66, 127.43, 128.15, 128.73, 128.92, 131.02, 131.36, 133.09, 133.95, 134.83, 147.87, 150.03, and 167.51 (S-C=N). HRMS (m/z): [M+1]⁺ calculated for C₁₈H₁₂N₄O₂S₂: 381.0474; found 381.0485.

4-(2,5-Dimethoxyphenyl)-2-{2-[(5-nitrothiophen-2-yl)methylene]hydrazinyl}thiazole (2i)

m. p. 217–218 °C, yield 71%, ¹HNMR (300 MHz, DMSO-d₆, ppm) δ = 3.73 (s, 3H, -OCH₃), 3.85 (s, 3H, -OCH₃), 6.84 (d, *J* = 3.21 Hz, 1H, Ar-H), 6.87 (d, *J* = 3.21 Hz, 1H, Ar-H), 7.02–7.05 (m, 1H, Ar-H), 7.42–7.45 (m, 1H, N-N-H), 7.50 (s, 1H, thiazole-H), 7.58 (d, *J* = 3.19 Hz, 1H, thiophene-H), 8.07–8.09 (m, 1H, thiophene-H), and 8.19 (s, 1H, H-C=N). ¹³C-NMR (75 MHz, DMSO-d₆, ppm) δ 55.79 (CH₃), 56.28 (CH₃), 109.74, 113.20, 114.25, 116.69, 123.40, 128.13 (-CH=N), 131.35, 134.69, 147.84, 151.35, 153.37, and 166.09 (S-C=N). HRMS (m/z): [M+1]⁺ calculated for C₁₆H₁₄N₄O₄S₂: 391.0529; found 391.0532.

4-(4-Methoxyphenyl)-2-{2-[(5-nitrothiophen-2-yl)methylene]hydrazinyl}thiazole (2j)

m. p. 214–215 °C, yield 89%, ¹HNMR (300 MHz, DMSO-d₆, ppm) δ = 3.78 (s, 3H, -OCH₃), 6.95–6.98 (m, 2H, Ar-H),

7.24 (s, 1H, thiazole-H), 7.42 (s, 1H, H-C=N), 7.77 (d, *J* = 3.88 Hz, 2H, Ar-H), 8.07 (d, *J* = 4.25 Hz, 1H, thiophene-H), 8.17 (d, *J* = 1.82 Hz, 1H, thiophene-H), and 12.72 (brs, 1H, N-N-H). ¹³C-NMR (75 MHz, DMSO-d₆, ppm) δ 55.58 (CH₃), 103.18, 114.46, 127.32 (-CH=N), 127.64, 128.10, 131.35, 134.62, 147.85, 149.98, 159.36, and 167.56 (S-C=N). HRMS (m/z): [M+1]⁺ calculated for C₁₅H₁₂N₄O₃S₂: 361.0424; found 361.0428.

AChE/BuChE Inhibition Assay

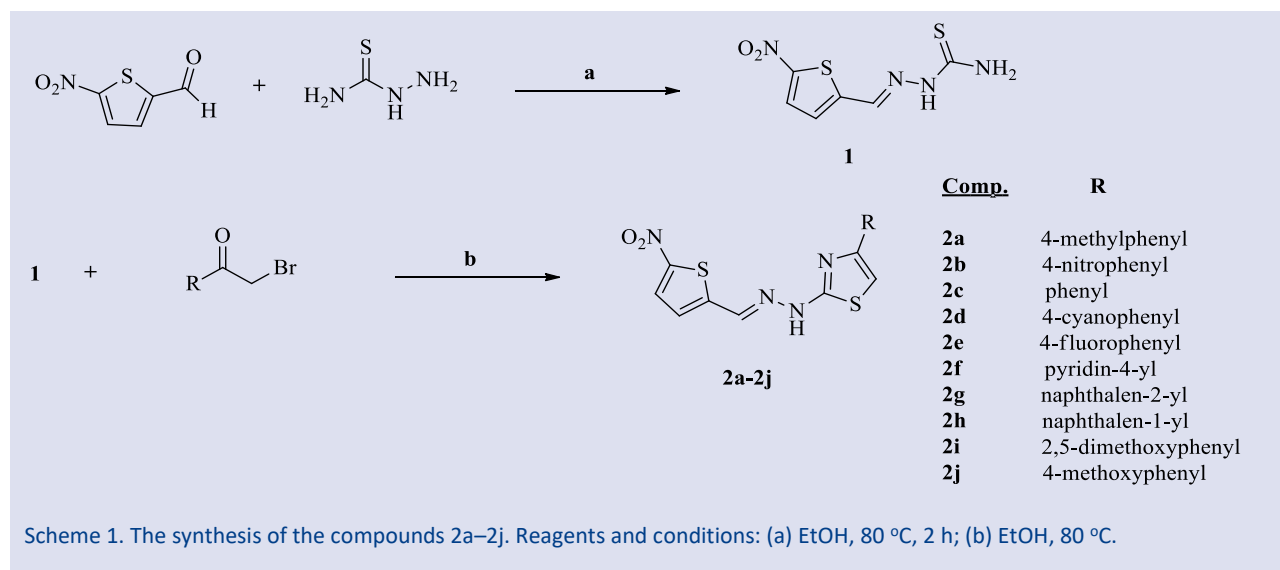
The inhibitory effects of title compounds on AChE/BuChE were studied using Ellman's approach[31], which was slightly modified. The reagents and materials used in the enzyme inhibition assay were supplied commercially by Sigma-Aldrich (St. Louis, MO, USA) and Fluka (Steinheim, Germany). A 10 L solution of studied compounds dissolved in 2 % dimethyl sulfoxide (DMSO, dilute with water) at final concentrations of 5, 10, 20, 40, and 80 g/mL, as well as a 20 L (1 unit/mL) solution of AChE, received a 2.4 mL 0.1 M phosphate buffer (from *Electrophorus electricus*, electric eel). After 15 minutes, the mixture was added to with 50 L of 0.01 M 5,5-dithio-bis(2-nitrobenzoic) acid (DTNB) and 20 L of 75 mM acetylthiocholine iodide (ATCI) or 25 mM butyrylthiocholine iodide (BTCl). Using polystyrol cuvettes and a spectrophotometer, the absorbance at 412 nm and 37 °C was measured after 30 minutes at room temperature (Shimadzu, UV-1700).

$$I (\%) = 100 - (\text{OD}_{\text{sample}} / \text{OD}_{\text{control}}) \times 100$$

Results and Discussion

Chemistry

The synthetic protocol of compounds 2a–2j was represented in Scheme 1 [29].



The core structures of ten compounds with the 2-2-[(5-nitrothiophen-2-yl)methylene]hydrazinylthiazole nucleus were synthesized in this work. To make 2-[(5-nitrothiophen-2-yl)methylene]hydrazinocarbothio-amide (1), the first stage involved reacting 5-nitrothiophene-2-carbaldehyde and thiosemicarbazide for 2 hours at 80 °C. Compound 1 and 2-bromo-1-phenylethanone derivatives were then reacted in ethanol to yield 2-2-[(5-nitrothiophen-2-yl)methylene]hydrazinylthiazole derivatives (2a–2j), as shown in Scheme 1 [29]. The structures of produced compounds (2a–2j) were verified using ¹H-NMR, ¹³C-NMR, and high-resolution mass spectroscopy (HRMS). Peaks were seen in the aromatic and aliphatic regions of the ¹H-NMR spectra. The peaks in the ¹³C-NMR spectra were evident in the expected aromatic and aliphatic regions. The peaks in the mass spectra (ESI-MS) of the compounds [M+1] corresponded to their predicted chemical formula (2a–2j).

In this study, we synthesized ten compounds with the 2-2-[(5-nitrothiophen-2-yl)methylene]hydrazinylthiazole nucleus in their core structures. The first stage included reacting 5-nitrothiophene-2-carbaldehyde and thiosemicarbazide for 2 hours at 80 °C to produce 2-[(5-nitrothiophen-2-yl)methylene]hydrazinocarbothio-amide (1) [32]. Then, as illustrated in Scheme 1, compound 1 and 2-bromo-1-phenylethanone derivatives were reacted in ethanol to provide the end products: 2-2-[(5-nitrothiophen-2-yl)methylene]hydrazinylthiazole derivatives (2a–2j). All of the generated substances were characterized using analytical and spectroscopic data. Compound ¹H-NMR spectra revealed doublets at δ 7.45–8.34 ppm for thiophene protons. The thiazole proton was detected as a singlet peak at δ 7.20–8.27 ppm. Azomethine proton (H-C=N) was detected as a singlet peak at δ 7.42–8.47 ppm. A broad singlet signal at δ 11.83–12.99 ppm identified the acetamide N–H proton. The aromatic protons of the aromatic rings caused the appearance of a pair of singlets, doublets, triplets, and/or multiplets at δ 6.84–8.10 ppm. Compound ¹³C-NMR spectra revealed signals at δ 125.94–128.93 ppm for methylene proton (H-C=N) carbon and δ 103.18–178.59 ppm for aromatic. The calculated molecular weights of the target compounds (2a–2j) matched the M \pm 1 peaks in the LC-MS/MS spectra.

Anticholinesterase Activity

To assess anticholinesterase activity, all ten compounds (2a–2j) were tested on the enzymes AChE and BuChE. In a previous study, blocking acetylcholinesterase (AChE) reduced cell proliferation in lung carcinoma cell lines [24-28]. It has also been observed that antiproliferation is associated with mitochondrial potential loss and apoptosis. Table 4 shows the inhibition percentages for the substances investigated at 80 μ g/mL concentration. At the studied concentrations, chemicals 2e, 2f, 2g, 2h, and 2j did not inhibit AChE. The inhibition percentages for AChE for compounds 2a, 2b, 2c, 2d, and 2i ranged from 33.66 % to 47.96 %, with compounds 2b and 2d inhibiting the enzyme the most. On the BuChE

enzyme, the inhibition percentages ranged from 13.03 % to 63.29 %. Compounds 2i and 2h inhibited BuChE the most, with 63.29 and 53.73 %, respectively, whereas compounds 2b and 2e inhibited it by more than 40 %.

Table 4. % AChE and BuChE enzyme inhibition percentages

Compounds	AChE%	BuChE%
2a	33.76 \pm 1.3	33.64 \pm 1.1
2b	45.71 \pm 1.5	41.08 \pm 1.5
2c	41.70 \pm 1.4	23.46 \pm 1.5
2d	47.96 \pm 1.0	23.09 \pm 1.2
2e	---	44.40 \pm 1.7
2f	---	13.96 \pm 1.6
2g	---	13.03 \pm 0.3
2h	---	53.73 \pm 1.3
2i	33.66 \pm 1.3	63.29 \pm 1.0
2j	---	---
Galantamin (IC ₅₀)	0.44 \pm 0.06	6.92 \pm 1.84

SAR for AChE and BChE inhibition

At the case of AChE inhibition, di-substitution of the phenyl ring with methoxy groups in the *ortho*-positions resulted in a significant drop-in inhibitory activity, as shown in compound 2i. Mono-substitution with a methyl group at the *para*-position of the phenyl ring reduced activity as well (compound 2a). The inhibitory action was boosted by adding to the phenyl ring highly electronegative species such as nitro (compound 2b) or cyano (compound 2d) group at the *para*-position.

In the case of BChE inhibition, naphthalene or pyridine resulted in a significant reduction in inhibitory activity, as shown in 2g and 2f, respectively. Mono-substitution with a methyl or cyano group at the *para*-position of the phenyl ring reduced activity as well (compound 2a and 2d, respectively). The highest inhibitory action was obtained by adding highly electronegative species on the phenyl ring, such as nitro group (compound 2b), fluoro group (compound 2e), and dimethoxy at *ortho* positions (compound 2i).

Conclusions

2-2-[(5-nitrothiophen-2-yl)methylene]hydrazinylthiazole derivatives (2a–2j) were synthesized and tested in vitro for their inhibitory effects on AChE and BuChE. The structures of the novel compounds were determined using spectroscopic methods such as ¹H-NMR, ¹³C-NMR, and high-resolution mass spectroscopy (HRMS). On AChE, the inhibition percentages ranged between 33.66%–47.96%, from where 4-cyanophenyl-substituted compound 2d was the most efficient AChE inhibitor (47.96 \pm 1.07%). On BuChE, the inhibition percentages ranged between 13.03%–63.29%, from where 2,5-dimethoxyphenyl-substituted compound 2i was the most effective BuChE inhibitor (63.29 \pm 1.01%).

Acknowledgments

The authors express their gratitude to the Anadolu University's DOPNA laboratory, Anadolu University and Scientific Research Projects.

Conflicts of Interest

The authors declare no conflict of interest.

Reference

- [1] Vaz M., Silvestre S., Alzheimer's disease: Recent treatment strategies, *Eur. J. Pharmacol.*, 887 (2020) 173554.
- [2] Bateman R.M., Glacial progress: do we finally understand the narrow-leaved marsh-orchids?, *New Journal of Botany*, 1(1) (2013) 2-15.
- [3] Zhou B., Li D., Cui J., Li D., Geng H., Gao J., Zhou B., Simple analogues of natural product chelerythrine: Discovery of a novel anticholinesterase 2-phenylisoquinolin-2-ium scaffold with excellent potency against acetylcholinesterase, *European Journal of Medicinal Chemistry*, 200 (2020) 1-11.
- [4] Zhao S., Xu J., Zhang H., Han C.K., Wu J., Li D., Hu C.J. (2021). Multivalent butyrylcholinesterase inhibitor discovered by exploiting dynamic combinatorial chemistry. *Bioorganic Chemistry*, 108, 104656.
- [5] Sun J., Wang H., Lei Z., Yue S., Chen J., Sun J., Development of 5-hydroxyl-1-azabenzanthrone derivatives as dual binding site and selective acetylcholinesterase inhibitors, *European Journal of Medicinal Chemistry*, 234 (2022) 114210.
- [6] Mao F., Wang H., Ni W., Zheng X., Wang M., Bao K., Ling D., Li X., Xu Y., Zhang H., Design, synthesis, and biological evaluation of orally available first-generation dual-target selective inhibitors of acetylcholinesterase (AChE) and phosphodiesterase 5 (PDE5) for the treatment of Alzheimer's disease, *ACS Chemical Neuroscience*, 9(2) (2018) 328-345.
- [7] Kurt B.Z., Gazioglu I., Basile L., Sonmez F., Ginex T., Kucukislamoglu M., Guccione S., Potential of aryl-urea-benzofuranylthiazoles hybrids as multitasking agents in Alzheimer's disease, *European Journal of Medicinal Chemistry*, 102 (2015) 80-92.
- [8] Romero A., Cacabelos R., Oset-Gasque M.J., Samadi A., Marco-Contelles J., Novel tacrine-related drugs as potential candidates for the treatment of Alzheimer's disease, *Bioorganic & Medicinal Chemistry Letters*, 23(7) (2013) 1916-1922.
- [9] Kandiah N., Pai M.-C., Senanarong V., Looi I., Ampil E., Park K.W., Karanam A.K., Christopher S., Rivastigmine: the advantages of dual inhibition of acetylcholinesterase and butyrylcholinesterase and its role in subcortical vascular dementia and Parkinson's disease dementia, *Clinical Interventions in Aging*, 12 (2017) 697.
- [10] Evren A.E., Nuha D., Dawbaa S., Saglik B.N., Yurttas L., Synthesis of novel thiazolyl hydrazone derivatives as potent dual monoamine oxidase-aromatase inhibitors, *Eur. J. Med. Chem.*, 229 (2022) 114097.
- [11] Sabry M.A., Ghaly M.A., Maarouf A.R., El-Subbagh H.I., New thiazole-based derivatives as EGFR/HER2 and DHFR inhibitors: Synthesis, molecular modeling simulations and anticancer activity, *Eur. J. Med. Chem.*, 241 (2022) 114661.
- [12] Nuha D., Evren A.E., Ciyanci Z.S., Temel H.E., Akalin Ciftci G., Yurttas L., Synthesis, density functional theory calculation, molecular docking studies, and evaluation of novel 5-nitrothiophene derivatives for anticancer activity, *Arch Pharm (Weinheim)*, e2200105 (2022).
- [13] Fayed E.A., Ragab A., Ezz Eldin R.R., Bayoumi A.H., Ammar Y.A., In vivo screening and toxicity studies of indolinone incorporated thiosemicarbazone, thiazole and piperidinosulfonyl moieties as anticonvulsant agents, *Bioorg. Chem.*, 116 (2021) 105300.
- [14] Paudel Y.N., Ali M.R., Shah S., Adil M., Akhtar M.S., Wadhwa R., Bawa S., Sharma M., 2-[(4-Chlorobenzyl) amino]-4-methyl-1,3-thiazole-5-carboxylic acid exhibits antidiabetic potential and raises insulin sensitivity via amelioration of oxidative enzymes and inflammatory cytokines in streptozotocin-induced diabetic rats, *Biomed. Pharmacother.*, 89 (2017) 651-659.
- [15] Nuha D., Evren A.E., Kapusiz Ö., ÜlküyeDudu G., Gundogdu-Karaburun N., Karaburun A.Ç., Berber H., Design, synthesis, and antimicrobial activity of novel coumarin derivatives: An in-silico and in-vitro study, *J. Mol. Struct.*, (2022) 134166.
- [16] Evren A.E., Dawbaa S., Nuha D., Yavuz Ş.A., Gül Ü.D., Yurttaş L., Design and synthesis of new 4-methylthiazole derivatives: In vitro and in silico studies of antimicrobial activity, *J. Mol. Struct.*, 1241 (2021) 130692.
- [17] Nuha D., Evren A.E., Yılmaz Cankılıç M., Yurttaş L., Design and synthesis of novel 2,4,5-thiazole derivatives as 6-APA mimics and antimicrobial activity evaluation, *Phosphorus Sulfur Silicon Relat Elem.*, 196(10) (2021) 954-960.
- [18] Modrić M., Božičević M., Farahó I., Bosnar M., Škorić I., Design, synthesis and biological evaluation of new 1,3-thiazole derivatives as potential anti-inflammatory agents, *J. Mol. Struct.*, 1239 (2021) 130526.
- [19] Kumar G., Singh N.P., Synthesis, anti-inflammatory and analgesic evaluation of thiazole/oxazole substituted benzothiazole derivatives, *Bioorg. Chem.*, 107 (2021) 104608.
- [20] Ghotbi G., Mahdavi M., Najafi Z., Moghadam F.H., Hamzeh-Mivehroud M., Davaran S., Dastmalchi S., Design, synthesis, biological evaluation, and docking study of novel dual-acting thiazole-pyridiniums inhibiting acetylcholinesterase and β -amyloid aggregation for Alzheimer's disease, *Bioorganic Chemistry*, 103 (2020) 104186.
- [21] Haroon M., Khalid M., Shahzadi K., Akhtar T., Saba S., Rafique J., Ali S., Irfan M., Alam M.M., Imran M., Alkyl 2-(2-(arylidene) alkylhydrazinyl) thiazole-4-carboxylates: Synthesis, acetyl cholinesterase inhibition and docking studies, *Journal of Molecular Structure*, 1245 (2021) 131063.
- [22] Sahin Z., Ertas M., Bender C., Bülbül E.F., Berk B., Biltekin S.N., Yurttaş L., Demirayak Ş., Thiazole-substituted benzoylpiperazine derivatives as acetylcholinesterase inhibitors, *Drug Development Research*, 79(8) (2018) 406-425.
- [23] Yurttaş L., Kaplancıklı Z.A., Özkay Y., Design, synthesis and evaluation of new thiazole-piperazines as acetylcholinesterase inhibitors, *Journal of Enzyme Inhibition and Medicinal Chemistry*, 28 (5) (2013) 1040-1047.
- [24] Karpel R., Aziz-Aloya R.B., Sternfeld M., Ehrlich G., Ginzberg D., Tarroni P., Clementi F., Zakut H., Soreq H., Expression of three alternative acetylcholinesterase messenger RNAs in human tumor cell lines of different

- tissue origins, *Experimental cell research*, 210(2) (1994). 268-277.
- [25] Perez-Aguilar B., Vidal C.J., Palomec G., Garcia-Dolores F., Gutierrez-Ruiz M.C., Bucio L., Gomez-Olivares J.L., Gomez-Quiroz L.E., Acetylcholinesterase is associated with a decrease in cell proliferation of hepatocellular carcinoma cells, *Biochimica et Biophysica Acta*, 1852(7) (2015) 1380-1387.
- [26] Richbart S.D., Merritt J.C., Nolan N.A., Dasgupta P., Acetylcholinesterase and human cancers, *Advances in Cancer Research*, 152 (2021) 1-66.
- [27] Xi H.J., Wu R.P., Liu J.J., Zhang L.J., Li Z.S., Role of acetylcholinesterase in lung cancer, *Thoracic Cancer*, 6(4) (2015) 390-398.
- [28] Cheng K., Samimi R., Xie G., Shant J., Drachenberg C., Wade M., Davis R.J., Nomikos G., Raufman J.-P., Acetylcholine release by human colon cancer cells mediates autocrine stimulation of cell proliferation, *American Journal of Physiology-Gastrointestinal and Liver Physiology*, 295(3) (2008) G591-G597.
- [29] Nuha D., Evren A.E., Çiyancı Z.Ş., Temel H.E., Akalin Çiftçi G., Yurttaş L., Synthesis, density functional theory calculation, molecular docking studies, and evaluation of novel 5-nitrothiophene derivatives for anticancer activity, *Archiv der Pharmazie*, (2022) e2200105.
- [30] Arif R., Rana M., Yasmeen S., Amaduddin Khan M.S., Abid M., Khan M.S., Rahisuddin, Facile synthesis of chalcone derivatives as antibacterial agents: Synthesis, DNA binding, molecular docking, DFT and antioxidant studies, *Journal of Molecular Structure*, (2020) 1208
- [31] Ellman G.L., Courtney K.D., Andres Jr V., Featherstone R.M., A new and rapid colorimetric determination of acetylcholinesterase activity, *Biochemical Pharmacology*, 7(2) (1961) 88-95.
- [32] Chauviere G., Bouteille B., Enanga B., Albuquerque C.D., Croft S.L., Dumas M., Perie J., Synthesis and Biological Activity of Nitro Heterocycles Analogous to Megazol, a Trypanocidal Lead, *Journal of Medicinal Chemistry*, 46 (2003) 427-440.

Design and Synthesis of Imidazole Derivatives as Anticancer Agents and Potential Aromatase Inhibitors

Hayrani Eren Bostancı^{1,a}, Ulviye Acar Çevik^{2,b}

¹ Department of Biochemistry, Faculty of Pharmacy, Sivas Cumhuriyet University, Sivas, Türkiye

² Department of Pharmaceutical Chemistry, Faculty of Pharmacy, Anadolu University, Eskişehir 26470, Türkiye

*Corresponding author

Research Article

History

Received: 15/06/2021

Accepted: 28/09/2022

Copyright



©2022 Faculty of Science,
Sivas Cumhuriyet University

ABSTRACT

In this study, imidazole derivative compounds were synthesized using the Debus-Radziszewski method. The chemical structures of the compounds were characterized by spectroscopic methods. The effects of target compounds on MCF7 (CRL-3435) were examined and their IC₅₀ values and percent viability were calculated. In addition, the cytotoxic effects on the L929 (CCL-1) normal cell line were evaluated in order to determine the selectivities of the compounds. Then, the inhibition values of aromatase enzyme of the compounds were calculated and compared to the reference compound. When the results were examined, it was observed that Compound 1a caused the death of breast cancer cells, although not as much as cisplatin, but did not harm healthy cells. In this respect, it was determined that compound 1a has a promising anticancer effect as an aromatase inhibitor.

Keywords: Imidazole, MTT, Anticancer, Aromatase.

erenbostanci@hotmail.com

<https://orcid.org/0000-0001-8511-2316>

uacar@anadolu.edu.tr

<https://orcid.org/0000-0003-1879-1034>

Introduction

Breast cancer is one of the most common types of cancer in our country and around the world [1]. Especially in postmenopausal women, the risk of breast cancer increases due to estrogen secretion in peripheral tissues [2]. Aromatase is a catalytic enzyme involved in the manufacture of estrogen from androgen. It catalyzes the last rate-limiting/crucial/key step in estrogen biosynthesis [3,4]. Figure 1. demonstrates the action and role of the aromatase enzyme.

According to their methods of action, aromatase inhibitors (AIs) can be divided into two classes. The steroidal AIs, such as exemestane and formestane (Figure 2), suppress the aromatase enzyme activity irreversibly. Nonsteroidal AIs, such as letrozole, vorozole, and anastrozole, are the second group of AIs that inhibit aromatase activity and have reversible inhibitory effects [5, 10].

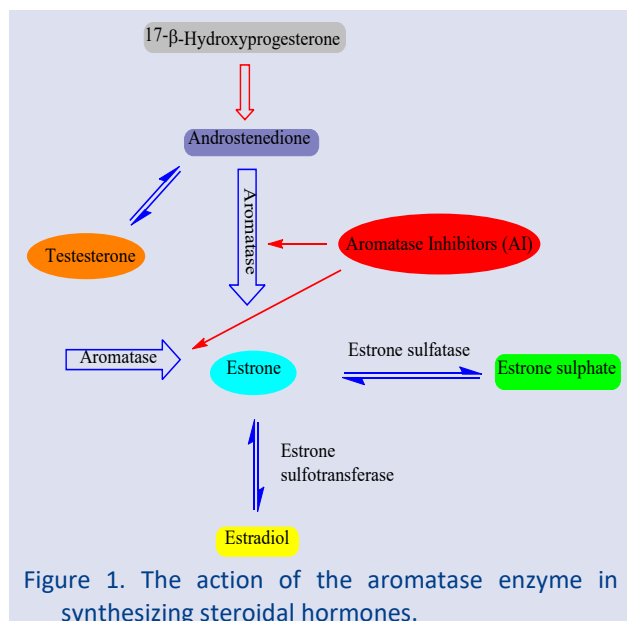


Figure 1. The action of the aromatase enzyme in synthesizing steroidal hormones.

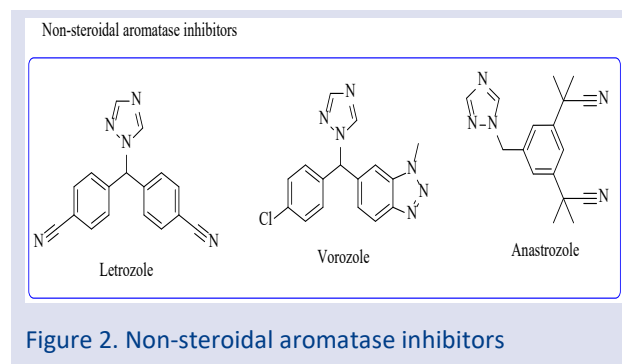


Figure 2. Non-steroidal aromatase inhibitors

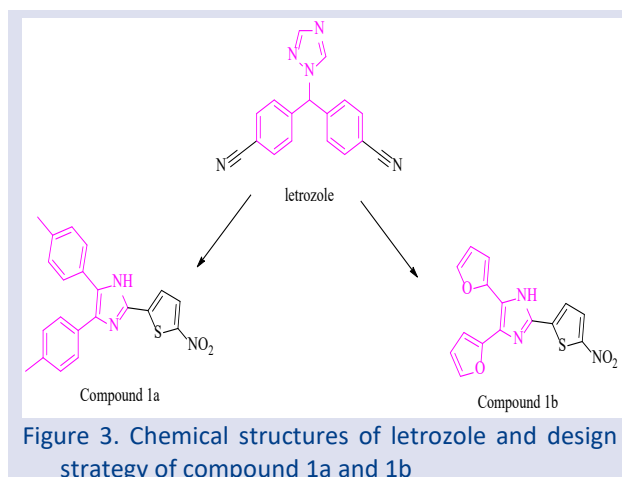
Based on their clinical development order, AIs are categorized into four generations: first, second, third, and fourth generation AIs. Third generation aromatase inhibitors such as letrozole and anastrozole are the most preferred inhibitors because of their low toxicity, selectivity and effectiveness. Third-generation inhibitors,

which provide an outstanding therapeutic benefit, show almost complete specificity in practice [6].

Heterocyclic rings containing nitrogen atoms can form an ionic bond with the iron part of hemoglobin and thus perform a very important function by suppressing the aromatase enzyme (HES). In addition to the contribution of the heterocyclic nitrogen atom to the activity, the presence of hydrogen bond acceptors in these structures is an important feature in terms of providing interactions in bonding algebra [7,8].

Nitrogen-containing heterocyclic rings are actively researched in the field of drug discovery, particularly in cancer research [9]. As possibly nonsteroidal AIs, triazole and imidazole rings are employed. The heterocyclic nitrogen atom of triazole and imidazole is significant because it coordinates the aromatase enzyme's heme iron. Some imidazole and triazole compounds have been produced and tested as antiaromatase drugs in the past [11-15].

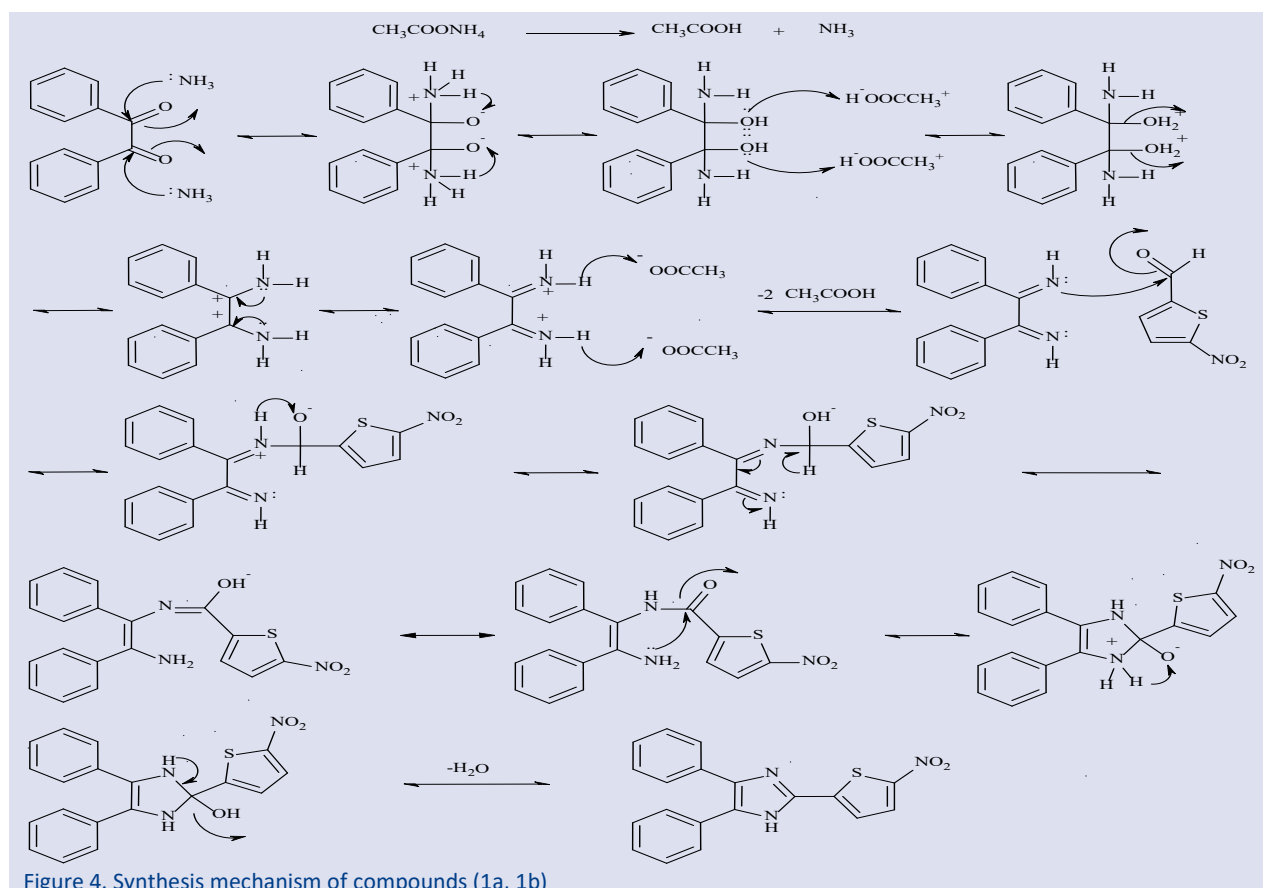
New imidazole derivative compounds with a structure comparable to letrozole were created in this work. The imidazole ring is employed instead of the triazole structure, and the imidazole ring is given an additional heteroaromatic group (Figure 3.). All final chemicals created on MCF7 (CRL-3435) breast cancer cells were tested for cell viability and cytotoxicity using the MTT assay. The aromatase inhibition potentials of the compounds were evaluated in a fluorimetric *in vitro* assay.



Materials and Methods

Chemistry

4,5-Disubstituted-2-(5-nitrothiophen-2-yl)-1H-imidazole (1a-1b): The mixture of benzyl derivative compound (4,4'-dimethylbenzyl (97 %) and α -furyl (98 %) (0.02 mol) and thiophene aldehyde (98 %) derivative compound (0.02 mol), ammonium acetate (> 98 %) (0.12 mol) and 10 mL acetic acid (> 99 %) is boiled under reflux for 3 hours with stirring. The product is precipitated by pouring the mixture into ice water. The raw product is washed with plenty of water and dried. The product is crystallized from aqueous ethanol. The synthesis mechanism of the compounds is given in Figure 4.



4,5-Bis(4-methylphenyl)-2-(5-nitrothiophen-2-yl)-1*H*-imidazole (1a); Yield: 77 %. ¹H NMR (500 MHz, DMSO-*d*₆): δ: 2.30 (3H, s, CH₃), 2.36 (3H, s, CH₃), 7.13 (2H, d, 5.76 Hz, Aromatic CH), 7.27 (2H, d, 5.79 Hz, Aromatic CH), 7.38-7.45 (4H, m, Aromatic CH), 7.68-7.69 (1H, m, Thiophen CH), 8.17-8.18 (1H, m, Thiophen CH), 12.60 (1H, s, NH). ¹³C NMR (125 MHz, DMSO-*d*₆): δ: 21.34, 21.51, 123.49, 124.94, 127.57, 128.66, 129.39, 129.84, 130.09, 130.51, 131.93, 139.41, 142.11. HRMS (m/z): [M+H]⁺ calcd for C₂₁H₁₇N₃O₂S 376.1114; found: 376.1110.

4,5-Di(furan-2-yl)-2-(5-nitrothiophen-2-yl)-1*H*-imidazole (1b); Yield: 78 %. ¹H NMR (500 MHz, DMSO-*d*₆): δ: 6.85-6.86 (2H, m, Furan CH), 7.67-7.68 (2H, m, Furan CH), 7.76-7.80 (1H, m, Furan CH), 8.12-8.16 (1H, m, Furan CH), 8.25 (2H, s, Thiophen CH), 12.50 (1H, s, NH). ¹³C NMR (125 MHz, DMSO-*d*₆): δ: 107.60, 108.75, 114.05, 118.27, 120.04, 125.32, 126.71, 131.05, 131.55, 149.10, 151.39. HRMS (m/z): [M+H]⁺ calcd for C₁₅H₉N₃O₄S 328.0334; found: 328.0640.

Anticancer Activity

The anticancer activities of compounds 1a and 1b were determined by the absorbance values obtained from MTT assays. The MTT method was performed as previously described [16]. The cells were seeded at a density of 1×10^4 cells/well and treated with different concentrations between 2-100 μM for each and incubated for 48 h. Untreated cells were used as control. Following incubation, the cells were treated with 20 μL of MTT solution (5 mg/mL in PBS, Sigma) and incubated at 37 °C for 3 h to let the metabolically active cells reduce MTT dye into formazan crystals. The formazan crystals were dissolved in DMSO (Sigma). The reduction of MTT was quantified by measuring the absorbance at 540 nm with a microplate reader (Thermo, Germany). Data were represented as mean ± standard deviation (± SD). The results obtained were evaluated with the MCF-7 breast cancer cell line versus the L929 (CCL-1) normal fibroblast cell line. In this section, cisplatin was used as a reference drug in cell lines.

Aromatase Inhibition Assay

This method was carried out according to the kit procedure (BioVision, Aromatase (CYP19A) Inhibitor Screening Kit (Fluorometric)). The compounds were dissolved in DMSO and added to the assay in at least 8 concentrations ranging from 1000 μM to 7.81 μM. Recombinant Human Aromatase stock was prepared by reconstituting with 1 ml of Aromatase Assay Buffer. The contents were mixed thoroughly by vortexing to obtain a homogeneous solution and transferred the solution to a 15 ml conical tube. The volume was brought to 2450 μl with Aromatase Assay Buffer and 50 μl of NADPH Production System (100X) was added for a final total volume of 2.5 ml. Letrozole was used as a positive inhibition control. For solvent control, a small aliquot of Aromatase Assay Buffer containing the organic solvent used to dissolve the test compounds were prepared. Reaction wells containing test compounds and corresponding no inhibitor controls

(which may also serve as a solvent control), as well as a background control (containing no fluorogenic Aromatase Substrate) were prepared. The plate was incubated for at least 10 min at 37°C to allow test ligands to interact with aromatase. After incubation, 30 μl of the Aromatase Substrate/NADP⁺ mixture was added to each well. Immediately (within 1 min), the fluorescence at Ex/Em = 488/527 nm was measured. The experiment was carried out in three repetitions.

Results and Discussion

In this study, 2,4,5-trisubstituted imidazole derivatives were obtained by boiling the diketone derivatives in acetic acid in the presence of ammonium acetate under reflux using the Debus-Radziszewski method. The general synthesis scheme of the compounds is shown in Figure 5. The structures of the compounds were elucidated by spectroscopic methods. Compound 1a has the *p*-tolyl structure. The -CH₃ protons in this structure were seen as singlet 2.30-2.36 ppm. Protons of the thiophene ring were observed in the range of 7.68-8.25 ppm. The NH protons of the imidazole ring were observed as singlet at 12.50 and 12.60 ppm.

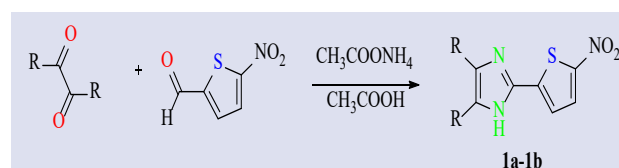


Figure 5. Chemical structure and general procedure for the synthesis of the final compounds 1a-1b

The anticancer activity results of compounds 1a-1b against MCF7 (CRL-3435) and L929 (CCL-1) are presented in Table 1. When the cytotoxic effects of the synthesized compounds on the MCF7 (CRL-3435) cell line were evaluated, it was determined that the compound 1a had promising effects in the series. Two different diketone derivatives, 4,4'-dimethylbenzyl and α-furyl were used in the synthesis of the compounds. It has been determined that the anticancer effect potential of the 4,4'-dimethylbenzyl derivative is particularly promising in terms of activity.

Table 1. IC₅₀ values (μM) and percent vitality of compounds 1a-1b and reference drug cisplatin for MCF-7 and L929 cell lines

Comp.	MCF7		L929	
	IC ₅₀	Percent Vitality	IC ₅₀	Percent Vitality
1a	82.7	43.3 ± 1.03	>100	63.5 ± 6.03
1b	>100	62.2 ± 8.8	>100	60.6 ± 3.02
Cisplatin	69.75	28.32 ± 3.78	>100	53.7 ± 4.83

The anti-aromatase activity of compounds 1a and 1b against the reference drug letrozole was evaluated using the commercial fluorimetric assay kit, Aromatase-CYP19A

(BioVision). The results found are shown in Table 2. The compound 1a one was found to have a higher activity with an IC₅₀ value of 55.780 ± 1.980 μM.

Table 2. IC₅₀ (μM) values of compounds

Compounds	Aromatase Inhibition (IC ₅₀)
1a	55.780 ± 1.980
1b	>100
Letrozole	0.114 ± 0.003

Conclusion

In this study, two imidazole derivative, 4,5-bis(4-methylphenyl)-2-(5-nitrothiophen-2-yl)-1H-imidazole (1a) and 4,5-di(furan-2-yl)-2-(5-nitrothiophen-2-yl)-1H-imidazole (1b), were synthesized. The anticancer effects of the compounds were evaluated on the MCF7 (CRL-3435) breast cancer cell line. Two different diketone derivatives, 4,4'-dimethylbenzyl and α-furyl were used in the synthesis of the compounds. When the effects of the compounds on the aromatase enzyme were evaluated, it was found that compound 1a had moderate activity, while the activity of compound 1b on the aromatase enzyme was not found.

Conflicts of interest

The authors declare that there are no conflicts of interest.

References

- [1] Lekgau K., Raphoko L.A., Lebepe C.M., Mongokoana D.F., Leboho T.C., Matsebatale T. M., ... & Nxumalo W., Design and Synthesis of 6-Amino-quinoline-alkynyl as Potential Aromatase (CYP19A1) Inhibitors, *J. Mol. Struct.*, 1255 (2022) 132473.
- [2] Osmaniye D., Karaca Ş., Kurban B., Baysal M., Ahmad I., Patel H., ... Kaplancıklı Z. A., Design, synthesis, molecular docking and molecular dynamics studies of novel triazolothiadiazine derivatives containing furan or thiophene rings as anticancer agents, *Bioorg. Chem.*, 122 (2022) 105709.
- [3] Sayyad N. B., Sabale P. M., Umare M. D., Bajaj K. K., (2022). Aromatase Inhibitors: Development and Current Perspectives, *Indian J. Pharm. Educ. Res.* 56 (2022) 311-320.
- [4] Shah V., Bhaliya J., Patel G. M., In silico docking and ADME study of deketene curcumin derivatives (DKC) as an aromatase inhibitor or antagonist to the estrogen-alpha positive receptor (E α +): potent application of breast cancer, *Struct. Chem.*, 33 (2022) 571-600.
- [5] Rashdan H. R., Shehadi I. A., Triazoles Synthesis & Applications as Nonsteroidal Aromatase Inhibitors for Hormone-Dependent Breast Cancer Treatment, *Heteroatom Chem.*, (2022).
- [6] Çevik U. A., Celik I., Mella J., Mellado M., Özkay Y., Kaplancıklı Z. A., Design, Synthesis, and Molecular Modeling Studies of a Novel Benzimidazole as an Aromatase Inhibitor, *ACS omega*. 7 (2022) 16152-16163.
- [7] Osmaniye D., Levent S., Sağlık B. N., Karaduman A. B., Özkay Y., Kaplancıklı Z. A., Novel imidazole derivatives as potential aromatase and monoamine oxidase-B inhibitors against breast cancer, *New J. Chem.*, 46 (2022) 7442-7451.
- [8] Ammazalorso A., Gallorini M., Fantacuzzi M., Gambacorta N., De Filippis B., Giampietro L., ... Amoroso R., Design, synthesis and biological evaluation of imidazole and triazole-based carbamates as novel aromatase inhibitors, *Eur. J. Med. Chem.*, 211 (2021) 113115.
- [9] Acar Çevik U., Celik I., Işık A., Ahmad I., Patel H., Özkay Y., & Kaplancıklı Z. A., Design, synthesis, molecular modeling, DFT, ADME and biological evaluation studies of some new 1,3,4-oxadiazole linked benzimidazoles as anticancer agents and aromatase inhibitors, *J. Biomol. Struct. Dyn.*, (2022) 1.
- [10] Ana G., Kelly P. M., Malebari A. M., Noorani S., Nathwani S. M., Twamley B., ... Meegan, M. J., Synthesis and Biological Evaluation of 1-(Diarylmethyl)-1H-1, 2, 4-Triazoles and 1-(Diarylmethyl)-1H-Imidazoles as a Novel Class of Anti-Mitotic Agent for Activity in Breast Cancer, *Pharma.*, 14 (2021) 169.
- [11] Asadi P., Khodarahmi G., Farrokhpour H., Hassanzadeh F., Saghaei L., Quantum mechanical/molecular mechanical and docking study of the novel analogues based on hybridization of common pharmacophores as potential anti-breast cancer agents, *Res. Pharm. Sci.*, 12 (2017) 233.
- [12] Mojaddami A., Sakhteman A., Fereidoonnehad M., Faghih Z., Najdian A., Khabnadideh S., ... Rezaei Z. Binding mode of triazole derivatives as aromatase inhibitors based on docking, protein ligand interaction fingerprinting, and molecular dynamics simulation studies, *Res. Pharm. Sci.*, 12 (2017) 21.
- [13] Song Z., Liu Y., Dai Z., Liu W., Zhao K., Zhang T., ... & Dai Y., Synthesis and aromatase inhibitory evaluation of 4-N-nitrophenyl substituted amino-4H-1,2,4-triazole derivatives, *Bioorg. Med. Chem.*, 24 (2016) 4723-4730.
- [14] Adhikari N., Amin S. A., Jha T., & Gayen S., Integrating regression and classification-based QSARs with molecular docking analyses to explore the structure-antiaromatase activity relationships of letrozole-based analogs, *Can. J. Chem.*, 95 (2017) 1285-1295.
- [15] Acar Çevik U., Sağlık B. N., Osmaniye D., Levent S., Kaya Çavuşoğlu B., Karaduman A. B., ... & Kaplancıklı Z. A., Synthesis and docking study of benzimidazole-triazolothiadiazine hybrids as aromatase inhibitors, *Arch. Pharm.*, 353 (2020) e2000008.
- [16] Acar Çevik U., Sağlık B.N., Osmaniye D., Levent S., Kaya Çavuşoğlu B., Karaduman A.B., ... & Kaplancıklı Z.A., Synthesis, anticancer evaluation and molecular docking studies of new benzimidazole-1,3,4-oxadiazole derivatives as human topoisomerase types I poison, *J. Enzyme Inhib. Med. Chem.*, 35 (2020) 1657-1673.

Investigation of Antimicrobial and Cytotoxic Activities of *Palmarosa (Cymbopogon martinii)* Essential Oil

Eda Sönmez Gürer ^{1,a,*}, Tutku Tunç ^{2,b}

¹ Department of Pharmacognosy, Faculty of Pharmacy, Sivas Cumhuriyet University, Sivas, Türkiye

² Department of Pharmaceutical Microbiology, Faculty of Pharmacy, Sivas Cumhuriyet University, Sivas, Türkiye

*Corresponding author

Research Article

History

Received: 27/07/2022

Accepted: 22/10/2022

Copyright



©2022 Faculty of Science,
Sivas Cumhuriyet University

ABSTRACT

In this study; It was aimed to investigate the cytotoxic activities and antimicrobial effects of Palmarosa essential oil obtained from *Cymbopogon martinii* plant. Content analyzes of Palmarosa essential oil were made by Gas Chromatography-Mass Spectrometry (GS-MS). The antimicrobial effects of Palmarosa essential oil were investigated using Disk Diffusion and Minimum Inhibition Concentration (MIC) methods. Cytotoxic effects of essential oil at different concentrations in breast cancer (MCF-7), prostate cancer (DU-145) and healthy human fibroblast (WI-38) cell lines XTT (2,3-bis-(2-methoxy-4-nitro-5)-sulfophenyl)-2H-tetrazolium-5-carboxanilide) test. In the disc diffusion method of Palmarosa; against *K. pneumoniae*, *S. aureus*, and *E. coli*, it was observed that the first concentrations formed zone diameters very close to the standard. It has been determined that the antifungal effect against *C. albicans* is present in the first two concentrations (200-100 µg/mL). Palmarosa, in the MIC method; Showed the highest antibacterial effect against *B. cereus* (MIC: <1.56 µg/mL). It has reached effective MIC values against other bacteria and fungi. In our cytotoxic activity studies; The IC50 value for DU-145 cells was 3.14 ±0.126, 6.29 ±0.56 for MCF-7 and 20.06 ±1.02 for WI-38. The antitumor activity of Palmarosa essential oil was found to be more effective in DU-145 cells, but it was observed that there was no toxicity in WI-38 cell line.

Keywords: Antimicrobial, *Cymbopogon martinii*, Cytotoxicity, Essential oil.

edagurer@cumhuriyet.edu.tr

<https://orcid.org/0000-0003-0319-6312>

ttunc@cumhuriyet.edu.tr

<https://orcid.org/0000-0002-8274-9386>

Introduction

Medicinal and aromatic plants have been used by people for many years to prevent and cure diseases [1]. Essential oils are volatile and aromatic compounds obtained from plants. These oils are found in special cells or cell groups such as leaves and stems of the plant [2]. 300 of the approximately 3000 essential oils known today are used in different industries such as medicine, food, cosmetics and perfume. In particular, some essential oils show medicinal properties and are used in the treatment of various systemic diseases [3]. Essential oils contain phytochemicals known as monoterpenes, sesquiterpenes and their oxygen derivatives. These phytochemicals (thymol, anethol, menthol, carvacrol, phenolic acids, flavones, etc.) show activity against bacterial and fungal species, and research has been carried out in this area for a long time [4,5]. Phenolic compounds constitute the main group of plant secondary metabolites with antioxidant effects. There are many studies on the beneficial properties of these phytochemical compounds on human health [6]. Secondary metabolites are compounds of natural origin that are not required for plant growth, but have biological and pharmacological activity, produced by different pathways. The source of natural antioxidants is phenolic compounds that can occur in all organs of plants. The main ones among these antioxidant compounds are flavonoids, phenolic acids, lignans, terpenes, tocopherols, phospholipids and organic acids [7].

Plants of the genus *Cymbopogon* belonging to the Poaceae family are economically very valuable as they are frequently preferred in the perfumery and pharmaceutical sectors with their characteristic odor in their essential oils. The genus *Cymbopogon* consists of about 140 species containing a wide variety of phytochemicals and their essential oils are obtained by steam distillation. Essential oils of the genus *Cymbopogon* contain components such as citral, geraniol, citronellol, citronellal, which have antibacterial, antifungal, insecticidal and insect repellent activities [8]. *Cymbopogon* species have important activities such as anthelmintic, anti-inflammatory, analgesic, antiaging, pesticide, antimicrobial, antifungal, antioxidant effects [9]. However, studies to determine the biological and pharmacological importance of these essential oils have increased rapidly in recent years; Besides its anticancer effects, many beneficial biological activities have been observed. Phytochemicals in the essential oil obtained from the *Cymbopogon* genus, It offers excellent biological activities and therefore can be used in the treatment of various types of cancer [8]. *C. flexuosus*, *C. nardus var. nardus*, *C. citratus*, *C. pendulus*, *C. winterianus* and *C. martinii var. motia* and *sofia* are among the other types with commercial value. Essential oils obtained from these species are widely used in many areas thanks to their typical lemon and rose-like aromas [9].

C. martinii is a perennial herb native to India with a height of 5-8 meters. Wide and leaves with an intense smell, long slender stems and structures with terminal flowers on the upper part are its distinctive physical properties. GC/GC-MS analysis studies reveal that *C. martinii* essential oil; geraniol, geranylacetate, farnesol, terpinene, myrsen, caryophyll, humulene, selinenes, linalool, nerolidol and limonene components [9]. *C. martinii* essential oil, known as Palmarosa, is particularly rich in geraniol [10]. Geraniol and geranylacetate compounds constitute approximately 75-90% of the total essential oil [11].

Microorganisms can gain resistance to drugs produced by utilizing antimicrobial properties over time. Due to this increase in resistance, studies on the development of new generation drugs in the fight against infections gain great importance [12]. In addition, it is observed that microorganisms do not acquire resistance against plants despite antibiotic resistance. This situation inevitably increases the importance of herbal drugs or plant extracts [13]. Antibiotic effects are the most widely known properties of essential oils because they are highly active against bacteria, viruses and protozoa. It is known that 60% of essential oils inhibit fungal growth and 30% inhibit bacterial growth [14].

In cancer treatment; various treatments are applied according to the location of the tumor in the body, the physiological condition of the patient and the structure of the tumor. Chemotherapy and radiotherapy are among the methods mostly used in the treatment of cancer in recent years. In radiotherapy, ionizing radiation is preferred to damage and destroy harmful tumors. Radiotherapy is locally effective in tumor treatment and is applied directly on the mass. The beam used in radiotherapy damages the DNA of the cell and causes its death [15]. If we look at the data in recent years; Cancer has a higher death rate than any other disease. Species observed more than others are; lung, breast, prostate, rectum and colon [16]. This has given great importance to research on cancer treatment.

The main feature that an antimicrobial agent should have is selective toxicity. The concept of selective toxicity was first introduced by Paul Ehrlich. Antimicrobial substances used in chemotherapy are required to be effective especially at low concentrations and to have extremely low toxic properties. In order to observe such a result; The antimicrobial agent must select microorganism cells as targets rather than mammalian cells. Bacteria are prokaryotic cells while mammalian cells are eukaryotic. Antimicrobial agents (penicillins, cephalosporins, sulfonamides) targeting a molecule in prokaryotic cells but not in eukaryotic cells have extremely selective toxicity [17].

In this study, it was aimed to investigate the antitumor activities of Palmarosa essential oil obtained from *Cymbopogon martinii* plant on MCF-7 breast cancer and DU 145 prostate cancer cells, cytotoxic activities on WI-38 human fibroblast cell line and antimicrobial effects on various bacteria and fungal cells.

Materials and Methods

Essential Oil Sample

Palmarosa essential oil was supplied by Art de Huile.

GC-MS (Gas Chromatography-Mess Spectrometry)

GC-MS analyzes for the determination of the components in the Palmarosa essential oil sample were commissioned by Art de Huile, which supplied the oil. The average values of the essential oil composition are given in (Table 1). These components are geranyl acetate, beta caryophyllene, cis beta ocimene, geranial, geraniol, limonene, linalol, myrcene, neral, nerol, trans beta ocimene, trans trans farnesol, geranyl hexanoate. When the GC-MS results were examined, it was determined that the content of Palmarosa essential oil had the highest rate of geraniol (81,41%) and the lowest rate of myrcene (0.15%). Geraniol was determined as the major essential oil component.

Table 1. Components of Palmarosa essential oil

Name of Component	Reference	GC-MS
Geranyl acetate	7,0-16,0	% 8,71
Beta caryophyllene	0,7-2,5	% 1,98
Cis beta ocimene	0,2-0,6	% 0,35
Geranial	0,2-6,0	% 0,43
Geraniol	72,0-86,0	% 81,41
Limonene	1,3	% 0,33
Linalol	1,0-5,5	% 2,79
Myrcene	5,0	% 0,15
Neral	0,5	% 0,30
Nerol	0,2-0,5	% 0,32
Trans beta ocimene	0,5-3,0	% 1,33
Trans trans farnesol	0,2-1,5	% 0,65
Geranyl hexanoate	0,4-0,8	% 0,50

Determination of Antimicrobial Activity

Disc diffusion (Kirby-Bauer) and microdilution broth methods were used to determine the antimicrobial activity of Palmarosa essential oil.

Disc Diffusion

In the disk diffusion test, *Escherichia coli* (ATCC 25922), *Pseudomonas aeruginosa* (ATCC 27853), *Staphylococcus aureus* (ATCC 29213), *Klebsiella pneumoniae* (ATCC 13883), *Bacillus cereus* (ATCC 14579), *Candida albicans* (ATCC 10231) strains were used. Dilutions of Palmarosa essential oil (200-1.56 µg/mL) were absorbed into blank discs with 20 µl. Mueller-Hinton Agar (MERCK) and Sabouraud Dextrose Agar (Neogen) agars were inoculated with 0.5 McFarland turbidity bacterial and yeast solutions using sterile swab sticks. Essential oil impregnated discs were placed. Antibiotic discs were used for positive control (OXOID). Bacterial plaques were incubated at 37 ± 0.1°C for 24 hours, and yeast plaques at 25 ± 0.1°C for 48 hours. At the end of the expected time, the diameters of the zones observed in the medium were measured in mm [18].

Minimum Inhibition Concentration (MIC)

For the experiment, 96-well microtiter plates with U-type wells were used. MHB was used for bacteria and SDB was used for yeast. 10 µl essential oil (200 µg/mL) was applied to the first well, followed by serial dilutions. Bacteria and yeasts adjusted to McFarland 0.5 turbidity were diluted to 5×10^5 CFU/mL for bacteria and 0.5-2.5 $\times 10^3$ CFU/mL for yeasts and 50 µl was added onto the wells [19, 20]. Plates were incubated for 24 hours at 37 °C. In order to better observe the growth at the end of the incubation, 50 µl of 2,3,5-Triphenyltetrazolium chloride (TTC) (Merck, Germany) solution of 2 mg/mL was applied to all. Incubation process complete at 37 °C for 2 hours. The first well in which a decrease in the color of Formazan due to the presence of live microorganisms in the wells was observed was accepted as the MIC. MIC results according to reference sources; It was evaluated as effective (MIC <100 µg/mL), Moderate (100 <MIC ≤ 625 µg/mL), Weak (MIC >625 µg/mL) [21, 22].

Cytotoxic Activity

In our study, MCF-7, DU-145, WI-38 cell lines were used for cytotoxic activity determination. Essential oils were prepared at different concentrations (200-1.56 µg/mL) and used. Cells were incubated in 5% CO₂ at 37°C. 1% penicillin (100 U/mL) and streptomycin (100 µg/mL) and 10% fetal bovine serum (FBS) were added to all wells.

Cytotoxicity was interpreted according to the XTT method. Cells were added to the wells in the appropriate medium, test compounds were applied in varying proportions and incubated in CO₂ medium at 37°C for 24 hours. When the time was up, 100 µL of XTT solution was added to all wells and incubated for an additional 2 hours and optical density values were determined at 475 nm [23].

Results and Discussion

According to the results of the disc diffusion test (Table 2), Palmarosa essential oil formed an inhibition zone against *E. coli*, *S. aureus* and *K. pneumoniae* bacteria at 1,2,3 and 4 concentrations (200-25 µg/mL) and against *C. albicans* yeast at 1st (200 µg/mL) and 2nd (100 µg/mL) concentrations.

Table 2. Disc diffusion results of Palmarosa essential oil

Mikroorganizma	Palmarosa Essential Oil								Positive Control	Negative Control
	Disc Diffusion Zone Diameters (mm)									
	Concentrations (µg/mL)									
	200	100	50	25	12.5	6.25	3.125	1.56		
<i>Escherichia coli</i>	10	10	10	9	7	7	7	7	1	9
<i>Pseudomonas aeruginosa</i>	-	-	-	-	-	-	-	-	1	7
<i>Staphylococcus aureus</i>	12	10	6	6	-	-	-	-	1	9
<i>Klebsiella pneumoniae</i>	20	16	12	9	-	-	-	-	2	2
<i>Bacillus cereus</i>	-	-	-	-	-	-	-	-	2	0
<i>Candida albicans</i>	10	6	-	-	-	-	-	-	1	8

The antimicrobial test results (MIC) of Palmarosa essential oil obtained from the *Cymbopogon martinii* plant

are shown in (Table 3). Palmarosa essential oil produced the best antibacterial activity in *B. cereus* bacteria compared to the others (MIC: <1.56 µg/mL). While it was moderately effective against *P. aeruginosa*, it reached MIC values effective against other bacteria and fungi.

Table 3. MIC results of Palmarosa essential oil

Microorganisms	Palmarosa Essential Oil
<i>Escherichia coli</i>	12,5
<i>Pseudomonas aeruginosa</i>	200
<i>Staphylococcus aureus</i>	>6,25
<i>Klebsiella pneumoniae</i>	3,125
<i>Bacillus cereus</i>	<1,56
<i>Candida albicans</i>	3,125

The color change caused by the addition of XTT solution to the wells in the microplate and caused by different concentrations of essential oils was measured in ELISA at a wavelength of 450 nm. % Inhibition was determined by making the calculations specified in the reference sources and the relevant tables and figures were obtained.

In studies with Palmarosa essential oil on DU-145 and MCF-7 cell lines, Palmarosa essential oil was observed to be more effective (Table 4) on DU-145 cell line. It has been observed that Palmarosa essential oil has no toxicity in healthy WI-38 cell lines at the effective doses.

Table 4. IC50 values of Palmarosa essential oil

IC ₅₀ (µg/mL)	MCF-7	DU-145	WI-38
Palmarosa	6,29 ±0,56	3,14 ±0,12	20,06 ±1,02

Chemotherapy drugs used in cancer treatment show severe side effects depending on the treatment. Methods such as radiotherapy, surgical treatment and hormone therapy, which are used in cancer treatment apart from existing cancer drugs, have increased the search for other methods that can be used in treatment because of the low probability of success in the treatment result and their side effects [24]. The importance of introducing alternative and complementary drugs and treatment methods for the treatment of cancer is emphasized in clinical, epidemiological and experimental studies. Plants are the leading natural resources preferred in the traditional treatment of different types of cancer diseases. About 60% of the sources used for anticancer treatment consist of plants, seafood or microorganisms [9].

Jain et al.; as a result of their examination in *C. martinii* oil with a chromatography device; they determined that it contains geraniol, geranylacetate, farnesol, terpinene, myrsen, caryophyll, humulene, selinenes, linalool, nerolidol and limonene [9]. *C. martinii* plant, known as Palmarosa, gives an essential oil especially rich in geraniol [10]. According to another study; The geraniol and geranyl acetate compounds of the essential oil obtained from the *C. martinii* plant constitute approximately 75-90% of the total essential oil [11].

Numerous studies have been conducted on the antimicrobial activities of essential oils.

According to the study of Verma R. et al.; the essential oil obtained from the *Cymbopogon martinii* plant was observed to provide broad-spectrum antibacterial effects with medium to very good effects against Gram-positive and Gram-negative strains [25].

From the works of Ganjewala D; essential oils of *Cymbopogon* species have emerged as having superior antifungal activities and significant antibacterial activities [8].

Bassole I.H.N. et al. in their study; essential oils distilled from *Cymbopogon citratus* and *Cymbopogon giganteus* plants were tested on nine bacteria by disc diffusion and microdilution methods. *C. giganteus* essential oil provided antimicrobial effects to all microorganisms used, while *C. citratus* essential oil could not inhibit *Pseudomonas aeruginosa* [26].

In a study by Khan and Ahmad in 2011; The effects of *Cymbopogon martinii* together with other essential oils on *Aspergillus fumigatus* and *Trichophyton rubrum* were investigated. As a result of this study, it was determined that the essential oil of *Cymbopogon martinii* showed high antimicrobial activity and therefore it could be evaluated as a new resource in the pharmaceutical industry [27].

Sharma R. et al.; investigated the effects of essential oil from *Cymbopogon flexuosus* on twelve human cancer cells. As a result; 502713 (colon), IMR-32 (neuroblastoma), Hep-g-2 (liver) and SiHa (cervix) showed significant cytotoxic activity against all cell lines, more specifically [28].

Thangam R. et al. *Cymbopogon citratus* in their study on the anticancer activities of essential oil; concluded that the essential oil provided cytotoxic and apoptotic activity in cancerous tissues [29].

Bayala B. et al. in their study; The reason for this study was to determine the cytotoxic activities of *Cymbopogon citratus* and *Cymbopogon giganteus* essential oils on cancerous cells. For this purpose, Antioxidant, potential anti-inflammatory effect and cytotoxic effect were studied on different prostate cancer and glioblastoma cell cultures. *C. citratus* essential oil gave significant results in prostate cell line PC-3 (IC₅₀ ¼ 32.1 mg/mL) and glioblastoma cell lines (SF-767 (IC₅₀ = 45.13 mg/mL) and SF-763 (IC₅₀ = 172.05 mg/mL) [30].

According to the GC-MS analysis in our study, geranyl acetate, beta caryophyllene, cis beta ocimene, geranial, geraniol, limonene, linalool, myrcene, neral, nerol, trans beta ocimene, trans trans farnesol, geranyl hexanoate components were determined in the content of Palmarosa essential oil. It was determined that geraniol (81.41%) was in the first place and geranyl acetate (8.71%) was in the second place in the composition of our essential oil. In our study; The content of our Palmarosa essential oil sample is very similar to the results obtained from studies conducted by different researchers in the literature.

As a result of the disc diffusion experiment studied at diverse dilutions of Palmarosa essential oil; first

concentration (200 µg/mL) formed a zone diameter (20mm) very close to the standard against *K. pneumoniae* bacteria. Against *S. aureus* and *E. coli* bacteria, It was determined that Palmarosa concentrations between 200-25 µg/mL formed zone diameters close to the standard. It was concluded that the first and second dilutions had a positive effect on *C. albicans* (200 µg/mL-10 mm, 100 µg/mL-6 mm).

As a result of the microdilution method studied with 8 different dilutions of Palmarosa essential oil, the strongest activity against *B. cereus* was determined (MIC: <1.56 µg/mL). While Palmarosa was moderately effective against *P. aeruginosa*, it reached MIC values effective against other bacteria and fungi.

To show the effect of essential oil on MCF-7 breast cancer and DU-145 prostate cancer cell lines, it was prepared at concentrations of 200 µg/mL, 100 µg/mL, 50 µg/mL, 25 µg/mL, 12.5 µg/mL, 6.25 µg/mL, 3.125 µg/mL, 1.56 µg/mL and the cells were found to be viable by the XTT method.

It has been determined that Palmarosa essential oil has a major activity on MCF-7 cells in the first 6 dilutions (200-6.25 µg/mL). At the first concentration (200 µg/mL), more than 100% effect was seen. Even at the sixth concentration (6.25 µg/mL), the rate of killing cancer cells, which is 92.79%, is quite high. Since the IC₅₀ value is 6.29 µg/mL, it is possible to see the effectiveness of Palmarosa essential oil even at low concentration.

It has been determined that Palmarosa essential oil has a major activity on DU-145 cells in the first 6 dilutions (200-6.25 µg/mL). At the first concentration (200 µg/mL), more than 100% effect was seen. Even at the lowest concentration (1.56 µg/mL), it has a very high killing rate of 75.43% cancer cells. Since the IC₅₀ value is 3.14 µg/mL, it is possible to see the effectiveness of Palmarosa essential oil even at very low concentrations.

In studies with Palmarosa essential oil on DU-145 and MCF-7 cell lines, it was observed that Palmarosa essential oil was more effective particularly on DU-145 prostate cancer cell line than MCF-7 breast cancer cell line. No antitumor activity study of the *Cymbopogon martinii* species was found in the studies. However, according to reference sources, antitumor activity has been detected in different species belonging to the genus *Cymbopogon*.

Eight different concentrations of Palmarosa essential oil were tested on the WI-38 cell line, which is a normal human lung fibroblast cell, and the cytotoxic activity results were evaluated as % cell viability.

Although a very low cell viability (5.81%) was observed at the first concentration of Palmarosa essential oil (200 µg/mL), an increasing percentage of cell viability was obtained at other concentrations. Cell viability reached 100% at the last 5 dilutions (25 µg/mL, 12.5 µg/mL, 6.25 µg/mL, 3.125 µg/mL, 1.56 µg/mL).

It has been observed that Palmarosa essential oil has no significant toxicity in healthy WI-38 cell lines at the effective doses.

According to the data we obtained as a result of research, there are no adequate publications on the

antitumor activity of Palmarosa essential oil. In order to investigate the antitumor effect of similar essential oils on other cancer cell lines and to determine whether they have any toxic effects on normal human cells, research can also be carried out on different human cell lines.

As a result; Palmarosa essential oil has been shown to have the capacity to be used as an another product in anticancer treatments. In the next stage, it may be suggested that these two essential oils be tested in animal experiments and then directed to clinical research and developed as a chemotherapy drug.

Acknowledgement

The study was funded by the Sivas Cumhuriyet University Scientific Research Project Fund (CUBAP). In this article; Eda SÖNMEZ GÜRER's 2019 Pharmaceutical Microbiology master's thesis was used. The authors thank the company "Art de Huile" for the supply of essential oil.

Conflicts of interest

All authors declare that they have no conflict of interest.

References

- Bayram E., Kırıcı S., Tansı S., Yılmaz G., Arabacı O., Kızıl S., Telci İ., Possibilities to Increase the Production of Medicinal and Aromatic Plants, Turkey Agricultural Eng. 7th Technical Congress, Ankara, Proceedings Book I, (2010) 437-456.
- Oussalah M., Caillet S., Saucier L., Lacroix M., Inhibitory Effects of Selected Plant Essential Oils on the Growth of Four Pathogenic Bacteria: *E. coli* O157:H7, *Salmonella* Typhimurium, *Staphylococcus Aureus* and *Listeria monocytogenes*, *Food Control*, 18 (2007) 414–420.
- Bakkali F., Averbeck S., Averbeck D., Idaomar M., Biological Effects of Essential Oils-A Review, *Food and Chemical Toxicology*, 46 (2008) 446-475.
- Souza E.L.D., Lima E.D.O., Freire K.R.D.L., Sousa C.P.D., Inhibitory Action of Some Essential Oils and Phytochemicals on the Growth of Various Moulds Isolated From Foods, *Brazilian Archives of Biology and Technology*, 48 (2005) 245-250.
- Burt S., Essential Oils: Their Antibacterial Properties and Potential Applications in Foods: A review, *International Journal of Food Microbiology*, (94) (2004) 223–253.
- Akalın G., Selamoğlu Z., Nutrition and Foods for Skin Health, *J Pharm Care*, 7(1-2) (2019) 31-33.
- Selamoğlu Z., Polyphenolic Compounds in Human Health with Pharmacological Properties, *Journal of Traditional Medicine & Clinical Naturopathy*, (2017) 6-4.
- Ganjewala D., *Cymbopogon* Essential Oils: Chemical Compositions and Bioactivities, *International Journal of Essential Oil Therapeutics*, (3) (2009) 56-65.
- Jain D., Pathak N., Khan S., Raghuram G.V., Bhargava A., Samarth R., Mishra P.K., Evaluation of Cytotoxicity and Anticarcinogenic Potential of Mentha Leaf Extracts, *International Journal of Toxicology*, 30(2) (2011) 225-236.
- Raina V.K., Srivastava S.K., Aggarwal K.K., Syamasundar K.V., Khanuja S.P.S., Essential Oil Composition of *Cymbopogon martinii* From Different Places in India, *Flavour Fragr. J.*, (18) (2003) 312–315.
- Chauhan K.N., Semwal M.P., Influence of Various Plant Spacing on Growth, Herbage Yield, Essential Oil Yield and Aroma Content of Palmarosa (*Cymbopogon martinii* Roxb.) at Different Harvest Under Agro-Climatic Condition of Doon Valley, *Journal of Essential Oil-bearing Plants*, 6(20) (2017) 1587-1593.
- Çelik E., Çelik G.Y., Antimicrobial Properties of Plant Essential Oils, *Orlab On-Line Journal of Microbiology*, 2(5) (2007) 1-6.
- Toroğlu S., Çenet M., Usage Areas of Some Plants Used for Therapeutic Purposes and Methods Used for Determination of Antimicrobial Activities, *KSU. Journal of Science and Engineering*, 9(2) (2006) 12-21.
- Cowan M.M., Plant Products as Antimicrobial Agents, *Clinical Microbiology Reviews*, 12(4) (1999) 564-582.
- Kiltie A., Knowles M.A., Selby P.J., Radiotherapy and Molecular Radiotherapy Introduction to The Cellular and Molecular Biology of Cancer, Oxford University Press, USA, (2005) 414.
- Cancer, World Health Organization, <https://www.who.int/news-room/fact-sheets/detail/cancer>, Retrieved July 20, (2022).
- Derbentli S., General Properties of Antimicrobial Substances, Antimicrobial Substances, Gazi Bookstore, Ankara, (2003) 141-142.
- CLSI., Performance Standards for Antimicrobial Disk Susceptibility Tests, Approved Standard, 13th Edition, CLSI document M02, Clinical and Laboratory Standards Institute Clinical and Laboratory Standards Institute, Pennsylvania, USA., (2018).
- CLSI., Methods for Dilution Antimicrobial Susceptibility Tests for Bacteria that Grow Aerobically, Approved Standard, 9th Edition, CLSI document M07-A9, Clinical and Laboratory Standards Institute, Pennsylvania, USA., 2012.
- CLSI. Reference Method for Broth Dilution Antifungal Susceptibility Testing of Yeasts, Approved Standard, 2th Edition, CLSI document M27-A2, Clinical and Laboratory Standards Institute, Pennsylvania, USA., 2012.
- Kuete V., Potential of Cameroonian Plants and Derived Products Against Microbial Infections, *Planta Med.*, 76 (2010) 1479–1491.
- Awouafack M.D., Mcgaw L.J., Gottfried S., Mbouangouere R., Tane P., Spitteller M., Eloff J.N., Antibacterial Activity and Cytotoxicity of the Ethanol Extract, Fractions and Eight Compounds Isolated From *Eriosema robustum*, *BMC Complementary Medicine and Therapies*, 13 (2013) 289.
- Adukwu E.C., Bowles M., Edwards-Jones V., Bone H., Antimicrobial Activity, Cytotoxicity and Chemical Analysis of Lemongrass Essential Oil (*Cymbopogon flexuosus*) and Pure Citral, *Appl. Microbiol. Biotechnol.*, 100 (2016) 9619–9627.
- Tekin A., Kaya E., Yazıcı S., Content Analysis of Cancer-Related Alternative Medicine Web Sites, *Mehmet Akif Ersoy University Journal of Social Sciences Institute*, 4(6) (2012) 14-34.
- Verma R.S., Padalia R.C., Goswami P., Verma S.K., Chauhan A., Singh V.R., Dorakar M.P., Chemical Composition and Antibacterial Activity of *p*-menthane Chemotype of *Cymbopogon martini* (Roxb.) W. Watson (Poaceae) From India, *Journal of Essential Oil Research*, 30(3) (2018) 182-188.
- Bassoléa I.H.N., Lamien-Medab A., Bayalaa B., Obamea L.C., Ilboudoa A.J., Franzb C., Novakb J., Nebié R.C., Dickoa M.H., Chemical Composition and Antimicrobial Activity of

- Cymbopogon citratus* and *Cymbopogon giganteus* Essential Oils Alone and in Combination, *Phytomedicine*, 18(12) (2011) 1070–1074.
- [27] Khan M.S.A., Ahmad I., In Vitro Antifungal, Anti-elastase and Anti-keratinase Activity of Essential Oils of Cinnamomum, Syzygium and Cymbopogon Species Against *Aspergillus fumigatus* and *Trichophyton rubrum*, *Phytomedicine*, 19 (2011) 48-55.
- [28] Sharma P.R., Mondhe D.M., Muthiah S., Pal H.C., Shahi A.K., Saxena A.K, Qazi G.N., Anticancer Activity of an Essential Oil From *Cymbopogon flexuosus*, *Chem. Biol. Interact.*, 179 (2009) 160-168.
- [29] Thangam R., Sathuvan M., Poongodi A., Suresh V., Pazhanichamy K., Sivasubramanian S., Kanipandian N., Ganesan N., Rengasamy R., Thirumurugan R., Kannan S., Activation of Intrinsic Apoptotic Signaling Pathway in Cancer Cells by *Cymbopogon citratus* Polysaccharide Fractions, *Carbohydrate Polymers*, 107 (2014) 138–150.
- [30] Bayala B., Bassole H.N., Maqdasy S., Baron S., Jean J.S., *Cymbopogon citratus* and *Cymbopogon giganteus* Essential Oils Have Cytotoxic Effects on Tumor Cell Cultures, Identification of Citral as a New Putative Anti-proliferative Molecule, *Biochimie*, 153 (2018) 162-170.

Sensitive Determination of Venlafaxine in Urine Samples by Using HPLC-DAD System After Fabric Phase Sorptive Extraction

Bezanur Özdemir ^{1,a}, Halil İbrahim Ulusoy ^{1,b}, Ümmügülüm Polat ^{1,c,*}, Marcello Locatelli ^{2,d}, Abuzar Kabir ^{3,e}

¹ Department of Analytical Chemistry, Faculty of Pharmacy, Sivas Cumhuriyet University, Sivas, Türkiye

² Department of Pharmacy, University of Chieti–Pescara “G. d’Annunzio”, Via dei Vestini 31, Chieti 66100, Italy

³ Department of Chemistry and Biochemistry, International Forensic Research Institute, Florida International University, 11200 SW 8th St, Miami, FL 33199, USA

*Corresponding author

Research Article

History

Received: 01/10/2022

Accepted: 09/12/2022

Copyright



©2022 Faculty of Science,
Sivas Cumhuriyet University

ABSTRACT

This study is focused on developing a sensitive analytical method for Venlafaxine molecule which is antidepressant drug belonging to the serotonin-noradrenaline reuptake inhibitors (SNRI) group. With this study, a separation and preconcentration method based on fabric phase sorptive extraction (FPSE) method was developed for low levels of Venlafaxine in urine samples. Experimental variables such as pH, ionic strength, desorption solvent, and other parameters were studied and optimized step by step. The linearity of method under optimized conditions is in the range of 15.00-750.00 ng mL⁻¹ while limit of detection is 4.28 ng mL⁻¹. The relative standard deviation (RSD %) obtained from model solutions containing 300 ng mL⁻¹ of Venlafaxine was lower than 3.1 % and pre-concentration factor was calculated as 62.50 for target molecule. In order to test accuracy of the method, recovery tests were carried out by means of spiked urine samples. As a result of recovery tests, quantitative values were obtained in the range of 97.5-104.2 % successively.

Keywords: HPLC, Fabric phase sorptive extraction, Venlafaxine, Analytical method development.

^a bezanur.587.35@gmail.com

^c gulsumorgul@gmail.com

^e akabir@fju.edu

^b <https://orcid.org/0000-0002-0634-837X>

^d <https://orcid.org/0000-0001-8393-2396>

^f <https://orcid.org/0000-0002-3740-8857>

^b hiulusoy@cumhuriyet.edu.tr

^d m.locatelli@unich.it

^b <https://orcid.org/0000-0002-8742-5145>

^f <https://orcid.org/0000-0002-0840-825X>

Introduction

Antidepressant drugs are widely and effectively used in the treatment of especially depression many mood disorders, psychotic disorders and substance abuse disorder mood disorders. Its use has become widespread in recent years and is an antidepressant belonging to the serotonin-noradrenaline reuptake inhibitors (SNRI) group. In addition to low doses of serotonin and noradrenaline, high doses of serotonin and noradrenaline, they inhibit dopamine reuptake. Side effects can include nausea-vomiting, headache, dizziness, constipation, anorexia, insomnia, dermatitis, irritability, and blurred vision [1,2]. Venlafaxine was first released in 1993 by Wyeth as a quick release tablet for use per more than one doses in day [3]. Venlafaxine, which is a tertiary, bicyclic compound in the phenylethylamine structure, differs from other antidepressants as chemical structure. It is racemic compound composed of R and S enantiomers combined in equal amounts [4]. It is also used in sleep, anxiety and eating disorders, pain syndromes, arrhythmia and some immune dysfunction cures [5].

Detection of antidepressant drugs in biological samples is used in various fields, especially toxicological and therapeutic drug monitoring. Due to the complexity of samples and low concentration levels of drugs, sample preparation is requisite for the development of chromatographic methods [6]. Separation and preconcentration methods are used for target analyte by

collect smaller volume than its volume so level that can be analysed by increase concentration of target analyte. Thus, concentration of target analyte increased and exist at measurable level. The separation process is done by removing the impurities and the other matrix components that may have an adverse effect on the analysis of the analyte or cause contamination of the analyser [7,8]. Conventional sample preparation techniques such as solid phase extraction (SPE) are still among the most frequently used for analytical sample preparation but, these techniques prone to error during extraction steps such as time consuming, exhausting, multistep, often toxic and hazardous organic solvents used in large volumes, solvent evaporation and sample dilution in the appropriate solvent [9]. So, solid phase micro extraction (SPME) technical are more popular in the last decades because they minimize solvent consumptions and total analysis time. The solid phase extraction method is based on collecting the analyte on a solid phase material. Although these method has superior advantage according to exist method, it has some lacking. Thus, researchers go on to study new material and led to the find of several microextraction techniques [10]. As a result of the evaluation of different micro-extraction techniques, it was revealed that the deficiency in all these techniques was caused by the coating technology used for fixed the sorbent on the substrate surface and the physical format

of the extraction systems determining PCSA [11]. Considering all these problems, a new, promising and wide-use extraction technique, called the fabric phase sorptive extraction method (FPSE), was developed by Kabir and Furton in 2014[12,13]. FPSE method provides a very efficient, green sample preparation technique by successfully integrating the advantages of sol-gel derivative sorbents used in microextraction and various fabric phases. Low sorbent capacity and long sample preparation time, two main limitations of absorbent extraction techniques, have been handled by fabric phase extraction [14].

In this work a sensitive determination method is developed for low concentrations of Venlafaxine molecule by using the HPLC-DAD system after the application of FPSE. The developed method was applied to simulated urine and normal urine samples after optimization procedures was completed successively.

Materials and Methods

Chemicals and Reagents

The reagents used during the experimental studies are all of analytical purity and were purchased from Merck and Sigma companies. All of the solutions used were prepared with ultra-pure water with 18.2 MΩ.cm resistance obtained from MP Minipure Dest Up device.

Venlafaxine was purchased from Sigma Aldrich (St. Louis, MO, USA). The standard stock solutions of venlafaxine were prepared in methanol by using brown flask. The standard solutions stocked in a dry place and protected from the light. The standard model solution was newly prepared after diluting of the main solutions with methanol. SPE frits and SPE cartridges were purchased from Agilent Technologies (California, USA).

Instrumentation

In all chromatographic measurements, Shimadzu (Prominence) HPLC (Kyoto, Japan) device was used. HPLC device used; It has equipped with LC 20 AD quaternary pump, SPD-M20 A DAD detector, DGU-20A vacuum degasser and CTO-10 AS VP column furnace equipment. Direct determination parameters for optimized with HPLC for venlafaxine active substance before enrichment experiments. Preliminary trials with different columns were performed as this fixed phase and good peak separation was obtained with the Phonomex Luna® Phenyl-Hexyl column. Many trials have been made in isocratic and gradient elution modes with aqueous solutions of organic characterizing phases such as methyl alcohol, ethyl alcohol and acetonitrile, containing buffers of different pH. Experiments continued until significant peaks for venlafaxine were obtained. A summarization of HPLC conditions after optimization was shown in Table 1. As can be seen in Figure 1, the peak of the venlafaxine molecule was observed clearly under the optimized conditions. Peak height and area increase with concentration as expected.

Table 1. HPLC Conditions for Venlafaxine Determinations

Parameter	HPLC Conditions
HPLC Mode	Isocratic elution
Mobil Phase	%10 Methyl alcohol % 60 pH 3 (0.02M) Phosphate Buffer %30 Acetonitrile
Flow Rate	1 mL/min
Execution time	20 dk
Colon	Luna® 15 µm Phenyl-Hexyl 100 Å, 250× 50 mm, AXIA™ Packed, Ea
Colon temperature	40 °C
Injection volume	10 µL

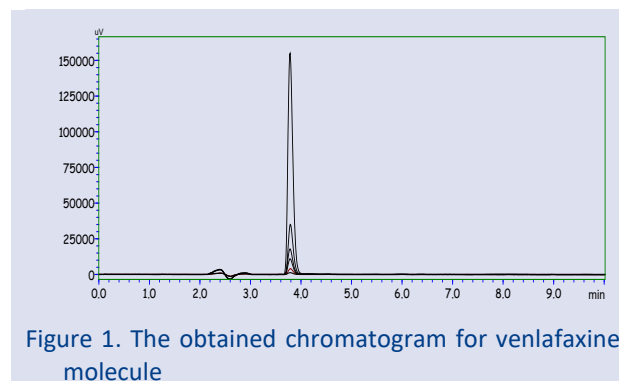


Figure 1. The obtained chromatogram for venlafaxine molecule

Fabrication and Characterization Fabric Phase Support Material

Among all tested membranes, sol-gel carbowax (CW-20 M) sorbent, coated on cellulose FPSE media, was the most efficient.

FPSE membranes were synthesized in the International Forensic Research Institute laboratory (Department of Chemistry and Biochemistry, Florida International University, Miami, FL, USA) according to the procedure described in our previous studies [15,16].

Briefly, a 100 cm² segment of cellulose fabric was first soaked with deionized water for 15 min under constant sonication. The fabric was then cleaned with deionized water, followed by soaking in 1 M NaOH solution for 1 h under sonication. The base treated fabric was then washed several times with ample deionized water, followed by treating with 0.1 M HCl solution for 1 h under sonication. Then, the material was washed with a deionized water and finally dried in an inert atmosphere overnight. The dried fabric was stored in a clean glass container until coating process. For modification of fabric phase surface, the sol-gel short-chain poly (ethylene glycol) sorbent was prepared by using a facile sol-gel synthesis approach developed in-house [17,18]. The sol solutions were prepared by sequential mixing of organic polymer or modified silane precursor/methyl trimethoxysilane (MTMS) (acting as sol-gel precursor)/acetone/CH₂Cl₂/TFA/water at various molar ratios as explained in these references. The solution was thoroughly mixed by vortexing for 3 min, centrifuged for 5 min, and sonicated for 2 min. Following centrifugation, the clear supernatant part of the sol solution was transferred to a clean, amber coloured reaction glass

bottle. The cleaned and pre-treated cellulose fabric substrate was then immersed into the sol solution, for a predetermined amount of time, to creating the sol-gel coating. The FPSE media was then cut into 1.5 cm pieces for future use and stored in air-tight containers to prevent contamination.

Characterization of fabric phase material was carried out by using FTIR, SEM technical in our previous studies. The detailed information can be found in these published articles [19–21].

FPSE Procedure

Separation and pre-concentration process based on FPSE were performed by optimizing parameters such as pH, desorption solvent selection and amount, adsorption time, vortexing time. This step permits to eliminate materials impurities and to activate functional groups for subsequently interactions. The membranes were then rinsed in ultra-pure water to remove organic solvent residues before the insertion into the sample for the extraction process.

1.5-cm² SOL-GEL CW20M fabric phases are added to 50 mL falcon tubes before they are passed through distilled water / ACN-MeOH solution / distilled water and washed. Then 20 mL of distilled water on them respectively; 2 mL of pH: 10 Br buffer 1 mL venlafaxine model solution is added and its volume is completed to 50 mL with distilled water. The covers of the falcon tubes are well closed and placed in the shaker device and left to shake at 100 rpm for 60 minutes. After shaking is completed, the tubes are taken and the fabric phase is separated from the liquid phase and 800 µL of ethyl alcohol solution is added to them and vortexed for 60 s. That is, the transition of analyte components attached to the fabric phase to solvent ethyl alcohol is provided. This solvent liquid phase samples are taken into the injectors and filtered through a 0.45 µm PTFE membrane filter and transferred to the vials. It is given to the HPLC device.

Preparation of Synthetic and Normal Urine Solution

As the application area of the developed method, two different samples were carried out including, synthetically and normal urine samples which were just used as spiked samples.

Normal urine sample was taken from a healthy volunteer was directly subjected to the developed method. The human urine samples were collected in a capped test tube from a healthy volunteer free from any kind of medication who had been informed about the perimental procedure and the nature of the study.

Synthetic urine solutions were prepared to be used in the literature to represent urine, which is one of the sample groups where antidepressant agents are most frequently monitored, and was used during the application [11]. Synthetic urine solution was prepared as explained [11]: 6.25 g urea, 0.27 g CaCl₂·2H₂O, 0.25 g NH₃Cl, 0.4 g KCl, 0.35 g Na₂SO₄, 0.35 g KH₂PO₄, 0.73 g NaCl were weighed and dissolved in some distilled water and its volume was

completed to 250 mL in volumetric flask. The pH was then adjusted to pH6 with 0.1 M HCl solution. It was transferred to an amber coloured bottle and stored at + 4°C.

Results and Discussion

Extraction Optimization Experiments

The objective is to keep the analyte type in the fabric phase at the highest possible level and to separate it from other substances in the environment, and after the separation process is achieved, all of the analytes in the solid phase pass into the solvent. Preliminary trials were made to determine the necessary parameters to achieve this. It was aimed to obtain a fast and easy separation process and to obtain the highest concentration of analyte by using as little amount of organic solvent as possible. Accordingly, a chromatographic method before FPSE experiments was developed for Venlafaxine molecule by optimizing all parameters.

pH Effect

The pH of the medium is a very important parameter for it affects the interaction of the analyte with the fabric phase and the reactions between the species. 2 mL range of pH 2-10 Britton Robinson (BR) buffer was added to all tubes including 200 ng mL⁻¹ venlafaxine, and their volume was completed to 50 mL by ultrapure water. After FPSE method was applied, the content of venlafaxine was determined by HPLC-DAD system. The obtained results were shown in Figure 2. It is seen that the optimum pH value in the enrichment processes is pH 10. As a result, it has been understood that pKa value of venlafaxine in the alkaline region. It becomes positively charged in the alkaline region. We investigated from the literature that venlafaxine has a pKa value of 9.40[22], which shows suitability with our study.

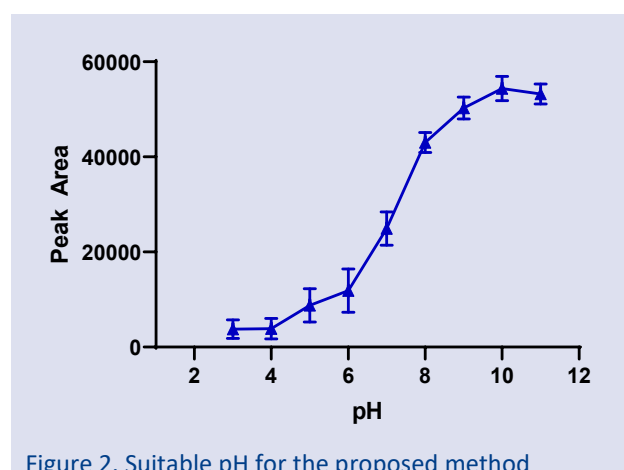


Figure 2. Suitable pH for the proposed method

Eluent Type and Volume

Selecting of eluent for desorption process is an important factor that a solvent can completely desorbed analyte molecule from solid phase surface without damaging the HPLC device. The target molecules are separated from the liquid phase and cling to the phase

after shaking. The solvent chosen for this purpose should be in accordance with the executive phase of the HPLC system. For this purpose, a solvent series were used containing methanol, ACN, isopropyl alcohol (IPA), ethanol, water and acetone. The results of this study were showed in Figure 3. It is seen that the most suitable solvent for desorption in FPSE was determined as ethanol. This result shows that our active substance can be taken better in solvents with high organic character.

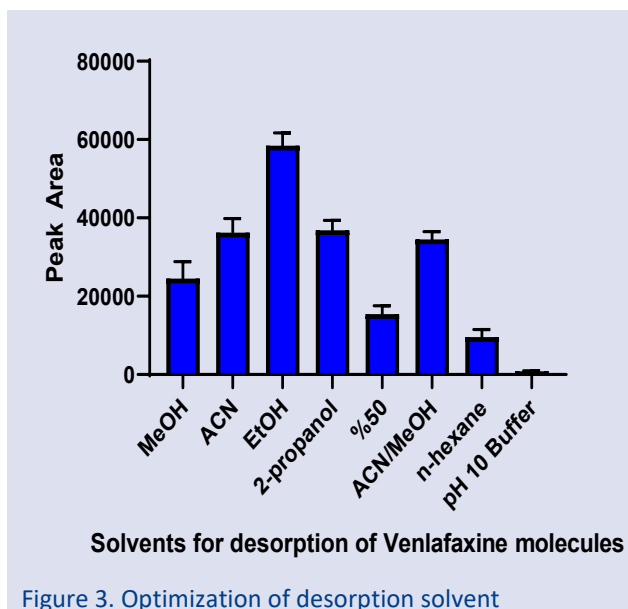


Figure 3. Optimization of desorption solvent

The amount of solvent must be within the range that can be analysed in the HPLC instrument. Volume of desorption solvent was studied by adding ethanol in the range of 200-1500 µL. At the end of these processes, the analyte components attached to the fabric phase were transferred to ethanol phase and this solvent phase were taken with an injector filtered through a 0.45 µm PTFE membrane filter and put into vials to submit to the HPLC device. As can be seen in Figure 4, the highest signals were obtained with 800 µL of ethanol and this volume was selected for desorption process.

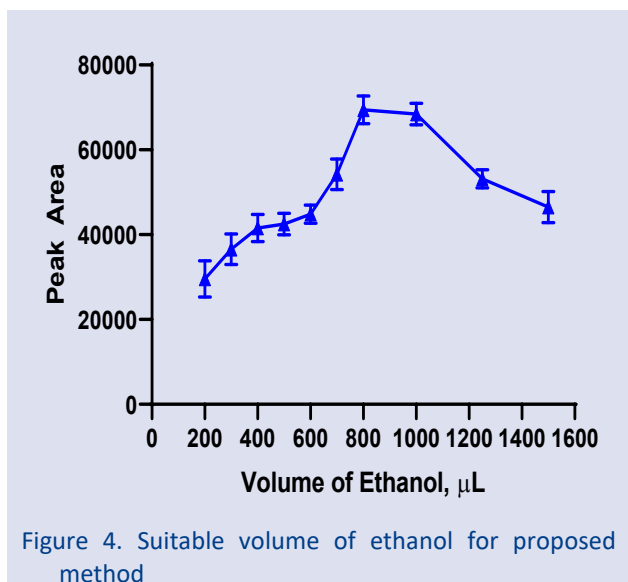


Figure 4. Suitable volume of ethanol for proposed method

Adsorption Time

The adsorption time, also known as the contact time required for the transition of analyte types from the environment where the analyte is located, is an important parameter. The tubes were shaken in shaker at 1000 rpm for 5, 10, 20, 30, 40, 50, 60, 70, 80, 90 minutes, respectively. The results obtained are shown in Figure 5. It is seen that the optimum adsorption time in enrichment processes to be made after that is 60 minutes. It keeps the maximum amount it can hold after 60 minutes. If the tubes are left in more shakers, the adhering substances start releasing, because the interaction is physical, so the signal starts to decrease as the time increases.

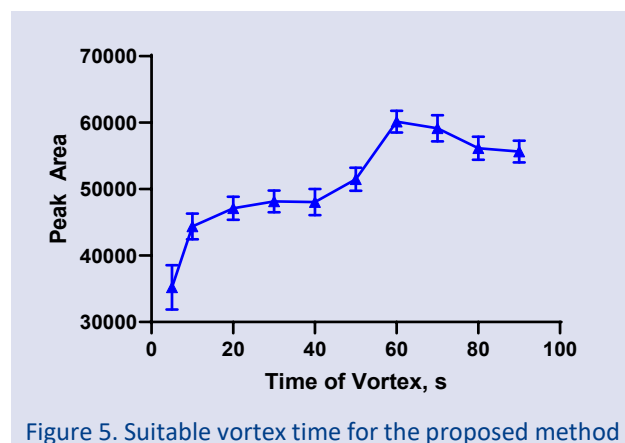


Figure 5. Suitable vortex time for the proposed method

Analytical Performance of the Developed Method

After determining the most suitable experimental conditions for fabric phase extraction, model solutions containing venlafaxine in different concentrations were prepared and each developed FPSE method was applied to determine the linear working range. With the help of analytical signals monitored with the DAD detector, the linear working range for venlafaxine molecule was determined to be 15-750 ng mL⁻¹. All analytical parameters of the developed method are collectively presented in Table 2.

Table 2. Analytical merits of the proposed method

Parameter	Before FPSE	After FPSE
Linear dynamic range	1.00-20.00 µg mL ⁻¹	15.00-750.00 ng mL ⁻¹
Limit of detection, LOD	0.32 µg mL ⁻¹	4.28 ng mL ⁻¹
Limit of quantification, LOQ	0.96 µg mL ⁻¹	14.14 ng mL ⁻¹
RSD(%) (for 300 ng mL ⁻¹)	3.10	2.40
Calibration sensitivity	11.42	822.24
Correlation Coefficient (R ²)	0.9972	0.9972
Pre-Concentration Factor ^a	-	62.50
Enhancement Factor ^b	-	72.00

^a Pre-concentration factors (PF) were calculated by using the ratio of the initial solution volume (50 mL) to the last elution solvent volume (0.8 mL).

^b The enhancement factors (EF) were found from the ratio of the slope of calibration curve of the analytes after MSPE application to that of prior FPSE application.

Analysis of Urine Samples

Simulated urine and normal urine samples were analysed in order to investigate the applicability of the proposed method by means of recovery tests. Venlafaxine concentration of the studied samples were analysed by using the optimized method and results were shown in Table 3. A known concentration of Venlafaxine was spiked to samples because none of samples was contained it as expected. The recoveries of target molecule in the spiked samples were in the range of 97.5-104.2 %. These satisfactory results demonstrate that the developed FPSE based HPLC-DAD method is suitable for trace determination of venlafaxine molecule in the urine samples.

Table 3. Analysis of urine samples

Sample	Added ng mL ⁻¹	Found ^{a,b} ng mL ⁻¹	%RSD	% Recovery
Synthetic urine solution	-	<LOD	-	-
	100.0	97.5 ± 5.4	5.5	97.5
Normal urine sample	200.0	195.1 ± 9.4	4.8	97.8
	-	<LOD	-	-
Normal urine sample	100.0	103.7 ± 3.9	3.8	103.7
	200.0	208.4 ± 9.8	4.7	104.2

^aMean value ± standard deviation found for three replicate measurements at 95% confidence level

^bConcentrations in a 50 mL solution obtained after sample preparation

Conclusions

A new, sensitive, simple and reliable HPLC based method was developed for the determination of Venlafaxine. The present method offers a simple extraction procedure. The proposed FPSE-HPLC-DAD procedure allows the reliable analysis of Venlafaxine which have not been determined in previously reported analytical method. When we consider it from this perspective even also, it can be concluded that the study is original. It offers a different perspective to the literature in terms of contributing to future studies. The developed method has the advantage of being fast and easy. Analysis of drug active ingredients, especially in complex biological environments, is a very difficult task. For this purpose, mostly complex analysis setups and expensive devices are used. In order to perform these analyses with basic laboratory equipment and a classical HPLC system that can be found in every laboratory, fabric phase extraction was applied as a pre-treatment and the analytical validation of the FPSE-HPLC-DAD-based method developed with trace levels of venlafaxine in model solutions was performed and all parameters were given in Table 2.

In this study, a method for chromatographic determination of venlafaxine molecule after enrichment was applied for the first time. The method increases the low concentrations of the active ingredient of venlafaxine to levels that can be determined by conventional HPLC systems with a simple pre-application system that can be found in every laboratory.

Acknowledgment

This study has been supported by The Scientific and Technological Research Council of Turkey (TUBITAK) as a 2209-A project with the 1919B011903961 code.

Conflicts of interest

All authors declare that they have no conflict of interest.

References

- [1] M. Leblanc, L. Thibault, Effect of sibutramine on macronutrient selection in male and female rats, *Physiol. Behav.*, 80 (2003) 243–252.
- [2] A.R. Chaves, S.M. Silva, R.H.C. Queiroz, F.M. Lanças, M.E.C. Queiroz, Stir bar sorptive extraction and liquid chromatography with UV detection for determination of antidepressants in plasma samples, *J. Chromatogr. B Anal. Technol. Biomed. Life Sci.*, 850 (2007) 295-302.
- [3] N. Dilbaz, A.R. Özen, M. Ay, H. Güz, S. Karademir, Venlafaksin'in major depresyonda etkinlik ve emniyeti; ümitsizlik, intihar düşüncesi ve anksiyete üzerine etkisi: Bir açık çalışma, *Psikofarmakoloji. Org.*, 9 (1999) 197–202.
- [4] H. Juan, Z. Zhiling, L. Huande, Simultaneous determination of fluoxetine, citalopram, paroxetine, venlafaxine in plasma by high performance liquid chromatography-electrospray ionization mass spectrometry (HPLC-MS/ESI), *J. Chromatogr. B Anal. Technol. Biomed. Life Sci.*, 820 (2005) 33-39.
- [5] S. Rani, A.K. Malik, R. Kaur, R. Kaur, A Review for the Analysis of Antidepressant, Antiepileptic and Quinolone Type Drugs in Pharmaceuticals and Environmental Samples, *Crit. Rev. Anal. Chem.*, 46 (2016) 424-442.
- [6] A. Khan, Vilazodone, a novel dual-acting serotonergic antidepressant for managing major depression, *Expert Opin. Investig. Drugs.*, 18 (2009) 1753-1764.
- [7] P.L. Kole, G. Venkatesh, J. Kotecha, R. Sheshala, Recent advances in sample preparation techniques for effective bioanalytical methods, *Biomed. Chromatogr.*, 25 (2011) 199-217.
- [8] A.G. Canlı, B. Sürücü, H.I. Ulusoy, E. Yılmaz, A. Kabir, M. Locatelli, Analytical methodology for trace determination of propoxur and fenitrothion pesticide residues by decanoic acid modified magnetic nanoparticles, *Molecule*, 24 (2019) 4621.
- [9] E. Karaca, S. Ulusoy, U. Morgül, H.İ. Ulusoy, Development of Analytical Method for Sensitive Determination of Streptozotocin based on Solid Phase Extraction, *Cumhuriyet Sci. J.*, 41 (2020) 826–831.
- [10] S. Ulusoy, M. Locatelli, A. Tartaglia, A. Kabir, H.İ. Ulusoy, Sensitive determination of Anastrozole and Letrozole in urine samples by novel magnetic nanoparticles containing tetraethylenepentamine (TEPA) prior to analysis by high - performance liquid chromatography - diode array detection, *Chem. Pap.*, 76 (2022) 3649–3659.
- [11] M. Sarıkaya, H.I. Ulusoy, U. Morgul, S. Ulusoy, A. Tartaglia, E. Yılmaz, M. Soylak, M. Locatelli, A. Kabir, Sensitive determination of Fluoxetine and Citalopram antidepressants in urine and wastewater samples by liquid chromatography coupled with photodiode array detector, *J. Chromatogr. A.*, 1648 (2021) 462215.
- [12] A. Kabir, R. Mesa, J. Jurmain, K. Furton, Fabric Phase Sorptive Extraction Explained, *Separations.*, 4 (2017) 21.

- [13] V. Kazantzi, A. Anthemidis, Fabric sol-gel phase sorptive extraction technique: A review, *Separations*, 4 (2017) 1–20.
- [14] E. Agadellis, A. Tartaglia, M. Locatelli, A. Kabir, K.G. Furton, V. Samanidou, Mixed-mode fabric phase sorptive extraction of multiple tetracycline residues from milk samples prior to high performance liquid chromatography-ultraviolet analysis, *Microchem. J.*, 159 (2020) 105437.
- [15] E. Zilfidou, A. Kabir, K.G. Furton, V. Samanidou, An improved fabric phase sorptive extraction method for the determination of five selected antidepressant drug residues in human blood serum prior to high performance liquid chromatography with diode array detection, *J. Chromatogr. B Anal. Technol. Biomed. Life Sci.*, 1125 (2019) 1–11.
- [16] A. Kabir, R. Mesa, J. Jurmain, K. Furton, Fabric Phase Sorptive Extraction Explained, *Separations*, 4 (2017) 21.
- [17] V. Samanidou, K. Michaelidou, A. Kabir, K.G. Furton, Fabric phase sorptive extraction of selected penicillin antibiotic residues from intact milk followed by high performance liquid chromatography with diode array detection, *Food Chem.*, 224 (2017) 131-138.
- [18] S. Gülle, H.I. Ulusoy, A. Kabir, A. Tartaglia, K.G. Furton, M. Locatelli, V.F. Samanidou, Application of a fabric phase sorptive extraction-high performance liquid chromatography-photodiode array detection method for the trace determination of methyl paraben, propyl paraben and butyl paraben in cosmetic and environmental samples, *Anal. Methods.*, 11 (2019) 6136–6145.
- [19] A. Tartaglia, M. Locatelli, A. Kabir, K.G. Furton, D. Macerola, E. Sperandio, S. Piccolantonio, H.I. Ulusoy, F. Maroni, P. Bruni, F. Croce, V.F. Samanidou, Comparison between exhaustive and equilibrium extraction using different SPE sorbents and sol-gel carbowax 20M coated FPSE media, *Molecule*, 24 (2019) 382.
- [20] A. Kabir, K.G. Furton, N. Tinari, L. Grossi, D. Innosa, D. Macerola, A. Tartaglia, V. Di Donato, C. D’Ovidio, M. Locatelli, Fabric phase sorptive extraction-high performance liquid chromatography-photo diode array detection method for simultaneous monitoring of three inflammatory bowel disease treatment drugs in whole blood, plasma and urine, *J. Chromatogr. B Anal. Technol. Biomed. Life Sci.*, 1084 (2018) 53-63.
- [21] H.I. Ulusoy, S. Gülle, E. Yilmaz, M. Soylak, Trace determination of vitamin B12 in food samples by using Fe₃O₄ magnetic particles including multi-walled carbon nanotubes and nanodiamonds, *Anal. Methods*, 11 (2019) 5108–5117.
- [22] N.F. de Rosa, N.A. Sharley, Stability of venlafaxine hydrochloride liquid formulations suitable for administration via enteral feeding tubes, *J. Pharm. Pract. Res.*, 38 (2008) 212–215.

Green Synthesis of C-quantum Dots Modified ZnO Nanophotocatalyst: The Effect of Different Solvents Used in Production of C-quantum Dots Modified ZnO Nanophotocatalyst on Photocatalytic Performance

Merve Vurucuel^{1,a}, Ali Duran^{2,3,b}, Abdullah İnci^{4,c}, Erkan Yılmaz^{1,3,5,6,d,*}

¹ERNAM-Erciyes University Nanotechnology Application and Research Center, Kayseri 38039, Türkiye

²Department of Nanotechnology Engineering, Faculty of Engineering, Abdullah Gul University, 38080, Kayseri, Türkiye

³ChemicaMed Chemical Inc., Erciyes University Technology Development Zone, Kayseri 38039, Türkiye

⁴Department of Parasitology, Faculty of Veterinary Medicine, Erciyes University, 38280, Kayseri, Türkiye

⁵Department of Analytical Chemistry, Faculty of Pharmacy, Erciyes University, Kayseri, 38039, Türkiye

⁶Technology Research & Application Center (ERU-TAUM), Erciyes University, Kayseri, 38039, Türkiye

*Corresponding author

Research Article

History

Received: 30/06/2021

Accepted: 09/11/2022

Copyright



©2022 Faculty of Science,
Sivas Cumhuriyet University

ABSTRACT

Access the quality and sufficient amount of water is started to being problem with population increasing. One of the way to behalf the solution of this problem is usage waste water treatment in industry and agriculture. Wastewater treatment methods have disadvantages of being costly and producing secondary pollutants, photocatalysis, which is one of the advanced oxidation methods that is more advantageous and effective in removing pollutants, is promising. The newest member of nanomaterial, C-quantum dots (CQDs) has been increasingly get attention on lots of field including photocatalyst. Semiconductors are commonly used in photocatalysis however, they have electron pair recombination problem that results decreasing of efficiency. Doping semiconductors with different nanomaterials is one of the easiest ways to get over the problem. Recently CQDs has been started to used as doping agent. Solvothermal method is among the easiest and environmentally friendly methods in nanomaterial synthesis. In this study, the effect of dimethylformamide, dimethylsulfoxide, ethylene glycol and water as solvothermal solvent on the photocatalytic efficiency of C-modified ZnO nanoparticles (CQDs@ZnO NPs) was investigated for the first time in the literature. Photocatalytic performance of CQDs@ZnO NPs was investigated on the photocatalytic degradation of methylene blue (MB). Angora mohair has been used as a CQDs source for the first time in the literature. Photocatalytic degradation performances of CQDs@ZnO NPs for MB at 300 min were 82.4%, 87.6% and 99% for ethylene glycol-water mixture, DMSO and DMF, respectively. The results proved that solvent type for solvothermal synthesis procedure has important role for photocatalytic performance of CQDs@ZnO NPs.

Keywords: Photocatalytic degradation, solvothermal synthesis, C-quantum dots, Angora mohair, ZnO NPs.

^a mervevurucuel@yahoo.com

^b <https://orcid.org/0000-0001-8054-1306>

^c ainci@erciyes.edu.tr

^d <https://orcid.org/0000-0003-1614-0756>

^b aliduran77@gmail.com

^d <https://orcid.org/0000-0002-6260-2424>

^d erkanyilmaz@erciyes.edu.tr

^d <https://orcid.org/0000-0001-8962-3199>

Introduction

One of the biggest humanity concern is access to clean and sufficient water owing to global warming, climate change and population growth. According to United Nations Water Development Report 2020, 2.2 million people do not have access to clean water beside %55 of population sanitation. In respect of report waste water treatment is consider as an essential solution to global warming because of waste water is source of methane gas due to undissociated organic waste that causes green gas effect [1]. Adsorption, membrane separation, coagulation and advanced oxidation processes such as photocatalysis are used as water treatment process. However adsorption, membrane separation and coagulation methods have disadvantages like high cost and occur secondary pollutant [2]. Photocatalysis, one of the advanced oxidation methods have a lot of promises thanks to being an effective way for degradation of pollutants [3]. Photocatalysis is the reaction by utilized light and semiconductor. The light is absorbed by

substrate and the catalytic reaction that named photocatalysis takes place on the substrat's surface [4]. Zinc Oxide (ZnO) and Titanium dioxide (TiO₂) are the most commonly used photocatalysts. TiO₂ has superhydrophobic, non toxic, chemically stabil properties beside it is strong oxidizer therefore degradation of organic pollutants [5]. Furthermore ZnO is physically and chemically stable, nontoxic and harmless beside it has low cost, biocompatible, high redox potential. Although ZnO and TiO₂ has the almost same band gap (3.37 eV and 3.2 eV), ZnO exhibit greater photocatalytic activity thanks to electron mobility of ZnO is much higher than TiO₂ [6,7]. One of photocatalysis disadvantages is rapid recombination of photogenerated electrons and hole that lead to low quantum yield

When a semiconductor like ZnO is excited by light the photocatalysis process starts. Firstly electrons are moved from valance band to conductive band therefore the valence band is charged positively. The conduction band

electrons catches protons from oxygen that is presented on weather or water hence the oxygen is charged negatively and become superoxide ion. The superoxide ion is react with organic pollutants and makes the pollutant decomposed to CO_2 and H_2O . On the other hand, protons in the valence band react with H_2O in water or moisture and OH^- ions are formed as a product. The reactive OH^- ions are carried out reaction with organic pollutants and makes the pollutants have degraded to CO_2 and H_2O [8].

Doping metal nanoparticles and carbon nanomaterials over the semiconductor's surface is one of the way to overcome the electron hole recombination drawbacks [8]. Recently many research proved that CQDs as the new class of nanoparticles is promising doping agent for semiconductor photocatalysts. CQDs are zero dimensional, water soluble, chemically stable, highly photo adsorbent nanomaterials. CQDs are cheap and non toxic thereby usage in catalysis, bioimaging and energy storage processes are desirable [9]. CQDs has been light absorber and electron reservoir therefore it has perfect electrical and optical properties. Many report has been published about CQDs being highly efficient photocatalytic material. The nano size of CQDs is resulted to difficulties to reusable therefore CQDs is doped to matrix like metal particles [10]. CQDs are synthesized by such as solvothermal, electrochemical oxidation, chemical oxidation, microwave excitation methods using a carbon source [11]. Electrochemical oxidation method has disadvantages that being complex chemical reaction. The inability to synthesize homogeneous particles is the main problem of the chemical oxidation method. Microwave method is inexpensive and rapid. However it needs a lot of energy beside reaction conditions are uncontrollable. Solvothermal synthesis method is considered as one of the most effective methods in the production of CQDs doped materials. Solvothermal method has advantages like being environment friendly, taking place by one step reaction, having good dispersion and facile reaction condition comparing the other methods. The synthesis occur in solvent like water, ethanol, dimethylformamide, dimethylsulfoxide, stainless closed vessel named autoclave [12]. Solvent type has an important role in the carbonization rate of the carbon source and therefore in different performances in the methods in which it is used [13-15].

In this study, the effects of the use of aprotic solvents dimethylformamide (DMF) and dimethyl sulfoxide (DMSO) and a protic solvent ethylene glycol-water mixture on the photocatalytic performance of CQDs@ZnO NPs were compared on the photocatalytic degradation of MB.

Another important parameter that affects the morphology, chemical content, and thus the in-use performance of CQDs is the type of carbon source used. Many studies have carried out about different organic carbon source usage for green synthesis of CQDs. For instance, instant coffee [9], citric acid [15] and urea anthracite [16] and aloe [17] have been used for carbon

sources. In the present work, mohair was used as carbon source of CQDs for the first time in literature. Mohair is Angora goat's feather which has unique properties such as being resistant, dirt-proof, showing excellent insulation properties. Mohair has slippery and softness unlike the other goat's wool thanks to the oil layer on the surface that named as yolk [18]. Herein, C-quantum dots modified ZnO nanophotocatalyst was synthesized from mohair by using DMF, DMSO and water-glycol mixture as solvothermal solvent. This study was carried out to examine how the photocatalytic efficiency of carbon dots will change in different hydrothermal synthesis solvent medium.

Experimental

Materials and Apparatus

Angora mohair was obtained from Republic of Turkey Ministry of Agriculture and Forestry Çankırı Directorate of Provincial Agriculture and Forestry. Zinc chloride (ZnCl_2) and ethylene glycol with 99% purity were obtained from Merck. NaOH pellets and N,N-dimethylformamide (%99) were purchased from Sigma-Aldrich. The degradation reactions of MB was carried out in a photochemical reactor had a UV irradiation source of 380 nm wavelength with a power of 400 W. The degradation rate of MB was calculated using the decrease in absorbance values measured by the UV-visible spectrophotometer (Perkin-Elmer Lambda 25 UV Visible Spectrophotometer). To study the morphology and size of nanomaterials, SEM images was taken by Gemini SEM500-71-08.

Synthesis of ZnO NPs

ZnO NPs were fabricated using the hydrothermal synthesis process according to the previous work of Şakir et al. [19] Briefly 2 g ZnCl_2 was dissolved in 25 ml ultra pure water and 5 g NaOH was dissolved in 25 mL ultra pure water NaOH solution was added dropwise to the ZnCl_2 solution stirred in the magnetic stirrer, and the resulting solution was then subjected to the hydrothermal synthesis procedure at 180 °C for 12 hours. ZnO NPs synthesized was centrifuged for separating to liquid phase from solid phase. The solid phase was washed with distilled water for twice and ethyl alcohol for three times to remove contaminants. The resulting solid ZnO NPs was dried on oven at 60 °C [19].

Synthesis of CQDs@ZnO NPs

As pre-treatment, the mohair was washed with soap to clean and dried in the oven at 40 °C. 500 mg of ZnO NPs, 50 mL from one of the solvothermal solvents (DMF, DMSO, ethylene glycol/water (35/25)) was added into erlenmeyer and mixed for 30 min. Afterward 500 mg mohair is added to the solvent medium and mixed 30 min. The mixture was transferred to the autoclave of solvothermal reactor and put in an oven 180 °C for 12 hours. The reaction for DMSO was carried out at 220 °C. after the reaction was complete, the mixture was

centrifuged to separate CQDs@ZnO NPs from the liquid phase. CQDs@ZnO NPs was washed with distilled water for twice and ethyl alcohol for three times and dried at 60 °C.

Photocatalytic experiments

100 mg of each nanomaterial was placed in 100 mL of 10 ppm methylene blue solution and stirred for 15 hours in the dark for the solution to reach adsorption equilibrium. The mixture was exposed to 400 W UV light to carry out the photocatalytic reaction. The samples have taken every 30 minutes. The decrease in MB concentration versus photocatalytic degradation time was calculated using the ratio of the decrease in the absorbance peak of MB at 664 nm wavelength in the UV-Vis spectrometer.

Results And Discussion

Characterization of Nanomaterials

To study the morphology and size of nanomaterials, SEM characterization studies were carried out (Figure 1). The average size of novel ZnO was 212 nm as shown in Figure 1A-C). When the synthesis of CQDs@ZnO NPs carried out via DMF, average ZnO size was around 80 nm and average CQDs size on the ZnO surface was 4 nm as shown in Figure 1D-F). While the synthesis reached out in DMSO solvent, average size of ZnO was 5.89 μm and CQDs size on the ZnO surface was 420 nm as shown in c) and g) by, lastly the average ZnO and CQDs size by ethylene glycol- water mixture were 200 nm and 35 nm, respectively.

Near IR analysis show that fingerprint of materials, difference between doped ZnO in the graph prove that doping has made changing on ZnO structure (Figure 2). According to the FTIR graph, entire NPs exhibit Zn-O characteristic stretch bonds peaks at around 400 cm^{-1} . ZnO NPs shows double peak on around 2900 cm^{-1} which represent C-H stretch bonds, peak around 1500 cm^{-1} that attributed C-O and also peak around 1000 cm^{-1} that represent C-C bond. CQDs@ZnO Nps in DMF shows peak on 1020 cm^{-1} , 1262 cm^{-1} , 1655 cm^{-1} and 2900 cm^{-1} that means C-N, CH₂, C-O-C and C-N bonds in addition 2966 cm^{-1} peak represent N-H bonds. C@ZnO NPs (DMSO) exhibit peaks on 1662 cm^{-1} and 2930 that are C-H, C=H bonds. CQDs@ZnO NPs (Ethylene Glycol+Water) exhibits peaks on about 1000 cm^{-1} , 1412 cm^{-1} , 1638 cm^{-1} , 2930 cm^{-1} and 3749 cm^{-1} which attributed C-C, C-N, N-H, C-H and O- H respectively (Figure 2). To sum up of all the FTIR results prove that functional groups on NPs depend on the solvent type. Therefore photocatalytic efficiency is depend on solvent type, either.

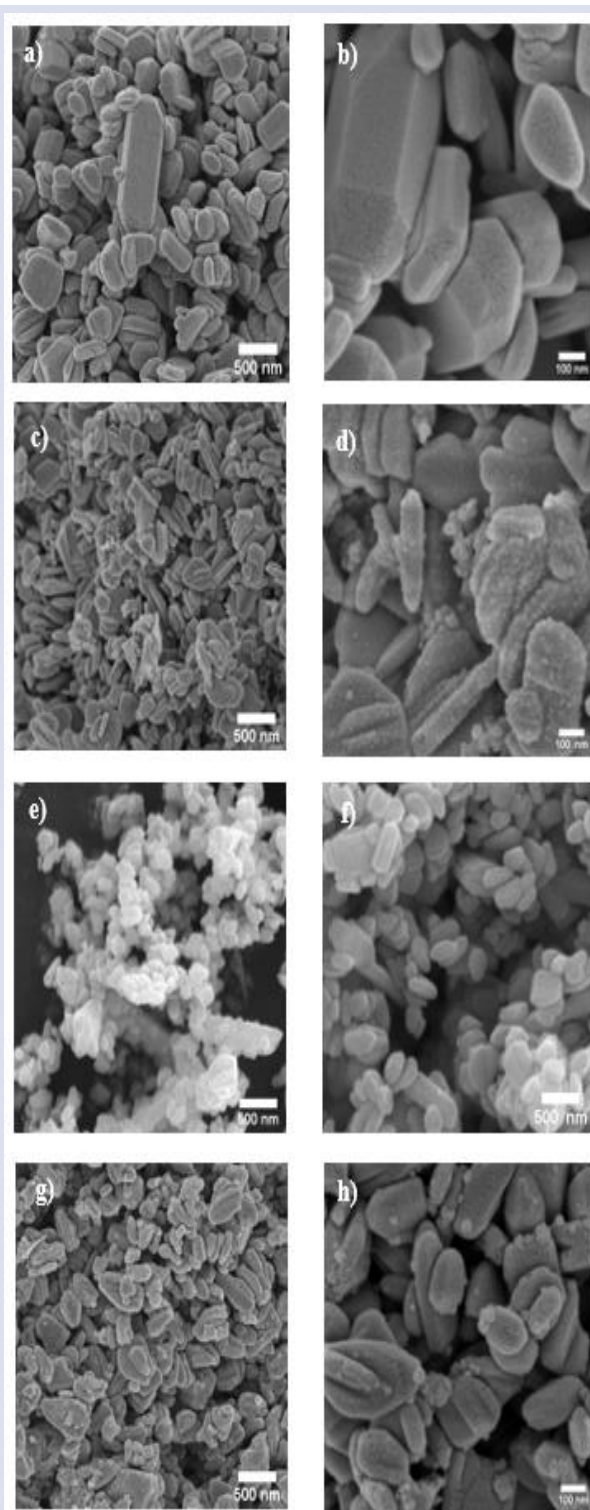


Figure 1. SEM images of nanomaterials, a-b) ZnO NPS (50K-10K), c-d) CQDs@ZnO NPs in DMF (50K-10K), e-f) C@ZnO NPs in DMSO (25K-15K), g-h) CDs@ZnO NPs (50K-10K).

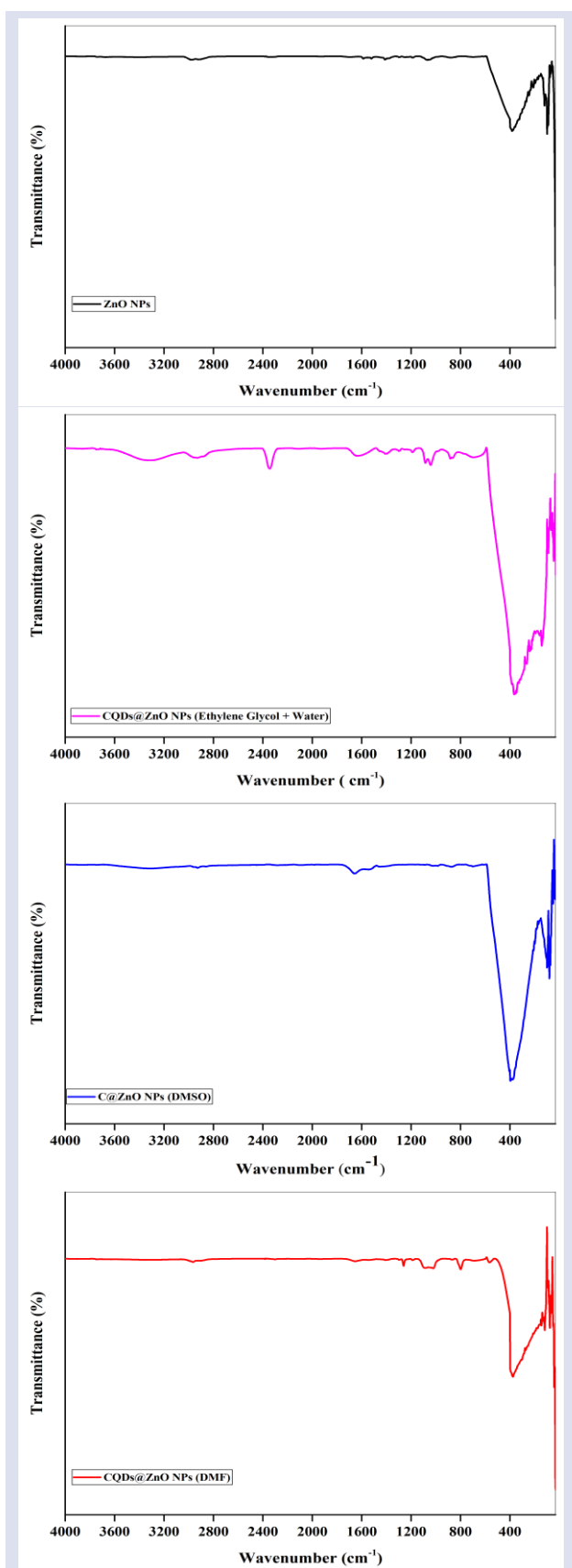


Figure 2. FTIR spectrums of ZnO NPs, CQDs@ZnO NPs in DMF, C@ZnO NPs in DMSO, CQDs@ZnO NPs in EthyleneGlycol+Water.

According to the Figure 3, XRD analysis result, the material shows ZnO NPs characteristic peaks which are

located at 2θ , 31.90, 34.50, 36.40, 47.60, 56.70, 62.90, 66.50, 68.00 and 69.20 corresponded to the (100), (002), (101), (110), (103), (200), (112) and (201). The XRD analysis demonstrate that different solvent usage on the synthesis was not made changing on main structure of ZnO NPs. The results can be interpreted that density of CQDs on ZnO was lower than %4 percent and CQDs distributed uniformly [20].

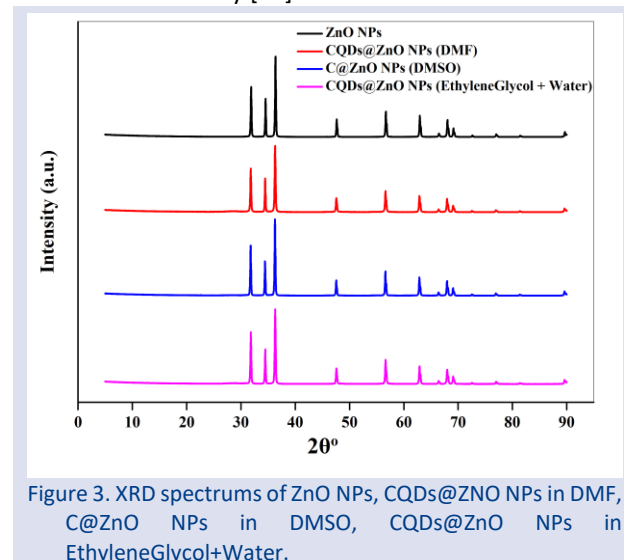


Figure 3. XRD spectrums of ZnO NPs, CQDs@ZnO NPs in DMF, C@ZnO NPs in DMSO, CQDs@ZnO NPs in EthyleneGlycol+Water.

In the manner of the Raman spectrum (Figure 4), all NPs shows ZnO characteristic peaks which are 308 cm^{-1} , 495 cm^{-1} , 607 cm^{-1} and 758 cm^{-1} , respectively. CQDs doped to ZnO did not cause a change in ZnO structure as can be seen in Raman Analysis.

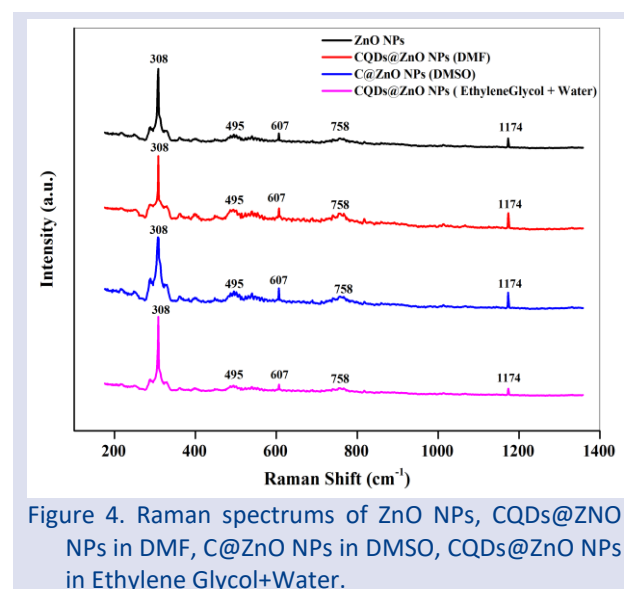


Figure 4. Raman spectrums of ZnO NPs, CQDs@ZnO NPs in DMF, C@ZnO NPs in DMSO, CQDs@ZnO NPs in Ethylene Glycol+Water.

Photocatalytic Efficiency of Different Doped Nanomaterials

The effect of dimethylformamide, dimethylsulfoxide, ethylene glycol and water as solvothermal solvent on the photocatalytic efficiency of C quantum dots-modified ZnO nanoparticles (CQDs@ZnO NPs) was investigated by adding 100 mg of CQDs@ZnO NPs in 100 mL of $10\text{ mg}\cdot\text{L}^{-1}$ of MB solution and then these mixtures subjected to 400

W UV irradiation for 300 min. The decrease in MB concentration was measured by using the ratio of the decrease in the absorbance peak of MB at 664 nm wavelength in the UV-Vis spectrometer (Figure 5). The reaction rate constant was calculated according to Langmuire Hinshelwood kinetics models. In the equation; Co represents initial MB dye concentration and C is MB dye concentration at irradiation time 't', in addition k is reaction rate constant [21].

$$\ln\left(\frac{C_0}{C}\right) = -kt$$

The methylene blue degradation by CQDs@ZnO NPs that synthesis via ethylene glycol-water mixture, DMSO and DMF were calculated as 82.4%, 87.6% and 99%, respectively.

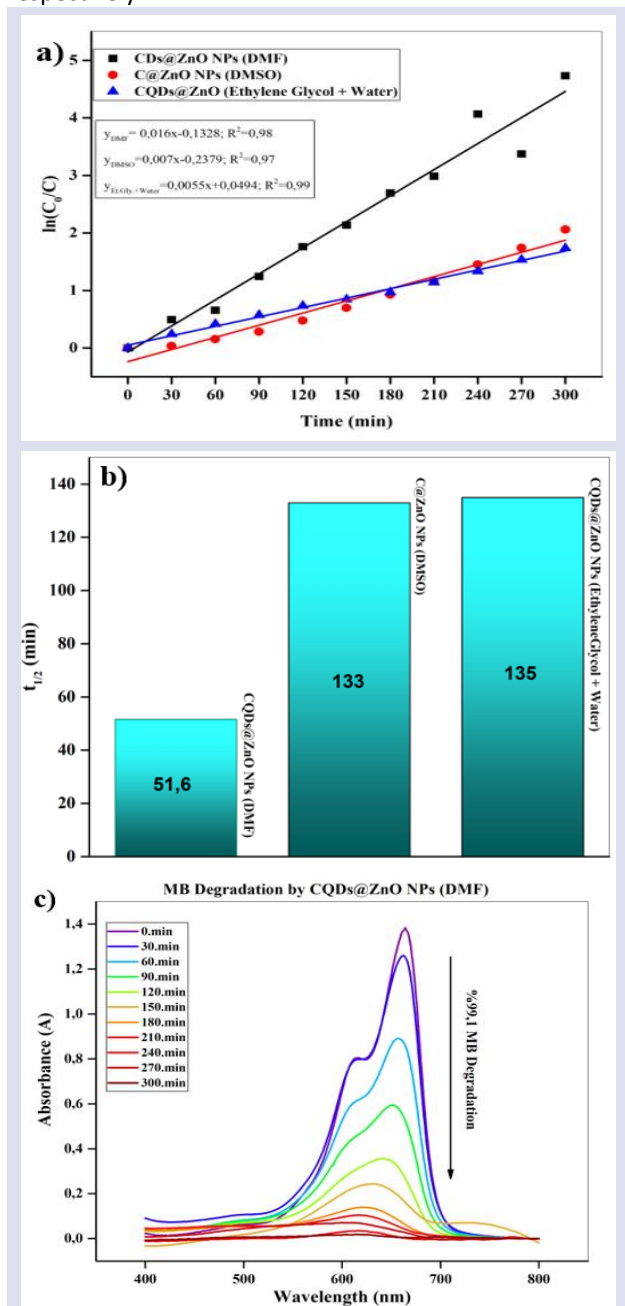


Figure 5. a) ln(C₀/C) Graph of different NPs, b) Time taken for MB concentration to half by different NPs, c) UV-Vis result of MB degradation by CQDs@ZnO NPs (DMF).

The results shows that the most efficient material is CQDs@ZnO NPs that synthesized by DMF. This situation can be explained by the particle sizes of the nanomaterials synthesized with 3 different solvents. The ZnO nanoparticles in the CQDs@ZnO NPs produced using the DMF solvent had a smaller particle size, that is, a larger surface area. Higher surface area means that there are more regions where the photocatalytic reaction takes place and therefore higher photocatalytic performance. The half life of MB concentration were calculated as 51.62 min, 133 min and 135 min by CQDs@ZnO NPs that synthesis via ethylene DMF, DMSO and glycol-water mixture, respectively (Figure 5). The graph show that the methylene blue concentration is rapidly decreased when CQDs@ZnO synthesis by DMF solvent comparing to other nanomaterial. Beside reaction kinetic constants were calculated 0.0134 min⁻¹, 0.0052 min⁻¹ and 0.0051 min⁻¹ with the same row.

Reusability of CDs@ZnO NPs Photocatalyst

Besides being effective, the reusability of photocatalysts is important in terms of eliminating repetitive material production, cheapness of the process, minimizing the post-process waste problem and sustainability. For reusability studies, 100 mg of photocatalysis which synthesized with DMF was used. When first cycle was completed, the mixture was centrifugated, after that the liquid phase was removed. The remained CQDs@ZnO NPs was washed with distilled water and ethyl alcohol. Afterward the washed CQDs@ZnO NPs was added into 100 mL of 10 ppm MB solution and the procedure was cycled. MB has been almost entirely degraded by the CDs@ZnO in DMF when 100 mg of the photocatalysis's reusability is studied four times subjected by 400 W UV lamp for 300 minutes. The results obtained proved that the carbon photocatalyst could be used at least 3 times without any change in its performance (Figure 6). MB concentration were dropped 98.31%, 98.70%, 98.64% and 14.69% when CQDs@ZnO NPs used four times respectively. Reaction kinetic constants were calculated as 0.0134 min⁻¹, 0.016 min⁻¹, 0.0177 min⁻¹ and 0.0085 min⁻¹. Half lifes of MB for each cycle were calculated as 31.62 min, 43.46 min, 33.07 min and 81.92 min.

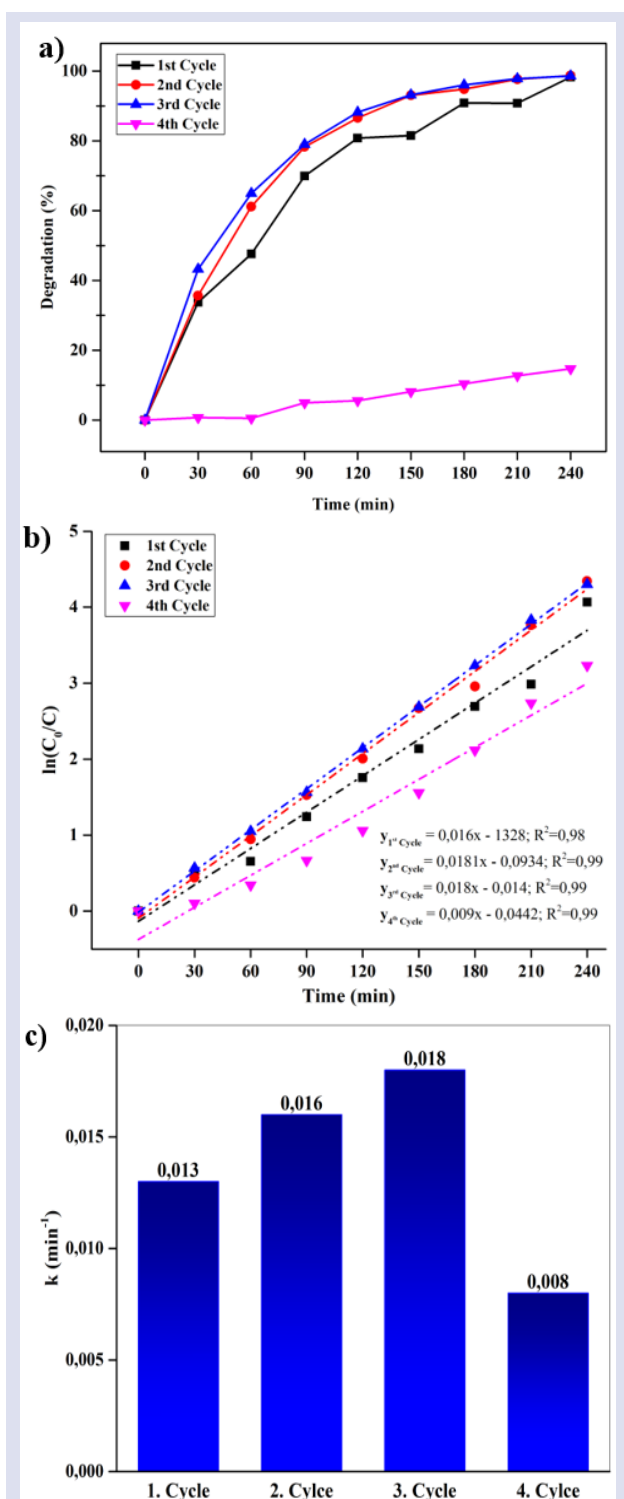


Figure 6. a) Reusability studies degradation percentage of MB concentration b) $\ln(C_0/C)$ result of reusability studies. C) Reaction kinetic constants of each reusing reaction.

Conclusion

To conclude, angora mohair was used as carbon source for green synthesis of CQDs on ZnO NPs for the first time in the literature. Thus, one of a special Turkey's precious mohair has acquired a scientific usage field. CQDs@ZnO NPs were synthesized in three different

solvothermal solvent environments and proved that the solvent type significantly affects the morphology, size and photocatalytic properties of ZnO NPs. When DMF is used as solvent, the particles exhibit smaller size as shown in SEM images; therefore, the photocatalytic efficiency increases. Doping semiconductors with CQDs is a promising way to improve the photocatalytic efficiency of semiconductors.

Acknowledgements

Authors acknowledge the Republic of Turkey Ministry of Agriculture and Forestry Çankırı Directorate of Provincial Agriculture and Forestry.

Conflicts of interest

The authors declare that there are no conflicts of interest.

References

- [1] UN World, UN World Water Development Report 2020 'Water and Climate Change', Paris (2020).
- [2] Wang C.-C., Li J.-R., Lv X.-L., Zhang Y.-Q., and Guo G., Photocatalytic organic pollutants degradation in metal-organic frameworks, *Energy Environ. Sci.*, 7(9) (2014) 2831–2867.
- [3] Lopes J. L., Martins M. J., Nogueira H. I. S., Estrada A. C., and Trindade T., Carbon-based heterogeneous photocatalysts for water cleaning technologies: a review, *Environmental Chemistry Letters*, 19 (2021) 1–26.
- [4] Ameta R., Solanki M. S., Benjamin S., and Ameta S. C., Photocatalysis, in *Advanced Oxidation Processes for Waste Water Treatment*, Elsevier, (2018) 135–175.
- [5] Nakata K. and Fujishima A., TiO₂ photocatalysis: Design and applications, *Journal of Photochemistry and Photobiology C: Photochemistry Reviews*, 13(3) (2012) 169–189.
- [6] Qi K., Cheng B., Yu J., and Ho W., Review on the improvement of the photocatalytic and antibacterial activities of ZnO, *Journal of Alloys and Compounds*, 727 (2017) 792–820.
- [7] Dagherir R., Drogui P., and Robert D., Modified TiO₂ For Environmental Photocatalytic Applications: A Review, *Industrial & Engineering Chemistry Research*, 52 (10) (2013) 3581–3599.
- [8] Bhati A., Anand S. R., Gunture, Garg A. K., Khare P., and Sonkar S. K., Sunlight-Induced Photocatalytic Degradation of Pollutant Dye by Highly Fluorescent Red-Emitting Mg-N-Embedded Carbon Dots, *ACS Sustainable Chemistry & Engineering*, 6 (7) (2018) 9246–9256.
- [9] Omer K. M., Mohammad N. N., and Baban S. O., Up-Conversion Fluorescence of Phosphorous and Nitrogen Co-Doped Carbon Quantum Dots (CDs) Coupled with Weak LED Light Source for Full-Spectrum Driven Photocatalytic Degradation via ZnO-CDs Nanocomposites, *Catalysis Letters*, 148(9) (2018) 2746–2755.
- [10] De B., Carbon dots and their polymeric nanocomposites, *Nanomaterials and Polymer Nanocomposites*, Elsevier, (2019) 217–260.
- [11] Liu J., Wang Y., Ma J., Peng Y., and Wang A., A review on bidirectional analogies between the photocatalysis and

- antibacterial properties of ZnO, *Journal of Alloys and Compounds*, 783 (2019) 898–918.
- [12] Wang Z., Zhang L., Zhang K., Lu Y., Chen J., Wang S., Hu B., Wang X., Application of carbon dots and their composite materials for the detection and removal of radioactive ions: A review, *Chemosphere*, 287 (3) (2022) 1-15.
- [13] Kurian M. and Paul A., Recent trends in the use of green sources for carbon dot synthesis-A short review, *Carbon Trends*, 3 (2021) 100032.
- [14] Mohammad-Jafarieh P., Akbarzadeh A., Salamat-Ahangari R., Pourhassan-Moghaddam M., and Jamshidi-Ghaleh K., Solvent effect on the absorption and emission spectra of carbon dots: evaluation of ground and excited state dipole moment, *BMC Chemistry*, 15 (2021) 53.
- [15] Yu R., Liang S., Ru Y., Li L., Wang Z., Chen J., A Facile Preparation of Multicolor Carbon Dots, *Nanoscale Research Letter*, (2022) 1–9
- [16] Li M., Yu C., Hu C., Yang W., Zhao C., Wang S., Zhang M., Zhao J., Wang X., Qui J., Solvothermal conversion of coal into nitrogen-doped carbon dots with singlet oxygen generation and high quantum yield, *Chemical Engineering Journal*, 320 (2017) 570–575.
- [17] Xu H., Yang X., Li G., Zhao C., and Liao X., Green Synthesis of Fluorescent Carbon Dots for Selective Detection of Tartrazine in Food Samples, *Journal of Agricultural and Food Chemistry*, 63(30) (2015) 6707-6714.
- [18] Şahin G., Coğrafi bir simge olarak Ankara keçisinin Türkiye’deki mevcut durumu, *Millî Folklor Dergisi*, 25(97) (2013)195–209.
- [19] Sakir M., Salem S., Sarduvac S.T., Sahmetlioglu E., Sarp G., Onses M.S., Yilmaz E., Photocatalytic green fabrication of Au nanoparticles on ZnO nanorods modified membrane as flexible and photocatalytic active reusable SERS substrates, *Colloids and Surfaces A: Physicochemical and Engineering Aspects*, 585 (2020) 1-11.
- [20] Song S., Wu K., Wu H., Guo J., and Zhang L., Multi-shelled ZnO decorated with nitrogen and phosphorus co-doped carbon quantum dots: synthesis and enhanced photodegradation activity of methylene blue in aqueous solutions, *RSC Advances*, 9 (13) (2019) 7362–7374.
- [21] Vasanthkumar K., Porkodi K., Selvaganapathi A., Constrain in solving Langmuir–Hinshelwood kinetic expression for the photocatalytic degradation of Auramine O aqueous solutions by ZnO catalyst, *Dyes and Pigments*, 75(1) (2007) 246–249.

Synthesis, Structural Characterization and Investigation of DNA/BSA Binding Properties of a Homo-disulphide Schiff Base Compound Carrying Oxo Propargyl Group

Aysegul Kose ^{1, a, *}¹ Department of Property Protection and Safety, Elbistan Vocational School, Kahramanmaraş İstiklal University, Kahramanmaraş, Türkiye

*Corresponding author

Research Article

History

Received: 09/05/2022

Accepted: 07/09/2022

Copyright

©2022 Faculty of Science,
Sivas Cumhuriyet University

ABSTRACT

In this work, a new homo-disulphide Schiff base compound (HDSB) was prepared and its structure was characterised by common spectroscopic and analytical methods. The compound was obtained from the condensation reaction of 2-aminothiophenol and 2-hydroxy-4-(prop-2-yn-1-yloxy)benzaldehyde in benzene. In the reaction, both Schiff base condensation and oxidation of thiols into disulphide formed. The isolated compound was structurally characterized by single crystal X-ray diffraction experiment. The homo-disulphide Schiff base compound (HDSB) was screened for its DNA/BSA binding properties using UV-Vis absorption and emission spectral studies. The compound showed considerable binding affinity to double-stranded fish sperm DNA (FSds-DNA) with binding constant of $4.1 \times 10^4 \text{ M}^{-1}$. Spectral measurements suggest that HDSB interacts with DNA in a minor groove binding mode. The compound also showed binding properties towards BSA (bovine serum albumin). The incremental addition of HDSB to the BSA solution resulted in a significant decrease in the characteristic emission band of BSA in the range of 320-500 nm (λ_{exc} : 280 nm) showing the binding interactions between HDSB and BSA.

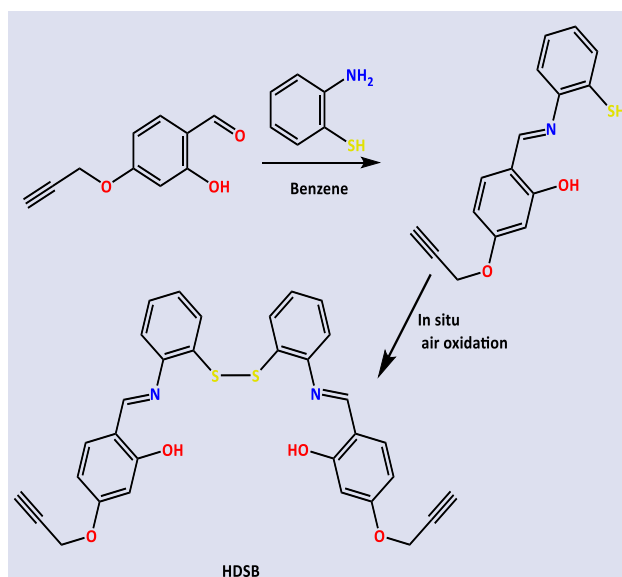
Keywords: Homo-disulphide Schiff base, Structural characterization, DNA/BSA binding, Spectroscopy.^a aysegul.kose@istiklal.edu.tr <https://orcid.org/0000-0003-3323-8149>

Introduction

In recent years, promising studies on drugs targeting tumors, arthritis, diabetes and neurological disorders have been conducted [1,2]. By studying the factors that affect the biological activities, molecules with specific properties as drugs are designed and their activities are examined [3]. The serious side effects of metal-based chemotherapy agents such as cisplatin and their limited use in some cancer types have led scientists to use organic compounds as anticancer agents [3]. Since cisplatin-based compounds show antitumor activity by binding to DNA, small organic or metal-organic molecules targeting DNA have been synthesized [4]. Examining the interactions of small molecules with DNA has created an important field of study. Molecules can bind to DNA by non-covalent interactions such as electrostatic, groove, intercalative, and partial intercalative bonding [5]. Schiff bases, also known as imine compounds, are compounds with a wide variety of biological activity such as antibacterial, antifungal, herbicide, anti-inflammatory, anticancer, anti-diabetic and antitumor activity [6, 7]. On the other hand, it has been reported that Schiff base compounds of the oxo-propargyl group increase biological activity [8, 9].

Synthesis and structural studies of Schiff bases containing disulphide groups attract attention due to their chelating properties, electron transfer abilities and biological properties [10,11]. Disulphides formed by oxidative dimerization of thiols attract attention in organic chemistry and biochemistry, and various oxidizers are used for this conversion [12–15]. It has been reported that

the thiol to disulphide conversion can be done under different experimental conditions [16]. Various Schiff bases containing disulphide groups were synthesized and their biological properties and chemosensor properties were investigated [11,17–20]. In this study, a new homo-disulphide compound HDSB (Scheme 1) was synthesized from the reaction of the salicylaldehyde compound carrying the oxo propargyl group and 2-aminothiophenol.



Scheme 1. Synthesis reaction of homo-disulphide Schiff base compound (HDSB)

The structure of the synthesized compound HDSB was characterized by FTIR, ¹H NMR and elemental analysis methods. In addition, the crystal structure of the compound was elucidated by single crystal X-ray diffraction study. DNA and BSA binding properties of the synthesized homo-disulphide compound were investigated by spectrophotometric methods.

Materials and Methods

All reagents and solvents were obtained from commercial sources (Aldrich or Merck). The starting 2-hydroxy-4-(prop-2-yn-1-yloxy)benzaldehyde was prepared according to the reported procedure [8, 21]. The structural characterization data are provided in the supplementary documents. Elemental analyses (C, H and N) were performed using a LECO CHNS 932. Infrared spectrum was obtained using KBr disc (4000-400 cm⁻¹) on a Perkin Elmer Spectrum 400 FT-IR. The electronic spectra in the 200-900 nm range were obtained on a Perkin Elmer Lambda 45 spectrophotometer. Mass spectra of the ligands were recorded on a LC/MS APCI AGILENT 1100 MSD spectrophotometer. ¹H NMR spectrum in CDCl₃ was recorded on a Bruker 400 MHz instrument. TMS was used as internal standard.

Synthesis of Homo-disulphide Schiff Base Compound (HDSB)

2-Hydroxy-4-(prop-2-yn-1-yloxy)benzaldehyde (0.88 g, 5 mmol) was dissolved in benzene. 2-amino benzenethiol (0.625 g 5mmol) was added to this solution. The colour turned to yellow with the addition of aldehyde. The mixture was refluxed at 80 °C for 8 hours. The progress of the reaction was checked by TLC. Upon consumption of starting compounds, the reaction solution was allowed to cool to the room temperature. Yellow needle-like crystals formed were filtered and dried in air.

Molecular Formula: C₃₂H₂₄N₂O₄S₂. Molecular weight: 564.65 g/mol. Yield: 85%. Colour: Yellow. E.N.: 119 °C. FTIR (ATR, cm⁻¹): 3274, 3241, 3060, 2857, 2692, 2115, 1606, 1506, 1377, 1339, 1282, 1232, 1188, 1115, 1020, 963, 883, 784, 752, 638, 558. Elemental analyses found (calculated for C₃₂H₂₄N₂O₄S₂) %: C, 67.79(68.06); H, 4.13(4.28); N, 4.83(4.96). ¹H NMR (CDCl₃, ppm) δ: 13.45 (b, OH, 2H), 9.05 (s, CH=N, 2H), 7.80-6.55 (m, CH_{aromatic} 14 H), 4.63 (s, OCH₂, 4H), 2.58 (s, C≡CH, 2H).

DNA Binding Studies

Absorption spectral measurements

The DNA binding properties of the homo-disulphide compound (HDSB) was studied by UV-Vis spectroscopic measurements. The absorption spectra of HDSB in DMSO (2.0 × 10⁻⁵ M) containing Tris-HCl buffer solution (pH = 7.0) were taken in the presence of increasing amount of double-stranded fish sperm DNA (FSds-DNA) at 230-730 nm range. The spectral changes of HDSB in the presence

of DNA were taken into account to determine the binding properties.

The absorbance was measured for calculating the percentage of DNA binding using equation given below.

$$[DNA]/(\epsilon_a - \epsilon_f) = [DNA]/(\epsilon_b - \epsilon_f) + 1/K_b(\epsilon_b - \epsilon_f)$$

In the equation given above, where ϵ_a is the apparent extinction coefficient obtained by the calculation of $A_{obs}/[Ligands \text{ or complexes}]$, ϵ_f is the extinction coefficient of the compounds in its free form, ϵ_b = extinction coefficient for the compounds in the fully bound form, and $[FSdsDNA]$ is the concentration of dsDNA in terms of base-pairs: K_b indicates the binding constant of the compound with DNA and is calculated from the slope of the line drawn between $[DNA]/(\epsilon_a - \epsilon_f)$ and $[DNA]$.

Competitive Binding Studies

Ethidium bromide (EB) is a DNA intercalating agent and it gives a characteristic emission band at 500-700 nm range ($\lambda_{exc} = 526$) when it binds to the DNA. The replacement of EB in the DNA-EB complex by another molecule results in quenching in the emission band. The quenching of the emission band of the DNA-EB are often referred to the competitive binding of the molecule via intercalation or groove binding. In the emission spectral measurements, to the constant concentration of FSds-DNA (75 μ M) solution pre-treated with 5 μ M EB in Tris-HCl, increasing amount of the compound (HDSB, 0-100 μ M in DMSO) were added. The emission spectra of the solutions were recorded in the wavelength range of 570-750 nm upon irradiation at 526 nm. The quenching of the emission band was followed and the quenching constants (K_{sv}) was calculated from the Stern-Volmer equation given below:

$$F_0/F = 1 + K_{SV}[Q]$$

Where; F_0 : emission intensity of DNA-EB in the absence of HDSB, F : emission intensity of DNA-EB in the presence of HDSB and $[Q]$: the total concentration of HDSB.

Bsa Binding Studies

The bovine serum albumin (BSA) properties of the homo-disulphide Schiff base compound (HDSB) was investigated by fluorescence spectral measurements [22]. The emission spectra of BSA (2.5 μ M) solution in Tris-HCl buffer (pH = 7.4) were recorded in the range of 320-500 nm (λ_{exc} : 280 nm) upon incremental addition of HDSB (0-100 μ M in DMSO). For each measurement, the mixtures were shaken and stands for 20 min at three different temperatures (288, 300 and 310 K). Concentration of BSA was determined by using the molar absorption coefficient of BSA at 279 nm (43824 mol⁻¹cm⁻¹). The quenching constant of the emission band of BSA in the presence of HDSB was calculated using Stern-Volmer equation (F_0/F) versus $\log [Q]$.

X-ray crystallography

Single crystal X-ray crystallographic data for the homo-disulphide Schiff base compounds (HDSB) were recorded at 293(2) K on a Bruker APEX 2 CCD diffractometer using Mo- $K\alpha$ radiation ($\lambda = 0.71073$ Å). Data reduction was performed using Bruker SAINT [23]. SHELXT was used to solve and SHELXL to refine the structure [24, 25]. The structure of the compound was solved by direct method and refined on F^2 using all the reflections. The hydrogen atoms bonded to carbon and oxygen atoms were inserted at calculated positions using a riding model.

Results and Discussion

Chemistry

The reactions between the 2-aminothiophenol and salicylaldehyde derivatives results in thiol Schiff base compounds. However, thiol Schiff base compounds are often susceptible to air oxidation that usually gave homo-disulphide Schiff base derivatives [26]. Moreover, it was reported that solvents can induce air oxidation of thiophenols into and homo-disulphides [27]. A speculated mechanism of conversion of the thiol Schiff bases to their homo-disulphide derivatives through reaction with oxygen have been proposed [26]. In this study, a homo-disulphide Schiff base compound (HDSB) was directly prepared by the condensation reaction of 2-aminothiophenol and 2-hydroxy-4-(prop-2-yn-1-yloxy)benzaldehyde in benzene. In the reaction, both Schiff base condensation and oxidation of thiols into disulphide occurred. The yellow-coloured homo-disulphide Schiff base compound (HDSB) is soluble in MeOH, EtOH, $CHCl_3$, diethyl ether, THF, DMF and DMSO. The structure of the compound was characterized by common spectroscopic and analytical methods (FTIR, 1H NMR and elemental analysis). Furthermore, the crystal structure of the compound was also examined by single crystal X-ray diffraction study. The FTIR spectrum of the compound was carried out and spectral data are given in the experimental section. The spectrum of the compound is shown in Figure 1. The FTIR spectrum of the compound showed peaks at 3274, 3060 and 2857 cm^{-1} due to the $\nu(C-H)$ stretching frequencies. In the spectrum, a relatively weak band at 3400-3500 cm^{-1} range is due to the phenolic group stretching's $\nu(O-H)$. The thiol Schiff base compounds show the $\nu(S-H)$ stretching frequency at 2500-2600 cm^{-1} range [28]. In the spectrum of the synthesized compound, no peak due to the $\nu(S-H)$ group stretching was observed and this is indicative of a stoichiometric formation of homo-disulphide Schiff base compound in the reaction [29]. Moreover, a weaker peak at 553 cm^{-1} due to the $\nu(S-S)$ stretching frequency confirms the homo-disulphide structure. In the spectrum of the compound, a relatively weaker peak at 2115 cm^{-1} can be assigned to the alkyne group $\nu(C\equiv N)$ on the phenol ring [30]. The IR spectrum of the compound displayed a strong peak at 1606 cm^{-1} and this peak is assigned to the which could be due to $\nu(C=N)$ stretching frequency. The FTIR spectral data of the homo-disulphide compound are similar to those of

similar homo-disulphide Schiff base compounds reported in literature [12].

The 1H NMR spectrum of the compound was recorded in $CDCl_3$ and the obtained data are presented in the experimental section. The spectrum of the compound displayed a signal at 13.45 ppm due to the phenolic OH protons. The presence of the signal due to the phenolic OH is indicative of enolic structure in solution. The azomethine proton ($HC=N$) resonance appears as a singlet at 9.05 ppm. The aromatic protons of the compounds were observed as multiplets at 7.80-6.55 ppm range. In addition, sharp signals at 4.63 and 2.54 ppm are assigned to the $O-CH_2$ and terminal acetylenic $C\equiv CH$ protons. Integration values in the spectrum is in well agreement with the proposed structure.

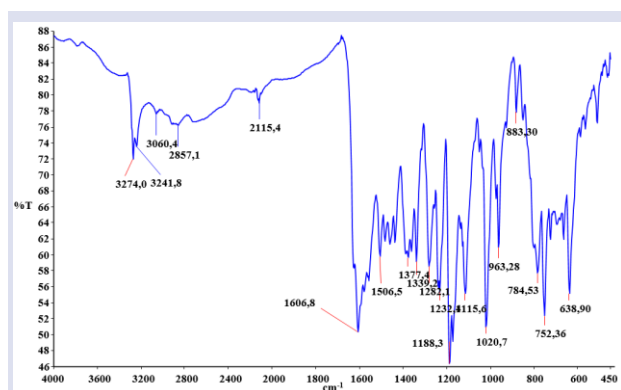


Figure 1. FTIR spectrum of the homo-disulphide Schiff base compound (HDSB)

Molecular Structure of Homo-Disulphide Schiff Base Compound (Hdsb)

Single crystals suitable for X-ray diffraction studies were obtained by recrystallization of the compound from chloroform solution. The definite structure of the compound was obtained from X-ray diffraction study. The X-ray refinement values and other crystallographic data obtained from X-ray diffraction studies of the compound are presented in Table 1. The structure of the compound was solved in the triclinic unit cell and P-1 space group. Molecular structure of the compound obtained from X-ray study is given in Figure 2. The disulphide bond (S-S) in the molecule form by the dimerization of two identical thiol units. The S1-S2 disulphide bond in dimeric molecule has a distance of 2.0215(10) Å (Table 2), which is very close to the S-S single bond distance observed in reported similar structures [12]. The N1-C10 and N2-C23 imine bond distances are 1.271(3) and 1.282(3) Å, respectively, and these distances are within the expected $C=N$ double bond distance [31]. In addition, O2-C6 and O3-C25 distances have characteristic C-O single bonds. The propargyl groups (C1-C2-C3 and C30-C31-C32) in the phenolic rings in the compound have an approximate linear geometry. The bond lengths of the C1-C2 and C31-C32 alkyne groups in the propargyl group are 1.160(4) and 1.153(4) Å, respectively, showing a $C\equiv C$ triple bond character. The phenolic groups (O2H and O3H) in the compound made intramolecular hydrogen bonds ($O2-H\cdots N1$ and $O3-H\cdots$

N2) with the imine bond nitrogen atoms (N1 and N2). In addition, phenolic groups interacted weakly with the sulphur atoms (O2-H \cdots S1 and O3-H \cdots S2) in the disulphide bond.

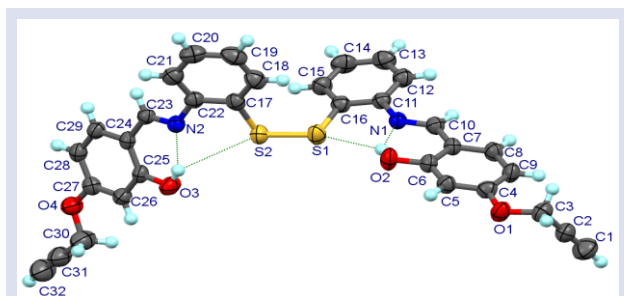


Figure 2. Molecular structure of the compound with atom numbering (thermal ellipsoid 50% probability). Hydrogen bonds are shown as dashed lines.

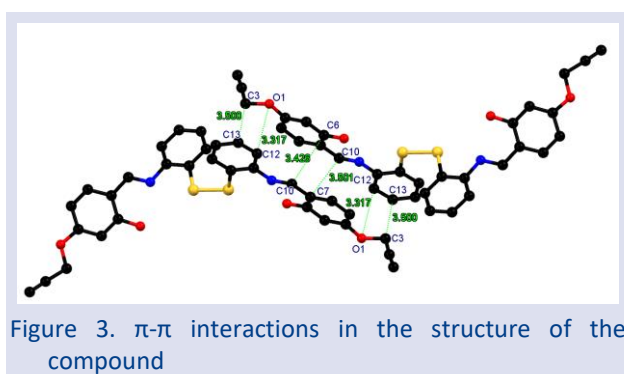


Figure 3. π - π interactions in the structure of the compound

When the data obtained from the X-ray diffraction studies of the compound were examined, it was determined that there were repeated π - π interactions between the molecules. One edge of the phenol and benzene rings in the compound formed head-tail type π - π interactions with the same edge in the neighbouring molecule (Figure 3). In addition, weak intermolecular C-H \cdots O, C-H \cdots S and C-H \cdots π interactions ensured the stability of the crystal lattice. The packing diagram of the molecule showing the π - π stacking interactions is given in Figure 4.

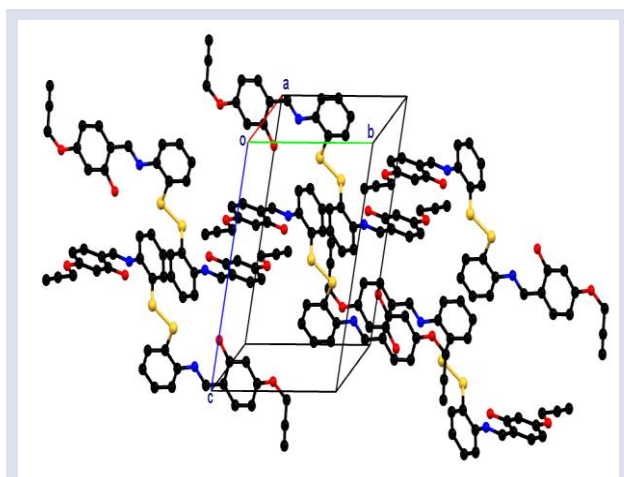


Figure 4. Packing diagram of HDSB

Table 1. Single crystal X-ray crystallographic data for the compound

Molecular formula	C ₃₂ H ₂₄ N ₂ O ₄ S ₂
Molecular weight (g/mol)	564.65
Temperature/K	298.0
Crystal system	Triclinic
Space group	P-1
a/Å	10.8703(11)
b/Å	12.2621(11)
c/Å	13.2290(9)
α /°	107.894(7)
β /°	91.944(7)
γ /°	115.300(9)
Volume/Å ³	1488.8(3)
Z	2
Crystal size/mm ³	0.15 × 0.13 × 0.11
Irradiation	Mo-K α (λ = 0.71073)
Refl. collected	12448
Independent refl.	6550 [R_{int} = 0.0317, R_{σ} = 0.0644]
Final R indexes [$I \geq 2\sigma(I)$]	R_1 = 0.0521, wR_2 = 0.1191
Final R indexes [all data]	R_1 = 0.0953, wR_2 = 0.1426
CCDC	2171343

Table 2. Bond distances for the Schiff base compound (Å)

S(1)-S(2)	2.0215(10)	C(4)-C(5)	1.382(3)	C(18)-C(19)	1.373(4)
S(1)-C(16)	1.778(2)	C(4)-C(9)	1.392(3)	C(19)-C(20)	1.383(4)
S(2)-C(17)	1.780(3)	C(5)-C(6)	1.370(3)	C(20)-C(21)	1.386(4)
O(1)-C(3)	1.426(3)	C(6)-C(7)	1.417(3)	C(21)-C(22)	1.385(3)
O(1)-C(4)	1.367(3)	C(7)-C(8)	1.389(3)	C(23)-C(24)	1.450(3)
O(2)-C(6)	1.343(3)	C(7)-C(10)	1.446(3)	C(24)-C(25)	1.398(3)
O(3)-C(25)	1.342(3)	C(8)-C(9)	1.370(3)	C(24)-C(29)	1.399(3)
O(4)-C(27)	1.369(3)	C(11)-C(12)	1.391(3)	C(25)-C(26)	1.383(3)
O(4)-C(30)	1.405(3)	C(11)-C(16)	1.391(3)	C(26)-C(27)	1.379(3)
N(1)-C(10)	1.271(3)	C(12)-C(13)	1.374(4)	C(27)-C(28)	1.388(3)
N(1)-C(11)	1.413(3)	C(13)-C(14)	1.376(4)	C(28)-C(29)	1.369(3)
N(2)-C(22)	1.412(3)	C(14)-C(15)	1.379(3)	C(30)-C(31)	1.466(4)
N(2)-C(23)	1.282(3)	C(15)-C(16)	1.385(3)	C(31)-C(32)	1.153(4)
C(1)-C(2)	1.160(4)	C(17)-C(18)	1.378(3)		
C(2)-C(3)	1.463(4)	C(17)-C(22)	1.402(3)		

UV-Vis Absorption and Photoluminescence Properties

The UV-Vis absorption and emission properties of the compounds were investigated in solution medium. The effect of the solvent on the absorption and emission properties were examined in different solvents (diethyl ether, chloroform, methanol and dimethyl sulfoxide). The absorption spectra and emission spectra of the compound are given in Figure 5. In methanol, the compound shows two well separated absorption bands in the range of 260-420 nm. The first band at 260-300 nm range (λ_{max} : 287 nm) can assigned to the π - π^* electronic transition due to the π -electrons in the structure of the compound. The latter band with higher absorbance values was seen at 306-420 nm range (λ_{max} : 341 nm) and this electronic absorption were assigned to the π - π^* and n - π^* transitions. Two separated absorption bands were preserved when the solvent was changed. However, depending on solvents,

the absorption values and position of the bands showed some shifts. The absorption bands of the compound showed bathochromic shifts in chloroform and diethyl ether. Moreover, the absorption values also increased (hyperchromic effect). The bathochromic shifts in low polar solvents (chloroform and diethyl ether) showed the interactions of the solvent with apolar groups of the compound. In DMSO, the absorption bands were also shifted longer wavelengths. The photoluminescence properties of the compound in the solutions were also studied. The solution of the compound was excited with the maximum absorption wavelength. The compound exhibited emission band at 350-550 nm range. In dimethyl sulfoxide and methanol, the compound showed an emission band at 350-500 nm range (λ_{exc} : 341 nm for dimethyl sulfoxide and 335 nm for methanol). In chloroform and diethyl ether, the compound exhibited dramatically different emission properties. In diethyl ether, the compound showed dual emission when irradiated at 345 nm, two emission bands were observed at 350-600 nm range. The first band with lower emission intensity at 350-380 nm range (λ_{max} : 365 nm) is narrow. The second band was broad and observed at 380-600 nm range. In chloroform solution, the compound showed similar emission characteristic to that of diethyl ether solution.

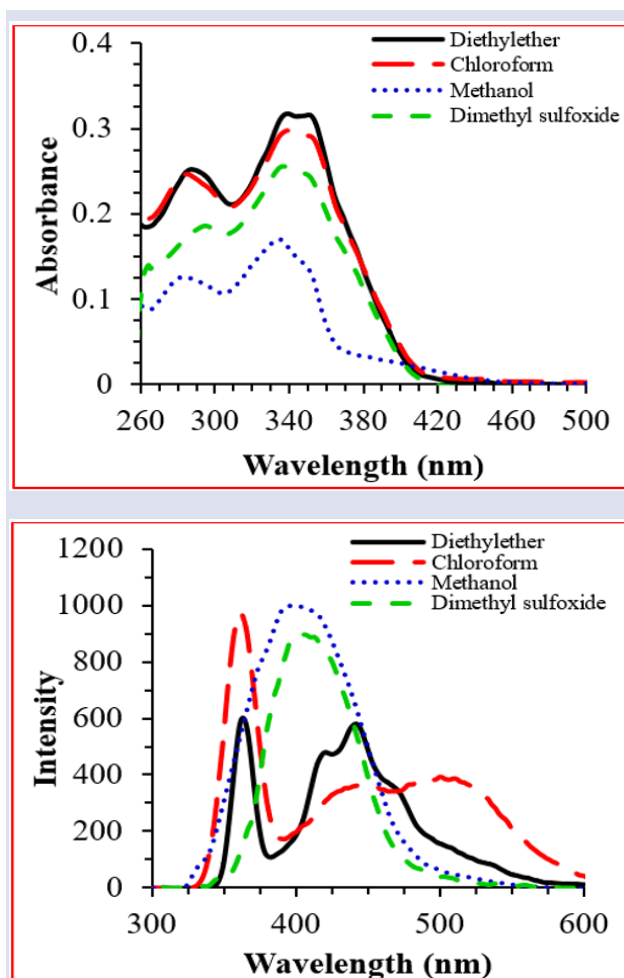


Figure 5. Absorption and emission spectra of the HDSB in different solvents (10^{-5} M)

Dna Binding Properties

DNA-targeting drugs are of great interest because the cause of many types of cancer is associated with DNA damage. There are many metal-organic and organic structures interacting with DNA in the literature [7]. DNA-targeted molecules interact with DNA in three modes (intercalation between base pairs, groove bonding, and electrostatic interactions). In order to examine the interactions between homo-disulphide compound and dsDNA synthesized within the scope of this study, UV-Vis spectra were obtained by adding increasing concentrations of FS-dsDNA to the compound solution. The UV-Vis absorption spectra obtained at increasing DNA concentrations of the compound are given in Figure 6. The interaction of small molecules with DNA usually results in a change in the UV-Vis absorption spectrum (hyperchromic or hypochromic effect and red or blue shift). The synthesized homo-disulphide compound showed two absorption bands of π - π^* and n - π^* electronic transitions in the 230-550 nm range. Addition of DNA at increasing concentrations (constant compound concentration) caused shifts in the absorption bands of the compound and decreased absorbance values. While no significant change was observed in the maximum absorption wavelength in the 230-300 nm range in the spectrum of the compound, the absorbance values gradually decreased. On the other hand, with increasing DNA addition, a noticeable red shift was observed in the absorption band observed in the 330-530 nm range. In addition, the addition of DNA caused a gradual decrease in the absorption values of this band. The DNA binding constant (K_b) of the HDSB compound was calculated taking into account the change in the absorption band (with the addition of DNA) observed in the 330-530 nm range [32]. The compound had a DNA binding constant of $4.1 \times 10^4 \text{ M}^{-1}$ and showed lower DNA binding affinity than ethidium bromide, a DNA intercalating molecule ($K_b = 1.4 \times 10^6 \text{ M}^{-1}$). It is thought that HDSB compound synthesized according to this obtained binding constant value interacts with DNA in minor groove binding mode. Also, the DNA binding constant of HDSB compound is within the range of minor groove binding agents reported in the literature [33].

In order to further investigate the DNA binding mode of the synthesized homo-disulphide Schiff base compound, competitive DNA binding studies were carried out with ethidium bromide (EB). As it is known, EB is a DNA binding agent and interacts with DNA by intercalating. The EB molecule is inserted between the DNA base pairs. The DNA-EB complex formed by the interaction of EB with DNA creates a characteristic emission in the range of 550-800 nm when excited at 526 nm [34]. In the presence of a second molecule that can intercalate with DNA close to or better than EB, a competition for DNA binding is expected. The decrease in the intensity of the emission band formed by the DNA-EB complex is generally attributed to the release of DNA-bound EB from the DNA-EtBr complex, the excited state energy transfer, or the conformational change of DNA [35]. The emission spectrum obtained by

adding increasing concentrations of the synthesized compound (HDSB) to the solution containing DNA-EB is shown in Figure 7.

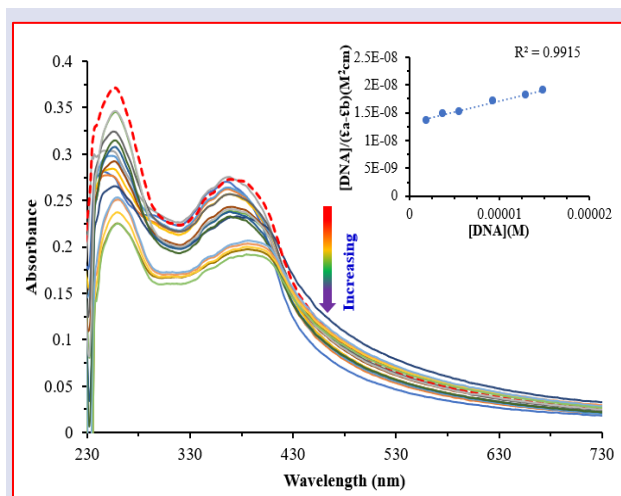


Figure 6 Absorption spectra of HDSB, in 2 mM Tris-HCl/2 mM NaCl buffer at pH 7.1 upon the addition of FSdsDNA. Inset: plot of $[DNA]/\epsilon_a - \epsilon_f$ vs. $[DNA]$ in for the titration of FSdsDNA with HDSB (0-100 μM)

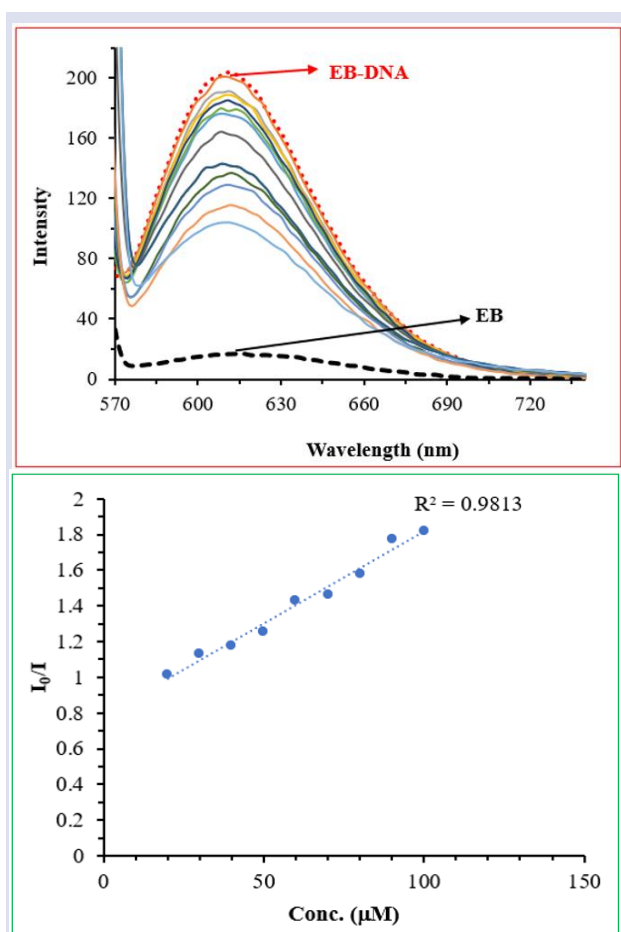


Figure 7. The emission spectra of the FSdsDNA-EB complex (75 μM) in the presence of various concentrations (0-100 μM) of HDSB in 2 mM Tris-HCl buffer (pH 7.1). Stern-Volmer plot of fluorescence titrations of HDSB with FSdsDNA. (λ_{exc} : 526 nm).

As seen in Figure 7, DNA-EB emission intensity decreased with HDSB addition and showed fluorescence quenching effect. This decrease observed in the fluorescence spectrum does not clearly show the intercalation of the compound with DNA, but confirms that it exhibits significant interaction with DNA. The slope of the I_0/I versus $[concentration]$ graph obtained from the Stern-Volmer equation gives the quenching constant K_{sv} . The nonlinearity of the plot of I_0/I versus $[concentration]$ suggests that emission quantification occurs through both dynamic and static damping mechanisms [36]. The fact that HDSB compound showed almost linear damping effect in the range of 20-100 μM indicates that the damping mechanism is static [36]. The K_{sv} value for the compound calculated from the Stern-Volmer equation is $1.02 \times 10^4 \text{ M}^{-1}$, which is close to some compounds that competitively bind to DNA with ethidium bromide.

Bsa Binding Properties

In addition to many important physiological functions of biomolecules such as serum albumins, they have very important roles in the transport and metabolism of many endogenous and exogenous compounds in metabolism. Due to its structural similarity to human serum albumin, bovine serum albumin (BSA) is the most studied protein for the investigation drug-protein interactions. Fluorescence spectroscopy is one of the most commonly used methods to investigate the interaction of small molecules with proteins. BSA is a fluorescent due to the presence of the amino acid residues such as phenylalanine, tyrosine and tryptophan. The interaction of BSA with small molecules generally results in a reduction in emission intensity (fluorescence quenching) [37]. BSA solution shows an emission band in the range of 320-400 nm when irradiated at 280 nm. The gradual addition of synthesized homo-disulphide Schiff base (HDSB) to the BSA solution causes an obvious decline in the emission band (Figure 8) showing the interactions of HDSB with BSA. With the increase of HDSB, a linear decrease in the emission intensity of BSA was observed. On the other hand, in the presence of HDSB, a new emission band appeared at 420-500 nm range (λ_{exc} : 280 nm). The formation of the new band is due to the emission characteristic of HDSB and the emission characteristic of the HDSB was discussed in section 3.3. The quenching constant (K_{sv}) was calculated using the Stern-Volmer equation [38]. The quenching constant (K_{sv}) was found to be $1.88 \times 10^5 \text{ M}^{-1}$, showing significant BSA-HDSB interaction.

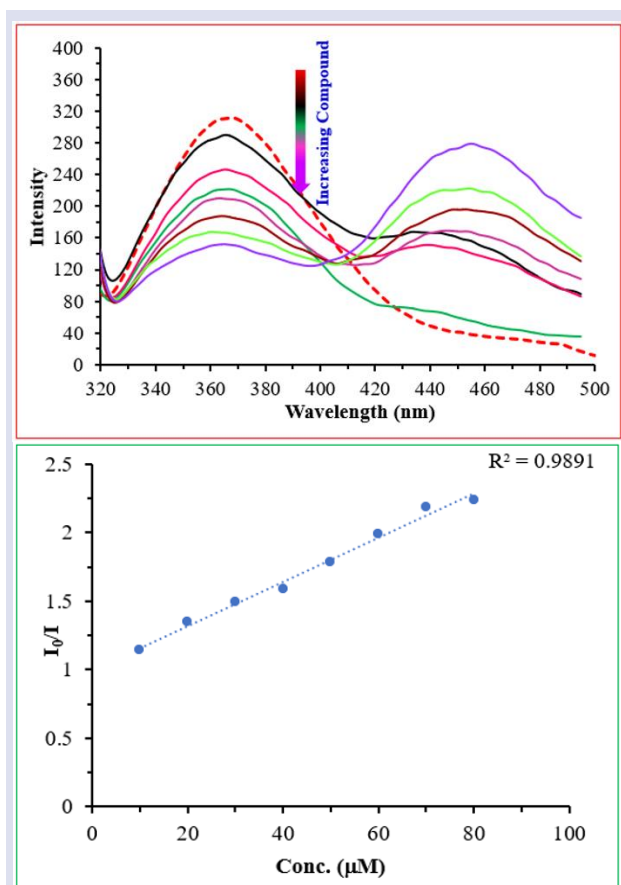


Figure 8 Emission spectra of BSA (λ_{exc} : 280 nm, λ_{em} : 362 nm) in the presence of increasing amounts of HDSB (0-100 μ M in DMSO). Stern-Volmer plot for HDSB with BSA protein

Conclusion

A homo-disulphide Schiff base compound (HDSB) was prepared and its DNA/BSA binding properties were investigated. The crystal structure of the compound was determined by single crystal X-ray diffraction experiment. The synthesised compound showed binding affinities towards both DNA and BSA. The spectral measurements suggested that the compound can be considered as a new DNA minor groove binding agent.

Conflicts of interest

There are no conflicts of interest in this work.

References

- [1] Abdel-Mohsen H. T., Sudheendran K., Conrad J., Beifuss U., Synthesis of disulfides by laccase-catalyzed oxidative coupling of heterocyclic thiols, *Green Chem.*, 15 (2013) 1490–1495.
- [2] Ali A. Q., Teoh S. G., Salhin A., Eltayeb N. E., Khadeer Ahamed, M. B., Majid A. M. S. A., Synthesis of isatin thiosemicarbazones derivatives: In vitro anti-cancer, DNA binding and cleavage activities, *Spectrochim. Acta - Part A Mol. Biomol. Spectrosc.*, 125 (2014) 440–448.
- [3] Amirnasr M., Bagheri M., Farrokhpour H., Schenk K. J., Mereiter K., Ford P. C., New Zn(II) complexes with N2S2 Schiff base ligands. Experimental and theoretical studies of the role of Zn(II) in disulfide thiolate-exchange, *Polyhedron*, 71 (2014) 1–7.
- [4] Annaraj B., Balakrishnan C., Neelakantan M. A., Synthesis, structure information, DNA/BSA binding affinity and in vitro cytotoxic studies of mixed ligand copper(II) complexes containing a phenylalanine derivative and diimine co-ligands, *J. Photochem. Photobiol. B Biol.*, 160 (2016) 278–291.
- [5] Annaraj B., Neelakantan M. A., Synthesis, crystal structure, spectral characterization and biological exploration of water soluble Cu(II) complexes of vitamin B6 derivative, *Eur. J. Med. Chem.*, 102 (2015) 1–8.
- [6] Behpour M., Ghoreishi S. M., Mohammadi N., Soltani N., Salavati-Niasari M., Investigation of some Schiff base compounds containing disulfide bond as HCl corrosion inhibitors for mild steel, *Corros. Sci.*, 52 (2010) 4046–4057.
- [7] Bharti S., Choudhary M., Mohan B., Rawat S. P., Sharma S. R., Ahmad K., Syntheses, spectroscopic characterization, SOD-like properties and antibacterial activities of dimer copper (II) and nickel (II) complexes based on imine ligands containing 2-aminothiophenol moiety: X-ray crystal structure determination of disulfide Schiff, *J. Mol. Struct.*, 1164 (2018) 137–154.
- [8] Bhowan M. G., Jhaumeer Lalloo S., Hosten E. C., Khodabaccus M. M., Rhyman L., Ramasami P., Synthesis, spectroscopic, biological and DFT studies of new t-butyl substituted salicylaldehydes having disulfide moiety, *J. Mol. Struct.*, 1175 (2019) 13–23.
- [9] Chen Y., Ren J. Q., Zhang X. G., Wu D. Y., Shen A. G., Hu J. M., Alkyne-Modulated Surface-Enhanced Raman Scattering-Palette for Optical Interference-Free and Multiplex Cellular Imaging, *Anal. Chem.*, 88 (2016) 6115–6119.
- [10] Demircioğlu Z., Synthesis, crystal structure, spectroscopic characterization, chemical activity and molecular docking studies of (E) - 2 - ((3 - chloro - 4 - methylphenyl) imino) methyl) - 6 - ethoxyphenol , *J. Mol. Struct.*, 1246 (2021) 131114.
- [11] Gandhimathi S., Theetharappan M., Bhuvanesh N. S. P., Neelakantan M. A., Crystal structure, theoretical and experimental electronic structure and DNA/BSA protein interactions of nickel(II) N2O2 tetradentate Schiff base complexes, *Polyhedron*, 138 (2017) 88–102.
- [12] Geethanjali H. S., Nagaraja D., Melavanki R. M., Exploring the mechanism of fluorescence quenching in two biologically active boronic acid derivatives using Stern-Volmer kinetics, *J. Mol. Liq.*, 209 (2015) 669–675.
- [13] Gu J., Codd R., Copper(II)-based metal affinity chromatography for the isolation of the anticancer agent bleomycin from *Streptomyces verticillus* culture, *J. Inorg. Biochem.*, 115 (2012) 198–203.
- [14] Gungor O., Kocer F., Kose M., Cu(II) complexes of biguanidine ligands: Structural characterisation, DNA binding and antimicrobial properties, *J. Mol. Struct.*, 1204 (2020) 127533.
- [15] Güngör S. A., Tümer M., Köse M., Erkan S., Benzaldehyde derivatives with functional propargyl groups as α -glucosidase inhibitors, *J. Mol. Struct.*, 1206 (2020).
- [16] Güngör S. A., Tümer M., Köse M., Erkan S., N-substituted benzenesulfonamide compounds: DNA binding properties and molecular docking studies, *J. Biomol. Struct. Dyn.*, (2021) 1–15.
- [17] Jamshidvand A., Sahihi M., Mirkhani V., Moghadam M.,

- Mohammadpoor-Baltork I., Tangestaninejad S., Studies on DNA binding properties of new Schiff base ligands using spectroscopic, electrochemical and computational methods: Influence of substitutions on DNA-binding, *J. Mol. Liq.*, 253 (2018) 61–71.
- [18] Kumar S., Pandya P., Pandav K., Gupta S. P., Chopra A., Structural studies on ligand–DNA systems: A robust approach in drug design, *J. Biosci.*, 37 (2012) 553–561.
- [19] Lehrer S., Corrections - Solute Perturbation of Protein Fluorescence. The Quenching of the Tryptophyl Fluorescence of Model Compounds and Lysozyme by Iodide Ion, *Biochemistry*, 10 (1971) 4995–4995.
- [20] Liu S., Chen B., Yang Y., Yang Y., Chen Q., Zeng X., Electrochemical oxidations of thioethers: Modulation of oxidation potential using a hydrogen bonding network, *Electrochem. Commun.*, 109 (2019) 106583.
- [21] Manivel J., Sangeetha S., Murali M., DNA and BSA Interaction, DNA Cleavage and *In Vitro* Cytotoxicity of Copper(II) Complexes: [Cu(bba)(phen)](ClO₄)₂ is Promising Chemotherapeutic Scaffold, *J. Sci. Res.*, 12 (2020) 111–133.
- [22] Moosun S. B., Bhowon M. G., Hosten E. C., Jhaumeer-Laulloo S., Crystal structures, antibacterial, antioxidant and nucleic acid interactions of mononuclear, and tetranuclear palladium(II) complexes containing Schiff base ligands, *J. Coord. Chem.*, 69 (2016) 2736–2753.
- [23] Moosun S. B., Jhaumeer-Laulloo S., Hosten E. C., Gerber T. I. A., Bhowon M. G., Antioxidant and DNA binding studies of Cu(II) complexes of N,N'-(1,1'-dithio-bis(phenylene))-bis(salicylideneimine): synthesis and characterization, *Transit. Met. Chem.*, 40 (2015) 445–458.
- [24] Moubeen S. A. M., El-Shahat M. F., Aziz A. A. A., Attia A. S., Synthesis, characterization and biological evaluation of novel octahedral Ru(III) complexes containing pentadentate Schiff base ligands, *Curr. Chem. Lett.*, 10 (2021) 17–32.
- [25] Neelakantan M. A., Balakrishnan C., Balamurugan K., Mariappan S. S., Zinc(II)-N₂O₂ ligation complex-based DNA/protein binder and cleaver having enhanced cytotoxic and phosphatase activity, *Appl. Organomet. Chem.*, 32 (2018) 1–18.
- [26] Neelakantan M. A., Balakrishnan C., Selvarani V., Theetharappan M., DNA/BSA binding interactions and VHPO mimicking potential of vanadium(IV) complexes: Synthesis, structural characterization and DFT studies, *Appl. Organomet. Chem.*, 32 (2018) 1–16.
- [27] Ramadan R. M., Elantabli F. M., El-Medani S. M., Conversion of thiol to homodisulfide-Schiff base derivative: Synthesis, molecular structure, crystal structure and DFT studies, *J. Mol. Struct.*, 1196 (2019) 547–554.
- [28] Raman N., Sobha S., Thamarachelvan A., A novel bioactive tyramine derived Schiff base and its transition metal complexes as selective DNA binding agents, *Spectrochim. Acta Part A Mol. Biomol. Spectrosc.*, 78 (2011) 888–898.
- [29] S. Bruker, APEX2 and SAINT Bruker, (1998).
- [30] Shafaatian B., Mousavi S. S., Afshari S., Synthesis, characterization, spectroscopic and theoretical studies of new zinc(II), copper(II) and nickel(II) complexes based on imine ligand containing 2-aminothiophenol moiety, *J. Mol. Struct.*, 1123 (2016) 191–198.
- [31] Shafaatian B., Ozbakzai Z., Notash B., Rezvani, S. A., Synthesis, characterization, single crystal X-ray determination, fluorescence and electrochemical studies of new dinuclear nickel(II) and oxovanadium(IV) complexes containing double Schiff base ligands, *Spectrochim. Acta-Part A Mol. Biomol. Spectrosc.*, 140 (2015) 248–255.
- [32] Sharma A. K., Chandra S., Complexation of nitrogen and sulphur donor Schiff's base ligand to Cr(III) and Ni(II) metal ions: Synthesis, spectroscopic and antipathogenic studies, *Spectrochim. Acta-Part A Mol. Biomol. Spectrosc.*, 78 (2011) 337–342.
- [33] Sheldrick G. M., Crystal structure refinement with SHELXL, *Acta Crystallogr., Sect. C Struct. Chem.* 71 (2015) 3–8.
- [34] Sheldrick G. M., SHELXT - Integrated space-group and crystal-structure determination, *Acta Crystallogr. Sect. A Found. Crystallogr.*, 71 (2015) 3–8.
- [35] Shi J. H., Chen J., Wang J., Zhu Y. Y., Binding interaction between sorafenib and calf thymus DNA: Spectroscopic methodology, viscosity measurement and molecular docking, *Spectrochim. Acta-Part A Mol. Biomol. Spectrosc.*, 136 (2015) 443–450.
- [36] Vardhan H., Yusubov M., Verpoort F., Self-assembled metal-organic polyhedra: An overview of various applications, *Coord. Chem. Rev.*, 306 (2016) 171–194.
- [37] Wu W. Bin, Wong Y. C., Tan Z. K., Wu J., Photo-induced thiol coupling and C-H activation using nanocrystalline lead-halide perovskite catalysts, *Catal. Sci. Technol.*, 8 (2018) 4257–4263.
- [38] Zhang Q., Ni Y., Kokot S., Combined voltammetric and spectroscopic analysis of small molecule-biopolymer interactions: The levodopa and serum albumin system, *Talanta*, 88 (2012) 524–532.

Activity Improvement and Thermal Stability Enhancement of D-Aminoacylase Using Protein-Polymer Conjugates

Sema Bilgin ^{1,a}, Nazan Gökşen Tosun ^{2,b,*}, Cemil Alkan ^{1,c}, Esra Koç ^{1,d}, Seçil Erden Tayhan ^{3,e}, İsa Gökçe ^{3,f}

¹ Department of Chemistry, University of Tokat Gaziosmanpaşa, Tokat 60010, Türkiye

² Department of Biomaterial and Tissue Engineering, University of Tokat Gaziosmanpaşa, Tokat 60010, Türkiye

³ Department of Genetic and Bioengineering, University of Tokat Gaziosmanpaşa, Tokat 60010, Türkiye

*Corresponding author

Research Article

History

Received: 01/10/2021

Accepted: 02/10/2022

Copyright




©2022 Faculty of Science,
Sivas Cumhuriyet University


ABSTRACT


In this study, the synthesis of new polymer-protein conjugates using a grafting-from strategy was performed by employing photo-induced electron transfer reversible addition-fragmentation chain transfer (PET-RAFT) polymerization. D-aminoacylase is an industrially significant enzyme for the preparation of chiral amino acids and it is coupled with reversible addition-fragmentation (RAFT) chain transfer agent (CTA) using-activated ester chemistry. The effects of polymeric side chain compositions on the activity of D-aminoacylase were studied with two different polymeric side chain lengths. For this reason, two monomers, a hydrophilic N-(2-aminoethyl acrylamide) and a hydrophobic and N-(iso-butoxymethyl) acrylamide were used, respectively. It was found that modification by grafting from strategy increased the thermal stability of the D-aminoacylase enzyme. Additionally, the hydrophobic monomer conjugate has been reported to increase the activity of the enzyme more than the hydrophilic monomer.


Keywords: PET-RAFT polymerization, Grafting from method, Bioconjugation, D-aminoacylase, Acrylamide


 sema.bilgin@gop.edu.tr

 cemil.alkan@gop.edu.tr


 ysecilerden@gmail.com


 <https://orcid.org/0000-0001-5921-5437>

 <https://orcid.org/0000-0002-1509-4789>


 <https://orcid.org/0000-0001-8473-5896>


 nazan_goksen@hotmail.com

 esrafndk@gmail.com

 isa.gokce@gop.edu.tr

 <https://orcid.org/0000-0001-5269-1067>

 <https://orcid.org/0000-0001-7171-608X>

 <https://orcid.org/0000-0002-5023-9947>

Introduction

Enzymes have drawn attention in industrial applications such as food processing [1], detergents, textiles, and, organic synthesis [2] in recent years. However, environmental conditions such as high temperature and pH value are significant drawbacks to their use in these applications requiring enzymes that are very active and stable. Polymers are extensively used to overcome these drawbacks by ligating onto proteins. [3, 4]. The protein-polymer hybrids, known as bio-conjugates, have modulated various properties of the protein, such as stability, activity, and reusability, so they could be used as potential materials in industrial usage, drug delivery, biocatalysts, and biosensors [3]. Research in the previously reported studies in the literature demonstrated that the polymer-protein conjugation greatly modified the properties of the attached enzyme, especially its activity and stability [4]. As an example, Griebenow and coworkers studied with α - Chymotrypsin that hydrolyses site-specific peptide bonds of proteins and they increased the long-term stability of α - chymotrypsin using pegylation since α -chymotrypsin is autolyzed while hydrolyzing peptide bonds [5].

Bioconjugates are formed using 'grafting from' and 'grafting to' methods. While in grafting to method, polymer are initially synthesized before ligation, in grafting from method, the polymer grows on the protein attached to the chain transfer agent by addition of

monomer [6]. The grafting to method has some disadvantages, such as requiring the use of a low-weight polymer. The 'grafting-from' method may bring about considerably high grafting density and therefore simpler purification [7]. Surely, there are some challenges in this method like poor control of polymer growth and a limited monomer selection [8]. The present methods like atom transfer radical polymerization (ATRP) [9], and reversible addition-fragmentation chain transfer (RAFT) [10,11] have been validated in the polymerization of acrylates and acrylamides. Also, ATRP with low copper contend and some photo-catalyzed reactions have led to grafting-from metal sensitive proteins [12,13]. RAFT has been one of the families of reversible deactivation radical polymerization (RDRP) methods and has become one of the most preferred polymerization techniques due to its versatility [14,15]. Synthesizing polymers with RDRP techniques has been interesting because of its advantages such as predictability of the chain length of the polymer, low dispersion, and constantly growing chain length, which has been defined as 'livingness' [16-18]. One of RDRP techniques RAFT has been the focus of attention due to its facilitation of use and functional group tolerance. However, conventional RAFT, in particular, has advantages as it relies on the thermal radical produced, as well as similar handicaps with other radical polymerization techniques, such as termination reactions

that restrict chain growth. In addition, the completion time of the RAFT polymerization should not be too long to provide control over the chain length distribution, but it can sometimes take a long time [19]. Photo-chemical RAFT polymerization could be carried out at low temperatures such as room conditions and with a light source, which can provide sustainable and environmentally friendly green chemistry applications [20-22]. Therefore, photochemistry has opened new horizons in polymer chemistry [23,24]. In this context, photo-induced electron/energy transfer reversible addition-fragmentation chain transfer polymerization (PET-RAFT) has been put forth as one of the interesting photochemical polymerization techniques. PET-RAFT technique differs from the conventional RAFT method in that the chain transfer agent (CTA) used also acts as an initiator type. PET-RAFT method provides convenience such as using the inductive energy of light at low temperatures and recognizing functional group tolerance [25]. Recently, studies on the handicaps of RAFT polymerization have developed methods that perform RAFT polymerization photochemically rather than thermally. PET-RAFT method has been preferred in protein-polymer conjugations, especially because the polymerization occurs at ambient temperature, visible light has been used to induce, the reaction has been fast and the chain length could be easily controlled [26]. Sumerlin and coworkers have recently reported that polymer-protein hybrids were generated using grafting from method and photo-induced electron transfer (PET) RAFT polymerization method was used for the synthesis of polymer [27]. They declared that a chain transfer agent (CTA) and a photocatalyst agent Eosin pair were used to synthesize of lysozyme polymer hybrid by grafted-from method. These conditions were used to grow polymers from D-aminoacylase enzyme in this study.

D-amino acids and their derivatives are widely used in the industries such as medicine and cosmetics [28]. D-amino acids are produced using enzymatic transformation in the recent manufacturing processes [29]. Recombinant D-aminoacylase enzyme (EcD) was produced using *E. coli* DH5 α host strain. EcD was modified with a chain transfer agent and the subsequent grafting of monomers of N-(isobutoxymethyl) acrylamide (NIBMA) and N-(2-aminoethyl acrylamide) (AEA) using the photo RAFT method was reported here in this work. N-(isobutoxymethyl) acrylamide (NIBMA) is water-miscible monomer and also significantly hydrophobic since it does not dissolve in aqueous media when polymerized [30]. It is a fact that, there are a few reporting on the polymerization of NIBMA via reversible deactivation radical polymerization (RDRP) in the literature. NIBMA has been incorporated to block copolymers for the formation of nanoassemblies of coatings and some polymer films [31]. AEA is a hydrophilic monomer and the polymer synthesized from it is known as a hydrogel, its hydrophilicity offers several advantages such as being used as a drug delivery system regardless of pH [32]. These enzyme grafted polymers (pNIBMA and

pAEA) are expected to increase thermal stability of the enzyme and improve its enzymatic activity.

Here, we aimed to report the synthesis of D-aminoacylase-polymer conjugates using grafting from method. Two different monomers were used for the enzyme conjugation in this work and the effects of these two monomers on the D-aminoacylase enzyme were investigated and compared.

Experimental Section

Production of Recombinant D-aminoacylase Enzyme

D-aminoacylase coding nucleic acid sequence was purchased from BIOMATIK. amn gene (GenBank: CP033635.1) was amplified by PCR using two primers;

P1 (5'TTTTCCATGGATATGCAGGTTGACTGGCTGATC3')

and

P2 (5'TTTTCTCGAGGTGAGAGGTCTGACGACGAG3')

contained unique NcoI and XhoI (Promega Corporation) restriction sites. The PCR product was cloned into the pET 22b (+) expression vector with an N-terminal six-histidine tag. Chemically and electrocompetent *E. coli* DH5 α cells were transformed by heat shock at 42 °C with the pET22bAmn plasmid. Transformation mix was spread on LB agar culture plates including ampicillin (100 μ g /mL) and they were incubated at 37°C overnight. After transformation, plasmids were isolated from positive clones and confirmed by DNA sequencing. Rosetta-gamiTM (DE3) cells were transformed with pET22bAmn plasmid for recombinant D-aminoacylase expression. Rosetta-gamiTM (DE3) transformants were subcultured at 37 °C for 16 h in Luria-Bertani (LB) medium containing 100 μ g/mL ampicillin, 50 μ g/mL streptomycin, 50 μ g/mL chloramphenicol, 10 μ g/mL tetracycline. The subculture was cultured until the OD₆₀₀ reached 0.6 after transfer to a fresh medium., and IPTG (final concentration 0.1 mM) was used for induction. Rosetta-gamiTM (DE3) cells were grown with vigorous shaking at 37 °C for 4 h after induction and these cells were harvested by centrifugation at 8000 rpm for 10 min at 4 °C.

All operations in D-aminoacylase purification were performed at 4°C unless otherwise mentioned. Harvested cells were re-suspended in buffer A (100 mM NaCl, 100 mM NaH₂PO₄ buffer, pH 8.00) and disrupted by ultrasonic treatment. The supernatant was acquired as raw enzyme solution by centrifugation at 30 000 rpm for 20 minutes at 4 °C. Cleared cell lysate having crude enzyme solution was loaded onto a column filled with a Ni-NTA agarose affinity matrix (Qiagen, USA) pre-equilibrated with buffer A. The weakly bound histidine-rich proteins were washed away from the column after extensive washing of the resin with buffer A. Then the recombinant D-aminoacylase enzyme was eluted with buffer B (300 mM imidazole; 100 mM NaH₂PO₄, 100 mM NaCl, pH 8.00) at a flow rate of 0.5 mL/min. The fractions were collected and the d-aminoacylase activity was analyzed. Fractions containing higher enzyme activity were pooled [33,34].

Synthesis of Chain Transfer Agent (CTA)

Chain transfer agent (CTA) was synthesized as previously reported [35]. Briefly, potassium hydroxide (14.6 g, 0.26 mol) was dissolved in distilled water (15.0 mL) and ethanethiol (18.6 mL, 0.26 mol) was dissolved in acetone (150 mL) then the potassium hydroxide solution was added slowly to the prepared ethanethiol solution by stirring on an ice bath. After adding carbon disulphide (16.1 mL, 0.27 mol) to the reaction mixture, the mixture was stirred for 30 min on ice bath. End of the time, the mixture was left to heat up to room temperature and 2-bromopropionic acid (22.0 mL, 0.25 mol) was supplemented dropwise and the reaction mixture was left to stir overnight at room temperature. Solution was evaporated to remove solvent using rotary evaporator.

The residue was dissolved in ether (200 mL) first in a separator funnel, and then water (200 mL) was added. The yellow ether layer was collected and washed with 200 mL water six times subsequently, and then once with saturated sodium chloride solution. CTA, a viscous yellow liquid solidifying upon freezing, was obtained by removing solvent using rotary evaporation. CTA was defined by proton NMR spectroscopy.

Synthesis of N-hydroxysuccinimide- Based CTA (NHS-CTA)

NHS-CTA was synthesized similar to the previously reported literature [36]. N-hydroxysuccinimide (NHS, 3.3 g, 29.7 mmol) was suspended in dry dichloromethane (100 mL) and then added dropwise into the solution consisting of 2-(1-isobutyl) sulfanylthiocarbonylsulfanyl-2-methyl propionic acid (CTA, 5.0 g, 19.8 mmol) and dicyclohexylcarbodiimide (DCC, 6.5 g, 29.7 mmol) in dichloromethane (150 mL) under nitrogen atmosphere on ice bath and the mixture was left to stir overnight at room temperature. After solvent evaporation and column chromatography (SiO₂: ethyl acetate/ petroleum ether 3:1) were carried out, the bright yellow solid product at high yield product was obtained and it was characterized by H-NMR.

Synthesis of D-aminoacylase- CTA

Grafting from method was modified to previously reported study [37]. Briefly, the concentration of D-aminoacylase (EcD) (3 mg/ml) was adjusted using 1×PBS solution (pH 7.5) in a total volume (10 mL). After that NHS-CTA (30 mg) was dissolved in 2 mL dimethyl sulfoxide (DMSO) and added dropwise to the stirring D-aminoacylase solution and the mixture was stirred for 2 h. Finally, the modified enzymes were dialyzed against 1×PBS containing 10% glycerine using a 25 k MWCO dialysis membrane (Spectrum Labs).

Grafting from D-aminoacylase- CTA

Grafting from the method reported in previous studies was modified for this study [37]. EcD was conjugated with two different acrylamide monomers, hydrophilic and hydrophobic. These are AEA (N-(2-aminoethyl

acrylamide)) and NIBMA (N-(iso-butoxymethyl) acrylamide), respectively and the conjugated enzymes were called EcD-pAEA and EcD-pNIBMA. For the synthesis of EcD-pAEA, N-(2-aminoethyl acrylamide) (AEA) (31 mg, 0.2 mmol) was firstly added to EcD-CTA solution and then Eosin Y (0.015 mg, 0.023 mmol), TEMED (N,N,N',N'-Tetramethylethylenediamine, 0.5 mL, 0.38 mg, 0.0023 mmol) and 75 µL of DMF were added to the 10 mL round bottom flask with a stir bar then the reaction mixture was exposed to nitrogen for degassing and sealing process for 30 min. Polymerization process was started with blue light while stirring. The blue light was extinguished to quench polymerization after 15 min, 30 min and 60 min and the obtained products were named as EcD-pAEA-S, EcD-pAEA-M and EcD-pAEA-L respectively. The synthesized products (EcD-pAEA-S, EcD-pAEA-M and EcD-pAEA-L) were characterized using ¹H NMR spectroscopy to confirm that polymerization had occurred. The products were lastly purified using dialysis against 100 mM NaH₂PO₄ (pH 8.00) solution.

For the synthesis of EcD-pNIBMA, this time NIBMA (34 mg, 0.2 mmol) was placed into the round bottom flask containing the EcD-CTA solution. After that the same reagents (Eosin Y, TEMED and DMF) which were mentioned above were added to reaction mixture while stirring then the reaction mixture was exposed to nitrogen for degassing and sealing process for 30 min. Polymerization was irradiated with blue light while stirring after that the products were named EcD-pNIBMA-S after 15 min, EcD-pNIBMA-M after 30 min and EcD-pNIBMA-L after 60 min. To confirm the polymerization, the obtained crude reaction products were characterized by using ¹H NMR spectroscopy. The crude reaction mixture was purified by dialysis against 100 mM NaH₂PO₄ (pH 8.00) solution. Conjugates were analyzed by SDS-PAGE.

To the best of our knowledge, functional group concentration decreases with molecular weight as shown in Fig.1, drawn theoretically. The best-fitting equation could also be used to calculate average molecular weight from the ratio of the weight of H of OH functional groups to the weight of H in CH₂ groups.

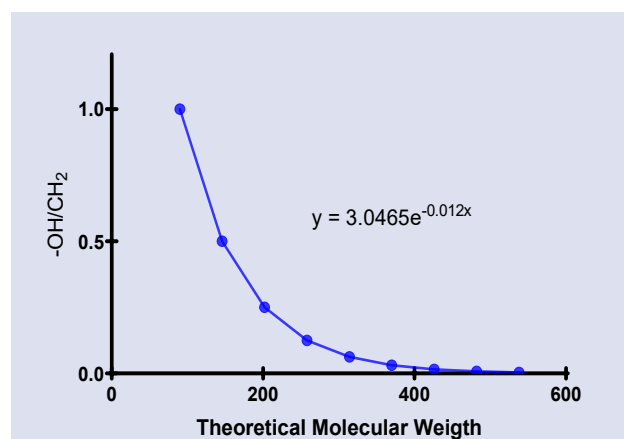


Figure 1. Mathematical expression of the increase in the theoretical molecular weight based on the decreasing ratio of side groups.

Hydrolysis Activity and Thermal Stability of D-Aminoacylase and its Polymer Conjugates

D-aminoacylase and their conjugates activities were determined with the 2,4,6-trinitrobenzenesulfonic acid method (TNBS) [38] and used N-acetyl-D-leucine as a substrate. The standard reaction mixture was prepared using 100 mM sodium phosphate buffer (pH 8), 50 mM N-acyl-d-leucine and an appropriate amount of the enzyme for the determination of enzymatic activity and incubated at optimum temperature 45°C for 30 min. End of the incubation time, the absorbance value of the reaction mixtures containing D-aminoacylase and their conjugates were measured at 335 nm using a Nanodrop DeNovIX spectrophotometer (Wilmington, USA). The relative enzymatic activities of EcD-pNIBMA and EcD-AEA conjugates were calculated based on D-aminoacylase activity and drawn using Graphpad Prism 8.1 software.

To determine the thermal stability of D-aminoacylase and their conjugates, they were pre-incubated at 45°C and pH 8 for different times (0, 30, 60, 90, 120 minute) after pre-incubation, the substrate was added to these enzymes' solutions and the observed orange colour was indicated that the enzymes were active and also the absorbance values were determined using a spectroscopy.

Thermal stability graph was plotted using Graphpad Prism 8.1 software of the enzyme solutions in absence of substrate for various at optimum temperature 45°C, respectively. Residual activities were determined under D-aminoacylase activity assay conditions.

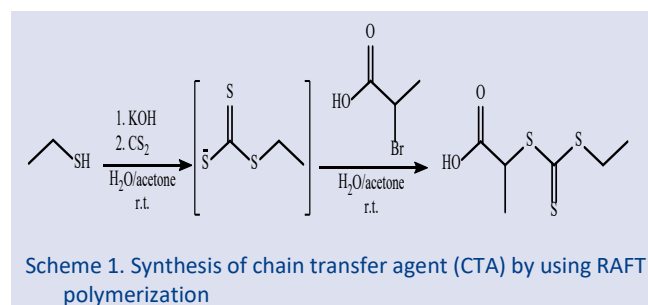
Results and Discussion

The ligation of polymers to proteins is recently used to improve proteins' biological activities [39]. The polymer-protein conjugates are usually occurred using grafting-to method, but this approach has disadvantages such as requiring polymer with low molecular weight. On the other hand, the grafting from approach allows high molecular weight polymers to be used, easy to purify and grow directly on proteins [40,41]. Consequently, grafting from method is commonly preferred instead grafting to method in the bio-conjugation process.

PET-RAFT, a polymerization method, occurs at room temperature by inducing visible light in the presence of a photocatalyst. PET-RAFT method has remarkable advantages such as low temperature requirement, visible light induction and regulation, and it is also

environmentally friendly [42]. Therefore, in this study, we decided to use PET-RAFT method to acquire grafting from polymerization of D-aminoacylase-conjugates. Eosin Y was preferred as a photocatalyst to inspect synthesis of acrylates and ethylacrylates in DMSO. To catalyze the polymerization process, Eosin Y was used with TEMED.

CTA, 2-(((ethylthio)- carbonothioyl) thio) propanoic acid was synthesized to use in production of polymers by RAFT polymerization as shown in Scheme 1. [43].



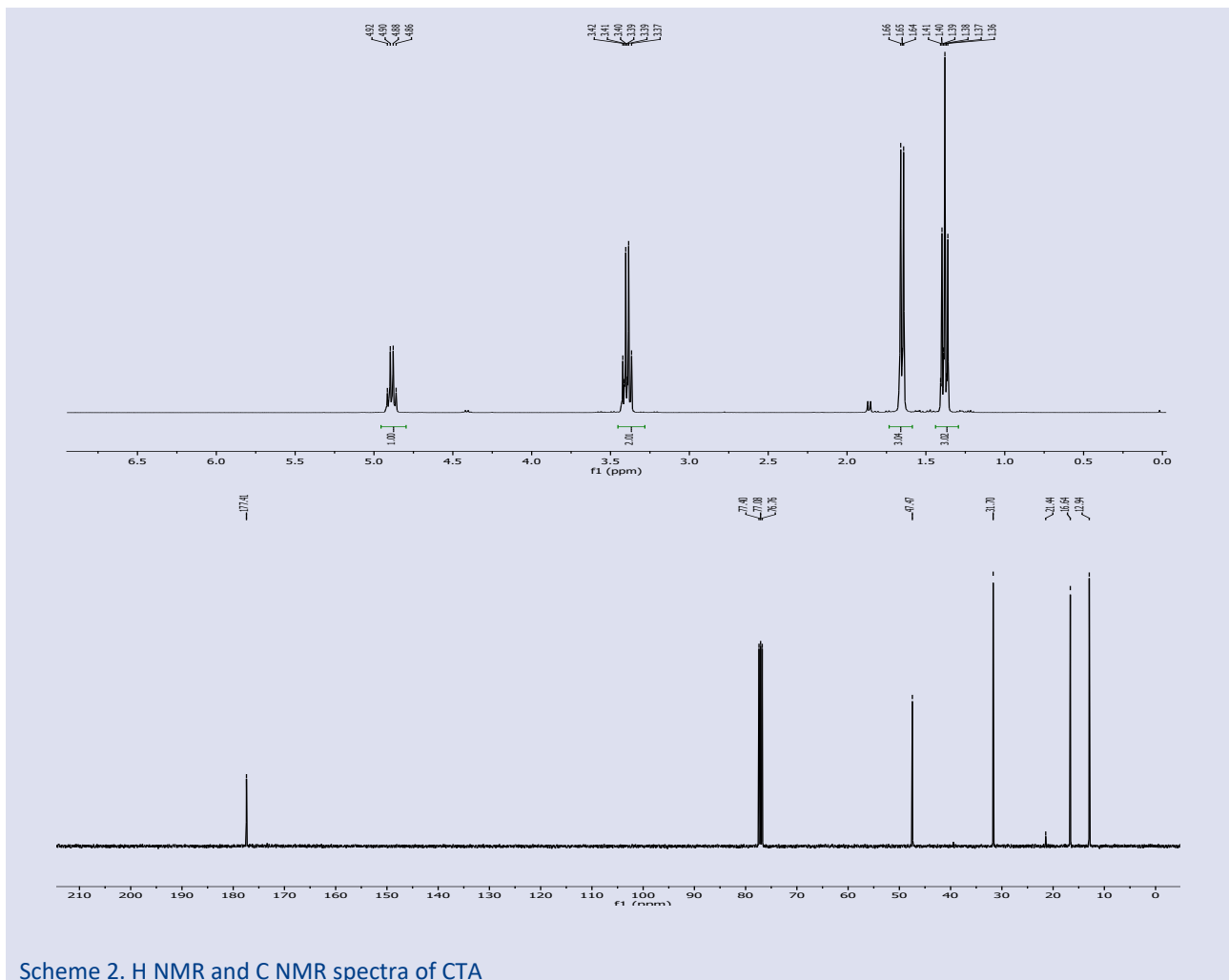
¹H-NMR and ¹³C-NMR data of CTA were given below, and these data were also presented in Scheme 2.

¹H-NMR (400 MHz, CDCl₃, ppm): δ = 4.92-4.86 (q, J = 8 Hz, 1H), 3.42-3.37 (q, J = 8 Hz, 2H), 1.66-1.64 (d, J = 8 Hz, 3H), 1.40-1.36 (t, J = 8 Hz, 3H).

¹³C-NMR (100 MHz, CDCl₃, ppm): δ = 177.4, 47.5, 31.7, 16.6, 150.4, 12.9.

N-hydroxysuccinimide esters (NHS) are significant vehicles used in bio-conjugate chemistry and provide a handle for growth polymers [44]. NHS-CTA was generated by adding CTA on N-hydroxysuccinimide ester. Recombinantly produced EcD was prepared 1×PBS solution in at a concentration of 3 mg/ml, it was added slowly dropwise on the enzyme solution after NHS-CTA was dissolved in DMSO. DMSO, as a solvent was required to dissolve CTA and slowly feeding, was prevented the enzyme precipitation that might result from high concentration of DMSO in reaction medium [45].

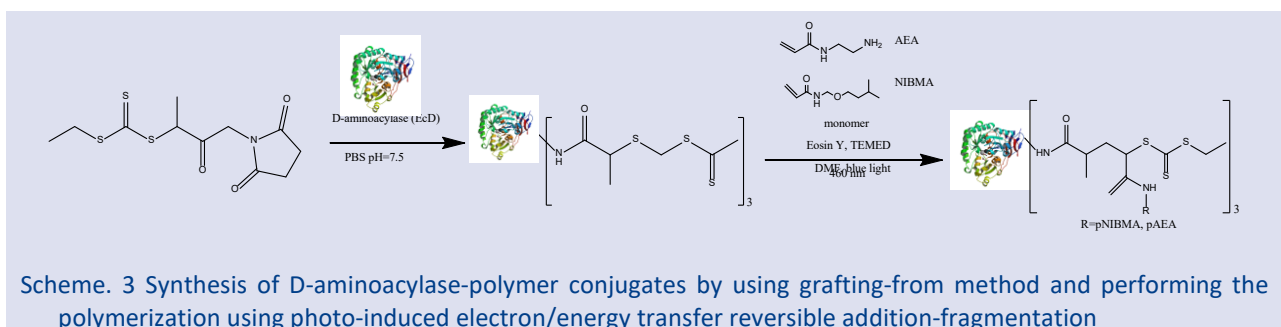
Subsequently, the obtained EcD-CTA was dialyzed to remove DMSO against 1× PBS with 10% glycerine using 25 k MWCO dialysis membrane tubing bag. The grafting from the polymerization was carried out using a polymerization catalyst TEMED together with Eosin Y as a photocatalyst in the presence of monomer. During the reaction period, it was observed that the color of the reaction medium changed from red to yellowish due to photodegradation of Eosin Y.



Scheme 2. H NMR and C NMR spectra of CTA

Throughout the grafting-from polymerization with D-aminoacylase-CTA using NIBMA and AEA monomers, bio-conjugates with different molecular weights were synthesized at different time periods and produced bio-

conjugates were called dependent on their lengths (short: EcD-pAEA-S, EcD-pNIBMA-S; medium: EcD-pAEA-M, EcD-pNIBMA-M; and long EcD-pAEA-L, EcD-pNIBMA-L) (Scheme 3.)



Scheme. 3 Synthesis of D-aminoacylase-polymer conjugates by using grafting-from method and performing the polymerization using photo-induced electron/energy transfer reversible addition-fragmentation

The polymerization ended quenching blue light after 60 min and the milky appearance of reaction media confirmed the suspension formation. After the polymerization completed, bio-conjugates were purified using dialysis membrane tubing.

The molecular weights of conjugates were calculated by using H-NMR data of the grafted side polymers of pNIBMA and pAEA from D-aminoacylase. Theoretically drawn molecular weight versus integral weight ratio curve of hydroxyl to aliphatic hydrogen (Fig 1) and best fitting equation were used for calculation. Molecular weights data were tabulated in Table 1.

Table. 1 Molecular weight data for grafted side polymers of pNIBMA and pAEA from D-aminoacylase – -graft-pNIBMA and D-aminoacylase -graft- pAEA produced using PET-RAFT polymerization

D-aminoacylase polymer conjugates	Molecular Weights of Bio-conjugates (g/mol)		
	Reaction Time (min)		
	15	30	60
EcD-pNIBMA	465	620	632
EcD-pAEA	532	544	560

According to the molecular weight results, it is observed that the molecular weight of the side groups could be controlled by the reaction time. Molecular weights of bio-conjugates were increased dependent on reaction time and these data were plotted using Graphpad Prisms 8.1 Software as shown in Fig 2.

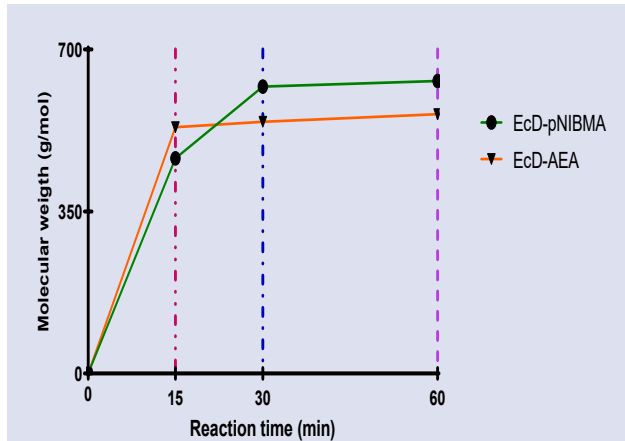


Figure 2. Variation of molecular weights of EcD-pNIBMA and EcD-AEA dependent on reaction time points.

Sodium dodecyl sulfate polyacrylamide gel electrophoresis (SDS-PAGE) of EcD-pNIBMA and EcD-pAEA demonstrated the polymers were ligated on the D-aminoacylase (Fig. 3). Besides that, SDS-PAGE results of the EcD-pNIBMA and EcD-pAEA confirmed that there was no free D-aminoacylase pointing out accomplished grafting from reactions.

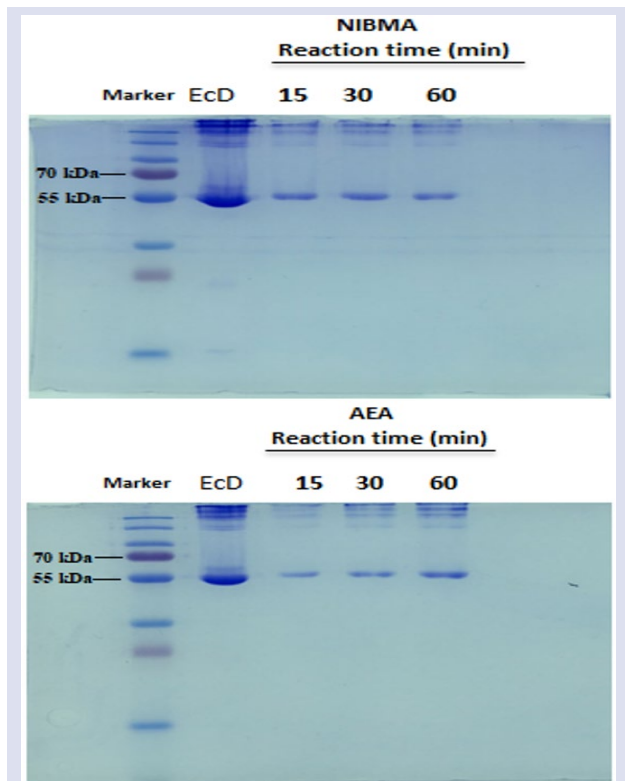


Figure 3. SDS-PAGE images of the obtained bio-conjugates at different reaction time

To evaluate the enzymatic activity of the EcD-pNIBMA and EcD-AEA bioconjugates, the enzyme activity was determined by using N-Acetyl-D-leucine as substrate with a method of 2, 4, 6-trinitrobenzene sulfonic acid (TNBS). TNBS is a highly sensitive and rapid chemical that is used to quantitate the free amino groups. A highly chromogenic product generated by the reaction of TNBS with primary amines was used for monitoring at 335 nm. Enzymatic activities of EcD, EcD-pNIBMA, and EcD-pAEA were measured at 335 nm using UV-visible spectroscopy and also observed changing the colour of substrate from colourless to orange. The activity results of bioconjugates were normalized comparing with enzymatic activity of native D-aminoacylase (EcD) and statistical analysis was carried out between groups using Graphpad 8.0 Prism Software as drawn in Fig 4.

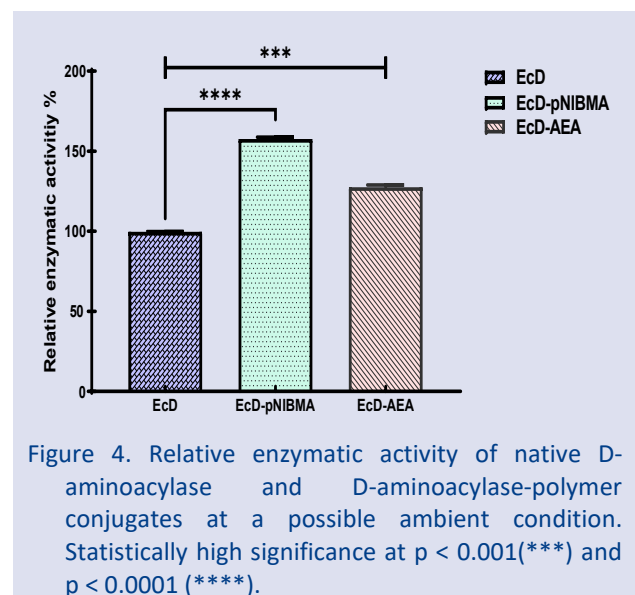
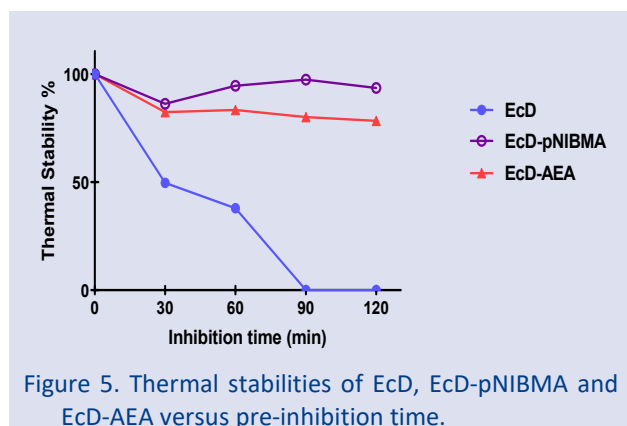


Figure 4. Relative enzymatic activity of native D-aminoacylase and D-aminoacylase-polymer conjugates at a possible ambient condition. Statistically high significance at $p < 0.001$ (***) and $p < 0.0001$ (****).

The bioconjugates exhibited high enzymatic activities than native enzyme. Moreover, EcD-pNIBMA occurred using hydrophobic monomer was more efficient than the other and the results were also found statically significant. Our results were similar to the studies in the literature [46]. Polymeric amine groups bounded to proteins increased enzymatic activity by removing water molecules from the hydrophobic regions of the protein, forming a local environment that increases enzyme-substrate-hydrophobic-hydrophobic interactions.

The thermal stabilities of the EcD-pNIBMA, EcD-AEA, EcD were investigated by thermal stability assay. For this reason, each material was subjected to an optimum temperature and an optimum pH by incubating each sample at different times (30, 60, 90, 120 min). D-aminoacylase and the bio-conjugates were analyzed using TNBS method, using N-acetyl-D-leucine as substrate. The native enzyme and bioconjugates were incubated for a certain period at specified conditions and then the substrate was added to each group (EcD-pNIBMA, EcD-AEA, EcD) and measured at 335 nm. The results were calculated using Graphpad 8.0 Prims Software as shown in Fig 5. The results revealed that grafting from method

could increase the thermal stability of enzymes. While the thermal stability of the native enzyme decreased linearly depending on the incubation time, it was determined that the grafted enzymes maintained their thermal stability. In addition, comparison of bio-conjugates EcD-pNIBMA was found more stable than EcD-pAEA and EcD-pNIBMA was remained stable as the time-dependent manner while thermal stability of EcD-pAEA was very slightly changed.



Conclusions

Well-defined, monodisperse protein-polymer bioconjugates have the potential to be important macromolecules for biotechnology and biomedicine. In particular, polymers could be synthesized by grafting from the method without damaging the structure and function of enzymes, increasing the activities of enzymes and allowing them to work in extreme conditions. In the present study, D-aminoacylase was first produced by the grafting from method and by PET-RAFT polymerization of protein-polymer bioconjugates using two different monomers. The PET-RAFT technique was successfully used to produce modified protein with extended bioactivity at optimum temperature and optimum pH. The PET-RAFT technique offered a versatile and high-throughput approach with effective control over polymerization while allowing the reaction to take place under room conditions. At the same time, the RAFT technique offered the opportunity to compare monomers with different properties by testing. Side chain lengths could be controlled over time for both grafted polymers, pNIBMA and pAEA. Compared with pAEA, pNIBMA was found to be more effective in biological activity. pNIBMA is more hydrophobic than pAEA and leads to better substrate conversion due to its protective effect on the enzyme environment. In addition, the bioconjugates were purified in one step by dialysis without the need for post-polymerization purification, and the absence of the need for serious chemicals makes this method both inexpensive and environmentally friendly. This study reveals that the bioconjugates obtained by the grafting from method using monomers with different properties of D-aminoacylase have increased activity compared to D aminoacylase. Polymers synthesized by PET-RAFT polymerization over D-aminoacylase by grafting from method acted as a thermal

shield for D-aminoacylase and it was determined that the thermal stability of bioconjugates increased compared to D-aminoacylase.

Acknowledgment

This work was supported by grants from Tokat Gaziosmanpaşa University, Foundation of Scientific Researches Projects (Project number: 2014/59).

Conflicts of interest

The authors declare that they have no conflict of interest.

References

- [1] Filice M., Aragon C., Mateo C., Palomo J., Enzymatic Transformations in Food Chemistry, *Current Organic Chemistry*, 21(2) (2016) 139–148.
- [2] Sheldon R. A., ve Pereira P. C., Biocatalysis engineering: The big picture, *Chemical Society Reviews*, 46(10) (2017) 2678–2691.
- [3] Wright T. A., Page R. C., Konkolewicz D., Polymer conjugation of proteins as a synthetic post-translational modification to impact their stability and activity, *Polymer Chemistry*, 10 (2019), 434-454.
- [4] Lucius M., Falatach R., McGlone C., Makaroff K., Danielson A., Williams C., Nix J. C., Konkolewicz D., Page R. C., Berberich J. A., Investigating the Impact of Polymer Functional Groups on the Stability and Activity of Lysozyme-Polymer Conjugates, *Biomacromolecules*, 17(3) (2016) 1123-1134.
- [5] Rodriguez-Martinez J. A., Rivera-Rivera I., Sola R. J., Griebenow K., Enzymatic activity and thermal stability of PEG- α -chymotrypsin conjugates, *Biotechnology Letters*, 31(6) (2009) 883-887.
- [6] Kaupbayeva B., Russell A. J., Polymer-enhanced biomacromolecules, *Progress in Polymer Science*, 101 (2020) 101194.
- [7] Xie Y., An J., Yang G., Wu G., Zhang Y., Cui L., Feng Y., Enhanced enzyme kinetic stability by increasing rigidity within the active site, *Journal of Biological Chemistry*, 289(11) (2014) 7994-8006.
- [8] Wallat J. D., Rose K. A., Pokorski J. K., Proteins as substrates for controlled radical polymerization, *Polymer Chemistry*, 5 (2014) 1545-1558.
- [9] Li S., Chung H. S., Simakova A., Wang Z., Park S., Fu L., Cohen-Karni D., Averick S., Matyjaszewski K., Biocompatible Polymeric Analogues of DMSO Prepared by Atom Transfer Radical Polymerization, *Biomacromolecules*, 18(2) (2017) 475–482.
- [10] Li H., Li M., Yu X., Bapat A. P., Sumerlin B. S., Block copolymer conjugates prepared by sequentially grafting from proteins via RAFT, *Polymer Chemistry*, 2 (2011) 1531-1535.
- [11] Li M., Li H., De P., Sumerlin B. S., Thermoresponsive block copolymer-protein conjugates prepared by grafting-from via RAFT polymerization, *Macromolecular Rapid Communications*, 32 (2011) 354-359.
- [12] Liu J., Bulmus V., Herlambang D. L., Barner-Kowollik C., Stenzel M. H., Davis T. P., In situ formation of protein-polymer conjugates through reversible addition-fragmentation chain transfer polymerization, *Angewandte Chemie - International Edition*, 46(17) (2007) 3099-3103.
- [13] Li X., Wang L., Chen G., Haddleton D. M., Chen H., Visible light-induced fast synthesis of protein-polymer conjugates:

- Controllable polymerization and protein activity, *Chemical Communications* 50 (2014) 6506-6508.
- [14] Jenkins A. D., Jones R. G., Moad G., Terminology for Reversible-Deactivation Radical Polymerization Previously Called 'Controlled' Radical or 'Living' Radical Polymerization (IUPAC Recommendations 2010), *Pure Appl. Chem.*, 82 (2) (2009) 483-491.
- [15] Parkatzidis K. Wang H. S., Truong N. P., Anastasaki A., Recent Developments and Future Challenges in Controlled Radical Polymerization: A 2020 Update, *Chem.*, 6(7) (2020) 1575-1588.
- [16] Braunecker W. A., Matyjaszewski K., Controlled/Living Radical Polymerization: Features, Developments, and Perspectives, *Prog. Polym. Sci.*, 32 (1) (2007) 93-146.
- [17] Goto A., Fukuda T., Kinetics of Living Radical Polymerization, *Prog. Polym. Sci.*, 29 (4) (2004) 329-385.
- [18] Chong B. Y. K., Le T. P. T., Moad G., Rizzardo E., Thang S.H., More Versatile Route to Block Copolymers and Other Polymers of Complex Architecture by Living Radical Polymerization: The RAFT Process, *Macromolecules*, 32 (6) (1999) 2071-2074.
- [19] Perrier S., 50th Anniversary Perspective: RAFT Polymerization - A User Guide, *Macromolecules*, 50 (19) (2017) 7433-7447.
- [20] McKenzie T. G., Fu Q., Uchiyama M., Satoh K., Xu J., Boyer C., Kamigaito M., Qiao G. G., Beyond Traditional RAFT: Alternative Activation of Thiocarbonylthio Compounds for Controlled Polymerization, *Adv. Sci.*, 3 (9) (2016) 1-9.
- [21] Dolinski N. D., Page Z. A., Discekici E. H., Meis D., Lee I.-H., Jones G. R., Whitfield R., Pan X., McCarthy B. G., Shanmugam S., Kottisch V., Fors B. P., Boyer C., Miyake G. M., Matyjaszewski K., Haddleton D. M., Alaniz J. R., Anastasaki A., Hawker C. J., What Happens in the Dark? Assessing the Temporal Control of Photo Mediated Controlled Radical Polymerizations, *J. Polym. Sci., Part A: Polym. Chem.*, 57 (3) (2019) 268-273.
- [22] Pan X., Tasdelen M. A., Laun J., Junkers T., Yagci Y., Matyjaszewski K., Photomediated Controlled Radical Polymerization, *Prog. Polym. Sci.*, 62 (2016) 73-125.
- [23] Theodorou A., Liarou E., Haddleton D. M., Stavrakaki I. G., Skordalidis P., Whitfield R., Anastasaki A., Velonia K., Protein Polymer Bioconjugates via a Versatile Oxygen Tolerant Photoinduced Controlled Radical Polymerization Approach, *Nat. Commun.*, 11(1) (2020) 1-11.
- [24] Jung K., Corrigan N., Ciftci M., Xu J., Seo S. E., Hawker C. J., Boyer C., Designing with Light: Advanced 2D, 3D, and 4D, Materials, *Adv. Mater.*, 32 (18) (2020) 1-21.
- [25] Allegrezza M. L., Konkolewicz D., PET-RAFT Polymerization: Mechanistic Perspectives for Future Materials, *ACS Macro Letters*, 10(4) (2021) 433-446.
- [26] Li X., Wang L., Chen G., Haddleton D. M., Chen H., Visible light-induced fast synthesis of protein-polymer conjugates: controllable polymerization and protein activity, *Chem. Commun.*, 50 (2014) 6506-6508.
- [27] Tucker B. S., Coughlin M. L., Figg C. A., Sumerlin B. S., Grafting-From Proteins using Metal-Free PET-RAFT Polymerizations under Mild Visible-Light Irradiation, *ACS Macro Letters*, 6 (4) (2017) 452-457.
- [28] Wang W., Xi H., Bi Q., Hu Y., Zhang Y., Ni M., Cloning, expression, and characterization of d-aminoacylase from *Achromobacter xylosoxidans* subsp. *denitrificans* ATCC 15173, *Microbiological Research*, 168(6) (2013) 360-366.
- [29] Schulze B., Wubbolts M. G., Biocatalysis for industrial production of fine chemicals, *Current Opinion in Biotechnology*, 10(6) (1999) 609-615.
- [30] King B., Lessard B. H., Controlled Synthesis and Degradation of Poly(N-(isobutoxymethyl) acrylamide) Homopolymers and Block Copolymers, *Macromolecular Reaction Engineering* 11(2) (2017) 1600073.
- [31] Kotsuchibashi Y., Ebara M., Idota N., Narain R., Aoyagi T., A 'smart' approach towards the formation of multifunctional nano-assemblies by simple mixing of block copolymers having a common temperature sensitive segment, *Polymer Chemistry*, 3(5) (2012) 1150-1157.
- [32] Dragan E. S., Perju M. M., Preparation and Swelling Behavior of Chitosan Poly (N-2-Aminoethyl Acrylamide) Composite Hydrogels, *Soft Materials*, 8(1) (2010) 49-62.
- [33] İncir İ., Kaplan Ö., Bilgin S., Gökçe İ., Development of a Fluorescent Protein-Based FRET Biosensor for Determination of Protease Activity, *Sakarya University Journal of Science*, 25(5) (2021) 1235-1244.
- [34] Kaplan Ö., İmamoğlu R., Şahingöz İ., Gökçe İ., Recombinant production of *Thermus aquaticus* single-strand binding protein for usage as PCR enhancer, *International Advanced Researches and Engineering Journal* 05(01) (2021) 042-046.
- [35] Paeth M., Stapleton J., Dougherty M. L., Fischesser H., Shepherd J., McCauley M., Falatach R., Page R. C., Berberich J. A., Konkolewicz D., Approaches for Conjugating Tailor-Made Polymers to Proteins, *Methods in Enzymology*, 590 (2017) 193-224.
- [36] Zobrist C., Sobocinski J., Lyskawa J., Fournier D., Miri V., Traisnel M., Jimenez M., Woisel P., Functionalization of titanium surfaces with polymer brushes prepared from a biomimetic RAFT agent, *Macromolecules*, 44(15) (2011) 5883-5892.
- [37] Kovaliov M., Allegrezza M. L., Richter B., Konkolewicz D., Averick S., Synthesis of lipase polymer hybrids with retained or enhanced activity using the grafting-from strategy, *Polymer*, 137 (2018) 337-345.
- [38] Fields R., The Rapid Determination of Amino Groups with TNBS, *Methods in Enzymology*, 25 (1972) 464-468.
- [39] Obermeyer A. C., Olsen, B. D., Synthesis and application of protein-containing block copolymers, *ACS Macro Letters*, 4(1) (2015) 101-110.
- [40] Heredia K. L., Maynard H. D., Synthesis of protein-polymer conjugates, *Organic and Biomolecular Chemistry*, 5 (2007) 45-53.
- [41] Wallat J. D., Rose K. A., Pokorski J. K., Proteins as substrates for controlled radical polymerization, *Polymer Chemistry*, 5 (2014) 1545-1558.
- [42] Cai J., Chen T., Xu Y., Wei S., Huang W., Liu R., Liu J., A versatile signal-enhanced ECL sensing platform based on molecular imprinting technique via PET-RAFT cross-linking polymerization using bifunctional ruthenium complex as both catalyst and sensing probes, *Biosensors and Bioelectronics*, 124 (125) (2019) 15-24.
- [43] Falatach R., McGlone C., Al-Abdul-Wahid M. S., Averick S., Page R. C., Berberich J. A., Konkolewicz D., The best of both worlds: Active enzymes by grafting-to followed by grafting-from a protein, *Chemical Communications*, 51 (2015) 5343-5346.
- [44] Barre A., Tintas M. L., Levacher V., Papamicael C., Gembus V., An Overview of the Synthesis of Highly Versatile N-Hydroxysuccinimide Esters, *Synthesis*, (49) (2017) 472-483.
- [45] Sumerlin B. S., Proteins as initiators of controlled radical polymerization: Grafting from via ATRP and RAFT, *ACS Macro Letters*, 1 (2012) 141-145.
- [46] Messina M. S., Messina K. M. M., Bhattacharya A., Montgomery H. R., Maynard H. D., Preparation of biomolecule-polymer conjugates by grafting-from using ATRP, RAFT, or ROMP, *Progress in Polymer Science*, 100 (2020) 101186.

Synthesis and Characterization of Novel Calix[4]arene Schiff Base Derivatives and Cytotoxicity Effect Evaluation on Cancer Cell Lines

Ayşen Işık ^{1,a,*}, Kezban Uçar Çiççi ^{2,b}, Hayrani Eren Bostancı ^{3,c}, Yusuf Tutar ^{4,d}, Ahmet Koçak ^{5,e}, Mustafa Yılmaz ^{5,f}

¹ Department of Biochemistry, Faculty of Science, Selcuk University, Konya, Türkiye

² Division of Basic Sciences and Health, Hemp Research Institute, Yozgat Bozok University, Yozgat, Türkiye

³ Department of Biochemistry, Faculty of Pharmacy, Cumhuriyet University, Sivas, Türkiye

⁴ Department of Biochemistry, Faculty of Pharmacy, University of Health Sciences, İstanbul, Türkiye

⁵ Department of Chemistry, Faculty of Science, Selcuk University, Konya, Türkiye

*Corresponding author

Research Article

History

Received: 10/09/2022

Accepted: 10/12/2022

Copyright



©2022 Faculty of Science,
Sivas Cumhuriyet University

ABSTRACT

In this study, four stages were used to create brand-new *p*-tert-butyl-calix [4] arene Schiff base derivatives. First, *p*-tert-butyl-phenol and formaldehyde are reacted to create *p*-tert-butyl-calix [4] arene (1). In the following step, methyl bromoacetate and *p*-ter-butyl-calix [4] arene (1) were combined with acetone and reflux to create the *p*-tert-butyl-calix [4] arene diester complex (2). The third step involves reacting the diester compound (2) and hydrazine hydrate to create the *p*-tert-butyl-calix [4] arene hydrazinamide molecule (3). In the final stage, calix [4] arene Schiff base derivatives (4a-d) were produced in good yields by combining compound (3), *p*-tert-butyl-calix [4] arene hydrazinamide, and various aldehyde derivatives with reflux in EtOH. Through the use of ¹H-NMR, ¹³C-NMR, infrared spectroscopy, and elemental analysis, the structures of produced compounds were verified. Four distinct cancer lines are linked to the antitumor activity of synthetic chemicals. (HT-29, a human colon cancer cell line, PC-3, a human prostate cancer cell line, C6, a rat glioma cell line and MCF-7, a human breast cancer cell line). Weak antitumor activity was seen in synthetic substances. However, only compound 4b was found to have potential efficacy against C6 and HT-29. It is clear that compound 4b, which has a nitro substitute on the phenyl ring, draws attention due to its increased activity.

Keywords: Calix[4]arene, Anticancer activity, Schiff Base.

^a isik.aysen@selcuk.edu.tr

^b <https://orcid.org/0000-0002-1280-0019>

^c erenbostanci@cumhuriyet.edu.tr

^d <https://orcid.org/0000-0001-8511-2316>

^e akocak@selcuk.edu.tr

^f <https://orcid.org/0000-0002-2487-2431>

^b ucarkezban@gmail.com

^e <https://orcid.org/0000-0002-4758-4141>

^d ytutar@yahoo.com

^f <https://orcid.org/0000-0003-2613-9644>

^f myilmaz42@yahoo.com

^f <https://orcid.org/0000-0003-2904-160X>

Introduction

A malignant condition characterized by unchecked and aberrant cell proliferation is referred to as cancer in general. Although different types of cancer have specific causes that lead to the abnormality, all types of cancer involve many mysterious phenomena [1]. Even though they were first developed as traditional anticancer medications, the most of them have negative side effects and primarily are unable to distinguish specifically between cancer cells and healthy cells. Selectivity is one of the primary issues with all current and forthcoming anticancer medications. As a result, throughout the past three decades, new developments in targeted chemotherapy have emerged. A scientific answer is clearly required in the area. From a comprehensive standpoint, it is possible to develop more potent medications and treatment plans to combat the tumor's resistance to therapy [2]. The use of supramolecular systems, such as macrocycles, has attracted attention in the realm of cancer therapy as a possible strategy to solve this issue.

Supramolecules typically form when two or more molecules come together under the influence of non-covalent bonding forces. Crown ethers, cyclodextrins, cucurbiturils, calixarenes, and pillar[n]arenes are examples of macrocyclic compounds [3-7]. The third generation of supramolecular chemistry is represented by

a significant class of cyclic oligomers known as calixarenes. These are made of phenolic units linked by methylene in the ortho positions. There are numerous more structural features of calixarenes, such as the simplicity modification of their basic core and their low toxicity, and their lack of immunological reactions [8]. Among all its biological characteristics, calix[n]arenes' capacity to inhibit the growth of cancer cells is one of the most extensively researched therapeutic areas. The cause is most likely a result of their distinct physicochemical characteristics, biocompatibility, and a variety of biological functions [9]. Numerous research teams have looked at the anticancer properties of molecules based on calixarene. Clinical trial data for anticancer drugs based on calixarene are among the most crucial. Only one Phase I investigation of OTX008, a calixarene-based molecule and galectin-1 inhibitor with potential antiangiogenic and antineoplastic activity, has been documented to date in the US clinical trials database [10]. According to this viewpoint, there is still a critical need for further research into the molecular mechanisms underlying the effects of novel functionalized calixarenes as anticancer agents.

On the other hand, due to their adaptability, Schiff bases are significant chemical substances in a variety of domains, including inorganic, analytical, and

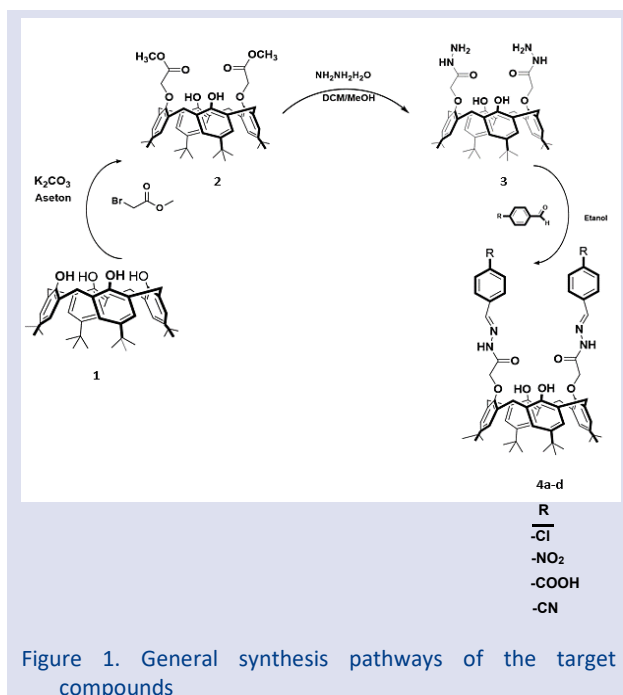
pharmaceutical chemistry. The carbonyl group of an aldehyde or beta diketone interacts with an amine moiety to generate Schiff bases. Because its active group ($-N=CH-$) contains active electrons, Schiff bases are excellent candidates for the development of novel medications [11-12]. Because of their extensive variety of pharmacokinetic properties and their popularity in drug development programs, the derivatives of Schiff bases represent a large category of substances that have found several applications in medicinal chemistry [13-14].

In the light of this information, we report the preparation, characterization four new calix [4] arene Schiff base derivatives (4a-d) and evaluate their anticancer activity against C6 (a rat brain glioma adenocarcinoma cell line), HT-29 (human colon carcinoma cell line), PC-3 (human prostate cancer cell line), and MCF-7 (human breast cancer cell line).

Materials and Methods

Chemistry

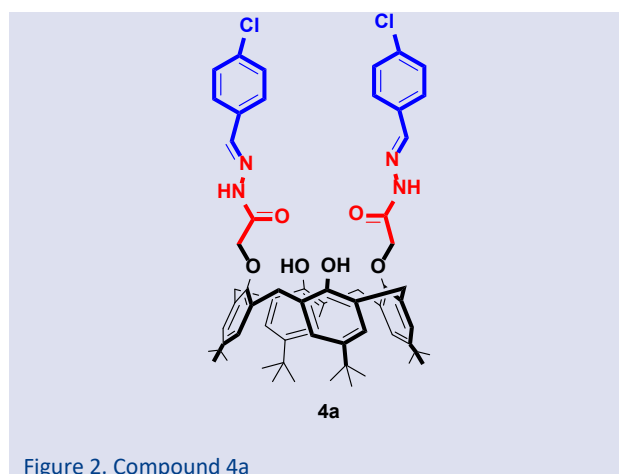
The different derivatives of calixarenes presented in Figure 1 (1, 2, and 3) were synthesized according to the literature [15-17].



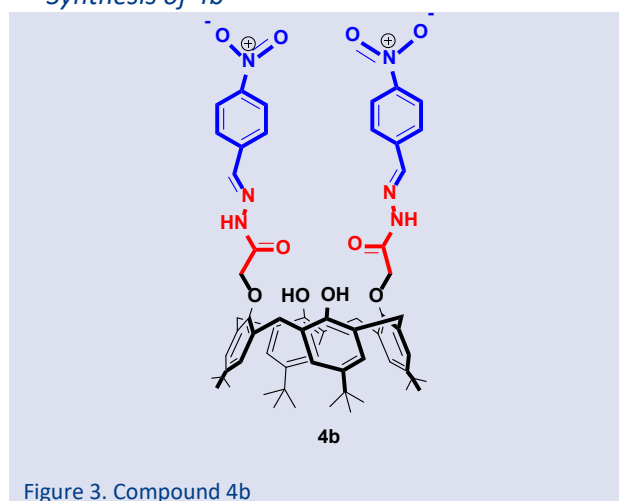
Synthesis of 4a

Compound (3) (0.30 g, 0.38 mmol) and 4-chlorobenzaldehyde (0.13 g, 0.91 mmol) are in ethanol solution under reflux with stirring for 12 hours. The reaction was checked with thin layer chromatography, and after this time, the solvent is removed and the target product is crystallized from ethanol. Yield 0.35 g (% 90), M.p.: 299.8-301.5 °C. IR (ATR) $\nu_{max}(cm^{-1})$: 1598 (HC=N), 1691 (C=O), 3373 (N-H). 1H -NMR (300 MHz, $CDCl_3$): δ (ppm) 1.07 (18H, s, Bu^t),

1.31 (18H, s, Bu^t), 3.56 (4H, d, $J = 13.44$ Hz, $ArCH_2Ar$), 4.19 (4H, d, $J = 13.38$ Hz, $ArCH_2Ar$), 4.74 (4H, s, $-OCH_2CO$), 6.99 (4H, s, $Ar-H$), 7.17 (4H, s, $Ar-H$), 7.37 (4H, d, $J=8.49$ Hz, 1,4-disubstituebenzene), 7.60 (4H, d, $J=8.52$ Hz, 1,4-disubstituebenzene), 7.90 (2H, s, OH), 8.26 (2H, s, $-CH=N$), 11.43 (2H, s, $-NH$). ^{13}C -NMR (75 MHz, $CDCl_3$): δ (ppm) 30.95, 31.57, 34.23, 74.38, 125.90, 126.49, 127.34, 128.97, 129.13, 132.05, 144.12, 147.97, 149.17, 163.59. Anal. Calcd for $C_{62}H_{70}Cl_2N_4O_6$: C, 71.73; H, 6.80; N, 5.40 %. Found: C, 71.48; H, 6.81; N, 5.39 %.



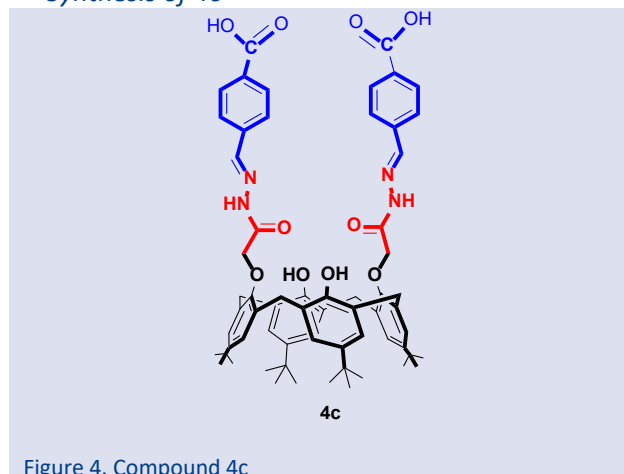
Synthesis of 4b



Compound (3) (0.30 g, 0.38 mmol) and 4-nitrobenzaldehyde (0.14 g, 0.91 mmol) are in ethanol solution under reflux with stirring for 12 hours. The reaction was checked with thin layer chromatography, and after this time, the solvent is removed and the target product is crystallized from ethanol. Yield 0.37 g (% 92), M.p.: 327.2-329.4 °C. IR (ATR) $\nu_{max}(cm^{-1})$: 1620 (HC=N), 1699 (C=O), 3234 (N-H). 1H -NMR (300 MHz, $CDCl_3$): δ (ppm) 1.10 (18H, s, Bu^t), 1.31 (18H, s, Bu^t), 3.59 (4H, d, $J = 13.47$ Hz, $ArCH_2Ar$), 4.19 (4H, d, $J = 13.35$ Hz, $ArCH_2Ar$), 4.76 (4H, s, $-OCH_2CO$), 7.03 (4H, s, $Ar-H$), 7.18 (4H, s, $Ar-H$), 7.82 (4H, d, $J=8.88$ Hz, 1,4-disubstituebenzene), 8.09

(2H, s, OH), 8.28 (4H, d, $J=8.82$ Hz, 1,4-disubstituebenzene), 8.42 (2H, s, $-\text{CH}=\text{N}$), 11.73 (2H, s, $-\text{NH}$). ^{13}C -NMR (75 MHz, CDCl_3): δ (ppm) 30.98, 31.56, 32.36, 74.37, 124.02, 126.04, 126.63, 127.28, 128.46, 132.08, 146.87, 148.95, 149.45, 163.91. Anal. Calcd. for $\text{C}_{62}\text{H}_{70}\text{N}_6\text{O}_{10}$: C, 70.3; H, 6.66; N, 7.93 %. Found: C, 70.12; H, 6.64; N, 7.94 %.

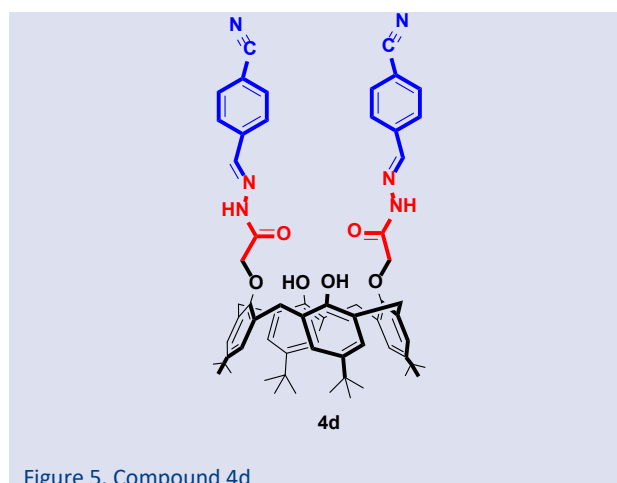
Synthesis of 4c



Compound (3) (0.30 g, 0.38 mmol) and 4-carboxybenzaldehyde (0.14 g, 0.91 mmol) are in ethanol solution under reflux with stirring for 12 hours. The reaction was checked with thin layer chromatography, and after this time, the solvent is removed and the target product is crystallized from ethanol. Yield 0.29 g (% 75), M.p.: 321.8-323.1 °C. IR (ATR) $\nu_{\text{max}}(\text{cm}^{-1})$: 1604 (HC=N), 1681 (C=O), 3498 (N-H). ^1H -NMR (300 MHz, CDCl_3): δ (ppm) 1.07 (18H, s, Bu^t), 1.31 (18H, s, Bu^t), 3.56 (4H, d, $J = 13.17$ Hz, ArCH_2Ar), 4.19 (4H, d, $J = 13.83$ Hz, ArCH_2Ar), 4.74 (4H, s, $-\text{OCH}_2\text{CO}$), 6.98 (4H, s, Ar-H), 7.17 (4H, s, Ar-H), 7.36 (4H, d, $J=7.77$ Hz, 1,4-disubstituebenzene), 7.47-7.51 (4H, m, 1,4-disubstituebenzene), 7.86 (2H, s, OH), 8.26 (2H, s, $-\text{CH}=\text{N}$), 11.43 (2H, s, $-\text{NH}$). ^{13}C -NMR (75 MHz, CDCl_3): δ (ppm) 30.95, 31.57, 34.01, 74.40, 125.90, 126.48, 127.36, 129.89, 130.79, 132.06, 135.06, 144.10, 148.30, 149.14, 175.31. Anal. Calcd. for $\text{C}_{62}\text{H}_{72}\text{N}_4\text{O}_{10}$: C, 72.70; H, 6.86; N, 5.30 %. Found: C, 72.51; H, 6.84; N, 5.28 %.

Synthesis of 4d

Compound (3) (0.30 g, 0.38 mmol) and 4-cyanobenzaldehyde (0.14 g, 0.91 mmol) are in ethanol solution under reflux with stirring for 12 hours. The reaction was checked with thin layer chromatography, and after this time, the solvent is removed and the target product is crystallized from ethanol.



Yield 0.35 g (% 88), M.p.: 328.9-330.2 °C. IR (ATR) $\nu_{\text{max}}(\text{cm}^{-1})$: 1600 (HC=N), 1707 (C=O), 3278 (N-H). ^1H -NMR (300 MHz, CDCl_3): δ (ppm) 1.08 (18H, s, Bu^t), 1.31 (18H, s, Bu^t), 3.55 (4H, d, $J = 13.44$ Hz, ArCH_2Ar), 4.20 (4H, d, $J = 13.35$ Hz, ArCH_2Ar), 4.75 (4H, s, $-\text{OCH}_2\text{CO}$), 7.00 (4H, s, Ar-H), 7.16 (4H, s, Ar-H), 7.30-7.43 (4H, m, 1,4-disubstituebenzene), 8.02-8.10 (4H, m, 1,4-disubstituebenzene), 8.74 (2H, s, $-\text{CH}=\text{N}$), 11.79 (2H, s, $-\text{NH}$). ^{13}C -NMR (75 MHz, $\text{DMSO}-d_6$): δ (ppm) 31.32, 31.82, 34.11, 74.05, 112.39, 126.08, 127.33, 128.28, 133.42, 133.56, 138.56, 142.20, 148.23, 150.05, 165.18. Anal. Calcd. for $\text{C}_{64}\text{H}_{70}\text{N}_6\text{O}_6$: C, 75.41; H, 6.92; N, 8.25 %. Found: C, 75.21; H, 6.93; N, 8.22 %.

Anticancer Activity Studies

L929, a healthy human fibroblast cell line; PC-3, the human prostate cancer cell line; MCF-7, the human breast cancer cell line; and the C6, rat brain glioma adenocarcinoma cell line are all purchased from the American Type Culture Collection and grown in Dulbecco's modified Eagle's medium (DMEM; Gibco, Thermo Fisher Scientific), which is supplemented with 10% fetal bovine serum (FBS; Sigma Aldrich), the cultivated cells were kept at 37 °C in a humid environment with 5% CO_2 . All recently created substances were dissolved in DMSO, and stock solutions were diluted with DMEM because the final DMSO concentration was less than 0.5%.

The MTT (3-(4,5-dimethylthiazole-2-yl)-2,5-diphenyl tetrazolium bromide) cell proliferation test was used to determine the viability of the cells. In a common colorimetric experiment, the mitochondrial activity of living cells is determined by splitting tetrazolium salts with mitochondrial dehydrogenases. [18,19]. The MTT assay was used to examine how the compounds in range 4a-4d affected the survival of the C6, HT-29, PC-3, MCF-7, and L929 cell lines. The cells were treated with 100 μM doses of each after being seeded at a density of 1×10^4 cells per well for 48 hours.

The control group consisted of untreated cells. To allow the metabolically active cells to convert MTT dye into

formazan crystals, the cells were treated with 20 μL of MTT solution (5 mg/mL in PBS, Sigma) and incubated at 37 $^{\circ}\text{C}$ for 3 h. DMSO was used to dissolve the formazan crystals for medicinal chemistry research (Sigma). Utilizing a microplate reader to measure the absorbance at 540 nm, the decrease of MTT was measured. The IC_{50} values were represented as mean \pm standard deviation (\pm SD).

Result and Discussion

Data on $^1\text{H-NMR}$, $^{13}\text{C-NMR}$, IR, and elemental analysis results were used to deduce the structures of four produced original compounds, 4a–4d. Reaction times are reduced, efficiency is raised, fewer resources are needed, and it is more environmentally and economically friendly when the final compounds are synthesized. With the aid of spectroscopic data, the IR investigations of four novel compounds derived from calix [4] arene Schiff bases that were synthesized as part of the study were clarified. All synthetic substances have an aromatic ring system when their chemical structures are analyzed. The voltage band of the HC=N group in the range of 1598 – 1620 cm^{-1} . In the literature, it has been reported that C=N stretching vibrations in Schiff bases are generally observed as a sharp peak at 1610-1640 cm^{-1} , and peaks are observed at 1600-1637 cm^{-1} in those that do not carry the methylene group attached to the azomethine group, that is, those that are directly attached to the aromatic ring [20]. Therefore, the obtained data are in accordance with the literature data. The 1,4-disubstituted benzene rings are a further structure that is present in all synthesis products. For this ring, the unique non-plane deformation bands were measured between 812 and 871 cm^{-1} . The voltage bands of the C=O group in the range of 1681 to 1707 cm^{-1} and the N-H group in the region of 3234 to 3498 cm^{-1} are additional structures that are present in all synthesis products. In the $^1\text{H-NMR}$ spectra, due to the presence of two *p*-tert butyl signals ($-\text{C}(\text{CH}_3)_3$) at 1.07-1.10 ppm and 1.31 ppm. Protons of ArCH₂Ar methylene bridges located on *p*-tert-butyl-calix [4] arene were observed as two doublets, in the range of 3.55-3.59 ppm and 4.19-4.20 ppm. Therefore, our observation of both doublets in this way provides evidence that the calix [4] arene compound was synthesized in the cone conformation. When the benzene ring is in the 1,4-disubstituted state, it conforms to the AA'BB' spin system. In this case, there are changes in the value and shape of the peak that the aromatic protons of the benzene ring give as singlet at 7.27 ppm, according to the electron donating or electron withdrawing properties of the substituents attached to the ring. The excess electron density around the proton causes resonance at higher field intensity by shielding the proton, and therefore the ppm value decreases accordingly. The low electron density around the proton, on the other hand, does not shield the proton, causing resonance at lower field strength, causing the current peak to be higher in ppm. When an electron withdrawing group is attached to the aromatic ring, since the electron density in the ring will decrease, the shielding of the ring protons also decreases,

and accordingly, the chemical shift values of the aromatic ring protons shift downward. While the benzene ring is in the 1,4-disubstituted state, singlet, doublet or quartet-shaped peaks can be observed in the spectrum depending on the electronic properties of the substituents on the ring. The 1,4-disubstituted phenyl ring peaks, which are usually observed as two doublets, can be obtained in quartet or even singlet form if the electronic properties of the substituents are very close to each other [21, 22]. In this context, the presence of the 1,4-disubstituted benzene ring is demonstrated at 7.37 and 8.28 ppm and Ar-H signals at 6.98 ppm and 7.18 ppm and the doublet four proton peaks. The signals belonging to -CH=N- proton was found at 8.26-8.74 ppm. Around 11.43-11.79 ppm, a wide singlet caused by the -N-H proton of the phenyl ring was detected. For the compounds included by the study, percentage studies of the C, H, and N components were carried out. The results show a 0.4% difference between experimental outcomes and theoretically predicted element percentages. This result suggests that there aren't many contaminants in the compounds. The anticancer activity of compounds 4a–4d was assessed against the cancer cell lines C6, HT-29, PC-3, and MCF-7 as well as the healthy cell line L929. The IC_{50} value of four new compounds synthesized was determined by MTT. Anticancer activity results of compounds 4a-4d are presented in Table 1. When the activity results of compounds were evaluated, it was seen that compounds 4a, 4c and 4d were ineffective cancer cells. However, compound 4b shows activity against C6, HT-29 cancer cell lines. The IC_{50} value of 93.421 \pm 4.282 and 96.622 \pm 4.518 μM , respectively. It was also found that compound 4b shows activity against L929 cell line. The IC_{50} value of compound 4b against L929 was 48,35 \pm 2.328 μM . It is a disadvantage that show cytotoxic effects are observed on healthy fibroblast cells (L929).

As a result of the study, four novel compounds were synthesized and characterized. Although synthesized compounds 4a, 4c, and 4d are ineffective against cancer, compound 4b seems to provide hope in anticancer activity. Future research aims to reach more potent molecules with various changes via this primary structure.

Table 1. IC_{50} values (0-100 μM) of calix[4]arene Schiff base derivatives on different cells

Compounds	C6	HT-29	PC-3	MCF-7	L929
4a	>100	>100	>100	>100	>100
4b	93.421 \pm 4.282	96.622 \pm 4.518	>100	>100	48,35 \pm 2.328
4c	>100	>100	>100	>100	>100
4d	>100	>100	>100	>100	>100

Conclusions

Using FT-IR, ^1H NMR, ^{13}C NMR, and elemental analysis, the structures of four novel calix [4] arene containing Schiff base derivatives that were developed and synthesized in this study were clarified. C6, HT-29, PC-3, MCF-7 cancer cell lines and L929 healthy cell line were tested for anticancer activity. The compounds **4a**, **4c**, **4d** were show no anticancer activity. However, compound **4b** shows activity against C6 ($\text{IC}_{50}=93.421\pm 4.282\ \mu\text{M}$), HT-29 ($\text{IC}_{50}=96.622\pm 4.518\ \mu\text{M}$) cancer cell lines and L929 ($\text{IC}_{50}=48,35\pm 2.328\ \mu\text{M}$) cell line. In future studies, by making use of the findings of this study, new compounds with similar chemical structures that are thought to be more effective can be synthesized and contribute to the pharmaceutical industry.

Acknowledgment

This study is derived from the a part of doctoral thesis of Ayşen İŞİK supported by the Selçuk University Scientific Research Project Center (Projects number 20111003). The authors are grateful to the Selçuk University Research Foundation for supporting this research.

Conflicts of interest

There are no conflicts of interest in this work.

References

- Baig S., Seevasant I., Mohamad J., Mukheem A., Huri H.Z., Kamarul T., Potential of apoptotic pathway-targeted cancer therapeutic research: Where do we stand?, *Cell Death Dis.*, 7(1) (2016) 2058.
- Narang A. S., & Desai D. S., Anticancer drug development, In *Pharmaceutical perspectives of cancer therapeutics*, New York, NY: Springer, (2009) 49-92.
- Guo S., Song Y., He Y., Hu X. Y., and Wang L., Highly efficient artificial light-harvesting systems constructed in aqueous solution based on supramolecular self-assembly, *Angew Chem. Int. Ed.*, 57 (2018) 3163–3167.
- Yokoyama T., and Mizuguchi M., Crown ethers as transthyretin amyloidogenesis inhibitors, *J. Med. Chem.*, 62 (2019) 2076–2082.
- Zhang Y. M., Xu Q. Y., and Liu Y., Molecular recognition, and biological application of modified β -cyclodextrins, *Sci. Chin.*, 62 (2019) 1–12.
- Böhmer V., Calixarenes, macrocycles with (almost) unlimited possibilities, *Angew. Chem. Int. Ed. Engl.*, 34 (2010) 713–745.
- Bauer D., Andrae B., Gaß P., Trenz D., Becker S., and Kubik S., Functionalizable acyclic cucurbiturils, *Org. Chem. Front.*, 6 (2019) 1555–1560.
- Geraci C., Consoli G. M., Galante E., Bousquet E., Pappalardo M., and Spadaro A., Calix[4]arene decorated with four Tn antiglycomimetic units and P3CS immunoadjuvant: synthesis, characterization, and anticancer immunological evaluation, *Bioconjugate Chem.*, 19 (2008) 751–758.
- Da Silva E., Lazar A. N., & Coleman A. W., Biopharmaceutical applications of calixarenes, *Journal of Drug Delivery Science and Technology*, 14(1) (2004) 3-20.
- Yousaf A., Abd Hamid S., Bunnori N. M., & Ishola A. A., Applications of calixarenes in cancer chemotherapy: facts and perspectives, *Drug design, development and therapy*, 9 (2015) 2831.
- Al-Hakimi A.N., Alminderej F., Aroua L., Alhag S.K., Alfaifi M.Y., Mahyoub, J.A., Eldin I., Elbehairi S., Alnafisah A.S., Design, synthesis, characterization of zirconium (IV), cadmium (II) and iron (III) complexes derived from Schiff base 2-aminomethylbenzimidazole, 2-hydroxynaphthadehyde and evaluation of their biological activity, *Arab. J. Chem.*, 13 (2020) 7378–7389.
- Maurya R.C., Chourasia J., Rajak D., Malik B.A., Mir J.M., Jain N., Batalia S., Oxovanadium(IV) complexes of bioinorganic and medicinal relevance: synthesis, characterization and 3D molecular modeling of some oxovanadium(IV) complexes involving O, N-donor environment of salicylaldehyde-based sulfa drug Schiff bases, *Arab. J. Chem.*, 9 (2016) 1084-1100.
- El-Saied F.A., Salem T.A., Shakhofa M.M.E., Al-Hakimi A.N., Radwan A.S., Antitumor activity of synthesized and characterized Cu (II), Ni (II) and Co (II) complexes of hydrazone-oxime ligands derived from 3-(hydroxyimino) butan-2-one, *Beni-Suef Univ. J. basic Appl. Sci.*, 7 (2018) 420-429.
- El-Saied F.A., Salem T.A., Shakhofa M.M.E., Al-Hakimi A.N., Anti-neurotoxic evaluation of synthetic and characterized metal complexes of thiosemicarbazone derivatives, *Appl. Organomet. Chem.*, 32 (2018) 4215.
- Gutsche C. D., and Iqbal M., p-ter-Butylcalix[4]arene, *Org. Synth.*, 68 (1990a) 234-237.
- Arnaud-Neu F., Collins E. M., Deasy M., Ferguson G., Harris S. J., Kaitner B., ... & Marques E., Synthesis, X-ray crystal structures, and cation-binding properties of alkyl calixaryl esters and ketones, a new family of macrocyclic molecular receptors, *Journal of the American Chemical Society*, 111(23) (1989) 8681-8691.
- Narang A. S., & Desai D. S., Anticancer drug development, In *Pharmaceutical perspectives of cancer therapeutics*, New York, NY: Springer, (2009) 49-92.
- Fang C., Tang S., Wang X., Sun X., Li H., Xu Y., Gu X., Xu J., Lasiokaurin derivatives: synthesis, antimicrobial and antitumor biological evaluation, and apoptosis-inducing effects, *Arch Pharm. Res. (Seoul)*, 40 (2017) 796e806.
- Mosmann T., Rapid colorimetric assay for cellular growth and survival: application to proliferation and cytotoxicity assays, *J. Immunol. Methods*, 65 (1983) 55e63.
- Karahan A., Yordan A., Yahsi Y., Kara H., Kurtaran R., N₂O₂ Tipi Schiff Bazı Ligandı ile Sentezlenen Cu(II) Kompleksinin X-Işını Yapısı ve Termal Özelliği, *SDU Journal of Science (E-Journal)*, 8(2) (2013) 163-174.
- Erdik E., , *Organik Kimyada Spektroskopik Yöntemler*, Fersa Matbaacılık San. Tic. Ltd. Şti., Ankara, (1993).
- Balcı M., Nükleer Manyetik Rezonans Spektroskopisi, Gökçe Ofset Matbaacılık Ambalaj, Tur. Org. San. Ve Tic. Ltd. Şti., Ankara, (2000) 25-206.

Proliferative and Antimicrobial Evaluation of the Benzalkonium Chloride Loaded Walnut Shell-Rich Chitosan Gels

Ahmet Kati^{1,2,a,*}, Sevde Altuntaş^{2,3,b}

¹Department of Biotechnology, University of Health Sciences Turkey, 34668, İstanbul, Türkiye

²Experimental Medicine Research and Application Center, University of Health Sciences, 34668, İstanbul, Türkiye

³Department of Tissue Engineering, University of Health Sciences Turkey, 34668, İstanbul, Türkiye

*Corresponding author

Research Article

History

Received: 29/05/2022

Accepted: 12/10/2022

Copyright




©2022 Faculty of Science,
Sivas Cumhuriyet University


ABSTRACT

Tissue engineering studies combine cells, biomaterials, and biomolecules to mimic native tissue. The selection of appropriate materials for tissue engineering applications encourages best practices from the lab to clinical trials, and natural biomaterials have the potential to offer desired features for these applications. Material abundance, ease of the process, and biocompatibility are the first milestones to choosing a suitable material. Lignocellulose is one of the most promising biomaterials for its biocompatible, antioxidant, and biodegradable features and is the most abundant material in nature. A walnut shell-added chitosan gel was developed in this study by exploiting chitosan's desired properties, such as biocompatibility, biodegradability, and mechanical capabilities, which boosted cell proliferation. Furthermore, the gel system was reinforced with benzalkonium chloride (BAC), a well-known eye drop sterilizing agent. The hydrogels were subjected to Fourier-transform infrared spectroscopy (FTIR) analyses, and BAC-related signals were observed. The results of BAC-loaded hydrogels revealed that the viability of the primary fibroblasts was enhanced on the BAC-loaded gels compared to tissue culture polystyrene, but the difference was not found statistically significant. Yet, antibacterial activity results demonstrated that only BAC-loaded gel systems have solid antibacterial activity. Additionally, the fibroblasts had the strongest proliferation profile on the walnut shell-added chitosan hydrogels compared to other test groups, but the films' bactericidal activity of the hydrogels was not apparent. After revising the BAC and walnut shell concentrations in the hydrogels, the findings demonstrated that the injectable gel system could be used for cell transplantation *in vitro* and *in vivo*.

Keywords: Chitosan, Injectable gel, Benzalkonium chloride, Toxicology, Bactericidal.

 ahmet.kati@sbu.edu.tr

 <https://orcid.org/0000-0002-9903-634X>

 sevde.altuntas@sbu.edu.tr

 <https://orcid.org/0000-0002-4803-9479>

Introduction

Because of major developments in 3D microtissue manufacturing and biomaterials, the recent decade has been dubbed the "golden era of tissue engineering." [1]. The development of materials that mimic the natural tissue environment or directly from nature has aided in advancing tissue engineering. The use of walnut shells, an industrial waste, in powder is one of the best examples. Thanks to its cellulose-containing structure, studies in which walnut shell powder has been added to scaffolds as a material that increases mechanical durability have been encountered more frequently in recent years. For example, in the study by Sharahi et al., electrospun fibers containing poly(caprolactone) and gelatin were enriched with walnut shell powder. It was shown that they did not have a toxic effect on mesenchymal stem cells in addition to the improved mechanical properties [2].

Another waste product is chitosan obtained from shellfish and is one of the biomaterial groups supporting cellular development with active amine and hydroxyl groups [3, 4]. Chitosan is employed in tissue engineering applications as nanoparticles, fiber mats, films, or directly

as a hydrogel due to similarities of chitosan with the extracellular matrix [5-8]. Furthermore, hydrogel forms that may release drugs and biomolecules have shown promise in skin or bone patch construction trials; however, the mechanical properties of chitosan-based biomaterials are limited and necessitate the addition of other additives such as gelatin, silk, or others [8]. Walnut powder, known as a thickener, can offer a solution with its nature and desirable mechanical properties [2].

The antibacterial capabilities of chitosan are affected by a variety of factors, including pH, molecular weight, concentration, degree of deacetylation, and the kind of bacterium utilized in the study. [9]. Due to their multi-parameter fabrication techniques, before employing the resultant chitosan-based materials as biomaterials, their antibacterial activity should be evaluated, and other antibacterial agent cues should be included in the materials, if necessary. Benzalkonium chloride (BAC) is an antibacterial agent that can be used as an alternative to alcohol in the growing usage of hand disinfectants in recent years. It is also utilized in skin care products, eye

drops, cosmetics, and medicinal purposes [10]. BAC also has virus inactivation potential against several viruses [11]. BAC, on the other hand, possesses antibacterial characteristics due to its ionic structure but is hazardous to mammalian cells at high doses, including skin and air track cells. Hence, the American College of Toxicology (ACT) recommends that the concentration of BAC in contact with the skin should be between 0.1% and 0.13% [12].

In the study, injectable chitosan-walnut shell gels enriched with BAC were created, and FTIR studies and primary fibroblast viability assessments of the gels were performed in addition to bactericidal testing. According to our findings, the chitosan: walnut shell: BAC has the potential for viable cell transplantation *in vitro* and *in vivo* analysis.

Materials and Methods

Walnut Shell Activation

The walnut shell powder was a generous gift from EcoShell, LP, Canada, with a 325-micrometer powder size. Following the deionized water washing and drying stages, 10 g of the powder was immersed in 64% (w/w) sulfuric acid (Sigma Aldrich, 258105) for four days; the powder was carried into a dialysis bag to remove excessive sulfuric acid for ten days. Each day, the dialysis bag's water was refreshed, and the final sample was centrifuged at 5000 rpm for 10 min. Then the sample was lyophilized for 24 hours to remove excess water and stabilize the active cellulosic part. The dried sample was stored at 4 °C for ten days.

Gel Preparation

Chitosan (Sigma Aldrich, 448877) gels were prepared in 1% (v/v) acetic acid (Sigma Aldrich, A6283) solution. The solution was kept at room temperature, and the 1% (w/v) processed walnut powder was added to the chitosan gel. The chitosan: walnut shell gel was mixed for 4 hours at 1000 rpm. To prepare chitosan: walnut shell: BAC gel, chitosan: walnut shell gel was mixed with 0.1% (v/v) BAC (Thor, Acticide BAC50), and the gel was mixed under the previous condition.

FT-IR Analysis

One ml of the three variations was frozen at -80 °C freezer for one night, and the samples were lyophilized overnight. The lyophilized samples were measured at the Thermo Fisher Nicolet ATR FTIR module between 400-4000 nm. The findings of each sample were recorded three times, and the average value is depicted in Figure 1.

MTT Analyses

Human dermal fibroblasts were grown in the human dermal fibroblast medium (Promocell, C-23020) until reaching %80-90 confluency in the humidified incubator at 37 °C. After the trypsinization step, 10⁴ cells/well was counted and applied to the 20 µl of the gel groups and

TCPS. Following one day of incubation, one mM MTT solution was added to the samples, and formazan salts were dissolved in isopropanol. The plate readout was completed using the Biotek Neo system at 590 nm (n>3). Tissue cultured polystyrene (TCPS) was used as a control group for the analysis. Additionally, bright field microscope images of the cells on the gels were recorded using an inverted microscope (AE2000, Motic).

Antimicrobial Analysis

An agar-well diffusion test was employed for the evaluation of the gel samples. The tested microorganisms are *Escherichia coli*, *Staphylococcus aureus*, *Shigella*, *Bacillus pumilis*, and *Pantoea agglomerans*. Each microorganism was grown in a Lurian Bertani broth at 35°C until reaching the optical density of 1.0. Following overnight incubation, the suspension of each examined microorganism was adjusted to OD 0.6 and uniformly spread on agar plates using a sterile cotton bud. To load 20 µL of the gel samples, a hole was punched in the bacteria spread agar with a sterile 100 µL volume tip. After the incubation at 35°C, the inhibition zones were measured by using a digital caliper. The 6 µg/mL concentration of ampicillin was used as a positive control. Each sample was done in triplicate.

Results and Discussion

BAC-loaded gels have a proper proliferative profile and bactericidal activity.

The cell viability analysis indicated that chitosan provides a more suitable environment for dermal fibroblasts than the control group (TCPS) since it presents many active -NH₂ and -OH groups at FTIR spectra. (Figure 1) The peak around 1589 cm⁻¹ (the N-H bending of the primary amine) in the spectra of the test groups indicates the functional amine group sourced from chitosan. Additionally, at 2917 and 2856 cm⁻¹, two new intensive peaks correspond to asymmetric and symmetric vibration stretching bands of the -CH₂ group, respectively, demonstrating chitosan-BAC interaction [10].

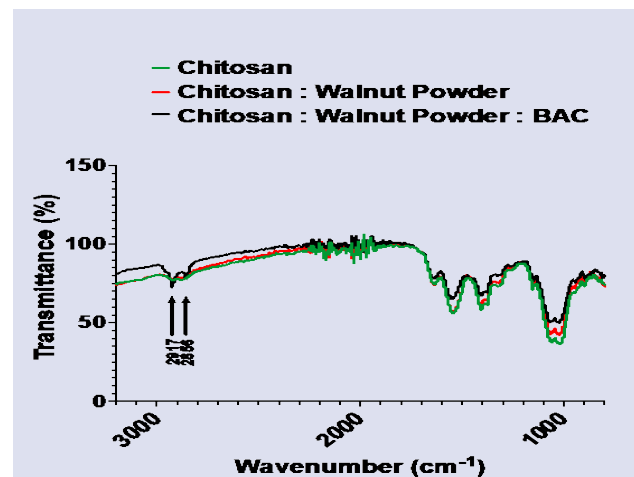


Figure 1. FTIR results of the chitosan, chitosan: walnut powder, and chitosan: walnut powder: BAC gel combinations, (n=3).

It is well-known that amine groups can increase protein concentration per surface area in a short time, and therefore cells show a tendency to attach to the surface [8]. There are different assumptions for protein adsorption on the hydroxyl group decorated surfaces, but it seems that the existence of the groups does not affect cell viability results [13, 14]. The cell viability results indicate that chitosan can provide the desired environment for fibroblast growth, but the difference is insignificant compared to a control group (Figure 2). Activated walnut shell powder-enriched gel form has the highest cell viability results (191.30 ± 8.60), and the difference is statistically significant compared to a control group (100 ± 16.09). Sharahi et al. reported that activated walnut powder supports cellular viability due to carrying many active groups, such as hydroxyl and carboxylic acid [2].

Interestingly, the BAC-loaded gel combination did not cause substantial toxicity even though it has been classified as a product type 1 disinfectant for personal hygiene in biocidal product regulation (BPR) [15]. The direct treatment of BAC solutions on the cells leads to membrane abnormalities because of the mode of action of quaternary ammonium compounds of BAC molecules. In a chitosan environment, the quaternary ammonium groups have the potential to reach different active groups, which may lead to controlling the cytotoxic effect of the BAC.

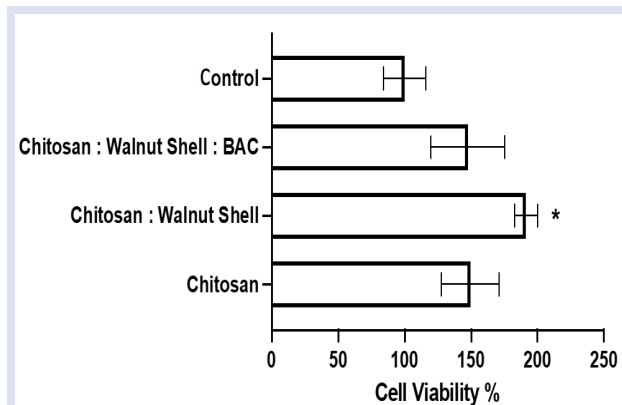


Figure 2. Cell viability results of the human dermal fibroblast on the gel formulations and TCPS control group. * represents $p < 0.05$ compared to TCPS. ($n > 3$ for each group)

In Figure 3, the cellular attachment on the gel was presented. The fibroblast on the gel formulations has shown a tendency to attach to the gel formulation surface, but the cells demonstrated a strong migration profile into the gel formulation. Therefore, for instance, the chitosan cell viability results on the chitosan gels showed around 50% proliferation, but the effect was not observed in figure 3A since the bright-field images could provide information on the top side of the gel formulations. The migration profile can be seen more clearly in Figure 3C. But, the cells that interacted with the formulation showed wide cell body presentation, unlike normal fibroblast morphology compared to other test groups, and it may be caused BAC toxicological effect (Figure 3C). The cell viability analysis also confirmed this finding since BAC-added formulation caused a decrement in the proliferation of the cells.

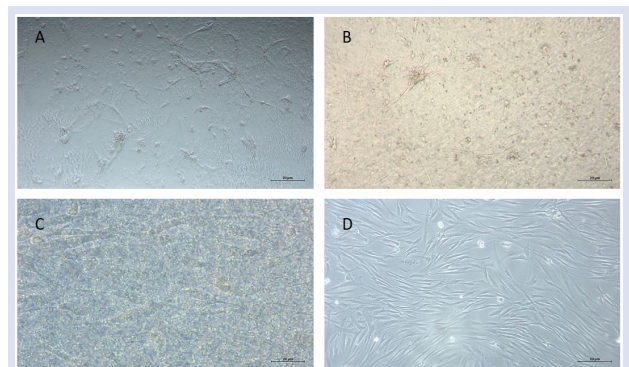


Figure 3. Optical microscope images of the human dermal fibroblast on the A) chitosan, B) Chitosan: Walnut shell, C) Chitosan: Walnut shell: BAC gel combinations, and D) TCPS control group. * represents $p < 0.05$ compared to TCPS. ($n > 3$ for each group)

Based on the well diffusion method, the antibacterial effectiveness of gel solutions on the microbes is shown in Table 1. According to the results, BAC-containing gel has a broad antibacterial activity on the microorganisms. Only chitosan and chitosan: walnut combination did not show any antibacterial effect. The experimental results showed that the BAC-containing gel had demonstrated bactericidal activity against gram-positive and gram-negative bacterial strains.

Table 1. Antibacterial effect of the gels on different microorganisms

Microorganisms	Diameter of Zone of Inhibition (mm)*									
	<i>Escherichia coli</i>		<i>Staphylococcus aureus</i>		Shigella		<i>Bacillus pumilis</i>		<i>Pantoea agglomerans</i>	
Samples	Mean	SD**	Mean	SD	Mean	SD	Mean	SD	Mean	SD
Chitosan:Walnut:BAC	17,19	0,82	24,83	1,08	19,22	0,82	24,18	0,67	29,19	0,55
Chitosan:Walnut	0	-	0	-	0	-	0	-	0	-
Chitosan	0	-	0	-	0	-	0	-	0	-
Positive Control (Ampicilin 6ug/mL)	34,04	1,04	56,87	1,08	36,19	0,96	38,39	1,18	29,19	0,55

* The zone of inhibition rate contains the 6mm diameter of well.

** SD: standard deviation

As a result, an injectable gel system has a critical potential for tissue engineering research and further reconstructing tissues in clinical applications [16]. In biomedical applications, in situ-forming gel systems have some troubleshooting which are defect geometries,

polymerization problems, and contamination risk [17, 18]. The injectable gel development studies mainly focus on antibacterial solutions, whether innate or doping exogenous materials [19, 20]. Our antibacterial properties of BAC-containing gel have provided good stability for the

different microorganisms in both clinical and laboratory research applications. However, additional research is needed to determine how concentration screening of BAC, grain size, and quantity of walnut shell powder in the gel system affects cellular activities.

Conclusion

In the study, a low-cost, biodegradable, and biocompatible antibacterial gel based on quaternary ammonium and benzalkonium chloride (BAC) was developed for tissue engineering studies. The gel promises the potential for a wide range of industrial applications. It has a resistant and broad antibacterial effect on gram-positive (*Staphylococcus aureus*, *Bacillus pumilis*) and gram-negative (*E. coli*, *Shigella*, *Pantoea agglomerans*). This study is the first research using walnut shell powder as a supporter material in injectable gel system technologies with a combination the chitosan and BAC. In the future, the injectable nature of the gels can be used as filling material in dentistry and orthopedic surgery, and the mechanical and physicochemical properties of the gels will be studied for further studies within the scope of our studies.

Conflicts of Interest

The author declares no conflicts of interest. No competing financial interests exist.

References

- [1] Cecen B., Ozturk A.B., Yasayan G., Alarcin E., Kocak P., Tutar R., Kozaci L.D., Ryon Shin S., Amir K. Miri, Selection of natural biomaterials for micro-tissue and organ-on-chip models., *Journal of Biomedical Materials Research Part A*, 110(5) (2022) 1147-1165.
- [2] Menon A., Haritha S., Preethi Soundarya V., Sanjay S., Viji C., Balagangadharan K., Selvamurugan N., Sustained release of chrysin from chitosan-based scaffolds promotes mesenchymal stem cell proliferation and osteoblast differentiation, *Carbohydrate Polymers*, 195 (2018) 356-367.
- [3] Menon A., Haritha S., Preethi Soundarya V., Sanjay S., Viji C., Balagangadharan K., Selvamurugan N., Sustained release of chrysin from chitosan-based scaffolds promotes mesenchymal stem cell proliferation and osteoblast differentiation, *Carbohydrate Polymers*, 195 (2018) 356-367.
- [4] Patel S., Shikha S., Manju Rawat S., Deependra S., Preparation and optimization of chitosan-gelatin films for sustained delivery of lupeol for wound healing, *International Journal of Biological Macromolecules*, 107 (2018) 1888-1897.
- [5] Ranganathan S., Kalimuthu B., Nagarajan S., Chitosan and gelatin-based electrospun fibers for bone tissue engineering, *International Journal of Biological Macromolecules*, 133 (2019) 354-364.
- [6] Qi L., Zirong X., Minli C., *In vitro* and *in vivo* suppression of hepatocellular carcinoma growth by chitosan nanoparticles, *European Journal of Cancer*, 43(1) (2007) 184-193.
- [7] Chen X., Xiaoming C., He J., Xiangxin C., Xiaoyuan X., Baicheng M., Jie Z., Tao H., SIKVAV-modified chitosan hydrogel as a skin substitutes for wound closure in mice, *Molecules*, 23(10) (2018) 2611.
- [8] Altuntas S., Harkiranpreet K. Dhaliwal, Nicole J. Bassous, Ahmed E. Radwan, Alpaslan P., Thomas W., Buyukserin F., Mansoor A., Nanopillared Chitosan/Gelatin Films: A Biomimetic Approach for Improved Osteogenesis, *ACS Biomaterials Science & Engineering*, 5(9) (2019) 4311-4322.
- [9] Li J., and Shaoling Z., Antibacterial activity of chitosan and its derivatives and their interaction mechanism with bacteria: Current state and perspectives, *European Polymer Journal* 138 (2020) 109984.
- [10] Zhou, N., Na M., Yinchen M., Xiangmin L., Jun Z., Li Li, Jian S., Evaluation of antithrombogenic and antibacterial activities of a graphite oxide/heparin–benzalkonium chloride composite, *Carbon*, 47(5) (2009) 1343-1350.
- [11] Armstrong J. A., Froelich E. J., Inactivation of viruses by benzalkonium chloride, *Applied Microbiology*, 12(2) (1964) 132-137.
- [12] Shadman Swarit A., Ishmamul Hoque S., Mohammed Sakib N., Mohidus Samad K., Development of a benzalkonium chloride based antibacterial paper for health and food applications, *ChemEngineering*, 5(1) (2021) 1.
- [13] Xian M., Liming F., Yili L., Qiang W., Lijing H., Zhonghang Y., Xianyun H., Gang W., Electrical field induce mBMSCs differentiation to osteoblast via protein adsorption enhancement, *Colloids and Surfaces B: Biointerfaces*, 209 (2022) 112158.
- [14] Kim M., Kyoichi S., Shintaro F., Takanobu S., Jiro O., Water flux and protein adsorption of a hollow fiber modified with hydroxyl groups, *Journal of Membrane Science*, 56(3) (1991) 289-302.
- [15] Choi Hye-Y., Yong-Hoon L., Cheol-Hong L., Yong-Soon K., In-Seop L., Ji-Min J., Ha-Young L., Hyo-Geun C., Hee Jong W., Dong-Seok S., Assessment of respiratory and systemic toxicity of Benzalkonium chloride following a 14-day inhalation study in rats, *Particle and Fibre Toxicology*, 17(1) (2020) 1-19.
- [16] Kang Yun M., Sang Hyo L., Ju Young L., Jin Soo S., Byung Soo K., Bong L., Heung Jae C., Byoung Hyun M., Jae Ho K., Moon Suk K., A biodegradable, injectable, gel system based on MPEG-b-(PCL-ran-PLLA) diblock copolymers with an adjustable therapeutic window, *Biomaterials*, 31(9) (2010) 2453-2460.
- [17] Pereira Rui C., M. Scaranari P., Castagnola M., Grandizio Helena S., Azevedo R. L., Reis Ranieri C., and Chiara G., Novel injectable gel (system) as a vehicle for human articular chondrocytes in cartilage tissue regeneration, *Journal of Tissue Engineering and Regenerative Medicine*, 3(2) (2009) 97-106.
- [18] Hoque J., Relekar G., Prakash Krishnamoorthy P., Bibek R. S., Jayanta H., Biocompatible injectable hydrogel with potent wound healing and antibacterial properties, *Molecular Pharmaceutics*, 14(4) (2017) 1218-1230.
- [19] Giano Michael C., Zuhair I., Scott H.M., Karim A.S., Joani M. C., Yuji Y., Gerald B, Joel P.S., Injectable bioadhesive hydrogels with innate antibacterial properties, *Nature Communications*, 5(1) (2014) 1-9.
- [20] Saito K., Tohru H., Rihito K., Daijiro M., Kazutaka K., *In vitro* antibacterial and cytotoxicity assessments of an orthodontic bonding agent containing benzalkonium chloride, *The Angle Orthodontist*, 79(2) (2009) 331-337

Decolourization of Methylene Blue in Aqueous Solution by Photocatalytic Oxidation, Fenton Oxidation and Biosorption

Nuket Kartal Temel^{*1,a}, Esra Bağda^{1,b}¹ Faculty of Science, Sivas Cumhuriyet University, Sivas, Türkiye² Faculty of Pharmacy, Sivas Cumhuriyet University, Sivas, Türkiye

*Corresponding author

Research Article

History

Received: 16/05/2022

Accepted: 04/12/2022

Copyright

©2022 Faculty of Science,
Sivas Cumhuriyet University

ABSTRACT

The aim of the study was to investigate decolourization of Methylene Blue (MB) in aqueous solution using advanced oxidation processes (AOPs) and biosorption comparatively. Photocatalytic decolourization of MB was studied using TiO₂ as catalyst. The photocatalytic decolourization of MB by direct UV irradiation alone, only TiO₂ and TiO₂/UV processes was investigated. It was found that decolourization by photocatalytic process of MB increased with decreasing pH, and decolourization rate also increased in the presence of TiO₂/UV when compared to UV irradiation alone. Decolourization of MB was also studied with using the Fenton process (Fe(II)/H₂O₂). Concentrations of Fe(II) and H₂O₂ on decolourization ratio were investigated. The optimum catalyst to H₂O₂ ratio was found 1:3 at pH 4.0. In the second part of the study, the biosorption process was conducted with using plant gall immobilised alumina. The removal percentages were calculated with both plant gall immobilised alumina and alumina alone. The immobilisation of plant gall increased the removal percentages from 60-70% to 90-95%. The proposed methods (AOPs and biosorption) have both advantages and disadvantages compared to each other.

Keywords: Biosorption, Dye, Fenton Oxidation, Photocatalytic Oxidation, TiO₂.

nkartal@cumhuriyet.edu.tr<https://orcid.org/0000-0002-3539-4930>esraer@cumhuriyet.edu.tr<https://orcid.org/0000-0003-1900-4944>

Introduction

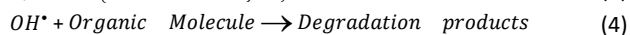
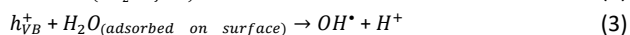
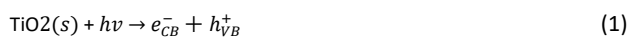
Dyes or colorant materials are important feedstock of many industries such as cosmetic, textile, paper dyeing, dyeing, drug and food processing [1]. The industrial effluents are generally heavily charged with unconsumed organic molecules such as dyes and inorganic molecules. Depositions of these molecules cause high damage to the environment [2,3]. According to researchers, even small quantities of colorant materials can colour large wetland and can cause reduction of penetration of light and photosynthetic activity [2]. Because of toxic effect of accumulated organic and inorganic substances, removal or degradation of these molecules has been an important task for scientist.

Several physicochemical and biological methods are being used to decompose, degrade or removal of waste effluents, but most of these methods are suffering from ineffective decolourization yield [4]. According to Hsueh et al., the ozonation process can effectively decolorize water soluble dyes, such as reactive dyes [5]. However, ozonation process is generally lead to inefficient decolourization yields for water insoluble dyes, such as disperse dyes. Water insoluble dyes can be decolorized by coagulation with high yield, but coagulation is ineffective for soluble dyes [5].

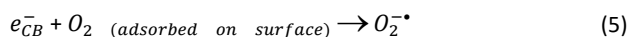
AOPs can be thought as a combination of different methods including ozonation, photocatalysis,

electrochemical oxidation techniques, Fenton and Fenton-like processes [6]. AOPs are very important techniques for the decolourization of organic compounds of wastewater as a pre- or post-treatment step [7]. The method can also be employed for removal of taste and odor compounds [8]. The techniques are mainly based on the generation of the hydroxyl radical (OH[•]) and generated hydroxyl radical has a great oxidation power and is able to oxidize nearly all organic substances to carbon dioxide and water [7,9,10]. Heterogeneous photocatalysis through illumination of UV on semiconductor surface is an attractive AOPs [11]. In AOPs, Titanium dioxide (TiO₂) is generally used for water and air purification since many environmental pollutants can be degraded by oxidation and reduction processes on TiO₂ [12]. Besides, TiO₂ is relatively inexpensive photocatalyst and has unique characteristics such as a chemically stability, non-toxicity, highly efficiency, and, has been widely used surface [7]. Photocatalytic oxidation processes are usually referred to as AOPs. When a photon with an energy which matches or exceeds the band gap energy of the semi-conductor is incident on a semiconductor surface, a conductive band electron will jump to its valence band leaving a positively charged hole behind [13]. The initial step in this type of photo-oxidation process is believed to be the formation of free hydroxyl radicals [14,15]. Hydroxyl radicals are

generated by the oxidation of water (OH^- ions) at the valence band positively charged holes.



On the other hand, the dissolved O_2 molecules are transformed to anionic superoxide ($\text{O}_2^{\bullet -}$) radicals via electrons from conductive band.



The most commonly studied photocatalysts are TiO_2 , ZnO , ZnS and CdS [16]. Additionally, In_2O_3 , SrTiO_3 , SnO_2 and WO_3 have been used as photocatalysts but all showed lower levels of photo-activity [16,17], and SiO_2 and MgO are found to be inactive. The usability of most metal oxides and sulphides as photocatalyst is not feasible due to their irreversible photo-corrosion on the surface for long term treatment processes [18]. Transition metal doping with silver which enhances the interfacial charge-transfer reactions of TiO_2 bulk phase and colloidal particles, can increase the photocatalytic activity of TiO_2 [19].

Another process named 'Fenton method' that is widely used for degradation of both water soluble and insoluble dyes [5]. According to Kim et. al., compared to other oxidation processes, such as UV-peroxide process, operation costs of Fenton method are quite low [20]. Fenton method has been lately and widely used for different chemical compounds because of its ease of operation, requires simple operation systems and the possibility to work in a wide temperatures ranges [20]. Fenton's reagent has been used extensively for oxidation of organic matter in water. The main advantage is the complete destruction of contaminant to harmless compounds, e.g. CO_2 , water and inorganic salts [21].

Adsorption has been reported as an effective way for the removal of dye molecules from waste waters [22]. An effective and expensive way of adsorption can be carried out with activated carbon. On the other hand, the operation cost is too expensive with activated carbon when treating high amount of waste effluents. The polymeric materials and resins are also widely employed for treatment of heavily contaminated dye effluents [23–26]. An important drawback of polymeric resins is the consumption of chemicals for the synthesis of adsorbent. Recently, a number of studies were about the removal or decolorization of dyes with using biomaterials [27]. The waste biomaterials such as agricultural wastes, plant materials, fungus and alga were used as sorbent with or without pre-treatment [4,28–31], . The main advantages of using biomaterials as sorbent are the low cost of the process and generally, the easy availability of these materials. Some of the biomaterials have reported that they have excellent exchange capacity [32]. Another important feature of biopolymers is that they generally

possess a number of different functional groups, such as hydroxyls and amines, which increase the efficiency of metal ion uptake and the maximum chemical loading possibility [33].

The present study consists of two main parts: the first is the decolorization of MB with AOPs (with TiO_2/UV system and Fenton method) and the second is removal of the dye with biosorption process. In second part of the study, the removal of MB was achieved with using alumina and plant gall modified alumina. The modification was easy and the removal percentage was increased significantly with modification of alumina. According to Bağda, plant galls contains huge amount of tannic acid and adjacent hydroxyl group of the molecule assumed as the active binding sides for adsorption process [2,34,35].

Material and Methods

The stock 10 ppm MB solution was prepared in deionized water. The pH of the dye solutions was adjusted with 0.1 mol L^{-1} of HCl and 0.1 mol L^{-1} of NaOH . TiO_2 (Anatase, 99.9%) was supplied by Aldrich chemical company (Surface area of TiO_2 $9.35 \text{ m}^2 \text{ g}^{-1}$). Hydrogen peroxide (33 %) and Alumina ($\alpha\text{-Al}_2\text{O}_3$) was supplied from Merck Chemicals (Darmstadt, Germany).

Photocatalytic Decolorization of Methylene Blue

0.1 g of TiO_2 and 100 mL of dye solution were placed in a Pyrex flask with a condenser. pH of dye solution were adjusted to desired level and the stirred solution was irradiated with an OSRAM-Ultra Vitalux 300 W low pressure mercury lamp with a flux output of approximately 5.8 W at about 254 nm. At regular time intervals, an aliquot of 5.0 mL of irradiated samples were withdrawn and centrifuged at 5000 rpm for 10 min to separate TiO_2 . The dye concentration was determined spectrophotometrically at 665 nm with Unicam UV 2 spectrophotometer.

Decolorization of Methylene Blue with Fenton Method

Experimental studies of Fenton's method were designed in a sealed flask. In the first stage 100 mL of dye solution and predetermined amount of catalysis were mixed. The pH of the solution was adjusted and H_2O_2 was added in to solution. The solution was stirred with a magnetic stirrer. 5 mL of sample solutions were withdrawn every 30 seconds and the dye concentrations were determined spectrophotometrically at 665 nm.

Plant Material and Modification of Alumina

The plant gall samples were collected from Karaçayır region of Sivas, Turkey. The crude dust of the sample was removed with soaking into water. The wet samples were dried in open air. The samples were granulated and stored in polyethylene bags.

The modification of Alumina was conducted as described below:

5.0 g of Al_2O_3 , 0.1 g sodium dodecylsulphate (SDS) and 0.5 g of dried gall sample were triturated well and heated at 50 °C in an incubator. These processes were repeated until the sample was completely homogeneous.

The same processes were done without plant material to obtain non-modified alumina sorbent.

Optimization of Removal Conditions

To obtain high removal efficiency, each experimental parameter was optimised individually. The effects of solution pH, concentration of inert salt, initial concentration of dye, and mass of sorbent were optimized. For removal of MB with gall modified alumina and non-modified alumina, 50 mL of dye solutions were treated with predetermined amount of sorbents after pH adjustment with a multi magnetic stirrer. The final dye concentration was determined spectrophotometrically mentioned above. All absorbance values were recorded after separation of sorbent particles via centrifugation. To eliminate the effect of loss of dye and the effect of any contribution to absorbance because of soluble materials released from sorbent absorbance values were taken against blank solution (without dye) prepared with the same way.

Results and Discussions

The Experimental Parameters that Affect the Photocatalytic Decolourization of Methylene Blue

The pH is an important parameter that affects the photocatalytic decomposition process. The differentiation of surface charge of catalysis as well as the oxidation state of pollutant are generally depend on the pH of the solution. The pH optimization is an unavoidable step for photocatalytic decomposition studies.

The effect of pH on photocatalytic decolourization was studied in the range of 2-11. As can be seen from figure 1a, changing the pH from acidic region to neutral region, the decolourization yield increased. Similar trends were also observed in other studies [36].

At acidic pH, the surface charge of TiO_2 is positive [16], so at highly acidic regions, electrostatic repulsion between cationic methylene blue and partially positively charged TiO_2 molecules might be the reason of low removal yield. According to Bubacz et al., pH has an important role and at more basic pH region, electrostatic interactions between negative TiO^- and methylene blue cation leads to a strong adsorption with a corresponding high rate of degradation. But, at extremely high pH (e.g. pH 11, fig. 1.a), the repulsion between negatively charged moieties of both TiO_2 and methylene blue was the main reason for depression in removal yield. From the figure 1.a. It could be concluded that neutral pHs were the optimum for the photocatalytic decolourization of methylene blue.

The effect of UV irradiation of solution was studied and it can be seen that the in the absence of irradiation the insufficient decolourization yields were achieved. Besides, the insufficient decolourization yields also achieved with using only UV irradiation. As can be seen from the figure

1b, decolourization of dye was significantly higher when conducting the process with both TiO_2 and UV irradiation.

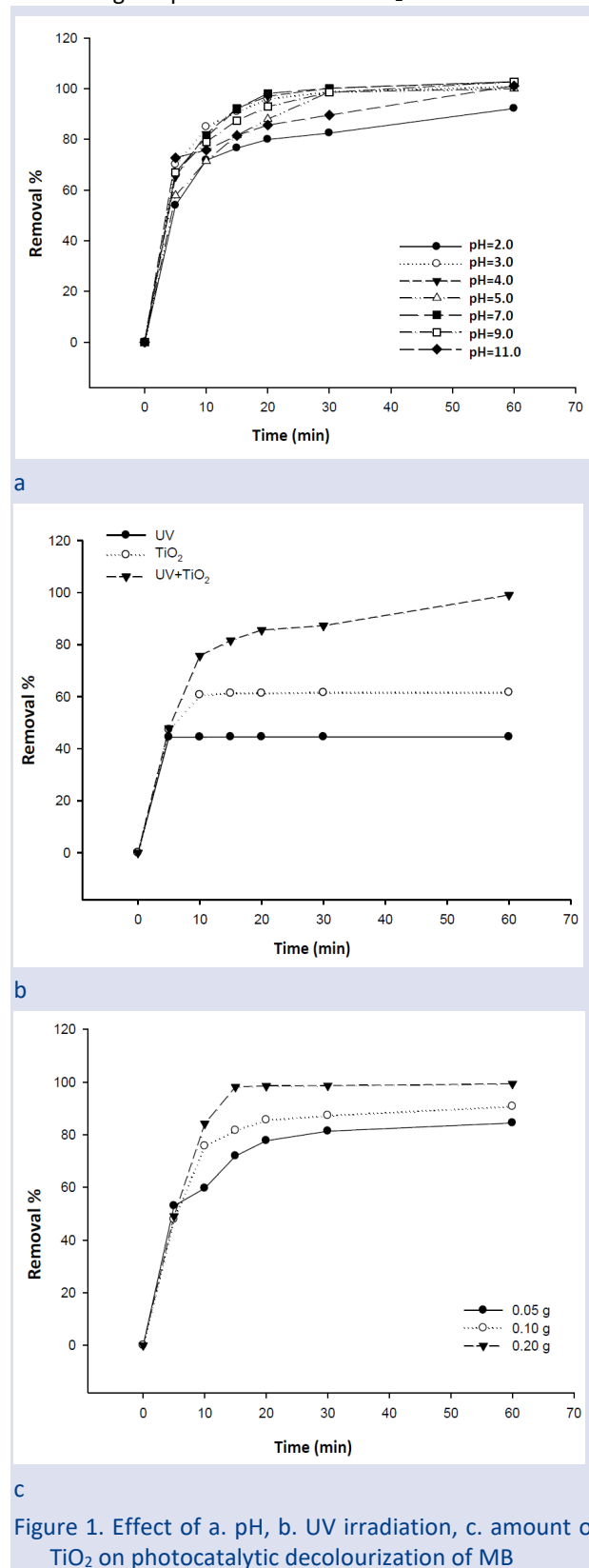


Figure 1. Effect of a. pH, b. UV irradiation, c. amount of TiO_2 on photocatalytic decolourization of MB

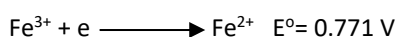
The decolourization yield was quantitative and almost 100 % of decolourization was achieved within only 60 min

The amount of TiO_2 affects decolourization of MB. It can be seen that, the decolourization degree increased as increasing the TiO_2 amount (figure 1c). As expected, an increase in available surface area was caused by an

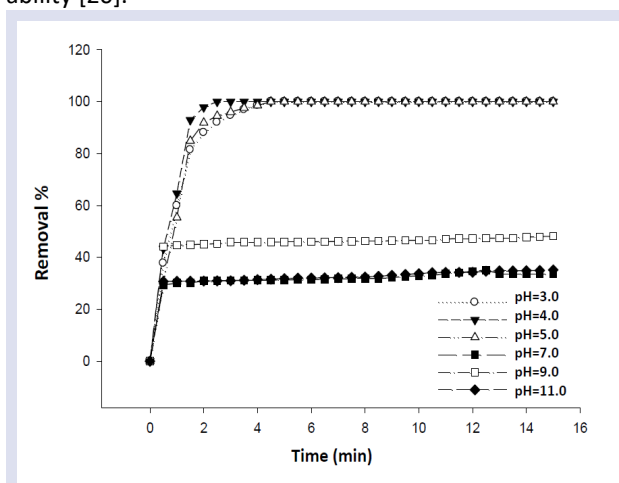
increase in the amount of TiO₂. So, increasing TiO₂ amount led an increase in the adsorption of dye molecules on to catalysis surface which resulted in an increase in decolourization rate.

The Experimental Parameters that Affect the Fenton's Decolourization of Methylene Blue

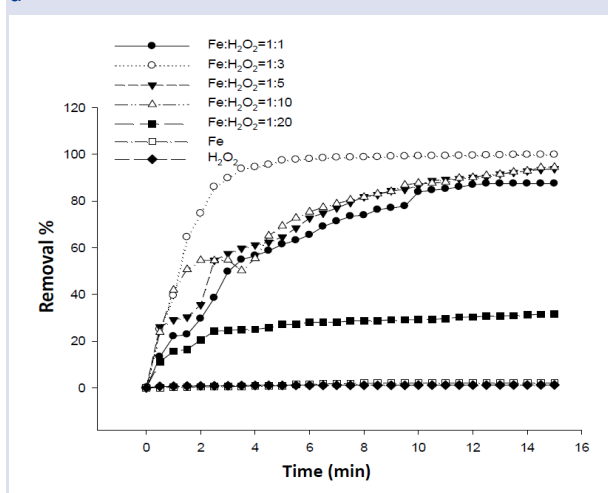
The effect of pH on decolourization of MB was studied in the range of 2-11. As shown from figure 2a, the decolourization of dye is higher at especially acidic region. This might be due to the reduction tendency of Fe³⁺ ions to Fe²⁺ ions in the acidic region according to reaction below:



On the other hand, at alkaline pH ranges, the precipitation of iron species as hydroxides causes low Fenton's decolourization yields. According to Kim et. al, the Fenton oxidation is not applicable in alkaline medium and iron (II) ion begins to form floc and precipitates and hydrogen peroxide is also unstable and may decompose to give oxygen and water, and finally loses its oxidation ability [20].



a



b

Figure 2. Effect of a. pH, b. Fe:H₂O₂ ratio on Fenton's degradation of MB.

The effect of catalysis to peroxide ratio was investigated in the range of 1:1, 1:3, 1:5, 1:10, and 1:20. As can be seen from the figure 2b, the maximum removal yield was achieved for the ratio 1:3.

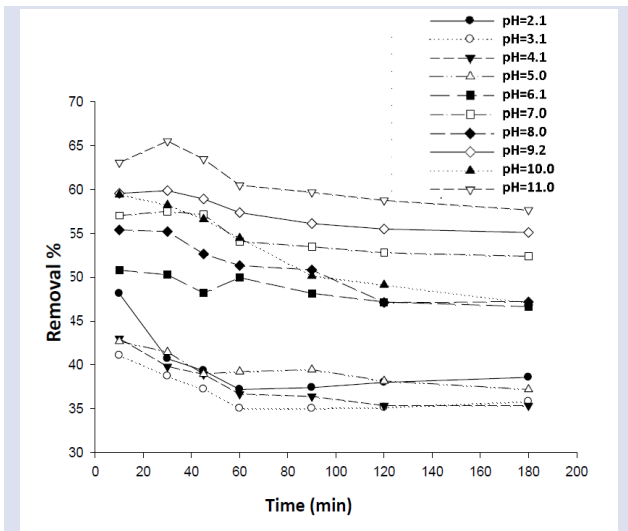
Parameters that Effect on Biosorption of Methylene Blue Yields

Adsorption is a cheap and easy alternative way for treatment of organic and inorganic pollutants. With using appropriate adsorbents, high removal of pollutants can be achieved. Due to their widely availability, low cost and high number of functional moieties, biological materials get attentions as alternative adsorbent.

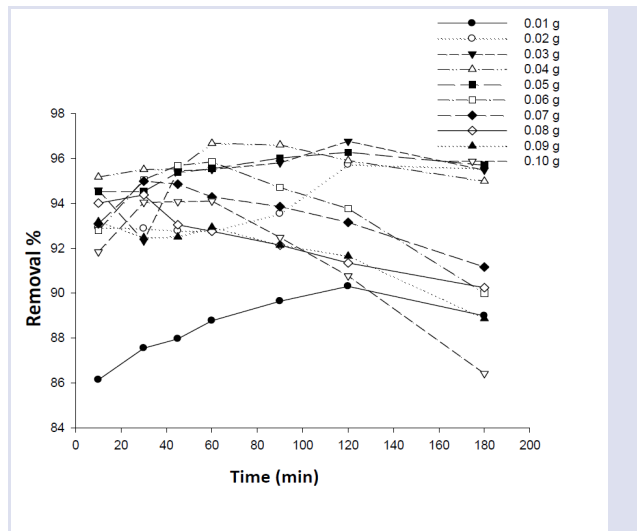
In the present study, alumina and plant gall modified alumina were employed as adsorbent. The parameters which affects the adsorption yield were investigated for high removal yield. The pH is may be the most important parameters that affect the adsorption of a molecule, for example of a dye. The surface charge of both sorbent and dye depends on the pH of solution. In the present study, the effect of solution pH was studied in the range of 2-12.

The pH dependence of dye removal is shown in figure 3a and 3b. As seen from figures, the removal of dye molecules at low pH range is significantly low; the low removal yield may be due to competition between cationic dye molecules with H₃O⁺ ions to bind active sides of surface. H₃O⁺ ions are smaller, might be more labile and can easily cover the active sides of the sorbent molecules. On the other hand, surface of the sorbent is mainly positive and the main interaction between sorbent and the cationic dye molecule was electrostatic repulsion at acidic region. As increasing the pH of the solution, the removal yield increased significantly as a result of high numbers of negatively charged active sides of the sorbent. At basic region predominant interaction between sorbent and dye molecules might be the electrostatic attraction.

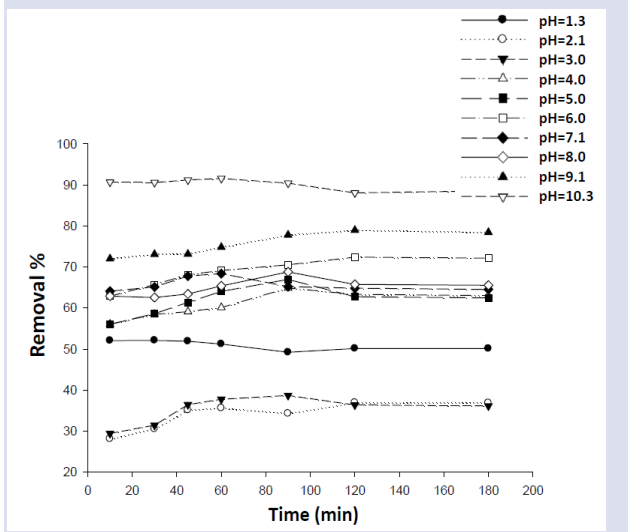
The effect of sorbent amount is generally thought to be elevating factor in an adsorption process. It is generally expected that, the higher the amount of the sorbent, the greater the adsorption is. It is seen from the figure 3c, it is valid for the adsorption of MB to non-modified alumina sorbent. On the other hand, removal yield significantly decreased for the biosorption of MB on to modified alumina as increasing the amount of sorbent (figure 3d). According to Yahaya et al., this unexpected results was due to a process named as 'screening effect'. The higher loading of sorbent protects the binding sides and results in lower removal yield [37].



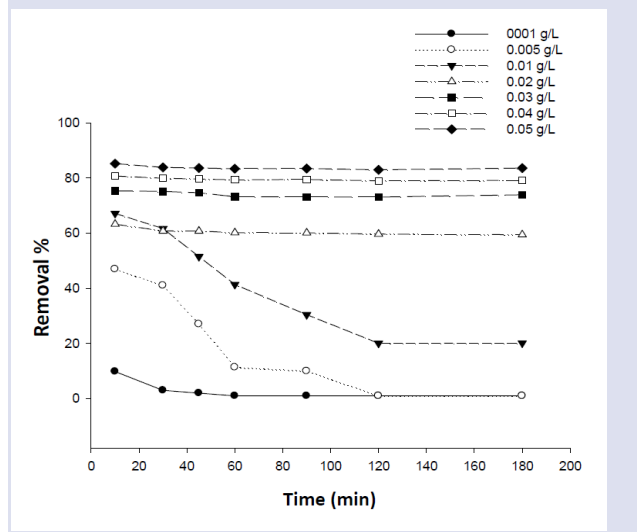
a



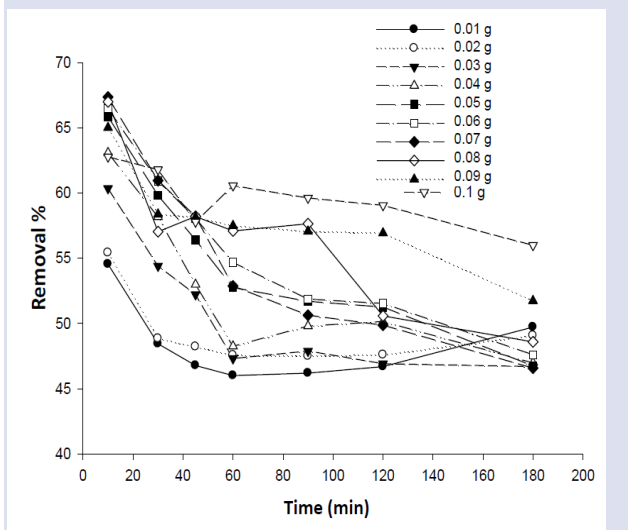
d



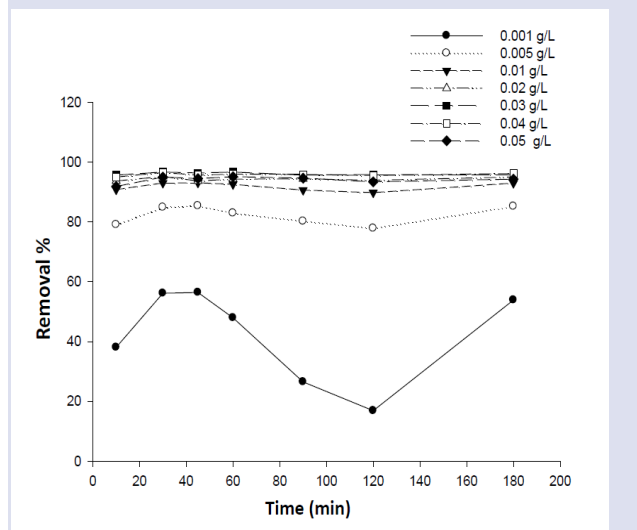
b



e



c



f

Figure 3 a. Effect of pH on removal of MB with non-modified alumina, b. Effect of pH on removal of MB with modified alumina, c. Effect of amount of sorbent on removal of MB with non-modified alumina, d. Effect of amount of sorbent on removal of MB with modified alumina, e. Effect of initial dye concentration on removal of MB with non-modified alumina, f. Effect of initial dye concentration on removal of MB with modified alumina.

The effect of initial dye concentration was also investigated in the range of 0.001-0.05 g L⁻¹. The modified and non-modified alumina sorbents were equilibrated in various concentration of MB and as shown from figure 3e and 3f, as expected, the removal yield increased, then reached equilibria almost at 0.01 g L⁻¹ for modified alumina. On the other hand, the removal yields increased all through the experiments for non-modified alumina. Maximum yield was about 85% for non-modified alumina.

The effect of presence of a salt was studied in the range of 0.01-0.08 mol L⁻¹ with using KNO₃. An increase in concentration of the salt is resulted in a decrease (about 15-20 percent for both modified and non-modified alumina sorbents) in the biosorption of the dye (Figure not shown). This might be due to coverage of the active sides of the sorbent with, small, more labile potassium ion rather than dye molecules.

Comparison of studied methods for decolourization of MB

The methods used in the present study have both advantageous and disadvantageous compared to each other. In terms of costs of the processes, required time to achieve high yields, ecological aspects are compared individually and given in Table 1.

Conclusion

In the present study, AOps and biosorption was employed for the efficient decolourization and the significant observations are briefly discussed below.

The effective and significantly higher removal yields were achieved with Fenton process for decolourization of MB. At especially acidic pH ranges, almost 100 % decolourization was obtained. The duration of the process for 100 % decolourization was about 2 minutes. The required time for complete decolourization was significantly shorter than the other studied process. However, in this process a strong oxidative agent, hydrogen peroxide and iron ions were used. This process can lead seconder environmental iron residues. Similarly, biosorption of MB with modified and non-modified alumina can lead seconder sludge. On the hand, biosorption process is thought to be economically quite feasible. The obtained maximum removal yield was above 90 % by modified alumina and was much lower for non-modified alumina. The modification of alumina by a simple modification procedure with an agricultural residue (with a type of plant gall) made the adsorption process more feasible. In photocatalytic decolorization method achieved maximum removal yield is > 98 % with using TiO₂/UV. In terms of ecological seconder residues and economically, TiO₂/UV decolorization method was rather feasible.

As a consequence, it can be said that all the used methods sufficiently capable of decolourization of MB dye solutions.

Table 1: Comparison of studied methods for decolourization of MB.

Method	pH	Amounts of Reagents (g)				
		Fe:H ₂ O ₂	TiO ₂	Non-modified Alumina	Modified Alumina	
Fenton	4 (~ 100%)	2 min. 1:3(>97%)	5 min. -	-	-	
Photocatalytic	Neutral to basic (>90%)	15 min. -	-	0.2 (>98)	15 min -	
Biosorption	Modified	11 (>92%)	10 min. -	-	-	0.03(> 96%) 240 min.
	Non-Modified	11 (>65 %)	30 min. -	-	-	0.07 (> 67) 10 min. -

Conflicts of Interest

The authors declare no conflict of interest

References

- [1] Pan Y., Wang J., Sun C., Liu X., Zhang H., Fabrication of highly hydrophobic organic-inorganic hybrid magnetic polysulfone microcapsules: A lab-scale feasibility study for removal of oil and organic dyes from environmental aqueous samples, *J. Hazard. Mater.*, 309 (2016) 65–76.
- [2] Bağda E., Galls As an Effective New Biosorbent for Removal of Methylene Blue and Crystal Violet, *Desalin. Water Treat.*, 43 (2012) 63–75.
- [3] More T.T., Yan S., Tyagi R.D., Surampalli R.Y., Potential use of filamentous fungi for wastewater sludge treatment, *Bioresour. Technol.*, 101 (2010) 7691–7700.
- [4] Deniz F., Karaman S., Removal of an azo-metal complex textile dye from colored aqueous solutions using an agro-residue, *Microchem. J.*, 99 (2011) 296–302.
- [5] Hsueh C.L., Huang Y.H., Wang C.C., Chen C.Y., Degradation of azo dyes using low iron concentration of Fenton and Fenton-like system, *Chemosphere*, 58 (2005) 1409–1414.
- [6] Asghar A., Raman A.A.A., Daud W.M.A.W. Advanced oxidation processes for in-situ production of hydrogen peroxide / hydroxyl radical for textile wastewater treatment : a review, *J. Clean. Prod.*, 87 (2015) 826–838.
- [7] Cheng M., Zeng G., Huang D., Lai C., Xu P., Zhang C., Liu Y., Hydroxyl radicals based advanced oxidation processes (AOPs) for remediation of soils contaminated with organic compounds: A review, *Chem. Eng. J.*, 284 (2016) 582–598.
- [8] Antonopoulou M., Evgenidou E., Lambropoulou D., Konstantinou I., A review on advanced oxidation processes for the removal of taste and odor compounds from aqueous media, *Water Res.*, 53 (2014) 215–234.

- [9] Bethi B., Sonawane S.H., Bhanvase B.A., Gumfekar S.P., Chemical Engineering and Processing : Process Intensification Nanomaterials-based advanced oxidation processes for wastewater treatment : A review, *Chem. Eng. Process. Process Intensif.*, 109 (2016) 178–189.
- [10] Bokare A.D., Choi W., Review of iron-free Fenton-like systems for activating H₂O₂ in advanced oxidation processes, *J. Hazard. Mater.*, 275 (2014) 121–135.
- [11] Temel N.K., Sökmen M., New catalyst systems for the degradation of chlorophenols, *Desalination.*, 281 (2011) 209–214.
- [12] Yang X., Cao C., Erickson L., Hohn K., Maghirang R., Klabunde K., Photo-catalytic degradation of Rhodamine B on C-, S-, N-, and Fe-doped TiO₂ under visible-light irradiation, *Appl. Catal. B Environ.*, 91 (2009) 657–662.
- [13] Saïen J., Ardjmand R.R., Iloukhanı H., Photocatalytic decomposition of sodium dodecyl benzene sulfonate under aqueous media in the presence of TiO₂, *Phys. Chem. Liq.*, 41 (5) (2003) 519–531.
- [14] Ollis D.F., Pelizzetti E., Serpone N., Photocatalyzed destruction of water contaminants, *Environ. Sci. Technol.*, 25 (9) (1991) 1522-1529.
- [15] Wu T., Lin T., Serpone N., TiO₂-Assisted Photodegradation of Dyes. 9. Photooxidation of a Squarylium Cyanine Dye in Aqueous Dispersions under Visible Light Irradiation, *Environ. Sci. Technol.*, 33 (1999) 1379–1387.
- [16] Temel N.K., Gürkan R., Ayan F., Photocatalytic TiO₂-catalyzed degradation of bromophenol blue-mediated Mo(VI)-peroxo complexes in the presence of SDS, *Desalin. Water Treat.*, 3994 (2015) 1–8.
- [17] Fox M.A., Dulay M.T., Heterogeneous Photocatalysis, *Chem. Rev.*, 93 (1) (1993) 341-357.
- [18] Kamat P.V., Photochemistry on nonreactive and reactive (semiconductor) surfaces. *Chem. Rev.*, 93 (1993) 267-300.
- [19] Sökmen M., Allen D.W., Akkaş F., Kartal N., Acar F., Photodegradation of some dyes using Ag-loaded titaniumdioxide, *Water. Air. Soil Pollut.*, 132 (2001) 153–163.
- [20] Kim T., Park C., Yang J., Kim S., Comparison of disperse and reactive dye removals by chemical coagulation and Fenton oxidation, *J. Hazard. Mater.*, 112 (2004) 95–103.
- [21] Dominguez A., Pastrana L., Longo M.A., Rua M.L., Sanroman M.A., Lipolytic enzyme production by *Thermus thermophilus* HB27 in a stirred tank bioreactor, *Biochem. Eng. J.*, 26 (2005) 95-99.
- [22] Hou P., Shi C., Wu L., Hou X., Chitosan/hydroxyapatite/Fe₃O₄ magnetic composite for metal-complex dye AY220 removal: Recyclable metal-promoted Fenton-like degradation, *Microchem. J.*, 128 (2016) 218-225.
- [23] Kono H., Ogasawara K., Kusumoto R., Oshima K., Hashimoto H., Cationic cellulose hydrogels cross-linked by poly (ethylene glycol): Preparation , molecular dynamics , and adsorption of anionic dyes, *Carbohydr. Polym.*, 152 (2016) 170–180.
- [24] Lin Q., Gao M., Chang J., Ma H., Adsorption properties of crosslinking carboxymethyl cellulose grafting dimethyldiallylammonium chloride for cationic and anionic dyes, *Carbohydr. Polym.*, 151 (2016) 283–294.
- [25] Wang Y., Xie Y., Zhang Y., Tang S., Guo C., Wu J., Lau R., Anionic and cationic dyes adsorption on porous poly-melamine-formaldehyde polymer, *Chem. Eng. Res. Des.*, 114 (2016) 258–267.
- [26] Zhu S., Guo H., Yang F., Wang Z., Synthesis and dye adsorption properties, *Chinese Chem. Lett.*, 26 (2015) 1091–1095.
- [27] Couto S.R., Dye removal by immobilised fungi, *Biotechnol. Adv.*, 27 (2009) 227–235.
- [28] Kumar P.S., Ramalingam S., Senthamarai C., Niranjana M., Vijayalakshmi P., Sivanesan S., Adsorption of dye from aqueous solution by cashew nut shell : Studies on equilibrium isotherm , kinetics and thermodynamics of interactions, *Desalination*, 261 (2010) 52–60.
- [29] Kumar S., Raut S., Bandyopadhyay P., Fungal decolouration and degradation of azo dyes : A review, *Fungal Biol. Rev.*, 30 (2016) 112–133.
- [30] Do M., Abak H., Alkan M., Adsorption of methylene blue onto hazelnut shell : Kinetics , mechanism and activation parameters, *J. Hazard. Mater.*, 164 (2009) 172–181.
- [31] Vijayaraghavan K., Yun Y.S., Bacterial biosorbents and biosorption, *Biotechnol. Adv.*, 26 (2008) 266–291.
- [32] Gupta V.K., Application of low-cost adsorbents for dye removal - A review, *J. Environ. Manage.*, 90 (2009) 2313–2342.
- [33] Barakat M.A., New trends in removing heavy metals from industrial wastewater, *Arab. J. Chem.*, 4 (2011) 361–377.
- [34] Bağda E., Bağda E., Removal of Basic Blue and Crystal Violet with a Novel Biosorbent : Oak Galls, *J. Environ. Prot. Ecol.*, 531 (2012) 517–531.
- [35] Bağda E., Erşan M., Bağda E., Investigation of adsorptive removal of tetracycline with sponge like, Rosa canina gall extract modified, polyacrylamide cryogels, *J. Environ. Chem. Eng.*, 1 (2013) 1079–1084.
- [36] Bubacz K., Choina J., Dolat D., Morawski A.W., Methylene Blue and Phenol Photocatalytic Degradation on Nanoparticles of Anatase TiO₂, *Pol. J. Environ. Stud.*, 19 (2010) 685–691.
- [37] Yahaya Y.A., Mat Don M., Bhatia S., Biosorption of copper (II) onto immobilized cells of *Pycnoporus sanguineus* from aqueous solution: Equilibrium and kinetic studies, *J. Hazard. Mater.*, 161 (2009) 189–195.

Simultaneous Manipulation and Imaging of Chemogenetically Induced Hydrogen Peroxide in Hardly Transfectable Endothelial Cells

Emrah Eroglu^{1,2,a,*}¹ Research Institute for Health Sciences and Technologies (SABITA), İstanbul Medipol University, İstanbul, Türkiye² Molecular Biology, Genetics and Bioengineering Program, Faculty of Engineering and Natural Sciences, Sabancı University, İstanbul, Türkiye.

*Corresponding author

Research Article

History

Received: 09/05/2022

Accepted: 28/09/2022

Copyright

©2022 Faculty of Science,
Sivas Cumhuriyet University

ABSTRACT

Hydrogen peroxide (H₂O₂) is a critical signaling molecule in vascular cells, which controls signaling events, yet it can cause pathological oxidative stress in excess. The lack of suitable tools undermined experimental approaches to study the role of oxidative eu- and distress in cellular ultra-locales. This study exploits a yeast-derived D-amino acid oxidase (mDAAO) as a chemogenetic tool to induce, visualize and test the cytotoxicity of H₂O₂ in hardly transfectable endothelial cells. Due to the poor transfectability of endothelial cells, lentiviral vectors have been used to generate cell lines stably expressing mDAAOs. mDAAOs are substrate-based chemogenetic enzymes that convert D-amino acids to their corresponding alpha-keto acids and generate H₂O₂ as a byproduct, which can be visualized with a novel ultrasensitive, and ratiometric H₂O₂ biosensor termed HyPer7. This study tested the suitability of two different D-amino acids, including D-alanine and D-methionine, to induce oxidative stress in endothelial cells. Live-cell imaging experiments unveiled that 10 mM D-methionine generated significantly higher and faster H₂O₂ signals than D-alanine. However, both D-amino acids induced comparable levels of cell death documented by a colorimetric cell metabolic activity assay (MTT). This study provides a guide for manipulating and monitoring the cytotoxic effect of H₂O₂ in endothelial cells.

Keywords: Chemogenetic tools, Endothelial cells, Hydrogen Peroxide, Genetically Encoded Biosensors, Cytotoxicity

^a dr.emrah.eroglu@gmail.com^{id} <https://orcid.org/0000-0002-9373-0808>

Introduction

Oxidative stress is characterized by the imbalance between sufficient generation and abundant accumulation of reactive oxygen species (ROS) in cells and tissues [1], which is a hallmark of many cardio- and neurovascular diseases like heart failure, atherosclerosis, ischemia, stroke, diabetes Mellitus, and Alzheimer's disease or dementia [2], all leading causes of death globally [3]. It has been established that increased levels of oxidative stress are implicated in the progression of cardio- and neurovascular diseases [4,5]. Thus, ROS have long been recognized as destructive molecules [6]. A more recent concept defines oxidative eustress as physiological oxidative stress required and essential for redox-dependent signaling pathways [7]. The relatively stable ROS hydrogen peroxide (H₂O₂) fine-tunes kinase-driven molecules such to control cell division, differentiation, and migration by reversible cysteine oxidation of these key signaling proteins [8]. However, excessive oxidative stress causes disturbed redox signaling and oxidative damage to macromolecules, termed oxidative distress, and the underlying mechanisms causative for the transition from healthy conditions to pathogenesis are not fully understood yet [9].

Potential sources of ROS for cardio- and neurovascular diseases can be found in all layers throughout the vasculature [10]. Of particular interest are endothelial cells, which form the inner layer of blood- and lymphatic vessels. Endothelial cells are rich in mitochondria and

NADPH oxidase (NOX), two critical sources for ROS generation [11]. ROS are usually produced by xanthine oxidase, nicotinamide adenine dinucleotide phosphate oxidase, lipoxygenases, or uncoupling endothelial nitric oxide synthase (eNOS) in vascular cells [12]. Any imbalance in the equilibrium between the production of reactive oxidants and antioxidant capacity triggers oxidative distress, which in turn leads to the progression of pathological conditions [13]. Thus, informative tools and technologies permitting real-time monitoring of ROS-dependent pathways are of the highest interest.

Genetically encodable biosensors are fluorescent protein-based nano-probes allowing the selective and ultrasensitive detection of their analytes in cellular ultra-locales [14-17]. Recent advances in the real-time detection and quantification of ROS levels with the aid of genetically encoded biosensors unveiled that spatial and temporal sources of ROS and reactive nitrogen species (RNS) have diverse functions within the cell [18-21]. Ever since the development of the first genetically encoded ROS, RNS, and reactive sulfur species (RSS) biosensors, much has been learned about the ultra-local role of these reactive molecules. However, the lack of suitable tools to manipulate the redox tone in subcellular locales undermined recapitulating in vivo conditions in cells and tissues. Conventional approaches, which administer physiologically irrelevant concentrations of H₂O₂ in micro-

and millimolar range directly to cells, failed to recapitulate H₂O₂-derived signaling pathways [20,22,23].

In recent years, the toolkit of redox biologists has been expanded by a yeast-derived enzyme D-amino acid oxidase (DAAO), which turned useful as a chemogenetic tool permitting the manipulation of redox levels on the level of tissues, cells, and even subcellular locales with high precision [22-24]. Chemogenetics refers to an experimental system that becomes activated in the presence of its substrate and remains silent in the absence of its biochemical stimulus [25]. In a recent study, our lab established and fine-tuned a mutated version of DAAOs, termed mDAAO, with improved enzymatic activity that is capable of efficiently converting various D-amino acids into their corresponding alpha-keto acids, producing the mild oxidant H₂O₂, ammonia (NH₄⁺), and pyruvate in the presence of molecular oxygen and the cofactor flavin

adenine dinucleotide (FAD) (Figure 1A). Because both NH₄⁺ and pyruvate are usually abundant in cells, the amount of these byproducts produced is negligible [25]. One mole of D-amino acid produces equimolar concentrations of H₂O₂ [26]. The type of D-amino acid and the amino acid uptake efficiency dictates the intracellular generation of mDAAO's byproducts (Figure 1A), which typically yields H₂O₂ in the lower micromolar range [24]. Pairing chemogenetic enzymes with genetically encoded biosensors allow multiparametric imaging and manipulation of cells and tissues with ultrahigh precision (Figure 1 B). mDAAOs are genetically encodable; thus, these enzymes can be tagged with fluorescent proteins and differentially targeted to defined subcellular locales such as the cytosol, nucleus, or mitochondria (Figure 1C) using leading peptides allowing manipulation of the redox state with a high spatial resolution.

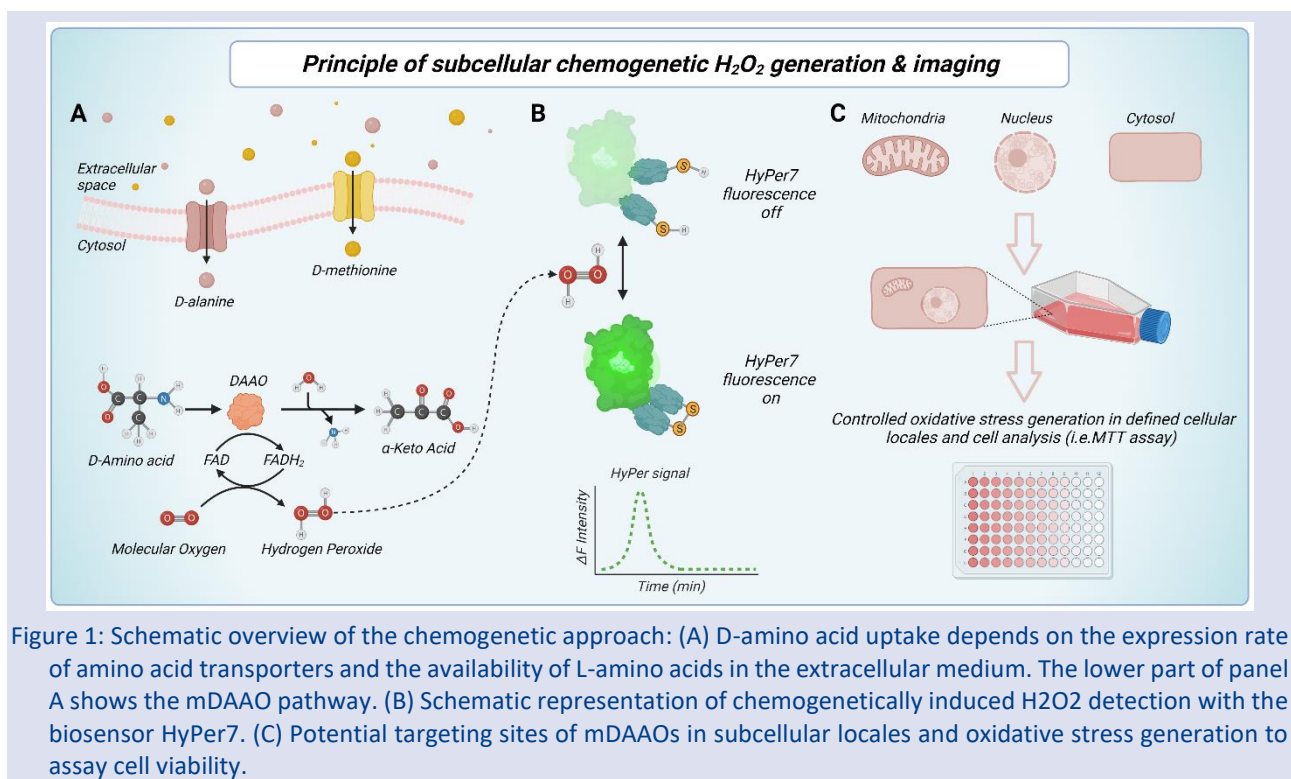


Figure 1: Schematic overview of the chemogenetic approach: (A) D-amino acid uptake depends on the expression rate of amino acid transporters and the availability of L-amino acids in the extracellular medium. The lower part of panel A shows the mDAAO pathway. (B) Schematic representation of chemogenetically induced H₂O₂ detection with the biosensor HyPer7. (C) Potential targeting sites of mDAAOs in subcellular locales and oxidative stress generation to assay cell viability.

This study employs these powerful approaches in hardly transfectable cells and guides how to manipulate and visualize H₂O₂ levels in subcellular locales of the immortalized human umbilical vein endothelial cell (HUVEC) line EA.hy926 [27]. Particularly, HUVECs, and its immortalized cell lines are accepted as hard-to-transfect primary cells, even with the most used transfection techniques because of their slow division [28]. Besides simultaneous generation and imaging of H₂O₂ signals in cells, this study also unveils the cytotoxic role of cytosolic H₂O₂ generation in endothelial cells using different D-amino acids.

Materials and Methods

Molecular Cloning

The differentially targeted chimera mCherry-mDAAO were subcloned into a 3rd-generation lentivirus shuttle vector pLenti-MP2 (Addgene #36097) via PCR techniques using the primers: forward 5'-ATACTCGAGATGGTGAGCAAGGGCGAG-3' including XhoI restriction site and reverse 5'-ATATCTAGATTACAGGGTCAGCCGCTC-3' including a stop codon and XbaI restriction site. HyPer7 [15] biosensor was a kind gift from the Vsevolod Belousov and is available at Addgene (#136467).

Cell Culture

HEK293T and EA.hy926 cells (ATCC, CRL-2922, Manassas, VA, USA) cells were grown in Dulbecco's Minimum Essential Medium (DMEM) supplemented with 10% fetal bovine serum (FBS) (Pan-Biotech, Aidenbach, Germany), 100 µg/mL Penicillin (Pan-Biotech, Aidenbach, Germany), and 100 U/mL Streptomycin (Pan-Biotech, Aidenbach, Germany). EA.hy926 cells were additionally supplemented with 100 µg/mL Normocin (InvivoGen, San Diego, CA, USA), and 2% HAT ((Sodium Hypoxanthine (5 mM), Aminopterin (20 µM), and Thymidine (0.8 mM)) (ATCC, VA, USA). Cells were maintained in a humidified CO₂ chamber (5% CO₂, 37 °C).

Lenti Virus Generation

At a confluency of 80–90%, HEK293T cells were co-transfected with 3 µg psPAX2 (Addgene #12260), 3 µg pMD2.G (Addgene #12259), and 6 µg of mCherry-mDAAO-NES lentivirus shuttle vector using PolyJet transfection reagent (SigmaGen Laboratories, Rockville, MD, USA). Following 24 hours posttransfection, the culture medium was replaced by fresh DMEM. Cells were further incubated for 24 h and 48 h before collecting the cell culture medium containing virus particles. The virus-containing culture medium was filtered using a 0.45 µm filter (TPP, Switzerland) to concentrate the lentivirus particles. A 100 kDa Amicon® Ultra15 Centrifugal Filter Unit was used for subsequent ultra-filtration at 3000× g, for 30 min, at 4 °C. Concentrated virus particles were aliquoted and used immediately or stored at –80 °C.

Stable Endothelial Cell Line Generation and Transient Transfection

Stable cell line generation was conducted following the guidelines as described elsewhere [27]. Briefly, EA.hy926 cells were seeded on a 30 mm well plate 24 hours before virus administration. At 50% - 60% confluency, the complete medium was replaced by an antibiotic-free transduction medium containing 10% FBS, 10 µg/mL Polybrene infection reagent (Sigma-Aldrich, St. Louis, MO, USA), and the lentivirus particles encoding for cytosolic targeted mCherry-mDAAO. Cells were incubated in the virus-containing medium for 48–72 h. Positive transduction was determined using conventional epifluorescence microscopy. If cell transduction was positive, cells were cultured for one week in fresh complete DMEM on a 10 cm culture dish. Fluorescence activated cell sorting (FACS) was used to select mCherry-mDAAO positive cells by detecting red fluorescence emission using an excitation wavelength of 555 nm laser (Filter type: BP 555/30 nm) in a BD-Influx Cell Sorter. Cells were then grown under standard culture conditions. Before imaging experiments, cells were seeded on a 30 mm glass coverslip (Glaswarenfabrik Karl Knecht Sondheim, Sondheim vor der Rhön, Germany) 24 hours before the experiment. For transient transfection of EA.hy926 cells, 1 µg of purified plasmid Hyper7 was used with 2.5 µL PolyJet transfection reagent according to manufacturer's instructions.

Imaging Buffers and Solutions

If not otherwise stated, all chemicals were purchased from NeoFroxx. Live-cell imaging experiments using gravity-based perfusion systems were conducted as described elsewhere [28,29]. Briefly, a cell storage buffer was used to adapt cells to a HEPES-buffered solution at room temperature containing 2 mM CaCl₂, 5 mM KCl, 138 mM NaCl, 1 mM MgCl, 1 mM HEPES (Pan-Biotech, Aidenbach, Germany), 0.44 mM KH₂PO₄, 2.6 mM NaHCO₃, 0.34 mM NaH₂PO₄, 10 mM D-Glucose, 0.1% MEM Vitamins (Pan-Biotech, Aidenbach, Germany), 0.2% essential amino acids (Pan-Biotech, Aidenbach, Germany), 100 µg/mL Penicillin (Pan-Biotech, Aidenbach, Germany), and 100 U/mL Streptomycin (Pan-Biotech, Aidenbach, Germany). Buffer pH was adjusted to 7.43 using 1 M NaOH and sterilized using a 0.45 µm medium filter (Isolab, Germany). For real-time imaging, a HEPES-buffered physiological salt solution was freshly prepared before each imaging experiment consisting of 2 mM CaCl₂, 5 mM KCl, 138 mM NaCl, 1 mM MgCl₂, 10 mM HEPES, 10 mM D-Glucose, and pH was adjusted to 7.43 using 1 M NaOH. All imaging buffers have been prepared and used immediately before imaging experiments.

Fluorescence Microscopy

Imaging was performed on an inverted widefield epifluorescence microscope Zeiss Axio Observer.Z1/7 (Carl Zeiss AG, Oberkochen, Germany). All experiments were performed using a PlanApochromat 20×/0.8 dry objective. The microscope was equipped with an LED. Light source Colibri 7 (423/44 nm, 469/38 nm, 555/30) for HyPer and mCherry imaging and a monochrome CCD. Camera AxioCam 503 for image acquisition. HyPer7 signals were collected by alternately exciting cells using a motorized dual-filter wheel decorated with beam splitters (FT455 (for HyPer low, F420) and FT495 (for HyPer high, F490)). Emissions were alternately collected using a bandpass filter (BP 525/50). mCherry-mDAAO signals were collected using the filter combinations FT570 (BS) and emission filter 605/70. Zen Blue 3.1 Pro software (Carl Zeiss AG, Oberkochen, Germany) was used for control and data acquisition. A custom-made gravity-based perfusion system was used to administer and withdraw D-amino acids or H₂O₂.

MTT (3-(4,5-dimethylthiazol-2-yl)-2,5-diphenyltetrazolium bromide) Assay

Cells were incubated for 24 hours with different concentrations of D-methionine or D-alanine, as described in the results section. Following cell treatment, 100 µL fresh culture medium and 10 µL of a 12 mM MTT stock solution was added to each well of a 96-well plate. Cells were further incubated at 37 °C for 4 hours. Culture medium except 25 µL was removed and 50 µL of DMSO was added to each well and mixed thoroughly with the pipette to dissolve the dye. Cells were further incubated at 37 °C for 10 minutes. The absorbance was determined spectrophotometrically at 540 nm using a reference

wavelength of 630 nm on a Tecan microplate reader Infinite 200 pro (DKSH, USA).

Statistics

GraphPad Prism software version 5.04 (GraphPad Software, San Diego, CA, USA) was used for data analysis. All experiments were performed at least in triplicates. Student's t-test was applied to test significant differences between group means. Statistical significance was considered meaningful if the p-value summary was $p < 0.0001$.

Results and Discussion

Endothelial cells are hardly transfectable cells with conventional transfection reagents [30]. Therefore, this study generated EA.hy926 cell lines stably expressing yeast-derived (from *R. gracilis*) D-amino acid oxidase - termed mDAAO - fused to a red fluorescent protein (mCherry) [24] using lentivirus approaches as described previously [27]. Purified lentiviral particles encoding for cytosolic targeted mCherry-mDAAO chimera were used to infect endothelial cells. After fluorescence-activated cell sorting (FACS), correct targeting and robust expression levels have been validated with high-resolution live-cell epifluorescence imaging. After FACS, the stable cell line displayed 100% transfection efficiency, documented by high-resolution live-cell imaging experiments in the red channel (Figure 2A).

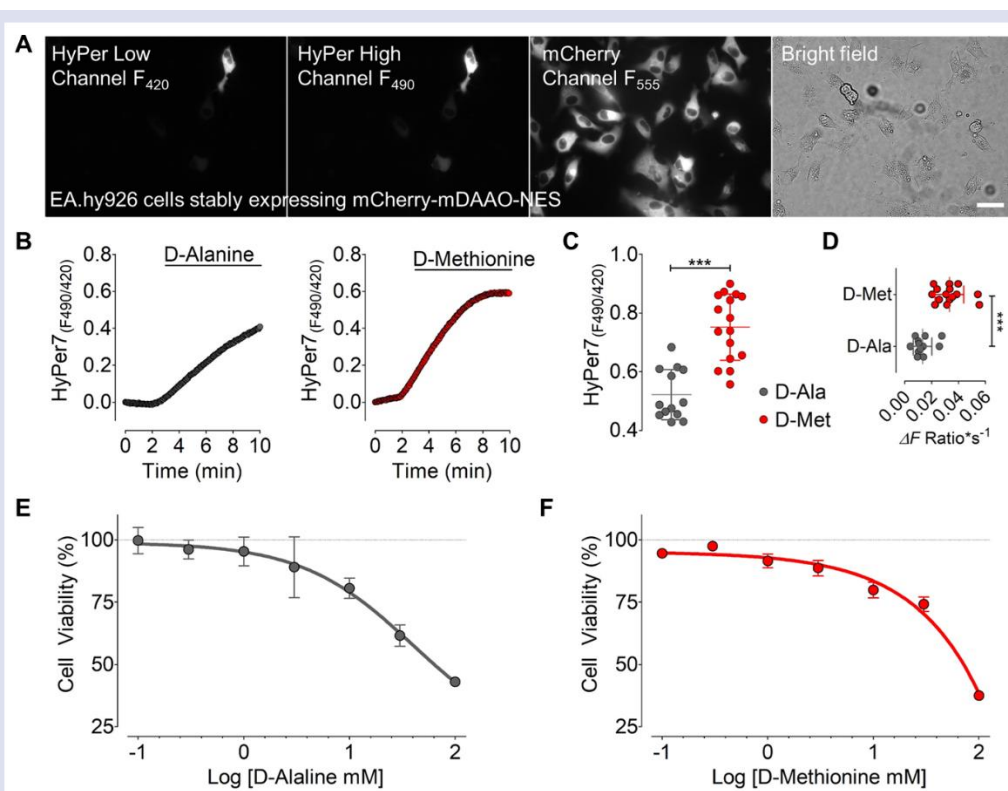


Figure 2: Chemogenetic generation, imaging, and testing of the cytotoxicity of H_2O_2 in endothelial cells. (A) Representative widefield images show EA.hy926 cells transiently expressing HyPer7 biosensor excited with 420 nm (1st image) and 490 nm (2nd image). The emission in both images was collected at 520 nm. The third image shows the same cells in the RFP channel excited with 555 nm. The very right panel shows brightfield images of the same cells. Micrographs are representative, and experiments were repeated $n=8$ with similar results. (B) Real-time traces of HyPer7 ratio signals of cells stably expressing mCherry-mDAAO-NES that are transiently transfected with HyPer7-NES in response to 10 mM D-alanine (left panel, $n=13$) and 10 mM D-methionine (right panel, $n=16$). (C) Scatter dot plot shows maximum HyPer7 ratio amplitudes in response to 10 mM D-alanine (grey dots, $n=13$) and 10 mM D-methionine (red dots, $n=16$). (D) Scatter dot plot shows the initial cytosolic invasion of H_2O_2 in the same cells described in panels B-C. (E, F) The normalized curves show cell viability of EA.hy926 cells stably expressing mCherry-mDAAO-NES using MTT assay in response to different D-alanine concentrations (grey dots, $n=3$) or D-methionine (red dots, $n=3$). Cells have been treated for 24 hours with 0 mM, 0.1 mM, 0.3 mM, 1mM, 3mM, 10mM, 30mM, and 100mM D-amino acids. An unpaired Student's t-test was applied to compare two columns. (P -value < 0.0001) All values are given as SD.

mDAAO functionality test has been validated with the ultrasensitive H_2O_2 biosensor HyPer7. HyPer7 biosensor is a ratiometric probe permitting the quantification of H_2O_2 levels [15]. Furthermore, these biosensors can be

differentially targeted to specific subcellular locales allowing simultaneous detection of the chemogenetically generated H_2O_2 . For this purpose, EA.hy926 cells stably expressing mCherry-mDAAO-NES were transiently

transfected using conventional transfection reagents. As shown in Figure 2A, transient transfection of EA.hy926 cells yielded only a few positively HyPer7 transfected cells, which is in line with numerous studies that document the hard transfectability of vascular cells [27,29,31,32]. Because this experiment aims to validate the functionality of mDAAOs in endothelial cells, the number of positively transfected HyPer7 cells ($13,3\% \pm 1,8$) was considered sufficient.

Most studies that employed mDAAOs utilized D-alanine as a substrate to activate the chemogenetic enzyme for H₂O₂ production [33]. D-alanine proved suitable as it causes robust and rapid H₂O₂ generation in most cell types, probably due to L-amino acid transporters' (LATs) abundant expression [34]. Luckily, amino acid transporters are selective for their respective amino acid, yet they are less stereoselective, permitting cellular uptake of D-amino acids and the activation of the chemogenetic enzyme [35].

As shown in Figure 2B, administration of 10 mM D-alanine to endothelial cells co-expressing targeted mCherry-mDAAO and HyPer7 triggered a detectable yet sluggish H₂O₂ signal in the cell cytosol. Our group's previous study showed that 10 mM D-alanine triggered robust and fast H₂O₂ generation in different cell types (i.e., HEK293T or U87MG) [24]. This observation suggests that endothelial cells hardly take up D-alanine, probably due to a tightly regulated membrane trafficking and import/export mechanisms in these cell types. Notably, endothelial cells have a barrier function to essential organs, such as the blood-brain, blood-retinal, gut-vascular, or blood-bile-barrier. Thus, the inner layer of vessels plays a critical role as a gatekeeper, firmly regulating the entry of biomolecules [36]. Thus, in contrast to most cell lines (mainly cancer cells), limited D-alanine uptake in endothelial cells might be causative for reduced chemogenetic generation of H₂O₂.

In contrast, D-methionine displayed a significantly higher HyPer7 ratio amplitude in EA.hy926 cells expressing mCherry-mDAAO-NES. However, it is unclear whether endothelial cells favor D-methionine over D-alanine or whether mDAAOs have higher catalytic activity for D-methionine. A likely effect is that both scenarios are valid, contributing to faster and more H₂O₂ generation in these cell types in response to D-methionine.

Nevertheless, both D-amino acids triggered cell death in endothelial cells equally. Cell treatment with up to 1 mM D-amino acid for 24 hours did not significantly affect cell death, while 10 mM and higher concentrations heavily influenced cell death. It is noteworthy that these findings demonstrate the robustness of endothelial cells against sustained oxidative stress that have been exposed to high levels of cytosolic H₂O₂ over 24 hours. Strikingly, only at maximum enzymatic (mDAAO) capacity activated by <10 mM D-alanine or D-methionine caused significant cell death.

Notably, this study focused on cytosolic oxidative stress, a cell compartment decorated with powerful antioxidant systems [37]. Employing the experimental approaches in

different cellular locales (i.e., mitochondria, caveolae, nucleus, mitochondria-associated membranes (MAMs)) might shed light on ultra-locale oxidative stress and its role in pathophysiology and cell death in the future.

Conclusion

This study demonstrates a reliable method for manipulating oxidative stress levels in cellular compartments with high spatial and temporal resolution in hardly transfectable endothelial cells. The choice of D-amino acids plays an essential role in modulating kinetic parameters in H₂O₂ generation, which is critical to investigating the acute effects of ROS levels on redox-sensitive enzymes such as the endothelial nitric oxide synthase (eNOS). This study has employed the ultrasensitive H₂O₂ biosensor HyPer7 as a direct read-out for H₂O₂ -generation. Alternative biosensors such as geNOps for nitric oxide (NO) [38], GCaMPs [39] for calcium, and MALions [40] for ATP-imaging can be combined with chemogenetic approaches presented in this study to investigate the acute or long-term effects of ultra-local H₂O₂ with differentially targeted mDAAOs. Notably, these signaling and metabolic parameters are hallmarks of most vascular-derived diseases.

Acknowledgments

This research was supported by funds from the Scientific and Technological Research Council of Turkey Grant 118C242. The author acknowledges Melike Seçilmiş for her technical support in culturing cells, Tuba Akgül Çağlar for Turkish language editing, Zeynep Çokluk for providing MTT protocols, and Asal Ghaffari Zaki for English language proof-reading. The HyPer7 biosensor was generously provided by Vsevolod Belousov. Figure 1 was generated with Biorender (Licence code: DN23VJT821).

Conflicts of interest

There are no conflicts of interest in this work.

References

- [1] Sies H., Belousov VV., Chandel N.S., Davies M.J., Jones D.P., Mann G.E., Murphy M.P., Yamamoto M., Winterbourn C., Defining roles of specific reactive oxygen species (ROS) in cell biology and physiology, *Nat Rev Mol Cell Biol.*, 23(7) (2022) 499-515
- [2] Panth N., Paudel K.R., Parajuli K., Reactive Oxygen Species: A Key Hallmark of Cardiovascular Disease, *Adv Med.*, 2016 (2016) 9152732
- [3] Rana J.S., Khan S.S., Lloyd-Jones D.M., Sidney S., Changes in Mortality in Top 10 Causes of Death from 2011 to 2018, *J. Gen. Intern Med.*, 36(8) (2021) 2517-2518.
- [4] Senoner T., Dichtl W., Oxidative Stress in Cardiovascular Diseases: Still a Therapeutic Target?, *Nutrients*, 11(9) (2019) 2090
- [5] Abdul-Muneer P.M., Chandra N., Haorah J., Interactions of oxidative stress and neurovascular inflammation in the

- pathogenesis of traumatic brain injury, *Mol. Neurobiol.*, 51(3) (2015) 966-79
- [6] Sharma P., Jha A. B., Dubey R. S., Pessarakli M., Reactive Oxygen Species, Oxidative Damage, and Antioxidative Defense Mechanism in Plants under Stressful Conditions, *Journal of Botany*, 217037 (2012) 2012
- [7] Sies H., Hydrogen peroxide as a central redox signaling molecule in physiological oxidative stress: Oxidative eustress, *Redox Biol.*, 11 (2017) 613-619.
- [8] Veal E., Day A., Hydrogen peroxide as a signaling molecule, *Antioxid Redox Signal.*, 15 (1) (2011) 147-51
- [9] Pizzino G., Irrera N., Cucinotta M., Pallio G., Mannino F., Arcoraci V., Squadrito F., Altavilla D., Bitto A., Oxidative Stress: Harms and Benefits for Human Health. *Oxid Med Cell Longev.*, 2017 8416763 (2017)
- [10] Chen Q., Wang Q., Zhu J., Xiao Q., Zhang L., Reactive oxygen species: key regulators in vascular health and diseases, *Br. J. Pharmacol.*, 175(8) (2018) 1279-1292.
- [11] Carvalho C., Moreira P.I., Oxidative Stress: A Major Player in Cerebrovascular Alterations Associated to Neurodegenerative Events, *Front Physiol.*, 9 (2018) 806.
- [12] Münzel T., Camici G.G., Maack C., Bonetti N.R., Fuster V., Kovacic J.C., Impact of Oxidative Stress on the Heart and Vasculature: Part 2 of a 3-Part Series, *J Am Coll Cardiol*, 70(2) (2017) 212-229.
- [13] Sies H., On the history of oxidative stress: Concept and some aspects of current development, *Current Opinion in Toxicology*, 7 (2018)
- [14] Eroglu E., Gottschalk B., Charoensin S., Blass S., Bischof H., Rost R., Madreiter-Sokolowski C.T., Pelzmann B., Bernhart E., Sattler W., Hallström S., Malinski T., Waldeck-Weiermair M., Graier W.F., Malli R., Development of novel FP-based probes for live-cell imaging of nitric oxide dynamics, *Nat Commun.*, 4 (2016) 7:10623.
- [15] Pak V.V., Ezeriņa D., Lyublinskaya O.G., Pedre B., Tyurin-Kuzmin P.A., Mishina N.M., Thauvin M., Young D., Wahni K., Martínez Gache S.A., Demidovich A.D., Ermakova Y.G., Maslova Y.D., Shokhina A.G., Eroglu E., Bilan D.S., Bogeski I., Michel T., Vriz S., Messens J., Belousov V.V., Ultrasensitive Genetically Encoded Indicator for Hydrogen Peroxide Identifies Roles for the Oxidant in Cell Migration and Mitochondrial Function, *Cell Metab.*, 31(3) (2020) 642-653.e6
- [16] Depaoli M.R., Bischof H., Eroglu E., Burgstaller S., Ramadani-Muja J., Rauter T., Schinagl M., Waldeck-Weiermair M., Hay J.C., Graier W.F., Malli R., Live cell imaging of signaling and metabolic activities, *Pharmacol Ther.*, 202 (2019) 98-119
- [17] Eroglu E., Charoensin S., Bischof H., Ramadani J., Gottschalk B., Depaoli M.R., Waldeck-Weiermair M., Graier W.F., Malli R., Genetic biosensors for imaging nitric oxide in single cells, *Free Radic Biol Med.*, 128 (2018) 50-58.
- [18] Collins J.A., Kapustina M., Bolduc J.A., Pike J.F.W., Diekman B.O., Mix K., Chubinskaya S., Eroglu E., Michel T., Poole L.B., Furdui C.M., Loeser R.F., Sirtuin 6 (SIRT6) regulates redox homeostasis and signaling events in human articular chondrocytes, *Free Radic Biol Med.*, 166 (2021) 90-103.
- [19] Eroglu E., Saravi S.S.S., Sorrentino A., Steinhorn B., Michel T., Discordance between eNOS phosphorylation and activation revealed by multispectral imaging and chemogenetic methods, *Proc. Natl. Acad. Sci. USA.*, 116(40) (2019) 20210-20217
- [20] Saravi S.S.S., Eroglu E., Waldeck-Weiermair M., Sorrentino A., Steinhorn B., Belousov V., Michel T., Differential endothelial signaling responses elicited by chemogenetic H₂O₂ synthesis, *Redox Biol.*, 36 (2020) 101605.
- [21] Sorrentino A., Steinhorn B., Troncone L., Saravi S.S.S., Badole S., Eroglu E., Kijewski M.F., Divakaran S., Di Carli M., Michel T., Reversal of heart failure in a chemogenetic model of persistent cardiac redox stress, *Am. J. Physiol. Heart Circ. Physiol.*, 317(3) (2019) H617-H626.
- [22] Ghaffari Zaki A., Erdoğan Y.C., Akgul Caglar T., Eroglu E., Chemogenetic approaches to dissect the role of H₂O₂ in redox-dependent pathways using genetically encoded biosensors, *Biochem. Soc. Trans.*, 50(1) (2022) 335-345.
- [23] Steinhorn B., Eroglu E., Michel T., Chemogenetic Approaches to Probe Redox Pathways: Implications for Cardiovascular Pharmacology and Toxicology, *Annu. Rev. Pharmacol. Toxicol.*, 62 (2022) 551-571.
- [24] Erdogan Y.C., Altun H.Y., Secilmis M., Ata B.N., Sevimli G., Cokluk Z., Zaki A.G., Sezen S., Akgul Caglar T., Sevgen İ., Steinhorn B., Ai H., Öztürk G., Belousov V.V., Michel T., Eroglu E., Complexities of the chemogenetic toolkit: Differential mDAAO activation by d-amino substrates and subcellular targeting, *Free Radic. Biol. Med.*, 177 (2021) 132-142.
- [25] Steinhorn B., Sorrentino A., Badole S., Bogdanova Y., Belousov V., Michel T., Author Correction: Chemogenetic generation of hydrogen peroxide in the heart induces severe cardiac dysfunction, *Nat. Commun.*, 12(1) (2021) 357.
- [26] Smolyarova D.D., Podgorny O.V., Bilan D.S., Belousov V.V., A guide to genetically encoded tools for the study of H₂O₂, *FEBS J.*, 289(18) (2021) 5382-5395.
- [27] Secilmis M., Altun H.Y., Pilic J., Erdogan Y.C., Cokluk Z., Ata B.N., Sevimli G., Zaki A.G., Yigit E.N., Öztürk G., Malli R., Eroglu E., A Co-Culture-Based Multiparametric Imaging Technique to Dissect Local H₂O₂ Signals with Targeted HyPer7, *Biosensors (Basel)*, 11(9) (2021) 338.
- [28] Kovala A.T., Harvey K.A., McGlynn P., Boguslawski G., Garcia J.G., English D., High-efficiency transient transfection of endothelial cells for functional analysis. *FASEB J.*, 14(15) (2000) 2486-94.
- [29] Eroglu E., Rost R., Bischof H., Blass S., Schreilechner A., Gottschalk B., Depaoli M.R., Klec C., Charoensin S., Madreiter-Sokolowski C.T., Ramadani J., Waldeck-Weiermair M., Graier W.F., Malli R., Application of Genetically Encoded Fluorescent Nitric Oxide (NO•) Probes, the geNOps, for Real-time Imaging of NO• Signals in Single Cells, *J. Vis. Exp.*, (121) (2017) 55486.
- [30] Yockell-Lelièvre J., Riendeau V., Gagnon S.N., Garenc C., Audette M., Efficient transfection of endothelial cells by a double-pulse electroporation method, *DNA Cell Biol.*, 28(11) (2009) 561-6.
- [31] Charoensin S., Eroglu E., Opelt M., Bischof H., Madreiter-Sokolowski C.T., Kirsch A., Depaoli M.R., Frank S., Schrammel A., Mayer B., Waldeck-Weiermair M., Graier W.F., Malli R., Intact mitochondrial Ca²⁺ uniport is essential for agonist-induced activation of endothelial nitric oxide synthase (eNOS), *Free Radic. Biol. Med.*, 102 (2017) 248-259.
- [32] Opelt M., Eroglu E., Waldeck-Weiermair M., Russwurm M., Koesling D., Malli R., Graier W.F., Fassett J.T., Schrammel A., Mayer B., Formation of Nitric Oxide by Aldehyde Dehydrogenase-2 Is Necessary and Sufficient for Vascular Bioactivation of Nitroglycerin, *J. Biol. Chem.*, 291(46) (2016) 24076-24084.
- [33] Pollegioni L., Caldinelli L., Molla G., Sacchi S., Pilone M.S., Catalytic properties of D-amino acid oxidase in cephalosporin C bioconversion: a comparison between

- proteins from different sources, *Biotechnol. Prog.*, 20(2) (2004) 467-73
- [34] Fraga S., Pinho M.J., Soares-da-Silva P., Expression of LAT1 and LAT2 amino acid transporters in human and rat intestinal epithelial cells, *Amino Acids*, 29(3) 2005) 229-33.
- [35] Sorrentino A., Michel T., Redox à la carte: Novel chemogenetic models of heart failure, *Br. J. Pharmacol*, 177(14) (2020) 3162-3167.
- [36] Faulkner A., Trans-endothelial trafficking of metabolic substrates and its importance in cardio-metabolic disease, *Biochem. Soc. Trans.*, 49(1) (2021) 507-517.
- [37] Kurutas E.B., The importance of antioxidants which play the role in cellular response against oxidative/nitrosative stress: current state, *Nutr. J.*, 15(1) (2016) 71.
- [38] Sevimli G., Smith M.J., Caglar T.A., Bilir Ş., Secilmis M., Altun H.Y., Yigit E.N., Yang F., Keeley T.P., Malli R., Öztürk G., Mann G.E., Eroglu E., Nitric oxide biosensor uncovers diminished ferrous iron-dependency of cultured cells adapted to physiological oxygen levels, *Redox Biol.*, 53 (2022) 102319.
- [39] Yang Y., Liu N., He Y., Liu Y., Ge L., Zou L., Song S., Xiong W., Liu X., Improved calcium sensor GCaMP-X overcomes the calcium channel perturbations induced by the calmodulin in GCaMP, *Nat. Commun.*, 9(1) (2018) 1504.
- [40] Arai S., Kriszt R., Harada K., Looi L.S., Matsuda S., Wongso D., Suo S., Ishiura S., Tseng Y.H., Raghunath M., Ito T., Tsuboi T., Kitaguchi T., RGB-Color Intensiometric Indicators to Visualize Spatiotemporal Dynamics of ATP in Single Cells, *Angew Chem. Int. Ed. Engl.*, 57(34) (2018) 10873-10878

Exactness of Proximal Group Homomorphisms

Mehmet Ali Öztürk^{1,a,*}

¹Department of Mathematics, Faculty of Arts and Sciences, Adıyaman University, 02040 Adıyaman, Türkiye.

*Corresponding author

Research Article

History

Received: 06/06/2022

Accepted: 01/09/2022

Copyright



©2022 Faculty of Science,
Sivas Cumhuriyet University

ABSTRACT

This research introduces groups in proximity spaces which endowed with a proximity relation. Two penultimate choices for such relations are the Efremovic (EF) proximity relation and its extension, namely, the descriptive EF-proximity relation. There is a strong relationship between sets (groups) and set (group) descriptions. Therefore, in this paper we consider this relationship via exactness of descriptive homomorphisms between ordinary descriptive groups and meta-descriptive groups. The definition of a short exact sequence of descriptive homomorphisms is given. Then, results were obtained giving the relationships between the two short exact sequences.

Keywords: Proximal group, EF-proximity space, Descriptive EF-proximity space, Descriptive homomorphism.

 mehaliozturk@gmail.com

 <https://orcid.org/0000-0002-1721-1053>

Introduction

The focus of this research is on algebraic structures in a descriptive EF-proximity space and exactness of proximal group homomorphisms which is an outgrowth of recent research [1, 2]. A descriptive proximity space [3, 4] is an extension of an Efremovič proximity space [5]. This extension is made possible by the introduction of feature vectors that describe each point in a proximity space. Sets A, B in a proximity space X are near, provided there is at least one pair of points $a \in A, b \in B$ with matching descriptions. The basic approach is to define binary operations on subsets in a space endowed with a proximity relation. By considering the features of points in a proximity space, it is then possible to define a descriptive proximity relation as well as descriptive binary operations. This leads to a study of groupoids in proximity spaces as well as other algebraic structures in proximity spaces such as semigroups and groups. In homological algebra, exact sequences play an important role. Exactness is a part of the fundamental concepts and is used, in particular, in the definition of some functors [6]. There is a strong relationship between sets (groups) and set (group) descriptions.

Preliminaries

Let X be a nonempty set of non-abstract points and let $\Phi = \{\phi_1, \phi_2, \dots, \phi_n\}$ be a set of probe functions that represent features of each $x \in X$. In a discrete space, a non-abstract point has a location and features that can be measured [7]. This leads to a proximal view of sets of picture points in digital images [8]. A *probe function* $\Phi: X \rightarrow \mathbb{R}$ represents a feature of a sample point in a picture. Let $\Phi(x) = (\phi_1, \phi_2, \dots, \phi_n)$ denote a feature vector for x , which provides a description of each $x \in X$. To obtain a descriptive proximity relation (denoted by

$\delta_{\{\Phi\}}$), one first chooses a set of probe functions. Let $A, B \in \mathcal{P}(X)$ and let $Q(A)$ and $Q(B)$ denote sets of descriptions of points in A and B , respectively (e.g., $Q(A) = \{\Phi(a) | a \in A\}$).

The expression $A\delta_{\Phi}B$ reads A is *descriptively near* B . Similarly, $A\overline{\delta}_{\Phi}B$ reads A is *descriptively far* from B . In an ordinary metric closure space X , the closure of $A \subset X$ is defined by $cl(A) = \{x \in X | d(x, A) = 0\}$ [9]. For a set X endowed with a descriptive proximity δ_{Φ} , the descriptive closure of $A \subset X$ is defined by $cl_{\Phi}(A) = \{x \in X | \Phi(x) \in Q(cl(A))\}$. The descriptive proximity of A and B is defined by $A\delta_{\Phi}B \iff Q(cl(A)) \cap Q(cl(B)) \neq \emptyset$. The *descriptive intersection* \bigcap_{Φ} of A and B is defined by $A\bigcap_{\Phi}B = \{x \in A \cup B | \Phi(x) \in Q(A), \Phi(x) \in Q(B)\}$. That is, $x \in A \cup B$ is in $A\bigcap_{\Phi}B$, provided $\Phi(x) = \Phi(a) = \Phi(b)$ for some $a \in A, b \in B$. Observe that A and B can be disjoint and yet $A\bigcap_{\Phi}B$ can be nonempty.

A *binary operation* on a set S is a mapping of $S \times S$ into S , where $S \times S$ is the set of all ordered pairs of elements of S . A *groupoid* is a system $S(*)$ consisting of a nonempty set S together with a binary operation " $*$ " on S .

Let $S(*)$ and $S'(\cdot)$ be groupoids. A mapping h of S into S' is called a homomorphism if $h(a * b) = h(a) \cdot h(b)$ for all $a, b \in S$. A one-to-one homomorphism h of S onto S' is called an *isomorphism* of S to S' [5].

Let us consider the groupoids $Q(A)(*_{1}), Q(B)(*_{2})$, where $A \subseteq X, B \subseteq Y$. A mapping $h_{\Phi}: Q(B) \rightarrow Q(A)$ is called a *descriptive homomorphism* if it provides $h_{\Phi}(\Phi_B(b_1) *_{2} \Phi_B(b_2)) = h_{\Phi}(\Phi_B(b_1)) *_{1} h_{\Phi}(\Phi_B(b_2))$ for all $\Phi_B(b_1), \Phi_B(b_2) \in Q(B)$. A one-to-one descriptive homomorphism h_{Φ} is called a *descriptive monomorphism*, a descriptive homomorphism h_{Φ} of $Q(B)$ onto $Q(A)$ is

called a *descriptive epimorphism* and one-to-one descriptive homomorphism h_Φ of $Q(B)$ onto $Q(A)$ is called a *descriptive isomorphism* [1].

Let $A(\cdot_1), B(\cdot_2)$ be groupoids, $h: B \rightarrow A$ be a homomorphism and $\Phi_A: A \rightarrow Q(A), a \mapsto \Phi(a)$ be an object description. The object description Φ_A of A into

$Q(A)$ is an object description homomorphism if $\Phi_A(a_1 \cdot_1 a_2) = \Phi_A(a_1) *_1 \Phi_A(a_2)$ for all $a_1, a_2 \in A$. Let we consider the descriptive homomorphism $h_\Phi: Q(B) \rightarrow Q(A)$ such that $h_\Phi(\Phi_B(b)) = \Phi_A(h(b))$ [1].

$$\begin{array}{ccc} B_\Phi & \xrightarrow{h'} & A_\Phi \\ \downarrow \Phi_B & & \downarrow \Phi_A \\ Q(B) & \xrightarrow{h_\Phi} & Q(A) \end{array} \quad (1)$$

Lemma 2.1: ([1]) $h_\Phi \circ \Phi_B = \Phi_A \circ h'$.

Theorem 2.2: ([1]) Let $(X, \delta_\Phi), (Y, \delta_\Phi)$ be descriptive EF-proximity spaces, $A(\cdot_1), B(\cdot_2), Q(B)(\circ_2)$ and $Q(A)(\circ_1)$ be groupoids and h be a homomorphism from $B(\cdot_2)$ to $A(\cdot_1)$. If there are a descriptive monomorphism h_Φ of $Q(B)$ to $Q(A)$ and an object description homomorphism Φ_A of A into $Q(A)$, then there is an object description homomorphism Φ_B of B into $Q(B)$.

Let $A_\Phi(*), B_\Phi(*), C_\Phi(*)$ be ordinary descriptive monoids, $h: B_\Phi \rightarrow A_\Phi$, and $h': C_\Phi \rightarrow B_\Phi$ be ordinary descriptive homomorphisms.

$$C_\Phi \xrightarrow{h'} B_\Phi \xrightarrow{h} A_\Phi \quad (2)$$

A pair of ordinary descriptive homomorphisms (the diagram (2)) is said to be exact at B_Φ , provided $Imh' = Kerh$.

$$\dots \xrightarrow{h_{n-1}} (A_\Phi)_{n-1} \xrightarrow{h_n} (A_\Phi)_n \xrightarrow{h_{n+1}} (A_\Phi)_{n+1} \xrightarrow{h_{n+2}} \dots \quad (3)$$

In general, a sequence of ordinary descriptive homomorphisms (the diagram (3)) is exact, provided each sequential pair h_n, h_{n+1} are exact at each $(A_\Phi)_n$ for $n \in \mathbb{N}$ [10].

$$\begin{array}{ccccc} C_\Phi & \xrightarrow{h'} & B_\Phi & \xrightarrow{h} & A_\Phi \\ \downarrow \Phi_C & & \downarrow \Phi_B & & \downarrow \Phi_A \\ Q(C) & \xrightarrow{h'_\Phi} & Q(B) & \xrightarrow{h_\Phi} & Q(A) \end{array} \quad (4)$$

Lemma 2.3: ([10]) Let $h: B_\Phi \rightarrow A_\Phi$ be an ordinary descriptive homomorphism, Φ_A, Φ_B be object descriptive homomorphisms and $h: Q(B) \rightarrow Q(A)$ be a meta-descriptive homomorphism represented in the diagram (4). If h and Φ_A are descriptive monomorphisms, then so is Φ_B .

Theorem 2.4: ([10]) Let $A_\Phi(*), B_\Phi(*), C_\Phi(*)$ be ordinary descriptive monoids, $A_\Phi(*_\Phi), B_\Phi(*_\Phi), C_\Phi(*_\Phi)$ be meta-descriptive monoids, and $C_\Phi \xrightarrow{h'} B_\Phi \xrightarrow{h} A_\Phi$ be exact, represented in the diagram (4). If Φ_A, Φ_B are object descriptive monomorphisms, then $Q(C) \xrightarrow{h'_\Phi} Q(B) \xrightarrow{h_\Phi} Q(A)$ is exact.

Theorem 2.5: ([10]) In the diagram (4), let $A_\Phi(*), B_\Phi(*), C_\Phi(*)$ be ordinary descriptive monoids, $A_\Phi(*_\Phi), B_\Phi(*_\Phi)$ and $C_\Phi(*_\Phi)$ be meta-descriptive monoids. Then

i) If Φ_A, Φ_C are object descriptive monomorphisms, h'_Φ is a meta-descriptive monomorphism, and $C_\Phi \xrightarrow{h'} B_\Phi \xrightarrow{h} A_\Phi$ is exact, then Φ_B is an object descriptive monomorphism.

ii) If Φ_B is an object descriptive epimorphism, Φ_A is an object descriptive monomorphism and h'_Φ is a meta-descriptive monomorphism, then Φ_C is an object descriptive epimorphism.

Corollary 2.6: ([10]) In the diagram (4), let $A_\Phi(*), B_\Phi(*), C_\Phi(*)$ be ordinary descriptive monoids, $A_\Phi(*_\Phi), B_\Phi(*_\Phi)$ and $C_\Phi(*_\Phi)$ be meta-descriptive monoids. Then

i) If Φ_A, Φ_C are object descriptive monomorphisms, h'_Φ is a meta-descriptive monomorphism, and $C_\Phi \xrightarrow{h'} B_\Phi \xrightarrow{h} A_\Phi$ is exact, then $Q(C) \xrightarrow{h'_\Phi} Q(B) \xrightarrow{h_\Phi} Q(A)$ is exact.

ii) If Φ_A, Φ_C are object descriptive monomorphisms, $e \rightarrow C_\Phi \xrightarrow{h'} B_\Phi \xrightarrow{h} A_\Phi \rightarrow e$ is short exact sequence, then $e_\Phi \rightarrow Q(C) \xrightarrow{h'_\Phi} Q(B) \xrightarrow{h_\Phi} Q(A) \rightarrow e_\Phi$ is a short exact sequence.

Exactness of Descriptive Group Homomorphisms

Theorem 3.1: Let $h: B_\Phi \rightarrow A_\Phi$ be an ordinary descriptive homomorphism, Φ_A, Φ_B be object descriptive homomorphisms, and $h_\Phi: Q(B) \rightarrow Q(A)$ be a meta-descriptive homomorphism in the diagram (1). If Φ_B is an object descriptive epimorphism and Φ_A is an object descriptive monomorphism, then $Imh = \Phi_A^{-1}(Imh_\Phi)$ and $Kerh_\Phi = \Phi_B(Kerh)$.

Proof: Since Φ_A is an object descriptive homomorphism, we get that $Imh = \Phi_A^{-1}(\Phi_A(Imh))$. Therefore, from Lemma 2.1,

$$Imh = \Phi_A^{-1}(Im(\Phi_A h)) = \Phi_A^{-1}(Im(h_\Phi \Phi_B)) = \Phi_A^{-1}(Imh_\Phi) \tag{5}$$

where Φ_B is an object descriptive epimorphism. Moreover, we obtain $Kerh_\Phi = h(h^{-1}(Kerh_\Phi))$. Thus $Kerh_\Phi = h(Ker(h_\Phi h))$, and so we have that $Kerh_\Phi = \Phi_B(Ker(\Phi_A h))$ by Lemma 2.1. Since Φ_A is an object descriptive monomorphism, we obtain $Kerh_\Phi = \Phi_B(Kerh)$.

Definition 3.2: Let $h: B_\Phi \rightarrow A_\Phi$ and $h': C_\Phi \rightarrow B_\Phi$ be ordinary descriptive homomorphisms.

$$e_\Phi \rightarrow C_\Phi \xrightarrow{h'} B_\Phi \xrightarrow{h} A_\Phi \rightarrow e_\Phi \tag{6}$$

The diagram (6) is said to be a short exact sequence if h' is a monomorphism and h is an epimorphism.

Theorem 3.3: In the diagram (4), let A_Φ, B_Φ , and C_Φ be ordinary descriptive groups and $Q(A), Q(B)$, and $Q(C)$ be meta-descriptive groups. Then

i) If Φ_A, Φ_C are object descriptive epimorphisms, h is an ordinary descriptive epimorphism, and $Q(C) \xrightarrow{h'_\Phi} Q(B) \xrightarrow{h_\Phi} Q(A)$ is exact, then Φ_B is an object descriptive epimorphism.

ii) If Φ_B is an object descriptive monomorphism, h is an ordinary descriptive epimorphism and h_Φ is a meta-descriptive monomorphism, then Φ_A is an object descriptive monomorphism.

Proof: i) Let $\Phi_B \in Q(B), b \in B_\Phi$. In this case $h_\Phi(\Phi_B(b)) \in Q(A)$, and since Φ_A is an object descriptive epimorphism, $h_\Phi(\Phi_B(b)) = \Phi_A(a)$ for some $a \in A_\Phi$. Since h is an ordinary descriptive epimorphism, we get $a = h(b')$ for some $b' \in B_\Phi$. From Lemma 2.1, $h_\Phi(\Phi_B(b')) = \Phi_A(h(b')) = \Phi_A(a) = h_\Phi(\Phi_B(b))$. Thus, $h_\Phi((\Phi_B(b'))^{-1} \Phi_B(b)) = e_{Q(A)}$ and then $(\Phi_B(b'))^{-1} \Phi_B(b) \in Kerh_\Phi = Imh'_\Phi$ by exactness. Hence, we obtain $(\Phi_B(b'))^{-1} \Phi_B(b) = h'_\Phi(\Phi_C(c)), c \in C_\Phi$ since Φ_C is an object descriptive epimorphism. Because of $h'(c) \in B_\Phi$ and $b' \in B_\Phi$, we have that $b'h'(c) \in B_\Phi$ and from Lemma 2.2, $\Phi_B(b'h'(c)) = \Phi_B(b')\Phi_B(h'(c)) = \Phi_B(b')h'_\Phi(\Phi_C(c)) = \Phi_B(b')(\Phi_B(b'))^{-1} \Phi_B(b) = \Phi_B(b)$. Therefore, Φ_B is an object descriptive epimorphism.

ii) Let $a \in Ker\Phi_A$. Since h is an ordinary descriptive epimorphism, there exists $b \in B$ such that $h(b) = a$. From Lemma 2.1, $h_\Phi(\Phi_B(b)) = \Phi_A(h(b)) = \Phi_A(a) = e_{Q(A)}$, and so $\Phi_B(b) = e_{Q(B)}$ by h_Φ is a meta-descriptive monomorphism. Therefore, we get $b = e_{Q(B)}$, since Φ_B is an object descriptive monomorphism. Consequently $a = h(b) = h(e_{B_\Phi}) = e_{A_\Phi}$. Thus $Ker\Phi_A = \{e_{A_\Phi}\}$.

$$\begin{array}{ccccccc} e_\Phi & \rightarrow & C_\Phi & \xrightarrow{h'} & B_\Phi & \xrightarrow{h} & A_\Phi \rightarrow e_\Phi \\ & & \Phi_C \downarrow \uparrow \Phi_C^{-1} & & \Phi_B \downarrow \uparrow \Phi_B^{-1} & & \Phi_A \downarrow \uparrow \Phi_A^{-1} \\ e_{Q(C)} & \rightarrow & Q(C) & \xrightarrow{h'_\Phi} & Q(B) & \xrightarrow{h_\Phi} & Q(A) \rightarrow e_{Q(A)} \end{array} \tag{7}$$

Corollary 3.4: Let A_Φ, B_Φ , and C_Φ be ordinary descriptive groups, $Q(A), Q(B)$, and $Q(C)$ be meta-descriptive groups, and in the diagram (7), each row be exact sequence.

i) If Φ_A and Φ_C are object descriptive monomorphisms, then Φ_B is an object descriptive monomorphism.

ii) If Φ_A and Φ_C are object descriptive epimorphisms, then Φ_B is an object descriptive epimorphism.

iii) If Φ_A and Φ_C are object descriptive isomorphisms, then Φ_B is an object descriptive isomorphism.

Two (short) exact sequences are called an isomorphic if there is a diagram of ordinary descriptive and meta-descriptive homomorphisms such that A_Φ, B_Φ , and C_Φ are object descriptive isomorphisms. In this case, it is easy to verify the diagram (7) with Φ_A^{-1}, Φ_B^{-1} and Φ_C^{-1} , is commutative.

In the diagram (7), exact sequence pairs are called ordinary-meta-descriptive homomorphism sequence or shortly called om-descriptive homomorphism sequence.

Proposition 3.5: Let A_Φ be ordinary descriptive group.

$$e_\Phi \rightarrow (Kerh)_\Phi \xrightarrow{i} A_\Phi \xrightarrow{\pi} (A/Kerh)_\Phi \rightarrow e_\Phi \tag{8}$$

Then, the diagram (8) is a short exact sequence.

Example 3.6: If $h: B_\Phi \rightarrow A_\Phi$ is an ordinary descriptive homomorphism, $\Phi_{Kerh}: (Kerh)_\Phi \rightarrow Q(Kerh)$ and $\Phi_B: (B)_\Phi \rightarrow Q(B)$ are object descriptive monomorphisms, then from Proposition 3.5 and Corollary 2.6. (ii), we have

$$e_{Q(Kerh)} \rightarrow Q(Kerh) \rightarrow Q(B) \rightarrow Q(B/Kerh) \rightarrow e_{Q(B/Kerh)}. \tag{9}$$

The diagram (8) is a short exact sequence. Therefore, we have that the diagram (10).

$$\begin{array}{ccccccc} e_\Phi & \rightarrow & (Kerh)_\Phi & \xrightarrow{i} & B_\Phi & \xrightarrow{\pi} & (B/Kerh)_\Phi \rightarrow e_\Phi \\ & & \downarrow \Phi_{Kerh} & & \downarrow \Phi_B & & \downarrow \Phi_{B/Kerh} \\ e_{Q(Kerh)} & \rightarrow & Q(Kerh) & \xrightarrow{i} & Q(B) & \xrightarrow{h_\Phi} & Q(B/Kerh) \rightarrow e_{Q(B/Kerh)} \end{array} \tag{10}$$

Conflicts of interest

There are no conflicts of interest in this work.

Acknowledgments

The author would like to thank the anonymous reviewers for their valuable suggestions.

References

- [1] Peters, J.F., İnan, E., Öztürk, M.A., Spatial and descriptive isometries in proximity spaces, *Gen. Math. Notes* 21(2) (2014) 1-10.
- [2] Peters, J.F., İnan, E., Öztürk, M.A., Monoids in proximal Banach spaces, *Int. J. Algebra* 8(18) (2014) 869-872.
- [3] Peters, J.F., Naimpally, S., Applications of near sets, *Notes of the Amer. Math. Soc.* 59(4) (2012) 536-542.
- [4] Peters, J.F., Near sets: An introduction, *Math. Comput. Sci.* 7(1) (2013) 3-9.
- [5] Efremovic, V.A., The geometry of proximity I (in Russian), *Mat. Sbornik N. S.* 31(73) (1952) 189-200.
- [6] Kasch, F., *Modules and Rings*, Academic Press Inc. Ltd., London, 1982.
- [7] Kovar, M.M., A new causal topology and why the universe is co-compact, arXiv:1112.0817 [math-ph] (2011) 1-15.
- [8] Peters, J.F., Local near sets: Pattern discovery in proximity spaces, *Math. Comput. Sci.* 7(1) (2013) 87-106.
- [9] Cech, E., *Topological Spaces*, John Wiley & Sons Ltd., London, 1966.
- [10] Peters, J.F., Öztürk, M.A., Uçkun, M., Exactness of Proximal Groupoid Homomorphisms, *Adıyaman University Journal of Science* 5(1) (2015) 1-13.

A Mathematical Model of Susceptible Diabetes Complication (SDC) Model in Discrete Time Fuzzy and Crisp Environment

Şeyma Şişman^{1,a}, Mehmet Merdan^{1,b,*}

³Department of Mathematical Engineering, Faculty Faculty of Engineering and Natural Sciences, Gümüşhane University, Gümüşhane, Türkiye.

*Corresponding author

Research Article

History

Received: 08/06/2022

Accepted: 01/09/2022

Copyright



©2022 Faculty of Science,
Sivas Cumhuriyet University

ABSTRACT

In this study, we examined the mathematical model of the discrete-time equation system with susceptible diabetes complication (SDC), which is known to be caused by environmental and genetic factors in a fuzzy environment. From the diabetes complication (DC) model, the susceptible diabetes complication (SDC) model is being developed. It was obtained using definitions of how the behavior of this model changes in a fuzzy environment. A nonlinear differential equation system transforms the sensitive diabetes complication (SDC) model into a discrete time equation system. Stability analysis of the model with jury criterion was examined. In addition, numerical solutions and graphics of the analysis of the discrete model in fuzzy environment are obtained by using the MATLAB package program.

Keywords: SDC model, Fuzzy difference equation, Generalized hukuhara.

 sseymasman@gmail.com

 <https://orcid.org/0000-0003-0756-4872>

 mmerdan@gumushane.edu.tr  <https://orcid.org/0000-0002-8509-3044>

Introduction

Mathematical modeling is used to, examine the epidemiology of a disease and to analyze important questions arising from real-world problems. It is also used in fields such as bio-science, chemistry, engineering and also in some real world problems. Analysis of these disease models can also be made with discrete-time equation systems. With the development of science, mathematical modeling is used to study not only the spread of infectious diseases, but also non-communicable diseases. Diabetes model is a biological problem and diabetes is a chronic disease. Diabetes is an indicator of irregular metabolism, where a combination of inherited and environmental factors leads to abnormally high blood sugar levels. There are two types of diabetes: type 1 diabetes, where without insulin, body cells cannot absorb and commit glucose, resulting in increased blood sugar levels, and in type 2 diabetes, where the body is unable to produce enough insulin. Recently, many researchers offered research on diabetes modeling [1]. Sergre. arc. [2] Creates a mathematical model about Blood Sugar and diabetes. In the human body various symptoms due to chronic diabetes, such as hyperglycemia, are based on the acute symptom of excessive diabetes as extreme urine production, compensative thirst and increased liquid intake, blurry seeing, weight loss and drowsiness. Rosado [3] limits hormone activity and affects blood glucose levels, they also present a mathematical model that detects diabetes in patients based on a 5-hour glucose intolerance test and the magnification results recommended by Ackerman [4]. Insulin-dependent diabetes Mellitus (IDDM) is discriminated by the inactivity of the pancreas. Based on the actual data of an IDDM patient recently, a few substantial systems in the bio-

system for mathematical modeling in diabetes mellitus have been obtained by Johansson and Stahl [5]. In 2004, Boutoyeb [6] et al. identified the diabetes complication model (DC) to find non-complicated diabetics (D) and complicated diabetics (C). One of the factors affecting lifestyle is sociable interplay. This interplay is an important factor influencing the lifestyle of a healthy sensitive individual to increase the potential in diabetes [6]. Hill et al. claims in [7] that it leads to interaction between patients with unhealthy lifestyles and healthy individuals, and a new group of individuals called (S), the number of susceptible individuals, is obtained to determine the number of likely interplays. The (DC) model is modified to the susceptible diabetes complication model (SDC), depending on the group of susceptible individuals[8].

$$\begin{aligned}\frac{dS}{dt} &= \vartheta S + \vartheta(1 - \rho)(D + C) - \frac{\beta SD}{N} - \mu S \\ \frac{dD}{dt} &= \frac{\beta SD}{N} + \vartheta\rho(D + C) - (\lambda + \mu)D + \gamma C \\ \frac{dC}{dt} &= \lambda D - (\gamma + \delta + \mu)C\end{aligned}$$

it is being transformed into a discrete-time system of equations. Where $S(0) > 0, D(0) > 0, C(0) > 0$, and $h = 0.01$. The parameters $\alpha, \beta, \gamma, \delta, \lambda, \mu, \rho > 0$ and $0 \leq \rho \leq 1$, respectively, are birth rate, interaction rate, recovery rate of complications, complication-related mortality rate, occurrence rate of complications, and rate of genetic disorder at birth [7-9].

In this study, we examined the mathematical model of the discrete-time equation system with sensitive diabetes complication (SDC). It has been applied to the SDC model

using the necessary definitions given in Chapter 2. In Chapter 3, the formulation of the model is shown with its analysis and symbols. In Chapter 4, the stability of the model and its numerical analyzes are obtained using the jury criterion. In Chapter 5, the analysis and stability of the model in fuzzy environment are examined.

Fuzzy Set and Fuzzy Difference Equations

The subject of Fuzzy difference equations has been developing rapidly recently. Applying Fuzzy difference equations is a natural way to model dynamical systems under probability uncertainty [10]. Fuzzy is a tool used for problems with uncertainty. Fuzzy derivative was first introduced by Lotfi A. Zadeh in 1965. The following studies were given by Prade and Dubois [11], Ralescu and Puri [12] and Voxman and Goetschel [13]. To solve the difference equation, there is an array that meets the equation, and this sequence is called a solution series of the equation. The Fuzzy difference equation is a difference equation in which the parameters and initial values are fuzzy numbers, and their solution is a sequence of fuzzy numbers. Fuzzy difference equations are developing rapidly.

Fuzzy difference equations were first introduced by Kandel and Byatt [14-15]. It was also rigorously studied by Kaleva for the initial value problem of these equations [16]. Zhang, Yang and Liao [17] investigated the positive solution and limitation of the fuzzy difference equation. These equations are suitable for financial problems and Chrysafis, Papadopoulos, Papaschinopoulos [18] have done studies on this subject. The Fuzzy difference equation is expressed as all derivative Hukuhara or generalized derivatives. Since the Hukahara difference is not always present, Bede et al. defined the generalized Hukuhara difference by generalizing the H-difference [19]. In recent years, there has been a great interest in research with fuzzy difference equations and stability of fuzzy difference equations. [20-32].

Definitions and Theorems

Definition 1 (Atanasov 1986). The intuitionistic fuzzy set defined on a non- empty set X as objects having the form $A = \{ \langle x, \alpha_A(x), \beta_A(x) \rangle : x \in X \}$, where the functions $\alpha_A(x) : X \rightarrow [0, 1]$ and $\beta_A(x) : X \rightarrow [0, 1]$, denote the degree of membership and the degree of non-membership of each element $x \in X$ to the set A respectively, and $0 \leq \alpha_A(x) + \beta_A(x) \leq 1$ for all $x \in X$. Clearly, when $\beta_A(x) = 1 - \alpha_A(x)$ for every $x \in X$, the set A becomes a fuzzy set [33].

Definition 2. Let the set $A \in F(\mathbb{R})$ be given. In this case

The set $A(0)$ is limited.

It is a A grade convex set.

The B grade set is normal. So, for $\exists x_0 \in \mathbb{R}, \mu_A(x_0) = 1$.

The $\mu_A(x)$ membership function is top-half continuous. So, the set $\{x \in \mathbb{R} : \mu_A(x) > \alpha\}$ is closed for $\forall \alpha \in [0, 1]$.

The set A that provides the conditions is called a graded number. Here the family of graded numbers on \mathbb{R} is denoted by $\mathcal{F}_N(\mathbb{R})$ [34].

Theorem 1 (Parametric form of the fuzzy number). Any fuzzy number can be stated by a couple functions such as $[q_i(\alpha), q_l(\alpha)], 0 \leq \alpha \leq 1$ that satisfy the circumstance given as follows [35]:

$q_i(\alpha)$, is a bounded, non-decreasing, left-continuous function when $\alpha \in (0, 1]$ and right-continuous function when $\alpha = 0$.

$q_l(\alpha)$ is a bounded, non-increasing, left-continuous function when $\alpha \in (0, 1]$ and right-continuous function when $\alpha = 0$.

$$q_i(\alpha) \leq q_l(\alpha) \text{ for any } \alpha \in (0, 1].$$

Definition 3. The membership function of the number of degrees $A \in \mathcal{F}_N(\mathbb{R})$ is $A_1 \leq A_2 \leq A_3$ so that the real numbers are,

$$\mu_A(x) = \begin{cases} 0 & , x < A_1 \\ \frac{x - A_1}{A_2 - A_1} & , A_1 \leq x \leq A_2 \\ \frac{A_3 - x}{A_3 - A_2} & , A_2 \leq x \leq A_3 \\ 0 & , A_3 < x \end{cases}$$

In this form, the number A is called the triangular grade number and is indicated by $A = (A_1, A_2, A_3)$ [19].

Definition 4 (α -cut of the fuzzy set). Let α -cut be given by $A = (A_1, A_2, A_3)$.

$$A_\alpha = [A_1 + \alpha(A_2 - A_1), A_3 - \alpha(A_3 - A_2)], \forall \alpha \in [0, 1].$$

Definition 5 (Hukuhara difference). Let $s, t \in \mathcal{F}_N(\mathbb{R})$. If $\exists v \in \mathcal{F}_N(\mathbb{R}^n)$ is present with $s = t + v$; Cluster v is called the Hukuhara difference (H-difference) of s and t clusters, denoted by $s \ominus_H t$. This is expressed as

$$s \ominus_H t = v \Leftrightarrow s = t + v$$

Theorem 2. Let s and $t \in \mathcal{F}_N(\mathbb{R})$. Single if $s \ominus_H t$ difference exists.

Theorem 3. Let s and $t \in \mathcal{F}_N(\mathbb{R})$ and let $s(\alpha) = [s_1(\alpha), s_2(\alpha)]$ and $t = [t_1(\alpha), t_2(\alpha)]$ be the α -cut of the graded numbers s and t respectively. α -cut of difference $s \ominus_H t$ is

$$(s \ominus_H t)(\alpha) = [s_1(\alpha) - t_1(\alpha), s_2(\alpha) - t_2(\alpha)]$$

Definition 6 (Hukuhara differentiable).

Let $f : (a, b) \rightarrow \mathcal{F}_N(\mathbb{R})$ and $x \in (a, b)$.

If $f(x + h) \ominus_H f(x), f(x) \ominus_H f(x - h)$ is present for $\forall h > 0$,

$$\lim_{h \rightarrow 0^+} \frac{f(x + h) \ominus_H f(x)}{h} = \lim_{h \rightarrow 0^+} \frac{f(x) \ominus_H f(x - h)}{h} = f'_H(x)$$

if $f'_H(x) \in \mathcal{F}_N(\mathbb{R})$ then f is called Hukuhara differentiable at x . This limit value is called the Hukuhara derivative of f in x .

Definition 7 (Generalized Hukuhara difference). Let s and $t \in \mathcal{F}_N(\mathbb{R})$. If,

$$s \ominus_{gH} t = v = \begin{cases} (i) & s = t + v \\ (ii) & t = s + (-1)v \end{cases}$$

the number of $\exists v \in \mathcal{F}_N(\mathbb{R}^n)$ grades is available, the number v is called the generalized Hukuhara difference (gH -difference) of s, t grades and is indicated by $s \ominus_{gH} t$.

Theorem 4. If $s, t \in \mathcal{F}_N(\mathbb{R})$ and α -cut sets

$s(\alpha) = [s_1(\alpha), s_2(\alpha)]$ and $t = [t_1(\alpha), t_2(\alpha)]$ $s \ominus_{gH} t$ are available, the α -cut set of the gH -difference is defined as [36]

$$[s \ominus_{gH} t](\alpha) = [\min\{s_1(\alpha) - t_1(\alpha), s_2(\alpha) - t_2(\alpha)\}, \max\{s_1(\alpha) - t_1(\alpha), s_2(\alpha) - t_2(\alpha)\}]$$

Definition 8 (Generalized Hukuhara differentiable). Let $f: (a, b) \rightarrow \mathcal{F}_N(\mathbb{R})$ and $x \in (a, b)$. If $f(x + h) \ominus_H f(x), f(x) \ominus_H f(x - h)$ is present for $\forall h > 0$,

$$\lim_{h \rightarrow 0^+} \frac{f(x + h) \ominus_{gH} f(x)}{h} = \lim_{h \rightarrow 0^+} \frac{f(x) \ominus_{gH} f(x - h)}{h} = f'_{gH}(x)$$

if $f'_{gH}(x) \in \mathcal{F}_N(\mathbb{R})$ then f is called Generalized Hukuhara differentiable at x . This limit value is called the Generalized Hukuhara differentiable of f in x [36].

Theorem 5. Let the α -cut section of the function $f: (a, b) \rightarrow \mathcal{F}_N(\mathbb{R})$ be $f(x, \alpha) = [f_1(x, \alpha), f_2(x, \alpha)]$ for each $\alpha \in [0, 1]$. In this case,

If f is differentiable in the sense of (i), the functions $f_1(x, \alpha)$ and $f_2(x, \alpha)$ are differentiable and $[f'(x)](\alpha) = [f'_1(x, \alpha), f'_2(x, \alpha)]$.

If f is differentiable in the sense of (ii), the functions $f_1(x, \alpha)$ and $f_2(x, \alpha)$ are differentiable and $[f'(x)](\alpha) = [f'_1(x, \alpha), f'_2(x, \alpha)]$.

Theorem 6 (Jury Theorem). For this criterion for $|\theta| < 1$ values

$$\theta^3 + a_3\theta^2 + a_2\theta + a_1 = 0$$

the roots of the cubic equation can be shown by the following conditions.

$$\begin{aligned} 1 + a_3 + a_2 + a_1 &> 0, \\ 3 + a_3 - a_2 - 3a_1 &> 0, \\ 1 - a_3 + a_2 - a_1 &> 0, \\ 1 + a_3a_1 - a_2 - a_1^2 &> 0, \end{aligned} \quad [37].$$

Mathematical Model of the Susceptible Diabetes Complication mModel (SDC)

The model is given below with the symbols to analyze and develop.

Notations

- S(n)**: Number of susceptible individuals
- D(n)**: Diabetes without complications (D)
- C(n)**: Complications of diabetes (C)
- γ : Recovery rate of complications
- ϑ : Birth rate
- δ : Complication-related mortality
- λ : Rate of occurrence of complications
- μ : Death rate
- ρ : Genetic disorder in childbirth
- β : Interaction rate

Formula of the model

The bio mathematical model examines the behavior of the system. This mathematical model for diabetes is used by Hill et al.[7]. It had been obtained before and is expressed in the following way by converting this model into the difference equation using the initial conditions previously accepted.

$$\begin{aligned} S(n + 1) &= S(n) + \vartheta S(n) + \vartheta(1 - \rho)(D(n) + C(n)) - \frac{\beta S(n)D(n)}{N} - \mu S(n) \\ D(n + 1) &= D(n) + \frac{\beta S(n)D(n)}{N} + \vartheta\rho(D(n) + C(n)) - (\lambda + \mu)D(n) + \gamma C(n) \\ C(n + 1) &= C(n) + \lambda D(n) - (\gamma + \delta + \mu)C(n) \end{aligned} \quad (1)$$

The equilibrium points are $S(n = 0) = S_0, D(n = 0) = D_0, C(n = 0) = C_0$.

Analysis of the Model

This section uses the information given about the SDC model to find stability and analysis.

Stability Analysis of the Model

The nonlinear difference system given above can be inscribed as follows [8]:

$$\begin{aligned} S(n + 1) &= S(n) + \vartheta S(n) + \vartheta(1 - \rho)(D(n) + C(n)) - \frac{\beta S(n)D(n)}{N} - \mu S(n) \\ D(n + 1) &= D(n) + \frac{\beta S(n)D(n)}{N} + \vartheta\rho(D(n) + C(n)) - (\lambda + \mu)D(n) + \gamma C(n) \\ C(n + 1) &= C(n) + \lambda D(n) - (\gamma + \delta + \mu)C(n) + 0S(n) \end{aligned}$$

Model (1) Linearized matrix in $E = (0,0,0)$ equilibrium points,

$$A = \begin{pmatrix} 1 + \vartheta - \mu & \vartheta(1 - \rho) & \vartheta(1 - \rho) \\ 0 & 1 + \vartheta\rho - \lambda - \mu & \vartheta\rho + \gamma \\ 0 & \lambda & 1 - \gamma - \delta - \mu \end{pmatrix}$$

Let us make the equation simpler here and say $X = \vartheta - \mu, Y = \vartheta(1 - \rho), Z = \vartheta\rho - \lambda - \mu, T = \vartheta\rho + \gamma, W = \gamma + \delta + \mu$.
Characteristic equation

$$|A - \theta I| = 0$$

and the cubic equation

$$\theta^3 + a_3\theta^2 + a_2\theta + a_1 = 0$$

is obtained where the first patient given in Table 1, the parameters $\vartheta, \beta, \gamma, \delta, \lambda, \mu, \rho > 0$ and $0 \leq \rho \leq 1$ written

$$\begin{aligned} a_3 &= X - Z + W - 3 < 0, \\ a_2 &= 3 + 2Z - 2W - 2X - XZ + XW - ZW - \lambda T > 0 \\ a_1 &= -1 + W - Z + ZW + \lambda T + X - XW + XZ - XZW - XT\lambda > 0 \end{aligned}$$

Therefore, according to theorem 6,

$$\begin{aligned} q_1 &= 1 + a_3 + a_2 + a_1 > 0, \\ q_2 &= 3 + a_3 - a_2 - 3a_1 > 0, \\ q_3 &= 1 - a_3 + a_2 - a_1 > 0, \\ q_4 &= 1 + a_3a_1 - a_2 - a_1^2 > 0 \text{ the system is stable.} \end{aligned}$$

Numerical Analysis on the Model

For the equation (1), the table (see Table 1) shown below shows the analysis of stability on three patients for different parameter values [24].

Table 1. Stability analysis of the SDC model

Parameters	First Patient	Second Patient	Third Patient
γ	0.37141	0	0
ϑ	0.01623	0.017	0.01642
δ	0.0068	0.0078	0.0588
λ	0.67758	0.77758	0.67765
μ	0.00764	1.91774	1.91864
ρ	0.077	0.077	0.077
β	0.16263	0.16263	0.16263
Value Of Variable	$a_1 = 2.9905 \times 10^{-5} > 0$	$a_1 = 10.0107 > 0$	$a_1 = 9.9082 > 0$
	$a_2 = 0.0535 > 0$	$a_2 = -1.8086 < 0$	$a_2 = -1.7880 < 0$
	$a_3 = 3.6788 > 0$	$a_3 = -0.0042 < 0$	$a_3 = -0.0016 < 0$
	$a_4 = 0.0285 > 0$	$a_4 = 0.0500 > 0$	$a_4 = 0.0285 > 0$
Stability Status	Stable	Unstable	Unstable

It was observed that the jury criterion was stable or unstable when evaluating parameter values taken for different patients.

Analysis of the Model in Fuzzy Environment

Let us assume that the initial conditions of the model $\tilde{S}_0, \tilde{D}_0, \tilde{C}_0$ are Fuzzy numbers. The model defined in the third section becomes

$$\begin{aligned} \tilde{S}(n+1) &= \tilde{S}(n) + \vartheta\tilde{S}(n) + \vartheta(1 - \rho) (\tilde{D}(n) + \tilde{C}(n)) - \frac{\beta\tilde{S}(n)\tilde{D}(n)}{N} - \mu\tilde{S}(n) \\ \tilde{D}(n+1) &= \tilde{D}(n) + \frac{\beta\tilde{S}(n)\tilde{D}(n)}{N} + \vartheta\rho (\tilde{D}(n) + \tilde{C}(n)) - (\lambda + \mu)\tilde{D}(n) + \gamma\tilde{C}(n) \\ \tilde{C}(n+1) &= \tilde{C}(n) + \lambda\tilde{D}(n) - (\gamma + \delta + \mu)\tilde{C}(n) \end{aligned} \tag{2}$$

with $\tilde{S}(n = 0) = \tilde{S}_0, \tilde{D}(n = 0) = \tilde{D}_0, \tilde{C}(n = 0) = \tilde{C}_0$.

Models are being converted to the fuzzy difference equation due to the presence of the fuzzy variable. Here we can use the fuzzy difference equation concept for the solution of the model and stability analysis.

Six different situations arise:

- i. $\tilde{S}(n), \tilde{D}(n)$ and $\tilde{C}(n)$, (i) – gH differentiable
- ii. $\tilde{S}(n)$, (i) – gH , $\tilde{D}(n)$, (i) – gH and $\tilde{C}(n)$, (ii) – gH differentiable
- iii. $\tilde{S}(n)$, (i) – gH , $\tilde{D}(n)$, (ii) – gH and $\tilde{C}(n)$, (i) – gH differentiable
- iv. $\tilde{S}(n)$, (ii) – gH , $\tilde{D}(n)$, (i) – gH and $\tilde{C}(n)$, (ii) – gH differentiable
- v. $\tilde{S}(n)$, (ii) – gH , $\tilde{D}(n)$, (ii) – gH and $\tilde{C}(n)$, (i) – gH differentiable
- vi. $\tilde{S}(n), \tilde{D}(n)$ and $\tilde{C}(n)$ (ii) – gH differentiable

It is not substantial to find all situations if we can understand the method for any of the situations, then we can find the result of other states.

In this study, we will consider the initial situation, i.e., $\tilde{S}(n), \tilde{D}(n)$ and $\tilde{C}(n)$, (i) – gH may be differentiable. The above difference equation $\tilde{S}(n), \tilde{D}(n)$ and $\tilde{C}(n)$, (i) – gH are differentiable

$$\begin{aligned}
 \tilde{S}_1(n+1, \alpha) &= \tilde{S}_2(n, \alpha) + \vartheta \tilde{S}_2(n, \alpha) + \vartheta(1-\rho) \left(\tilde{D}_1(n, \alpha) + \tilde{C}_1(n, \alpha) \right) - \frac{\beta \tilde{S}_2(n, \alpha) \tilde{D}_1(n, \alpha)}{N} - \mu \tilde{S}_2(n, \alpha) \\
 \tilde{S}_2(n+1, \alpha) &= \tilde{S}_1(n, \alpha) + \vartheta \tilde{S}_1(n, \alpha) + \vartheta(1-\rho) \left(\tilde{D}_2(n, \alpha) + \tilde{C}_2(n, \alpha) \right) - \frac{\beta \tilde{S}_1(n, \alpha) \tilde{D}_2(n, \alpha)}{N} - \mu \tilde{S}_1(n, \alpha) \\
 \tilde{D}_1(n+1, \alpha) &= \tilde{D}_2(n, \alpha) + \frac{\beta \tilde{S}_1(n, \alpha) \tilde{D}_2(n, \alpha)}{N} + \vartheta \rho \left(\tilde{D}_2(n, \alpha) + \tilde{C}_1(n, \alpha) \right) - (\lambda + \mu) \tilde{D}_2(n, \alpha) + \gamma \tilde{C}_1(n, \alpha) \\
 \tilde{D}_2(n+1, \alpha) &= \tilde{D}_1(n, \alpha) + \frac{\beta \tilde{S}_2(n, \alpha) \tilde{D}_1(n, \alpha)}{N} + \vartheta \rho \left(\tilde{D}_1(n, \alpha) + \tilde{C}_2(n, \alpha) \right) - (\lambda + \mu) \tilde{D}_1(n, \alpha) + \gamma \tilde{C}_2(n, \alpha) \\
 \tilde{C}_1(n+1, \alpha) &= \tilde{C}_2(n, \alpha) + \lambda \tilde{D}_1(n, \alpha) - (\gamma + \delta + \mu) \tilde{C}_2(n, \alpha) \\
 \tilde{C}_2(n+1, \alpha) &= \tilde{C}_1(n, \alpha) + \lambda \tilde{D}_2(n, \alpha) - (\gamma + \delta + \mu) \tilde{C}_1(n, \alpha)
 \end{aligned}
 \tag{3}$$

The above difference equations are crisp difference equations [24].

Stability analysis

The fuzzy SDC model indicated by (3), in matrix form, is as follows:

$$\begin{bmatrix} \tilde{S}_1(n+1, \alpha) \\ \tilde{S}_2(n+1, \alpha) \\ \tilde{D}_1(n+1, \alpha) \\ \tilde{D}_2(n+1, \alpha) \\ \tilde{C}_1(n+1, \alpha) \\ \tilde{C}_2(n+1, \alpha) \end{bmatrix} = \begin{bmatrix} 0 & 1 + \vartheta - \frac{\beta \tilde{D}_1(n, \alpha)}{N} - \mu & \vartheta(1-\rho) - \frac{\beta \tilde{S}_2(n, \alpha)}{N} & 0 & \vartheta(1-\rho) & 0 \\ 1 + \vartheta - \frac{\beta \tilde{D}_2(n, \alpha)}{N} - \mu & 0 & 0 & \vartheta(1-\rho) - \frac{\beta \tilde{S}_1(n, \alpha)}{N} & 0 & \vartheta(1-\rho) \\ \frac{\beta \tilde{D}_2(n, \alpha)}{N} & 0 & 0 & 1 + \frac{\beta \tilde{S}_1(n, \alpha)}{N} + \vartheta \rho - (\lambda + \mu) & \vartheta \rho + \gamma & 0 \\ 0 & \frac{\beta \tilde{D}_1(n, \alpha)}{N} & 1 + \frac{\beta \tilde{S}_2(n, \alpha)}{N} + \vartheta \rho - (\lambda + \mu) & 0 & 0 & \vartheta \rho + \gamma \\ 0 & 0 & \lambda & 0 & 0 & 1 - (\gamma + \delta + \mu) \\ 0 & 0 & 0 & \lambda & 1 - (\gamma + \delta + \mu) & 0 \end{bmatrix} \begin{bmatrix} \tilde{S}_1(n, \alpha) \\ \tilde{S}_2(n, \alpha) \\ \tilde{D}_1(n, \alpha) \\ \tilde{D}_2(n, \alpha) \\ \tilde{C}_1(n, \alpha) \\ \tilde{C}_2(n, \alpha) \end{bmatrix}$$

The stability of the solution is shown with the help of numerical simulations.

Numerical Solutions

Let us take into account the model, which includes the following fuzzy values. At $n = 0$, the number of susceptible individuals is $\tilde{S}_0 = (280,290,300)$, $\tilde{D}_0 = (7,9,11)$ for non-complicated diabetic, and $\tilde{C}_0 = (9,11,13)$. The values of other parameters are $\gamma = 0.37141, \vartheta = 0.01623, \delta = 0.0068, \lambda = 0.67758, \mu = 0.00764, \rho = 0.077, \beta = 0.16263$.

Numerical simulation: α -cut of initial conditions

$$\begin{aligned} \tilde{S}_1(0, \alpha) &= 280 + 10\alpha \\ \tilde{S}_2(0, \alpha) &= 300 - 10\alpha \\ \tilde{D}_1(0, \alpha) &= 7 + 2\alpha \\ \tilde{D}_2(0, \alpha) &= 11 - 2\alpha \\ \tilde{C}_1(0, \alpha) &= 9 + 2\alpha \\ \tilde{C}_2(0, \alpha) &= 13 - 2\alpha \end{aligned}$$

Now the solutions for a patient for the fuzzy initial conditions constant n are given as follows tables (see table 2, see table 3, see table 4) and figures (Figure 1, Figure 2, Figure 3):

Table 2. $S_1(n, \alpha), S_2(n, \alpha)$ n = 10 value

α	$S_1(n, \alpha)$	$S_2(n, \alpha)$
0	312.0297	294.1509
0.1	311.1297	295.0382
0.2	310.2303	295.9263
0.3	309.3315	296.8151
0.4	308.4333	297.7047
0.5	307.5357	298.5950
0.6	306.6387	299.4860
0.7	305.7423	300.3778
0.8	304.8466	301.2702
0.9	303.9515	302.1633
1	303.0571	303.0571

Table 3. $D_1(n, \alpha), D_2(n, \alpha)$ n = 10 value

α	$D_1(n, \alpha)$	$D_2(n, \alpha)$
0	14.3227	9.6775
0.1	14.0931	9.9128
0.2	13.8634	10.1477
0.3	13.6333	10.3823
0.4	13.4030	10.6165
0.5	13.1724	10.8504
0.6	12.9415	11.0840
0.7	12.7104	11.3173
0.8	12.4789	11.5502
0.9	12.2472	11.7828
1	12.0152	12.0152

Table 4. $C_1(n, \alpha), C_2(n, \alpha)$ n = 10 value

α	$C_1(n, \alpha)$	$C_2(n, \alpha)$
0	22.4534	15.1063
0.1	22.0892	15.4772
0.2	21.7248	15.8477
0.3	21.3601	16.2178
0.4	20.9950	16.5874
0.5	20.6296	16.9567
0.6	20.2639	17.3257
0.7	19.8978	17.6942
0.8	19.5314	18.0624
0.9	19.1647	18.4302
1	18.7976	18.7976

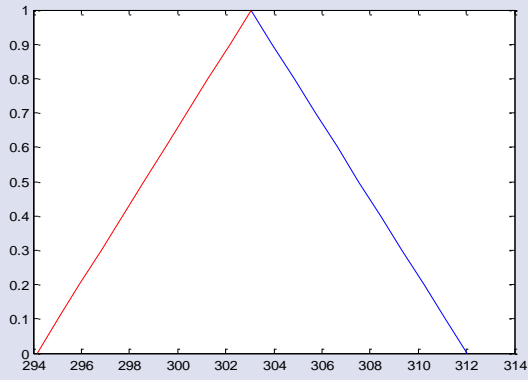


Figure 1. Graph of $S_1(n, \alpha), S_2(n, \alpha) n = 10$

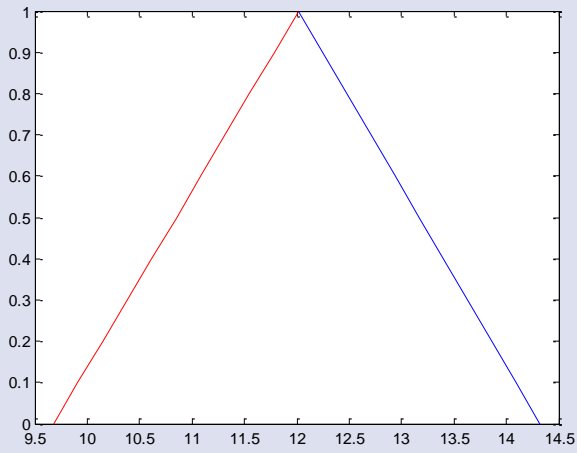


Figure 2. Graph of $D_1(n, \alpha), D_2(n, \alpha) n = 10$

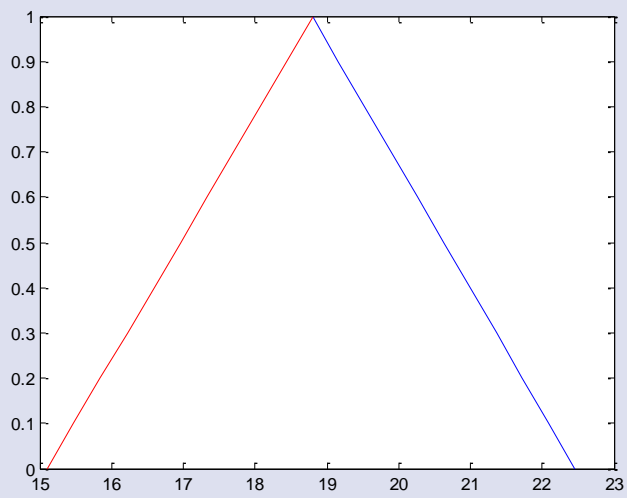


Figure 3. Graph of $C_1(n, \alpha), C_2(n, \alpha) n = 10$

Explanation: From the Table 2, Figure 1 we see that $S_1(n, \alpha)$ are decreasing and $S_2(n, \alpha)$ are increasing, Table 3, Figure 2 we see that $D_1(n, \alpha)$ are decreasing and $D_2(n, \alpha)$ are increasing and Table 4, Figure 3, we see that $C_1(n, \alpha)$ are decreasing, $C_2(n, \alpha)$ are increasing. For $\alpha \in [0,1]$ for $n = 10$. $\tilde{S}(n), \tilde{D}(n)$ and $\tilde{C}(n)$ provide a strong solution. Therefore, the system is stable in these situations.

Conclusions

In this study, we examined the mathematical model of the sensitive diabetes complication (SDC) system to determine the number of likely interactions that cause the interaction between unhealthy individuals and healthy individuals in the fuzzy and crisp environment Approaches to the generalized Hukuhara derivative notion have been applied to explain fuzzy solutions of the given model In addition, demonstration of the sensitive diabetes complication system in the fuzzy environment was used to better analyze the decision-making situation by ensuring that uncertain parameters were met. The gH -derivative approach method, which has a substantial place in fuzzy analysis, makes it likely to obtain the fuzzy solution of the model. Stability analysis was obtained for the model in Fuzzy environment.

Acknowledgments

The authors are grateful to the esteemed reviewers for their comments and suggestions based on which the manuscript has been significantly improved.

Conflicts of interest

There are no conflicts of interest in this work.

References

- [1] Nguyen, H.T., Walker, E.A., A First Course in Fuzzy Logic, CRC Press, New York, London, Tokyo, (1997).
- [2] Segre, G., Turco, G.L., and Vercellone, G.V., Modelling Blood Glucose and Insuline Kinetics Normal, *Diabetic and obsese Subjects*, 22(2) (1973) 94-103.
- [3] Rosado, Y.C., Mathematical model for Detecting Diabetes, Proceedings of The National Conference On Undergraduate Research (NCUR), *University of Wisconsin LaCrosse La-Crosse, Wisconsin*, (2009) 16 – 18.
- [4] Ackerman, E., Gatewood, I., Rosevear, J., and Molnar, G., Blood glucose regulation and diabetes, Concepts and Models of Biomathematics, F. Heinmets, Ed., *Marcel Decker*, (1969) 131-156.
- [5] Stahl, F., and Johansson, R., Diabetes mellitus modeling and short-term prediction based on blood glucose measurements, *Mathematical Biosciences* 217 (2009) 101–117.
- [6] Boutayeb, A., Twizell, E. H., Achouayb, K., Chetouani, A., A mathematical model for the burden of diabetes and its complications, *BioMedical Engineering Online* 3 (2004) 20.
- [7] Hill, J., Nielsen, M., Fox, M. H., Understanding the Social Factors That Contribute to Diabetes: A Means to Informing Health Care and Social Policies for the Chronically Ill, *The Permanente Journal*, 17(2) (2013) 67–72.
- [8] Şişman, Ş., Merdan, M., Global stability of Susceptible Diabetes Complication (SDC) model in discrete time, *Sigma J Eng Nat Sci*, 39 (3) (2021) 290–312.
- [9] Widyaningsih, P., Affan, R.C., Saputro, D.R.S. A Mathematical Model for The Epidemiology of Diabetes Mellitus with Lifestyle and Genetic Factors, *IOP Conf. Series: Journal of Physics: Conf. Series*, (2018) 1028-012110.
- [10] Zadeh, L., Toward a generalized theory of uncertainty (GTU) – an outline, *Information Sciences* 172 (2005) 1–40.
- [11] Dubois, D., Prade, H., Towards fuzzy differential calculus: Part 3, Differentiation, *Fuzzy Sets and Systems* 8 (1982) 225–233.
- [12] Puri, M.L., Ralescu, D.A., Differentials of fuzzy functions, *Journal of Mathematical Analysis and Application* 91 (1983) 552–558.
- [13] Goetschel, R., Voxman, W., Elementary fuzzy calculus, *Fuzzy Sets and Systems*, 31 (1986) 18–43.
- [14] Kandel, A., Byatt, W. J., Fuzzy differential equations, Proc. Int. Conf. Cybernetics and Society, Tokyo, November, (1978) 1213-1216.
- [15] Kandel, A., Byatt, W. J., Fuzzy sets, fuzzy algebra, and fuzzy statistics Proc. IEEE, 66 (1978) 1619-1639.
- [16] Kaleva, O., Fuzzy differential equations, *Fuzzy Sets and Systems*, 24 (1987) 301-317.
- [17] Zhang, Q., Yang, L., Liao, D., On the fuzzy difference equation $x_{n+1} = A + \sum_{i=0}^k \frac{B}{x_{n-i}}$, *Engineering and Technology*, 75 (2011).
- [18] Chrysafis, K.A., Papadopoulos, B.K., and Papischinopoulos, G., On the fuzzy difference equations of finance, *Fuzzy Sets and Systems*, 159 (2008) 3259-3270.
- [19] Bede, B., Mathematics of Fuzzy Sets and Fuzzy Logic, Springer, (2013)
- [20] Papischinopoulos, G., Stefanidou, G., Boundedness and asymptotic behavior of the solutions of a fuzzy difference equation, *Fuzzy Sets and Systems* 140 (2003) 523–539.
- [21] Zhang, Q., Zhang, W., Liu, J., Shao, Y., (2014). On a Fuzzy Logistic Difference Equation, *wseas transactions on mathematics*, E-ISSN: 2224-2880, 282-290.
- [22] Din, Q. Asymptotic Behavior of a Second-Order Fuzzy Rational Difference Equation, *Hindawi Publishing Corporation Journal of Discrete Mathematics* (2015) 7.
- [23] Mahata, A., Mondal, S.P., Alam, S., and Roy, B., Mathematical model of glucose-insulin regulatory system on diabetes mellitus in fuzzy and crisp environment, *Ecological Genetics and Genomics*, (2016).
- [24] Mahata, A., Roy, B., Mondal, S. P., Alam, S., Application of ordinary differential equation in glucose insulin regulatory system modeling in fuzzy environment, *Ecological Genetics and Genomics* 3(2017) 60-66.
- [25] Salahshour, S., Aliahmadian, Mahata, A., Mondal, S. P., Alam, S., The Behavior of Logistic Equation with Alley Effect in Fuzzy Environment : Fuzzy Differential Equation Approach, *International Journal of Applied and Computational Mathematics* 4 (2) (2018) 1-20.

- [26] Mahata, A., Mondal, S. P., Alam, S., Chakraborty, A., Dey, S.K., Goswami, A., Mathematical model for diabetes in fuzzy environment, *Journal of Intelligent and Fuzzy Systems*, 36 (3) (2018) 2923-2932.
- [27] Mahata, A., Mondal, S. P., Ahmadian, A., Ismail, F., Alam, S., and Salahshour, S., Different Solution Strategies for Solving Epidemic Model in Imprecise Environment, , *Complexity*, (2018) 4902142.
- [28] Khastan, A., Alijani, Z., On the new solutions to the fuzzy difference equation $x_n + 1 = A + \frac{B}{x_n}$, *Fuzzy Sets and Systems* 358, (2019), 64-83.
- [29] Zhang, Q., Zhang, W., Lin, F., Li, D. On dynamic behavior of second-order exponential-type fuzzy difference equation, *Fuzzy Sets and Systems*,(2021), 169-187.
- [30] Jia,L., Wang,C., Zhao, X., Wei,W. Dynamic Behavior of a Fractional-Type Fuzzy Difference System, *Symmetry* ,(2022), 14, 1337.
- [31] Han, C., Li, L., Su, G. And Sun, T. Dynamical behaviors of a k-order fuzzy difference equation, *Open Mathematics* (2022), 20: 391–403.
- [32] Darus, M., Wahab, A.F., Review on Fuzzy Difference Equation, *Malaysian Journal of Fundamental & Applied Sciences*, 8 (4) (2012) 176-180.
- [33] Atanasov,K.,T., Intuitionistic Fuzzy Set. *Fuzzy Set and Systems*, 20(1) (1986) 87-96.
- [34] Diamond, P., Kloeden, P., Metric topology of fuzzy numbers and fuzzy analysis, In *Fundamentals of Fuzzy Sets*, Springer, (2000) 583-641.
- [35] Goetschel Jr, R., Voxman, W., Elementary fuzzy calculus, *Fuzzy sets and systems*, 18(1) (1986) 31-43.
- [36] Stefanini, L., A generalization of Hukuhara difference for interval and fuzzy arithmetic, *Working Papers Series in Economics, Mathematics and Statistics*, 48 (2008) 1-13.
- [37] Samuelson, P.A., Conditions that a root of a polynomial be less than unity in absolute value, *Ann. Math. Stat.*,12 (1941) 360-364.

Dual-Gaussian Pell and Pell-Lucas Numbers

Hasan Gökbaşı^{1,a,*}

³Department of Mathematics, Faculty of Science and Literature, Bitlis Eren University, Bitlis, Türkiye.

*Corresponding author

Research Article

History

Received: 03/02/2022

Accepted: 02/10/2022

Copyright



©2022 Faculty of Science,
Sivas Cumhuriyet University

ABSTRACT

In this study, we define a new type of Pell and Pell-Lucas numbers which are called dual-Gaussian Pell and dual-Gaussian Pell-Lucas numbers. We also give the relationship between negadual-Gaussian Pell and Pell-Lucas numbers and dual-complex Pell and Pell-Lucas numbers. Also, some sum and product properties of Pell and Pell-Lucas numbers are given. Moreover, we obtain the Binet's formula, generating function, d'Ocagne's identity, Catalan's identity, Cassini's identity and some sum formulas for these new type numbers. Some algebraic properties of dual-Gaussian Pell and Pell-Lucas numbers are investigated. Furthermore, we give the matrix representation of dual-Gaussian Pell and Pell-Lucas numbers.

Keywords: Dual-Gaussian numbers, Dual-Gaussian Pell numbers, Dual-Gaussian Pell-Lucas numbers.

^ahgokbas@beu.edu.tr

^{id}<https://orcid.org/0000-0002-3323-8205>

Introduction

Complex numbers, Hyperbolic numbers and Dual numbers arise in many areas such as coordinate transformation, matrix modeling, displacement analysis, rigid body dynamics, velocity analysis, static analysis, dynamic analysis, transformation, mechanics, kinematics, physics, mathematics, and geometry. Horadam [1] introduced the concept, the complex Fibonacci numbers, called the Gaussian Fibonacci numbers $GF_n = F_n + iF_{n-1}$ where $F_n \in \mathbb{R}, i^2 = -1$ and F_n, nth Fibonacci numbers. Fjelstad and Gal [2] defined the hyperbolic numbers $H = h + jh^*$ where $h, h^* \in \mathbb{R}, j^2 = 1$ and $j \neq \pm 1$. Clifford [3] described the dual numbers $D = d + \varepsilon d^*$ where $d, d^* \in \mathbb{R}, \varepsilon^2 = 0$ and $\varepsilon \neq 0$. Messelmi [4] expressed the dual-complex numbers $Z = z + \varepsilon z^*$ where $z, z^* \in \mathbb{C}, \varepsilon^2 = 0$ and $\varepsilon \neq 0$. There are several studies in the literature that are concerned with these numbers [5-8].

Fjelstad and Gal [2] inspected the extensions of the hyperbolic complex numbers to n -dimensions and they gave n -dimensional dual complex numbers in algebra and analysis. Matsuda [9] et al. inspected the two-dimensional rigid transformation which is more concise and efficient than the standard matrix presentation, by modifying the ordinary dual number construction for the complex numbers. Akar et al. [10] introduced arithmetical operations on dual-hyperbolic numbers. They investigated dual hyperbolic number and hyperbolic complex number valued functions. Majernik [11] gave three types of the four-component number systems which are formed by using the complex, binary and dual two-component numbers. Aydın [12] formulated, if $z_1 = x_1 + ix_2$ and $z_2 = y_1 + iy_2$ any dual-complex number by $w = x_1 + ix_2 + \varepsilon y_1 + i\varepsilon y_2$.

Moreover, addition, subtraction, multiplication and division of dual-complex numbers and was defined by

$$w_1 \pm w_2 = (z_1 + \varepsilon z_2) \pm (z_3 + \varepsilon z_4) = (z_1 \pm z_3) + \varepsilon(z_2 \pm z_4)$$

$$w_1 \times w_2 = (z_1 + \varepsilon z_2) \times (z_3 + \varepsilon z_4) = (z_1 z_3) + \varepsilon(z_1 z_4 + z_2 z_3)$$

and

$$\frac{w_1}{w_2} = \frac{z_1 + \varepsilon z_2}{z_3 + \varepsilon z_4} = \frac{(z_1 + \varepsilon z_2)(z_3 - \varepsilon z_4)}{(z_3 + \varepsilon z_4)(z_3 - \varepsilon z_4)} = \frac{z_1}{z_3} + \varepsilon \frac{z_2 z_3 - z_1 z_4}{z_3^2}$$

Table 1. Multiplication scheme of dual-complex numbers

\times	1	i	ε	$i\varepsilon$
1	1	i	ε	$i\varepsilon$
i	i	-1	$i\varepsilon$	$-\varepsilon$
ε	ε	$i\varepsilon$	0	0
$i\varepsilon$	$i\varepsilon$	$-\varepsilon$	0	0

The conjugations can operate on dual-complex numbers as follows:

$$w = x_1 + ix_2 + \varepsilon y_1 + i\varepsilon y_2$$

$$w^{*1} = (x_1 - ix_2) + (\varepsilon y_1 - i\varepsilon y_2), \text{complex conjugation}$$

$$w^{*2} = (x_1 + ix_2) - (\varepsilon y_1 + i\varepsilon y_2), \text{dual conjugation}$$

$$w^{*3} = (x_1 - ix_2) - (\varepsilon y_1 - i\varepsilon y_2), \text{coupled conjugation}$$

$$w^{*4} = (x_1 - ix_2) \left(1 - \varepsilon \frac{y_1 + iy_2}{x_1 + ix_2}\right), \text{dual - complex conjugation}$$

$$w^{*5} = (y_1 + iy_2) - (\varepsilon x_1 + i\varepsilon x_2), \text{anti - dual conjugation}$$

Therefore, the norm of dual-complex numbers is defined as

$$N_w^{*1} = \|w \times w^{*1}\| = \sqrt{|z_1|^2 + 2\varepsilon \operatorname{Re}(z_1 z_2^*)}$$

$$N_w^{*2} = \|w \times w^{*2}\| = \sqrt{|z_1|^2}$$

$$N_w^{*3} = \|w \times w^{*3}\| = \sqrt{|z_1|^2 - 2i\varepsilon \operatorname{Im}(z_1 z_2^*)}$$

$$N_w^{*4} = \|w \times w^{*4}\| = \sqrt{|z_1|^2}$$

$$N_w^{*5} = \|w \times w^{*5}\| = \sqrt{z_1 z_2 + \varepsilon(z_2^2 - z_1^2)}$$

Beneficial point is the number sequences that have been studied over many years. For $n \in \mathbb{N}_0$, Pell and Pell-Lucas numbers are defined by the recurrence relations, respectively. $P_{n+2} = 2P_{n+1} + P_n$, $P_0 = 0$, $P_1 = 1$ and $Q_{n+2} = 2Q_{n+1} + Q_n$, $Q_0 = 2$, $Q_1 = 2$. Besides the n th Pell and Pell-Lucas number are formulized as $P_n = \frac{\alpha^n - \beta^n}{\alpha - \beta}$ and $Q_n = \alpha^n + \beta^n$, where $\alpha = 1 + \sqrt{2}$, $\beta = 1 - \sqrt{2}$. These formulas are called as Binet's formula [13, 14].

Many researchers studied several areas of this number sequence. Halıcı and Çürük [15] examined the dual numbers and investigated the characteristic properties of them. They also gave equations about conjugates and some important features of these newly defined numbers. Azak and Güngör [16] defined the dual complex Fibonacci and Lucas numbers and gave the well-known properties for these numbers. Aydın [17] defined dual-complex k-Pell numbers, dual-complex k-Pell quaternions and also gave some algebraic properties of them.

In the following sections, the dual-Gaussian Pell and the dual-Gaussian Pell-Lucas numbers will be defined. In this work, a variety of algebraic properties of dual-Gaussian Pell and dual-Gaussian Pell-Lucas numbers are presented in a unified manner. Some identities will be given for dual-Gaussian Pell and dual-Gaussian Pell-Lucas numbers such as Binet's formula, generating function, d'Ocagne's identity, Catalan's identity, Cassini's identity, and some sum formulas. The dual-Gaussian Pell and the dual-Gaussian Pell-Lucas numbers' properties will also be obtained using matrix representation.

Dual-Gaussian Pell and Pell-Lucas numbers

Definition 2.1: For $n \in \mathbb{N}_0$, the dual-Gaussian Pell and the dual-Gaussian Pell-Lucas numbers are defined by

$$DGP_{n+3} = P_{n+3} + iP_{n+2} + \varepsilon P_{n+1} + i\varepsilon P_n$$

$$DGQ_{n+3} = Q_{n+3} + iQ_{n+2} + \varepsilon Q_{n+1} + i\varepsilon Q_n$$

where P_n and Q_n , are the n th Pell and Pell-Lucas numbers. ε , denotes the pure dual unit ($\varepsilon^2 = 0$, $\varepsilon \neq 0$), i denotes the imaginary unit ($i^2 = -1$) and $i\varepsilon$ denotes the imaginary dual unit.

$$DGP_0 = i - 2\varepsilon + 5i\varepsilon, DGP_1 = 1 + \varepsilon - 2i\varepsilon \text{ and}$$

$$DGP_2 = 2 + i + i\varepsilon, \dots$$

$$DGQ_0 = 2 - 2i + 6\varepsilon - 14i\varepsilon, DGQ_1 = 2 + 2i - 2\varepsilon + 6i\varepsilon \text{ and } DGQ_2 = 6 + 2i + 2\varepsilon - 2i\varepsilon, \dots$$

Let DGQ_{n+3} and DGQ_{m+3} be two dual-Gaussian Pell-Lucas numbers. The addition, subtraction and multiplication of the dual-Gaussian Pell-Lucas numbers are given by

$$DGQ_{n+3} \pm DGQ_{m+3} = (Q_{n+3} \pm Q_{m+3}) + i(Q_{n+2} \pm Q_{m+2}) + \varepsilon(Q_{n+1} \pm Q_{m+1}) + i\varepsilon(Q_n \pm Q_m)$$

$$DGQ_{n+3} \times DGQ_{m+3} = (Q_{n+3}Q_{m+3} - Q_{n+2}Q_{m+2}) + i(Q_{n+3}Q_{m+2} + Q_{n+2}Q_{m+3}) + \varepsilon(Q_{n+3}Q_{m+1} - Q_{n+2}Q_m + Q_{n+1}Q_{m+3} - Q_nQ_{m+2}) + i\varepsilon(Q_{n+3}Q_m + Q_{n+2}Q_{m+1} + Q_{n+1}Q_{m+2} + Q_nQ_{m+3}).$$

There exist five different conjugations. Dual-Gaussian Pell-Lucas numbers can operate as follows:

$$DGQ_{n+3} = Q_{n+3} + iQ_{n+2} + \varepsilon Q_{n+1} + i\varepsilon Q_n$$

$$DGQ_{n+3}^{*1} = (Q_{n+3} - iQ_{n+2}) + (\varepsilon Q_{n+1} - i\varepsilon Q_n), \text{ complex conjugation}$$

$$DGQ_{n+3}^{*2} = (Q_{n+3} + iQ_{n+2}) - (\varepsilon Q_{n+1} + i\varepsilon Q_n), \text{ dual conjugation}$$

$$DGQ_{n+3}^{*3} = (Q_{n+3} - iQ_{n+2}) - (\varepsilon Q_{n+1} - i\varepsilon Q_n), \text{ coupled conjugation}$$

$$DGQ_{n+3}^{*4} = (Q_{n+3} - iQ_{n+2}) \left(1 - \varepsilon \frac{Q_{n+1} + iQ_n}{Q_{n+3} + iQ_{n+2}} \right), \text{ dual - complex conjugation}$$

$$DGQ_{n+3}^{*5} = (Q_{n+1} + iQ_n) - (\varepsilon Q_{n+3} + i\varepsilon Q_{n+2}), \text{ anti - dual conjugation}$$

Similarly, the properties for dual-Gaussian Pell numbers are obtained.

Lemma 2.2: Let P_n and Q_n be the Pell and the Pell-Lucas numbers, respectively. The following relations are satisfied

$$\begin{aligned}
 Q_{n+1}^2 + Q_n^2 &= 8P_{2n+1} \\
 Q_{n+1}^2 - Q_n^2 &= 8P_{2n+1} - 4(-1)^n \\
 Q_{2n+2} + Q_{2n} &= 8P_{2n+1} \\
 Q_{2n+2} - Q_{2n} &= 2Q_{2n+1} \\
 Q_{n+r}Q_n &= Q_{2n+r} + Q_r(-1)^n \\
 Q_mQ_{n+r} + Q_{m+r}Q_n &= 2Q_{m+n+r} + (-1)^nQ_{m-n}Q_r \\
 Q_mQ_{n+r} - Q_{m+r}Q_n &= (-8)(-1)^n P_{m-n}P_r
 \end{aligned}$$

Proof: The proofs are carried out with the help of the Binet’s formula.

Proposition 2.3: DGQ_n be a dual-Gaussian Pell-Lucas number. The following properties hold.

$$\begin{aligned}
 DGQ_{n+3} + DGQ_{n+3}^{*1} &= 2Q_{n+3} + 2\varepsilon Q_{n+1} \\
 DGQ_{n+3} \times DGQ_{n+3}^{*1} &= 8P_{2n+5} + 16\varepsilon P_{2n+3} \\
 DGQ_{n+3} + DGQ_{n+3}^{*2} &= 2Q_{n+3} + 2iQ_{n+2} \\
 DGQ_{n+3} \times DGQ_{n+3}^{*2} &= [8P_{2n+5} - 4(-1)^n] + 2i[Q_{2n+5} + 2(-1)^n] \\
 DGQ_{n+3} + DGQ_{n+3}^{*3} &= 2Q_{n+3} + 2i\varepsilon Q_n \\
 DGQ_{n+3} \times DGQ_{n+3}^{*3} &= 8P_{2n+5} + 32i\varepsilon(-1)^n
 \end{aligned}$$

Similarly, the proposition for dual-Gaussian Pell numbers is obtained.

Definition 2.4: For $n \in \mathbb{N}_0$, DCP_n and DCQ_n the dual-complex Pell and the dual-complex Pell-Lucas numbers, the negadual-Gaussian Pell and the negadual-Gaussian Pell-Lucas numbers are defined by

$$\begin{aligned}
 DGP_{-n} &= (-1)^{n+1}DGP_n^{*1} \\
 DGQ_{-n} &= (-1)^nDGQ_n^{*1}
 \end{aligned}$$

where P_n and Q_n , are the n th Pell and Pell-Lucas numbers. Also, DCP_n and DCQ_n , are the dual-complex Pell and dual-complex Pell-Lucas numbers. ε , denotes the pure dual unit ($\varepsilon^2 = 0, \varepsilon \neq 0$), i denotes the imaginary unit ($i^2 = -1$) and $i\varepsilon$ denotes the imaginary dual unit.

$$DGQ_{-n} = Q_{-n} + iQ_{-n-1} + \varepsilon Q_{-n-2} + i\varepsilon Q_{-n-3}$$

When the equality is established,

$$\begin{aligned}
 DGQ_{-n} &= (-1)^nQ_n + i(-1)^{n+1}Q_{n+1} + \varepsilon(-1)^{n+2}Q_{n+2} + i\varepsilon(-1)^{n+3}Q_{n+3} \\
 DGQ_{-n} &= (-1)^n[Q_n - iQ_{n+1} + \varepsilon Q_{n+2} - i\varepsilon Q_{n+3}] \\
 DGQ_{-n} &= (-1)^nDCQ_n^{*1}
 \end{aligned}$$

Similarly, DGP_{-n} is found.

Theorem 2.5: Let DGP_n and DGQ_n be the dual-Gaussian Pell and the dual-Gaussian Pell-Lucas numbers, respectively. The following relations are satisfied

$$\begin{aligned}
 2(DGP_{n+1} + DGP_n) &= DGQ_{n+1} \\
 2(DGP_{n+1} - DGP_n) &= DGQ_n \\
 DGP_{n+1} + DGP_{n-1} &= DGQ_n \\
 DGP_{n+1} - DGP_{n-1} &= 2DGP_n \\
 DGP_{n+2} + DGP_{n-2} &= 6DGP_n \\
 DGP_{n+2} - DGP_{n-2} &= 2DGQ_n
 \end{aligned}$$

$$DGQ_{n+1} + DGQ_n = 4DGP_{n+1}$$

$$DGQ_{n+1} - DGQ_n = 4DGP_n$$

$$DGQ_{n+1} + DGQ_{n-1} = 8DGP_n$$

$$DGQ_{n+1} - DGQ_{n-1} = 2DGQ_n$$

$$DGQ_{n+2} + DGQ_{n-2} = 6DGQ_n$$

$$DGQ_{n+2} - DGQ_{n-2} = 16DGP_n$$

Proof:

$$\begin{aligned} 2(DGP_{n+1} + DGP_n) &= 2(P_{n+1} + iP_n + \varepsilon P_{n-1} + i\varepsilon P_{n-2} + P_n + iP_{n-1} + \varepsilon P_{n-2} + i\varepsilon P_{n-3}) \\ &= 2(P_{n+1} + P_n) + 2i(P_n + P_{n-1}) + 2\varepsilon(P_{n-1} + P_{n-2}) + 2i\varepsilon(P_{n-2} + P_{n-3}) \\ &= Q_{n+1} + iQ_n + \varepsilon Q_{n-1} + i\varepsilon Q_{n-2} = DGQ_{n+1} \end{aligned}$$

The other steps of the theorem can be proved by a similar method.

Theorem 2.6: (Generating Function Formula) Let DGP_n and DGQ_n be the dual-Gaussian Pell and Pell-Lucas numbers. Generating function formula for this numbers is as follows

$$\begin{aligned} m(t) &= \frac{(i - 2\varepsilon + 5i\varepsilon) + t(1 - 2i + 5\varepsilon - 12i\varepsilon)}{1 - 2t - t^2} \\ h(t) &= \frac{(2 - 2i + 6\varepsilon - 14i\varepsilon) + t(-2 + 6i - 14\varepsilon + 34i\varepsilon)}{1 - 2t - t^2}. \end{aligned}$$

Proof: Let $h(t)$ be the generating function for dual-Gaussian Pell-Lucas numbers as

$$h(t) = \sum_{n=0}^{\infty} DGQ_n t^n. \text{ Using } h(t), 2th(t) \text{ and } t^2h(t), \text{ we get the following equations,}$$

$$th(t) = \sum_{n=0}^{\infty} DGQ_n t^{n+1}, t^2h(t) = \sum_{n=0}^{\infty} DGQ_n t^{n+2}. \text{ After the needed calculations, the generating function for dual-}$$

Gaussian Pell-Lucas numbers is obtained as

$$\begin{aligned} h(t) &= \frac{DGQ_0 + DGQ_1 t - 2DGQ_0 t}{1 - 2t - t^2} \\ h(t) &= \frac{(2 - 2i + 6\varepsilon - 14i\varepsilon) + t(-2 + 6i - 14\varepsilon + 34i\varepsilon)}{1 - 2t - t^2}. \end{aligned}$$

Similarly, generating function formula for dual-Gaussian Pell numbers is obtained.

Theorem 2.7: (Binet's Formula) Let DGP_n and DGQ_n be the dual-Gaussian Pell and Pell-Lucas numbers. Binet's formula for this number is as follows

$$DGP_n = \frac{\hat{\alpha}\alpha^{n-3} - \hat{\beta}\beta^{n-3}}{\alpha - \beta}$$

$$DGQ_n = \hat{\alpha}\alpha^{n-3} + \hat{\beta}\beta^{n-3}$$

$$\text{where } \hat{\alpha} = \alpha^3 + i\alpha^2 + \varepsilon\alpha^1 + i\varepsilon, \alpha = 1 + \sqrt{2} \text{ and } \hat{\beta} = \beta^3 + i\beta^2 + \varepsilon\beta^1 + i\varepsilon, \beta = 1 - \sqrt{2}.$$

Proof:

$$\begin{aligned} DGQ_n &= Q_n + iQ_{n-1} + \varepsilon Q_{n-2} + i\varepsilon Q_{n-3} \\ &= (\alpha^n + \beta^n) + i(\alpha^{n-1} + \beta^{n-1}) + \varepsilon(\alpha^{n-2} + \beta^{n-2}) + i\varepsilon(\alpha^{n-3} + \beta^{n-3}) \\ &= \alpha^{n-3}(\alpha^3 + i\alpha^2 + \varepsilon\alpha^1 + i\varepsilon) + \beta^{n-3}(\beta^3 + i\beta^2 + \varepsilon\beta^1 + i\varepsilon) \end{aligned}$$

$$DGQ_n = \hat{\alpha}\alpha^{n-3} + \hat{\beta}\beta^{n-3}.$$

Similarly, Binet's formula for dual-Gaussian Pell numbers is obtained.

Theorem 2.8: (d'Ocagne's Identity) Let DGP_n and DGQ_n be the dual-Gaussian Pell and Pell-Lucas numbers. d'Ocagne's identity for this number is as follows

$$DGP_m DGP_{n+1} - DGP_{m+1} DGP_n = 8(-1)^{n+1}P_{m-n} - 2i(-1)^n P_{m-n} - \varepsilon[6(-1)^n(P_{m-n}) + (-1)^n(P_{m-n-2} + P_{m-n+2})] - 12i\varepsilon(-1)^n P_{m-n}$$

$$DGQ_m DGQ_{n+1} - DGQ_{m+1} DGQ_n = 8[(-1)^n P_{m-n+1} + (-1)^m P_{n-m}] + 16i(-1)^n P_{m-n} + 8\varepsilon[(-1)^m (P_{n-m-2} + P_{n-m+2}) - (-1)^n (P_{m-n-2} + P_{m-n+2})]$$

Proof:

$$DGQ_m DGQ_{n+1} - DGQ_{m+1} DGQ_n = (Q_m + iQ_{m-1} + \varepsilon Q_{m-2} + i\varepsilon Q_{m-3})(Q_{n+1} + iQ_n + \varepsilon Q_{n-1} + i\varepsilon Q_{n-2}) - (Q_{m+1} + iQ_m + \varepsilon Q_{m-1} + i\varepsilon Q_{m-2})(Q_n + iQ_{n-1} + \varepsilon Q_{n-2} + i\varepsilon Q_{n-3}) = 8[(-1)^n P_{m-n+1} + (-1)^m P_{n-m}] + 16i(-1)^n P_{m-n} + 8\varepsilon[(-1)^m (P_{n-m-2} + P_{n-m+2}) - (-1)^n (P_{m-n-2} + P_{m-n+2})]$$

Similarly, d’Ocagne’s identity for dual-Gaussian Pell numbers is obtained.

Theorem 2.9: (Catalan’s Identity) Let DGP_n and DGQ_n be the dual-Gaussian Pell and Pell-Lucas numbers. Catalan’s identity for this number is as follows

$$DGP_n^2 - DGP_{n+r} DGP_{n-r} = P_r^2 [(-1)^{n-r} + (-1)^{n+r}] + iP_r (-1)^{n-r} [P_{r-1} - P_{r+1}] + \varepsilon P_r [(-1)^{n-1} (P_{-r-2} + P_{-r+2}) + (-1)^{n-r} (P_{r+2} + P_{-r+2})] + i\varepsilon P_r [(-1)^{n-r-1} (P_{r+3} + P_{r-1}) + (-1)^{n-r} (P_{r-3} + P_{r+1})]$$

$$DGQ_n^2 - DGQ_{n+r} DGQ_{n-r} = 4(-1)^n [2P_r^2 - P_r] + 16i(-1)^{n-r} [P_r^2] - 8\varepsilon P_r [(-1)^{n-r} (P_{r+2} + P_{r-2}) + (-1)^{n-1} (P_{-r+2} + P_{-r-2})] + 8i\varepsilon (-1)^{n-r} P_r [(P_{r+3} + P_{r-1}) - (P_{r-3} + P_{r+1})]$$

Proof:

$$DGQ_n^2 - DGQ_{n+r} DGQ_{n-r} = (Q_n + iQ_{n-1} + \varepsilon Q_{n-2} + i\varepsilon Q_{n-3})(Q_n + iQ_{n-1} + \varepsilon Q_{n-2} + i\varepsilon Q_{n-3}) - (Q_{n+r} + iQ_{n+r-1} + \varepsilon Q_{n+r-2} + i\varepsilon Q_{n+r-3})(Q_{n-r} + iQ_{n-r-1} + \varepsilon Q_{n-r-2} + i\varepsilon Q_{n-r-3}) = 4(-1)^n [2P_r^2 - P_r] + 16i(-1)^{n-r} [P_r^2] - 8\varepsilon P_r [(-1)^{n-r} (P_{r+2} + P_{r-2}) + (-1)^{n-1} (P_{-r+2} + P_{-r-2})] + 8i\varepsilon (-1)^{n-r} P_r [(P_{r+3} + P_{r-1}) - (P_{r-3} + P_{r+1})]$$

Similarly, Catalan’s identity for dual-Gaussian Pell numbers is obtained.

Theorem 2.10: (Cassini’s Identity) Let DGP_n and DGQ_n be the dual-Gaussian Pell and Pell-Lucas numbers. Cassini’s identity for this number is as follows

$$DGP_n^2 - DGP_{n+1} DGP_{n-1} = -2(-1)^n + 2i(-1)^n - 12\varepsilon(-1)^n + 12i\varepsilon(-1)^n$$

$$DGQ_n^2 - DGQ_{n+1} DGQ_{n-1} = 4(-1)^n - 16i(-1)^n + 96(-1)^n \varepsilon - 96i\varepsilon(-1)^n$$

Proof: If $r = 1$ is taken in the Catalan’s identity, Cassini’s identity is obtained. Similarly, Cassini’s identity for dual-Gaussian Pell numbers is obtained.

Theorem 2.11: Let DGP_n and DGQ_n be the dual-Gaussian Pell and Pell-Lucas numbers. In this case

$$\sum_{k=1}^n DGP_k = \left(\frac{Q_{n+1}-1}{2}\right) + i\left(\frac{Q_n-1}{2}\right) + \varepsilon\left(\frac{Q_{n-1}+1}{2}\right) + i\varepsilon\left(\frac{Q_{n-2}-3}{2}\right)$$

$$\sum_{k=1}^n DGP_{2k-1} = \left(\frac{P_{2n}}{2}\right) + i\left(\frac{P_{2n-1}-1}{2}\right) + \varepsilon\left(\frac{P_{2n-2}+2}{2}\right) + i\varepsilon\left(\frac{P_{2n-3}-5}{2}\right)$$

$$\sum_{k=1}^n DGP_{2k} = \left(\frac{P_{2n+1}-1}{2}\right) + i\left(\frac{P_{2n}}{2}\right) + \varepsilon\left(\frac{P_{2n-1}-1}{2}\right) + i\varepsilon\left(\frac{P_{2n-2}+2}{2}\right)$$

$$\sum_{k=1}^n DGQ_k = (2P_{n+1} - 2) + i(2P_n) + \varepsilon(2P_{n-1} - 2) + i\varepsilon(2P_{n-2} + 4)$$

$$\sum_{k=1}^n DGQ_{2k-1} = \left(\frac{Q_{2n}-1}{2}\right) + i\left(\frac{Q_{2n-1}+3}{2}\right) + \varepsilon\left(\frac{Q_{2n-2}-5}{2}\right) + i\varepsilon\left(\frac{Q_{2n-3}+15}{2}\right)$$

$$\sum_{k=1}^n DGQ_{2k} = \left(\frac{Q_{2n+1}-1}{2}\right) + i\left(\frac{Q_{2n}-1}{2}\right) + \varepsilon\left(\frac{Q_{2n-1}+3}{2}\right) + i\varepsilon\left(\frac{Q_{2n-2}-5}{2}\right)$$

Proof:

$$\sum_{k=1}^n DGQ_k = \sum_{k=1}^n (Q_k + iQ_{k-1} + \varepsilon Q_{k-2} + i\varepsilon Q_{k-3})$$

$$\begin{aligned}
 &= \sum_{k=1}^n Q_k + i \sum_{k=0}^{n-1} Q_k + \varepsilon \sum_{k=-1}^{n-2} Q_k + i\varepsilon \sum_{k=-2}^{n-3} Q_k \\
 &= (2P_{n+1} - 2) + i(2P_n) + \varepsilon(2P_{n-1} - 2) + i\varepsilon(2P_{n-2} + 4)
 \end{aligned}$$

Other sums are proven through the same method. Similarly, Sums are proven for dual-Gaussian Pell numbers is obtained.

Theorem 2.12: Let DGP_n and DGQ_n be the dual-Gaussian Pell-Lucas numbers. For $n \geq 1$ be integer. Then, the matrix representations of these sequences with both negative and positive indices are as follows

$$\begin{aligned}
 \begin{bmatrix} 2 & 1 \\ 1 & 0 \end{bmatrix}^n \begin{bmatrix} DGP_2 & DGP_1 \\ DGP_1 & DGP_0 \end{bmatrix} &= \begin{bmatrix} DGP_{n+2} & DGP_{n+1} \\ DGP_{n+1} & DGP_n \end{bmatrix} \\
 \begin{bmatrix} 0 & 1 \\ 1 & 2 \end{bmatrix}^n \begin{bmatrix} DGP_0 \\ DGP_1 \end{bmatrix} &= \begin{bmatrix} DGP_n \\ DGP_{n+1} \end{bmatrix} \\
 \begin{bmatrix} 2 & 1 \\ 1 & 0 \end{bmatrix}^n \begin{bmatrix} DGQ_2 & DGQ_1 \\ DGQ_1 & DGQ_0 \end{bmatrix} &= \begin{bmatrix} DGQ_{n+2} & DGQ_{n+1} \\ DGQ_{n+1} & DGQ_n \end{bmatrix} \\
 \begin{bmatrix} 0 & 1 \\ 1 & 2 \end{bmatrix}^n \begin{bmatrix} DGQ_0 \\ DGQ_1 \end{bmatrix} &= \begin{bmatrix} DGQ_n \\ DGQ_{n+1} \end{bmatrix} \\
 \begin{bmatrix} 0 & 1 \\ 1 & -2 \end{bmatrix}^n \begin{bmatrix} DGP_2 & DGP_1 \\ DGP_1 & DGP_0 \end{bmatrix} &= \begin{bmatrix} DGP_{-n+2} & DGP_{-n+1} \\ DGP_{-n+1} & DGP_{-n} \end{bmatrix} \\
 \begin{bmatrix} 0 & 1 \\ 1 & -2 \end{bmatrix}^n \begin{bmatrix} DGP_0 \\ DGP_1 \end{bmatrix} &= \begin{bmatrix} DGP_{-n} \\ DGP_{-n-1} \end{bmatrix} \\
 \begin{bmatrix} 0 & 1 \\ 1 & -2 \end{bmatrix}^n \begin{bmatrix} DGQ_2 & DGQ_1 \\ DGQ_1 & DGQ_0 \end{bmatrix} &= \begin{bmatrix} DGQ_{-n+2} & DGQ_{-n+1} \\ DGQ_{-n+1} & DGQ_{-n} \end{bmatrix} \\
 \begin{bmatrix} 0 & 1 \\ 1 & -2 \end{bmatrix}^n \begin{bmatrix} DGQ_0 \\ DGQ_1 \end{bmatrix} &= \begin{bmatrix} DGQ_{-n} \\ DGQ_{-n-1} \end{bmatrix}
 \end{aligned}$$

Proof:

For the prove, we utilize induction principle on n . The equality holds for $n = 1$. Now assume that the equality is true for $n > 1$. Then, we can verify for $n + 1$ as follows

$$\begin{aligned}
 \begin{bmatrix} 2 & 1 \\ 1 & 0 \end{bmatrix}^{n+1} \begin{bmatrix} DGP_2 & DGP_1 \\ DGP_1 & DGP_0 \end{bmatrix} &= \begin{bmatrix} 2 & 1 \\ 1 & 0 \end{bmatrix} \begin{bmatrix} 2 & 1 \\ 1 & 0 \end{bmatrix}^n \begin{bmatrix} DGP_2 & DGP_1 \\ DGP_1 & DGP_0 \end{bmatrix} \\
 &= \begin{bmatrix} 2 & 1 \\ 1 & 0 \end{bmatrix} \begin{bmatrix} DGP_{n+2} & DGP_{n+1} \\ DGP_{n+1} & DGP_n \end{bmatrix} = \begin{bmatrix} DGP_{n+3} & DGP_{n+2} \\ DGP_{n+2} & DGP_{n+1} \end{bmatrix}
 \end{aligned}$$

Thus, the first step of the theorem can be proved easily. Similarly, the other steps of the proof are seen by induction on n .

Conclusions

This study presents the dual-Gaussian Pell-Lucas and Pell numbers. We obtained these new numbers not defined in the literature before. These number sequences have great importance as they are used in quantum physics, applied mathematics, kinematic, differential equations and cryptology. Since this study includes some new results, it contributes to literature by providing essential information concerning these new numbers. Therefore, we hope that this new number system and properties that we have found will offer a new perspective to the researchers.

Acknowledgment

The author expresses his sincere thanks to the anonymous referees and the associate editor for their careful reading, suggestions, and comments, which improved the presentation of results.

Conflicts of interest

There are no conflicts of interest in this work.

References

- [1] Horadam A.F., Complex Fibonacci Numbers and Fibonacci Quaternions, *American Math. Monthly*, 70 (1963) 289-291.
- [2] Fjelstad P., Gal S.G., n -dimensional Dual Complex Numbers, *Advances in Applied Clifford Algebras*, 8(2) (1998) 309-322.
- [3] Clifford W.K., A Preliminary Sketch of Biquaternions, *The London Mathematical Society*, (1873) 381-395.
- [4] Messelmi F., Dual Complex Numbers and Their Holomorphic Functions, Available at: <https://hal.archives-ouvertes.fr/hal-01114178>. Retrieved January 7, 2022.

- [5] Catarino P., Bicomplex k -Pell Quaternions, *Computational Methods and Function Theory*, 19 (2019) 65-76.
- [6] Gül K., Dual Bicomplex Horadam Quaternions, *Notes on Numbers Theory and Discrete Mathematics*, 26 (2020) 187-205.
- [7] Soykan Y., On Dual Hyperbolic Generalized Fibonacci Numbers, *Indian Journal of Pure and Applied Mathematics*, 52 (2021) 62-78.
- [8] Vajda S., Fibonacci and Lucas Numbers and the Golden Section, Ellis Horwood Limited Publ., England, (1989) 47-52.
- [9] Matsuda G., Kaji S. Ochiai H., Anti-commutative Dual Complex Numbers and 2 Rigid Transformation, *Mathematical Progress in Expressive Image Synthesis I.*, Springer, (2014) 131-138.
- [10] Akar M., Yüce S., Şahin S., On the Dual Hyperbolic Numbers and the Complex Hyperbolic numbers, *Journal of Computer Science & Computational Mathematics*, 8 (2018) 1-6.
- [11] Majernik V., Multicomponent Number Systems, *Acta Physica Polonica A.*, 90(3) (1996) 491-498.
- [12] Aydın F.T., Dual-complex k -Fibonacci Numbers, *Chaos, Solitons & Fractals*, 115 (2018) 1-6.
- [13] Koshy T., Fibonacci and Lucas Numbers with Applications, A Wiley-Interscience Publication, USA, (2001) 83-91.
- [14] Koshy T., Pell and Pell-Lucas Numbers with Applications. London: Springer New York Heidelberg Dordrecht, (2014) 31-35.
- [15] Halıcı S., Çürük Ş., On Dual k -bicomplex Numbers and Some Identities Including Them, *Fundamental Journal of Mathematics and Applications*, 3 (2020) 86-93.
- [16] Azak Z., Güngör M.A., Investigation of Dual-complex Fibonacci, Dual-complex Lucas Numbers and Their Properties, *Adv. Appl. Clifford Algebras*, 27 (2017) 3083-3096.
- [17] Aydın F.T., Dual-complex k -Pell Quaternions, *Notes on Numbers Theory and Discrete Mathematics*, 25 (2019) 111-125.

On Hyperideals of Multiplicative Hyperrings

Betül Coşgun^{1,a}, Ummahan Acar^{1,b,*}

¹Department of Mathematics, Faculty of Science, Muğla Sıtkı Koçman University, Muğla, Türkiye.

*Corresponding author

Research Article

History

Received: 14/11/2021

Accepted: 18/10/2022

Copyright





©2022 Faculty of Science,
Sivas Cumhuriyet University

ABSTRACT


Let R be a commutative multiplicative hyperring. In this paper, we introduce and study the concepts of n -hyperideal and δ - n -hyperideal of R which are generalization of n -ideals and δ - n -ideals of the in a commutative ring. An element a is called a nilpotent element of R if there exists a positive integer n such that $0 \in a^n$. A hyperideal I ($I \neq R$) of R is called an n -hyperideal of R if for all $a, b \in R$, $a * b \subseteq I$ and a is non-nilpotent element implies that $b \in I$ [15]. Also, I is called a δ - n -hyperideal if for all $a, b \in R$, $a * b \subseteq I$ then either a is nilpotent or $b \in \delta(I)$, where δ is an expansion function over the set of all hyperideals of a multiplicative hyperring. In addition, we give the definition of z_δ -hyperideal. Some properties of n -hyperideals, δ - n -hyperideals and z_δ -hyperideals of the hyperring R are presented. Finally, the relations between these notions are investigated.

Keywords: Multiplicative hyperring, n -hyperideal, δ - n -hyperideal.

 betulcosgun93@gmail.com

 <https://orcid.org/0000-0003-1389-259X>

 uacar@mu.edu.tr

 <https://orcid.org/0000-0001-5762-9684>

Introduction

The first publications on algebraic hyperstructures, as a natural generalization of classical algebra, are first encountered in 1934. The group concept, the fundamental definition of algebraic structures, was first generalized to hypergroup theory by Marty [1]. After Marty's definition, many concepts of algebra, especially hypergroups, were generalized to hyperstructures. Subsequently, applications of hyperstructures theory to other branches of science are studied by many researchers. A detailed examination of this theory can be found at [2-4]. The concept of hyperring has been studied in different ways. The definition of hyperring, given by taking "+" hyperoperation and multiplication, was made by Krasner and is known by his name. A class of hyperrings is multiplicative hyperring which satisfies the axioms similar a ring, but product replaced by hyperproduct. The multiplicative hyperring defined by Rota in 1982 and its properties have been studied by many mathematicians [5-9].

In this paper, we consider the notions of n -ideal and δ - n -ideal in commutative rings and extend these notions n -hyperideals and δ - n -hyperideals to commutative multiplicative hyperrings. Furthermore, we characterize for the δ - n hyperideals of commutative multiplicative hyperring.

First of all, let us to introduce some notions and results of algebraic hyperstructures theory, which we will need to development our paper. Let H be a nonempty set and we mean the set of all nonempty subsets of H by $P^*(H)$. A map $\circ: H \times H \rightarrow P^*(H)$ is called a hyperoperation on H . Naturally, we can extend the hyperoperation \circ to subsets of H , as follows:

$$X \circ Y = \bigcup_{x \in X, y \in Y} x \circ y, \quad X \circ h = \bigcup_{x \in X} x \circ h, \quad h \circ Y = \bigcup_{y \in Y} h \circ y$$

where $\emptyset \neq X, Y \subseteq H$ and $h \in H$.

R is called a multiplicative hyperring with operation $+$ and hyperoperation \circ if

$(R, +)$ is an abelian group,

(R, \circ) is a semihypergroup, i.e, $(x \circ y) \circ z = x \circ (y \circ z)$, for all $x, y, z \in R$,

For all $x, y, z \in R$, we have $x \circ (y + z) \subseteq (x \circ y) + (x \circ z)$ and $(y + z) \circ x \subseteq (y \circ x) + (z \circ x)$,

For all $x, y \in R$, $x \circ (-y) = (-x) \circ y = -(x \circ y)$.

If in (iii) the equality holds, then R has a strongly distributive property. Also R is called commutative if $x \circ y = y \circ x$ for all $x, y \in R$ and an element $e \in R$ is said to be a left (resp. right) scalar identity if $e \circ x = x$, (resp. $x \circ e = x$), for all $x \in R$. An element e is called scalar identity element if it is both left and right scalar identity element [10]. If $0 \in x \circ y$ and $x \neq 0$, where $\forall x, y \in R$, then $y = 0$, then a commutative multiplicative hyperring R is called a strong hyperdomain [11].

A nonempty subset I of a multiplicative hyperring R is a hyperideal if

$$I - I \subseteq I$$

$$x \circ r \cup r \circ x \subseteq I \text{ for all } x \in I, \text{ for all } r \in R$$

The set of all hyperideals of R is denoted by $I(R)$. A hyperideal $I (\neq R)$ of a multiplicative hyperring R is called prime hyperideal if for all $a, b \in R$, $a \circ b \subseteq I$ implies that $a \in I$ or $b \in I$ [12]. An element a is called nilpotent element of R if there exists a positive

integer n such that $0 \in a^n$ where for any positive integer $n > 1, a^n = \underbrace{a \circ a \circ \dots \circ a}_{n\text{-times}}$ and $a^1 = \{a\}$ and we denoted the set of all nilpotent elements of R by $\text{nil}(R)$ (for more details see[8]).

Let $(R, +, \circ)$ and $(S, +', *)$ be two commutative multiplicative hyperrings and $g: R \rightarrow S$ be a map. Then g is called a homomorphism (resp. good homomorphism) if g satisfies the following conditions for all $a, b \in R$,

$$g(a + b) = g(a) + ' g(b),$$

$$g(a \circ b) \subseteq g(a) * g(b) \quad (\text{resp. } g(a \circ b) = g(a) * g(b))$$

In [10], an expansion function over the set of all hyperideals of a multiplicative hyperring is defined as following:

A function $\delta: I(R) \rightarrow I(R)$ that satisfies the following two conditions is called an expansion function of $I(R)$

- (1) $I \subseteq \delta(I)$,
- (2) If $I \subseteq J$, then $\delta(I) \subseteq \delta(J)$, for all $I, J \in I(R)$

In [13], G. Ulucak defined δ -primary hyperideal as follows; A proper hyperideal I of R is called δ -primary hyperideal of a multiplicative hyperring $(R, +, \circ)$ if for all $a, b \in R, a \circ b \subseteq I$ implies that either $a \in I$ or $b \in \delta(I)$, where δ is an expansion function of $I(R)$.

n-Hyperideals of the Multiplicative Hyperring

In this section, the definitions of n -ideal and δ - n -ideal given in [14] and [13], respectively, will be generalized to a commutative multiplicative hyperrings. Now we give a definition of n -hyperideal and some properties of this concept which is in [15]. For the safe of completeness, we will give the proofs of Theorem 2.1. and Theorem 2.2. Throughout this paper, unless otherwise stated, $(R, +, *)$ will be taken as a commutative multiplicative hyperring.

Definition 2.1. Let I be a hyperideal of $(R, +, *)$ and $I \neq R$. For all $a, b \in R$, if $a * b \subseteq I$ and a is non-nilpotent element implies that $b \in I$ then I is called a n -hyperideal of R .

Example 2.1. Let $(\mathbb{Z}_4, +, \cdot)$ be a ring and $I = \{\bar{0}, \bar{2}\}$ be an ideal of \mathbb{Z}_4 . We define hyperoperation \circ in \mathbb{Z}_4 . For all $\bar{m}, \bar{n} \in \mathbb{Z}_4, \bar{m} \circ \bar{n} = \overline{mn} + I$

\circ	$\bar{0}$	$\bar{1}$	$\bar{2}$	$\bar{3}$
$\bar{0}$	I	I	I	I
$\bar{1}$	I	$\bar{1} + I$	I	$\bar{1} + I$
$\bar{2}$	I	I	I	I
$\bar{3}$	I	$\bar{1} + I$	I	$\bar{1} + I$

Then $(\mathbb{Z}_4, +, \circ)$ is a multiplicative hyperring and $H = \{\bar{0}, \bar{2}\}$ is a hyperideal of \mathbb{Z}_4 . Since $\bar{m} \circ \bar{n} \subseteq H$ and \bar{m} is non-nilpotent implies that $\bar{n} \in H$, for all $\bar{m}, \bar{n} \in \mathbb{Z}_4$. Then H is a n -hyperideal of \mathbb{Z}_4 .

Example 2.2. Let $(\mathbb{Z}, +, *)$ be a multiplicative hyperring with respect to hyperoperation $*$ defined by $a * b = \{a \cdot b, 2a \cdot b, 3a \cdot b, \dots\}$, for all $a, b \in \mathbb{Z}$ in [4]. $2\mathbb{Z}$ is a hyperideal of \mathbb{Z} but it is not n -hyperideal. Because $4 * 3 \subseteq 2\mathbb{Z}$ and 4 is a non-nilpotent but $3 \notin 2\mathbb{Z}$.

Theorem 2.1. Let $K = \{I_k : k \in \Omega\}$ be a nonempty family of n -hyperideals of a multiplicative hyperring $(R, +, *)$. Then $\bigcap_{k \in \Omega} I_k$ is a n -hyperideal of R and if K is a chain, then $\bigcup_{k \in \Omega} I_k$ is a n -hyperideal of R .

Proof. $\bigcap_{k \in \Omega} I_k$ is a n -hyperideal, it is clear from Definition 2.3. We will show that $\bigcup_{k \in \Omega} I_k$ is a n -hyperideal. Let K be a chain. Since $I_k \subseteq R$ and $I_k \neq \emptyset$ for $k \in \Omega$. $\bigcup_{k \in \Omega} I_k \subseteq R$ and $\bigcup_{k \in \Omega} I_k \neq \emptyset$. For all $x, y \in \bigcup_{k \in \Omega} I_k$ and $r \in R$, then there exist $i, j \in \Omega$ such that $x \in I_i, y \in I_j$. Suppose $I_i \subseteq I_j$ then $x \in I_j$ since I_j is a hyperideal, $x - y \in I_j$ and $x * r \cup r * x \subseteq I_j$. Hence $x - y \in \bigcup_{k \in \Omega} I_k$ and $x * r \cup r * x \subseteq \bigcup_{k \in \Omega} I_k$. Let $x * y \subseteq \bigcup_{k \in \Omega} I_k$ and x is non-nilpotent element for $x, y \in R$. $x * y \subseteq \bigcup_{k \in \Omega} I_k \Rightarrow \exists i \in \Omega, x * y \subseteq I_i$. Since I_i is a n -hyperideal and x is non-nilpotent, $y \in I_i$. Hence $y \in \bigcup_{k \in \Omega} I_k$ and $\bigcup_{k \in \Omega} I_k$ is a n -hyperideal of R .

Theorem 2.2. Let $f: (R, +, \circ) \rightarrow (S, +', *)$ be a good homomorphism. Then

If J is a n -hyperideal of S , then $f^{-1}(J)$ is a n -hyperideal of R .

If f is an isomorphism and I is a n -hyperideal of R , then $f(I)$ is a n -hyperideal of S .

Proof. i. Since J is a hyperideal and f homomorphism, $f^{-1}(J) = \{r \in R: f(r) \in J\} \neq \emptyset$ is a hyperideal of R . Let us show that $f^{-1}(J)$ is a n -hyperideal. Let $r_1 \circ r_2 \subseteq f^{-1}(J)$ and r_1 is a non-nilpotent element. Then for all $n \in \mathbb{N}, 0 \notin (r_1)^n$ so $0_S = f(0) \notin f(r_1)^n$, thus $f(r_1)$ is a non-nilpotent element in S . Since $r_1 \circ r_2 \subseteq f^{-1}(J)$ and f is a homomorphism, $f(r_1 \circ r_2) = f(r_1) * f(r_2) \subseteq f(f^{-1}(J)) \subseteq J$. Therefore $f(r_2) \in J$ because J is a n -hyperideal and $f(r_1)$ is a non-nilpotent element. Hence $r_2 \in f^{-1}(J)$ and so $f^{-1}(J)$ is a n -hyperideal of R .

ii. It is clear that $f(I) = \{f(r): r \in I\} \subseteq S$ is a hyperideal of S . Now, we will show that $f(I)$ is a n -hyperideal. For all $s_1, s_2 \in S, s_1 * s_2 \subseteq f(I)$ and s_1 is non-nilpotent. Since f is an isomorphism, $f(r_1) = s_1$ and $f(r_2) = s_2$, for some $r_1, r_2 \in R$. Since s_1 is non-nilpotent, for all $n \in \mathbb{N}, 0 \notin f(r_1)^n = f((r_1)^n)$ and $0 \notin (r_1)^n$, i.e, r_1 is non-nilpotent. $f(r_1 \circ r_2) \subseteq f(I) \Rightarrow r_1 \circ r_2 \subseteq I$. From the definition of n -hyperideal, $r_2 \in I$. Hence $s_2 = f(r_2) \in S$, thus $f(I)$ is a n -hyperideal of S .

The set $\text{ann}(x) = \{r \in R: 0 \in r * x\}$ is called the annihilator of x in $(R, +, *)$ and x is said to be a zerodivisor element of R if $\text{ann}(x) \neq \emptyset$. The set of all zerodivisor elements of R denoted by $z_d(R)$.

Definition 2.2. Let I be a proper hyperideal of $(R, +, *)$. We say that I is a z_d -hyperideal, precisely when, whenever $a, b \in R$ with $a * b \subseteq I$ implies that $\text{ann}(a) \neq \{0\}$ or $b \in I$.

Example 2.3. Let $(\mathbb{Z}_6, +, \cdot)$ be a ring. We define the following hyperoperation $*$ on \mathbb{Z}_6 : For all $\bar{a}, \bar{b} \in \mathbb{Z}_6$,

$\bar{a} * \bar{b} = \{\bar{a} \cdot \bar{b}, 2\bar{a} \cdot \bar{b}, 3\bar{a} \cdot \bar{b}, 4 \cdot \bar{a} \cdot \bar{b}, 5\bar{a} \cdot \bar{b}\}$. Then $(\mathbb{Z}_6, +, *)$ is a commutative multiplicative hyperring. $H = \{\bar{0}, \bar{2}, \bar{4}\}$ is a z_d -hyperideal of \mathbb{Z}_6 .

Example 2.4. Let $(\mathbb{Z}, +, *)$ be a multiplicative hyperring w.r.t hyperoperation in Example 2.2. Then $4\mathbb{Z}$ is a hyperideal of \mathbb{Z} but it is not z_d -hyperideal. Because $4 * 3 \subseteq 4\mathbb{Z}$ but $\text{ann}(4) = \{0\}$ and $3 \notin 4\mathbb{Z}$.

Theorem 2.3. Every n -hyperideal of R is a z_d -hyperideal.

Proof. Let I be n -hyperideal of R . Assume that $r * s \in I$ and $ann(r) = 0$ for $r, s \in R$. Then $0 \notin r^n$ for all $n \in \mathbb{N}$. Since I is a n -hyperideal of R and r is non-nilpotent element in $R, s \in I$. Hence, I is a z_d -hyperideal of R .

Example 2.5 shows that the converse of the Theorem 2.3 is not true.

Example 2.5. Consider the commutative multiplicative hyperring \mathbb{Z}_6 in Example 2.3. $H = \{\bar{0}\}$ is a z_d -hyperideal of \mathbb{Z}_6 but H is not n -hyperideal.

Proposition 2.1. If R is a strong hyperdomain, then $\{0\}$ is a n -hyperideal of R .

Proof. Let $a * b \subseteq 0$ and a is a non nilpotent element for $a, b \in R$. Then $a * b \subseteq 0$ and $0 \notin a^n$ for all $n \in \mathbb{N}$ and so $a \neq 0$. Since R is a strong hyperdomain and $0 \in a * b, b = 0$. Therefore $b \in 0$ and so $\{0\}$ is a n -hyperideal.

In [12], Dasgupta defined the radical of the arbitrary hyperideal I as the intersection of all prime hyperideals containing I and denoted by $Rad(I) = \sqrt{I}$. He also showed that $D \subseteq Rad(I)$ by defining a set $D = \{r \in R : r^n \subseteq I \text{ for some } n \in \mathbb{N}\}$ for an arbitrary hyperideal I . We will denote this set D by $D(I)$ for any hyperideal I .

In [16], Anbarloei showed that for $a \in R, (I : a) = \{r \in R : r * a \subseteq I\}$ is a hyperideal of R . The following proposition prove that n -hyperideal can be characterization with $(I : a)$.

Proposition 2.2. Let I be a proper hyperideal of R . I is a n -hyperideal of R if and only if $I = (I : a)$ for every $a \notin D(0)$.

Proof. Suppose I is a n -hyperideal of R . Then $x * a \subseteq I$, for all $x \in I$. Therefore $x \in (I : a)$ and so $I \subseteq (I : a)$. Let $u \in (I : a)$ and $a \notin D(0)$. Then $a * u \subseteq I$. By Definition 2.1, $u \in I$. Thus $(I : a) \subseteq I$ and so $I = (I : a)$. Conversely, let $I = (I : a)$, for every $a \notin D(0)$. Suppose $a * u \subseteq I$ for all $a, u \in R, a$ is a non-nilpotent. Then $u \in (I : a) = I$ and so I is a n -hyperideal.

Proposition 2.3. Let N be a proper hyperideal of $(R, +, *)$ with identity 1. Then N is a n -hyperideal if and only if for $U, V \in I(R), U * V \subseteq N$, with $U \cap (R - D(0)) \neq \emptyset$ implies $V \subseteq N$.

Proof. Suppose that $U * V \subseteq N$ with $U \cap (R - D(0)) \neq \emptyset$ for hyperideals U and V of R . Since $U \cap (R - D(0)) \neq \emptyset$, there exists $x \in U$ such that $x \notin D(0)$. Then $x * V \subseteq N$ and so $V \subseteq (N : x)$. Therefore, $V \subseteq N$ by Proposition 2.2. Conversely, $u * v \subseteq N$ and u is non-nilpotent element for all $u, v \in R$. Then $u \notin D(0)$. Let $U = \langle u \rangle$ and $V = \langle v \rangle$. Then $U * V = \langle u * v \rangle \subseteq N$ and $U \cap (R - D(0)) \neq \emptyset$. Therefore $V \subseteq N$ and so $b \in N$. Thus, N is a n -hyperideal of R .

Theorem 2.4. Let K be a hyperideal of $(R, +, *)$ with $K \cap (R - D(0)) \neq \emptyset$. The following statements are hold:

If J_1, J_2 are n -hyperideals of R with $J_1 * K = J_2 * K$, then $J_1 = J_2$.

If $J * K$ is a n -hyperideal of R , then $J * K = J$.

Proof. i. Since J_1 is a hyperideal, $J_1 * K = J_2 * K \subseteq J_1$. Then $J_2 \subseteq J_1$, by Proposition 2.3. Because J_1 is a n -

hyperideal, $J_2 * K \subseteq J_1$ and $K \cap (R - D(0)) \neq \emptyset$. Similarly, $J_1 \subseteq J_2$. Thus, $J_1 = J_2$.

ii. Let $J * K$ be a n -hyperideal of R . Then $J * K$ is a hyperideal and so $J * (J * K) \subseteq J * K$. Since $J * K$ is a n -hyperideal and $K \cap (R - D(0)) \neq \emptyset, J \subseteq J * K$. Therefore $J = J * K$.

In Theorem 2.5, another characterization will be given for prime hyperideals to be n -hyperideal.

Theorem 2.5. Let $(R, +, *)$ be a commutative multiplicative hyperring with scalar identity (1) and Q be a prime hyperideal of R with $Q \cap D(0) \neq \emptyset$. Then Q is an n -hyperideal if and only if $Q = D(0)$.

Proof. $D(0) \subseteq Q$ is trivial. Now, we assume that $Q \not\subseteq D(0)$. Then there exist $a \in Q$ such that $0 \notin a^n$, for all $n \in \mathbb{N}$ and so a is non-nilpotent. Since Q is a n -hyperideal and $a = a * 1 \subseteq Q, 1 \in Q$ and $a * 1 \subseteq Q$, for all $a \in R$. Hence, $a \in Q$ and $R = Q$, which is a contradiction. Thus, $Q = D(0)$.

Conversely, suppose that $Q = D(0)$. Let for $x, y \in R, x * y \subseteq Q$ and x is a non-nilpotent. Then $x \notin Q = D(0)$ and $y \in Q$ because Q is a prime hyperideal. Hence, Q is a n -hyperideal of R .

Example 2.6. Let $(\mathbb{Z}, +, *)$ be a multiplicative hyperring in Example 2.2. $2\mathbb{Z}$ is a prime hyperideal of \mathbb{Z} but it is not n -hyperideal of \mathbb{Z} .

Example 2.7. Consider the multiplicative hyperring $(\mathbb{Z}, +, *)$ in Example 2.2, $H = 2\mathbb{Z}$ is a prime hyperideal of \mathbb{Z} and $S = \{2, 4, 6\} \subseteq \mathbb{Z}$. Then $(H : S) = \{x \in \mathbb{Z} : x * S \subseteq H\} = \mathbb{Z}$ is a n -hyperideal but H is not n -hyperideal, because $4 * 3 \subseteq H$ and 4 is a non-nilpotent element but $3 \notin H$.

δ – n- Hyperideal of Multiplicative Hyperring

In this section, we will introduce the definition of δ - n -hyperideal over the multiplicative hyperring with scalar identity and we will give a characterization of δ - n -hyperideal. Throughout this section, all hyperideals will be taken as \mathcal{C} -hyperideal. \mathcal{C} -hyperideals of a multiplicative hyperring defined by Das Gupta in [12] as follows, let $(R, +, *)$ be a multiplicative hyperring and $J \in I(R)$. J is said to be \mathcal{C} -ideal if for any $A \in \mathcal{C}, A \cap J \neq \emptyset \Rightarrow A \subseteq J$, where $\mathcal{C} = \{r_1 * r_2 * r_3 * \dots * r_n : r_i \in R, n \in \mathbb{N}\}$.

In the following definition, we are using definition of radical I , to state once again if I is \mathcal{C} -ideal, then $Rad(I) = D(I)$ in [12].

Definition 3.1. Let $J \in I(R), J \neq R$ and $\delta: I(R) \rightarrow I(R)$ be an expansion function. We say that J is a δ - n -hyperideal of R if for all $x, y \in R, x * y \subseteq J$ then either $x \in \sqrt{0}$ or $y \in \delta(J)$.

Example 3.1. Let $(\mathbb{Z}_8, +, \cdot)$ be a ring and $I = \{\bar{0}, \bar{4}\}$ be an ideal of \mathbb{Z}_8 . We define hyperoperation in \mathbb{Z}_8 : For all $\bar{a}, \bar{b} \in \mathbb{Z}_8, \bar{a} * \bar{b} = a \cdot b + I$. Then $(\mathbb{Z}_8, +, *)$ is a multiplicative hyperring. Let $\delta: I(\mathbb{Z}_8) \rightarrow I(\mathbb{Z}_8)$ be a function such that $\delta(H) = H$, for all H hyperideal of \mathbb{Z}_8 . Therefore, δ is an expansion function. $H = \{\bar{0}, \bar{2}, \bar{4}, \bar{6}\}$ is a δ - n -hyperideal.

Example 3.2. Consider the multiplicative hyperring $(\mathbb{Z}, +, *)$ in Example 2.2. Let $\delta: I(\mathbb{Z}) \rightarrow I(\mathbb{Z})$ be a function such that $\delta(H) = H$ for all H hyperideal. Then δ is an expansion function. $H = 2\mathbb{Z}$ is hyperideal of multiplicative hyperring \mathbb{Z} but H is not δ - n -hyperideal. Indeed, $4 * 3 \subseteq H$ but $4 \notin \sqrt{0}$ and $3 \notin \delta(H)$.

Proposition 3.1. Let R be multiplicative hyperring with scalar identity and δ be an expansion of hyperideals of R and J a proper hyperideal of R with $\delta(J) \neq R$. If J is a δ - n -hyperideal of R , then $J \subseteq \sqrt{0}$.

Proof. Suppose that $J \not\subseteq \sqrt{0}$. Then there exists element $a \in (J - \sqrt{0})$. Since $a \in 1 * a \subseteq J$ and $a \notin \sqrt{0}$, $1 \in \delta(J)$. Then for all $r \in R$, $r \in 1 * r \subseteq \delta(J)$ and so $\delta(J) = R$, a contradiction. Thus $J \subseteq \sqrt{0}$.

Theorem 3.1. Let J be a hyperideal of $(R, +, *)$. If $J = \sqrt{0}$, then J is a δ - n -hyperideal if and only if J is a δ -primary hyperideal.

Proof. Suppose that J is a δ - n -hyperideal and $x, y \in R, x * y \subseteq J$ and $x \notin J$. Then x is not nilpotent and so $y \in \delta(J)$ because J is a δ - n -hyperideal. Hence, J is a δ -primary hyperideal. Conversely, J is a δ -primary hyperideal, $x, y \in R, x * y \subseteq J$ and $x \notin \sqrt{0}$. Then $x \notin J$ and $y \in \delta(J)$ since J is a δ -primary hyperideal. Hence, J is a δ - n -hyperideal of R .

Proposition 3.2. Let δ be an expansion of hyperideals of R . Then the following are hold

- i. Let J be a δ -primary hyperideal of R with $\delta(J) \neq R$. Then J is a δ - n -hyperideal of R if and only if $J \subseteq \sqrt{0}$.
- ii. Let J be a prime hyperideal of R with $\delta(J) \neq R$. Then J is a δ - n -hyperideal of R if and only if $J = \sqrt{0}$.

Proof. i. It is clear by Proposition 3.1. and Theorem 3.1.

ii. Since J is prime hyperideal, $\sqrt{0} \subseteq J$. From Proposition 3.1, $J \subseteq \sqrt{0}$ and so $J = \sqrt{0}$. Conversely, since J is a prime hyperideal, J is a δ -primary hyperideal by [13]. From Theorem 3.1, J is a δ - n -hyperideal of R .

Theorem 3.2. For a proper hyperideal I of R and an expansion of function δ , the following statements are equivalent:

I is a δ - n -hyperideal of R .

$(I : a) \subseteq \sqrt{0}$ for all $a \in R - \delta(I)$.

If $a \circ J \subseteq I$ for some $a \in R$ and an hyperideal J of R , then $a \in \sqrt{0}$ or $J \subseteq \delta(I)$.

If $J \circ K \subseteq I$ for some hyperideals J and K of R implies $J \cap (R - \sqrt{0}) = \emptyset$ or $K \subseteq \delta(I)$.

Proof. (i) \Rightarrow (ii) Assume that any $x \in (I : a)$, then $x \circ a \subseteq I$. Since I is a δ - n -ideal of R and $a \notin \delta(I)$, $x \in \sqrt{0}$. Thus, $(I : a) \subseteq \sqrt{0}$.

(ii) \Rightarrow (iii) Suppose that if $a \circ J \subseteq I$ and $J \not\subseteq \delta(I)$. For any $j \in J, a \circ j \subseteq I$ and so $J \subseteq (a : I) \subseteq \sqrt{0}$. Since $J \not\subseteq \delta(I)$, there exist $j \in J$ but $j \notin \delta(I)$ and so $a \in \sqrt{0}$ by (ii).

(iii) \Rightarrow (iv) Let $J \circ K \subseteq I$ and suppose $J \cap (R - \sqrt{0}) \neq \emptyset$. Then there is an element $j \in J - \sqrt{0}$. For any $k \in K, j \circ k \subseteq I$. Then for $j \in J - \sqrt{0}, j \circ k \subseteq I$. From (iii), $k \in \delta(I)$ and so $K \subseteq \delta(I)$.

(iv) \Rightarrow (i) Let $x \circ y \subseteq I$ for some $x, y \in R$ and $J = (x), K = (y)$. Then $J \circ K \subseteq I$. If $J \cap (R - \sqrt{0}) \neq \emptyset$, then $x \in \sqrt{0}$. If $K \not\subseteq \delta(I)$, then $y \notin \delta(I)$ and so $K \not\subseteq I$, a contraction. Then, $x \in \sqrt{0}$ by our assumption. Thus, I is a δ - n -hyperideal of R .

Example 3.3. Consider the commutative multiplicative hyperring $(\mathbb{Z}_6, +, *)$ in Example 2.3. $H = \{\overline{0}, \overline{2}, \overline{4}\}, K = \{\overline{0}, \overline{3}\}, \overline{0}$ and \mathbb{Z}_6 are hyperideals of multiplicative hyperring \mathbb{Z}_6 . $\delta: I(\mathbb{Z}_6) \rightarrow I(\mathbb{Z}_6)$ be a function such that

$$\delta(X) = \begin{cases} \mathbb{Z}_6, & X = H, \mathbb{Z}_6 \\ K, & X = K, \{0\} \end{cases}$$

Therefore, δ is an expansion function. $\{0\}$ is a δ - n -hyperideal but it is not δ -primary hyperideal of \mathbb{Z}_6 .

Acknowledgment

This paper has been granted by the Muğla Sıtkı Koçman University Research Projects

Coordination Oce through Project Grant Number: (21/124/03/01).

Conflicts of interest

There are no conflicts of interest in this work.

References

- [1] Marty F., Sur une generalization de la notion de groupe, *8. Congress Math. Scandenaves*, Stockholm, (1934) 45-49.
- [2] Corsini S., Leoreanu V., Applications of Hyperstructure Theory, *Advances in Mathematics*, Kluwer Academic Publishers, (2003).
- [3] Corsini S., Prolegomena of Hypergroup Theory, Aviani Editore, Italy, (1993).
- [4] Dawvaz B., Leoreanu-Fotea V., Hyperring Theory and Applications. Palm Harbor, USA: International Academic Press (2007).
- [5] Rota R., Sugli iperanelli moltiplicativi, *Rend. Di. Math.*, Series VII, 4 (1982) 711-724.
- [6] Ameri R., Eyvazi M., Hoskova-Mayerova S., Superring of Polynomials over a Hyperring, *Mathematics*, 7(10) (2019) 1-15.
- [7] Dawvaz B., Salasi A., A Realization of Hyperrings, *Communications in Algebra*, 34(2007) 4389-4400.
- [8] Ameri R., Eyvazi M., Hoskova-Mayerova S., Multiplicative Hyperring of Fractions and Coprime Hyperideals, *An. St. Univ. Ovidius Constant*, 25(1) (2017) 5-23.
- [9] Bayrak D., Yamak S., A Note on The Lattice of Fuzzy Hyperideals of a Hyperring, *Afrika Matematika*, 28(2017) 1185-1192.
- [10] Procesi R., Rota R., On Some Classes of Hyperstructures, *Discrete Mathematics*, 208/209 (1999) 485-497.
- [11] Ameri R., Kordi A., Clean Multiplicative Hyperrings, *Italian Journal of Pure and Applied Mathematics*, 35 (2015) 625-636.
- [12] Dasgupta U., On Prime and Primary Hyperideals of a Multiplicative Hyperrings, *Annals of the Alexandru Ioan Cuza University-Mathematics*, LVIII (1) (2012) 19-36.
- [13] Ulucak G., On Expansions of Prime and 2-absorbing Hyperideals in Multiplicative Hyperrings, *Turkish Journal of Mathematics*, 43 (2019) 1504-1517.
- [14] Tekir U., Koç S., Oral K.H., N-ideals of Commutative Rings, *Filomat*, (2017) 2933-2941.
- [15] Coşgun B., Acar U. A Study on Hyperideals of Multiplicative Hyperring, *IFSCOM 2021*, Antalya, Türkiye, (2021).
- [16] Anbarloei M., On Almost Primary Hyperideals and Almost 2-Absorbing Primary Hyperideals of a Multiplicative Hyperring, *Southeast Asian Bulletin of Mathematics*, 44 (2020) 167-176.



Fixed Point Theorems In 2-Banach Spaces For Non-expansive Type Conditions

Mithun Paul ^{1,a}, Krishnadhan Sarkar ^{2,b,*}, Kalishankar Tiwary ^{1,c}

¹ Department of Mathematics, Raiganj University, West Bengal, 733134-India

² Department of Mathematics, Raniganj Girls' College, Raniganj, Paschim Bardhaman, West Bengal, 713358-India

*Corresponding author

Research Article

History

Received: 12/05/2022

Accepted: 16/11/2022

Copyright



©2022 Faculty of Science,
Sivas Cumhuriyet University

ABSTRACT

Fixed point theorems had been established and developed under various non-expansive type conditions on different metric spaces. In this paper, we have generalized (ψ, ϕ) -weak contractions, which is the generalizations of F-contraction, (ϕ, F) -contraction as well as (ψ, ϕ) -contractions. Then we have established some unique common fixed point results for a sequence of mappings for (ψ, ϕ) -weak contractions in 2-Banach spaces. Some basic definitions, properties and examples are given in the introduction and preliminaries part. Some corollaries are also given on the basis on the results.

Keywords: 2-Banach spaces, Coincidence points, Non-decreasing function, Cauchy sequence, Fixed point.

^a mithunmscmath@gmail.com

^b <https://orcid.org/0000-0001-5429-281X>

^c tiwarykalishankar@yahoo.com

^d <https://orcid.org/0000-0002-5773-2021>

^e sarkarkrishnadhan@gmail.com

^f <https://orcid.org/0000-0001-6890-8427>

Introduction and Preliminaries

In 1922, S. Banach first established the Banach contraction principle (BCP) and proved fixed point results in complete metric spaces. Since then lots of fixed point results have been proved in many contractive conditions on various spaces. In 2011, Mujahid Abbas, Talat Nazir and Stojan Radenovic [1] established some common fixed point results for four maps in partially ordered metric spaces. Also in 2018, Seonghoon Cho [2] obtained some fixed point theorems for generalized weakly contractive mappings in metric spaces.

In this paper we have established a unique common fixed point theorem on generalized (ψ, ϕ) -weak contractions for a sequence of mappings in 2-Banach spaces, which is a generalization of the results of Seonghoon Cho [2].

The concept of 2-Banach space has been initiated by S. Gahler [3] and then many authors established fixed point results on this space under different contractive conditions as in other spaces. In 2013, Liu and Chai [4] established fixed point theorem for weakly contractive mappings in generalized metric spaces. Later in 2021, Zhiquan and Guiwen Lv [5] also developed some fixed point results for generalized (ψ, ϕ) -weak contraction in Branciari-type generalized metric spaces.

We recall some basic definitions, properties and conclusions which are as follows:

Definition 1 [2] Let X be a real linear space and $\|\cdot, \cdot\|$ be a non-negative real valued function defined on $X \times X$ satisfying the following conditions:

$\|v, w\| = 0$, if and only if v and w are linearly dependent in X ;

$\|v, w\| = \|w, v\|$, for all $v, w \in X$;

$\|v, kw\| = |k|\|v, w\|$, $v, w \in X$; $k \in R$;

$\|v, w + z\| \leq \|v, w\| + \|w, z\|$, for all $v, w, z \in X$.

Then $\|\cdot, \cdot\|$ is called a 2-norm on X and the pair $(X, \|\cdot, \cdot\|)$ is called a linear 2-normed space.

Note: 2-Norm are non-negative and $\|v, w + kv\| = \|v, w\|$, for all $v, w \in X$; $k \in R$.

Definition 2 [6,7] A sequence $\{v_n\}$ in a linear 2-normed space $(X, \|\cdot, \cdot\|)$ is called Cauchy sequence if

$$\lim_{m, n \rightarrow \infty} \|v_m - v_n, a\| = 0, \text{ for all } a \in X.$$

Definition 3 [6] A sequence $\{v_n\}$ in a linear 2-normed space $(X, \|\cdot, \cdot\|)$ is said to be convergent in X , if there is a point v in $X \times X$ such that $\lim_{n \rightarrow \infty} \|v_n - v, a\| = 0$, for all $a \in X$.

Definition 4 [6] A linear 2-normed space X is said to be complete with respect to the 2-norm $\|\cdot, \cdot\|$ if every Cauchy sequence is convergent to an element of X . Then we call $(X, \|\cdot, \cdot\|)$ to be a 2-Banach space.

Definition 5 [6] Let X be a 2-Banach space and T be a self-mapping on X . T is said to be continuous at $x \in X$ if for every sequence $\{v_n\}$ in X , $v_n \rightarrow v$ as $n \rightarrow \infty$ implies $T(x_n) \rightarrow T(x)$ as $n \rightarrow \infty$.

Definition 6 [6] Let F and G be self maps on a set X (i.e, $F, G: X \rightarrow X$). If $u = Fw = Gw$ for some $w \in X$, then w is called a coincidence point of F and G ; and u is called a point of coincidence of F and G .

Example 1 Let $X = R^3$. Define 2-norm on X as

$$\begin{aligned} \|v, w\| &= 0, \text{ if and if } v, w \text{ are linearly dependent;} \\ &= |(v_1 \ v_2 \ v_3) \begin{pmatrix} w_1 \\ w_2 \\ w_3 \end{pmatrix}|, \text{ where, } v = (v_1, v_2, v_3), \\ w &= (w_1, w_2, w_3) \in R^3, \end{aligned}$$

Then $(X, \|\cdot, \cdot\|)$ is called a 2-Normed on X .

Example 2 [8]. Let Q_n denote the set of all real polynomials of degree $\leq n$ on the interval $[0,1]$. For usual addition and scalar multiplication, Q_n is a linear vector space over the real numbers. Let v_1, v_2, v_3, \dots be distinct

fixed points in $[0,1]$ and define the following 2-norm on Q_n as

$$\begin{aligned} \|F, G\| &= \sum_{k=0}^{2n} |F(v_k)|G(v_k), \text{ whenever } F \text{ and } \\ &= 0 \text{ if and only if } F \text{ and } G \text{ are linearly} \\ &\text{dependent.} \end{aligned}$$

Then $(Q_n, \|\cdot, \cdot\|)$ is a 2-Banach space.

In 2013, Liu and Chai [4] established some fixed point theorems in generalized metric spaces and 2018, Seonghoon Cho[2] obtained some fixed point results in a metric space using a generalised weakly contractive mapping.

Inspiring the results of Liu and Chai [4] and Seonghoon Cho[2] (c.f. Theorem 2.2) we have established the following results.

Main Results

To establish our main results we introduce two classes of functions Ψ and Φ which are given below:

$\Psi = \{\psi : [0, \infty) \rightarrow [0, \infty)$ satisfying the following conditions:

- (i) ψ is monotonic non-decreasing;
- (ii) $\lim_{t \rightarrow r} \psi(t) > 0$ for $r > 0$ and $\lim_{t \rightarrow 0^+} \psi(t) = 0$;
- (iii) $\psi(t) = 0$ if and only if $t = 0$.

$\Phi = \{\varphi : [0, \infty) \rightarrow [0, \infty)$ satisfying the following conditions:

- (i) $\lim_{t \rightarrow r} \inf \varphi(t) > 0$ for $r > 0$;
- (ii) $\varphi(t_n) \rightarrow 0$ implies $t_n \rightarrow 0$;
- (iii) $\varphi(t) = 0$ if and only if $t = 0$.

Theorem 1 Let $(X, \|\cdot, \cdot\|)$ be a 2-Banach space and $\{T_i\}_{i=1}^{\infty}$ be a sequence of self maps on X satisfying the following conditions:

$$\psi\{\|T_i x - T_j y, a\| + \phi(T_i x) + \phi(T_j y)\} \leq \psi\{Z^{(1)}(x, y, T_i, T_j, \phi)\} - \varphi\{Z^{(2)}(x, y, T_i, T_j, \phi)\}, \forall x, y \in X, \psi \in \Psi, \varphi \in \Phi; \quad (1)$$

where,

$$Z^{(1)}(x, y, T_i, T_j, \phi) = \max\{\|x - y, a\| + \phi(x) + \phi(y), \|x - T_i x, a\| + \phi(x) + \phi(T_i x), \|y - T_j y, a\| + \phi(y) + \phi(T_j y), \frac{1}{2}\{\|x - T_j y, a\| + \phi(x) + \phi(T_j y) + \|y - T_i x, a\| + \phi(y) + \phi(T_i x)\}\} \quad (2)$$

$$Z^{(2)}(x, y, T_i, T_j, \phi) = \max\{\|x - y, a\| + \phi(x) + \phi(y), \|x - T_i x, a\| + \phi(x) + \phi(T_i x), \|y - T_j y, a\| + \phi(y) + \phi(T_j y)\} \quad (3)$$

And $\phi: X \rightarrow [0, \infty)$ is a lower semi continuous function.

Then there exists a unique $z \in X$ such that $z = T_i z, \forall i = 1, 2, 3, \dots$ and $\phi(z) = 0$.

Proof: Let $x_0 \in X$ be a point and we define a sequence $\{x_n\}_{n=1}^{\infty} \subset X$ by

$$x_{n+1} = T_i x_n \quad \forall i = 1, 2, 3, \dots$$

Consider two cases:

Case-I: Let $\{x_n\}$ be periodic.

subcase-I.I: If for some $n \in N, x_n = x_{n+1}$, then $x_n = T_i x_n$ and hence x_n is a fixed point of $T_i \quad \forall i = 1, 2, 3, \dots$

subcase-I.II: If for some $n \in N, x_n = x_{n+p}$, for $p = 2, 3, \dots$, then $T_i^{p-1} x_n$ is a fixed point of T_i .

For $p = 2, x_n = x_{n+2}$, then $T_i x_n$ is a fixed point of T_i i.e., $T_i(x_n) = T_i(T_i(x_n))$, i.e., $x_{n+1} = x_{n+2}$

If not then, $\|x_{n+1} - x_{n+2}, a\| > 0, \quad \forall a \in X$.

From (2) we have,

$$Z^{(1)}(x_n, x_{n+1}, T_i, T_j, \phi)$$

$$= \max\{ ||x_n - x_{n+1}, a|| + \phi(x_n) + \phi(x_{n+1}), ||x_n - x_{n+1}, a|| + \phi(x_n) + \phi(x_{n+1}), ||x_{n+1} - x_{n+2}, a|| + \phi(x_{n+1}) + \phi(x_{n+2}), \frac{1}{2}\{||x_n - x_{n+1}, a|| + \phi(x_n) + \phi(x_{n+1}), ||x_{n+1} - x_{n+2}, a|| + \phi(x_{n+1}) + \phi(x_{n+2})\}\}$$

$$= \{||x_n - x_{n+1}, a|| + \phi(x_n) + \phi(x_{n+1})\}, \quad [as \ x_n = x_{n+2}]$$

and

$$Z^{(2)}(x_n, x_{n+1}, T_i, T_j, \phi) = \max\{ ||x_n - x_{n+1}, a|| + \phi(x_n) + \phi(x_{n+1}), ||x_n - x_{n+1}, a|| + \phi(x_n) + \phi(x_{n+1}), ||x_{n+1} - x_{n+2}, a|| + \phi(x_{n+1}) + \phi(x_{n+2}), \}$$

$$= \{||x_n - x_{n+1}, a|| + \phi(x_n) + \phi(x_{n+1})\} \quad [as \ x_n = x_{n+2}]$$

Therefore, by (1) we obtain

$$\begin{aligned} & \psi\{||x_{n+1} - x_{n+2}, a|| + \phi(x_{n+1}) + \phi(x_{n+2})\} \\ &= \psi\{||T_i x_n - T_j x_{n+1}, a|| + \phi(T_i x_n) + \phi(T_j x_{n+1})\} \\ &\leq \psi\{||x_n - x_{n+1}, a|| + \phi(x_n) + \phi(x_{n+1})\} - \phi\{||x_n - x_{n+1}, a|| + \phi(x_n) + \phi(x_{n+1})\}, \end{aligned}$$

which gives $\psi\{||x_{n+1} - x_n, a|| + \phi(x_{n+1}) + \phi(x_n)\} < \psi\{||x_n - x_{n+1}, a|| + \phi(x_n) + \phi(x_{n+1})\}$, which is a contradiction.

Hence, $T_i(T_i x_n) = T_i x_n$ i.e., $T_i x_n$ is a fixed point of $T_i, \forall i = 1, 2, 3, \dots$

Therefore the statement is true for $p = 2$.

Assume that the statement is true for $p = m, m \geq 2$, i.e., $T_i^{m-1} x_n$ is a fixed point of T_i .

$$Then \quad T_i^m x_n = T_i^{m-1} x_n \tag{4}$$

Applying T_i on both sides of (4), we get

$$T_i(T_i^m x_n) = T_i(T_i^{m-1} x_n) \quad \text{i.e.,} \quad T_i(T_i^m x_n) = T_i^m x_n.$$

Hence, $T_i^m x_n$ is a fixed point of T_i . Therefore the statement is true for $p = m + 1$.

Thus by the Principle of Mathematical Induction if $x_n = x_{n+p}$, then x_n is a fixed point of T_i , for $p = 1, 2, 3, \dots$

Case-II: Assume $x_n \neq x_{n+1}$, for all $n \in N$. Now from (2) we have

$$\begin{aligned} & Z^{(1)}(x_{n-1}, x_n, T_i, T_j, \phi) \\ &= \max\{||x_{n-1} - x_n, a|| + \phi(x_{n-1}) + \phi(x_n), ||x_{n-1} - x_n, a|| + \phi(x_{n-1}) + \phi(x_n), ||x_n - x_{n+1}, a|| + \phi(x_n) + \phi(x_{n+1}), \\ & \frac{1}{2}\{||x_{n-1} - x_n, a|| + \phi(x_{n-1}) + \phi(x_n) + ||x_n - x_{n+1}, a|| + \phi(x_n) + \phi(x_{n+1})\}\} \\ &= \max\{||x_{n-1} - x_n, a|| + \phi(x_{n-1}) + \phi(x_n), ||x_n - x_{n+1}, a|| + \phi(x_n) + \phi(x_{n+1})\} \\ & \phi(x_{n+1}) \} \end{aligned} \tag{5}$$

And from (3) we

$$Z^{(2)}(x_{n-1}, x_n, T_i, T_j, \phi) = \max\{||x_{n-1} - x_n, a|| + \phi(x_{n-1}) + \phi(x_n), ||x_{n-1} - x_n, a|| + \phi(x_{n-1}) + \phi(x_n), ||x_n - x_{n+1}, a|| + \phi(x_n) + \phi(x_{n+1})\}$$

$$= \max\{||x_{n-1} - x_n, a|| + \phi(x_{n-1}) + \phi(x_n), ||x_n - x_{n+1}, a|| + \phi(x_n) + \phi(x_{n+1})\}$$

$$\text{If } ||x_{n-1} - x_n, a|| + \phi(x_{n-1}) + \phi(x_n) \leq ||x_n - x_{n+1}, a|| + \phi(x_n) + \phi(x_{n+1}),$$

Then from (1) we get

$$\psi\{||x_n - x_{n+1}, a|| + \phi(x_n) + \phi(x_{n+1})\} \leq \psi\{||x_n - x_{n+1}, a|| + \phi(x_n) + \phi(x_{n+1})\} - \phi\{||x_n - x_{n+1}, a|| + \phi(x_n) + \phi(x_{n+1})\},$$

Which gives $\phi\{||x_n - x_{n+1}, a|| + \phi(x_n) + \phi(x_{n+1})\} = 0$.

By definition of ϕ function we have

$$\|x_n - x_{n+1}, a\| + \phi(x_n) + \phi(x_{n+1}) = 0.$$

Hence $x_{n+1} = x_n$ and $\phi(x_{n+1}) = \phi(x_n) = 0$, which is a contradiction. Therefore,

$$\|x_n - x_{n+1}, a\| + \phi(x_n) + \phi(x_{n+1}) < \|x_{n-1} - x_n, a\| + \phi(x_{n-1}) + \phi(x_n), \forall n = 1, 2, 3, \dots \tag{7}$$

and

$$Z^{(1)}(x_{n-1}, x_n, T_i, T_j, \phi) = \|x_{n-1} - x_n, a\| + \phi(x_{n-1}) + \phi(x_n) \tag{8}$$

and

$$Z^{(2)}(x_n, x_{n+1}, T_i, T_j, \phi) = \|x_{n-1} - x_n, a\| + \phi(x_{n-1}) + \phi(x_n) \tag{9}$$

From (1) we have

$$\psi\|x_n - x_{n+1}, a\| + \phi(x_n) + \phi(x_{n+1}) \leq \psi\{\|x_{n-1} - x_n, a\| + \phi(x_{n-1}) + \phi(x_n)\} - \varphi\{\|x_{n-1} - x_n, a\| + \phi(x_{n-1}) + \phi(x_n)\} \tag{10}$$

From (7) the sequence $\{\|x_{n-1} - x_n, a\| + \phi(x_{n-1}) + \phi(x_n)\}$ is monotonic decreasing and bounded below and hence convergent.

Let

$$\lim_{n \rightarrow \infty} \{\|x_{n-1} - x_n, a\| + \phi(x_{n-1}) + \phi(x_n)\} = r$$

and $\lim_{r \rightarrow \infty} \psi\{\|x_{n-1} - x_n, a\| + \phi(x_{n-1}) + \phi(x_n)\} = r^*$, where $r, r^* \geq 0$.

Claim: $r=0$.

If $r > 0$, then taking lower limit as $n \rightarrow \infty$ on both sides of (10), we have

$$\begin{aligned} & \lim_{n \rightarrow \infty} \psi\{\|x_n - x_{n+1}, a\| + \phi(x_n) + \phi(x_{n+1})\} \\ & \leq \lim_{n \rightarrow \infty} \psi\{\|x_{n-1} - x_n, a\| + \phi(x_{n-1}) + \phi(x_n)\} - \\ & \quad \lim_{n \rightarrow \infty} \varphi\{\|x_{n-1} - x_n, a\| + \phi(x_{n-1}) + \phi(x_n)\} \\ \text{or, } & \lim_{n \rightarrow \infty} \inf \varphi\{\|x_{n-1} - x_n, a\| + \phi(x_{n-1}) + \phi(x_n)\} \leq 0, \text{ which is a contradiction as} \\ & \lim_{n \rightarrow \infty} \{\|x_{n-1} - x_n, a\| + \phi(x_{n-1}) + \phi(x_n)\} = r > 0 \Rightarrow \lim_{n \rightarrow \infty} \inf \varphi\{\|x_{n-1} - x_n, a\| + \phi(x_{n-1}) + \\ & \quad \phi(x_n)\} \leq 0. \end{aligned}$$

Therefore $\lim_{n \rightarrow \infty} \{\|x_{n-1} - x_n, a\| + \phi(x_{n-1}) + \phi(x_n)\} = 0$, which gives

$$\|x_{n-1} - x_n, a\| = 0, \text{ and } \lim_{n \rightarrow \infty} \phi(x_n) = 0.$$

Now we prove that the sequence $\{x_n\}$ is Cauchy in X .

If $\{x_n\}$ is not Cauchy, then there exist $\epsilon > 0$ and two subsequences $\{x_{m(k)}\}$ and $\{x_{n(k)}\}$ of $\{x_n\}$ with $m(k)$ is the smallest index such that $m(k) > n(k) > k$, implies

$$\|x_{m(k)-1} - x_{n(k)}, a\| \geq \epsilon,$$

and

$$\|x_{m(k)-1} - x_{n(k)}, a\| < \epsilon.$$

Now,

$$\begin{aligned} \epsilon & \leq \|x_{m(k)} - x_{n(k)}, a\| + \phi(x_{m(k)}) + \phi(x_{n(k)}) \\ & \leq \|x_{m(k)} - x_{m(k)-1}, a\| + \|x_{m(k)-1} - x_{n(k)}, a\| + \phi(x_{m(k)}) + \phi(x_{n(k)}) \\ & < \|x_{m(k)} - x_{m(k)-1}, a\| + e + \phi(x_{m(k)}) + \phi(x_{n(k)}) \end{aligned}$$

Limiting as $k \rightarrow \infty$ we have

$$\lim_{k \rightarrow \infty} \{\|x_{m(k)} - x_{n(k)}, a\| + \phi(x_{m(k)}) + \phi(x_{n(k)})\} = \epsilon.$$

From (2) we have,

$$\begin{aligned} & Z^{(1)}(x_{n(k)}, x_{m(k)}, T_i, T_j, \phi) \\ &= \max\{\|x_{n(k)} - x_{m(k)}, a\| + \phi(x_{n(k)}) + \phi(x_{m(k)}), \|x_{n(k)} - T_i x_{n(k)}, a\| \\ & \phi(x_{n(k)}) + \phi(T_i x_{n(k)}), \|x_{m(k)} - T_j x_{m(k)}, a\| + \phi(x_{m(k)}) + \phi(T_j x_{m(k)}), \\ & \frac{1}{2}\{\|x_{n(k)} - T_j x_{m(k)}, a\| + \phi(x_{n(k)}) + \phi(T_j x_{m(k)}), \|x_{m(k)} - T_i x_{n(k)}, a\| + \\ & \phi(x_{m(k)}) + \phi(T_i x_{n(k)})\} \\ &= \max\{\|x_{n(k)} - x_{m(k)}, a\| + \phi(x_{n(k)}) + \phi(x_{m(k)}), \|x_{n(k)} - x_{n(k)+1}, a\| + \\ & \phi(x_{n(k)}) + \phi(x_{n(k)+1}), \|x_{m(k)} - x_{m(k)+1}, a\| + \phi(x_{m(k)}) + \phi(x_{m(k)+1}), \\ & \frac{1}{2}\{\|x_{n(k)} - x_{m(k)+1}, a\| + \phi(x_{n(k)}) + \phi(T x_{m(k)+1}), \|x_{m(k)} - x_{n(k)+1}, a\| + \\ & \phi(x_{m(k)}) + \phi(x_{n(k)+1})\} \end{aligned}$$

Taking limit as $k \rightarrow \infty$ on both sides of (15) and using (11) and (14) we have

$$\lim_{k \rightarrow \infty} Z^{(1)}(x_{n(k)}, x_{m(k)}, T_i, T_j, \phi) = \varepsilon.$$

Also it follows from (3) that

$$\begin{aligned} & Z^{(2)}(x_n(k), x_m(k), T_i, T_j, \phi) \\ &= \max\{\|x_n(k) - x_m(k), a\| + \phi(x_n(k)) + \phi(x_m(k)), \|x_n(k) - T_i x_n(k), a\| + \\ & \phi(x_n(k)) + \phi(T_i x_n(k)), \|x_m(k) - T_j x_m(k), a\| + \phi(x_m(k)) + \phi(T_j x_m(k))\} \\ &= \max\{\|x_n(k) - x_m(k), a\| + \phi(x_n(k)) + \phi(x_m(k)), \|x_n(k) - x_{n(k)+1}, a\| + \\ & \phi(x_n(k)) + \phi(x_{n(k)+1}), \|x_m(k) - x_{m(k)+1}, a\| + \phi(x_m(k)) + \phi(x_{m(k)+1})\} \end{aligned}$$

Taking limit as $k \rightarrow \infty$ on both sides of (17) and using (11) and (14) we have

$$\lim_{k \rightarrow \infty} Z^{(2)}(x_n(k), x_m(k), T_i, T_j, \phi) = \varepsilon.$$

Also from (1) we have,

$$\begin{aligned} & \psi\{\|x_{n(k)+1} - x_{m(k)+1}, a\| + \phi(x_{n(k)+1}) + \phi(x_{m(k)+1})\} \\ & \leq \psi\{Z^{(1)}(x_n(k), x_m(k), T_i, T_j, \phi)\} - \varphi\{Z^{(2)}(x_n(k), x_m(k), T_i, T_j, \phi)\} \end{aligned}$$

Taking lower limit as $k \rightarrow \infty$ on both sides of (19) we have

$$\begin{aligned} & \lim_{n \rightarrow \infty} \psi\{\|x_{n(k)+1} - x_{m(k)+1}, a\| + \phi(x_{n(k)+1}) + \phi(x_{m(k)+1})\} \\ & \leq \lim_{n \rightarrow \infty} \psi\{Z^{(1)}(x_n(k), x_m(k), T_i, T_j, \phi)\} - \liminf_{n \rightarrow \infty} \varphi\{Z^{(2)}(x_n(k), x_m(k), T_i, T_j, \phi)\}, \end{aligned}$$

[using (14) and (16)]

Which gives $\lim_{k \rightarrow \infty} Z^{(2)}(x_n(k), x_m(k), T_i, T_j, \phi) \leq 0$ which is a contradiction as

$$\lim_{k \rightarrow \infty} Z^{(2)}(x_n(k), x_m(k), T_i, T_j, \phi) = \varepsilon.$$

Hence $\{x_n\}$ is a Cauchy in X .

Since X is complete, there exist $z \in X$ such that $\lim_{n \rightarrow \infty} x_n = z$.

Since ϕ is lower semi-continuous, $\phi(z) \leq \liminf_{n \rightarrow \infty} \phi(x_n) \leq \lim_{n \rightarrow \infty} \phi(x_n) = 0$, which gives $\phi(z) = 0$.

Claim: $T_i(z) = z, \forall i = 1, 2, 3, \dots$

Now from (2) we have

$$Z^{(2)}(x_n(k), x_m(k), T_i, T_j, \phi)$$

$$= \max\{\|x_n - z, a\| + \phi(x_n) + \phi(z), \|x_n - T_i x_n, a\| + \phi(x_n) + \phi(T_i x_n), \|z - T_j z, a\| + \phi(z) + \phi(T_j z), \frac{1}{2}\{\|x_n - T_j z, a\| + \phi(x_n) + \phi(T_j z) + \|z - T_j x_n, a\| + \phi(z) + \phi(T_i x_n)\}\} \tag{20}$$

Taking lower as $n \rightarrow \infty$ on both side of (20) we have

$$\lim_{n \rightarrow \infty} Z^{(1)}(x_n, z, T_i, T_j, \phi) = \|z - T_j z, a\| + \phi(T_j z) \tag{21}$$

Also from (3)

$$Z^{(2)}(x_n, z, T_i, T_j, \phi) = \max\{\|x_n - z, a\| + \phi(x_n) + \phi(z), \|x_n - T_j z, a\| + \phi(x_n) + \phi(T_j z), \|z - T_j z, a\| + \phi(T_j z) + \phi(z)\} \tag{22}$$

Limiting as $n \rightarrow \infty$ on the both side of (22) we have

$$\lim_{n \rightarrow \infty} Z^{(2)}(x_n, z, T_i, T_j, \phi) = \|z - T_j z, a\| + \phi(T_j z) \tag{23}$$

Now from (1), we have

$$\begin{aligned} & \psi\{\|x_{n+1} - T_j z, a\| + \phi(x_{n+1}) + \phi(T_j z)\} \\ &= \psi\{\|T_i x_n - T_j z, a\| + \phi(T_i x_n) + \phi(T_j z)\} \\ & \leq \psi\{Z^{(1)}(x_n, z, T_i, T_j, \phi)\} - \phi\{Z^{(2)}(x_n, z, T_i, T_j, \phi)\} \end{aligned} \tag{24}$$

Taking lower limit as $n \rightarrow \infty$ on both side of (24) we have

$$\begin{aligned} & \lim_{n \rightarrow \infty} \psi\{\|x_{n+1} - T_j z, a\| + \phi(x_{n+1}) + \phi(T_j z)\} \\ &= \lim_{n \rightarrow \infty} \psi\{\|T_i x_n - T_j z, a\| + \phi(T_i x_n) + \phi(T_j z)\} \\ & \leq \lim_{n \rightarrow \infty} \psi\{Z^{(1)}(x_n, z, T_i, T_j, \phi)\} - \lim_{n \rightarrow \infty} \inf \phi\{Z^{(2)}(x_n, z, T_i, T_j, \phi)\} \end{aligned}$$

$$\text{Or, } \lim_{n \rightarrow \infty} \psi\{\|x_{n+1} - T_j z, a\| + \phi(x_{n+1}) + \phi(T_j z)\} \leq \lim_{n \rightarrow \infty} \psi\{Z^{(1)}(x_n, z, T_i, T_j, \phi)\} - \lim_{n \rightarrow \infty} \inf \phi\{Z^{(2)}(x_n, z, T_i, T_j, \phi)\},$$

$$[\text{As } \lim_{n \rightarrow \infty} Z^{(1)}(x_n, z, T_i, T_j, \phi) = \|z - T_j z, a\| + \phi(T_j z) = \lim_{n \rightarrow \infty} \{\|x_{n+1} - T_j z, a\| + \phi(x_{n+1}) + \phi(T_j z)\}]$$

which gives $\lim_{n \rightarrow \infty} \inf \psi\{Z^{(2)}(x_n, z, T_i, T_j, \phi)\} \leq 0$, which is a contradiction.

[As $\lim_{n \rightarrow \infty} \psi\{Z^{(2)}(x_n, z, T_i, T_j, \phi)\} > 0$ implies $\lim_{n \rightarrow \infty} \inf \phi\{Z^{(2)}(x_n, z, T_i, T_j, \phi)\} > 0$.]

Hence $T_i(z) = z \quad \forall i = 1, 2, 3, \dots$

Uniqueness: To prove the uniqueness , let us assume that u and z be two fixed points of T_i i.e., $T_i z = z$ and $T_i u = u$ with $\phi(z) = 0, \phi(u) = 0$ such that $z \neq u$.

Then from (2) we have

$$\begin{aligned} Z^{(1)}(z, u, T_i, T_j, \phi) &= \max\{\|z - u, a\| + \phi(z) + \phi(u), \|z - T_j u, a\| + \phi(u) + \\ & \quad \phi(T_j u), \frac{1}{2}\{\|u - T_j u, a\| + \phi(T_j z) + \phi(u)\}\} \\ &= \|z - u, a\| + \phi(z) + \phi(u) \\ &= \|z - u, a\| \end{aligned} \tag{25}$$

And from (3) we have

$$\begin{aligned} Z^{(2)}(z, u, T_i, T_j, \phi) &= \max\{\|z - u, a\| + \phi(z) + \phi(u), \|z - T_j u, a\| + \phi(z) + \\ & \quad \phi(T_j u), \|u - T_j z, a\| + \phi(T_j z) + \phi(u)\} \\ &= \|z - u, a\| + \phi(z) + \phi(u) \\ &= \|z - u, a\| \end{aligned} \tag{26}$$

Also from (1) we have

$$\begin{aligned} \psi\{\|z - u, a\| + \phi(z) + \phi(u)\} &= \psi\{\|T_i z - T_j u, a\|\} + \phi(T_i z) + \phi(T_j u) \\ &\leq \psi\{Z^{(1)}(z, u, T_i, T_j, \phi)\} - \phi\{Z^{(2)}(z, u, T_i, T_j, \phi)\} \\ &= \psi\{\|z - u, a\|\} - \phi\{\|z - u, a\|\}, \end{aligned}$$

which gives $\phi\{\|z - u, a\|\} \leq 0$, which is a contradiction as $\phi\{\|z - u, a\|\} > 0$.

Hence $z = u$.

This completes the proof.

Corollary 1 Let $(X, \|\cdot, \cdot\|)$ be a 2-Banach space and $\{T_i\}_{i=1}^\infty$ be a sequence of self maps on X satisfying the following conditions:

$$\begin{aligned} &\psi\{\|T_i^k x - T_j^k y, a\| + \phi(T_i^k x) + \phi(T_j^k y)\} \\ &\leq \psi\{Z^{(1)}(x, y, T_i^k, T_j^k, \phi)\} - \phi\{Z^{(2)}(x, y, T_i^k, T_j^k, \phi)\}, \quad \forall x, y \in X, \\ &\psi \in \Psi, \phi \in \Phi; \end{aligned}$$

where,

$$\begin{aligned} Z^{(1)}(x, y, T_i^k, T_j^k, \phi) &= \max\{\|x - y, a\| + \phi(x) + \phi(y), \|x - T_i^k x, a\| + \phi(x) + \phi(T_i^k x), \|y - T_j^k y, a\| + \phi(y) \\ &+ \phi(T_j^k y), \frac{1}{2}\{\|x - T_j^k y, a\| + \phi(x) + \phi(T_j^k y) + \|y - T_i^k x, a\| + \phi(y) \\ &+ \phi(T_i^k x)\}\} \\ Z^{(2)}(x, y, T_i^k, T_j^k, \phi) &= \max\{\|x - y, a\| + \phi(x) + \phi(y), \|x - T_i^k x, a\| + \phi(x) \\ &+ \phi(T_i^k x), \|y - T_j^k y, a\| + \phi(y) + \phi(T_j^k y)\} \end{aligned}$$

and $\phi : X \rightarrow [0, \infty)$ is a lower semi continuous function.

Then there exists a unique $z \in X$ such that $z = T_i z, \forall i = 1, 2, 3, \dots$ and $\phi(z) = 0$.

Proof: Let $S_i = T_i^k$. Then by Theorem 2.1, the sequence $\{S_i\}_{i=1}^\infty$ have a unique fixed point, say $z \in X$. $T_i^k z = S_i z = z$. Then $\phi(z) = \phi(T_i^k z) = \phi(S_i z) = 0$.

Since $T_i^{k+1} z = T_i z$, then $S_i(T_i z) = T_i^k(T_i z)$, so $T_i z$ is a fixed point of S_i .

By the uniqueness of the fixed point of $S_i, T_i z = z, \forall i = 1, 2, 3, \dots$

Corollary 2 Let $(X, \|\cdot, \cdot\|)$ be a 2-Banach space and T_1, T_2 be two self maps on X satisfying the following conditions:

$$\psi\{\|T_1 x - T_2 y, a\| + \phi(T_1 x) + \phi(T_2 y)\} \leq \psi\{Z^{(1)}(x, y, T_1, T_2, \phi)\} - \phi\{Z^{(2)}(x, y, T_1, T_2, \phi)\}, \quad \forall x, y \in X, \psi \in \Psi, \phi \in \Phi;$$

where,

$$\begin{aligned} Z^{(1)}(x, y, T_1, T_2, \phi) &= \max\{\|x - y, a\| + \phi(x) + \phi(y), \|x - T_1 x, a\| + \phi(x) + \phi(T_1 x), \|y - T_2 y, a\| + \phi(y) + \\ &\phi(T_2 y), \frac{1}{2}\{\|x - T_2 y, a\| + \phi(x) + \phi(T_2 y) + \|y - T_1 x, a\| + \phi(y) + \phi(T_1 x)\}\} \end{aligned}$$

$$Z^{(2)}(x, y, T_1, T_2, \phi) = \max\{\|x - y, a\| + \phi(x) + \phi(y), \|x - T_1 x, a\| + \phi(x) + \phi(T_1 x), \|y - T_2 y, a\| + \phi(y) + \phi(T_2 y)\}$$

And $\phi : X \rightarrow [0, \infty)$ is a lower semi continuous function.

Then there exists a unique $z \in X$ such that $T_1 z = T_2 z = z$ with $\phi(z) = 0$.

Acknowledgment

The authors would like to express their sincere thanks to the editor and the anonymous reviewers for their helpful comments and suggestion to improve the paper.

Conflicts of interest

There are no conflicts of interest in this work.

References

- [1] Abbas M., Nazir T., Radenovic S., Common fixed points of four maps in partially ordered metric spaces, *Applied Mathematics Letters*, 24 (2011) 1520-1526.
- [2] Cho S., Fixed point theorems for generalized weakly contractive mappings in metric spaces with applications, *Fixed Point Theory and Applications*, (2018) Article number 3(2018).
- [3] Gahler S., Linear 2 normierte Raume., *Math. Nachr.*, 28(1965) 1-43.
- [4] Liu B., Chai G.Q., Fixed point theorem for weakly contractive mappings in generalized metric spaces, *Hubei Shifan Xueyuan Xuebao*, 33(1) (2013) 60-65.
- [5] Xue Z., Lv G., A fixed point theorem for generalized (ψ, ϕ) -weak contractions in Branciari-type generalized metric spaces, *Fixed Point Theory and Algorithms for Sciences and Engineering*, (2021) Article number 1(2021).
- [6] Kumar D.R., Pitchaimani M., Approximation of common fixed points in 2-Banach spaces with applications, *Appl. Gen. Topol.*, 20(1) (2019) 43-55.
- [7] Pitchaimani M., Kumar D.R., Some common fixed point theorems using implicit relation in 2-Banach spaces, *Surveys in Mathematics and its Applications*, 10 (2015) 159-168.
- [8] Chouhan P., Malviya N., Fixed point of expansive mappings in 2-Banach Spaces, *International Journal of Analysis and Applications*, 3(1) (2013) 60-67.



Generalized Gamma, Beta and Hypergeometric Functions Defined by Wright Function and Applications to Fractional Differential Equations

Enes Ata ^{1,a,*}, İsmail Onur Kıymaz ^{1,b}

¹Department of Mathematics, Faculty of Arts and Science, Kırşehir Ahi Evran University, Kırşehir, Türkiye.

*Corresponding author

Research Article

History

Received: 06/10/2021

Accepted: 30/11/2022

Copyright



©2022 Faculty of Science,
Sivas Cumhuriyet University

ABSTRACT

When the literature is examined, it is seen that there are many studies on the generalizations of gamma, beta and hypergeometric functions. In this paper, new types of generalized gamma and beta functions are defined and examined using the Wright function. With the help of generalized beta function, new type of generalized Gauss and confluent hypergeometric functions are obtained. Furthermore, some properties of these functions such as integral representations, derivative formulas, Mellin transforms, Laplace transforms and transform formulas are determined. As examples, we obtained the solution of fractional differential equations involving the new generalized beta, Gauss hypergeometric and confluent hypergeometric functions. Finally, we presented their relationship with other generalized gamma, beta, Gauss hypergeometric and confluent hypergeometric functions, which can be found in the literature.

Keywords: Beta function, Wright function, Gauss hypergeometric function, Laplace transform, Fractional differential equation

enesata.tr@gmail.com

<https://orcid.org/0000-0001-6893-8693>

iokiymaz@ahievran.edu.tr

<https://orcid.org/0000-0003-2375-0202>

Introduction

Gamma and beta functions are very useful special functions in many sciences such as mathematics, physics, chemistry, biology, medicine and engineering. These functions have been the focus of attention of researchers due to their popularity. When the literature is examined, it is seen that the generalized gamma and beta functions are mostly obtained by using appropriate kernel functions in the integral representations of the original functions. For instance, generalized gamma and beta functions are defined by using exponential, confluent hypergeometric and Mittag-Leffler functions etc. as kernel functions in their integral representations. Gamma and beta functions can also be written using the Pochhammer symbol. Series representations of hypergeometric functions are also associated with the Pochhammer symbol. Many researchers have defined various generalizations for hypergeometric functions by making use of these relations. Historically, these generalizations began in 1994 and 1997 when Chaudhry et al., [1,2] selected exponential functions as the kernel of integral representations of original gamma and beta functions. Many researchers defined new generalizations of these functions inspired by the work of Chaudhry et al., (see for example [1-24] and reference therein).

All the studies mentioned above motivated us to describe a new generalization of gamma and beta functions. For this, we used the Wright function, which has a more general form than many special functions. We also defined the generalized Gauss and confluent hypergeometric functions with the help of generalized beta function. Then we presented some properties of these new functions. As examples, we obtained the solution of fractional differential equations involving the

new generalized beta, Gauss hypergeometric and confluent hypergeometric functions.

Preliminaries

In this section, we gave some preliminary information that is needed throughout this paper. Then we mentioned the generalized gamma, beta, Gauss hypergeometric, and confluent hypergeometric functions defined by Chaudhry et al.. Firstly we gave the Mellin, inverse Mellin, Laplace, inverse Laplace integral transformations and the Caputo fractional derivative operator below. The Mellin and inverse Mellin transforms [25] for $s \in \mathbb{C}$ respectively are defined by

$$\mathfrak{M}\{f(p)\} = F(s) = \int_0^{\infty} p^{s-1} f(p) dp,$$

and

$$\mathfrak{M}^{-1}\{F(s)\} = \frac{1}{2\pi i} \int_{c-i\infty}^{c+i\infty} p^{-s} F(s) ds, \quad (c > 0).$$

The Laplace and inverse Laplace transforms [25] for $Re(s) > 0$ respectively are given by

$$\mathfrak{L}\{f(p)\} = F(s) = \int_0^{\infty} \exp(-sp) f(p) dp,$$

and

$$\mathfrak{L}^{-1}\{F(s)\} = \frac{1}{2\pi i} \int_{c-i\infty}^{c+i\infty} \exp(sp) F(s) ds, \quad (c > 0).$$

The Caputo fractional derivative operator [26] of order $\varepsilon \in \mathbb{C}$ for $m \in \mathbb{N}$, $m - 1 < Re(\varepsilon) < m$ is given by

$${}^c D_p^\varepsilon [f(p)] = \frac{1}{\Gamma(m-\varepsilon)} \int_0^p (p-t)^{m-\varepsilon-1} f^{(m)}(t) dt, \quad (Re(\varepsilon) > 0; p > 0).$$

Also, Laplace transform of Caputo fractional derivative for $m \in N, m - 1 < Re(\varepsilon) \leq m$ as follows [26]:

$$\mathfrak{L}\{ {}^c D_p^\varepsilon [f(p)] \} = s^\varepsilon F(s) - \sum_{k=0}^{m-1} s^{\varepsilon-k-1} f^{(k)}(0). \tag{1}$$

We presented the generalized gamma, beta, Gauss hypergeometric, and confluent hypergeometric functions defined by Chaudhry et al. chronologically below.

In 1994, Chaudhry and Zubair [1] gave the extended gamma function for $Re(x) > 0, Re(p) > 0$ as follows:

$$\Gamma_p(x) = \int_0^\infty t^{x-1} \exp\left(-t - \frac{p}{t}\right) dt.$$

In 1997, Chaudhry et al. [2] gave the extended beta function for $Re(x) > 0, Re(y) > 0, Re(p) > 0$ as follows:

$$B(x, y; p) = \int_0^1 t^{x-1} (1-t)^{y-1} \exp\left(-\frac{p}{t(1-t)}\right) dt.$$

In 2004, Chaudhry et al. [3] gave the extended Gauss and confluent hypergeometric functions respectively as:

$$F_p(a, b; c; z) = \sum_{n=0}^\infty (a)_n \frac{B(b+n, c-b; p) z^n}{B(b, c-b) n!}$$

$$(p \geq 0; |z| < 1; Re(c) > Re(b) > 0),$$

and

$$\Phi_p(b; c; z) = \sum_{n=0}^\infty \frac{B(b+n, c-b; p) z^n}{B(b, c-b) n!}$$

$$(p \geq 0; Re(c) > Re(b) > 0).$$

Here, value expressed by $(\lambda)_n$ is the Pochhammer symbol [28] and is given as follows:

$$(\lambda)_0 \equiv 1 \text{ and } (\lambda)_n = \frac{\Gamma(\lambda+n)}{\Gamma(\lambda)}, \quad (Re(\lambda) > -n; n \in N; \lambda \neq 0, -1, -2, \dots).$$

The integral representations of the above series are as follows, respectively:

$$F_p(a, b; c; z) = \frac{1}{B(b, c-b)} \int_0^1 t^{b-1} (1-t)^{c-b-1} (1-zt)^{-a} \exp\left(-\frac{p}{t(1-t)}\right) dt,$$

$$(p > 0; p = 0 \text{ and } |arg(1-z)| < \pi; Re(c) > Re(b) > 0),$$

and

$$\Phi_p(b; c; z) = \frac{1}{B(b, c-b)} \int_0^1 t^{b-1} (1-t)^{c-b-1} \exp\left(zt - \frac{p}{t(1-t)}\right) dt,$$

$$(p > 0; p = 0 \text{ and } Re(c) > Re(b) > 0).$$

In this paper, we use Wright function to define new generalizations of gamma and beta functions, which defined in [28] as:

$${}_0\Psi_1(\alpha, \beta; z) = \sum_{n=0}^\infty \frac{1}{\Gamma(\alpha n + \beta)} \frac{z^n}{n!}$$

where $\alpha, \beta \in \mathbb{C}$ and $Re(\alpha) > -1$.

New Generalized Gamma and Beta Functions

In this section, we introduced new generalized gamma and beta functions and presented some of their properties.

Definition 1. The new generalized gamma and beta functions for $Re(x) > 0$, $Re(y) > 0$, $Re(\alpha) > -1$, $Re(p) > 0$, respectively are defined by

$${}^{\Psi}\Gamma_p^{(\alpha,\beta)}(x) = \int_0^{\infty} t^{x-1} {}_0\Psi_1\left(\alpha, \beta; -t - \frac{p}{t}\right) dt, \quad (2)$$

and

$${}^{\Psi}B_p^{(\alpha,\beta)}(x, y) = \int_0^1 t^{x-1}(1-t)^{y-1} {}_0\Psi_1\left(\alpha, \beta; -\frac{p}{t(1-t)}\right) dt. \quad (3)$$

We call the new generalizations of gamma and beta functions as Ψ -gamma and Ψ -beta functions, respectively.

Theorem 1. Let $Re(s) > 0$, $Re(x+s) > 0$, $Re(y+s) > 0$, $Re(p) > 0$, $Re(\alpha) > -1$. Then,

$$\mathfrak{M}\left\{{}^{\Psi}B_p^{(\alpha,\beta)}(x, y)\right\} = B(x+s, y+s) {}^{\Psi}\Gamma^{(\alpha,\beta)}(s).$$

Proof. Multiplying the equation (3) by p^{s-1} and integrating from $p = 0$ to $p = \infty$, we have

$$\mathfrak{M}\left\{{}^{\Psi}B_p^{(\alpha,\beta)}(x, y)\right\} = \int_0^{\infty} p^{s-1} \int_0^1 t^{x-1}(1-t)^{y-1} {}_0\Psi_1\left(\alpha, \beta; -\frac{p}{t(1-t)}\right) dt dp.$$

By interchanging the integrals, we get

$$\mathfrak{M}\left\{{}^{\Psi}B_p^{(\alpha,\beta)}(x, y)\right\} = \int_0^1 t^{x-1}(1-t)^{y-1} \int_0^{\infty} p^{s-1} {}_0\Psi_1\left(\alpha, \beta; -\frac{p}{t(1-t)}\right) dp dt.$$

By substituting $v = \frac{p}{t(1-t)}$, we obtain

$$\begin{aligned} \mathfrak{M}\left\{{}^{\Psi}B_p^{(\alpha,\beta)}(x, y)\right\} &= \int_0^1 t^{x+s-1}(1-t)^{y+s-1} dt \int_0^{\infty} v^{s-1} {}_0\Psi_1(\alpha, \beta; -v) dv \\ &= B(x+s, y+s) {}^{\Psi}\Gamma^{(\alpha,\beta)}(s). \end{aligned}$$

Corollary 1. The inverse Mellin transform of the above equation is obtained as:

$${}^{\Psi}B_p^{(\alpha,\beta)}(x, y) = \frac{1}{2\pi i} \int_{c-i\infty}^{c+i\infty} B(x+s, y+s) {}^{\Psi}\Gamma^{(\alpha,\beta)}(s) p^{-s} ds, \quad (c > 0).$$

Theorem 2. Let $Re(x) > 0$, $Re(y) > 0$, $Re(p) > 0$, $Re(s) > 0$, $Re(\alpha) > -1$. Then,

$$\mathfrak{L}\left\{{}^{\Psi}B_p^{(\alpha,\beta)}(x, y)\right\} = \frac{1}{s} {}^{\Psi}B_{\frac{1}{s}}\left[\begin{matrix} (1,1)_{1,1} \\ (\beta, \alpha)_{1,1} \end{matrix} \middle| x, y\right].$$

Proof. Applying the Laplace transform to the Ψ -beta function, we have

$$\begin{aligned} \mathfrak{L}\left\{{}^{\Psi}B_p^{(\alpha,\beta)}(x, y)\right\} &= \int_0^{\infty} \exp(-sp) {}^{\Psi}B_p^{(\alpha,\beta)}(x, y) dp \\ &= \int_0^1 t^{x-1}(1-t)^{y-1} \int_0^{\infty} \exp(-sp) {}_0\Psi_1\left(\alpha, \beta; -\frac{p}{t(1-t)}\right) dp dt \\ &= \int_0^1 t^{x-1}(1-t)^{y-1} \int_0^{\infty} \exp(-sp) \sum_{n=0}^{\infty} \frac{1}{\Gamma(\alpha n + \beta)} \frac{\left(-\frac{p}{t(1-t)}\right)^n}{n!} dp dt \end{aligned}$$

$$\begin{aligned}
 &= \frac{1}{s} \int_0^1 t^{x-1} (1-t)^{y-1} \sum_{n=0}^{\infty} \frac{\left(-\frac{1}{s}\right)^n}{\Gamma(\alpha n + \beta)} dt \\
 &= \frac{1}{s} {}^{\psi} B_{\frac{1}{s}} \left[\begin{matrix} (1,1)_{1,1} \\ (\beta, \alpha)_{1,1} \end{matrix} \middle| x, y \right].
 \end{aligned}$$

Corollary 2. The inverse Laplace transform of the above equation is obtained as:

$${}^{\psi} B_p^{(\alpha, \beta)}(x, y) = \frac{1}{2\pi i} \int_{c-i\infty}^{c+i\infty} \exp(sp) \frac{1}{s} {}^{\psi} B_{\frac{1}{s}} \left[\begin{matrix} (1,1)_{1,1} \\ (\beta, \alpha)_{1,1} \end{matrix} \middle| x, y \right] ds, \quad (c > 0).$$

Remark 1. Note that, ${}^{\psi} B_{\frac{1}{s}} \left[\begin{matrix} (1,1)_{1,1} \\ (\beta, \alpha)_{1,1} \end{matrix} \middle| x, y \right]$ is special case of the generalized beta function defined by Ata and Kıymaz [4].

Theorem 3. Let $Re(x) > 0, Re(y) > 0, Re(p) > 0, Re(\alpha) > -1$. Then,

$$\begin{aligned}
 {}^{\psi} B_p^{(\alpha, \beta)}(x, y) &= 2 \int_0^{\frac{\pi}{2}} \cos^{2x-1}(\theta) \sin^{2y-1}(\theta) {}_0\Psi_1(\alpha, \beta; -p \sec^2(\theta) \csc^2(\theta)) d\theta, \\
 {}^{\psi} B_p^{(\alpha, \beta)}(x, y) &= \int_0^{\infty} \frac{u^{x-1}}{(1+u)^{x+y}} {}_0\Psi_1\left(\alpha, \beta; -2p - p\left(u + \frac{1}{u}\right)\right) du.
 \end{aligned}$$

Proof. The desired results are obtained by putting $t = \cos^2(\theta)$ and $t = \frac{u}{1+u}$ in equation (3), respectively.

Theorem 4. Let $Re(x) > 0, Re(y) > 0, Re(p) > 0, Re(s) > 0, Re(\alpha) > -1$. Then,

$${}^{\psi} B_p^{(\alpha, \beta)}(x, y + 1) + {}^{\psi} B_p^{(\alpha, \beta)}(x + 1, y) = {}^{\psi} B_p^{(\alpha, \beta)}(x, y).$$

Proof. By making the necessary calculations, we get

$$\begin{aligned}
 &{}^{\psi} B_p^{(\alpha, \beta)}(x, y + 1) + {}^{\psi} B_p^{(\alpha, \beta)}(x + 1, y) \\
 &= \int_0^1 t^{x-1} (1-t)^y {}_0\Psi_1\left(\alpha, \beta; -\frac{p}{t(1-t)}\right) dt + \int_0^1 t^x (1-t)^{y-1} {}_0\Psi_1\left(\alpha, \beta; -\frac{p}{t(1-t)}\right) dt \\
 &= \int_0^1 (t^{x-1} (1-t)^y + t^x (1-t)^{y-1}) {}_0\Psi_1\left(\alpha, \beta; -\frac{p}{t(1-t)}\right) dt \\
 &= \int_0^1 t^{x-1} (1-t)^{y-1} {}_0\Psi_1\left(\alpha, \beta; -\frac{p}{t(1-t)}\right) dt \\
 &= {}^{\psi} B_p^{(\alpha, \beta)}(x, y).
 \end{aligned}$$

Theorem 5. Let $Re(x) > 0, Re(y) > 0, Re(p) > 0, Re(\alpha) > -1$. Then,

$$\begin{aligned}
 {}^{\psi} \Gamma_p^{(\alpha, \beta)}(x) {}^{\psi} \Gamma_p^{(\alpha, \beta)}(y) &= 4 \int_0^{\frac{\pi}{2}} \int_0^{\infty} r^{2(x+y)-1} \cos^{2x-1}(\theta) \sin^{2y-1}(\theta) \\
 &\quad \times {}_0\Psi_1\left(\alpha, \beta; -r^2 \cos^2(\theta) - \frac{p}{r^2 \cos^2(\theta)}\right) \\
 &\quad \times {}_0\Psi_1\left(\alpha, \beta; -r^2 \sin^2(\theta) - \frac{p}{r^2 \sin^2(\theta)}\right) dr d\theta.
 \end{aligned}$$

Proof. By writing $t = \eta^2$ in (2), we have

$${}^{\Psi}\Gamma_p^{(\alpha,\beta)}(x) = 2 \int_0^{\infty} \eta^{2x-1} {}_0\Psi_1\left(\alpha, \beta; -\eta^2 - \frac{p}{\eta^2}\right) d\eta.$$

Therefore,

$${}^{\Psi}\Gamma_p^{(\alpha,\beta)}(x) {}^{\Psi}\Gamma_p^{(\alpha,\beta)}(y) = 4 \int_0^{\infty} \int_0^{\infty} \eta^{2x-1} \xi^{2y-1} {}_0\Psi_1\left(\alpha, \beta; -\eta^2 - \frac{p}{\eta^2}\right) {}_0\Psi_1\left(\alpha, \beta; -\xi^2 - \frac{p}{\xi^2}\right) d\eta d\xi.$$

Taking $\eta = r\cos(\theta)$ and $\xi = r\sin(\theta)$, the desired result is obtained.

Theorem 6. Let $Re(x) > 0, Re(y) < 1, Re(p) > 0, Re(\alpha) > -1$. Then,

$${}^{\Psi}B_p^{(\alpha,\beta)}(x, 1-y) = \sum_{n=0}^{\infty} \frac{(y)_n}{n!} {}^{\Psi}B_p^{(\alpha,\beta)}(x+n, 1).$$

Proof. Using equation (3), we have

$${}^{\Psi}B_p^{(\alpha,\beta)}(x, 1-y) = \int_0^1 t^{x-1} (1-t)^{-y} {}_0\Psi_1\left(\alpha, \beta; -\frac{p}{t(1-t)}\right) dt.$$

The binomial series is as follows:

$$(1-t)^{-y} = \sum_{n=0}^{\infty} (y)_n \frac{t^n}{n!} \quad (|t| < 1).$$

Considering binomial series and interchanging summation and integration, we get

$$\begin{aligned} {}^{\Psi}B_p^{(\alpha,\beta)}(x, 1-y) &= \sum_{n=0}^{\infty} \frac{(y)_n}{n!} \int_0^1 t^{x+n-1} {}_0\Psi_1\left(\alpha, \beta; -\frac{p}{t(1-t)}\right) dt \\ &= \sum_{n=0}^{\infty} \frac{(y)_n}{n!} {}^{\Psi}B_p^{(\alpha,\beta)}(x+n, 1). \end{aligned}$$

New Generalized Gauss and Confluent Hypergeometric Functions

In this section, we introduced new generalized Gauss and confluent hypergeometric functions and presented some of their properties.

Definition 2. The new generalized Gauss and confluent hypergeometric functions for $Re(c) > Re(b) > 0, Re(p) > 0, Re(\alpha) > -1$, respectively are defined by

$${}^{\Psi}F_p^{(\alpha,\beta)}(a, b; c; z) = \sum_{n=0}^{\infty} (a)_n \frac{{}^{\Psi}B_p^{(\alpha,\beta)}(b+n, c-b) z^n}{B(b, c-b) n!}, \quad (|z| < 1),$$

and

$${}^{\Psi}\Phi_p^{(\alpha,\beta)}(b; c; z) = \sum_{n=0}^{\infty} \frac{{}^{\Psi}B_p^{(\alpha,\beta)}(b+n, c-b) z^n}{B(b, c-b) n!}.$$

We call ${}^{\Psi}F_p^{(\alpha,\beta)}(a, b; c; z)$ as Ψ -Gauss hypergeometric function and ${}^{\Psi}\Phi_p^{(\alpha,\beta)}(b; c; z)$ as Ψ -confluent hypergeometric function.

Theorem 7. Let $Re(c) > Re(b) > 0, Re(p) > 0, Re(\alpha) > -1$. Then,

$${}_{\psi}F_p^{(\alpha, \beta)}(a, b; c; z) = \frac{1}{B(b, c-b)} \int_0^1 t^{b-1} (1-t)^{c-b-1} {}_0\Psi_1\left(\alpha, \beta; -\frac{p}{t(1-t)}\right) (1-zt)^{-a} dt, \quad (4)$$

$${}_{\psi}F_p^{(\alpha, \beta)}(a, b; c; z) = \frac{1}{B(b, c-b)} \int_0^{\infty} u^{b-1} (1+u)^{a-c} (1+u(1-z))^{-a} {}_0\Psi_1\left(\alpha, \beta; -2p-p\left(u+\frac{1}{u}\right)\right) du, \quad (5)$$

$${}_{\psi}F_p^{(\alpha, \beta)}(a, b; c; z) = \frac{2}{B(b, c-b)} \int_0^{\frac{\pi}{2}} \sin^{2b-1}(\theta) \cos^{2c-2b-1}(\theta) (1-z\sin^2(\theta))^{-a} \\ \times {}_0\Psi_1\left(\alpha, \beta; -\frac{p}{\sin^2(\theta)\cos^2(\theta)}\right) d\theta. \quad (6)$$

Proof. By making the necessary calculations for equation (4), we have

$$\begin{aligned} {}_{\psi}F_p^{(\alpha, \beta)}(a, b; c; z) &= \sum_{n=0}^{\infty} (a)_n \frac{{}_{\psi}B_p^{(\alpha, \beta)}(b+n, c-b) z^n}{B(b, c-b) n!} \\ &= \frac{1}{B(b, c-b)} \sum_{n=0}^{\infty} (a)_n \int_0^1 t^{b+n-1} (1-t)^{c-b-1} {}_0\Psi_1\left(\alpha, \beta; -\frac{p}{t(1-t)}\right) \frac{z^n}{n!} dt \\ &= \frac{1}{B(b, c-b)} \int_0^1 t^{b-1} (1-t)^{c-b-1} {}_0\Psi_1\left(\alpha, \beta; -\frac{p}{t(1-t)}\right) \sum_{n=0}^{\infty} (a)_n \frac{(zt)^n}{n!} dt \\ &= \frac{1}{B(b, c-b)} \int_0^1 t^{b-1} (1-t)^{c-b-1} {}_0\Psi_1\left(\alpha, \beta; -\frac{p}{t(1-t)}\right) (1-zt)^{-a} dt. \end{aligned}$$

By putting $u = \frac{t}{1-t}$ and $t = \sin^2(\theta)$ in the last equation, equations (5) and (6) are obtained.

Theorem 8. Let $\operatorname{Re}(c) > \operatorname{Re}(b) > 0$, $\operatorname{Re}(p) > 0$, $\operatorname{Re}(\alpha) > -1$. Then,

$${}_{\psi}\Phi_p^{(\alpha, \beta)}(b; c; z) = \frac{1}{B(b, c-b)} \int_0^1 t^{b-1} (1-t)^{c-b-1} \exp(zt) {}_0\Psi_1\left(\alpha, \beta; -\frac{p}{t(1-t)}\right) dt, \quad (7)$$

$${}_{\psi}\Phi_p^{(\alpha, \beta)}(b; c; z) = \frac{1}{B(b, c-b)} \int_0^1 u^{c-b-1} (1-u)^{b-1} \exp(z(1-u)) {}_0\Psi_1\left(\alpha, \beta; -\frac{p}{u(1-u)}\right) du.$$

Proof. Similarly, using equation (3) desired results are achieved.

Note 1. The beta function and the Pochhammer symbol provide the following equations:

$$B(b, c-b) = \frac{c}{b} B(b+1, c-b),$$

and

$$(a)_{n+1} = a(a+1)_n.$$

These equations are used to calculate the theorems given below.

Theorem 9. Let $\operatorname{Re}(c) > \operatorname{Re}(b) > 0$, $\operatorname{Re}(p) > 0$, $\operatorname{Re}(\alpha) > -1$. Then,

$$\frac{d^n}{dz^n} \left\{ {}_{\psi}F_p^{(\alpha, \beta)}(a, b; c; z) \right\} = \frac{(a)_n (b)_n}{(c)_n} {}_{\psi}F_p^{(\alpha, \beta)}(a+n, b+n; c+n; z).$$

Proof. Differentiating the ${}^\psi F_p^{(\alpha,\beta)}(a, b; c; z)$ function, we have

$$\begin{aligned} \frac{d}{dz} \left\{ {}^\psi F_p^{(\alpha,\beta)}(a, b; c; z) \right\} &= \frac{d}{dz} \left\{ \sum_{n=0}^{\infty} (a)_n \frac{{}^\psi B_p^{(\alpha,\beta)}(b+n, c-b) z^n}{B(b, c-b) n!} \right\} \\ &= \sum_{n=1}^{\infty} (a)_n \frac{{}^\psi B_p^{(\alpha,\beta)}(b+n, c-b) z^{n-1}}{B(b, c-b) (n-1)!}. \end{aligned}$$

By writing $n \rightarrow n + 1$, we get

$$\begin{aligned} \frac{d}{dz} \left\{ {}^\psi F_p^{(\alpha,\beta)}(a, b; c; z) \right\} &= \frac{(a)(b)}{(c)} \sum_{n=0}^{\infty} (a+1)_n \frac{{}^\psi B_p^{(\alpha,\beta)}(b+n+1, c-b) z^n}{B(b+1, c-b) n!} \\ &= \frac{(a)(b)}{(c)} {}^\psi F_p^{(\alpha,\beta)}(a+1, b+1; c+1; z). \end{aligned}$$

By the inductive method, the more general form is obtained as:

$$\frac{d^n}{dz^n} \left\{ {}^\psi F_p^{(\alpha,\beta)}(a, b; c; z) \right\} = \frac{(a)_n (b)_n}{(c)_n} {}^\psi F_p^{(\alpha,\beta)}(a+n, b+n; c+n; z).$$

Theorem 10. Let $Re(c) > Re(b) > 0, Re(p) > 0, Re(\alpha) > -1$. Then,

$$\frac{d^n}{dz^n} \left\{ {}^\psi \Phi_p^{(\alpha,\beta)}(b; c; z) \right\} = \frac{(b)_n}{(c)_n} {}^\psi \Phi_p^{(\alpha,\beta)}(b+n; c+n; z).$$

Proof. The desired result is obtained by performing similar operations as in the proof of Theorem 9.

Theorem 11. Let $Re(c) > Re(b) > 0, Re(p) > 0, Re(s) > 0, Re(\alpha) > -1$. Then,

$$\mathfrak{M} \left\{ {}^\psi F_p^{(\alpha,\beta)}(a, b; c; z) \right\} = \frac{{}^\psi \Gamma^{(\alpha,\beta)}(s) B(b+s, c+s-b)}{B(b, c-b)} {}_2F_1(a, b+s; c+2s; z).$$

Proof. Multiplying the equation (4) by p^{s-1} and integrating from $p = 0$ to $p = \infty$, we have

$$\begin{aligned} \mathfrak{M} \left\{ {}^\psi F_p^{(\alpha,\beta)}(a, b; c; z) \right\} &= \int_0^\infty p^{s-1} {}^\psi F_p^{(\alpha,\beta)}(a, b; c; z) dp \\ &= \int_0^\infty p^{s-1} \sum_{n=0}^{\infty} \frac{{}^\psi B_p^{(\alpha,\beta)}(b+n, c-b)}{B(b, c-b)} (a)_n \frac{z^n}{n!} dp \\ &= \frac{1}{B(b, c-b)} \int_0^1 t^{b-1} (1-t)^{c-b-1} (1-zt)^{-a} \int_0^\infty p^{s-1} {}_0\Psi_1 \left(\alpha, \beta; -\frac{p}{t(1-t)} \right) dp dt. \end{aligned}$$

Putting $u = \frac{p}{t(1-t)}$ for the second integral to the right of the last equation, we get

$$\int_0^\infty p^{s-1} {}_0\Psi_1 \left(\alpha, \beta; -\frac{p}{t(1-t)} \right) dp = t^s (1-t)^s {}^\psi \Gamma^{(\alpha,\beta)}(s),$$

and then using this equation in the above equation, we obtain

$$\mathfrak{M} \left\{ {}^\psi F_p^{(\alpha,\beta)}(a, b; c; z) \right\} = \frac{{}^\psi \Gamma^{(\alpha,\beta)}(s) B(b+s, c+s-b)}{B(b, c-b)} {}_2F_1(a, b+s; c+2s; z).$$

Corollary 3. The inverse Mellin transform of the above equation is obtained as:

$${}^{\psi}F_p^{(\alpha,\beta)}(a, b; c; z) = \frac{1}{2\pi i} \int_{c-i\infty}^{c+i\infty} \frac{{}^{\psi}\Gamma^{(\alpha,\beta)}(s)B(b+s, c+s-b)}{B(b, c-b)} {}_2F_1(a, b+s; c+2s; z)p^{-s} ds, \quad (c > 0).$$

Theorem 12. Let $Re(c) > Re(b) > 0, Re(p) > 0, Re(s) > 0, Re(\alpha) > -1$. Then,

$$\mathfrak{M}\left\{{}^{\psi}\Phi_p^{(\alpha,\beta)}(b; c; z)\right\} = \frac{{}^{\psi}\Gamma^{(\alpha,\beta)}(s)B(b+s, c+s-b)}{B(b, c-b)} \Phi(b+s; c+2s; z).$$

Proof. The desired result is obtained by performing similar operations as in the proof of Theorem 11.

Corollary 4. The inverse Mellin transform of the above equation is obtained as:

$${}^{\psi}\Phi_p^{(\alpha,\beta)}(b; c; z) = \frac{1}{2\pi i} \int_{c-i\infty}^{c+i\infty} \frac{{}^{\psi}\Gamma^{(\alpha,\beta)}(s)B(b+s, c+s-b)}{B(b, c-b)} \Phi(b+s; c+2s; z)p^{-s} ds, \quad (c > 0).$$

Theorem 13. Let $Re(c) > Re(b) > 0, Re(p) > 0, Re(s) > 0, Re(\alpha) > -1$. Then,

$$\mathfrak{L}\left\{{}^{\psi}F_p^{(\alpha,\beta)}(a, b; c; z)\right\} = \frac{1}{s} {}^{\psi}F_{\frac{1}{s}}\left[\begin{matrix} (1,1)_{1,1} \\ (\beta, \alpha)_{1,1} \end{matrix} \middle| a, b; c; z\right].$$

Proof. Using Laplace transform and making necessary calculation, we have

$$\begin{aligned} \mathfrak{L}\left\{{}^{\psi}F_p^{(\alpha,\beta)}(a, b; c; z)\right\} &= \int_0^{\infty} \exp(-sp) {}^{\psi}F_p^{(\alpha,\beta)}(a, b; c; z) dp \\ &= \frac{1}{B(b, c-b)} \int_0^1 t^{b-1}(1-t)^{c-b-1}(1-zt)^{-a} \int_0^{\infty} \exp(-sp) {}_0\Psi_1\left(\alpha, \beta; -\frac{p}{t(1-t)}\right) dp dt \\ &= \frac{1}{s} \frac{1}{B(b, c-b)} \int_0^1 t^{b-1}(1-t)^{c-b-1}(1-zt)^{-a} \sum_{n=0}^{\infty} \frac{\left(-\frac{1}{t(1-t)}\right)^n}{\Gamma(\alpha n + \beta)} dt \\ &= \frac{1}{s} {}^{\psi}F_{\frac{1}{s}}\left[\begin{matrix} (1,1)_{1,1} \\ (\beta, \alpha)_{1,1} \end{matrix} \middle| a, b; c; z\right]. \end{aligned}$$

Corollary 5. The inverse Laplace transform of the above equation is obtained as:

$${}^{\psi}F_p^{(\alpha,\beta)}(a, b; c; z) = \frac{1}{2\pi i} \int_{c-i\infty}^{c+i\infty} \exp(sp) \frac{1}{s} {}^{\psi}F_{\frac{1}{s}}\left[\begin{matrix} (1,1)_{1,1} \\ (\beta, \alpha)_{1,1} \end{matrix} \middle| a, b; c; z\right] ds, \quad (c > 0).$$

Remark 2. Note that, ${}^{\psi}F_{\frac{1}{s}}\left[\begin{matrix} (1,1)_{1,1} \\ (\beta, \alpha)_{1,1} \end{matrix} \middle| a, b; c; z\right]$ is special case of the generalized Gauss hypergeometric function defined by Ata and Kıymaz [4].

Theorem 14. Let $Re(c) > Re(b) > 0, Re(p) > 0, Re(s) > 0, Re(\alpha) > -1$. Then,

$$\mathfrak{L}\left\{{}^{\psi}\Phi_p^{(\alpha,\beta)}(b; c; z)\right\} = \frac{1}{s} {}^{\psi}\Phi_{\frac{1}{s}}\left[\begin{matrix} (1,1)_{1,1} \\ (\beta, \alpha)_{1,1} \end{matrix} \middle| b; c; z\right].$$

Proof. The desired result is obtained by performing similar operations as in the proof of Theorem 13.

Corollary 6. The inverse Laplace transform of the above equation is obtained as:

$${}^{\psi}\Phi_p^{(\alpha,\beta)}(b; c; z) = \frac{1}{2\pi i} \int_{c-i\infty}^{c+i\infty} \exp(sp) \frac{1}{s} {}^{\psi}\Phi_{\frac{1}{s}}\left[\begin{matrix} (1,1)_{1,1} \\ (\beta, \alpha)_{1,1} \end{matrix} \middle| b; c; z\right] ds, \quad (c > 0).$$

Remark 3. Note that, ${}_{\frac{s}{s}}\Psi_1\left[\begin{matrix} (1,1)_{1,1} \\ (\beta, \alpha)_{1,1} \end{matrix} \middle| b; c; z\right]$ is special case of the generalized confluent hypergeometric function defined by Ata and Kıymaz [4].

Theorem 15. Let $Re(c) > Re(b) > 0, Re(p) > 0, Re(\alpha) > -1$. Then,

$${}_{\Psi}F_p^{(\alpha, \beta)}(a, b; c; z) = (1 - z)^{-a} {}_{\Psi}F_p^{(\alpha, \beta)}\left(a, c - b; c; \frac{z}{z - 1}\right).$$

Proof. Using equation

$$(1 - z(1 - t))^{-a} = (1 - z)^{-a} \left(1 + \frac{zt}{1 - z}\right)^{-a}$$

and by writing $t \rightarrow 1 - t$ in (4), we have

$$\begin{aligned} {}_{\Psi}F_p^{(\alpha, \beta)}(a, b; c; z) &= \frac{(1 - z)^{-a}}{B(b, c - b)} \int_0^1 t^{c-b-1} (1 - t)^{b-1} \left(1 - \frac{zt}{z - 1}\right)^{-a} {}_0\Psi_1\left(\alpha, \beta; -\frac{p}{t(1 - t)}\right) dt \\ &= (1 - z)^{-a} {}_{\Psi}F_p^{(\alpha, \beta)}\left(a, c - b; c; \frac{z}{z - 1}\right). \end{aligned}$$

Theorem 16. Let $Re(c) > Re(b) > 0, Re(p) > 0, Re(\alpha) > -1$. Then,

$${}_{\Psi}\Phi_p^{(\alpha, \beta)}(b; c; z) = \exp(z) {}_{\Psi}\Phi_p^{(\alpha, \beta)}(c - b; c; -z).$$

Proof. By writing $t \rightarrow 1 - t$ in equation (7), the desired result is achieved.

Applications to Fractional Differential Equations

In this section, we obtained the solution of fractional differential equations involving the newly generalized beta, Gauss hypergeometric and confluent hypergeometric functions.

Example 1. Let $1 < Re(\varepsilon) \leq 2, Re(x) > 0, Re(y) > 0, Re(p) > 0, Re(\alpha) > -1$. Assume that the fractional differential equation

$${}^c D_p^\varepsilon[f(p)] = p^{\beta-1} {}_{\Psi}B_{\varepsilon p^\alpha}^{(\alpha, \beta)}(x, y)$$

and initial conditions

$$f(0) = f'(0) = 0$$

are given. Considering equation (1) and applying Laplace transform to the fractional differential equation, we have

$$\mathfrak{L}\{ {}^c D_p^\varepsilon[f(p)]\} = \mathfrak{L}\{p^{\beta-1} {}_{\Psi}B_{\varepsilon p^\alpha}^{(\alpha, \beta)}(x, y)\}$$

and then

$$s^\varepsilon F(s) - s^{\varepsilon-1} f(0) - s^{\varepsilon-2} f'(0) = s^{-\beta} B_{\frac{\varepsilon}{s^\alpha}}(x, y).$$

By using initial conditions, we get

$$F(s) = s^{-\varepsilon-\beta} B_{\frac{\varepsilon}{s^\alpha}}(x, y).$$

Applying inverse Laplace transform to both sides of the last equation, we obtain the solution function as:

$$f(p) = p^{\beta+\varepsilon-1} {}_{\Psi}B_{\varepsilon p^\alpha}^{(\alpha, \beta+\varepsilon)}(x, y).$$

Example 2. Let $1 < \text{Re}(\varepsilon) \leq 2$, $\text{Re}(c) > \text{Re}(b) > 0$, $\text{Re}(p) > 0$, $\text{Re}(\alpha) > -1$. Assume that the fractional differential equation

$${}^c D_p^\varepsilon[f(p)] = p^{\beta-1} \Psi F_{\varepsilon p^\alpha}^{(\alpha, \beta)}(a, b; c; z)$$

and initial conditions

$$f(0) = f'(0) = 0$$

are given. Considering equation (1) and applying Laplace transform to the fractional differential equation, we have

$$\Omega\{{}^c D_p^\varepsilon[f(p)]\} = \Omega\{p^{\beta-1} \Psi F_{\varepsilon p^\alpha}^{(\alpha, \beta)}(a, b; c; z)\}$$

and then

$$s^\varepsilon F(s) - s^{\varepsilon-1}f(0) - s^{\varepsilon-2}f'(0) = s^{-\beta} F_{\frac{\varepsilon}{s^\alpha}}(a, b; c; z).$$

By using initial conditions, we get

$$F(s) = s^{-\varepsilon-\beta} F_{\frac{\varepsilon}{s^\alpha}}(a, b; c; z).$$

Applying inverse Laplace transform to both sides of the last equation, we obtain the solution function as:

$$f(p) = p^{\beta+\varepsilon-1} \Psi F_{\varepsilon p^\alpha}^{(\alpha, \beta+\varepsilon)}(a, b; c; z).$$

Example 3. Let $1 < \text{Re}(\varepsilon) \leq 2$, $\text{Re}(c) > \text{Re}(b) > 0$, $\text{Re}(p) > 0$, $\text{Re}(\alpha) > -1$. Assume that the fractional differential equation

$${}^c D_p^\varepsilon[f(p)] = p^{\beta-1} \Psi \Phi_{\varepsilon p^\alpha}^{(\alpha, \beta)}(b; c; z)$$

and initial conditions

$$f(0) = f'(0) = 0$$

are given. Considering equation (1) and applying Laplace transform to the fractional differential equation, we have

$$\Omega\{{}^c D_p^\varepsilon[f(p)]\} = \Omega\{p^{\beta-1} \Psi \Phi_{\varepsilon p^\alpha}^{(\alpha, \beta)}(b; c; z)\}$$

and then

$$s^\varepsilon F(s) - s^{\varepsilon-1}f(0) - s^{\varepsilon-2}f'(0) = s^{-\beta} \Phi_{\frac{\varepsilon}{s^\alpha}}(b; c; z).$$

By using initial conditions, we get

$$F(s) = s^{-\varepsilon-\beta} \Phi_{\frac{\varepsilon}{s^\alpha}}(b; c; z).$$

Applying inverse Laplace transform to both sides of the last equation, we obtain the solution function as:

$$f(p) = p^{\beta+\varepsilon-1} \Psi \Phi_{\varepsilon p^\alpha}^{(\alpha, \beta+\varepsilon)}(b; c; z).$$

Conclusion

In this paper, we defined Ψ -gamma and Ψ -beta functions involving Wright function in the kernels and then we defined Ψ -Gauss and Ψ -confluent hypergeometric functions with the help of Ψ -beta function. Furthermore, we gave some properties of these functions and we presented their applications to fractional differential equations. In fact, most of the generalized gamma, beta, and hypergeometric functions in the literature seem to be special cases of the new generalized functions introduced in this article, such that: Chaudhry et al. [1,2,3],

$${}^{\Psi}\Gamma_p^{(0,1)}(x) = \Gamma_p(x),$$

$${}^{\Psi}B_p^{(0,1)}(x, y) = B(x, y; p),$$

$${}^{\Psi}F_p^{(0,1)}(a, b; c; z) = F_p(a, b; c; z),$$

$${}^{\Psi}\Phi_p^{(0,1)}(b; c; z) = \Phi_p(b; c; z).$$

Özergin et al. [5],

$${}^{\Psi}\Gamma_p^{(0,1)}(x) = \Gamma_p^{(\alpha, \alpha)}(x),$$

$${}^{\Psi}B_p^{(0,1)}(x, y) = B_p^{(\alpha, \alpha)}(x, y),$$

$${}^{\Psi}F_p^{(0,1)}(a, b; c; z) = F_p^{(\alpha, \alpha)}(a, b; c; z),$$

$${}^{\Psi}\Phi_p^{(0,1)}(b; c; z) = \Phi_p^{(\alpha, \alpha)}(b; c; z).$$

Lee et al. [6],

$${}^{\Psi}B_p^{(0,1)}(x, y) = B(x, y; p; 1),$$

$${}^{\Psi}F_p^{(0,1)}(a, b; c; z) = F_p(a, b; c; z; 1),$$

$${}^{\Psi}\Phi_p^{(0,1)}(b; c; z) = \Phi_p(b; c; z; 1).$$

Parmar [7],

$${}^{\Psi}\Gamma_p^{(0,1)}(x) = \Gamma_p^{(\alpha, \alpha; 1)}(x),$$

$${}^{\Psi}B_p^{(0,1)}(x, y) = B_p^{(\alpha, \alpha; 1)}(x, y),$$

$${}^{\Psi}F_p^{(0,1)}(a, b; c; z) = F_p^{(\alpha, \alpha; 1)}(a, b; c; z),$$

$${}^{\Psi}\Phi_p^{(0,1)}(b; c; z) = \Phi_p^{(\alpha, \alpha; 1)}(b; c; z).$$

Srivastava et al. [8],

$${}^{\Psi}B_p^{(0,1)}(x, y) = B_p^{(\alpha, \alpha; 1, 1)}(x, y),$$

$${}^{\Psi}F_p^{(0,1)}(a, b; c; z) = F_p^{(\alpha, \alpha; 1, 1)}(a, b; c; z).$$

Shadab et al. [9],

$${}^{\Psi}B_p^{(0,1)}(x, y) = B_1^p(x, y),$$

$${}^{\Psi}F_p^{(0,1)}(a, b; c; z) = F_{p,1}(a, b; c; z),$$

$${}^{\Psi}\Phi_p^{(0,1)}(b; c; z) = \Phi_{p,1}(b; c; z).$$

Rahman et al. [10],

$${}^{\Psi}B_p^{(0,1)}(x, y) = B_p^{1;1}(x, y),$$

$${}^{\Psi}F_p^{(0,1)}(a, b; c; z) = F_p^{1;1}(a, b; c; z),$$

$${}^{\Psi}\Phi_p^{(0,1)}(b; c; z) = \Phi_p^{1;1}(b; c; z).$$

Classic functions [27],

$${}^{\Psi}\Gamma_0^{(0,1)}(x) = \Gamma(x),$$

$${}^{\Psi}B_0^{(0,1)}(x, y) = B(x, y),$$

$${}^{\Psi}F_0^{(0,1)}(a, b; c; z) = {}_2F_1(a, b; c; z),$$

$${}^{\Psi}\Phi_0^{(0,1)}(b; c; z) = \Phi(b; c; z).$$

Acknowledgment

Note that, a part of this work was published without peer review at Cornell University arXiv.org on March 5, 2018 as preprint arXiv:1803.03121 [math.CA]. Then on March 12, 2021, it was revised to arXiv:1803.03121v3 [math.CA] [24]. The authors are thankful to the referees for their valuable remarks, comments and suggestions that led to the improvement of this research and to the editors for their interest.

Conflicts of interest

There are no conflicts of interest in this work.

References

- [1] Chaudhry M.A., Zubair S.M., Generalized Incomplete Gamma Functions with Applications, J.Comput. Appl. Math., 55 (1) (1994) 99-124.
- [2] Chaudhry M.A., Qadir A., Rafique M., Zubair S.M., Extension of Euler's Beta Function, J. Comput. Appl. Math., 78 (1) (1997) 19-32.
- [3] Chaudhry M.A., Qadir A., Srivastava H.M., Paris R.B., Extended Hypergeometric and Confluent Hypergeometric Functions, Appl. Math. Comput., 159 (2) (2004) 589-602.
- [4] Ata E., Kıymaz İ.O., A Study on Certain Properties of Generalized Special Functions Defined by Fox-Wright Function, Appl. Math. Nonlinear Sci., 5 (1) (2020) 147-162.

- [5] Özergin E., Özarslan M.A., Altın A., Extension of Gamma, Beta and Hypergeometric Functions, *J. Comput. Appl. Math.*, 235 (16) (2011) 4601-4610.
- [6] Lee D.M., Rathie A.K., Parmar R.K., Kim Y.S., Generalization of Extended Beta Function, Hypergeometric and Confluent Hypergeometric Functions, *Honam Math. J.*, 33 (2) (2011) 187-206.
- [7] Parmar R.K., A New Generalization of Gamma, Beta, Hypergeometric and Confluent Hypergeometric Functions, *Le Matematiche*, 68 (2) (2013) 33-52.
- [8] Srivastava H.M., Agarwal P., Jain S., Generating Functions for the Generalized Gauss Hypergeometric Functions, *Appl. Math. Comput.*, 247 (C) (2014) 348-352.
- [9] Shadab M., Saime J., Choi J., An Extended Beta Function and Its Applications, *J. Math. Sci.*, 103 (1) (2018) 235-251.
- [10] Rahman G., Mubeen S., Nisar K.S., A New Generalization of Extended Beta and Hypergeometric Functions, *J. Frac. Calc. Appl.*, 11 (2) (2020) 32-44.
- [11] Çetinkaya A., Kıymaz İ.O., Agarwal P., Agarwal R.A., A Comparative Study on Generating Relations for Generalized Hypergeometric Functions via Generalized Fractional Operators, *Adv. Differ. Equ.*, 2018 (1) (2018) 1-11.
- [12] Goswami A., Jain S., Agarwal P., Araci S., A Note on the New Extended Beta and Gauss Hypergeometric Functions, *Appl. Math. Infor. Sci.*, 12 (1) (2018) 139-144.
- [13] Choi J., Rathie A.K., Parmar R.K., Extension of Extended Beta, Hypergeometric and Confluent Hypergeometric Functions, *Honam Math. J.*, 36 (2) (2014) 357-385.
- [14] Kulip M.A.H., Mohsen F.F., Barahmah S.S., Futher Extended Gamma and Beta Functions in Term of Generalized Wright Function, *Electronic J. Uni. Aden Basic Appl. Sci.*, 1 (2) (2020) 78-83.
- [15] Şahin R., Yağcı O., Yağbasan M.B., Kıymaz İ.O., Çetinkaya A., Further Generalizations of Gamma, Beta and Related Functions, *J. Inequalities Spec. Func.*, 9 (4) (2018) 1-7.
- [16] Mubeen S., Rahman G., Nisar K.S., Choi J., An Extended Beta Function and Its Properties, *J. Math. Sci.*, 102 (7) (2017) 1545-1557.
- [17] Abubakar U.M., A Study of Extended Beta and Associated Functions Connected to Fox-Wright Function, *J. Frac. Calc. Appl.*, 12 (3) (13) (2021) 1-23.
- [18] Yağcı, O., Şahin, R., Degenerate Pochhammer Symbol, Degenerate Sumudu Transform, and Degenerate Hypergeometric Function with Applications, *Hacet. J. Math. Stat.*, 50 (5) (2021) 1448-1465.
- [19] Şahin, R., Yağcı, O., A New Generalization of Pochhammer Symbol and its Applications, *Appl. Math. Nonlinear Sci.*, 5 (1) (2020) 255-266.
- [20] Şahin, R., & Yağcı, O., Fractional Calculus of the Extended Hypergeometric Function, *Appl. Math. Nonlinear Sci.*, 5 (1) (2020) 369-384.
- [21] Abdalla, M., Hidan, M., Boulaaras, S.M., Cherif, B.B., Investigation of Extended k-Hypergeometric Functions and Associated Fractional Integrals, *Math. Prob. Eng.*, 2021 (2021) 1-11.
- [22] Saboor, A., Rahman, G., Ali, H., Nisar, K.S., Abdeljawad, T., Properties and Applications of a New Extended Gamma Function Involving Confluent Hypergeometric Function, *J. Math.*, 2021 (2021) 1-12.
- [23] Ata E., Modified Special Functions Defined by Generalized M-Series and their Properties, *arXiv:2201.00867v1 [math.CA]*, (2022).
- [24] Ata E., Generalized Beta Function Defined by Wright Function, *arXiv:1803.03121v3 [math.CA]*, (2021).
- [25] Debnath, L., Bhatta, D., *Integral transforms and their applications*, Third edition, CRC Pres, Boca Raton, London, New York, (2015) 143-398.
- [26] Podlubny, I., *Fractional differential equations: an introduction to fractional derivatives, fractional differential equations, to methods of their solution and some of their applications*, Elsevier, (1998) 103-109.
- [27] Andrews G.E., Askey R., Roy R., *Special functions*, Cambridge university press, Cambridge, (1999) 1-60.
- [28] Kilbas A.A., Srivastava H.M., Trujillo J.J., *Theory and applications of fractional differential*, Elsevier, North-Holland mathematics studies 204, Amsterdam, (2006) 1-68.

Some Identities with Special Numbers

Neşe Ömür^{1,a}, Kübra Nur Südemem^{1,b}, Sibel Koparal^{2,c,*}

¹ Department of Mathematics, Faculty of Sciences and Arts, Kocaeli University, Kocaeli, Türkiye.

² Department of Mathematics, Faculty of Sciences and Arts, Bursa Uludağ University, Bursa, Türkiye.

*Corresponding author

Research Article

History

Received: 14/12/2021

Accepted: 05/12/2022

Copyright



©2022 Faculty of Science,
Sivas Cumhuriyet University

ABSTRACT

In this paper, we derive new identities which are related to some special numbers and generalized harmonic numbers $H_n(\alpha)$ by using the argument of the generating function given in [3] and comparing the coefficients of the generating functions. Also considering q -numbers involving q -Changhee numbers $Ch_{n,q}$ and q -Daehee numbers $D_{n,q}$, some sums are given. For example, for any positive integer n and any positive real number $q > 1$, when $\alpha = \frac{q}{q-1}$, we have the relationship between generalized harmonic numbers and q -Daehee numbers.

Keywords: Harmonic numbers, Cauchy numbers of order r , q -Changhee number, Generating functions

^a sibelkoparal1@gmail.com

^{id} <https://orcid.org/0000-0003-2889-2832>

^b neseomur@gmail.com

^{id} <https://orcid.org/0000-0002-3972-9910>

^c kubranursudemem@hotmail.com ^{id} <https://orcid.org/0000-0003-4695-7855>

Introduction

In [1], for any $\alpha \in \mathbb{R}^+$ and $n \in \mathbb{N}$, the generalized harmonic numbers $H_n(\alpha)$ are defined by

$$H_0(\alpha) = 0 \text{ and } H_n(\alpha) = \sum_{i=1}^n \frac{1}{i\alpha^i} \text{ for } n \geq 1. \quad (1)$$

For $\alpha = 1$, the usual harmonic numbers are $H_n(1) = H_n$ and the generating function of $H_n(\alpha)$ is

$$\sum_{n=1}^{\infty} H_n(\alpha) t^n = -\frac{\ln\left(1 - \frac{t}{\alpha}\right)}{1-t}. \quad (2)$$

The works of Cauchy numbers of order r C_n^r , Daehee numbers of order r D_n^r , q -Changhee numbers $Ch_{n,q}$, q -Daehee numbers $D_{n,q}$ are given. Their combinatorial identities and relations have received much attention [2-7].

The Cauchy numbers of order r , denoted by C_n^r , are defined by the generating function

$$\sum_{n=0}^{\infty} C_n^r \frac{t^n}{n!} = \left(\frac{t}{\ln(1+t)}\right)^r \quad [13]. \quad (3)$$

For $r = 1$, $C_n^1 = C_n$ are called Cauchy numbers.

The Daehee numbers of order r , denoted by D_n^r , are defined by the generating function

$$\sum_{n=0}^{\infty} D_n^r \frac{t^n}{n!} = \left(\frac{\ln(1+t)}{t}\right)^r \quad [11-13]. \quad (4)$$

For $r = 1$, $D_n^1 = D_n$ are called Daehee numbers.

The Stirling numbers of the first kind $S_1(n, k)$ are defined by

$$x^n = \sum_{k=0}^n S_1(n, k) x^k,$$

and the Stirling numbers of the second kind $S_2(n, k)$ are defined by

$$x^n = \sum_{k=0}^n S_2(n, k) x^k,$$

where $x^{\underline{n}}$ stands for the falling factorial defined by $x^{\underline{0}} = 1$ and $x^{\underline{n}} = x(x-1)\cdots(x-n+1)$. It is known that $S_1(n, k) = 0$ for $k > n$ and $S_1(n, n) = 1$.

The generating function of the Stirling numbers of the first kind $S_1(n, k)$ is given by

$$\sum_{n=k}^{\infty} S_1(n, k) \frac{t^n}{n!} = \frac{(\ln(1+t))^k}{k!}, \quad k \geq 0, \quad (5)$$

and the generating function of the Stirling numbers of the second kind $S_2(n, k)$ is given by

$$\sum_{n=k}^{\infty} S_2(n, k) \frac{t^n}{n!} = \frac{(e^t - 1)^k}{k!}, \quad k \geq 0 \quad [10]. \quad (6)$$

Let $|S_1(n, k)|$ be the unsigned Stirling numbers of the first kind given by

$$x^{\bar{n}} = \sum_{k=0}^n |S_1(n, k)| x^k,$$

where $x^{\bar{n}}$ stands for the rising factorial defined by $x^{\bar{0}} = 1$ and $x^{\bar{n}} = x(x+1) \cdots (x+n-1)$. It is clear that $S_1(n, k) = (-1)^{n-k} |S_1(n, k)|$ [5].

The generating function of $|S_1(n, k)|$ is given by

$$\sum_{n=k}^{\infty} |S_1(n, k)| \frac{t^n}{n!} = \frac{(-\ln(1-t))^k}{k!}.$$

The numbers associated with $S_1(n, k)$ are given as follows: For $n < k$,

$$\rho(n, k) = \frac{|S_1(k, k-n)|}{\binom{k-1}{n}},$$

and for $n \geq k$,

$$\rho(n, k) = n! \sigma_n(k),$$

where $\sigma_n(x)$ is the Stirling polynomial [5]. The generating function of these numbers is

$$\sum_{n=0}^{\infty} \rho(n, k) \frac{t^n}{n!} = \left(\frac{t}{1-e^{-t}} \right)^k. \tag{7}$$

It is clearly that $\rho(n, k) = B_n^{(k)}(k)$ is known as the classical Bernoulli polynomials of order k [9].

Let p be a fixed odd prime number. $\mathbb{Z}_p, \mathbb{Q}_p$ and \mathbb{C}_p will denote the ring of p -adic integers, the field of p -adic rational numbers and the completion of the algebraic closure of \mathbb{Q}_p . The p -adic norm $|\cdot|_p$ is normalized by $|p|_p = \frac{1}{p}$. Let q be an indeterminate in \mathbb{C}_p such that $|1-q|_p < p^{\frac{-1}{p-1}}$. The q -extension of number x is defined as $[x]_q = \frac{1-q^x}{1-q}$. It is clear that $\lim_{q \rightarrow 1} [x]_q = x$.

The q -Changhee polynomials $Ch_{n,q}(x)$ [4] are defined by the generating function

$$\sum_{n=0}^{\infty} Ch_{n,q}(x) \frac{t^n}{n!} = \frac{1+q}{1+q(1+t)} (1+t)^x. \tag{8}$$

When $x = 0$, $Ch_{n,q} = Ch_{n,q}(0)$ are called q -Changhee numbers and when $q = 1$, $Ch_n = Ch_{n,1}(0)$ are called Changhee numbers.

The q -Daehee polynomials $D_{n,q}(x)$ [7] are defined by the generating function

$$\sum_{n=0}^{\infty} D_{n,q}(x) \frac{t^n}{n!} = \frac{1-q + \frac{1-q}{\ln q} \ln(1+t)}{1-q-qt} (1+t)^x. \tag{9}$$

In the special case, when $q = 1$, $D_n(x) = D_{n,1}(x)$ are called Daehee polynomials and when $x = 0$, $D_{n,q} = D_{n,q}(0)$ are called q -Daehee numbers.

Let $f(t)$ be a generating function (a power series) for a sequence $\{A_n\}$, the sequence of coefficients of the expansion of $f(t)^r$ is defined by $A_n^{(r)}$, where r is a fixed real nonzero number:

$$f(t) = \sum_{n=0}^{\infty} A_n \frac{t^n}{n!}, \quad f(t)^r = \sum_{n=0}^{\infty} A_n^{(r)} \frac{t^n}{n!} \tag{10}$$

absolutely convergent in a neighborhood of the origin.

Suppose $f(t)$ has a subsidiary generating function $g(t)$ so that

$$f(t) = (1+g(t))^{-1}, \quad |g(t)| < 1 \quad \text{and} \quad g(t)^n = \sum_{m=M(n)}^{\infty} a_m^{(n)} \frac{t^m}{m!}, \tag{11}$$

where $M(n)$ is a non-negative integer. Note that $g(t) = \sum_{m=0}^{\infty} a_m \frac{t^m}{m!}$ [8].

In [2], let

$$a(m, k) = (-1)^k \sum_{n=k}^{M^{-1}(m)} \frac{1}{n!} S_1(n, k) a_m^{(n)}, \tag{12}$$

where $M^{-1}(m)$ indicates the inverse function of M (in most cases, it is simply $M^{-1}(m) = m$). Then

$$A_m^{(r)} = \sum_{k=1}^{M^{-1}(m)} a(m, k) r^k, \quad m \geq 1. \tag{13}$$

Also Liu gave the sum as follows:

$$A_m^{(r)} = \sum_{i=0}^{M^{-1}(m)} \binom{-r}{i} a_m^{(i)}. \tag{14}$$

In [3], Kim et. al. gave obvious formula for coefficients of the expansion of given generating function, when that function has a suitable form, the coefficients can be represented by the Daehee numbers of order r and the Changhee numbers of order r . By the classical method of comparing the coefficients of the generating function, some identities related to these numbers were shown. For example,

$$D_n^r = \sum_{m=0}^n B_m^{(r)} S_1(n, m),$$

where $B_n^{(r)}$ are the Bernoulli numbers of order r .

In this paper, we derive new identities which are related to some special numbers by using the argument of the generating function given in [2]. For example, for any positive integer n and any positive real number $q \neq 1$,

$$\sum_{i=0}^{n-1} \left(\frac{1-q}{q} \right)^{i+1} \frac{D_i}{i!} = \ln q \left(D_{n,q} \frac{(1-q)^n}{n! q^n} - 1 \right),$$

and for any positive integers n and r ,

$$C_n^r = \sum_{m=0}^n \sum_{k=0}^m (-1)^k \binom{m}{k} \binom{r+m-1}{m} D_n^k.$$

Some identities with special numbers

In this section, we will give some identities involving generalized harmonic numbers, Cauchy numbers of order r , q -Changhee numbers and q -Daehee numbers.

Theorem 1. For any positive integer n and any positive real number $q > 1$, we have

$$H_n\left(\frac{q}{q-1}\right) = \ln q \left(1 - D_{n,q} \frac{(1-q)^n}{n! q^n}\right).$$

Proof. From (2) and (9), we have

$$\begin{aligned} \sum_{n=0}^{\infty} (-1)^n D_{n,q} \frac{t^n}{n!} &= \frac{1-q}{1-q+qt} + \frac{1-q}{\ln q} \frac{1-t}{1-q+qt} \frac{\ln(1-t)}{1-t} \\ &= \frac{1-q}{1-q+qt} - \frac{1-q}{\ln q} \frac{1-t}{1-q+qt} \sum_{k=0}^{\infty} H_k t^k \\ &= \frac{1-q}{1-q+qt} + \frac{1}{\ln q} \frac{1-q}{1-q+qt} \left(\sum_{k=0}^{\infty} H_k t^{k+1} - \sum_{k=0}^{\infty} H_k t^k \right) \end{aligned}$$

and by $\sum_{k=0}^{\infty} x^k = \frac{1}{1-x}$, equals to

$$\begin{aligned} \sum_{n=0}^{\infty} (-1)^n \frac{q^n}{(1-q)^n} t^n + \frac{1}{\ln q} \sum_{n=0}^{\infty} (-1)^n \frac{q^n}{(1-q)^n} t^n \left(\sum_{k=1}^{\infty} H_{k-1} t^k - \sum_{k=0}^{\infty} H_k t^k \right) \\ = \sum_{n=0}^{\infty} (-1)^n \frac{q^n}{(1-q)^n} t^n - \frac{1}{\ln q} \sum_{n=0}^{\infty} (-1)^n \frac{q^n}{(1-q)^n} t^n \sum_{k=0}^{\infty} H_k t^k + \frac{1}{\ln q} \sum_{n=0}^{\infty} (-1)^n \frac{q^n}{(1-q)^n} t^n \sum_{k=1}^{\infty} H_{k-1} t^k \end{aligned}$$

and by some combinatoric operations,

$$\begin{aligned} \sum_{n=0}^{\infty} (-1)^n D_{n,q} \frac{t^n}{n!} \\ = \sum_{n=0}^{\infty} (-1)^n \frac{q^n}{(1-q)^n} t^n - \frac{1}{\ln q} \sum_{n=0}^{\infty} \sum_{k=0}^n (-1)^k \frac{q^k}{(1-q)^k} H_{n-k} t^n + \frac{1}{\ln q} \sum_{n=1}^{\infty} \sum_{k=0}^{n-1} (-1)^k \frac{q^k}{(1-q)^k} H_{n-k-1} t^n \\ = \sum_{n=0}^{\infty} \left((-1)^n \frac{q^n}{(1-q)^n} + \frac{1}{\ln q} \sum_{k=0}^{n-1} (-1)^{k+1} \frac{q^k}{(1-q)^k} \frac{1}{n-k} \right) t^n. \end{aligned}$$

Hence, by comparing the coefficients of t^n above gives

$$\frac{D_{n,q}}{n!} = \frac{q^n}{(1-q)^n} + \frac{1}{\ln q} \sum_{k=0}^{n-1} (-1)^{n+k+1} \frac{q^k}{(1-q)^k} \frac{1}{n-k}.$$

Thus, from (1), the desired result is obtained.

Corollary 1. For any positive integer n and any positive real number $q \neq 1$, we have

$$\sum_{i=0}^{n-1} \left(\frac{1-q}{q}\right)^{i+1} \frac{D_i}{i!} = \ln q \left(D_{n,q} \frac{(1-q)^n}{n! q^n} - 1 \right).$$

Proof. From Theorem 1, we obtain

$$\ln q \left(1 - D_{n,q} \frac{(1-q)^n}{n! q^n} \right) = \sum_{i=1}^n \frac{(-1)^i (1-q)^i}{i q^i} = - \sum_{i=0}^{n-1} \frac{(-1)^i (1-q)^{i+1}}{q^{i+1}} \frac{i!}{(i+1)!}$$

and by Daehee number $D_n = \frac{(-1)^n}{n+1} n!$,

$$\ln q \left(D_{n,q} \frac{(1-q)^n}{n! q^n} - 1 \right) = \sum_{i=0}^{n-1} \left(\frac{1-q}{q} \right)^{i+1} \frac{D_i}{i!},$$

as claimed.

Theorem 2. For any positive integers n and r , we have

$$\rho(n, r) = \sum_{i=0}^n \sum_{m=0}^n \sum_{k=0}^i (-1)^{k+n} \binom{r+i-1}{i} \binom{i}{k} S_2(n, m) C_m^k.$$

Proof. For $f(t) = \frac{t}{1-e^{-t}}$ by (11) and Binomial theorem, we have

$$g(t)^i = \left(\frac{e^{-t} - 1}{\ln(1 + (e^{-t} - 1))} - 1 \right)^i = \sum_{k=0}^i (-1)^{i-k} \binom{i}{k} \left(\frac{e^{-t} - 1}{\ln(1 + (e^{-t} - 1))} \right)^k.$$

From (3) and (6), we have

$$\begin{aligned} g(t)^i &= \sum_{k=0}^i (-1)^{i-k} \binom{i}{k} \sum_{m=0}^{\infty} C_m^k \frac{(e^{-t} - 1)^m}{m!} \\ &= \sum_{n=0}^{\infty} \sum_{m=0}^n \sum_{k=0}^i (-1)^{i-k+n} \binom{i}{k} C_m^k S_2(n, m) \frac{t^n}{n!}, \end{aligned}$$

and by (11),

$$a_n^{(i)} = \sum_{m=0}^n \sum_{k=0}^i (-1)^{i-k+n} \binom{i}{k} C_m^k S_2(n, m).$$

Note that for integers $r \geq 1$ and $j \geq 0$,

$$\binom{-r}{j} = (-1)^j \binom{r+j-1}{j}. \tag{15}$$

Then, by (14), we have

$$A_n^{(r)} = \sum_{i=0}^n \sum_{m=0}^n \sum_{k=0}^i (-1)^{k+n} \binom{r+i-1}{i} \binom{i}{k} S_2(n, m) C_m^k.$$

(7) and (10) give that

$$\sum_{n=0}^{\infty} A_n^{(r)} \frac{t^n}{n!} = \left(\frac{t}{1-e^{-t}} \right)^r = \sum_{n=0}^{\infty} \rho(n, r) \frac{t^n}{n!}.$$

Thus, comparing the coefficients of $\frac{t^n}{n!}$, the desired result is obtained.

Theorem 3. For any positive integers n and r , we have

$$C_n^r = \sum_{i=0}^n \sum_{k=0}^i (-1)^k \binom{r+i-1}{i} \binom{i}{k} D_n^k.$$

Proof. We take $f(t) = \frac{t}{\ln(1+t)}$ for using (11). From Binomial theorem and (4), we have

$$\begin{aligned} g(t)^i &= \left(\frac{\ln(1+t)}{t} - 1 \right)^i = \sum_{k=0}^i (-1)^{i-k} \binom{i}{k} \left(\frac{\ln(1+t)}{t} \right)^k \\ &= \sum_{k=0}^i (-1)^{i-k} \binom{i}{k} \sum_{n=0}^{\infty} D_n^k \frac{t^n}{n!} = \sum_{n=0}^{\infty} \sum_{k=0}^i (-1)^{i-k} \binom{i}{k} D_n^k \frac{t^n}{n!}, \end{aligned}$$

which equals by (11),

$$a_n^{(i)} = \sum_{k=0}^i (-1)^{i-k} \binom{i}{k} D_n^k.$$

From here, by (14) and (15), we obtain that

$$A_n^{(r)} = \sum_{i=0}^n \sum_{k=0}^i (-1)^k \binom{i}{k} \binom{r+i-1}{i} D_n^k,$$

and from (7) and (10),

$$\sum_{n=0}^{\infty} A_n^{(r)} \frac{t^n}{n!} = \sum_{n=0}^{\infty} C_n^r \frac{t^n}{n!}.$$

Thus, we have the proof.

Theorem 4. For any positive integers n and r , we have

$$\sum_{i=0}^n (-1)^n S_2(n, i) C_i^r = \sum_{i=0}^n \sum_{k=0}^i (-1)^k \binom{i}{k} \binom{r+i-1}{i} \rho(n, k).$$

Proof. By (11), we note that

$$f(t) = \frac{e^{-t} - 1}{\ln(1 + (e^{-t} - 1))} \quad \text{and} \quad g(t) = \frac{t - 1 + e^{-t}}{1 - e^{-t}}.$$

From Binomial theorem, (6) and (7), we have

$$\begin{aligned} g(t)^i &= \left(\frac{t}{1 - e^{-t}} - 1 \right)^i = \sum_{k=0}^i (-1)^{i-k} \binom{i}{k} \left(\frac{t}{1 - e^{-t}} \right)^k \\ &= \sum_{k=0}^i (-1)^{i-k} \binom{i}{k} \sum_{n=0}^{\infty} \rho(n, k) \frac{t^n}{n!} \\ &= \sum_{n=0}^{\infty} \sum_{k=0}^i (-1)^{i-k} \binom{i}{k} \rho(n, k) \frac{t^n}{n!}, \end{aligned}$$

and using (11),

$$a_n^{(i)} = \sum_{k=0}^i (-1)^{i-k} \binom{i}{k} \rho(n, k).$$

Hence, (14) and (15) yield that

$$A_n^{(r)} = \sum_{i=0}^n \sum_{k=0}^i (-1)^k \binom{i}{k} \binom{r+i-1}{i} \rho(n, k).$$

From (3), (6) and (10), we obtain that

$$\begin{aligned} \sum_{n=0}^{\infty} A_n^{(r)} \frac{t^n}{n!} &= f(t)^r = \left(\frac{e^{-t} - 1}{\ln(1 + (e^{-t} - 1))} \right)^r \\ &= \sum_{i=0}^{\infty} C_i^r \frac{(e^{-t} - 1)^i}{i!} = \sum_{i=0}^{\infty} C_i^r \sum_{n=i}^{\infty} (-1)^n S_2(n, i) \frac{t^n}{n!} \\ &= \sum_{n=0}^{\infty} \sum_{i=0}^n (-1)^n S_2(n, i) C_i^r \frac{t^n}{n!}. \end{aligned}$$

Thus, comparing the coefficients of $\frac{t^n}{n!}$, we have the proof.

Now, for any positive integers r , we have q – numbers $\binom{n+r-1}{r-1} Ch_{n,q}$ given by

$$\left(\frac{1+q}{q(1+t)+1} \right)^r = \sum_{n=0}^{\infty} \binom{n+r-1}{r-1} Ch_{n,q} \frac{t^n}{n!}. \tag{16}$$

Theorem 5. For any positive integers n and r , we have

$$\binom{r}{n} \sum_{i=0}^r \binom{r-n}{i-n} q^i = \frac{(1+q)^r}{n!} Ch_{n,q} \sum_{i=0}^n \sum_{k=0}^i (-1)^k \binom{i}{k} \binom{r+i-1}{i} \binom{n+k-1}{k-1}.$$

Proof. For $f(t) = \frac{q(1+t)+1}{1+q}$, by (11), we have

$$g(t) = \frac{-qt}{q(1+t)+1}.$$

From Binomial theorem, we have

$$\begin{aligned} f(t)^r &= \left(\frac{q(1+t)+1}{1+q} \right)^r = \frac{1}{(1+q)^r} (q(1+t)+1)^r \\ &= \frac{1}{(1+q)^r} \sum_{i=0}^r \binom{r}{i} q^i (1+t)^i = \frac{1}{(1+q)^r} \sum_{n=0}^{\infty} \sum_{i=0}^r \binom{r}{i} \binom{i}{n} q^i t^n \end{aligned} \tag{17}$$

which, by Binomial theorem and (16), we write

$$\begin{aligned} g(t)^i &= \left(\frac{1+q}{q(1+t)+1} - 1 \right)^i = \sum_{k=0}^i (-1)^{i-k} \binom{i}{k} \left(\frac{1+q}{q(1+t)+1} \right)^k \\ &= \sum_{n=0}^{\infty} \sum_{k=0}^i (-1)^{i-k} \binom{i}{k} \binom{n+k-1}{k-1} Ch_{n,q} \frac{t^n}{n!}. \end{aligned}$$

Hence, with the help of (11), by comparing coefficients of t^n , we obtain that

$$a_n^{(i)} = \sum_{k=0}^i (-1)^{i-k} \binom{i}{k} \binom{n+k-1}{k-1} Ch_{n,q}.$$

By (10), (14) and (15), we get

$$A_n^{(r)} = \sum_{i=0}^n \sum_{k=0}^i (-1)^k \binom{i}{k} \binom{r+i-1}{i} \binom{n+k-1}{k-1} Ch_{n,q},$$

and

$$f(t)^r = \sum_{n=0}^{\infty} \sum_{i=0}^n \sum_{k=0}^i (-1)^k \binom{i}{k} \binom{r+i-1}{i} \binom{n+k-1}{k-1} Ch_{n,q} \frac{t^n}{n!}. \tag{18}$$

Finally, (17) and (18) give that

$$\sum_{i=0}^r \binom{r}{i} \binom{i}{n} q^i = \frac{(1+q)^r}{n!} Ch_{n,q} \sum_{i=0}^n \sum_{k=0}^i (-1)^k \binom{i}{k} \binom{r+i-1}{i} \binom{n+k-1}{k-1}.$$

By the equality $\binom{r}{i} \binom{i}{n} = \binom{r}{n} \binom{r-n}{i-n}$, we have the proof.

Theorem 6. For any positive integers n and r , we have

$$\sum_{i=1}^n \sum_{k=0}^i \sum_{j=0}^k (-1)^k \binom{i}{k} \binom{k}{j} \binom{r+i-1}{i} \binom{n+j-1}{j-1} \frac{q^j}{(1+q)^k} = (1+q)^{r-n} \sum_{k=0}^r (-1)^k \binom{r}{k} \binom{n+k-1}{k-1} \frac{q^k}{(1+q)^k}.$$

Proof. The proof is similar to the proof of above theorems, taking $f(t) = (1+q) \frac{1+t}{1+q+t}$ and using the generating function

$$\sum_{n=0}^{\infty} \binom{n+r-1}{r-1} \frac{(-1)^n}{(1+q)^n} t^n = \frac{(1+q)^r}{(1+q+t)^r}.$$

Acknowledgment

We would like thank the anonymous reviewers for their valuable suggestions.

Conflicts of interest.

There are no conflicts of interest in this work.

References

[1] Genčev M., Binomial sums involving harmonic numbers, *Math. Slovaca*, 61(2) (2011) 215-226.
 [2] Liu G., Generating functions and generalized Euler numbers, *Proc. Japan Acad.*, 84(A) (2008) 29-34.
 [3] Wang N.L., Li H., Some identities on the higher-order Daehee and Changhee numbers, *Pure and Applied Mathematics Journal*, 4(5-1) (2015) 33-37.
 [4] Kim T., Mansour T., Rim S.-H., Seo J.-J., A note on q -Changhee polynomials and numbers, *Adv. Studies Theor. Phys.*, 8(1) (2014) 35-41.
 [5] Graham R.L., Knuth D.E., Patashnik O., Concrete Mathematics. 2nd. Edition, Addison-Wesley Publishing Company, (1994).
 [6] Kim D.S., Kim T., Lee S.-H., Seo J.-J., Higher-order Daehee numbers and polynomials, *International Journal of Mathematical Analysis*, 8 (5-6) (2014) 273-283.
 [7] Kim T., Lee S.-H., Mansour T., Seo J.-J., A note on q -Daehee polynomials and numbers, *Adv. Stud. Comtemp. Math.*, 24(2) (2014) 155-160.
 [8] Srivastava H.M., Choi J.-S., Series associated with the zeta and related functions. Dordrecht, Boston and London, Kluwer Acad. Publ., (2001).
 [9] Charalambides C.A., Enumerative Combinatorics. Boca Raton, London, New York, Chapman & Hall/CRC, (2002).
 [10] Comtet L., Advanced Combinatorics. Reidel, Dordrecht, (1974).
 [11] Kwon H.I., Jang G.W., Kim T., Some Identities of Derangement Numbers Arising from Differential Equations, *Advanced Studies in Contemporary Mathematics*, 28(1) (2018) 73-82.
 [12] Park J.W., Kwon J., A note on the degenerate high order Daehee polynomials, *Appl. Math. Sci.*, 9 (2015) 4635-4642.
 [13] Rim S.-H., Kim T., Pyo S.-S., Identities between harmonic, hyperharmonic and Daehee numbers, *J. Inequal. Appl.*, 2018 (2018) 168.

Analysis of Exact Solutions of a Mathematical Model by New Function Method

Yusuf Gürefe^{1,a}, Yusuf Pandir^{2,b,*}, Tolga Akturk^{3,c}

¹ Department of Mathematics, Faculty of Science, Mersin University, Mersin, Türkiye.

² Department of Mathematics, Faculty of Arts and Science, Yozgat Bozok University, Yozgat, Türkiye.

³ Department of Mathematics and Science Education, Faculty of Education, Ordu University, Ordu, Türkiye.

*Corresponding author

Research Article

History

Received: 04/03/2022

Accepted: 09/12/2022

Copyright



©2022 Faculty of Science,
Sivas Cumhuriyet University

ABSTRACT

In this article, the new function method is used to obtain the wave solutions of the nonlinear Klein-Gordon equation. Since the Klein-Gordon equation is a nonlinear partial differential equation containing exponential functions, it was decided to apply the new function method, which was defined on the assumption of a nonlinear auxiliary differential equation containing exponential functions. Thus, it aims to reach wave solutions not found in the literature. The considered method can be easily applied to this type of nonlinear problem that is difficult to solve and gives us solutions. Here, two new exact solutions are obtained. Then two and three-dimensional density and contour graphs are drawn by selecting the appropriate parameters to analyze the physical behavior of these solutions. The Mathematica package program was effectively used in all calculations and graphic drawings.

Keywords: New function method, Klein-Gordon Equation with an exponential nonlinearity, Mathematical model.

^a ygurefe@gmail.com

^b <https://orcid.org/0000-0002-7210-5683>

^c yusuf.pandir@bozok.edu.tr

^d <https://orcid.org/0000-0003-0274-7901>

^e tolgaakturk@gmail.com

^f <https://orcid.org/0000-0002-8873-0424>

Introduction

Each of the nonlinear partial differential equations is a mathematical model of problems in physics, chemistry, biology, mechanics, and health. Therefore, the solutions to such equations are essential to researchers. Based on this thought, various methods have been developed and applied to investigate the exact or approximate solutions of nonlinear mathematical models. Some of those methods are, respectively, the trial equation method [1], the Kudryashov method [2], the first integral method [3], the extended trial equation method [4], the new extended direct algebraic method [5], the modified exponential function method [6], the sine-cosine method [7], the extended tanh-function method [8], the variational iteration method [9], Adomian decomposition method [10], the Chebyshev-Tau method [11]. Apart from these, a new method called the "new function method" has been proposed in the paper [12]. Subsequently, some authors have applied this approach to various nonlinear partial differential equations [13-18]. This method makes it easy to find the exact solutions of the nonlinear partial differential equations that contain exponential, trigonometric, or hyperbolic functions and are difficult to solve. Because the nonlinear partial differential equations containing such functions can be easily solved by assuming an auxiliary ordinary differential equation containing functions of the same type and thus by simplifying the derivative term and hyperbolic, trigonometric, or exponential functions in these equations, for this reason, the new function method was used to determine the exact solutions of the nonlinear

Klein-Gordon equation containing the exponential function in this study. All details about this method and its applications to nonlinear partial differential equations can be found in the articles published on this subject in the literature.

In this study, the new function method is used for the equation given below as the Klein-Gordon equation with exponential nonlinearity [19]

$$\phi_{tt} = \phi_{xx} + ae^{\beta\phi} + be^{2\beta\phi}. \quad (1)$$

The nonlinear Klein-Gordon equations are considered to model some nonlinear phenomena. Also, this nonlinear physical model has exponential nonlinearity. Detailed information on modeling these equations is given in the paper [20].

New Function Method

In this study, we analyze the traveling wave solutions of the Klein-Gordon equation using the new function method. First of all, the general form of the nonlinear mathematical model is given as

$$P(\phi_{xx}, \phi_t, e^{\beta\phi}, e^{2\beta\phi}, \dots) = 0 \quad (2)$$

and then the wave transforms $\phi(x,t) = \phi(\eta)$, $\eta = k(x-ct)$ is substituted into Eq. (2), where $c \neq 0$ is the velocity of the wave and k is wave number. Thus, the

nonlinear partial differential equation is obtained in the form of a nonlinear ordinary differential equation as follows

$$N(\phi', \phi'' \dots) = 0. \tag{3}$$

According to the method, suppose that the function ϕ satisfies the following equation

$$H(\phi'') = R(r(\phi)), \tag{4}$$

where H, R and r are continuous or differentiable functions on R . Also, the derivative concepts required in Eq. (4) are considered as

$$\phi' = h(r(\phi)), \quad \phi'' = h(r(\phi))r'(\phi)h'(r(\phi)). \tag{5}$$

Substituting Eq. (5) into Eq. (4), we obtain

$$H(h(r(\phi))r'(\phi)h'(r(\phi))) = R(r(\phi)). \tag{6}$$

If we take $\varpi = r(\phi)$, then we can write

$$H(\varpi'h(\varpi)h'(\varpi)) = R(\varpi). \tag{7}$$

Thus, an ordinary differential equation containing the single variable function h and its derivatives up to the requested order is obtained from Equation (7). Then, integrating the obtained ordinary differential equation, it is easily converted into a form as follows:

$$\frac{d\phi}{h(r(\phi))} = d\eta \Rightarrow \int \frac{d\phi}{h(r(\phi))} = \int d\eta = \eta + S. \tag{8}$$

Here, S is an integral constant. The traveling wave solutions of Eq. (1) can be constructed by calculating these integrals.

Applications for The Klein-Gordon Equation with An Exponential Nonlinearity

By using the wave transform, the Klein-Gordon equation with exponential nonlinearity is reduced to the following nonlinear ordinary differential equation form:

$$k^2(c^2 - 1)\phi'' = ae^{\beta\phi} + be^{2\beta\phi}. \tag{9}$$

We suppose that the auxiliary equation based on the exponential function is as follows

$$\phi' = h(e^{\beta\phi}). \tag{10}$$

Both sides of Eq. (10) are derived with respect to η , we get

$$\phi'' = \beta e^{\beta\phi} h(e^{\beta\phi}) h'(e^{\beta\phi}). \tag{11}$$

Substituting Eq. (11) into Eq. (9), we have

$$k^2(c^2 - 1)\beta h(e^{\beta\phi})h'(e^{\beta\phi}) = a + be^{\beta\phi}. \tag{12}$$

If λ is written instead of $e^{\beta\phi}$ in Eq. (12), then the new form of the ordinary differential equation is given as

$$k^2(c^2 - 1)\beta h(\lambda)h'(\lambda) = a + b\lambda. \tag{13}$$

When Eq. (13) is integrated with respect to λ , we obtain

$$h^2(\lambda) = \frac{1}{\beta k^2(c^2 - 1)}(b\lambda^2 + 2a\lambda + S), \tag{14}$$

where S is an integration constant. From Eq. (14), we can easily write the following function

$$h(\lambda) = \pm \sqrt{\frac{1}{\beta k^2(c^2 - 1)}(b\lambda^2 + 2a\lambda + S)}. \tag{15}$$

Letting $e^{\beta\phi} = \lambda$, we have $\phi = \frac{1}{\beta} \ln \lambda$. Differentiating both sides of this equality with respect to η , we get

$$\phi' = \frac{1}{\beta} \frac{\lambda'}{\lambda} = h(e^{\beta\phi}) = h(\lambda). \tag{16}$$

From Eq. (16), the following differential equation is obtained

$$\lambda' = \frac{d\lambda}{d\eta} = \beta \lambda h(\lambda) = \sqrt{\frac{\beta}{k^2(c^2 - 1)}} \lambda^2 (b\lambda^2 + 2a\lambda + S) \tag{17}$$

When Eq. (17) is solved by using the Mathematica program, the equality is obtained as

$$\eta + Q = \frac{\sqrt{bk^2(c^2 - 1)} \arctan \left[\frac{S + a\lambda}{\sqrt{S^2 + \lambda S(2a + b\lambda)}} \right]}{\sqrt{\beta S}}, \tag{18}$$

where Q is an integration constant. λ_i ($i = 1, \dots, 4$) are roots of equation $(b\lambda^4 + 2a\lambda^3 + S\lambda^2) = 0$

$$\lambda_1 = 0, \lambda_2 = 0, \lambda_3 = -\frac{a + \sqrt{a^2 - bS}}{b}, \lambda_4 = \frac{-a + \sqrt{a^2 - bS}}{b} \tag{19}$$

Then, we obtain the following cases.

CASE-1:

$$\lambda(x, t) = \frac{S \left(-a \operatorname{sech}[\sigma]^2 + \sqrt{(-a^2 + bS) \operatorname{sech}[\sigma]^2 \tanh[\sigma]^2} \right)}{a^2 - bS \tanh[\sigma]^2}, \tag{20}$$

where $\sigma = \left(\frac{\sqrt{S\beta}(Q+k(x-ct))}{bk^2(c^2-1)} \right)$, $k \neq 0$ and $c \neq \pm 1$

. Substituting the function λ in Eq. (20) into the relation $\phi = \frac{1}{\beta} \ln \lambda$, we get

$$\phi(\eta) = \frac{1}{\beta} \ln \left[\frac{S \left(-a \operatorname{sech}[\sigma]^2 + \sqrt{(-a^2 + bS) \operatorname{sech}[\sigma]^2 \tanh[\sigma]^2} \right)}{a^2 - bS \tanh[\sigma]^2} \right] \quad (21)$$

By determining the suitable values of the parameters in the exact solution of the nonlinear mathematical model, two-dimensional, three-dimensional, density, and contour graphs of this function were drawn. The Mathematica program is used to obtain these graphics.

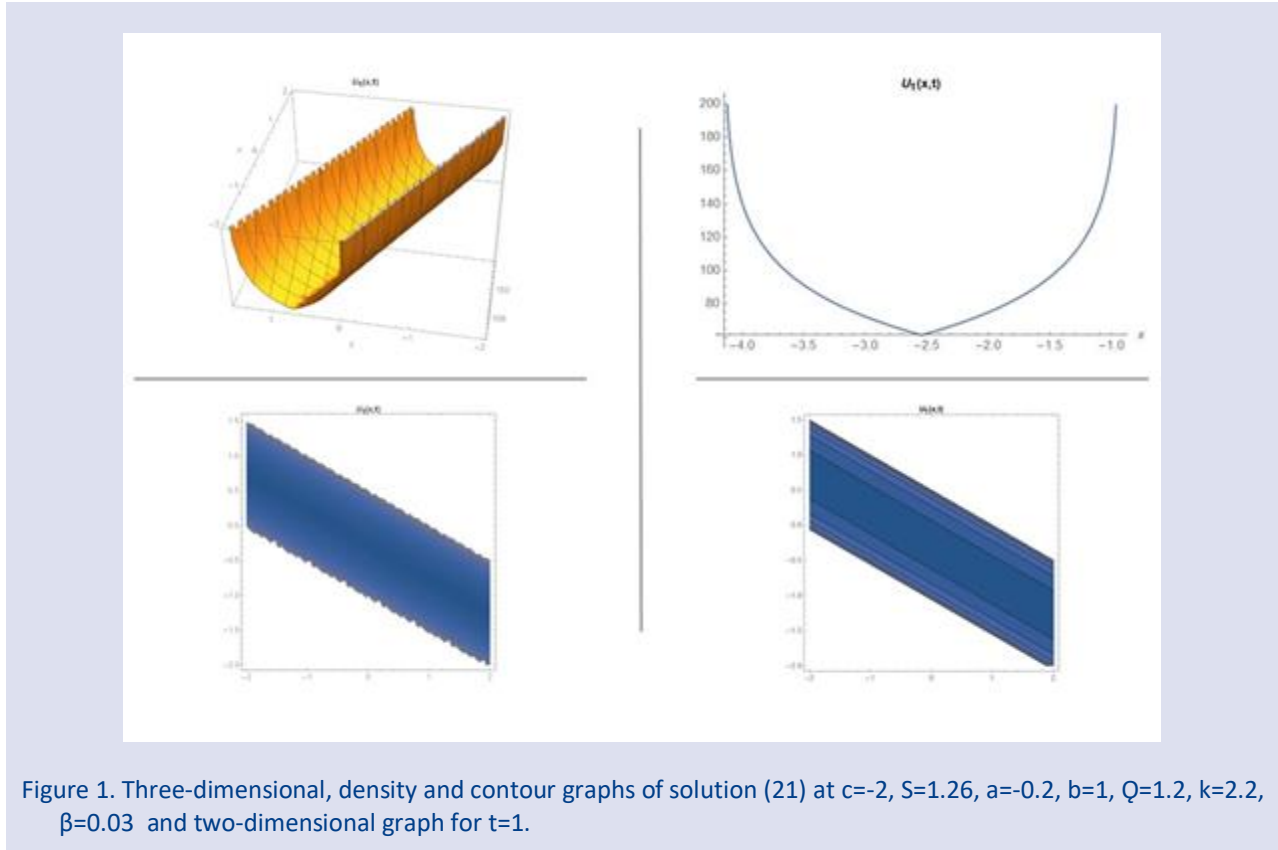


Figure 1. Three-dimensional, density and contour graphs of solution (21) at $c=-2, S=1.26, a=-0.2, b=1, Q=1.2, k=2.2, \beta=0.03$ and two-dimensional graph for $t=1$.

CASE-2:

$$\lambda(x,t) = \frac{S \left(a \operatorname{sech}[\sigma]^2 + \sqrt{(-a^2 + bS) \operatorname{sech}[\sigma]^2 \tanh[\sigma]^2} \right)}{-a^2 + bS \tanh[\sigma]^2} \quad (22)$$

$$\phi(\eta) = \frac{1}{\beta} \ln \left[\frac{S \left(a \operatorname{sech}[\sigma]^2 + \sqrt{(-a^2 + bS) \operatorname{sech}[\sigma]^2 \tanh[\sigma]^2} \right)}{-a^2 + bS \tanh[\sigma]^2} \right] \quad (23)$$

where $\sigma = \left(\frac{\sqrt{S\beta}(Q+k(x-ct))}{bk^2(c^2-1)} \right)$, $k \neq 0$ and $c \neq \pm 1$.

Substituting the function λ in Eq. (22) into the relation $\phi = \frac{1}{\beta} \ln \lambda$, we get

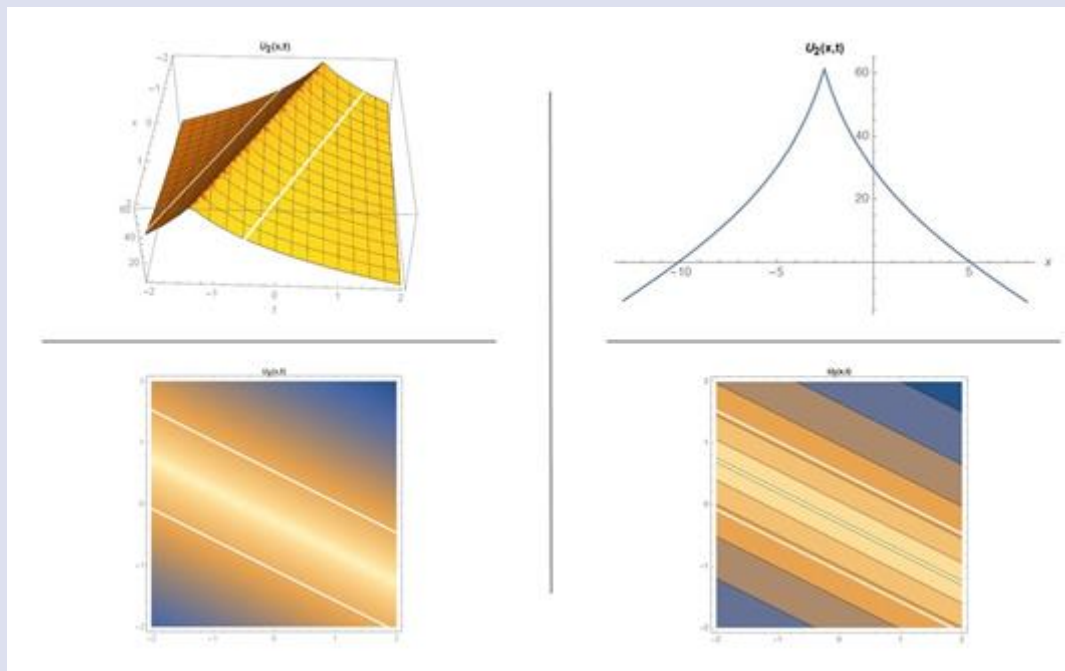


Figure 2. Three-dimensional, density and contour graphs of solution (23) at $c=-2$, $S=1.26$, $a=-0.2$, $b=1$, $Q=1.2$, $k=2.2$, $\beta=0.03$ and two-dimensional graph for $t=1$.

Conclusions

A new function method is used to obtain the soliton solutions of the Klein-Gordon equation. Thus, functions with periodic characteristics were obtained with the help of this method. Finding functions with this type of property provides an advantage in interpreting and making assumptions about the behavior of the mathematical model. Since periodic functions exhibit similar motion behaviors in all intervals, it allows interpretation of the behavior pattern for any interval beforehand. The solutions of trigonometric functions can be written in a logarithmic function. In addition, when the two-three dimensional density and contour graphs of the obtained solution function were examined, the periodic functions obtained as the solution function of the mathematical model represented the behavioral models. The results show that the new function technique is a very effective and convenient mathematical tool for solving nonlinear partial differential equations.

Conflicts of interest

The authors declared no conflict of interests.

References

- [1] Liu C.S., Trial Equation Method and Its Applications to Nonlinear Evolution Equations, *Acta. Phys. Sin.*, 54 (2005) 2505-2509.
- [2] Kudryashov N.A., One Method for Finding Exact Solutions of Nonlinear Differential Equations, *Commun. Nonl. Sci. Numer. Simul.*, 17 (2012) 2248-2253.
- [3] Lu B., The First Integral Method for Some Time Fractional Differential Equations, *J. Math. Anal. Appl.*, 395 (2) (2012) 684-693.
- [4] Gurefe Y., Misirli E., Sonmezoglu A., Ekici M., Extended Trial Equation Method to Generalized Nonlinear Partial Differential Equations, *Appl. Math. Comput.*, 219 (10) (2013) 5253-5260.
- [5] Hussain A., Jabeen F., Abbas N., Optical Soliton Solutions of Multi-Dimensional Boiti-Leon-Manna-Pempinelli Equations, *Mod. Phys. Lett. B*, 36(10) (2021) 2250035.
- [6] Aktürk, T., Modified Exponential Function Method for Nonlinear Mathematical Models with Atangana Conformable Derivative, *Rev. Mex. Fis.*, 67(4) (2021) 1-18.
- [7] Sherriffe D., Behera D., Analytical Approach for Travelling Wave Solution of Non-Linear Fifth-Order Time-Fractional Korteweg-De Vries Equation, *Pramana-J. Phys.*, 96(64) (2022) 1-8.
- [8] Zaman U.H.M., Arefin M.A., Akbar M.A., Uddin M.H., Analytical Behavior of Soliton Solutions to the Couple Type Fractional-Order Nonlinear Evolution Equations Utilizing a Novel Technique, *Alex. Eng. J.*, 61(12) (2022) 11947-11958.
- [9] He J.H., Some Asymptotic Methods for Strongly Nonlinear Equations, *Int. J. Modern Phys. B*, 20 (10) (2006) 1141-1199.
- [10] Alkarawi A.H., Al-Saiq I.R., Adomian Decomposition Method Applied to Klein Gordon and Nonlinear Wave Equation, *J. Interdiscip. Math.*, 24 (5) (2021) 1149-1157.
- [11] Gurefe N., Kocer E.G., Gurefe Y., Chebyshev-Tau Method for the Linear Klein-Gordon Equation, *Int. J. Phys. Sci.*, 7 (43) (2012) 5723-5728.
- [12] Shen G., Sun Y., Xiong Y., New Travelling-Wave Solutions for Dodd-Bullough Equation, *J. Appl. Math.*, 2013 (2013) 1-6.
- [13] Sun Y., New Travelling Wave Solutions for Sine-Gordon Equation, *J. Appl. Math.*, 2014 (2014) 1-5.
- [14] Bulut H., Akturk T., Gurefe Y., Travelling Wave Solutions of the (N+1)-dimensional Sine-Cosine-Gordon Equation, *AIP Conf. Proc.*, 1637 (2014) 145-149.

- [15] Bulut H., Akturk T., Gürefe Y., An Application of the New Function Method to the Generalized Double Sinh-Gordon Equation, *AIP Conf. Proc.*, 1648 (2015) 370014.
- [16] Akturk T., Gürefe Y., Bulut H., New Function Method to the (n+1)-dimensional Nonlinear Problems, *Int. J. Optim. Control: Theor. Appl.*, 7 (3) (2017) 234-239.
- [17] Akturk T., Gürefe Y., Pandir Y., An Application of the New Function Method to the Zhiber-Shabat Equation, *Int. J. Optim. Control: Theor. Appl.*, 7 (3) (2017) 271-274.
- [18] Gürefe Y., Akturk T., Pandir Y., An Application of the New Function Method for a Coupled Sine-Gordon Equation, *Adv. Differ. Equ. Control Process.*, 19 (3) (2018) 287-294.
- [19] Wazwaz A.M., The tanh and the Sine-Cosine Methods for Compact and Noncompact Solutions of the Nonlinear Klein-Gordon Equation, *Appl. Math. Comput.*, 167(2) (2005) 1179-1195.
- [20] Duncan D.B., Symplectic Finite Difference Approximations of the Nonlinear Klein-Gordon Equation, *SIAM J. Numer. Anal.*, 34 (5) (1997) 1742-1760.

Retinoblastoma Radiotherapy Treatment Optimizations Through GATE Simulations

İbrahim Etem Gül^{1,a}, Sinan Kuday^{2,b,*}

¹ Medical Physics, Health Science Institute, Istanbul Aydın University, 34295, Istanbul, Türkiye

² Department of Physics, Ankara University, Tandogan, 06100, Ankara, Türkiye

*Corresponding author

Research Article

History

Received: 03/08/2022

Accepted: 25/08/2022

Copyright



©2022 Faculty of Science,
Sivas Cumhuriyet University

ABSTRACT

One of the most frequent children tumors in the area around the eyes is defined as retinoblastoma. Proton radiotherapy treatment is a particularly effective type of radiation therapy due to the prolonged survival rates of children with childhood cancers such as retinoblastoma, continued growth of nearby organs and tissues, low radiation dose restriction of vision-related tissues and systems of these tissues. In this study, a geometry phantom including eyeball, lens, lacrimal gland, optic nerve, optic chiasm, retina, cancer, cornea and bone structures was modeled with Monte Carlo simulation tool GATE (vGATE 9.0). With this simulation, the doses absorbed by the tissues were calculated using the DoseActor and TLEDoseActor algorithms. Secondary doses were determined by the TLEDoseActor algorithm. Determination of secondary radiations is important because of the low radiation dose limit of tissues and systems that affect vision. The best treatment results were tried to be obtained by giving the beam thickness of the radiation used in our study, 4 different angles towards the target and different energies. These results show that it can be helpful in calculating a treatment plan for proton therapy in clinical practice.

Keywords: GATE, DoseActor, TLEDoseActor, Proton therapy, Retinoblastoma, Radiotherapy.

iethemgul@gmail.com

<https://orcid.org/0000-0001-6972-3635>

kuday@cern.ch

<https://orcid.org/0000-0002-0116-5494>

Introduction

Proton therapy affects the proliferation time of cancer cells, disrupts the nutrition of the cells in question, and is an external beam radiotherapy used to break the DNA helix, stop or destroy the proliferation of these unwanted cells. The aim of all external beam treatments is to try to protect the healthy organs from the negative effects of radiation while targeting the unwanted tumor area in the body with radiation therapy [1]. The risk of secondary cancer after traditional radiotherapy, the longer life expectancy in pediatric cancers, the more radiosensitive tissues and organs, while the tissues continue to grow, while the presence of radiation-induced growth disorders makes proton therapy more preferable. Clinical studies on this subject support that proton therapy gives less dose to healthy tissues compared to other radiotherapy techniques [2]. Although proton therapy facilities are quite expensive, the first facilities are built in the USA, Europe and Japan, but the number of facilities has been increasing in China and South Korea in recent years. Significant advances in proton therapy are expected in the next 10 years. Forecasts include: proton therapy systems will continue to shrink in volume, proton dosimetry will become more sophisticated, and devices that change the size and shape of the proton beam, such as multileaf collimators, will allow the treatment of complex tumors, but will also be more effective in very small lesions such as eye tumors. Recent advances have reduced the volumes of proton therapy technology by up to 40

percent. In particular, the development of superconducting magnet technology was influential in the size of the cyclotron that produced the proton beam. In addition, the revolving portal, in the volume of a three storey building, could be significantly reduced. Thus, proton therapy will be considered more cost effective and in the treatment of different types of cancer, and there will be a significant reduction in operating costs. Scientists are working on very finely tuned collimation systems made of different materials to reduce neutron production, which has a high share in secondary radiation. This will be of great importance, especially in patients receiving repeat proton therapy. [3] Proton Interactions Numerous interactions slow down atomic orbital electrons by the Coulomb force. They are deflected from their direction as a result of numerous collisions with the atomic nucleus. Apart from these, in inelastic collisions that occur occasionally with nuclear interactions, the proton collides with one or more protons in the nucleus, releasing the particles, thereby releasing secondary radiations especially neutrons and gamma rays. In particular, the neutron dose is considered unfavorable in proton therapy because of possible long-term effects. Secondary radiations can cause cancer to recur in patients and healthy tissues to receive an extra dose of radiation. [4]

The content of the article is as follows: In the next section, there will be phantom simulation preparation of eye organ geometry, GATE software, algorithms and

calculations used to calculate secondary radiation doses. In the findings section, we conclude our study with the results and interpretation part, which will find the dose values obtained in the cancerous region in the retina and healthy tissues, and the dose distributions out of the area with the GATE software.

Materials and Methods

Geant4 is a program that allows wide use for simulating the penetration of defined particles through matter. Areas of application include studies in high energy, nuclear and accelerator physics, as well as medicine and space sciences. [5]

GATE combines the advantages of reality-tested physics models of the GEANT4 simulation toolset with extensive geometry definition and powerful 3D visualization and original features unique to emission tomography. The program, which consists of several hundred C++ codes, the mechanisms used to manage time, geometry and radioactive resources, creates with C++ codes thanks to GEANT4.

GATE specifically provides modeling capability. It is a program that allows simulating time-dependent physical events such as detector movements or source decay kinetics, time curves based on realistic conditions. [6]

In the Cartesian coordinate system, the Earth volume which we have determined as 5 m, is created in the x, y and z coordinates. Eye globe, Retina, Cornea, Lacrimal gland, Optic nerve, Temporal bone, Nasal bone, Optic chiasm, Lens, and Cancer tissue geometry, element contents were taken from various anatomy books, articles, ICRU Journal, 46, 1992, ICRP 89 data. [7,8,9,10,11,12,13,14]

If we accept the tumor tissue as the center, 800 Thousand Total Number Of Applications protons with the same characteristics of 20 Mev energy and 4 mm

emittance from 4 different points with 45 degree angles target the cancer tissue. By using the Pen Beam Scanning (PBS) method, Secondary Radiation Generation at the beam source is avoided. In treatments with PBS method, Secondary Radiation is caused by nuclear interactions with atoms of cells and tissues within the beam range of the patient. DoseActor and TLDoseActor are deployed to calculate the absorbed doses in all tissues inside and outside the field. DoseActor and TLEDoseActor algorithms will be discussed in the section.

In the simulation, proton beams with 20 MeV energies targeting the cancerous area from 4 different angles were selected and irradiation was carried out with Pen Beam Scanning Method (PBS). Also known as Active Scanning Proton Therapy, PBS uses a magnet system to conduct protons across the entire cross-section and deflect them at the particle exit, thus leading to the development of density modulated proton therapy (IMPT).

IMPT allows use of the entire tumor area to provide a homogeneously dispersed therapy to the target dose. The use of a range deflector in PBS dulls the flank edge, while collimation allows sharpening of the edge with precision from 2 to 4 mm, depending on the depth of the target tumor. The volume defined in the DoseActor is divided into three-dimensional pixels, namely Voxels, and the energies left by the particles passing through the voxels in these three-dimensional boxes are calculated cumulatively, and the total absorbed energy in the tissue is calculated. The TLE trace length estimator quickly calculates the absorbed energies of secondary particles such as photons and neutrons by using the position, velocity and time parameters as in the fog chamber. We put the DoseActor and TLEDoseActors actors which we evaluated in the simulation on all tissues that we defined with codes, and we determined the doses accumulated in these tissues by opening the root file and integrating the cumulative dose values in the graph.

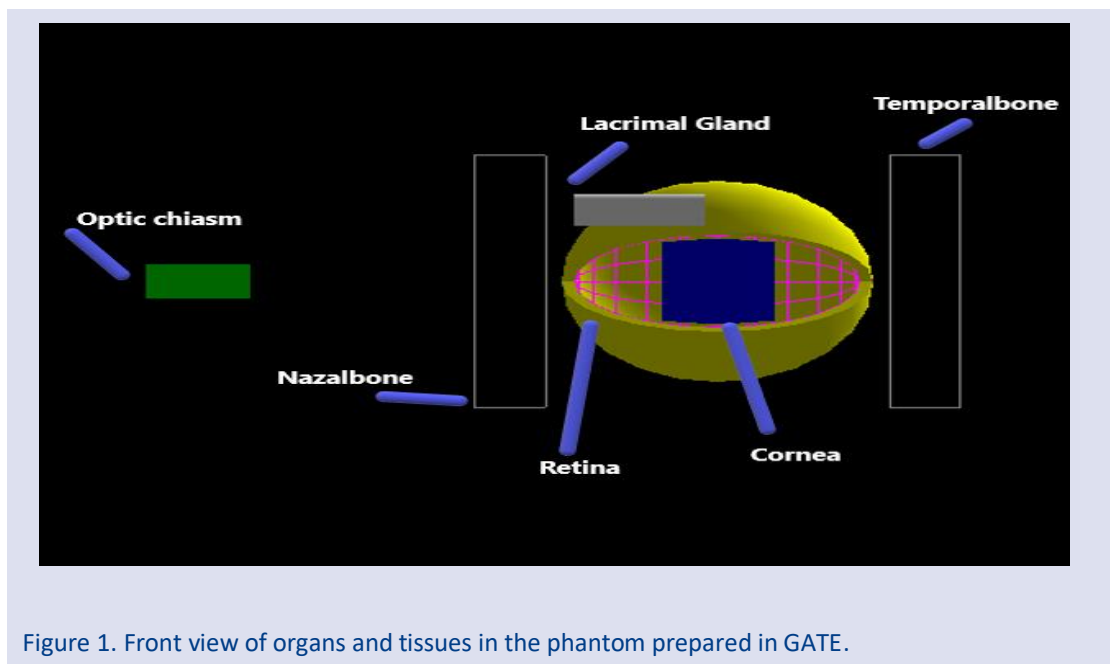


Figure 1. Front view of organs and tissues in the phantom prepared in GATE.

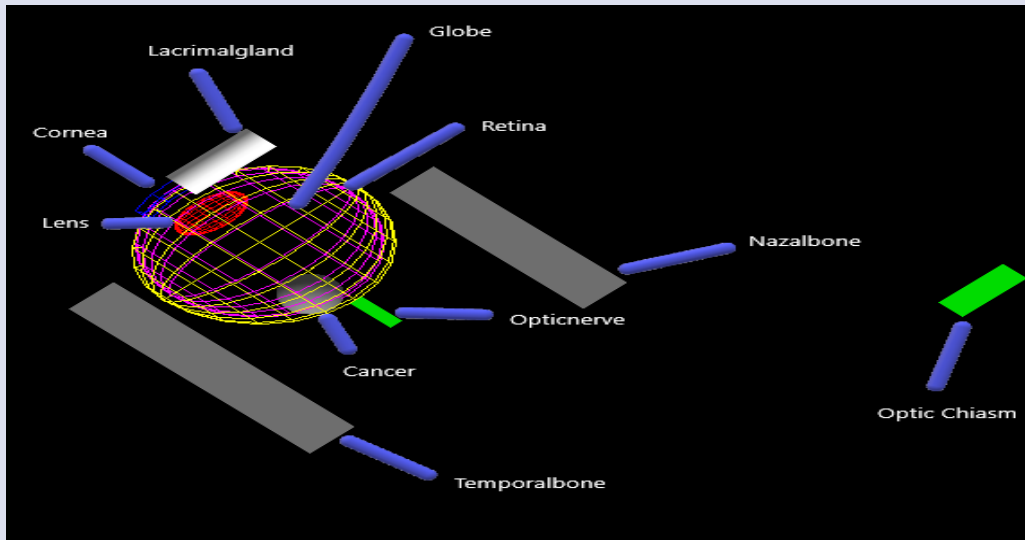


Figure 2. Top view representation of organs and tissues in the phantom prepared in GATE

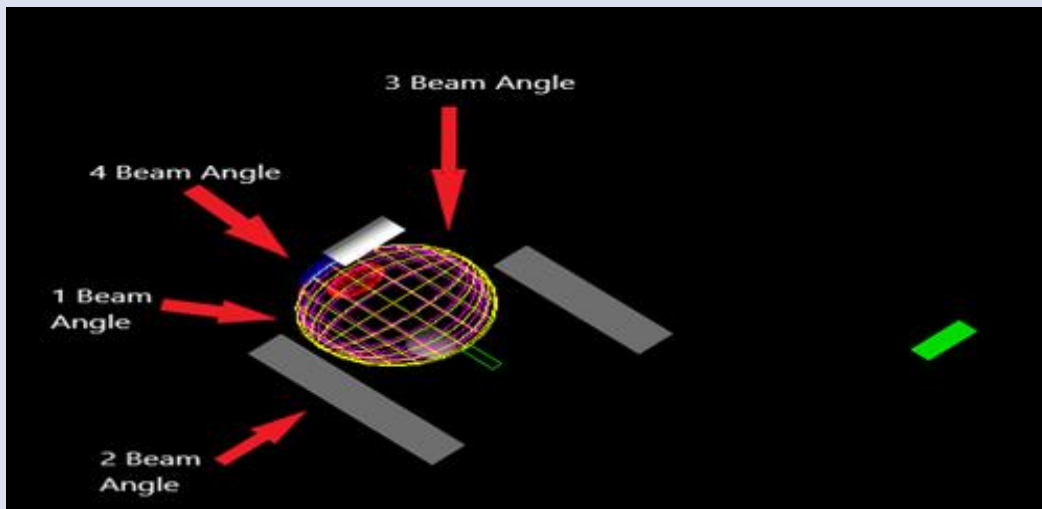


Figure 3. Top view representation of the directions of the source rays in the phantom prepared in GATE.

DoseActor and TLEDoseActor Algorithms

With the GATE 6.2 update made in 2014, DoseActor three-dimensional dose calculation has been enabled. DoseActor can display three-dimensional images and distribution of the energy collected in a certain area. While determining the DoseActor parameters, it is important to choose the voxel sizes according to the needs, the size of the selected volume and the emittance of the beam from the source. It also allows to choose resolution and position. When the DoseActor library is added to the desired volume, it divides it into particles called dosels, and stores all the energies collected in this volume, the uncertainties in the stored energy and dose, the square of the values in the stored energy and dose data, and the values such as the number of interacting particles with the ROOT file. In the volumes we determined in our study, the biochemical composition of

the material was determined beforehand. The DoseActors we place are calculated by dividing the total energy of the material in which it is located by the total volume and density. [17]

The track length estimator (TLE) deterministically calculates the values of secondary radiations (Rayleigh, Compton scattering) occurring after primary interactions using a hybrid algorithm. It calculates the path followed by the particles and the absorbed dose. This calculation is done much faster than conventional methods and can be seen clearly. It is used in MCNPX and MC codes. With the TLE method, it is based on the principle that all voxels in the volumes it encounters throughout the photon range leave their energy behind. For GATE, an algorithm called TLE application EPDL97 is employed. The selected energy range for each element, the coefficients drawn from the table before the simulation starts are loaded and these values are calculated deterministically. [17,18]

Results and Discussion

The secondary radiation values resulting from the interaction of protons with atoms throughout the interval for 10 tissues with different locations and biochemical structures, the cumulative dose values absorbed in the tissues, normalization values and percentage values are given in Table 1 and Table 2. At energies of 15, 20, 25, 30 Mev, a total of 32 different variations are made from 4 different angles with 4mm and 9mm emittance, and different angles are followed. Paired simple t-test was used when calculating statistics. For different values of energy, beam thickness and beam angle, at 5% significance level. The difference was evaluated.

H0: There is no statistically significant difference between 4 mm and 9 mm beam emittance values.

H1: There is a statistically significant difference between the 4 mm and 9 mm beam emittance values. In the second statistical evaluation, different angles were evaluated.

H0: There is no statistically significant difference between the 2nd beam angle and 4th mm beam angle values.

H1: There is a statistically significant difference between the 2nd beam angle and 4th mm beam angle values. In the third statistical analysis, beam energies were evaluated.

H0: There is no statistically significant difference between the values of 15 Mev and 30 Mev.

H1: There is a statistically significant difference between the values of 15 Mev and 30 Mev.

As a result, null hypotheses and alternative hypotheses were established. In the analysis, it was determined that there was a difference in energy values and beam emittance values at the 5% significance level, and there was no difference in the angle values at the same significance level. The confidence interval of the data was calculated. The values we obtained are given in Table 3.

When all energies were analyzed, the optimum values were found to be at 20 Mev energy. It was used at all angles and the advantageous 4mm beam thickness was used. Dose geometries in which tissues were absorbed were determined. 75.44% of the total dose was absorbed

in the tumor. 12.32% of the absorbed dose is absorbed by the Temporalbone, 8.34% by the Globe and 2.84% by the Retina. Dose percentages in non-target tissues remain below 1%. In addition, we could not get dose values in the out-of-range Optic Chiasma, which is very small and very small in volume, and in the Cornea, where we avoided the beam direction. In our study, it was determined that the Proton Emitted Bragg Peak (SOBP) provided high doses to the target volume, while the doses in the organs outside the area were within the dose limit values. Clinically, the treatment of retinalblastoma tumor relies on tumor volume, location, recurrence of cancer primarily in vital organs, and secondarily affecting visual sensation, with a radiation absorption of approximately 1.8 Gy per week traditionally according to the International Classification of Retinoblastoma, issued in 2003 for about 4-5 weeks. It is planned to be treated for only 5 days. At the end of the treatment, it is aimed to give a dose of approximately 45 Gy to the tumor.[1]

In our study, the value exposed to the temporal bone, which is the most dosed healthy structure at a total dose of 45 Gy given for tumor shadow treatment, was calculated as 7.34 Gy. [20] In other sensitive tissues, the dose was well below the limit values. Dose absorption from other tissues was calculated as 4.97 Gy in the eye fluid or globe, 1.69 Gy in the retina, and between 0.01 mGy and 0.53 Gy in other tissues.

In addition to the total absorbed doses in the simulation, the maximum dose was calculated as 1.065 mGy in the cancerous tissue and 0.088 mGy, 0.373 in the lens, retina, optic nerve and optic at the undesired secondary doses and the total doses cooled in the tissues. Chiasmatic tissues which are critical for vision and high radiation sensitivity, respectively. mGy were measured as < 0.001 mGy, < 0.001 mGy. As with Doseactor, no dose value was obtained in the cornea in TLE DoseActor. These values show that proton therapy has a low effect on secondary cancer formation and in tissues with high radiation sensitivity.

Total absorbed doses and percentage values resulting from secondary radiation produced as a result of nuclear interactions during irradiation of retinalblastoma cancer are given in Table 2

Table 1. Dose values cooled in organs and tissues in DoseActor algorithms, percentage values, normalization calculation.

Dose Actor, 800 Thousand Total Number Of Applications, 4 mm Beam Emittance, 20 Mev- 1,2,3,4. Beam Angle			
Organs and Tissue	Total Dose Values	Dosage Value Percentage Values	Normalization Accounts In Gy
Globe	0,064934287	8,34%	4.974 Gy
Cancer	0.58723832	75,43%	45.00Gy
Retina	0.02212048	2,84%	1.694 Gy
Temporalbone	0.095942601	12,32%	7.348 Gy
Nazalbone	1.1824136 e -5	<0.01%	6 mGy
Opticnerve	0.0012386610	0,16%	9,54 mGy
Lacrimalgland	1.0504367 e -5	<0.01%	6 mGy
Lens	0.0069477997	0,89%	0.53 Gy
Opticchiasm	2.7057855 e -8	<0.01%	<0.01 mGY
Cornea			

Table 2. Dose values cooled in organs and tissues in TLEDoseActor algorithms, percentage values, normalization calculation.

TLEDose Actor, 800 Thousand Total Number Of Applications, 4 mm Beam Emittance, 20 Mev- 1,2,3,4. Beam Angle				
Organs and Tissue	Total Dose Values	Dosage Value	Percentage Values	Normalization Accounts In Gy
Globe	1.2168534 e -5	26,29%		0.932 mGy
Cancer	1.3902021 e -5	30,03%		1.065 mGy
Retina	4.8661112 e -6	10,51%		0.373 mGy
Temporalbone	9.7501176 e -6	21,07%		0.747 mGy
Nazalbone	4.3429290 e -6	9,38%		0.332 mGy
Opticnerve	1.555112 e -10	<0.01%		<0.01 mGY
Lacrimalgland	8.2597376 e -8	0,02%		<0.01 mGY
Lens	1.1616141 e -6	2,51%		0.088 mGy
Opticchiasm	8.031298 e -9	<0.01%		<0.01 mGY
Cornea				

Table 3. In the paired sample t test table, the total dose values of all organs include t significance values and confidence intervals.

TLE DOSEACTOR+DOSEACTOR 200 Thousand Total Number Of Applications, 1 Beam Angle , 15 Mev Energy				
Organs and Tissue	4mm Beam Emittance Total Dose Total	9mm Beam Emittance Total Dose Total	D total	D ² total
Total	0,01482031	0,005717856208	9,10238187 . 10 ⁻³	2,039262820042. 10 ⁻⁴
Data	\bar{D}	SD	t account/ t 7,0.05	Confidence Interval
Values	0,001137798	0,0011973757	2,6796 / \pm 2.365	-2,8306 \leq μ D \leq 2,8329
TLE DOSEACTOR+DOSEACTOR 200 Thousand Total Number Of Applications, 4 mm Beam Emittance, 30 Mev Energy				
Organs and Tissue	2. Beam Angle Dose	4. Beam Angle Dose	D total	D ² total
Total	0,01603558534	0,0431035901	9,10238187 . 10 ⁻³	2,039262820042. 10 ⁻⁴
Data	\bar{D}	SD	t account / t 7,0.05	Confidence Interval
Values	-0,00338349591	0,0142164629	-0,6711 / \pm 2.365	-0,0355 \leq μ D \leq 0,02877
TLE DOSEACTOR+DOSEACTOR 200 Thousand Total Number Of Applications, 4 mm Beam Emittance, 2 Beam Angle Dose				
Organs and Tissue	15 Mev Energy	30 Mev Energy	D total	D ² total
Total	0,01777254	0,01665754	0,00175632286405	0,0001716112098014
Data	\bar{D}	SD	t account / t 7,0.05	Confidence Interval
Values	2,1954.10 ⁻⁴	2,1408 .10 ⁻⁵	29,533 / \pm 2.365	1,7.10 ⁻⁴ \leq μ D \leq 2,6.10 ⁻⁴

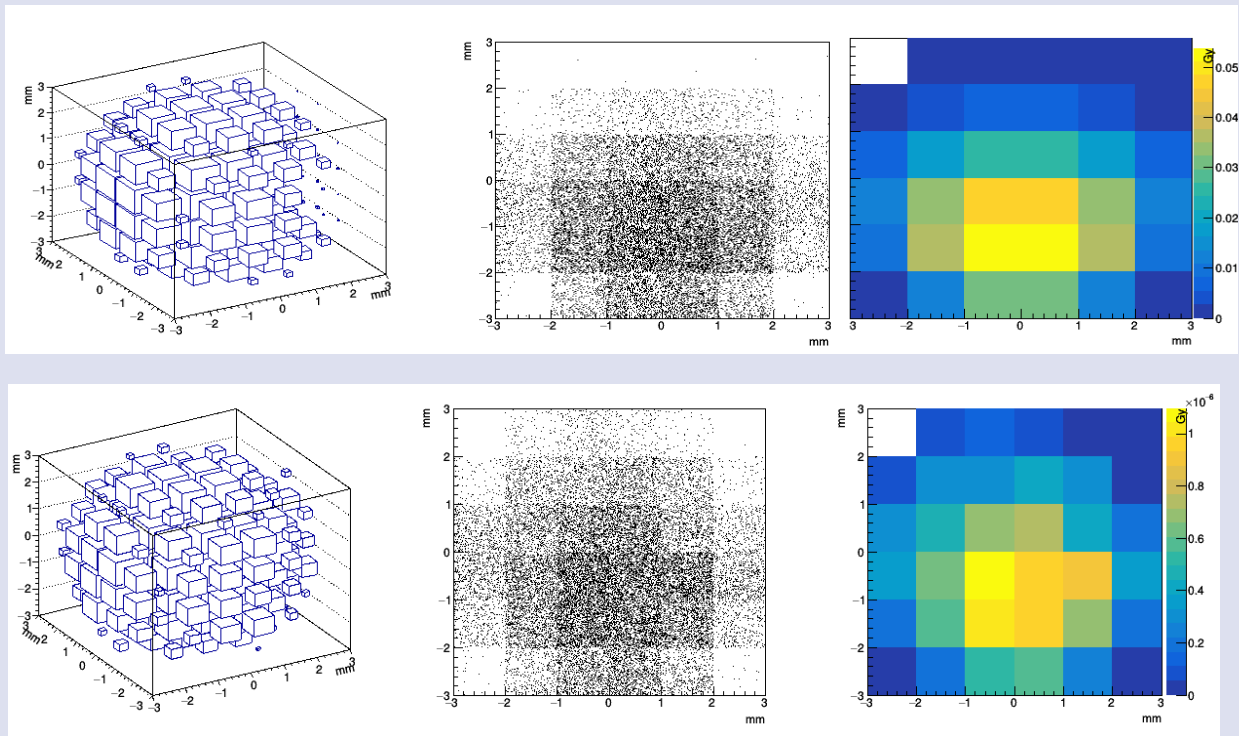


Figure 4. Measured by simulation in cancer tissue; 3B particle distribution (left), 2B particle distribution (centre) dose distribution (right) DoseActor algorithm (top) and TLE algorithm (bottom) dose data.

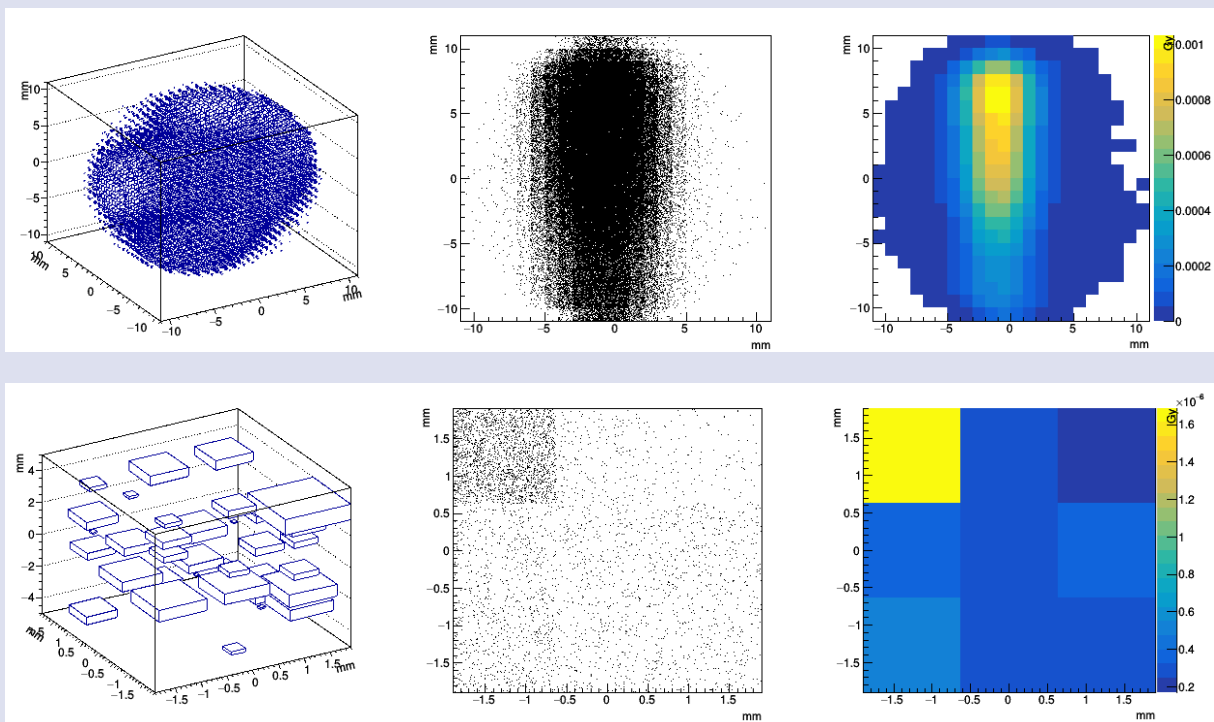


Figure 5. Measured by simulation in globe organ; 3B particle distribution (left), 2B particle distribution (centre) dose distribution (right) DoseActor algorithm (top) and TLE algorithm (bottom) dose data.

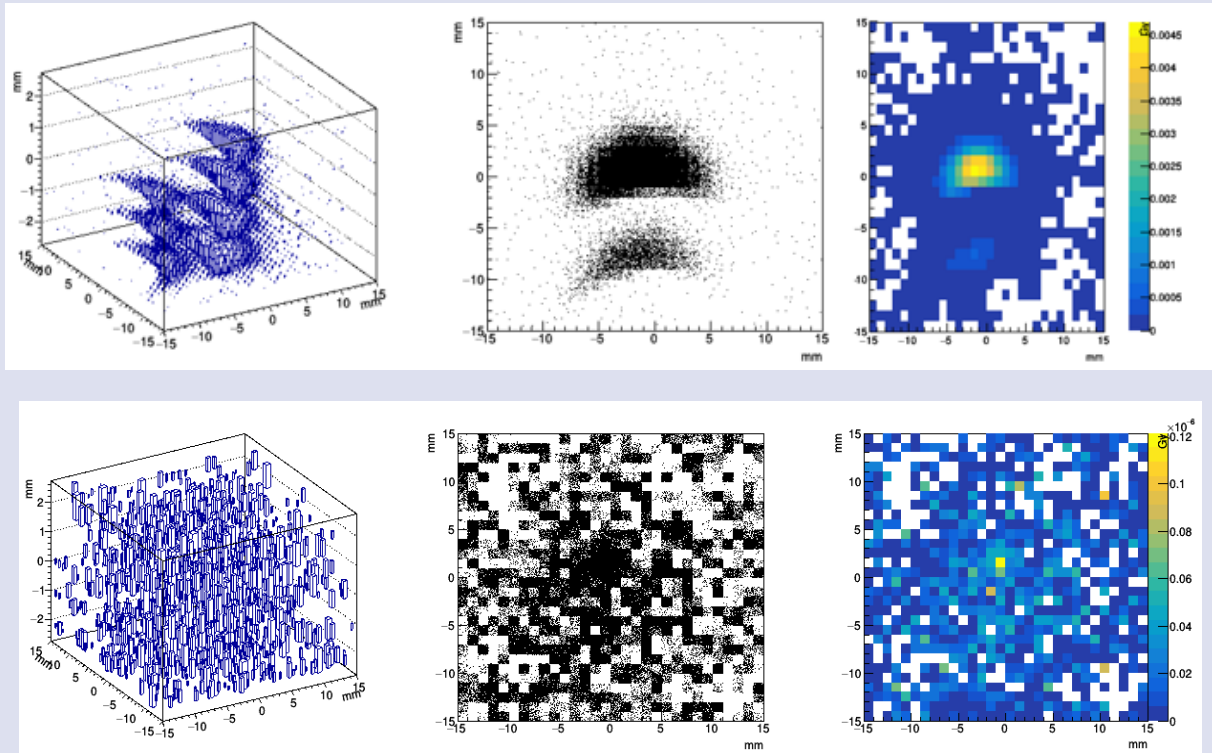


Figure 6. Measured by simulation in temporal bone tissue; 3B particle distribution (left), 2B particle distribution (centre) dose distribution (right) DoseActor algorithm (top) and TLE algorithm (bottom) dose data.

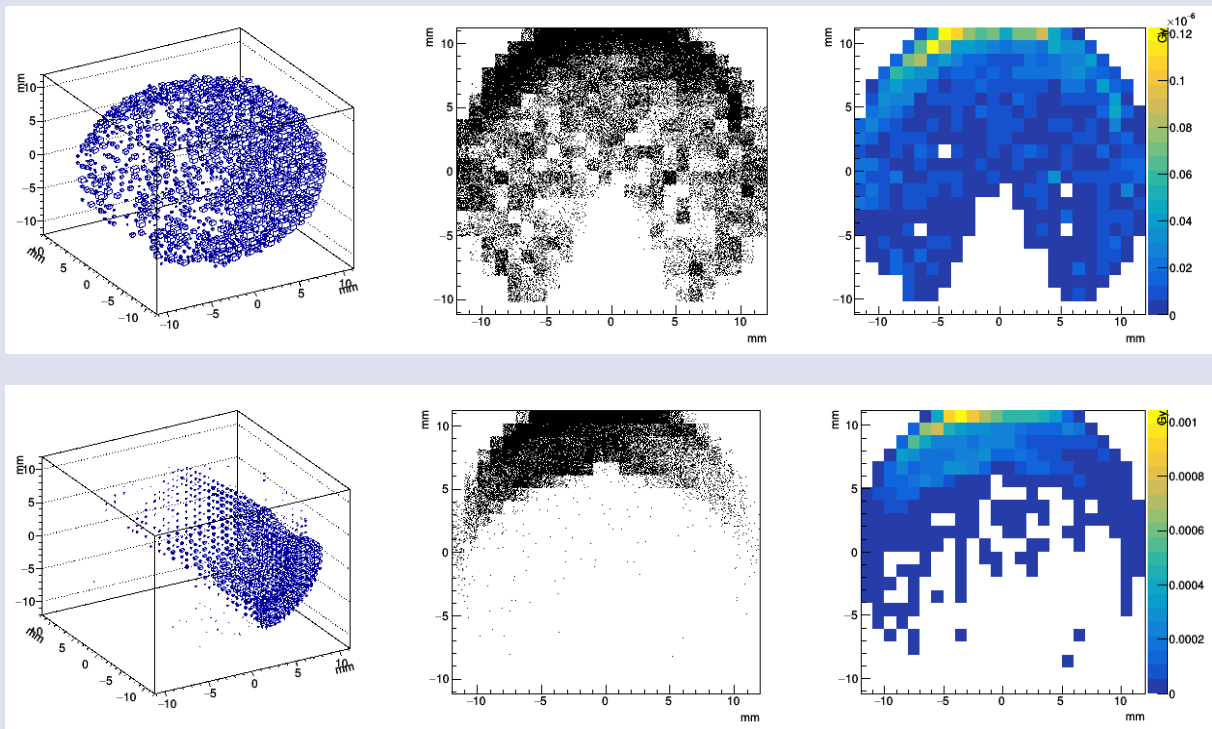


Figure 7. Measured by simulation in cancer tissue; 3B particle distribution (left), 2B particle distribution (centre) dose distribution (right) DoseActor algorithm (top) and TLE algorithm (bottom) dose data.

Conclusion

In our study, we determined the tissue to be given to cancer with a comprehensive trial. When different energy

values, different beam emittance and 4 different angles and paired simple t test values were compared in total dose calculations. A significant difference was found at 5% significance level in beam emittance and different energy

values. When evaluated for radiation given at different angles, no significant difference was observed at the 5% significance level. In the light of these statistics, we experimentally observed that by using different angles to reach the optimum dose. Least damage has been given to different tissues and that there was an improvement as expected. The best target dose was obtained using the beam thickness of 4mm. We also determined that the optimum energy is 20 MeV. It also showed the importance of Geant 4 software for accurate treatment planning because visual sensory tissues are radiosensitive before treatment. It is understood from the data that the effects of secondary radiations originating from unwanted neutrons and photons originating from atomic interactions on tissues are quite limited. At the end of our treatment plan, it was observed that the dose did not accumulate in the tissues above the critical dose value. In addition, the fact that the dose values are seen outside the area shows the importance of using dosimetry in the department employees working with higher energies in the long term.

Conflicts of interest

The authors state that did not have conflict of interests.

References

- [1] Munier F., Verwey J., Pica A., (Eds). New Developments in External Beam Radiotherapy for Retinoblastoma: From Lens To Normal Tissue-Sparing Techniques, *Clinical Experiments Ophthalmology*, 36 (2008) 78-89.
- [2] Lee T., Bilton D., Famiglietti R., (Eds). Treatment Planning With Protons For Pediatric Retinoblastoma, Medulloblastoma, And Pelvic Sarcoma: How Do Protons Compare With Other Conformal Techniques, *International Journal Radiation Oncology Biology Physics*, 36 (2005) 362-372.
- [3] M P Mehta, Proton Therapy Predictions for the Next Decade, Miami Cancer Institute, July 06, 2020.
- [4] Paganetti H. (Eds). Proton Therapy Physics. 1 nd ed. Boston, (2012) 516-544.
- [5] Geant 4 A Simulation Toolkit Available at: https://geant4.web.cern.ch/?statfacts_page=corp. Retrieved August 17, 2022.
- [6] GateOpenGate Collaboration Available at: https://opengate.readthedocs.io/en/latest/introduction/html?statfacts_page=corp. Retrieved August 17, 2022.
- [7] Başmak H., Gözün Anatomisi ve Fizyolojisi. 1 nd ed. Eskişehir, (2005) 12-44.
- [8] Valentin J.,(Eds). International Commission On Radiological Protection Basic Anatomical and Physiological Data for Use in Radiological Protection Reference Values, *ICRP Publication 89*, 32 (3-4) (2002) 217-220
- [9] Allisy A. (Eds). Reports of the International Commission on Radiation Units and Measurements, *ICRU Publication 46*, 24 (1) (1992) 19-24
- [10] Stafford S., Pollock B., Leavitt J., A Study Of The Radiation Tolerance Of The Optic Nerves And Chiasm After Stereotactic Radiosurgery, *International Journal Radiation Oncology Biology Physics*, 55, (2003) 77-81.
- [11] Vincent Gregoire, Wilfried De Neve, Avraham Eisbruch, Nancy Lee, Danielle Van den Weyngaert, Dirk Van Gestel, Intensity-Modulated Radiation Therapy For Head And Neck Carcinoma, *Oncologist*, 12 (2007) 555-564.
- [12] Haegin Hana, Yeon Soo Yeoma, Thang Tat Nguyen, Chansoo Choia, Hanjin Leea, Bangho Shina, Chan Hyeong Kima, Development of Detailed Eye Models for Pediatric Phantoms, *Transactions of the Korean Nuclear Society Autumn Meeting Gyeongju*, 103 (2017) 6.
- [13] Steven Nguyen, Julian Sison, Marjorie Jones, Jesse L Berry, Jonathan W Kim, A Linn Murphree, Vanessa Salinas, Arthur J Olch, Eric L Chang, Kenneth K Wong, Lens Dose-Response Prediction Modeling and Cataract Incidence in Patients With Retinoblastoma After Lens-Sparing or Whole-Eye Radiation Therapy, *International Journal Radiation Oncology Biology Physics*, 103 (5) (2019) 1143-1150.
- [14] Jones B., Errington D., Proton Beam Radiotherapy, *British Journal Of Radiology*, 73 (2000) 802-805.
- [15] Frances C., Charlwood, A., H., Aitkenhead, Ronald I. Mackay, A Monte Carlo Study On The Collimation Of Pencil Beam Scanning Proton Therapy Beams, *Medical Phys.*, 43 (2016) 1462-1472
- [16] Baldacci F., Mittone A., Bravin A., (Eds). A Track Length Estimator Method For Dose Calculations In Low-Energy X-Ray Irradiations, *Implementation, Properties And Performance, Zeitschrift Für Medizinische Physik*, 25 (2015) 36-47.
- [17] Smekens F., Freud N., (Eds). Simulation Of Dose Deposition In Stereotactic Synchrotron Radiation Therapy, *A Fast Approach Combining Monte Carlo And Deterministic Algorithms*, 54 (2009) 4671-4685
- [18] Stewart, F., Akleyev A., Hauer J., (Eds). ICRP Statement on Tissue Reactions and Early and late Effects of Radiation in Normal Tissues and Organs Threshold Doses for Tissue Reactions, *ICRP Publication*, 41 (1-2) (2012) 293-300.

Production Cross-section and Reaction Yield of ^{82}Sr for $^{82}\text{Sr}/^{82}\text{Rb}$ Generator

Şevki Şentürk^{1,a,*}, Tuncay Bayram^{1,b}, Serkan Akkoyun^{2,c}

¹Department of Physics, Faculty of Science, Karadeniz Technical University, Trabzon, Türkiye.

²Department of Physics, Faculty of Science, Sivas Cumhuriyet University, Sivas, Türkiye.

*Corresponding author

Research Article

History

Received: 11/02/2022

Accepted: 10/10/2022

Copyright




©2022 Faculty of Science,
Sivas Cumhuriyet University

ABSTRACT

There are many radioisotopes used for diagnostic and therapeutic purposes in nuclear medicine. One of the radioisotopes used for diagnostic purposes is ^{82}Rb . It is used in positron emission tomography (PET) as to be positron emitter and commonly obtained from $^{82}\text{Sr}/^{82}\text{Rb}$ generator. In this study, we have investigated some possible production mechanisms of ^{82}Sr by regarding $^{82}\text{Sr}/^{82}\text{Rb}$ generator. $^{85,87}\text{Rb}(p,xn)^{82}\text{Sr}$ and $^{80,82,83,84,86}\text{Kr}(^3\text{He},xn)^{82}\text{Sr}$ reaction channels have been investigated using the Constant Temperature Fermi Gas Model (CTFGM), Back Shifted Fermi Gas Model (BSFGM), and Generalised Superfluid Model (GSM) models within the framework of TALYS 1.9 nuclear reaction code. It has been seen that the production cross-sections, reaction yields and total activation values calculated up to 60 MeV beam energy value are in agreement with the available data in the literature.


Keywords: Production cross-section, Reaction yield, Strontium-82.


 sevkiisenturk61@gmail.com

 <https://orcid.org/0000-0001-8355-1307>

 t.bayram@ymail.com

 <https://orcid.org/0000-0003-3704-0818>

 sakkoyun@cumhuriyet.edu.tr

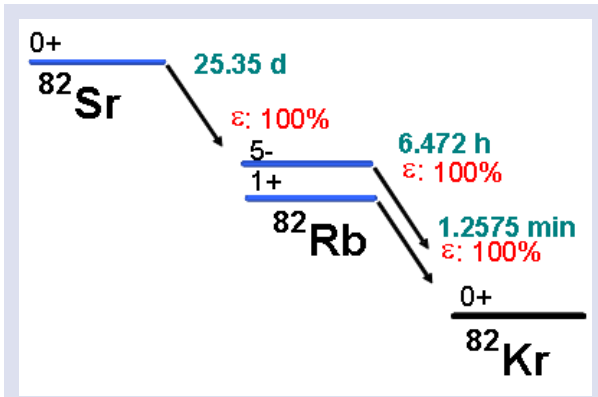
 <https://orcid.org/0000-0002-8996-3385>

Introduction

Today, radioisotopes are commonly used in the diagnosis and treatment of many diseases in nuclear medicine. While gamma or positron emitting radioisotopes are preferred for diagnostic use ($^{99\text{m}}\text{Tc}$, ^{18}F), beta emitter radioisotopes are preferred for therapeutic use (^{67}Cu , ^{188}Re , ^{90}Y , ^{131}I) [1]. Studies on these commonly used radioisotopes and potential radioisotopes are still ongoing [2]. One of the commonly used radioisotopes in nuclear medicine is ^{82}Rb radioisotope, which is obtained from $^{82}\text{Sr}/^{82}\text{Rb}$ generator. ^{82}Sr has a half-life of approximately 25.55 days. It transforms into the short half-life (76.38 s) radioisotope ^{82}Rb by 100% EC [3] as shown in Figure 1. ^{82}Rb is used in Positron Emission Tomography (PET) applications in nuclear medicine. ^{82}Rb is obtained from the decay its parent, ^{82}Sr , which is commercially available as $^{82}\text{Sr}/^{82}\text{Rb}$ generator system [4]. Radionuclide generators are a convenient method for in situ radioisotope production and provide an alternative to cyclotrons for rapid and regular production of short half-life radionuclides for clinical use [5,6].

In the process from past to present, many studies have been carried out on the production of ^{82}Sr by different nuclear reaction channels. For example, one of the proton bombardment studies, such as the $^{85}\text{Rb}(p,4n)^{82}\text{Sr}$ reaction [7,8], has been done by Kastleiner et al. in 2001. In the experimental study using the stacked foil technique, the margin of error has been calculated as 13-26% and best reaction cross section value obtained has been determined as 195 mb at 45 MeV [9]. Another study has been conducted by Buthelezi et al. in 2006 [10] for the $^{85}\text{Rb}(p,xn)^{82}\text{Sr}$ [10,11] reaction. In the experimental study, Rb target nuclei has been bombarded with proton and

cross section measurements has been taken in the energy range of 1-100 MeV and compared with the theoretical values obtained with the help of ALICE nuclear reaction program for the same reaction values. Maximum cross section value obtained has been determined as 148 mb at 67,37 MeV. In 2019, Zagryadskii et al., in their experimental study using a different reaction channel ($^{82,83,84}\text{Kr}(^3\text{He},xn)^{82}\text{Sr}$), bombarded $^{82,83,84}\text{Kr}$ target with ^3He , and cross section measurements has been made in the energy range of 20-75 MeV. Determined the best values obtained as 193, 173 and 110 mb at 33, 45 and 64 MeV, respectively [12]. Apart from these, many different studies are available in the literature for the production of ^{82}Sr radioisotope; $^{85,87}\text{Rb}(d,xn)^{82}\text{Sr}$ [13], and $^{80,82,83}\text{Kr}(\alpha,xn)^{82}\text{Sr}$ [14]. In this study, we have investigated some possible production mechanisms of ^{82}Sr by regarding $^{82}\text{Sr}/^{82}\text{Rb}$ generator. In this study, it is aimed to examine the nuclear reaction channels at low energy values and to provide preliminary data for the experimental studies to be made for the radioisotope production of the optimal values obtained. In this context, $^{85,87}\text{Rb}(p,xn)^{82}\text{Sr}$ and $^{80,82,83,84,86}\text{Kr}(^3\text{He},xn)^{82}\text{Sr}$ reaction channels have been investigated using the Constant Temperature Fermi Gas Model (CTFGM), Back Shifted Fermi Gas Model (BSFGM), and Generalised Superfluid Model (GSM) models within the framework of TALYS nuclear reaction code. It has been discussed the production cross-section, reaction yields and total activation values calculated up to 60 MeV beam energy value are agreement with the available data in the literature.

Figure 1. ^{82}Sr decay scheme.

Calculations

In this study, we have investigated some possible production mechanisms of ^{82}Sr by regarding $^{82}\text{Sr}/^{82}\text{Rb}$ generator using the TALYS nuclear reaction code. $^{85,87}\text{Rb}(p,xn)^{82}\text{Sr}$ and $^{80,82,83,84,86}\text{Kr}(^3\text{He},xn)^{82}\text{Sr}$ reaction channels have been investigated using the Constant Temperature Fermi Gas Model (CTFGM), Back Shifted Fermi Gas Model (BSFGM), and Generalised Superfluid Model (GSM) models of Level Density Model up to 60 MeV energy value within the framework of TALYS nuclear reaction code. TALYS is a simulation program used for the analysis of nuclear reaction experiments and obtaining nuclear data. This program provides information about the interaction between particles and nuclei such as protons, neutrons and ^3He at energies in the energy range of 1 keV-200 MeV, helping to provide an optimization between experimental and theoretical data [15].

TALYS nuclear reaction code includes several nuclear reaction models that allow for a better understanding of nuclear reactions, which allows for a better evaluation of nuclear reactions. For example, Fermi Gas Model (FGM) is one of the best known level density models. Since it is based on the assumption that the single particle states that make up the excited energy levels of the nucleus are equally spaced, it is a successful model at low energy levels but fails at high energy levels. In the CTFGM, the excitation energy was examined in two ways. In the low energy region (from 0 MeV up to matching energy E_M), the law of Constant Temperature was applied and in the high energy region, Fermi Gas law was applied. The constant temperature part of the total level density model is given in the equation below. The nuclear temperature T and E_0 are parameters that serve to adjust the formula to the experimental discrete levels [16].

$$\rho_T^{tot} = \frac{dN(E_x)}{dE_x} = \frac{1}{T} \exp\left(\frac{E_x - E_0}{T}\right)$$

BSFGM has been developed to allow the coupling energy to be considered as a modifiable parameter at low energies. The expression for the total BFM level density is given by the following expression [17].

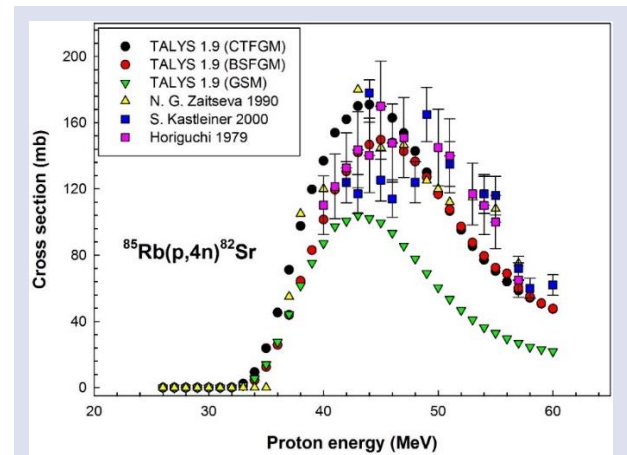
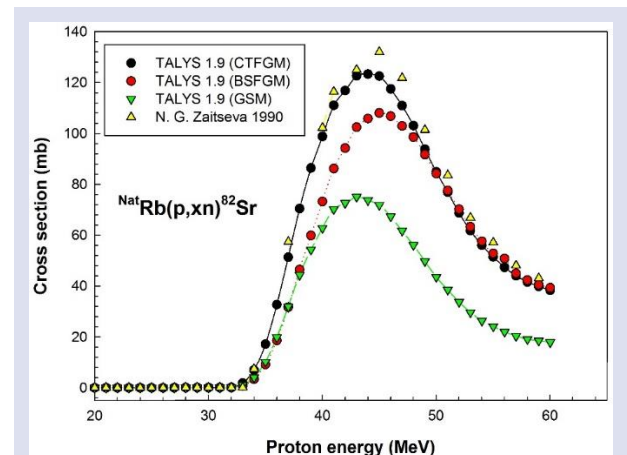
$$\rho_{BFM}^{tot}(E_x) = \left[\frac{1}{\rho_F^{tot}(E_x)} + \frac{1}{\rho_0(E)} \right]^{-1}$$

In addition, GSM is a model used to characterize phase transitions from superfluid behavior in the low energy region to the high energy region. The expression for the total GSM level density is given by the following expression [18].

$$\rho_{GSM}^{tot}(E_x) = \frac{1}{\sqrt{2\pi\sigma}} \frac{\sqrt{\pi}}{12} \frac{\exp[2\sqrt{\sigma U}]}{a^{1/4} U^{1/4}}$$

Results and Discussion

In this study, we have calculated the production cross sections, reaction yields and total activation values up to 60 MeV beam energy value for $^{85,87}\text{Rb}(p,xn)^{82}\text{Sr}$ and $^{80,82,83,84,86}\text{Kr}(^3\text{He},xn)^{82}\text{Sr}$ reaction channels via TALYS 1.9 code. The obtained production cross-section calculations are shown in Figures 2-7.

Figure 2. Cross-section for the $^{85}\text{Rb}(p,4n)^{82}\text{Sr}$ nuclear reaction.Figure 3. Cross-section for the $^{\text{Nat}}\text{Rb}(p,xn)^{82}\text{Sr}$ nuclear reaction.

In Figures 2 and 3, comparisons of $^{85}\text{Rb}(p,4n)^{82}\text{Sr}$ and $^{85}\text{Rb}(p,xn)^{82}\text{Sr}$ reactions cross section calculations with available data in the literature has been given in Ref. [9,19,20]. As seen in Figure 2 and 3, the calculated cross-section values up to energy values of approximately 32 MeV with the considered three TALYS models are around zero. Considering both reactions, the results of GSM model are not so compatible with the experimental data. GSM model gives low cross-section values. The other two models were generally found to be more compatible with the available data, especially in the high energy region. The best level density model for ^{82}Sr production by both reaction channels has been determined as CTFGM. According to the best model, maximum cross-section for $^{85}\text{Rb}(p,4n)^{82}\text{Sr}$ and $^{85}\text{Rb}(p,xn)^{82}\text{Sr}$ has been calculated as 170.982 mb at 44 MeV and 123 mb at 42 MeV, respectively. Considering the margins of error of the studies in the literature used in the comparison (margins of error are approximately 10-20%), it seems that the values obtained are acceptable.

In Figures 4-7, the production cross-section of $^{82,83,84}\text{Kr}(^3\text{He},xn)^{82}\text{Sr}$ reactions are presented. As can be seen in figure 4, significant peak values in the energy range of 18-30 MeV were obtained for the $^{82}\text{Kr}(^3\text{He},3n)^{82}\text{Sr}$ reaction channel and they were seen that CTFGM was the model that best fitted the available data. Maximum cross-section value for this reaction channel has been calculated as 202.393 mb at 22 MeV. Figure 5 and 6 show the cross-section values for the $^{83,84}\text{Kr}(^3\text{He},xn)^{82}\text{Sr}$ reaction channels. As can be seen, the data in the low energy region were not obtained, the cross-section values showed a significant peak in the range of 40-60 MeV and the BSFGM model is the most compatible model with the available experimental data. In addition they were observed that the maximum cross-section value for these reaction channels were obtained from CTFGM, that GSM was not compatible with the available data and low cross-section values were obtained. Maximum cross-section value for this reaction channel has been calculated as 22.637 mb and 17.019 mb at 44 MeV and 58 MeV, respectively. The figure 7 was indicated the BSFGM for $^{84}\text{Kr}(^3\text{He},xn)^{82}\text{Sr}$ reaction channel more consistent with the available data although the best cross-section values are obtained from CTFGM that indicated. The obtained data has been compared with the accessible data in the literature, and it was seen that the results are found acceptable when the margins of error in the studies has been taken into account (margins of error are approximately 13-26%) [12,13].

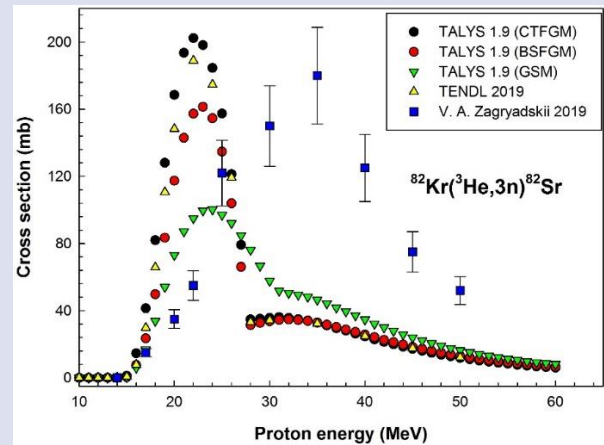


Figure 4. Cross-section for the $^{82}\text{Kr}(^3\text{He},3n)^{82}\text{Sr}$ nuclear reaction.

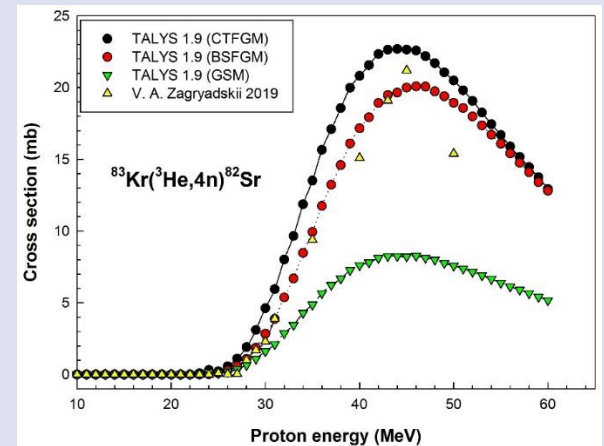


Figure 5. Cross-section for the $^{83}\text{Kr}(^3\text{He},4n)^{82}\text{Sr}$ nuclear reaction.

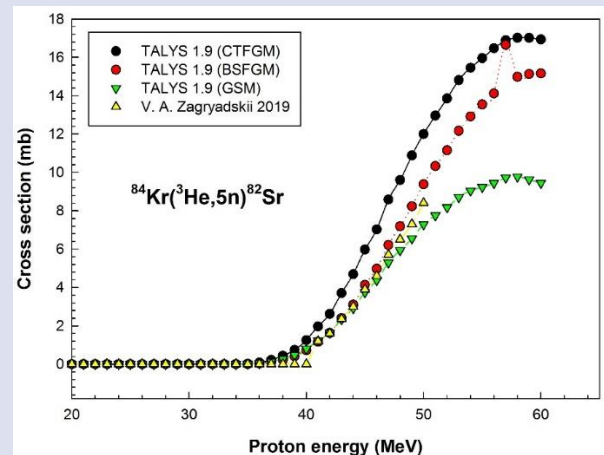


Figure 6. Cross-section for the $^{84}\text{Kr}(^3\text{He},5n)^{82}\text{Sr}$ nuclear reaction.

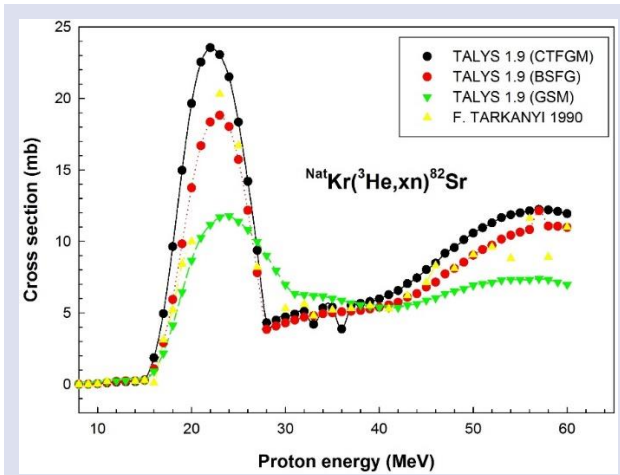


Figure 7. Cross-section for the $^{nat}\text{Kr}(^3\text{He},x\text{n})^{82}\text{Sr}$ nuclear reaction.

Another important part of radioisotope production is reaction yield. Reaction yield allows us to obtain information about the different possible radioisotope production values of nuclear reactions. In this study, we have calculated reaction yield of $^{80,82}\text{Kr}(^3\text{He},x\text{n})^{82}\text{Sr}$ reactions for 5 mA. As can be clearly seen in Figure 8, $^{80,82}\text{Kr}(^3\text{He},x\text{n})^{82}\text{Sr}$ reaction yields are 0.01248 and 0.2160 GBq/mAh, respectively.

In addition, total activation values has been calculated as seen in Figures 9 and 10. Maximum total activities values for $^{80}\text{Kr}(^3\text{He},\text{n})^{82}\text{Sr}$ and $^{82}\text{Kr}(^3\text{He},3\text{n})^{82}\text{Sr}$ reactions are 1.4782 and 25.5668 GBq, respectively. As seen in Figures 9 and 10, total activities are constant up to after cutting of the irradiation.

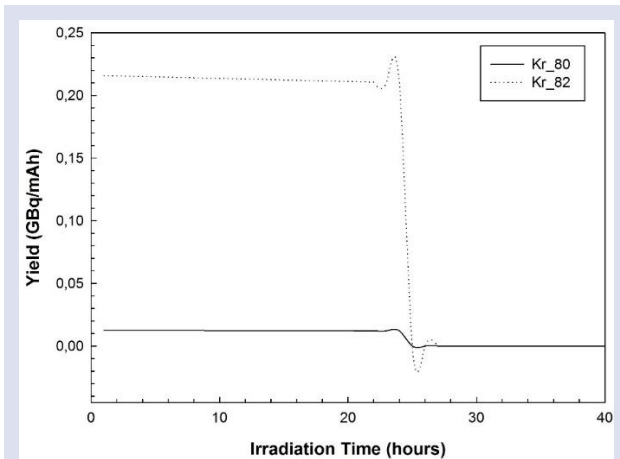


Figure 8. Reaction yields of $^{80,82}\text{Kr}(^3\text{He},x\text{n})^{82}\text{Sr}$ reactions.

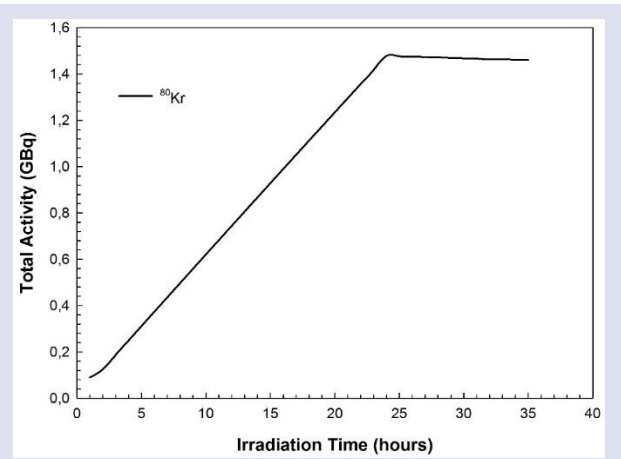


Figure 9. Total activity of $^{80}\text{Kr}(^3\text{He},\text{n})^{82}\text{Sr}$ nuclear reaction.

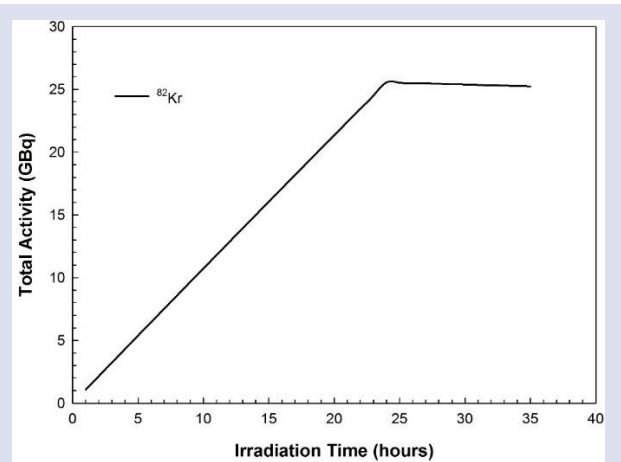


Figure 10. Total activity of $^{82}\text{Kr}(^3\text{He},3\text{n})^{82}\text{Sr}$ nuclear reaction.

Conclusion

The aim of this study was to examine the production cross sections of the ^{82}Sr radioisotope used in nuclear medicine at low energy levels [0-60 MeV]. In this context, some possible production mechanisms of $^{85,87}\text{Rb}(p,x\text{n})^{82}\text{Sr}$ and $^{80,82,83,84,86}\text{Kr}(^3\text{He},x\text{n})^{82}\text{Sr}$ reaction channels have been investigated within the framework of TALYS nuclear reaction code. As a result of this study, it has been seen that the GSM calculations were inconsistent with the existing data and low cross-section values were obtained. CTFGM and BSFGM calculations generally yielded results consistent with the available data. But the maximum production cross-section values were obtained from CTFGM. Best production cross-section for $^{82}\text{Sr}/^{82}\text{Rb}$ generator were 170.982 mb for $^{85}\text{Rb}(p,4\text{n})^{82}\text{Sr}$ reaction and 202.393 mb for $^{82}\text{Kr}(^3\text{He},3\text{n})^{82}\text{Sr}$ reaction at 44 MeV and 22 MeV, respectively. In addition, maximum reaction yield values for 5 mA current have been calculated as 0.01248 and 0.2160 GBq/mAh for $^{80}\text{Kr}(^3\text{He},\text{n})^{82}\text{Sr}$ reaction and $^{82}\text{Kr}(^3\text{He},3\text{n})^{82}\text{Sr}$ reaction, respectively.

The total activation values have been calculated as 1.4782 and 25.5668 GBq, respectively. Considering the margins of error in existing experimental studies and the inadequacy of specific experimental studies in this field, the comparison of the obtained results is open to discussion.

Conflicts of interest

There are no conflicts of interest in this work.

References

- [1] Gündoğdu E.A., Özgenç E., Ekinci M., Nükleer Tıpta Görüntüleme ve Tedavide Kullanılan Radyofarmasötikler, *J Lit Pharm.*, 7 (1) (2018) 24-34.
- [2] Azaam A., Excitation functions for proton-induced reactions on Te and ^{nat}Ti targets: Measurements and model calculations special relevant to the ¹²⁸Te(p,n)¹²⁸I reaction, *Nuclear Physics A.*, 121790 (2020) 999.
- [3] ⁸²Sr Decay scheme, NOS. Available at: <https://www.google.com/search?q=sr82+decay+scheme&rlz>. Retrieved October 4, 2022.
- [4] Aardenah K., van der Walt T.N., Davids C., Radiochemical separation of ⁸²Sr and preparation of sterile ⁸²Sr/⁸²Rb generator column, *J. Radionucl. Chem.*, 270 (2006) 385-390.
- [5] Hoffman I., Medical isotope production, research reactors and their contribution to the global xenon background, *Journal of Radioanalytical and Nuclear Chemistry*, 318 (2018) 165-173.
- [6] Phillips D.R., Peterson E.J., Production of strontium-82 for the Cardiogen PET generator: a project of the Department of Energy Virtual Isotope Center, *Radiochim. Acta.*, 88 (2000) 149-155.
- [7] Horiguchi T., Noma H., Yoshizawa Y., Excitation functions of proton-induced nuclear reaction on ⁸⁵Rb, *J. Appl. Rad. Isot.*, 36 (1980) 141-151.
- [8] Vereshchagin Yu.I., Zagryadskiy V.A., Prusakov V.N., Cyclotron ⁸²Sr production for medical applications, *Nuclear Instruments and Methods to Physics Research A.*, 334 (1993) 246-248.
- [9] Kastleiner S., Qaim S.M., Nortier F., Excitation functions of ⁸⁵Rb(p,xn)^{85m,g,83,82,81}Sr reactions up to 100 MeV integral test of cross section data, comparison of production routes of ⁸³Sr and thick target yield of ⁸²Sr, *Applied Radiation and Isotopes*, 56 (2002) 685-695.
- [10] Buthelezi E.Z., Nortier F.M., Schroeder I.W., Excitation functions for the production of ⁸²Sr by proton bombardment of ^{nat}Rb at energies up to 100 MeV, *Applied Radiation and Isotopes*, 64 (2006) 915-924.
- [11] Deptula C., et al., Excitation functions and yields for medically important generators ⁸²Sr-⁸²Rb, ¹²⁵Xe-¹²³I and ²⁰¹Bi-²⁰⁰Tl obtained with 100 MeV protons, *Nukleonika*, 35 (1-3) (1990) 3-22.
- [12] Zagryadskii V.A., Latushkin S.T., Measurement of ^{82,83,84}Kr(³He,xn)⁸²Sr cross sections in kurchatov institute U-150 Cyclotron, *Atomic Energy*, 126 (2019) 5.
- [13] Tarkanyi F., Hermanne A., Activation cross section data of deuteron induced nuclear reactions on rubidium up to 50 MeV, *Eur. Phys. J. A.*, (2021) 57-21.
- [14] Zagryadskii V.A., Latushkin S.T., Experimental determination of ^{80,82,83}Kr(α,xn)⁸²Sr cross sections for reaction threshold to 60 MeV α-particles, *Atomic Energy*, 110 (2011) 2.
- [15] Koning A., Hilare S., Goriely S., TALYS user manual, 2015.
- [16] Ignatyuk A.V., Istekov K.K., The role of collective effects in the systematics of nuclear level densities, *Yad. Fiz.*, 29(4) (1979) 875-883.
- [17] Baba H., Nucl. Phys. A., A shell-model nuclear level density, 159(2) (1970) 625641.
- [18] Ignatyuk A.V., Smirenkin G.N., Tishin A.S., Phenomenological description of energy dependence of the level density parameter, *Sov. J. Nucl. Phys.*, 21 (1975) 255.
- [19] Horiguchi T., Noma H., Yoshizawa Y., Excitation functions of proton induced nuclear reactions on ⁸⁵Rb, *International J. of Appl. rad. and Isotopes*, 31 (1979) 141-151.
- [20] Zeitseva N.G., et al., Cross section for the 100 MeV proton induced nuclear reactions and yields of some radionuclides used in nuclear medicine, *Radiochimica Acta.*, 54 (1991) 57-72.

Calculation of One- and Two-Center Overlap Like Quantum Similarity Integrals over $\psi^{(\alpha)}$ Exponential Type Functions

Ercan Şahin^{1,a,*}¹Taşova Yüksel Akın Vocational School, Amasya University, Amasya, Türkiye.

*Corresponding author

Research Article

History

Received: 28/06/2022

Accepted: 17/10/2022

Copyright

©2022 Faculty of Science,
Sivas Cumhuriyet University

ABSTRACT

One- and two-center overlap like quantum similarity integrals over $\psi^{(\alpha)}$ functions are evaluated using the one-center expansion method. These integrals are expressed through expansion coefficients and usual two-center overlap integrals. The expressions derived in this work have no restrictions for the values of orbital parameters, quantum numbers and internuclear distances. Since these integrals of $\psi^{(\alpha)}$ functions are calculated for the first time, the comparison is made with literature values obtained from Slater type functions. The computation results are in good agreement with literature values. The algorithm presented in this study could be useful when exponential type functions are employed in quantum similarity measures of atomic and molecular systems.

Keywords: $\psi^{(\alpha)}$ function, Expansion theorem, Overlap-like quantum similarity integral, Exponential type function

 ercan.sahin@amasya.edu.tr <https://orcid.org/0000-0002-4588-1257>

Introduction

Quantum similarity measure (QSM) was firstly introduced in early 1980s as a quantitative comparison tool between molecules via their electron density functions [1]. Nowadays, QSM has a wide range of application area in quantitative structure-activity/property relationship (QSAR and QSPR) problems. The main idea of the QSM concept is that molecular electron density distribution can be used as a descriptor to compare molecular structures. Further details and extensive bibliography can be found in refs. [2-6]. The QSM is also extended to atomic [7] and nuclear [8] systems to analyze periodicity of the properties of them.

Electron density is used as information carrier of the system in QSM approach. Hence, description of the electron density is important subject to obtain reliable results. In most of the ab initio methods, density is defined by means of one-particle wave functions of investigated system and therefore used basis functions have significance. Gaussian type functions are the most popular basis functions and the first choice in QSM calculations due to their computational simplicity. Molecular electronic densities are modeled by spherical Gaussians with the help of atomic shell approximation [9, 10]. However, it is well known that the electronic wave function of atomic or molecular systems can be better represented with exponential type functions (ETFs) [11]. For this reason, the simplest form of ETFs called Slater type functions (STFs) were tested in atomic QSM studies. Larger

electron charge concentration was obtained near the nuclei with STFs, and this led to better description of atomic overlap self-similarities [12]. Molecular overlap-like quantum similarity (OLQS) integrals of STFs were also investigated by using one-center two-range expansion [13] and Fourier transform [14-17] methods. The accuracy in Fourier transform method was improved through the convergence acceleration techniques such as epsilon algorithm of Wynn [14], nonlinear \bar{D} transformation [15, 16] and nonlinear $S\bar{D}$ transformation [17].

In the present work, we use $\psi^{(\alpha)}$ functions [18, 19] as basis function to express electron density in molecular QSM calculations. These functions collect a large class of ETFs. Each value of the α parameter in the range $-\infty < \alpha < 3$ corresponds to a different complete orthonormal set of ETFs. For instance, Coulomb-Sturmian and Lambda functions can be obtained from $\psi^{(\alpha)}$ functions for $\alpha = 1$ and $\alpha = 0$ cases, respectively. The $\psi^{(\alpha)}$ functions play a significant role in different topics of atomic and molecular physics such as electronic structure studies, momentum and four-dimensional space representations of ETFs, and molecular integral solutions of STFs [20]. The aim of this study is to perform one- and two-center OLQS integrals of $\psi^{(\alpha)}$ functions. This can be considered as a first step for the usage of these functions in QSMs.

General Definitions and Properties

$\psi^{(\alpha)}$ Complete Orthonormal Sets of Exponential Type Functions

In this study, we have used standard definition of $\psi^{(\alpha)}$ ETFs for integer values of α parameter ($\alpha = 2, 1, 0, -1, \dots$) given by [18]:

$$\psi_{nlm}^{(\alpha)}(\zeta, \vec{r}) = N_{nl}^{\alpha}(\zeta)(2\zeta r)^l e^{-\zeta r} L_{n+l-1}^{2l+2-\alpha}(2\zeta r) S_{lm}(\theta, \varphi), \quad (1)$$

where ζ and $S_{lm}(\theta, \varphi)$ stand for orbital parameter and real spherical harmonics, respectively. Here $N_{nl}^\alpha(\zeta)$ and $L_q^p(x)$ refer to the normalization constant and generalized Laguerre polynomials, respectively, and they are given by

$$N_{nl}^\alpha(\zeta) = (-1)^\alpha \left(\frac{(2\zeta)^3 (n-l-1)!}{(2n)^\alpha ((n+l+1-\alpha)!)^3} \right)^{1/2} \tag{2}$$

$$L_q^p(x) = \sum_{i=0}^{q-p} \gamma_{qi}^p x^i, \quad \gamma_{qi}^p = \frac{(-1)^{p+i} (q!)^2}{i!(p+i)!(q-p-i)!} \tag{3}$$

Orthonormality condition satisfied with the weight function $(n/\zeta r)^\alpha$:

$$\int \psi_{nlm}^{(\alpha)*}(\zeta, \vec{r}) \left(\frac{n}{\zeta r} \right)^\alpha \psi_{n'l'm'}^{(\alpha)}(\zeta, \vec{r}) dV = \delta_{nn'} \delta_{ll'} \delta_{mm'} \tag{4}$$

The products of the $\psi^{(\alpha)}$ functions at the same center can be expressed by linear combinations with the help of expansion theorem of them [21]:

$$\psi_{nlm}^{(\alpha)}(\zeta, \vec{r}) \psi_{n'l'm'}^{(\alpha)}(\zeta', \vec{r}) = \frac{(2z)^{3/2}}{\sqrt{4\pi}} \sum_{N=1}^{n+n'-1} \sum_{L=0}^{N-1} \sum_{M=-L}^L B_{nlm, n'l'm'}^{\alpha NLM}(\zeta, \zeta') \psi_{NLM}^{(\alpha)}(z, \vec{r}), \tag{5}$$

where $z = \zeta + \zeta'$. The analytical expression of $B_{nlm, n'l'm'}^{\alpha NLM}$ coefficients is given in ref. [21].

STFs defined by

$$\chi_{nlm}(\zeta, \vec{r}) = (2\zeta)^{2n+1} / (2n)!^{1/2} r^{n-1} e^{-\zeta r} S_{lm}(\theta, \varphi) \tag{6}$$

are written as finite linear combinations of $\psi^{(\alpha)}$ functions [18]:

$$\chi_{nlm}(\zeta, \vec{r}) = \sum_{n'=l+1}^n \bar{\omega}_{nn'}^{\alpha l} \psi_{n'm}^{(\alpha)}(\zeta, \vec{r}), \tag{7}$$

see ref. [18] for the definition of $\bar{\omega}_{nn'}^{\alpha l}$ coefficients. Using eq. (7), molecular integrals of STFs can be obtained as finite linear combinations of integrals with $\psi^{(\alpha)}$ functions.

Molecular Overlap-like Quantum Similarity Integrals

The QSMs of molecules A and B require multicenter integrals involving molecular electron density functions $\rho_A(\vec{r})$ and $\rho_B(\vec{r})$, and a positive definite operator $\Omega(\vec{r}_1, \vec{r}_2)$ as below:

$$Z_{AB} = \iint \rho_A(\vec{r}_1) \Omega(\vec{r}_1, \vec{r}_2) \rho_B(\vec{r}_2) d\vec{r}_1 d\vec{r}_2 \tag{8}$$

Various QSMs can be defined by selecting different Hermitian bielectronic operators [2-6]. The most common and simple choice of mentioned operator is Dirac's delta function, $\Omega(\vec{r}_1, \vec{r}_2) = \delta(\vec{r}_1 - \vec{r}_2)$, and then similarity integral in eq. (8) transforms into overlap-like QSM:

$$Z_{AB} = \iint \rho_A(\vec{r}) \rho_B(\vec{r}) d\vec{r} \tag{9}$$

If compared molecules are the same, the self-similarity measure is obtained as

$$Z_{AA} = \iint \rho_A(\vec{r})^2 d\vec{r} \tag{10}$$

Z_{AA} is also used in general definition of the similarity indices called "Carbo index" [1]:

$$C_{AB} = \frac{Z_{AB}}{\sqrt{Z_{AA} Z_{BB}}} \tag{11}$$

The Carbo index transforms QSM into a number in the interval (0,1] and allows the quantitative comparison of quantum systems. When C_{AB} approaches 1, the compared systems can be considered as more similar. The exact unity value is only achieved in the case of A=B.

In the Hartree-Fock-Roothaan or other linear combination of atomic orbitals (LCAO) based ab initio methods, the electron density of the molecular systems is expanded with appropriate basis functions and QSM integral in eq. (9) becomes a molecular integral up to four centers. The general form of OLQS integrals can be written as below:

$$Z_{1234}^{abcd} = \iint \phi_1^*(\vec{r}_a) \phi_2(\vec{r}_b) \phi_3^*(\vec{r}_c) \phi_4(\vec{r}_d) d\vec{r} \tag{12}$$

Here $\phi_i(\vec{r}_x)$ represents the basis function centered at atom "x" with quantum numbers n_i, l_i and m_i . In this work, we have used $\psi^{(\alpha)}$ basis functions and calculated one- and two-center integrals.

One-Center Overlap-Like Quantum Similarity Integrals

One-center, atomic, OLQS integrals over $\psi^{(\alpha)}$ functions are given by using eq. (12) in the case of a=b=c=d:

$$Z_{1234}^{aaaa} = \iint \psi_{n_1 l_1 m_1}^{(\alpha)}(\zeta_1, \vec{r}) \psi_{n_2 l_2 m_2}^{(\alpha)}(\zeta_2, \vec{r}) \psi_{n_3 l_3 m_3}^{(\alpha)}(\zeta_3, \vec{r}) \psi_{n_4 l_4 m_4}^{(\alpha)}(\zeta_4, \vec{r}) d\vec{r} \tag{13}$$

Using expansion formula in eq. (5), orthonormality of the spherical harmonics and auxiliary radial integrals [22]

$$\int_0^\infty x^n e^{-qx} dx = \frac{n!}{q^{n+1}} \tag{14}$$

one can express the one-center integrals as follow:

$$Z_{1234}^{aaaa} = \sum_{N,N',L,M} N_{NL}^\alpha(\zeta_1 + \zeta_2) N_{N'L}^\alpha(\zeta_3 + \zeta_4) B_{n_1 l_1 m_1, n_2 l_2 m_2}^{\alpha NLM}(\zeta_1, \zeta_2) B_{n_3 l_3 m_3, n_4 l_4 m_4}^{\alpha N'LM}(\zeta_3, \zeta_4) \times \sum_{i,j'} \gamma_{\alpha i}^p \gamma_{\alpha' i'}^p \frac{2^{2L+i+i'+1} (2L+i+i'+2)!}{\pi(\zeta_1 + \zeta_2 + \zeta_3 + \zeta_4)^{2L+i+i'+3}} (\zeta_1 + \zeta_2)^{L+i+(3/2)} (\zeta_3 + \zeta_4)^{L+i'+(3/2)}, \tag{15}$$

where $1 \leq N \leq n_1 + n_2 - 1, 1 \leq N' \leq n_3 + n_4 - 1, \max(|l_1 - l_2|, |l_3 - l_4|) \leq L \leq \min(l_1 + l_2, l_3 + l_4), -L \leq M \leq L, 0 \leq i \leq N - L - 1, 0 \leq i' \leq N' - L - 1, Q = N + L + 1 - \alpha, Q' = N' + L + 1 - \alpha$ and $P = 2L + 2 - \alpha$.

Two-Center Overlap-Like Quantum Similarity Integrals

Two-center integrals are divided into two groups according to the number of basis functions found in the same atom.

- Two-center integrals of the first kind:

$$Z_{123_4}^{aa_b} = \int \int \psi_{n_1 l_1 m_1}^{(\alpha)}(\zeta_1, \vec{r}_a) \psi_{n_2 l_2 m_2}^{(\alpha)}(\zeta_2, \vec{r}_a) \psi_{n_3 l_3 m_3}^{(\alpha)}(\zeta_3, \vec{r}_a) \psi_{n_4 l_4 m_4}^{(\alpha)}(\zeta_4, \vec{r}_b) d\vec{r}. \tag{16}$$

- Two-center integrals of the second kind:

$$Z_{12_34}^{aa_bb} = \int \int \psi_{n_1 l_1 m_1}^{(\alpha)}(\zeta_1, \vec{r}_a) \psi_{n_2 l_2 m_2}^{(\alpha)}(\zeta_2, \vec{r}_a) \psi_{n_3 l_3 m_3}^{(\alpha)}(\zeta_3, \vec{r}_b) \psi_{n_4 l_4 m_4}^{(\alpha)}(\zeta_4, \vec{r}_b) d\vec{r}. \tag{17}$$

Now by using eq. (5), we can express two-center OLQS integrals in terms of usual overlap integrals as follow:

- Two-center integrals of the first kind:

$$Z_{123_4}^{aaa_b} = 2(\zeta_1 + \zeta_2)^{3/2} (\zeta_3 + \zeta_4)^{3/2} (\pi)^{-1} \sum_{N,L,M,N',L',M'} B_{n_1 l_1 m_1, n_2 l_2 m_2}^{\alpha NLM}(\zeta_1, \zeta_2) B_{n_3 l_3 m_3, n_4 l_4 m_4}^{\alpha N'L'M'}(\zeta_3 + \zeta_4, \zeta_3) \times S_{N'L'M',n_4 l_4 m_4}^\alpha(\zeta_1 + \zeta_2 + \zeta_3, \zeta_4; \vec{R}_{ab}), \tag{18}$$

where $1 \leq N \leq n_1 + n_2 - 1, |l_1 - l_2| \leq L \leq l_1 + l_2, -L \leq M \leq L, 1 \leq N' \leq N + n_3 - 1, |L - l_3| \leq L' \leq L + l_3$ and $-L' \leq M' \leq L'$.

- Two-center integrals of the second kind:

$$Z_{12_34}^{aa_bb} = 2(\zeta_1 + \zeta_2)^{3/2} (\zeta_3 + \zeta_4)^{3/2} (\pi)^{-1} \sum_{N,L,M,N',L',M'} B_{n_1 l_1 m_1, n_2 l_2 m_2}^{\alpha NLM}(\zeta_1, \zeta_2) B_{n_3 l_3 m_3, n_4 l_4 m_4}^{\alpha N'L'M'}(\zeta_3, \zeta_4) \times S_{NLM,N'L'M'}^\alpha(\zeta_1 + \zeta_2, \zeta_3 + \zeta_4; \vec{R}_{ab}), \tag{19}$$

where $1 \leq N \leq n_1 + n_2 - 1, |l_1 - l_2| \leq L \leq l_1 + l_2, -L \leq M \leq L, 1 \leq N' \leq n_3 + n_4 - 1, |l_3 - l_4| \leq L' \leq l_3 + l_4$ and $-L' \leq M' \leq L'$.

In the above equations (18) and (19), S^α stand for two-center overlap integrals over $\psi^{(\alpha)}$ functions which are given by the following expression:

$$S_{nlm,n'l'm'}^\alpha(\zeta, \zeta'; \vec{R}_{ab}) = \int \psi_{nlm}^{(\alpha)*}(\zeta, \vec{r}_a) \psi_{n'l'm'}^{(\alpha)}(\zeta', \vec{r}_b) dV, \tag{20}$$

where $\vec{R}_{ab} = \vec{r}_a - \vec{r}_b$. With the help of Fourier transform method, analytic expressions of S^α were developed for $\zeta = \zeta'$ case in ref. [21]. The more general solutions for $\zeta = \zeta'$ or $\zeta \neq \zeta'$ were derived by using ellipsoidal coordinates [23].

All two-center OLQS integrals involving other combinations of functions can be expressed by eqs. (18) and (19) using symmetry properties. It should be noted that we have used real spherical harmonics in $\psi^{(\alpha)}$ functions for simplicity. If complex spherical harmonics are used in basis functions, symmetry properties of them must be considered according to eq. (12).

Numerical Results and Discussion

The algorithm for evaluating one- and two-center OLQS integrals over $\psi^{(\alpha)}$ functions was described. For this purpose, we have used one-center expansion of functions. For two-center cases, OLQS integrals are expressed in terms of the standard two-center overlap integrals which can be calculated accurately and efficiently [21, 23]. The algorithm was implemented in a computer program written in Mathematica 12 software that capable to perform calculations with a high pre-determined accuracy.

Since there is not any calculation about OLQS integrals over $\psi^{(\alpha)}$ functions up to now, we have used STF results found in the literature to support the reliability of our

procedures. We present numerical results for one- and two-center OLQS integrals over STFs obtained from those with $\psi^{(\alpha)}$ functions using eq. (7). Table 1 contains orbital parameters of STFs used for the calculations. In table 2, we listed values of one-center, atomic, OLQS integrals. Numerical results for two-center OLQS integrals of the first and second kind are given in tables 3 and 4, respectively. The numbers in parentheses in the tables show powers of 10. All values are given in atomic units. As can be seen from tables 2-4, our results for OLQS integrals are in good agreement with literature values [13, 16]. Accurate calculations of expansion coefficients and two-center overlap integrals of $\psi^{(\alpha)}$ functions, and integral transformations from $\psi^{(\alpha)}$ functions to STFs are performed efficiently.

The accuracy of molecular quantum similarity measurements and the quantum similarity index are highly dependent on the description of the electron density of systems. Effective one-electron basis functions must be employed to construct reliable electron density. Asymptotic properties of the electronic wave functions are well represented by $\psi^{(\alpha)}$ functions. Therefore, the use of these functions in molecular similarity calculations were proposed in this work. We demonstrate that the algorithm constructed in this study could be useful when

ETFs containing Laguerre functions are employed in the QSM of atoms and diatomic molecular systems. The expressions derived for one- and two-center OLQS integrals have no restrictions for the values of orbital parameters, quantum numbers and internuclear distances. Application of presented procedure to molecular systems using specific ETFs such as Coulomb - Sturmian or Hydrogen-like functions, and evaluation of remaining three- and four-center integrals can be considered as the next step of this work.

Table 1. Orbital parameters of Slater type functions

Orbitals	Carbon	Nitrogen
1s	5.6727	6.6651
2s	1.6083	1.9237
2p _z (2z)	1.5679	1.9170

Table 2. One-center integrals over Slater type functions. *

Integrals	Carbon	Nitrogen
$Z_{1s1s1s1s}^{aaaa}$	7.263 226 539 889	11.780 945 572 070
	7.263 226 534	11.780 945 572
$Z_{1s1s1s2s}^{aaaa}$	0.296 453 696 849	0.499 679 084 708
	0.296 453 696	0.499 679 084
$Z_{1s1s2s2s}^{aaaa}$	0.030 556 227 264	0.053 124 445 791
	0.030 556 227	0.053 124 445
$Z_{1s2s2s2s}^{aaaa}$	0.010 478 691 378	0.018 493 682 096
	0.010 478 691	0.018 493 682
$Z_{2s2s2s2s}^{aaaa}$	0.025 863 146 042	0.044 258 042 479
	0.025 863 146	0.044 258 042
$Z_{1s1s2z2z}^{aaaa}$	0.027 665 504 721	0.052 409 841 641
	0.027 665 504	0.052 409 841
$Z_{2z2z2z2z}^{aaaa}$	0.043 132 809 946	0.078 834 988 765
	0.043 132 809	0.078 834 988

* The values in the first line were calculated in this work using eqs. (7) and (15). The values in the second line were taken from ref. [13].

Table 3. Two-center integrals of the first kind $Z_{123_4}^{aaa-b}$ over Slater type functions. a and b denote carbon and nitrogen atoms, respectively. a = (0, 0, 0) and b = (0, 0, z_b).

Integrals	z _b	Eqs. (7) and (18)	Ref. [16]
$Z_{1s1s1s_1s}^{aaa_b}$	0.5	0.858 425 675 390 877(0)	0.858 425 675 391(0)
	1.0	0.347 537 588 662 945(-1)	0.347 537 588 663(-1)
	1.5	0.129 121 127 852 282(-2)	0.129 121 127 852(-2)
	2.0	0.469 994 519 132 161(-4)	0.469 994 519 132(-4)
$Z_{1s1s2s_2s}^{aaa_b}$	0.5	0.501 691 891 383 981(-1)	0.501 691 891 384(-1)
	1.0	0.390 207 911 608 111(-1)	0.390 207 911 608(-1)
	1.5	0.230 014 520 893 589(-1)	0.230 014 520 894(-1)
	2.0	0.119 332 536 416 542(-1)	0.119 332 536 417(-1)
$Z_{1s1s2s_2z}^{aaa_b}$	0.5	-0.737 349 020 140 985(-1)	-0.737 349 020 141(-1)
	1.0	-0.646 924 813 965 509(-1)	-0.646 924 813 966(-1)
	1.5	-0.391 558 341 502 100(-1)	-0.391 558 341 502(-1)
	2.0	-0.205 470 626 696 680(-1)	-0.205 470 626 697(-1)

Table 4. Two-center integrals of the second kind $Z_{12_34}^{aa_bb}$ over Slater type functions. a and b denote carbon and nitrogen atoms, respectively. a = (0, 0, 0) and b = (0, 0, z_b).

Integrals	z_b	Eqs. (7) and (19)	Ref. [16]
$Z_{1s1s_1s1s}^{aa_bb}$	0.5	0.392 518 041 234 902(0)	0.392 518 041 235(0)
	1.0	0.287 291 441 055 918(-2)	0.287 291 441 056(-2)
	1.5	0.142 141 502 024 259(-4)	0.142 141 502 024(-4)
	2.0	0.600 438 755 929 345(-7)	0.600 438 755 929(-7)
$Z_{1s2s_1s2s}^{aa_bb}$	0.5	0.185 319 053 139 597(-1)	0.185 319 053 140(-1)
	1.0	0.266 806 719 446 299(-2)	0.266 806 719 446(-2)
	1.5	0.206 888 508 259 901(-3)	0.206 888 508 260(-3)
	2.0	0.115 769 691 748 916(-4)	0.115 769 691 749(-4)
$Z_{1s2s_1s2z}^{aa_bb}$	0.5	-0.159 539 790 120 835(-1)	-0.159 539 790 121(-1)
	1.0	-0.324 008 018 849 674(-2)	-0.324 008 018 850(-2)
	1.5	-0.280 545 795 502 279(-3)	-0.280 545 795 502(-3)
	2.0	-0.165 259 528 950 509(-4)	-0.165 259 528 951(-4)

Conflicts of interest

There are no conflicts of interest in this work.

References

- [1] Carbo R., Leyda L., Arnau M., How Similar is a Molecule to Another? An Electron Density Measure of Similarity Between Two Molecular Structures, *Int. J. Quantum Chem.*, 17 (1980) 1185-1189.
- [2] Carbo-Dorca R., Besalu E., A General Survey of Molecular Quantum Similarity, *J. Mol. Struct. (Theochem)*, 451 (1998) 11-23.
- [3] Robert D., Girones X., Carbo-Dorca R., Molecular Quantum Similarity Measures As Descriptors for Quantum QSAR, *Polycycl. Aromat. Comp.*, 19 (2000) 51-71.
- [4] Carbo-Dorca R., Robert D., Amat L., Girones X., Besalu E., Molecular quantum similarity in QSAR and drug design. 1st ed. Berlin, (2000) 26-38.
- [5] Carbo-Dorca R., Girones X., Mezey P.G., Fundamentals of molecular similarity. 1st ed. New York, (2001) 187-320.
- [6] Bultinck P., Girones X., Carbo-Dorca R., Molecular Quantum Similarity: Theory and Applications. In: Lipkowitz K.B., Larter R., Cundari T., (Eds). Reviews in computational chemistry. 1st ed. Hoboken: Wiley, (2005) 127-207.
- [7] Borgoo A., Godefroid M., Sen K.D., De Profit F., Geerlings P., Quantum Similarity of Atoms: A Numerical Hartree-Fock and Information Theory Approach, *Chem. Phys. Lett.*, 399 (2004) 363-367.
- [8] Robert D., Carbo-Dorca R., On the Extension of Quantum Similarity to Atomic Nuclei: Nuclear Quantum Similarity, *J. Math. Chem.*, 23 (1998) 327-351.
- [9] Amat L., Carbo-Dorca R., Quantum Similarity Measures Under Atomic Shell Approximation: First Order Density Fitting Using Elementary Jacobi Rotations, *J. Comput. Chem.*, 18 (1997) 2023-2039.
- [10] Amat L., Carbo-Dorca R., Molecular Electronic Density Fitting Using Elementary Jacobi Rotations Under Atomic Shell Approximation, *J. Chem. Inf. Comput. Sci.*, 40 (2000) 1188-1198.
- [11] Hoggan P.E., How Exponential Type Orbitals Recently Became a Viable Basis Set Choice in Molecular Electronic Structure Work and When to Use Them. In: Russo N., Antonchenko V.Y., Kryachko E.S., (Eds). Self-organization of molecular systems. 1st ed. Dordrecht: Springer, (2009) 199-219.
- [12] Sola M., Mestres J., Oliva J.M., Duran M., Carbo R., The Use of Ab Initio Quantum Molecular Self-Similarity Measures to Analyze Electronic Charge Density Distributions, *Int. J. Quantum Chem.*, 58 (1996) 361-372.
- [13] Berlu L., Hoggan P.E., Useful Integrals for Ab Initio Molecular Quantum Similarity Measurements Using Slater Type Atomic Orbitals, *J. Theor. Comput. Chem.*, 2 (2003) 147-161.
- [14] Berlu L., A Fourier Transform Approach for Two-Center Overlap-Like Quantum Similarity Integrals Over Slater Type Orbitals, *J. Theor. Comput. Chem.*, 3 (2004) 257-267.
- [15] Berlu L., Safouhi H., Analytical Development of Multicenter Overlap-Like Quantum Similarity Integrals Over Slater Type Orbitals and Numerical Evaluation, *J. Theor. Comput. Chem.*, 4 (2005) 787-801.
- [16] Safouhi H., Analytical and Numerical Development for The Two-Centre Overlap-Like Quantum Similarity Integrals Over Slater Type Functions, *J. Phys. A*, 38 (2005) 7341-7361.
- [17] Safouhi H., Berlu L., The Fourier Transform Method and The SD Approach for The Analytical and Numerical Treatment of Multicenter Overlap-Like Quantum Similarity Integrals, *J. Comput. Phys.*, 216 (2006) 19-36.
- [18] Guseinov I.I., New Complete Orthonormal Sets of Exponential Type Orbitals and Their Application to Translation of Slater Orbitals, *Int. J. Quantum Chem.*, 90 (2002) 114-118.
- [19] Guseinov I.I., New Complete Orthonormal Sets of Exponential Type Orbitals in Standard Convention and Their Origin, *Bull. Chem. Soc. Jpn.*, 85 (2012) 1306-1309.
- [20] Mamedov B.A., Israfil I. Guseinov: A Pioneer of The Quantum Theory of Atomic, Molecular, and Nuclear Systems, *Int. J. Quantum Chem.*, 114 (2014) 361-366.
- [21] Guseinov I.I., Unified Treatment of Complete Orthonormal Sets of Functions in Coordinate, Momentum and Four-Dimensional Spaces and Their Expansion and One-Range Addition Theorems, *J. Math. Chem.*, 42 (2007) 991-1001.
- [22] Arfken G.B., Weber H.J., Mathematical methods for physicists. 6th ed. Amsterdam, (2005) 499-533.
- [23] Guseinov I.I., Sahin E., Evaluation of One-Electron Molecular Integrals Over Complete Orthonormal Sets of ψ^α -ETO Using Auxiliary Functions, *Int. J. Quantum Chem.*, 110 (2010) 1803-1808.

Machine Learning Applications to the One-speed Neutron Transport Problems

Recep Gökhan Türeci^{1,a,*}

¹Kırıkkale Vocational School, Kırıkkale University, Kırıkkale, Türkiye.

*Corresponding author

Research Article

History

Received: 17/08/2022

Accepted: 26/10/2022

Copyright



©2022 Faculty of Science,
Sivas Cumhuriyet University

ABSTRACT

Machine learning is a branch of artificial intelligence and computer science. The purpose of machine learning is to predict new data by using the existing data. In this study, two different machine learning methods which are Polynomial Regression (PR) and Artificial Neural Network (ANN) are applied to the neutron transport problems which are albedo problem, the Milne problem, and the criticality problem. ANN applications contain two different activation functions, Leaky Relu and Elu. The training data set is calculated by using the H_N method. PR and ANN results are compared with the literature data. The study is only based on the existing data; therefore, the study could be thought only data mining on the one-speed neutron transport problems for isotropic scattering.

Keywords: Polynomial Regression, Artificial Neural Network, Leaky Relu activation function, Elu activation functions, Machine Learning.

tureci@gmail.com

<https://orcid.org/0000-0001-6309-6300>

Introduction

The neutron distribution is essential in nuclear reactor operations. Although the diffusion theory results are used in the nuclear reactor theory, the solution of the neutron transport equation is also important. However, the neutron transport equation has seven independent variables. Therefore, reasonable approximations can be used, and thus the one-speed, homogeneous medium and plane geometry neutron transport equation can be written. All neutrons have the same energy in the one-speed approximation. The secondary neutron number, c , is a constant in a homogeneous medium. There are two variables, which are spatial and angular variables, in the plane geometry approximation.

The one-speed, homogeneous medium and plane geometry neutron transport equation is given by

$$\mu \frac{\partial \Psi(x, \mu)}{\partial x} + \Psi(x, \mu) = \frac{c}{2} \int_{-1}^1 \Psi(x, \mu') d\mu' \quad (1)$$

where x and μ correspond to the spatial and the cosine of direction respectively. $\Psi(x, \mu)$ is the neutron distribution at x point and μ direction, and c corresponds to the secondary neutron number. The solution of Eq. (1) has been studied with different numerical methods such as the S_N method [1], P_N and DP_N [2], and semi-numerical methods such as the Case method [3,4], the C_N method [5], the F_N method [6] and H_N method [7].

Machine Learning is the research topic that computer programs can learn from data [8]. After the learning process, the new data can be predicted by the learned programs. Especially as a result of the discovery of quantum mechanics and the breakthroughs in technology

and computer systems, data scientists claim that we have a large pile of data that should be analysed. Machine learning studies are important today in terms of analysing this large data pile and creating smart systems that can decide on its own.

Machine learning applications are now an issue that is studied in neutron transport and reactor calculations like many fields with different applications. Chen *et al.* [9] investigated kinetic models in linear transport theory by deep neural network. The mathematical structure of ANN is well defined in this reference. So we are not interested in the details of the mathematical background of ANN here. We are interested in only application of ANN to data. Whewell and McClarren [10] investigated the data reduction for neutron scattering and fission sources by DJINN (Deep Jointly Informed Neural Networks). The data requirements are reduced by 94 % of the original data according to this study. Xie *et al.* [11] developed ANN to solve neutron diffusion problems. They investigated two different approach which are boundary dependent method and boundary independent method. Zolfaghari *et al.* [12] searched the thermalization devices, which include collimators and moderators, by multilayer perceptron neural network. Chen *et al.* [13] investigated neutron and X-ray scatterings by machine learning.

In this study, we are not interested in solving any equation. We are interested in only data. Therefore, our study can be considered as data mining for one-speed neutron transport theory. The data required for machine learning is calculated by H_N method. The data is the training data for the one-speed neutron transport problems. These problems are half-space albedo, the Milne problem, and the criticality problem respectively. The albedo is defined as the ratio between the net

outgoing and the net incoming neutron fluxes over a surface. The Milne problem deals with the finding of the extrapolation length which is the point where the flux is zero. The criticality problem is studied to find the criticality equation. This equation gives the relation between the secondary neutron number and the reactor thickness. These problems data, which are calculated with HN method, are examined with polynomial regression (PR) and the artificial neural network (ANN) in this study.

PR algorithm is run with the least squares method. The aim of PR is to find a regression relation which provides the training data set. To apply PR, numpy [14], scipy [15] and scikit-learn (sklearn) [16] modules in Python can be used to data. ANN algorithm is different from PR. ANN is an improved algorithm of the Logistic regression (LR) algorithm which gives only two different results, true or false. Moreover, ANN includes some hyperparameters which are dependent to the data set and the programmer. To determine these hyperparameters is based on experience over studying the data. To apply ANN, keras [17] and tensorflow [18] modules in Python can be used to data. ANN hyperparameters are given in the Table, but particularly two different activation functions, which are Leaky Relu (Leaky Rectified Linear Unit) [19] and Elu (Exponential Linear Unit) [20] activation functions, are studied in this study.

Material and Methods

The Polynomial Regression (PR) and the Results with PR

The PR is a fit application between (x, y) , which are independent variable and the dependent variable, respectively. The polyfit method [14] in numpy module was used to the imported data for PR in this study. The polyfit method is based on the least squares method. The squares of the residuals, which are the differences between a calculated or an observed data and the fitted value, is performed minimizing in this method. Thus, the coefficients of the polynomial are determined. The polynomial is given as below:

$$P(x) = \sum_n^N a_n x^n = a_0 x^0 + a_1 x^1 + a_2 x^2 + \dots + a_N x^N \quad (2)$$

The independent variable is the secondary neutron number, c , in all studies. The dependent variables are albedo values, extrapolation distance, and critical thickness for each problem, respectively. Therefore, Equation (2) can be written as in Eq. (3).

$$P(c) = \sum_{n=0}^7 a_n c^n = a_0 c^0 + a_1 c^1 + a_2 c^2 + \dots + a_7 c^7 \quad (3)$$

The Artificial Neural Network (ANN)

The basic of artificial neural networks is based on logistic regression [8]. A logistic regression, Figure 1,

consists of an input layer, a summation layer, and an output layer. The result of the summation is applied to the activation function. If the activation value is bigger than a threshold value, then the output is determined. The output gives only two different results. Therefore, the logistic regression is also called as binary classification. This structure runs as a biological neuron cell. It consists of dendrites, nuclei of the cell, and axon. The dendrite is the input, and the axon is the output. The signals are collected by dendrites in the nucleus. This determines the status of the cell. If the collected signal value is bigger than a threshold value, then the next cell is activated. An artificial neural cell in Figure 2 works similarly to a biological cell.

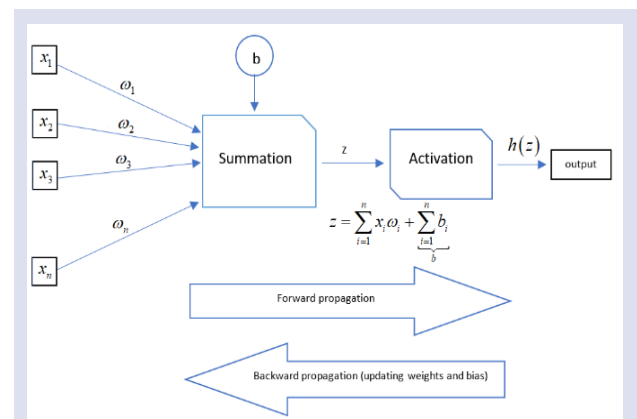


Figure 1. A logistic regression with computation graph.

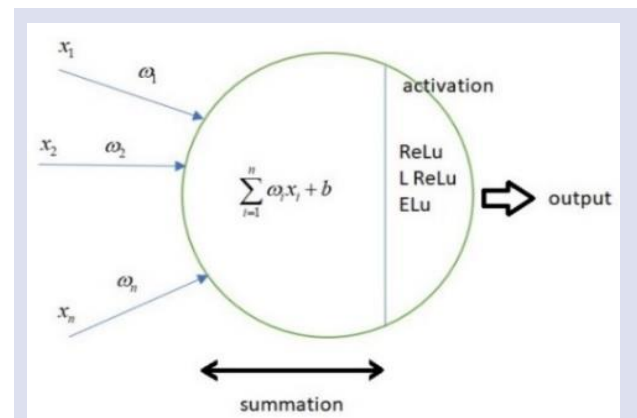


Figure 2. An artificial neuron cell in ANN.

Here x_i , w_i and b correspond to input data, weights and bias in machine learning, respectively. The first transition from input to output doesn't generally give a good result, and it is called as the forward propagation. Therefore, the backward propagation is used. Thus, the weights and bias values are updated in the backward propagation process. The optimization function is used in this stage. It tries to minimize the loss value.

An ANN includes hidden layers unlike logistic regression. Thus, a typical ANN consists of an input layer, hidden layer, and the output layer as in Figure 3. An ANN study tries to find the weights, ω_i , and the bias, b , of the interested in problem.

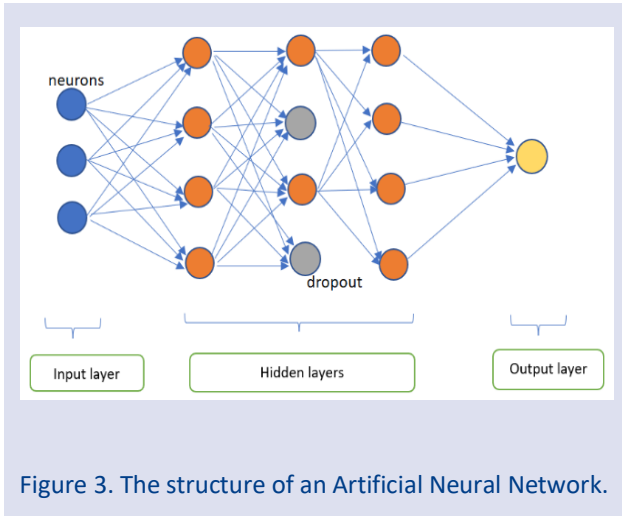


Figure 3. The structure of an Artificial Neural Network.

The connection of the layers is also important. Keras module gives us different model structures. If we have only one input layer and only one output layer, and if we don't use the output of another layer, then the sequential model [21] will be a good option to use.

In this study, ANN model is created by the sequential model, and the optimization function is selected as adam (adaptive moment estimation) [22] for the optimization function. There are different activation functions in ANN algorithms, and there are certain advantages and disadvantages of these functions. The properties of the activation functions used in this study are given in Table 1.

Leaky Relu activation function is focused to zero, and there are no killed neutrons. The function has 0.01x for the negative value. Elu (Exponential Linear Unit) activation function includes an exponential term and there are no killed neurons. However, it runs slowly in terms of the calculation time since it includes an exponential term.

Table 1. Activation functions and its properties used in this study

Mathematical definition of the activation function	The behaviour of the activation function
$h_{LeakyReLU}(x) = \max(0.01x, x)$	<p>The graph shows a coordinate system with a horizontal axis and a vertical axis. Two lines originate from the origin (0,0). One line, labeled 'y = 0.01 x', has a very shallow positive slope. The other line, labeled 'y = x', has a steeper positive slope. The function follows the shallower line for negative x values and the steeper line for positive x values.</p>
$h_{ELu} = \begin{cases} \alpha(e^x - 1), & x < 0 \\ x, & x \geq 0 \end{cases}$	<p>The graph shows a coordinate system with a horizontal axis and a vertical axis. The horizontal axis is labeled with values -3, -2, -1, 0, 1, 2, 3. The vertical axis is labeled with values 1, 2, 3. A curve starts from the left, passing through the origin (0,0), and follows a linear path 'y = x' for positive x values. For negative x values, the curve follows an exponential-like path 'y = \alpha(e^x - 1)'. Dotted lines connect the points on the curve to the axes.</p>

Application of PR

Since we are interested in the data mining for one-speed neutron transport problems, we need a training data set. This data set is calculated by using the H_N method. The H_N calculations were performed with Mathematica 12.2 software, and *WorkingPrecision* value was selected as 32.

It is important that the data should contain thousands of data for the success of ANN. However, we calculated only 11 different data according to the secondary neutron number. We could calculate much more data at shorter intervals and calculate hundreds or thousands of data, but since we have not examined complex problems, we work with these 11 data, especially by forcing the neural network. The training data set is given in Table 2

Table 2. The training data set for varying c with HN method

c	Albedo	c	Extrapolation distance	c	Critical thickness
0.10	0.0216976569566343	0.10	8.5382882681302200	1.10	4.2266192698707600
0.20	0.0462648688682488	0.20	3.9239076951733300	1.20	2.5787585222225100
0.30	0.0744514267270763	0.30	2.4947273586756700	1.30	1.8754510915842200
0.40	0.1073349048799300	0.40	1.8249003850628600	1.40	1.4732070964173800
0.50	0.1465444012833310	0.50	1.4408497695258000	1.50	1.2101130830389700
0.60	0.1947164506629280	0.60	1.1922598119270000	1.60	1.0239260606883200
0.70	0.2565567261583740	0.70	1.0180610666686400	1.70	0.8850734307673520
0.80	0.3418664995580910	0.80	0.8890546020955310	1.80	0.7775459392298720
0.90	0.4780245341005770	0.90	0.7895694514644200	1.90	0.6918667133043400
0.95	0.5966629255385620	0.95	0.7478782683064080	2.00	0.6220468763406790
0.98	0.7210172380719860	0.98	0.7249509445737220	2.50	0.4064698693764990

PR Application for Albedo Data

First, we should try to understand the correlation matrix. It gives the correlations between the variables which are called as features in the machine learning language. If the correlation between the two features is close to the unit value, then these features have a linear relation. If the correlation is close to the negative unit

value, then the relation between the features is again linear, but the slope of the line is negative. If the correlation is close to zero, then it is understood that there is no relationship between the two features. The correlation matrix for the albedo is given in Figure 4-a.

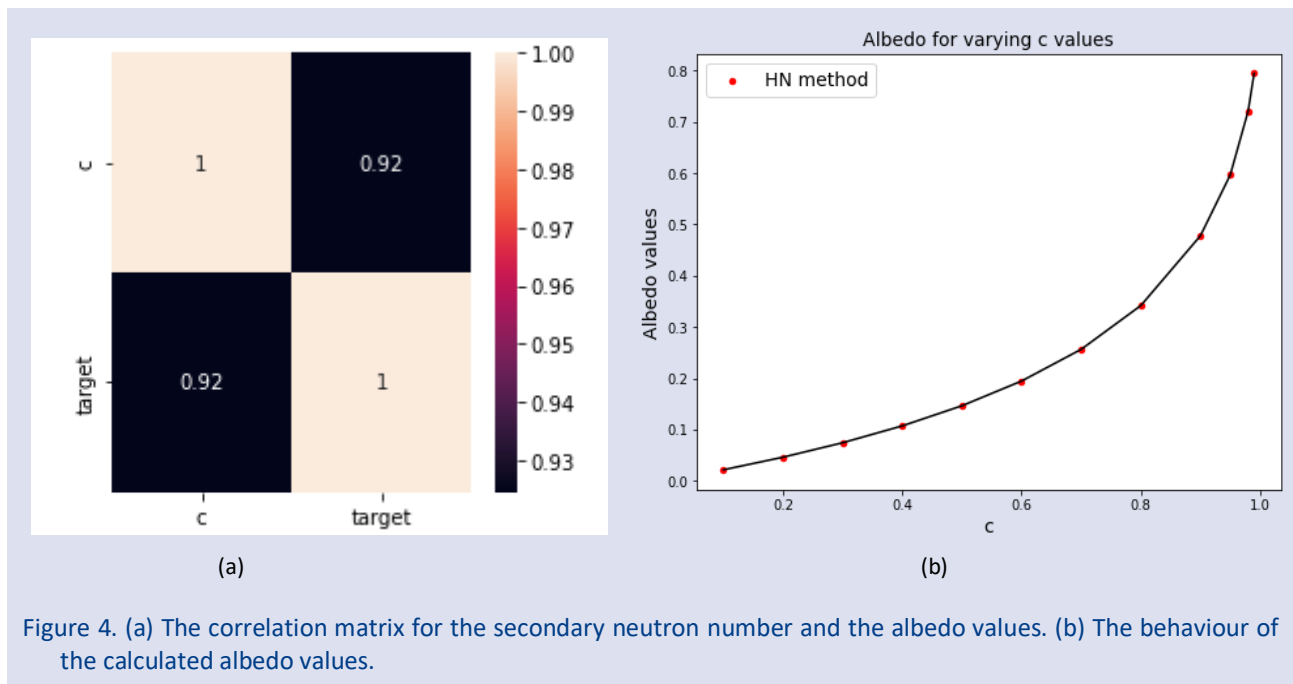


Figure 4. (a) The correlation matrix for the secondary neutron number and the albedo values. (b) The behaviour of the calculated albedo values.

The target in Figure 4-a corresponds to the albedo. According to Figure 4-a, the correlation between the secondary neutron number and the albedo values is 0.92. This means that there is a strong relationship between c and albedo, and this relationship is a close linear behaviour. Figure 4-b represents the H_N results for the albedo and supports to the result of Figure 4-a.

Polyfit method in *numpy* module is used on the training data to apply polynomial regression. This analysis is performed for third-order, 4th order, 5th order, and 6th

order polynomials. The coefficients for each polynomial regression and R^2 values are given in Table 3, and the graphics of the polynomials on the training data are given in Figure 5.

Table 3. The polynomial coefficients for the albedo problem

Polynomial Coefficients	Third order	4 th order polynomial	5 th order polynomial	6 th order polynomial
a_0	-0.097160764740	0.102653259668	-0.122656652880	0.160801117064
a_1	1.268863094720	-1.301081444528	2.414879932232	-3.161361500426
a_2	-2.828679335978	6.614462062288	-12.913954563141	24.992183953605
a_3	2.426921750454	-10.538806383260	33.205888658331	-86.116136609767
a_4	-	5.925015300984	-37.689181901735	151.820348299569
a_5	-	-	15.929876969293	-131.434216376403
a_6	-	-	-	44.578524178006
R^2	0.9892459906109	0.9960750831911	0.9985235712740	0.9993852906092

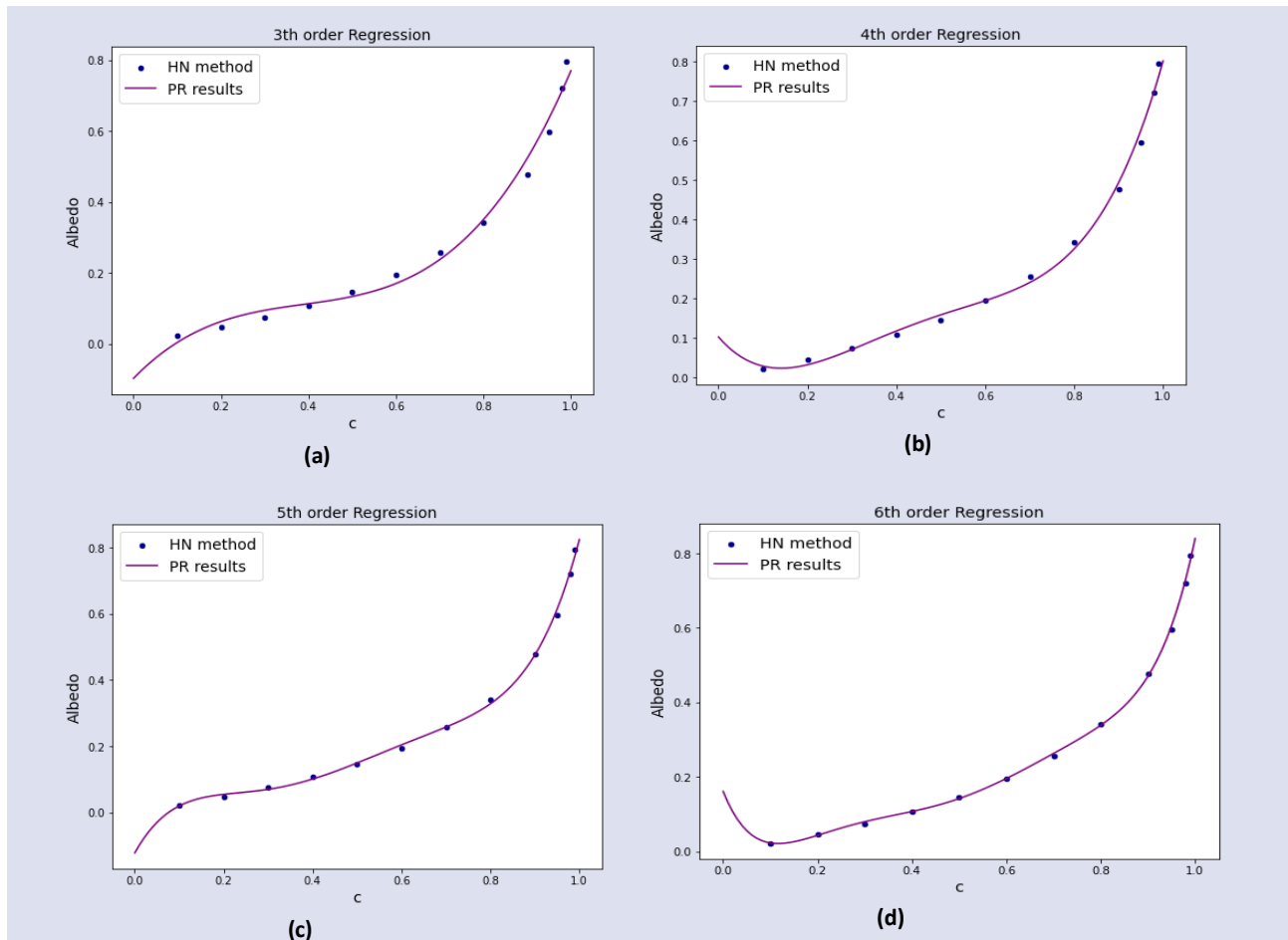


Figure 5. Polynomial regression for the albedo values with (a) third order, (b) 4th order, (c) 5th order and, (d) 6th order polynomials.

Since we know the polynomial coefficients, we can predict the new data. The predicted values will be given in ANN section together with the ANN results.

PR Application for The Milne Problem

The correlation matrix and the HN method results are given in Figure 6 where the target corresponds to the extrapolation distance. The correlation between the

extrapolation distance values and c values has negative value. It corresponds to the extrapolation distance values decrease as c values increase. The polynomial coefficients are given in Table 4 with the R^2 values. The behaviours of the polynomials are given in Figure 7. The predicted PR results for the extrapolation distance are given together with the ANN results.

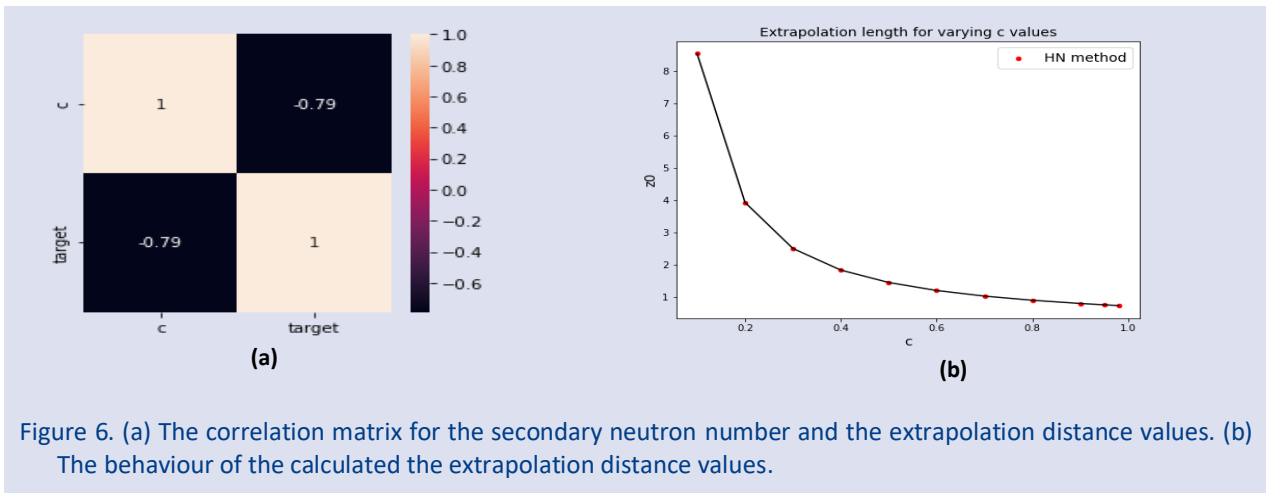


Figure 6. (a) The correlation matrix for the secondary neutron number and the extrapolation distance values. (b) The behaviour of the calculated the extrapolation distance values.

Table 4. The polynomial coefficients for the Milne problem

Polynomial Coefficients	Third order	4 th order polynomial	5 th order polynomial	6 th order polynomial
a_0	12.73103959077	15.788245491725	18.485254724793	20.894687303262
a_1	-54.931030528914	-94.652754304187	-139.480703388677	-187.134618844626
a_2	83.735974910281	231.577867207033	469.633521969347	795.996424716015
a_3	-41.293833149226	-	-786.754877968709	-1823.178700875148
a_4	-	247.138836479952	640.269808323104	2302.409952872807
a_5	-	95.432074098969	-201.601504460371	-1507.521802226705
a_6	-	-	-	399.319132359482
R^2	0.9714452701730	0.9940761925904	0.9990018141316	0.999872681941

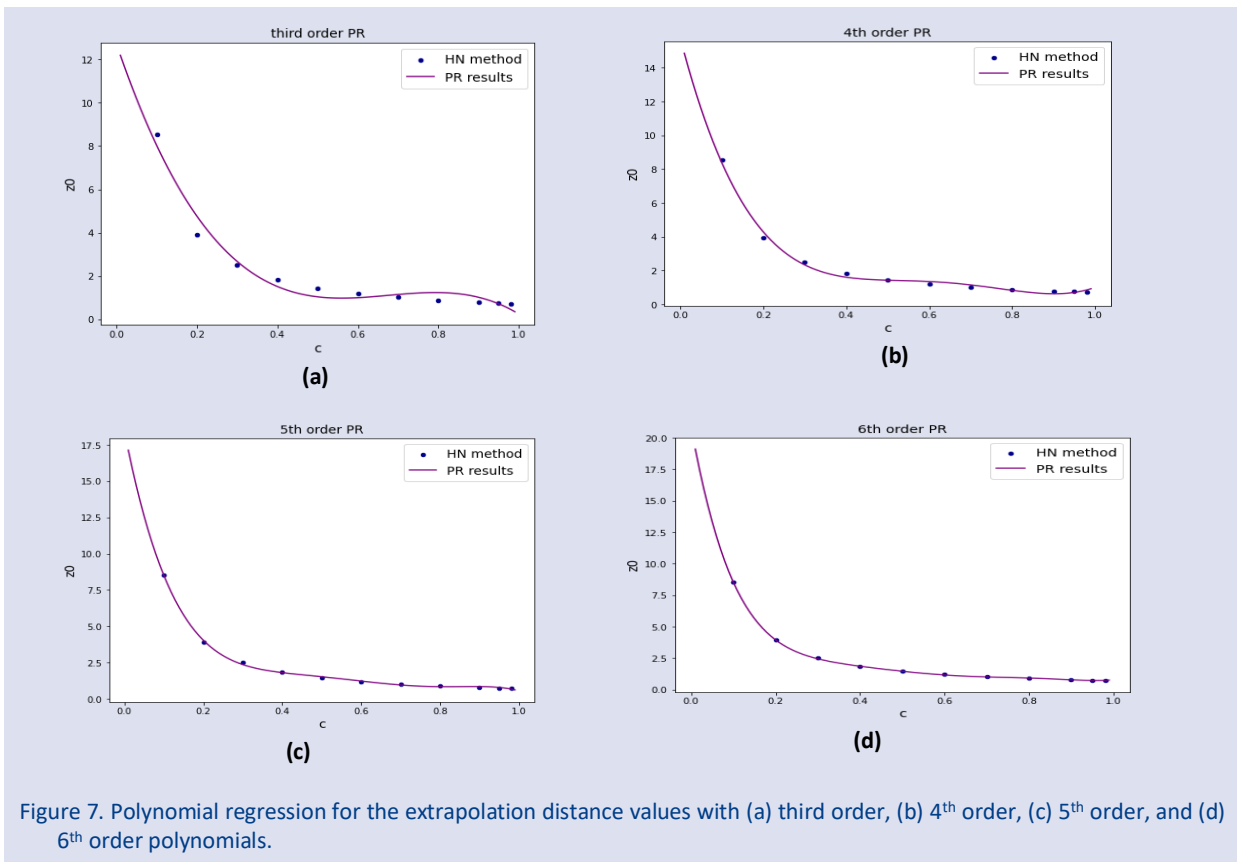


Figure 7. Polynomial regression for the extrapolation distance values with (a) third order, (b) 4th order, (c) 5th order, and (d) 6th order polynomials.

PR Application for The Criticality Problem

The correlation matrix and the H_N method results are given in Figure 8 where the target corresponds to the critical thickness values. The correlation between the criticality thickness values and c values has

negative value. It corresponds to the critical thickness values decrease as c values increase. The polynomial coefficients are given in Table 5 with the R^2 values. The behaviours of the polynomials are given in Figure 9.

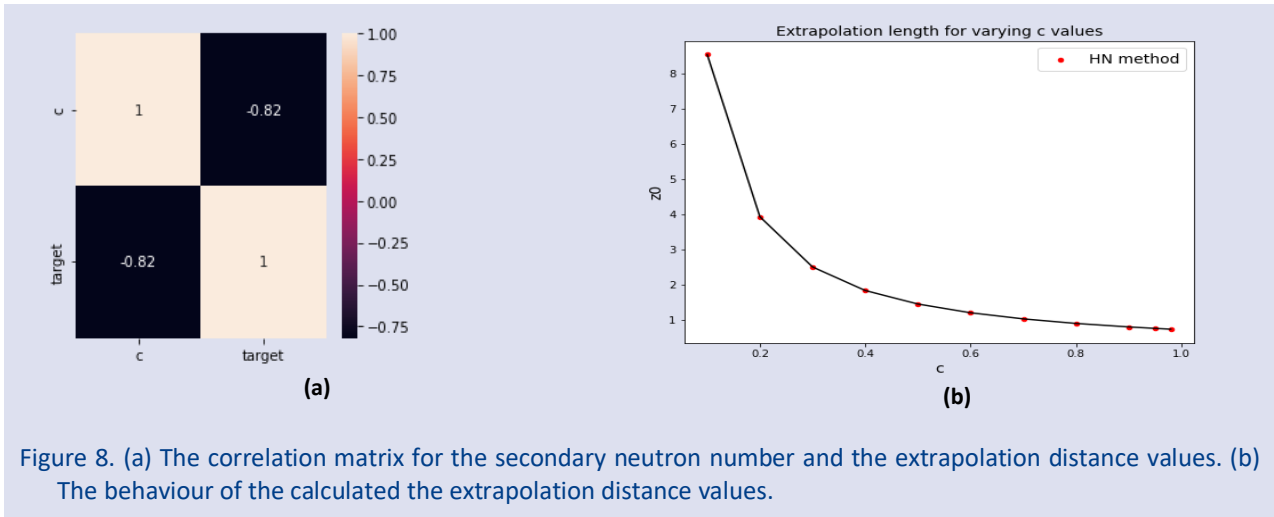


Table 5. The polynomial coefficients for the critically problem

Polynomial Coefficients	Third order	4 th order polynomial	5 th order polynomial	6 th order polynomial
a_0	36.033612931841	94.467135307170	244.733526359218	627.280616843006
a_1	-	-193.416454497710	-646.162511121329	-2030.175944634479
a_2	52.875734964750	149.504546920933	683.519407553603	2733.972521931903
a_3	26.241293304929	-51.117712902239	-359.541070193650	-1952.377568565584
a_4	-4.326510203990	6.498778152535	93.803659999828	778.418589815078
a_5	-	-	-9.700542427477	-164.163088552406
a_6	-	-	-	14.302087604165
R^2	0.9707663267140	0.992025771469	0.9980065173723	0.9995529480494

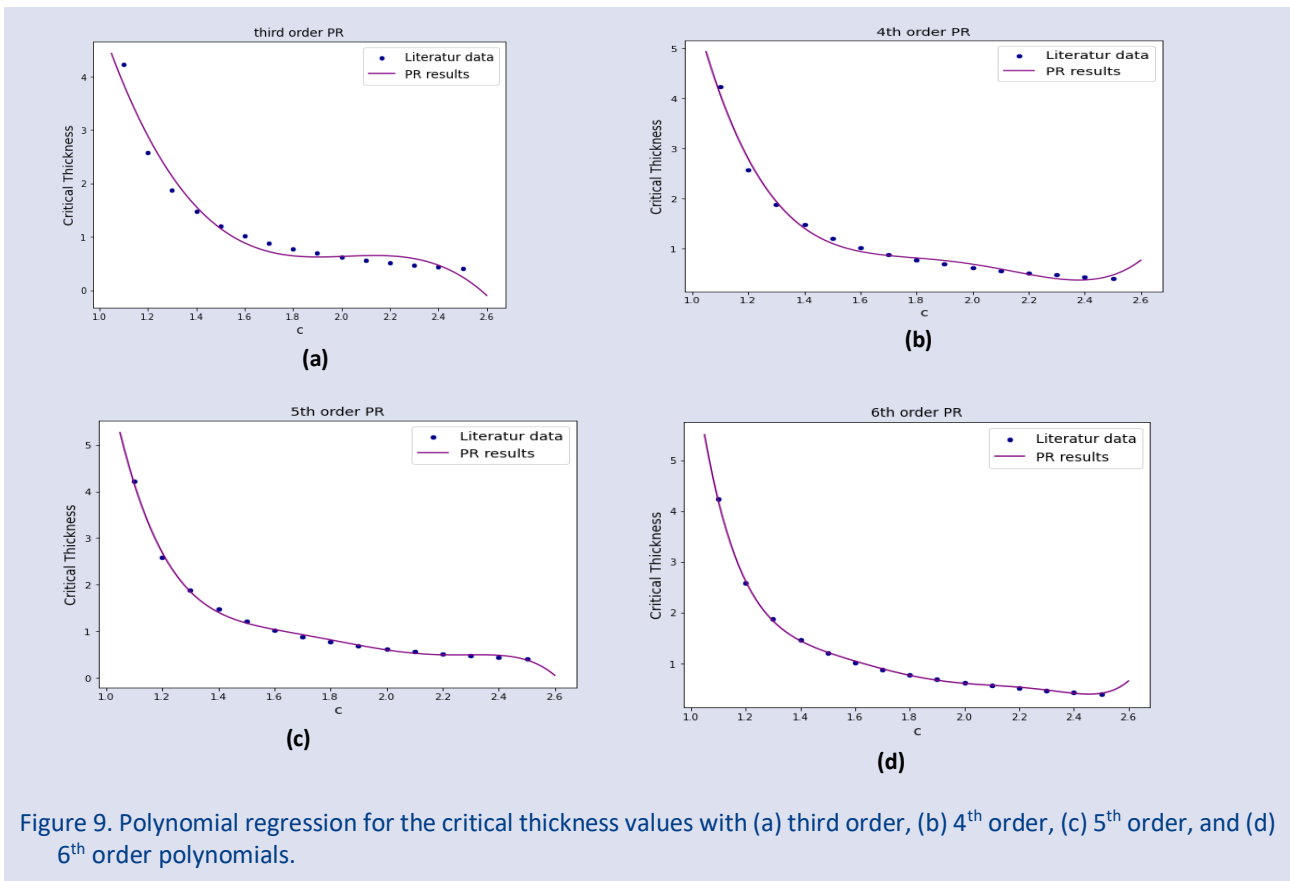


Figure 9. Polynomial regression for the critical thickness values with (a) third order, (b) 4th order, (c) 5th order, and (d) 6th order polynomials.

Application of ANN

ANN application is different from PR application. ANN includes hyperparameters which are depend on the problem and the user. It is important that there is no any linearity among these hyperparameters. The used

hyperparameters for each problem are given in Table 6. Unfortunately, the values or situations of these hyperparameters depend on the experience and the type of problem. The ANN results for albedo are given in Figure 10 with the loss functions.

Table 6. The ANN hyperparameters used in this study

Hyperparameters	Albedo	The Milne problem	Criticality
Number of neurons	200	200	200
Epoch number	300	600	600
Batch size parameter	8	8	8
Test size	0.2	0.2	0.2
Validation split parameter	0.2	0.2	0.2
Number of hidden layers	5	5	10
Loss function	msle	msle	msle
Optimization function	adam	adam	adam
Activation function	LRelu / Elu(a=0.1)	LRelu / Elu(a=0.1)	LRelu / Elu(a=0.4)

msle: Mean square logarithmic error

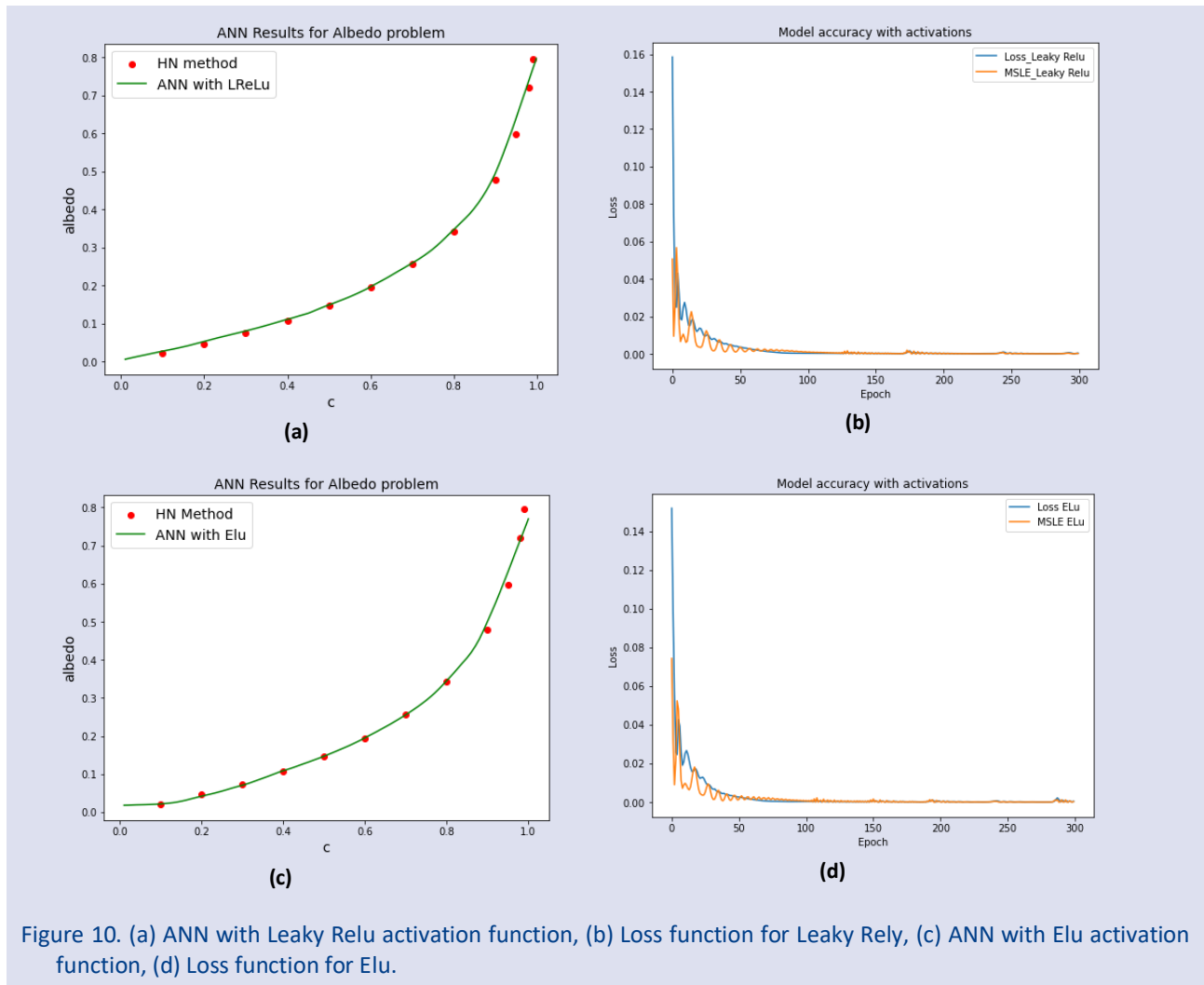


Figure 10. (a) ANN with Leaky Relu activation function, (b) Loss function for Leaky Rely, (c) ANN with Elu activation function, (d) Loss function for Elu.

Figures 11 and 12 show the ANN results with Leaky Relu and Elu activation functions and PR results with third order and 4th order and with 5th and 6th order PR results. These figures are given as separated not to cause confusion. According to the results PR gives good results for the training data set range. But PR results are not good

for out of the training data set. While ANN results are reasonable. Table 7 represents the predicted values by PR and ANN predictions and the calculated data by H_N method. According to the tabulated results, ANN results are better than the PR results in the training data range.

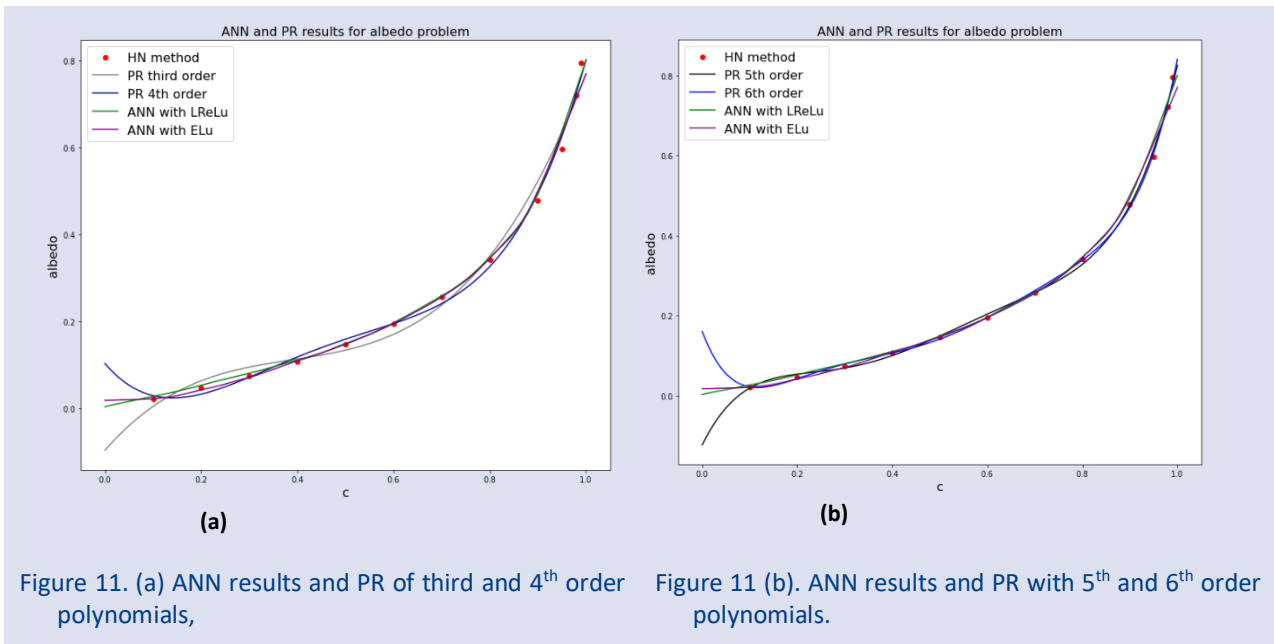


Figure 11. (a) ANN results and PR of third and 4th order polynomials,

Figure 11 (b). ANN results and PR with 5th and 6th order polynomials.

Table 7. The predicted albedo values with PR and ANN, HN results and the literature data

c	PR third order	PR 4th order	PR 5th order	PR 6th order	ANN LeakyRelu	ANN ELu	HN results	Ref [6]
0.05	-0.040485943	0.052855023	-0.030277386	0.055357485	0.015550368	0.019501526	0.010527886	-
0.10	0.003865673	0.028743431	0.019288064	0.022382941	0.027096316	0.021702837	0.021697657	0.0217
0.15	0.037714275	0.023747507	0.043210760	0.025665113	0.038747564	0.028760070	0.021697317	-
0.20	0.062880055	0.032185027	0.054203130	0.042993716	0.052679956	0.041934598	0.046264869	0.04626
0.25	0.081183203	0.049262519	0.061116334	0.062485542	0.066931598	0.055374168	0.059847996	-
0.30	0.094443911	0.071075264	0.069537638	0.079410954	0.080342233	0.070764676	0.074451427	0.07445
0.35	0.104482370	0.094607294	0.082387780	0.093521891	0.095019184	0.089193664	0.090220877	-
0.40	0.113118771	0.117731395	0.100518348	0.106881382	0.110837251	0.108875334	0.107334905	0.1073
0.45	0.122173307	0.139209104	0.123309139	0.122194567	0.126786008	0.127226219	0.126015681	-
0.50	0.133466167	0.158690711	0.149265541	0.141641226	0.148766205	0.147058889	0.146544401	-
0.55	0.148817544	0.176715258	0.176615896	0.166209819	0.170162231	0.169510245	0.169284290	-
0.60	0.170047629	0.194710540	0.203908873	0.195533031	0.196252808	0.195216626	0.194716451	0.1947
0.65	0.198976613	0.214993102	0.230610837	0.228224827	0.226612359	0.224009961	0.223497145	-
0.70	0.237424687	0.240768243	0.257703221	0.262719018	0.258634686	0.255775630	0.256556726	-
0.75	0.287212043	0.276130016	0.288279897	0.298609331	0.295483530	0.293667436	0.295279357	-
0.80	0.350158872	0.326061223	0.328144544	0.338490986	0.346499681	0.344976991	0.341866500	0.3419
0.85	0.428085366	0.396433420	0.386408019	0.390303793	0.403047055	0.405470312	0.400170417	-
0.90	0.522811714	0.494006916	0.476085728	0.470176740	0.494039237	0.500720441	0.478024534	0.4780
0.95	0.636158110	0.626430770	0.614694997	0.605774103	0.638666987	0.630749643	0.596668782	-

The Milne problem results with ANN are given in Figure 12. The predicted values are given in Table 8. ANN results are better than the PR results as in the albedo investigation. The comparisons are given in Figures 13 and 14. The critical thickness results with ANN are given in Figure 15 with the loss functions. The comparisons of the

results with both ANN and PR are given in Figures 16 and 17. The predicted values and calculated values with H_N method are given in Table 9. Table 10 represents the CPU times for ANN calculations.

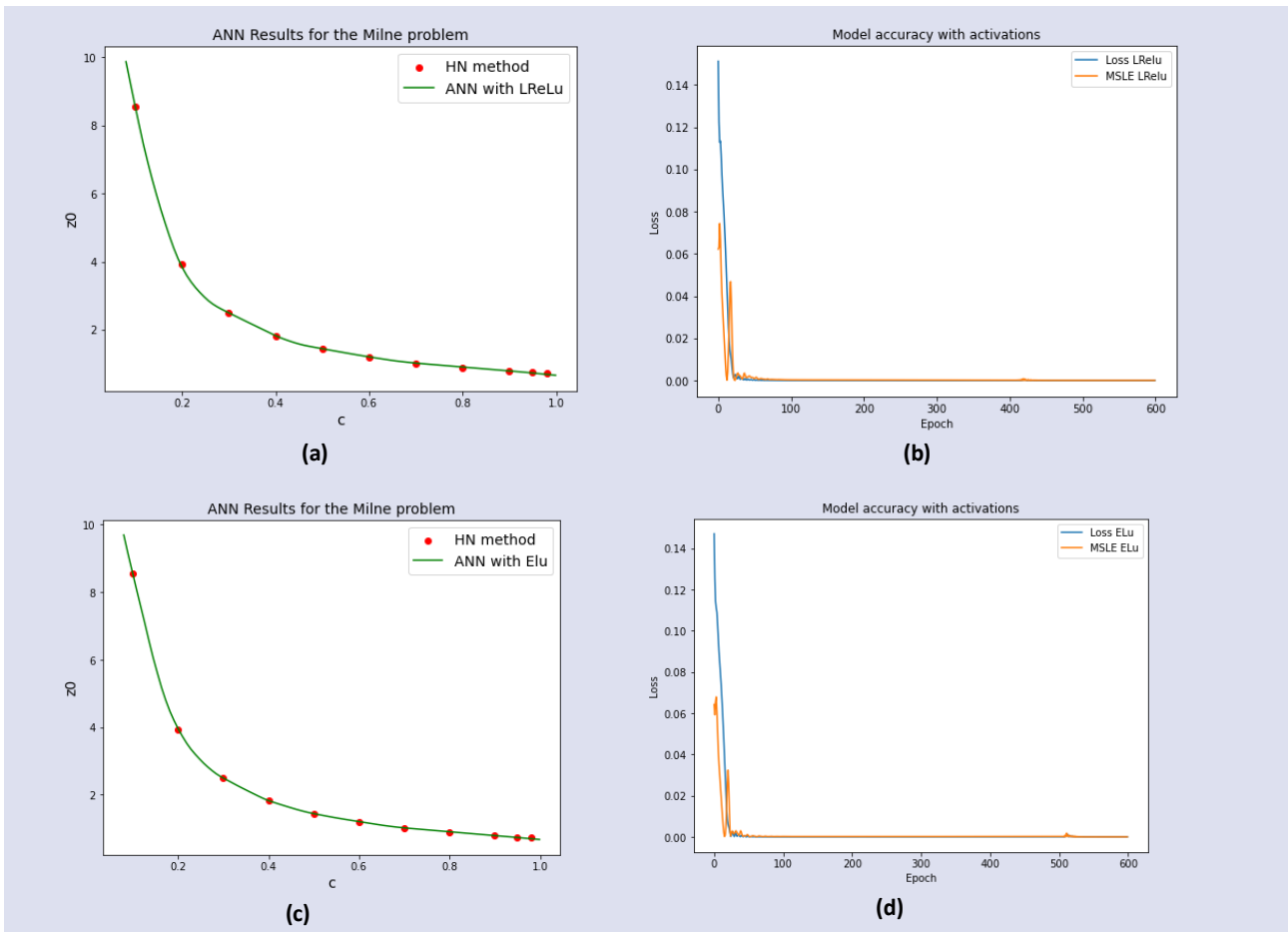


Figure 12. (a) ANN with Leaky Relu activation function, (b) Loss function for Leaky Relu, (c) ANN with Elu activation function, (d) Loss function for Elu.

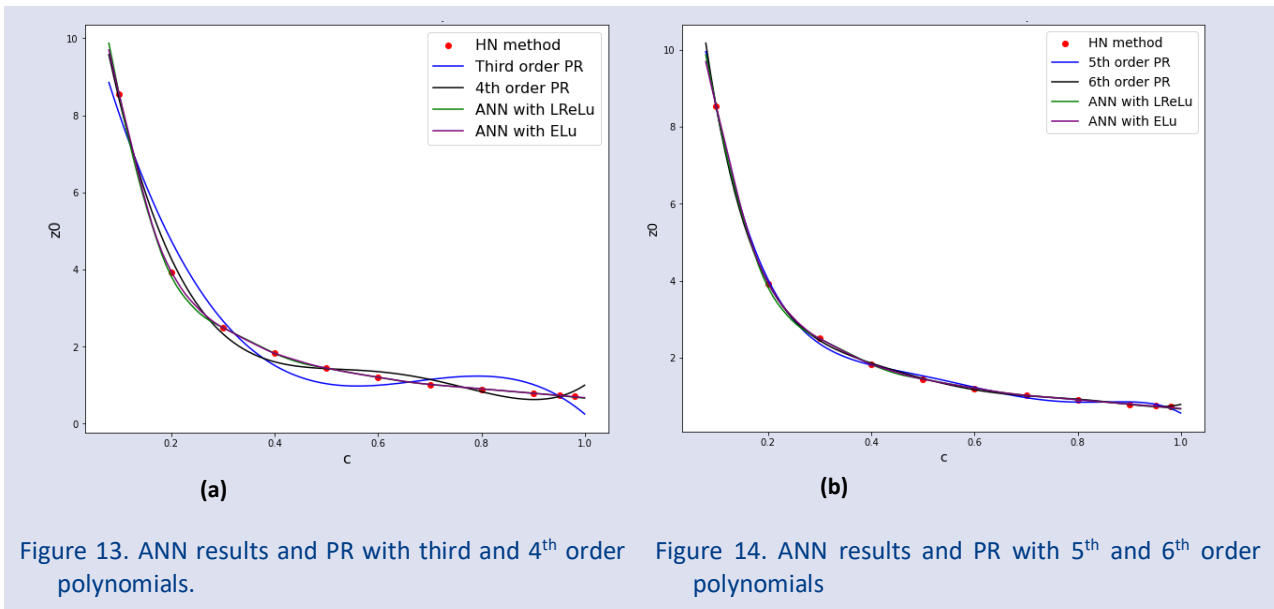


Figure 13. ANN results and PR with third and 4th order polynomials.

Figure 14. ANN results and PR with 5th and 6th order polynomials

Table 8. The predicted albedo values with PR and ANN, HN results and the literature data

c	PR third order	PR 4th order	PR 5th order	PR 6th order	ANN LeakyRelu	ANN ELu	HN results	Ref [6]
0.05	10.188666273	11.604256540	12.590897686	13.313975286	11.840276718	11.550756454	18.17324720	-
0.10	8.034002454	8.401153104	8.508775693	8.533576061	8.537860870	8.543089867	8.538288268	8.53829
0.15	6.236077760	6.015053273	5.783433224	5.636852014	5.736626625	5.809600353	5.426971982	-
0.20	4.763921816	4.296389946	4.040335114	3.949196288	3.837925434	3.960925341	3.923907695	3.92391
0.25	3.586564248	3.109910836	2.978306502	2.992731577	2.928089142	3.025303841	3.054278391	-
0.30	2.673034679	2.334678464	2.361972772	2.445501237	2.494558573	2.496745348	2.494727359	2.49473
0.35	1.992362736	1.864070166	2.014199497	2.105152759	2.157500029	2.143542767	2.107561555	-
0.40	1.513578044	1.605778085	1.808532382	1.857113569	1.824761152	1.826388121	1.824900385	1.82490
0.45	1.205710227	1.481809179	1.661637210	1.647259169	1.581019044	1.614304304	1.609850598	-
0.50	1.037788910	1.428485213	1.525739783	1.459073629	1.440720677	1.441888928	1.440849770	1.44085
0.55	0.978843720	1.396442766	1.381065865	1.295302402	1.319161654	1.315809488	1.304544227	-
0.60	0.997904281	1.350633227	1.228281131	1.164097496	1.203084111	1.206238747	1.192259812	1.19226
0.65	1.064000218	1.270322798	1.080931103	1.069654976	1.096536160	1.100451231	1.098132352	-
0.70	1.146161157	1.149092489	0.957881098	1.007344810	1.017981768	1.019245267	1.018061067	1.01806
0.75	1.213416721	0.994838123	0.875756172	0.963333053	0.960831523	0.961277604	0.949094398	-
0.80	1.234796538	0.829770334	0.841381062	0.918696374	0.903681397	0.903938890	0.889054602	0.889055
0.85	1.179330231	0.690414567	0.844220129	0.858028921	0.846531689	0.846978545	0.836299972	-
0.90	1.016047426	0.627611078	0.848817303	0.782541528	0.789381742	0.790483654	0.789569451	0.789569
0.95	0.713977749	0.706514934	0.787236027	0.727653262	0.728278637	0.733815908	0.747878268	-

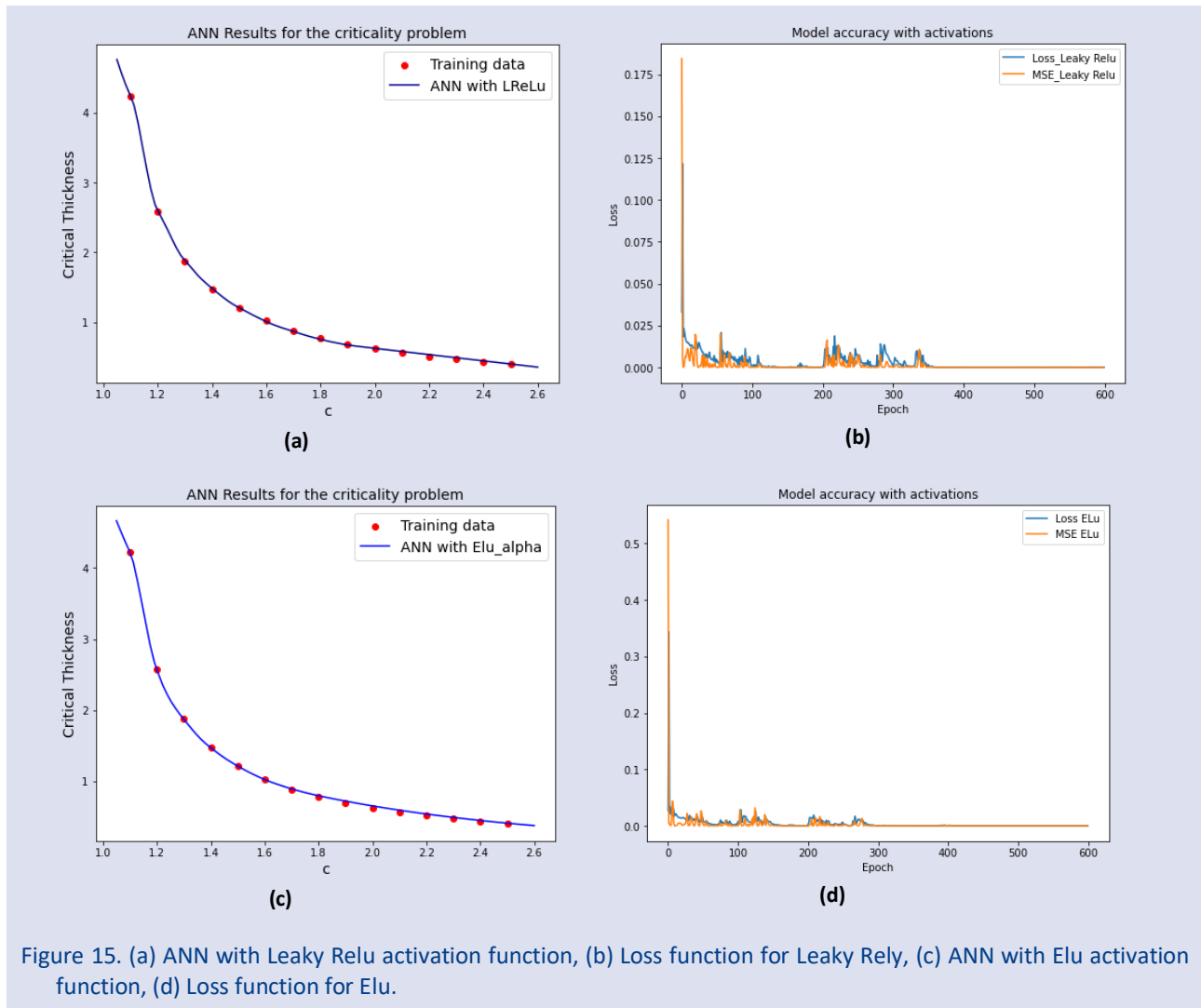


Figure 15. (a) ANN with Leaky Relu activation function, (b) Loss function for Leaky Relu, (c) ANN with Elu activation function, (d) Loss function for Elu.

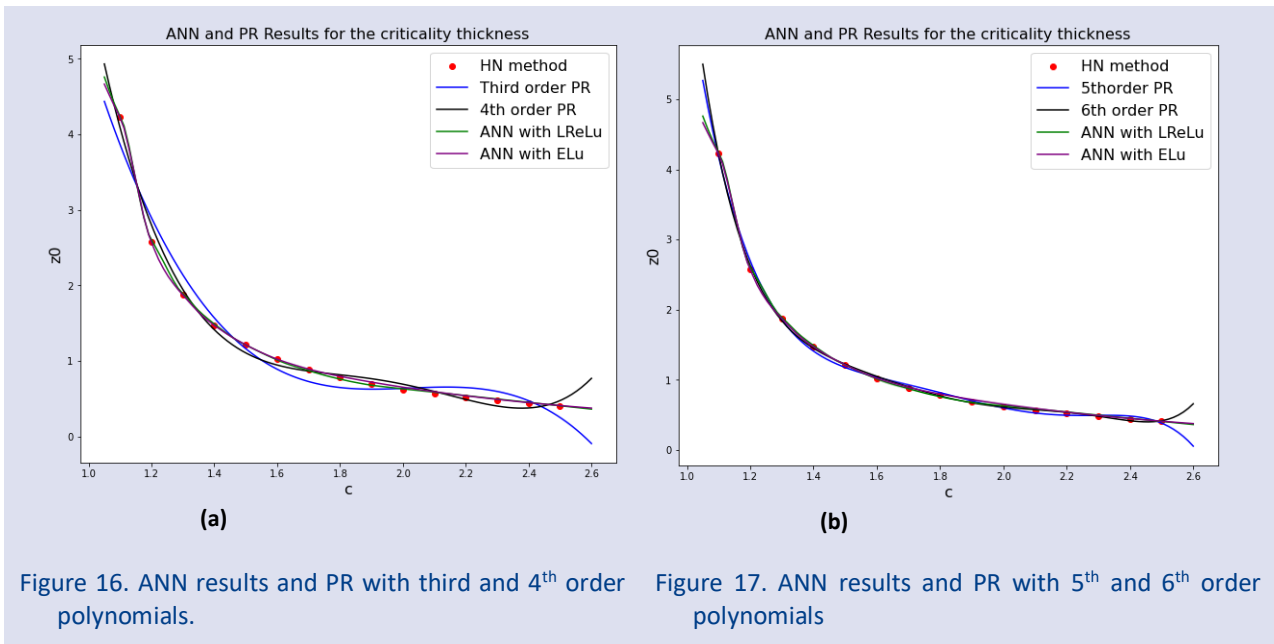


Figure 16. ANN results and PR with third and 4th order polynomials. Figure 17. ANN results and PR with 5th and 6th order polynomials

Table 9. The predicted critical thickness values with PR and ANN, HN results and the literature data

c	PR third order	PR 4th order	PR 5th order	PR 6th order	ANN LeakyRelu	ANN ELu	HN results	Ref [6]
1.05	4.436640713	4.932784128	5.267616683	5.500000720	4.759516716	4.665410995	6.600527483	-
1.10	3.863684288	4.086722354	4.179200859	4.212667744	4.239711285	4.222702503	4.226619270	4.22674
1.15	3.350546912	3.380727934	3.335961807	3.284674501	3.389765739	3.397710323	3.187897630	-
1.20	2.893983701	2.798395958	2.692706239	2.625772469	2.603260517	2.569414139	2.578758522	-
1.25	2.490749773	2.324296336	2.209944696	2.163469717	2.217116833	2.138610840	2.170721623	-
1.30	2.137600245	1.943973792	1.853527782	1.840655903	1.889006495	1.871923208	1.875451092	1.87766
1.35	1.831290235	1.643947868	1.594282390	1.613388171	1.664572239	1.643992543	1.650649761	-
1.40	1.568574859	1.411712922	1.407647933	1.448837946	1.487948179	1.470546722	1.473207096	1.47688
1.45	1.346209236	1.235738131	1.273312576	1.323398629	1.332890511	1.329103589	1.329304314	-
1.50	1.160948482	1.105467485	1.174849460	1.220954189	1.210703254	1.213001370	1.210113083	-
1.55	1.009547716	1.011319793	1.099352938	1.131308657	1.107202888	1.109943986	1.109702483	-
1.60	0.888762053	0.944688681	1.037074800	1.048776508	1.012116909	1.021637082	1.023926061	1.03039
1.65	0.795346613	0.897942591	0.981060505	0.970933957	0.933853269	0.952186227	0.949789829	-
1.70	0.726056511	0.864424782	0.926785412	0.897531141	0.871189833	0.891013980	0.885073431	0.89275
1.75	0.677646865	0.838453328	0.871791003	0.829565207	0.809955120	0.839110076	0.828092811	-
1.80	0.646872794	0.815321123	0.815321123	0.768514291	0.758651495	0.795110703	0.777545939	0.7863
1.85	0.630489413	0.791295876	0.757958201	0.715732404	0.714092731	0.755685329	0.732409325	-
1.90	0.625251840	0.763620111	0.701259481	0.672005211	0.677867234	0.718870461	0.691866713	0.70157
1.95	0.627915194	0.730511172	0.647393258	0.637266710	0.652532697	0.684144139	0.655258774	-
2.00	0.635234590	0.691161218	0.598775100	0.610476808	0.629557252	0.651447415	0.622046876	0.63257
2.05	0.643965147	0.645737224	0.557704080	0.589659799	0.607055962	0.620682538	0.591786523	-
2.10	0.650861981	0.595380984	0.525999009	0.572103739	0.584608793	0.591545403	0.564107544	-
2.15	0.652680211	0.542209106	0.504634661	0.554720714	0.562175453	0.563958168	0.538665175	-
2.20	0.646174953	0.489313017	0.493378006	0.534568018	0.539779484	0.537853360	0.515298304	-
2.25	0.628101325	0.440758958	0.490424436	0.509530217	0.517384887	0.513141751	0.493649386	-
2.30	0.595214444	0.401587991	0.492034001	0.479162122	0.494980454	0.489778817	0.473655588	-
2.35	0.544269428	0.377815991	0.492167630	0.445692651	0.472600222	0.467705846	0.455029751	-
2.40	0.472021393	0.376433650	0.482123370	0.415189600	0.450304508	0.446859717	0.437739484	-
2.45	0.375225457	0.405406479	0.450172606	0.398885300	0.427969217	0.427191317	0.421561906	-
2.50	0.250636738	0.473674805	0.381196300	0.414663185	0.405631959	0.408649623	0.406469869	-
2.55	0.095010353	0.591153769	0.256321214	0.488705251	0.383291245	0.391174197	0.392302667	-

Table 10. The CPU times in seconds

Activation function	Albedo	Milne's problem	Criticality
Leaky Relu	7.81	14.20	18.60
Elu	7.66	14.90	21.30

Conclusions

In this study, two different machine learning algorithms, polynomial regression and artificial neural network, were applied to isotropic scattering neutron transport theory problems. This study is about the data mining for the existing data for albedo, Milne problem, and criticality problem. These data are the training data. The training data for each problem was calculated by H_N method.

The success of machine learning applications depends on the size of the training data. We studied here with restricted data. We have only 11 different data for each problem. We could have created a larger data set, but we especially wanted to force the artificial neural network.

According to the results

Polynomial regression could give reasonable results for only training data range. PR results are not good for out of data ranges. Therefore, the predictions used PR should belong to the training data range.

ANN results are more successful both the training data range and out of the training data range. Although ANN calculations take more time than polynomial regression, the success of ANN is worth it.

ANN includes hyperparameters. Unfortunately, there is no any linearity among these hyperparameters. Used hyperparameters in this study are given in Table 6. When we create a larger neural network of 10 or 20 hidden layers, we see that ANN result becomes an underfitting situation, a linear behaviour. When we create a smaller neural network, we again see that ANN gives an underfitting result. This comparison is only for the number of hidden layers. Similar comparisons are valid for other hyperparameters such as neuron number, activation function, optimizers. For example, if we think that we can choose much more neuron number then, ANN will give underfitting results. The hyperparameters in this study are the valid for the training data set in this study. If we use richer data set, then the hyperparameters could be updated.

Although the values are completely different for the extrapolation distance and the criticality problem, the behaviour is similar. The extrapolation distance and the critical thickness values decrease as the secondary neutron number increase. However, ANN includes 5 hidden layers in the extrapolation distance calculations, 10 hidden layers in the critical thickness calculations.

Acknowledgment

This work was studied with the computer system which was collected with personal opportunities.

Conflicts of interest

There are no conflicts of interest in this work.

References

- [1] Carlson B.G., Solution of the Transport Equation by SN Approximations. Los Alamos Scientific Laboratory, LA-1599, United States, (1955) 1-29.
- [2] Lewis E.E., Miller W.F., Computational Methods of Neutron Transport. United States, (1984).
- [3] Case K.M., Zweifel P.F., Linear Transport Theory. Addison-Wesley: MA, (1967) 1-270.
- [4] Case K.M., Elementary solutions of the transport equation and their applications, *Annals of Phys.*, 9 (1) (1960) 1–23.
- [5] Kavenoky A., The CN Method of Solving the Transport Equation: Application to Plane Geometry, *Nuclear Science and Eng.*, 65 (2) (1978) 209-225.
- [6] Grandjean P., Siewert C.E., The FN method in neutron-transport theory. Part II: applications and numerical results, *Nucl. Sci. Eng.*, 69 (2) (1979) 161-168.
- [7] Tezcan C., Kaşkaş A., Güleçyüz M.Ç., The HN method for solving linear transport equation: *theory and applications*, *JQSRT.*, 78 (2) (2003) 243-254.
- [8] Géron A., Hands-On Machine Learning with Scikit-Learn, Keras and TensorFlow, 2nd ed. O'Reilly Media, (2019).
- [9] Chen Z., Andrejevic N., Drucker N.C., Nguyen T., Xian R.P., Smidt T., Wang Y., Ernstorfer R., Tennant D.A., Chan M., Li M., Machine learning on neutron and x-ray scattering and spectroscopies, *Chem. Phys. Rev.*, 2 (2021) 031301.
- [10] Whewell B., McClarren R.G., Data reduction in deterministic neutron transport calculations using machine learning, *Annals of Nuclear Energy.*, 176 (1) (2022) 109276.
- [11] Xie Y., Wang Y., Ma Y., Wu Z., Neural Network Based Deep Learning Method for Multi-Dimensional Neutron Diffusion Problems with Novel Treatment to Boundary, *J. Nucl. Eng.*, 2 (2021) 533-552.
- [12] Zolfaghari M., Masoudi S.F., Rahmani F., Fathi A., Thermal neutron beam optimization for PGNAA applications using Q-learning algorithm and neural network, *Sci. Rep.*, 12 (2022) 8635.
- [13] Zheng C., Liub L., Muc L., Solving the linear transport equation by a deep neural network approach, *Preprint submitted to Journal of Discrete and Continuous Dynamical System-S.*, 15 (4) (2021) 669-686.
- [14] Numpy. Available at: <https://numpy.org/doc/stable/user/index.html#user> Retrieved August 2022.
- [15] Scipy. Available at: <https://scipy.org/> Retrieved August 2022.
- [16] Sklearn. Available at: <https://scikit-learn.org/stable/> Retrieved August 2022.
- [17] Keras. Available at: <https://keras.io/> Retrieved August 2022.
- [18] Tensorflow. Available at: <https://www.tensorflow.org/> Retrieved August 2022.
- [19] Polyfit. Available at: <https://numpy.org/doc/stable/reference/generated/numpy.polyfit.html> Retrieved August 2022.
- [20] Sutskever, I., Vinyals O., Le Q.V., Sequence to Sequence Learning with Neural Networks, arXiv:1409.3215v3., (2014).
- [21] Kingma D.P., Ba J.L., Adam: A Method for Stochastic Optimization, arXiv:1412.6980v9., (2017).
- [22] Xu B., Wang N., Chen T., Li M., Empirical Evaluation of Rectified Activations in Convolution Network, arXiv:1505.00853v2., (2015).
- [23] Clevert D., Unterthiner T., Hochreiter S., Fast and accurate deep network learning by exponential linear units (Elus), arXiv:1511.07289v5., (2016).
- [24] Atalay M.A. The critical slab problem for reflecting boundary conditions in one-speed neutron transport theory, *Annals of Nuclear Energy.*, 23 (3) (1996) 183-193.

Molecular Docking and ADME Analysis of L-Phe -L-Tyr Dipeptide

Bilge Bıçak^{1,a,*}, Serda Kecel Gunduz^{1,b}

¹Department of Physics, Faculty of Science, İstanbul University, İstanbul, Türkiye.

*Corresponding author

Research Article

History

Received: 20/07/2022

Accepted: 01/11/2022

Copyright



©2022 Faculty of Science,
Sivas Cumhuriyet University

ABSTRACT

Hypertension is a serious risk factor for various diseases. Therefore, lowering and preventing high blood pressure is a significant issue. Blockage of the renin-angiotensin-aldosterone system (RAAS), which controls blood pressure, is important to reduce blood pressure and consequently reduce symptoms of heart failure. This blockage can be carried out by angiotensin-converting enzyme (ACE) and angiotensin II receptor blockers (ARBs). The phenylalanyltyrosine (H-Phe-Tyr-OH, Phe-Tyr, L-Phe-L-Tyr, L-phenylalanyl-L-tyrosine) dipeptide examined in this study is an important structure that shows blood pressure lowering properties. For this reason, the potential of the peptide to be an ACE inhibitor or ARB was investigated. The molecular activity of the Phe-Tyr dipeptide was compared with antihypertensive drugs using theoretical calculations. Molecular docking method, one of these theoretical methods, has a considerable process in illuminating biochemical processes by investigating the interactions of drugs (ligands) with targeted receptors. In this theoretical study, molecular docking analyses of H-Phe-Tyr-OH dipeptide with ACE and Angiotensin II type 1 receptor (AT1R) were implemented. The interaction types and interaction regions of the peptide were also determined in comparison with drug molecules (Captopril, Enalapril, Telmisartan and Eprosartan) that are ACE inhibitors and ARBs. Lastly, ADME (absorption, distribution, metabolism, and excretion) analysis of the H-Phe-Tyr-OH dipeptide was also performed to estimate its drug potential. In this study, the pharmacokinetic properties of Phe-Tyr dipeptide and its mechanism of action with ACE and AT1R were investigated for the first time by molecular docking and ADME calculations.

Keywords: Antihypertensive, Peptide, Docking, ADME.

 bbicak@istanbul.edu.tr

 <https://orcid.org/0000-0003-1147-006X>

 skecel@istanbul.edu.tr

 <https://orcid.org/0000-0003-0973-8223>

Introduction

Hypertension, which has been a subject of pharmacological research for many years, is a very serious and common risk factor for human health and stands out as an important risk group especially in cardiovascular diseases [1]. The renin-angiotensin-aldosterone system (RAAS) is important for regulating arterial blood pressure. The blockage of RAAS come forward in the treatment of several diseases including hypertension [2,3]. The blockage can be realized by renin inhibitors, ACE inhibitors and Angiotensin receptor blockers (ARBs) [4]. To better understand what type of hypertension a pharmacological class of antihypertensive is, its mechanism of action is being studied closely. Molecular receptor targets are of great importance in studies examining the mechanism of action. Various antihypertensive drugs can be used as angiotensin II receptor blockers (ARBs) and angiotensin converting enzyme inhibitors (ACEIs) [5]. Angiotensin-converting enzyme (ACE) inhibitors, i.e. drugs, help relax the veins and arteries to reduce blood pressure. These drugs are used to treat and manage hypertension, which is a significant risk factor for coronary disease, and other cardiovascular conditions [6]. The treatment of patients who have difficulty in tolerating ACE inhibitors due to cough that occurs as a side effect is continued with angiotensin receptor blockers [2]. Angiotensin receptor blockers (ARBs) interact and inhibit with the angiotensin II type 1 receptor (AT1R). Therefore, ARBs can be used to treat hypertension and hypertension-related diseases [2].

Amino acid metabolism is an effective system for controlling blood pressure. In a L-phenylalanine (Phe) study, it was reported that L-phenylalanine reduces the high salt-induced hypertension in rats [7]. Additionally, in a tyrosine study, it was reported that tyrosine reduces blood pressure in spontaneously for hypertensive rats [8]. Phe-Tyr dipeptide has also antihypertensive effect, reduce blood pressure and can be used as a pharmaceutical drug for the treatment of hypertension and cardiovascular diseases [9,10]. Molecular docking method has an important perspective in elucidating biochemical processes by examining the interactions of drugs or drug candidates (ligands) with targeted receptors at the atomic level. This method provides an estimation of the ligand-receptor complex structure and enables the determination of the optimal pose of the ligand to obtain the lowest energy complex structure [11-13]. Determining the pharmacokinetic information of drug candidate molecules is of great importance for drug development studies in biological systems. Estimates of absorption, distribution, metabolism, and excretion can be determined by ADME analysis. In this study, to elucidate the ACE inhibitor activity and AT1R blockage mechanism of Phe-Tyr, its interactions with the ACE and AT1R were investigated by molecular docking method, and the binding mechanisms of the peptide were presented with ACE inhibitors and ARBs comparatively. Pharmacokinetic properties for the predictions of the drug potential of the Phe-Tyr dipeptide were also determined by the ADME study.

Methods

The aim of molecular docking is to provide the prediction of a ligand and receptor complex [14]. To understand the reported antihypertensive activity of Phe-Tyr dipeptide, molecular docking studies were carried out using specific target receptor (ACE and AT1R). The binding mode of the Phe-Tyr dipeptide with the binding sites of ACE and AT1R were explored [15,16]. In this study, Phe-Tyr (antihypertensive dipeptide) was optimized at Gaussian09 with DFT method and B3LYP/6-31++G(d,p) basis set [17,18]. Phe-Tyr dipeptide was prepared as ligand by AutoDock Tools 1.5.6. Crystal structure of human angiotensin converting enzyme (PDB Code: 1O8A) and Angiotensin II type 1 receptor (PDB Code: 4ZUD) were downloaded from PDB DataBank (<https://www.rcsb.org/>). Receptors were prepared by deleting water, ions, and other ligands and adding polar hydrogens. After pdbqt files were obtained and grid box was adjusted, molecular docking study was run using AutoDock Vina [19]. After the binding affinities were obtained as a result of molecular docking analyses, the interaction region and interaction types of ligand-receptor complexes were determined with the help of Discovery Studio Visualizer 2019 [20]. Pharmacokinetic profile (ADME properties) of Phe-Tyr dipeptide were determined with the help of SwissADME online servers [21]. Docking studies and ADME analysis were carried out using Intel Core i7-6700HQ, up to 3.5 GHz workstation.

Result and Discussion

Molecular Docking Analysis

Molecular docking method investigates the behavior of small drug/drug candidate molecules in the binding site of a target receptor (protein, enzyme etc.). When the molecule is bound to a protein or enzyme receptor, this method presents an estimation about the ligand (small molecule) behavior using structure and electrostatic interactions [22]. Before molecular docking analyses, Phe-Tyr was optimized with DFT/B3LYP/6-31++G(d,p) basis set and the energy of optimized Phe-Tyr dipeptide was calculated as -695576.07609184 kcal/mol.

ACE receptor (PDB ID: 1O8A)

Phe-Tyr dipeptide was docked with ACE receptor using AutoDock Vina program. The best docking pose of Phe-Tyr

dipeptide at the ACE active site was shown in Figure 1. The results of binding energies and close interactions of ligand-receptor complex were shown in Figure 2 and Table 1. As a result of molecular docking, the best binding energy was obtained as -7.8 kcal/mol (see Table 2). Gln-281, Asp-415 and Tyr-520 residues in the ACE formed hydrogen bonds having 2.99 Å, 2.30 Å and 3.08 Å bond lengths with Phe-Tyr dipeptide. Asp-453, Val-379, Val-380 and His383 residues formed pi interactions with Phe-Tyr. While Val-379 and Val-380 residues formed pi-alkyl interactions with Phe-Tyr, Asp-453 and His-383 formed pi-anion and pi-pi stacked interactions with dipeptide. In the literature, it was reported that ACE has three active site pockets. While Ala354, Glu384 and Tyr523 residues are included in S1 pocket, Gln281, His353, Lys511, His513 and Tyr520 residues are included in S2 pocket and Glu162 residue is included in S1' pocket [23,24]. When looking at close interactions in this study, Phe-Tyr formed hydrogen bonds (Gln-281 and Tyr-520) with S2 pocket of ACE. When the binding energy of the dipeptide with ACE in our study was compared with the docking studies performed with other peptides in the literature, it was observed that the binding energies with ACE were lower or close to that of our study [24,25]. In docking studies performed with various small peptide structures, it was observed that the binding energies with ACE ranged from -3.6 to -7.9 kcal/mol [24,25]. The binding energies of captopril and enalapril, which are antihypertensive drugs and defined as ACE inhibitors, with ACE were calculated as -5.99 kcal/mol and -6.38 kcal/mol in a literature study, respectively [26]. Accordingly, the peptide structure in our study was found to have a close binding energy or high binding energy profile with the peptides and drugs in the literature. In addition, when the binding sites were examined, it was determined that both the studied peptides and the antihypertensive drugs (captopril, enalapril) bind from the same region with ACE and interact with the same residues [24-27]. It was observed that there is interaction between ACE residues, especially Gln-281 and Tyr-520, and both captopril and peptides studied in the literature [24-27]. In this study, it was determined that Phe-Tyr dipeptide made H-bonds with these two important residues. According to these results, Phe-Tyr can have a good inhibition activity depending on its effective interaction with the active site of ACE.



Figure 1. Phe-Tyr dipeptide at ACE active site.

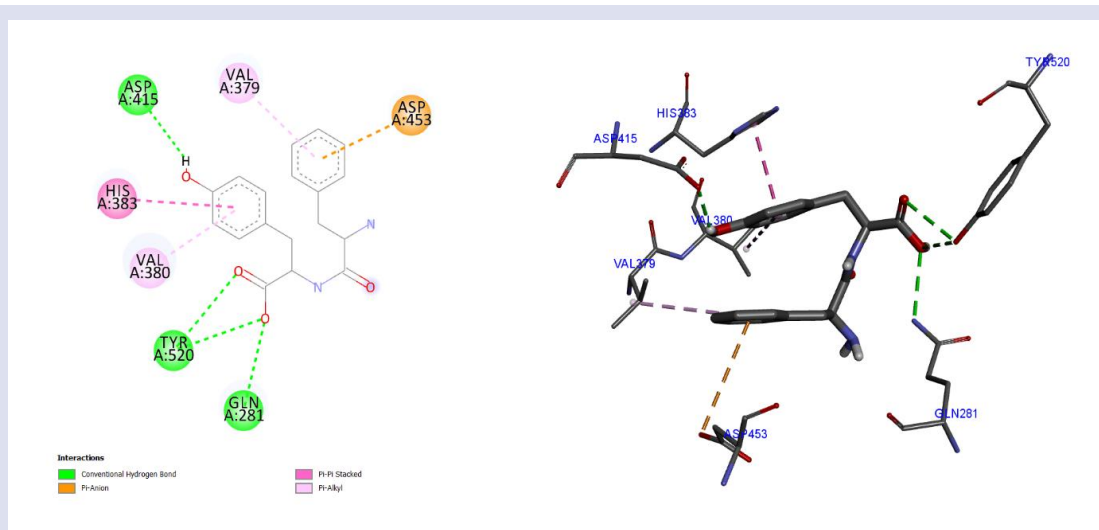


Figure 2. The close interactions of Phe-Tyr dipeptide with ACE.

Table 1. The interaction types of ligand-receptor complex.

Residue	Interaction Type	Distance (Å)
GLN-281	H-Bond	2.99
TYR-520	H-Bond	3.03
		3.04
ASP-415	H-Bond	2.30
HIS-383	Pi-Pi Stacked	3.81
VAL-380	Pi-Alkyl	5.32
VAL-379	Pi-Alkyl	5.33
Asp-453	Pi-Anion	4.91

Table 2. The binding affinities and RMSD values as a result of molecular docking analysis.

Mode	Affinity (kcal/mol)	Dist from best mode	
		rmsd l. b.	rmsd u. b.
1	-7.8	0.000	0.000
2	-7.4	2.375	4.633
3	-7.3	1.856	2.988
4	-7.3	2.381	4.618
5	-7.2	1.729	4.489
6	-7.0	1.659	2.333
7	-7.0	2.819	5.000
8	-7.0	2.239	5.123
9	-6.9	1.693	4.492

AT1 receptor (PDB ID:4ZUD)

Phe-Tyr dipeptide was docked with AT1 receptor and the best docking pose of Phe-Tyr dipeptide at the AT1R active site was shown in Figure 3. The results of binding energies and close interactions of ligand-receptor complex were shown in Figure 4 and Table 3. As a result of molecular docking, the best binding energy was obtained as -8.6 kcal/mol (see Table 4). Tyr-35 and Thr-88 residues in the AT1R formed hydrogen bonds having 3.01 Å and 3.00 Å bond lengths with Phe-Tyr dipeptide. Ile-288 and Pro-285 residues in the AT1R formed pi-alkyl interactions with Phe-Tyr. Tyr-92, Val-108 and Tyr-292 residues formed pi-pi stacked, pi-sigma and pi-pi T-shaped interactions with Phe-Tyr dipeptide, respectively. When the literature was searched, it was seen that Phe-Tyr dipeptide binds with AT1R from the same region with angiotensin receptor blocking drugs and other drug candidate compounds in the literature, but each molecule interacts with different residue groups uniquely [28,29]. In

the literature, it was emphasized that while most of the ARBs interact with residues Tyr-35, Trp-84 and Arg-167, the binding conformation and interact residues of each ARB differ [28]. It was also determined by Zhang et al that Telmisartan, an ARB, has pi-interaction with Tyr-92 [30]. In our study, it was determined that Phe-Tyr also has pi-pi stacked interaction with Tyr-92. It has been reported that eprosartan, which is an ARB, tends to have alkyl interactions with Tyr-292 and Ile-288 [30]. In our study, it was determined that Phe-Tyr has pi-alkyl interaction with Ile-288 and pi-pi t-shaped interaction with Tyr-292. In another literature study, docking studies of AT1R with quercetin and chlorogenic acid were performed and H-bond, Van der Waals and electrostatic interactions with Tyr-35, Trp-84, Thr-88, Ser-105, Val-108, Ser-109, Arg-167, Ile-288 residues were detected [29]. In our study, similar to the literature, it was determined that Phe-Tyr dipeptide form hydrogen bonds with Tyr-35 and Thr-88, and pi interactions with Val-108 and Ile-288.

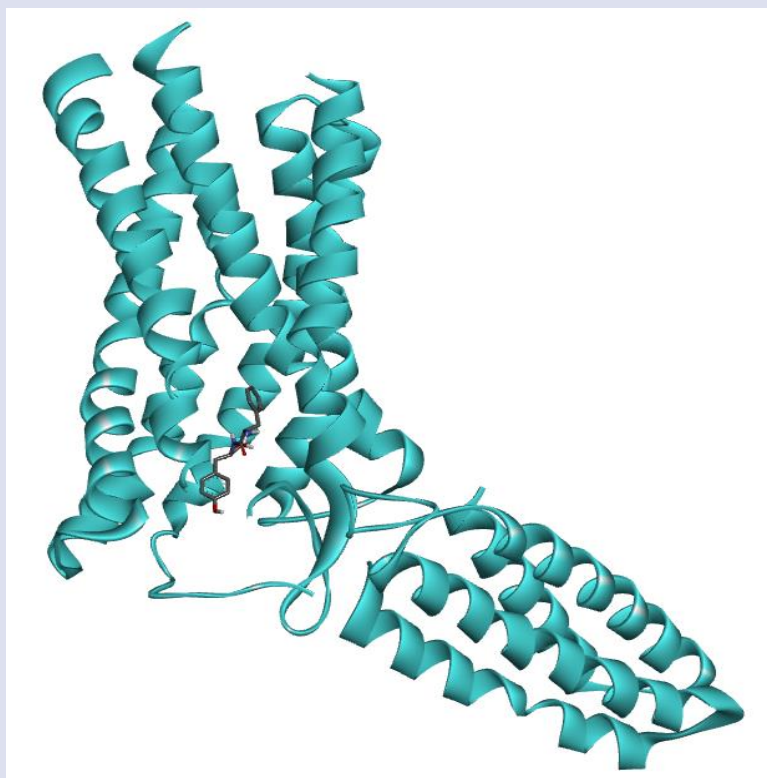


Figure 3. Phe-Tyr dipeptide at AT1R active site.

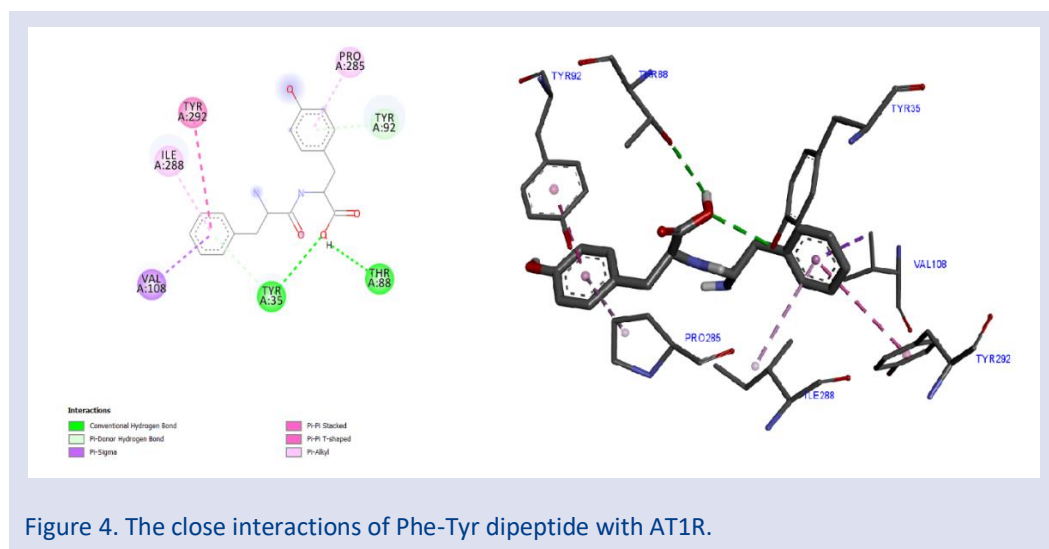


Figure 4. The close interactions of Phe-Tyr dipeptide with AT1R.

Table 3. The interaction types of ligand-receptor complex.

Residue	Interaction Type	Distance (Å)
TYR-35	H-Bond	3.01
THR-88	H-Bond	3.00
TYR-92	Pi-Pi Stacked	3.84
VAL-108	Pi-Sigma	3.90
TYR-292	Pi-Pi T-Shaped	5.21
ILE-288	Pi-Alkyl	5.11
PRO-285	Pi-Alkyl	5.28

Table 4. The binding affinities and RMSD values as a result of molecular docking analysis.

Mode	Affinity (kcal/mol)	Dist from best mode	
		rmsd l. b.	rmsd u. b.
1	-8.6	0.000	0.000
2	-8.4	2.158	4.289
3	-7.8	2.490	4.509
4	-7.6	2.421	7.767
5	-7.5	2.090	3.551
6	-7.5	2.263	8.316
7	-7.4	2.284	4.602
8	-7.3	1.982	7.935
9	-7.2	2.904	8.174

ADME Analysis

ADME (absorption, distribution, metabolism, excretion) analysis is used to obtain pharmacokinetic information for drug candidate molecules. ADME profile of Phe-Tyr dipeptide was determined by using SwissADME and was given in Table 5.

When looking at druglikeness profile of Phe-Tyr, this dipeptide has the potential to be an oral drug. The most important proof of this is that the molecule obeys the Lipinski's rule of 5 [31]. 4 parameters (molecular weight <500 g/mol, have no more than 5 hydrogen bond donors and 10 hydrogen bond acceptors, and octanol/water partition coefficient <5) were determined by Lipinski using the common characteristics of most of the oral drug candidates that passed the phase II clinical stage. In this study, physicochemical and lipophilicity properties of Phe-Tyr were given in Table 5. In physicochemical and lipophilicity properties parts, it was seen that Phe-Tyr has a molecular weight of 328.36 g/mol, five H-bond acceptors, four H-bond donors and its octanol/water partition coefficient is less than five. In addition, it was determined that Phe-Tyr dipeptide is very soluble and has a high absorption

property in the gastrointestinal system. It is important that drugs developed for CNS diseases pass through the BBB and other drugs do not affect the CNS [32]. The Phe-Tyr dipeptide is a drug candidate that does not affect the CNS, which has not BBB permeability. PSA is used to characterize the transport process of drug molecules and relates to various causes of drug absorption [33]. PSA value of Phe-Tyr was calculated as 112.65 Å². Some drugs can be inhibited or induced Cytochrome P450 enzymes. These conditions may cause drug-drug interactions and cause undesirable reactions [34]. Phe-Tyr didn't inhibit CYP450 enzymes in the result of SwissADME server. When the ADME profiles of the antihypertensive drugs losartan and captopril were compared [35], it was observed that the Phe-Tyr dipeptide also fully complied with the Lipinski's rule of 5. It has been determined to be high in gastrointestinal absorption like antihypertensive drugs. The profile of CYP3A4 inhibitor of Phe-Tyr dipeptide was similar to Captopril [35].

Table 5. ADME properties of Phe-Tyr dipeptide

Physicochemical Properties	Phe-Tyr
MW	328.36 g/mol
No. of heavy atoms	24
No. of arom. heavy atoms	12
No. rotatable bonds	8
No. of H-bond acceptors	5
No. of H-bond donors	4
Polar surface area	112.65 Å ²
Lipophilicity	
LogP _{o/w} (iLOGP)	1.78
LogP _{o/w} (XLOGP3)	-1.68
LogP _{o/w} (WLOGP)	1.07
LogP _{o/w} (MLOGP)	1.35
LogP _{o/w} (SILICOS-IT)	1.75
Consensus LogPO/W	0.85
Water Solubility	
Log S (ESOL)	-0.66
Log S (Ali)	-0.17
Log S (SILICOS-IT)	-4.24
Pharmacokinetics	
GI absorption	High
BBB permeant	No
P-gp substrate	No
CYP1A2 inhibitor	No
CYP2C19 inhibitor	No
CYP2C9 inhibitor	No
CYP2D6 inhibitor	No
CYP3A4 inhibitor	No
Log K _p (skin permeation)	-9.50 cm/s
Druglikeness	
Lipinski	Yes, 0 violation
Ghose	Yes
Veber	Yes
Muegge	Yes
Bioavailability Score	0.55

Conclusion

In conclusion, a novel study of Phe-Tyr dipeptide having antihypertensive were theoretically carried out using *in silico* methods. Molecular activity of Phe-Tyr dipeptide was compared with antihypertensive drugs by using theoretical calculations. Molecular docking method was used to obtain an estimate of the biological activity of the molecule. The interactions of the Phe-Tyr dipeptide with ACE and AT1 receptors were investigated by molecular docking method. It was determined that Phe-Tyr dipeptide interacts more with the S2 region (Gln-281 and Tyr-520), which is one of the active sites of ACE, where synthetic drugs like Captopril used in hypertension studies interact. In another molecular docking study, it was determined that the Phe-Tyr dipeptide interacted with AT1R and formed H-bond and pi interactions similar to ARBs like Telmisartan and Eprosartan synthetic drugs with Tyr-92 and Ile-288, Tyr-292 residues, respectively. In addition, the ADME profile was determined for Phe-Tyr, which has the potential to be an antihypertensive drug according to low molecular weight, appropriate H-bond acceptors and H-bond donor counts and favorable

octanol/water partition coefficient. As a result of *in silico* ADME analysis, it was determined that the Phe-Tyr dipeptide is a drug candidate in accordance with Lipinski's rule of 5 and had an ADME profile similar to antihypertensive drugs. Finally, it can be said that this study will be helpful experimental studies.

Conflicts of interest

The authors stated that did not have conflict of interests.

References

- [1] Laurent, S., Antihypertensive drugs, *Pharmacol. Res.*, 124 (2017) 116-125.
- [2] Hill R.D., Vaidya P.N., Angiotensin II Receptor Blockers (ARB). In: StatPearls [Internet]. StatPearls Publishing, Treasure Island (FL), (2022).
- [3] Shahoud, J. S., Terrence S., and Narothama R.A., Physiology, arterial pressure regulation. In: StatPearls [Internet]. StatPearls Publishing, Treasure Island (FL), (2022).
- [4] Kritsi, E., Matsoukas, M.T., Potamitis, C., Karageorgos, V., Detsi, A., Magafa, V., Liapakis, G., Mavromoustakos, T., Zoumpoulakis, P., Exploring new scaffolds for angiotensin II receptor antagonism, *Bioorg. Med. Chem.*, 24 (18) (2016) 4444-4451.
- [5] Amaya, J.A.G., Cabrera, D.Z., Matallana, A.M., Arevalo, K.G., Guevara-Pulido, J., In-silico design of new enalapril analogs (ACE inhibitors) using QSAR and molecular docking models, *Inform. Med. Unlocked.*, 19 (2020) 100336.
- [6] Herman, L.L., Padala, S.A., Ahmed, I., Bashir, K., Angiotensin converting enzyme inhibitors (ACEI). In: StatPearls [Internet]. StatPearls Publishing, Treasure Island (FL), (2022).
- [7] Wang, Z., Cheng, C., Yang, X., Zhang, C., L-phenylalanine attenuates high salt-induced hypertension in Dahl SS rats through activation of GCH1-BH4, *PLoS One*, 16 (4) (2021) e0250126.
- [8] Sved, A.F., Fernstrom, J.D., Wurtman, R.J., Tyrosine administration reduces blood pressure and enhances brain norepinephrine release in spontaneously hypertensive rats, *Proc. Natl. Acad. Sci. U.S.A.*, 76 (7) (1979) 3511-3514.
- [9] Suetsuna, K., Maekawa, K., Chen, J.R., Antihypertensive effects of Undaria pinnatifida (wakame) peptide on blood pressure in spontaneously hypertensive rats, *J. Nutr. Biochem.*, 15 (5) (2004) 267-272.
- [10] Kecel-Gündüz, S., Budama-Kilinc, Y., Cakir Koc, R., Kökcü, Y., Bıcak, B., Aslan, B., Özel, A.E., Computational design of Phe-Tyr dipeptide and preparation, characterization, cytotoxicity studies of Phe-Tyr dipeptide loaded PLGA nanoparticles for the treatment of hypertension, *J. Biomol. Struct. Dyn.*, 36 (11) (2018) 2893-2907.
- [11] Khan, T., Lawrence, A.J., Azad, I., Raza, S., Khan, A.R., Molecular Docking Simulation with Special Reference to Flexible Docking Approach, *JSM Chem.*, 6 (1) (2018) 1053-1057.
- [12] [Meng, X.Y., Zhang, H.X., Mezei, M., Cui, M., Molecular docking: a powerful approach for structure-based drug discovery, *Curr. Comput.-Aided Drug Des.*, 7 (2) (2011) 146-157.

- [13] McConkey, B.J., Sobolev, V., Edelman, M., The performance of current methods in ligand–protein docking, *Curr. Sci.*, 83 (7) (2002) 845-856.
- [14] Bıçak, B., Gündüz, S.K., Kökcü, Y., Özel, A.E., Akyüz, S., Molecular docking and molecular dynamics studies of L-glycyl-L-glutamic acid dipeptide, *Bilgesci*, 3 (1) (2019) 1-9.
- [15] Lakhri, Y., Rbaa, M., Tuzun, B., Hichar, A., Anouar, E.H., Ounine, K., Almalki, F., Hadda, T.B., Zarrouk, A., Lakhri, B., Synthesis, structural confirmation, antibacterial properties and bio-informatics computational analyses of new pyrrole based on 8-hydroxyquinoline, *J. Mol. Struct.*, 1259 (2022) 132683.
- [16] Jayarajan, R., Satheeshkumar, R., Kottha, T., Subbaramanian, S., Sayin, K., Vasuki, G., Water mediated synthesis of 6-amino-5-cyano-2-oxo-N-(pyridin-2-yl)-4-(p-tolyl)-2H-[1, 2'-bipyridine]-3-carboxamide and 6-amino-5-cyano-4-(4-fluorophenyl)-2-oxo-N-(pyridin-2-yl)-2H-[1, 2'-bipyridine]-3-carboxamide—An experimental and computational studies with non-linear optical (NLO) and molecular docking analyses, *Spectrochim. Acta A Mol. Biomol. Spectrosc.*, 229 (2020) 117861.
- [17] Lehtola, S., Automatic algorithms for completeness-optimization of Gaussian basis sets, *J. Comput. Chem.*, 36 (5) (2015) 335-347.
- [18] Frisch M.J., Trucks G.W., Schlegel H.B., Scuseria G.E., Robb M.A., Cheeseman J.R., Scalmani G., Barone V., Petersson G.A., Nakatsuji H., et.al., Gaussian 16 Rev. B.01, Wallingford, CT, 2016.
- [19] Trott, O., Arthur J. O., AutoDock Vina: improving the speed and accuracy of docking with a new scoring function, efficient optimization, and multithreading, *J. Comput. Chem.*, 31 (2) (2010) 455-461.
- [20] Biovia Discovery Studio, Available at: <https://www.3ds.com/products-services/biovia/products/molecular-modeling-simulation/biovia-discovery-studio/>. Retrieved May 14, 2022.
- [21] Daina, A., Michielin, O., Zoete, V., SwissADME: a free web tool to evaluate pharmacokinetics, drug-likeness and medicinal chemistry friendliness of small molecules, *Sci. Rep.*, 7 (1) (2017) 1-13.
- [22] Pagadala, N.S., Syed, K., Tuszynski, J., Software for molecular docking: a review, *Biophys. Rev.*, 9 (2) (2017) 91-102.
- [23] Andújar-Sánchez, M., Cámara-Artigas, A., Jara-Pérez, V., A calorimetric study of the binding of lisinopril, enalaprilat and captopril to angiotensin-converting enzyme, *Biophys. Chem.*, 111 (2) (2004) 183-189.
- [24] Pina, A.S., Roque, A.C.A., Studies on the molecular recognition between bioactive peptides and angiotensin-converting enzyme, *J. Mol. Recognit.*, 22 (2) (2009) 162-168.
- [25] Wang, X., Chen, H., Fu, X., Li, S., Wei, J., A novel antioxidant and ACE inhibitory peptide from rice bran protein: Biochemical characterization and molecular docking study, *Lwt*, 75 (2017) 93-99.
- [26] Amaya, J.A.G., Cabrera, D.Z., Matallana, A.M., Arevalo, K.G., Guevara-Pulido, J., In-silico design of new enalapril analogs (ACE inhibitors) using QSAR and molecular docking models, *Inform. Med. Unlocked.*, 19 (2020) 100336.
- [27] Dalkas, G.A., Marchand, D., Galleyrand, J.C., Martinez, J., Spyroulias, G.A., Cordopatis, P., Cavelier, F., Study of a lipophilic captopril analogue binding to angiotensin I converting enzyme, *J. Pept. Sci.*, 16 (2) (2010) 91-97.
- [28] Singh, K.D., Unal, H., Desnoyer, R., Karnik, S.S., Divergent spatiotemporal interaction of angiotensin receptor blocking drugs with angiotensin type 1 receptor, *J. Chem. Inf. Model.*, 58 (1) (2018) 182-193.
- [29] Sant'Anna, L.S., Merlugo, L., Ehle, C.S., Limberger, J., Fernandes, M.B., Santos, M.C., Mendez, A.S.L., Paula, F.R., Moreira, C.M., Chemical composition and hypotensive effect of *Campomanesia xanthocarpa*, *J. Evid. Based Complementary Altern. Med.*, 2017 (2017).
- [30] Zhang, H., Unal, H., Desnoyer, R., Han, G.W., Patel, N., Katritch, V., Karnik, S.S., Cherezov, V., Stevens, R.C., Structural Basis for Ligand Recognition and Functional Selectivity at Angiotensin Receptor, *J. Biol. Chem.*, 290 (49) (2015) 29127-29139.
- [31] Lipinski, C.A., Lead-and drug-like compounds: the rule-of-five revolution, *Drug Discov. Today Technol.*, 1 (4) (2004) 337-341.
- [32] Carpenter, T.S., Kirshner, D.A., Lau, E.Y., Wong, S.E., Nilmeier, J.P., Lightstone, F.C., A method to predict blood-brain barrier permeability of drug-like compounds using molecular dynamics simulations, *Biophys. J.*, 107 (3) (2014) 630-641.
- [33] Mannhold, R., Kubinyi, H., Folkers, G., Molecular drug properties: measurement and prediction, Weinheim, Wiley-VCH, 37 (2008) 111-123.
- [34] Lynch, T., Neff, A.P., The effect of cytochrome P450 metabolism on drug response, interactions, and adverse effects, *Am. Fam. Physician.*, 76 (3) (2007) 391-396.
- [35] Ji, D., Xu, M., Udenigwe, C.C., Agyei, D., Physicochemical characterisation, molecular docking, and drug-likeness evaluation of hypotensive peptides encrypted in flaxseed proteome, *Curr. Res. Food Sci.*, 3 (2020) 41-50.

Carbon Radiotherapy For Head and Neck Cancer: Dosimetric Comparison with Photon Plans

Deniz Erkal^{1,a,*}, Sinan Kuday^{2,b}

¹ Mediaci Physics, Institute of Graduate School of Sciences, Istanbul Aydın University, Istanbul, Türkiye.

² Department of Physics, Faculty of Sciences, Ankara University, 06100, Ankara, Türkiye.

*Corresponding author

Research Article

History

Received: 03/09/2022

Accepted: 11/11/2022

Copyright



©2022 Faculty of Science,
Sivas Cumhuriyet University

^a turerceci@gmail.com

^b <https://orcid.org/0000-0001-6309-6300>

ABSTRACT

Radiation therapy is one of the most widely used treatment methods for tumors. The therapeutic use of carbon ions is more advantageous than other radiotherapy techniques especially photon-based irradiation due to its physical properties and radiobiological effects, and therefore it has received more attention. One of the most important reasons for that carbon ion beams are more effective than photon beams while minimizing the dose in the normal tissues around the target, it offers an improved dose distribution that leads to sufficient dose concentration in tumors. In addition, the carbon beam reaches its maximum at the end of its range, which increases with depth, and due to this feature, it provides a higher biological efficiency. In radiotherapy studies, Monte Carlo simulation is widely used to determine the dose distributions and to obtain the correct properties of the beams. With MC simulation, it helps to understand the relative biological efficiency as well as the spatial model of energy storages. In this study, a geometry with critical organs (skull, brain, nasopharynx and thyroid) based on a MIRD phantom was modeled with the Monte Carlo simulation tool GATE (vGATE 9.0). In this experiment, the tumor was irradiated with different carbon beam energies and photon beams. The aim is to calculate the energy accumulations in the region and surrounding organs with the MC method, and as a result, to show the dosimetric advantages of carbon radiotherapy over photon radiotherapy.

Keywords: Breast cancer, Proton therapy, Photon therapy, GATE, Monte Carlo .

Introduction

Among the head and neck cancers, nasopharyngeal cancer makes surgical intervention impossible due to its epidemiological and histological features, as well as its anatomical localization, and therefore it shows sensitivity to radiotherapy and chemotherapy, which are effective treatment methods in order to destroy the tumor [1]. For this reason, radiotherapy is the main treatment method for nasopharyngeal cancer. New radiotherapy techniques allow the preservation of brain areas with low tolerance to radiation, such as the pituitary gland and brain.

During the application of radiotherapy, some healthy cells may be affected by radiation, but they can repair themselves faster than cancer cells or cause side effects and secondary cancer formation as a result of exposure to high doses. With a good treatment planning, it is critical to protect the healthy tissues around the target volume at the highest level by giving the highest dose to the target volume.

Carbon ion therapy, which is a new radiotherapy method recently, has given very successful results in cancer treatment. Carbon ion therapy is a new form of radiation that fights to the extent that it destroys the unwanted mass by damaging the DNA in the cancer cell [2]. It is a modern treatment method based on the interaction of heavy ion beams such as carbon with living tissue. In photon radiotherapy, the rays are scattered by

Compton scattering as they move through the living tissue and when they reach the cancerous area, they leave most of their energy on the healthy tissue, in which case it damages the healthy tissue. The carbon radiotherapy method ensures that the target cancer cells are destroyed by leaving minimal effects on the surrounding healthy tissue [3].

The use of the Monte Carlo (MC) method in radiotherapy dosimetry has increased exponentially recently, and even this computer simulation technique has been taken as a reference and has become a common tool in treatment plans and dosimetry calculations [4]. The most accurate way to calculate the dose distribution in treatment planning is the geometry of the source, the transport of energy to the desired tissue and the monitoring of energy accumulation by using the particle transport MC method. Geant4 (GEneration ANd Tracking) is software that can simulate particles interacting with and passing through matter [4]. Geant4 is a widely used MC code in health physics for various applications such as dosimetry, imaging, nuclear medicine and radiation protection. This code library is constantly evolving, so Geant4 is a fully automated system for health physics that compares this MC code with reference data and performs regression testing. The tests performed in Geant4-med are carried out on the CERN computing infrastructure by

using the geant-val web application developed for Geant4 testing at CERN [5].

In this study, the dosimetric advantages of carbon radiotherapy over photon radiotherapy for head and neck cancers were investigated with the MC method in terms of the rays exposed to the healthy tissues around the malignant tumor cells.

Materials and Methods

GATE is open source software, developed jointly by the world's leading medical physics laboratories, that allows simulating medical physics using the Geant4 code library.. Geant4 is an object-oriented and C++ programming language that simulates particle transition in matter and simulates real-world processes or systems very close to reality. Geant4 (C++) is a software package developed in 1998 after Geant3 (based on Fortran), which was developed at CERN (European Nuclear Research Council) in 1993 for high energy physics experiments [6]. By using the Geant4 simulation, the possible interactions of the particle with the atom and nucleus of the target material during its progression in the matter and physical events such as position and energy in this process can be monitored.

The phantom was placed on the x, y, z coordinates with the dimensions of 2.0 x 2.0 x 2.0 m³. The average sized skull, brain, nasopharynx and thyroid organs of an

adult human were scaled and defined inside the world geometry created in the Cartesian coordinate system. Maximum x, y and z lengths were measured as 20.00 21.20 12.80 cm for the skull, 7.00, 3.50, 11.20 cm for the brain, 4.00, 4.50, 3.00 cm for the nasopharynx, and the skull volume is 5.427.2 cm³ [7]. Thyroid with 0.83, 1.85, 4.50 cm dimensions were defined in the phantom created. Materials and tissues to fill the phantom volume were selected over the textures defined in the GateDatabase.db file based on the NIST Standards [8].

In this study, the vGATE 9.0 version of GATE was used and the teleportation was performed on a personal computer with 10 million events. Figure 1 below shows the image of the created geometry and Figure 2 shows the image formed during irradiation.

DoseActors with voxel dimensions of 1.0 mm x 1.0 mm x 1.0 mm were attached to the organs defined in the simulation code. The targeting of the cancerous area was completed by sending carbon ion beams and photon beams from different points for typical MeV values of each irradiations shown in Table 1. Radiation exposure of surrounding organs was measured with DoseActor. The dose value (Gy) stored in DoseActor was saved by taking the output files in root format. Cut regions for each tissue and each particle (electron, positron, gamma) has been set to 0.01 mm.

Table 1: Doses absorbed by organs (Gy) for each energy levels (MeV) with 1M events using a particle filter.

Energy For Carbon(MeV)	Energy For Photon(MeV)	Carbon DoseActor (Gy)		Photon DoseActor (Gy)	
160 MeV	12 MeV	Nazofarengal	3.9122 e-08	Nazofarengal	1.7570 e-08
		Brain	7.1320 e-10	Brain	4.2980 e-08
		Thyroid	3.6452 e-10	Thyroid	3.1052 e-08
140 MeV	10 MeV	Nazofarengal	4.6213 e-08	Nazofarengal	9.4296 e-09
		Brain	1.8312 e-10	Brain	3.3480 e-09
		Thyroid	5.2590 e-11	Thyroid	4.0096 e-09
120 MeV	9 MeV	Nazofarengal	3.7962 e-08	Nazofarengal	2.2865 e-07
		Brain	2.1590 e-10	Brain	3.0870 e-07
		Thyroid	3.7125 e-11	Thyroid	4.4290 e-10
110 MeV	8 MeV	Nazofarengal	3.0596 e-08	Nazofarengal	5.1355 e-08
		Brain	6.1599 e-10	Brain	3.3012 e-09
		Thyroid	3.6500 e-10	Thyroid	7.1230 e-08
100 MeV	7 MeV	Nazofarengal	3.0713 e-08	Nazofarengal	9.3361 e-09
		Brain	6.1560 e-10	Brain	4.3000 e-08
		Thyroid	5.2031 e-11	Thyroid	3.9810 e-10

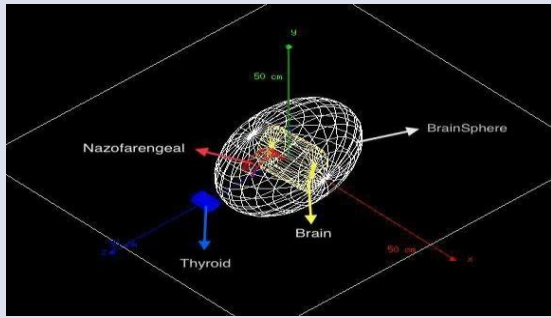


Figure 1. Geometric shape designed with the help of Gate simulation package [8]

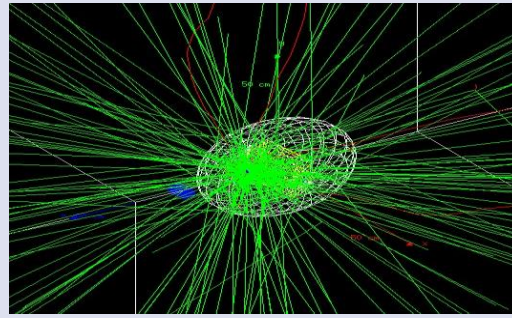


Figure 2. Schematic view of particle beams interacting towards the nasopharynx.

During the carbon-ion and photon simulations, we considered 2D circular shaped mono-energetic beam with 2 mm σ_x and 2 mm σ_y distribution targeting the centre of the phantom assuming the cancer cells are not larger than the beam size. For the physical interactions, built-in physics lists are used together as QGSP_BERT_HP and FTFP_BERT_HP within the Geant4 code. Statistical outputs showed that 1K events correspond to 2.235 minutes of irradiation without initializations in photon simulations while 7.16 minutes of irradiation in carbon simulations.

Results

In this study, we calculated the radiation absorbed by the cancerous mass and neighboring organs with the help of virtual dosimetry called doseActor in GATE. Carbon ion beams with energies of 160 MeV, 140MeV, 120MeV, 110MeV and 100 MeV were delivered to the target mass

and five different simulations were performed. We also delivered the photon beams with energies of 10 MeV, 9 MeV, 8 MeV and 7 MeV. Then the dose values are calculated by the voxel algorithms for each simulation from the 2D and 3D absorbed dose distributions formed in the phantom that we designed to use together with the photon and carbon simulation as in Figure 3 and Figure 4.

The amount of doses stored in each organ and the percentage of doses absorbed are given in Table 2. As expected, carbon doses absorbed a very high percentage of the total dose in the target organ, the nasopharynx, while the percentile of doses absorbed by organs outside the area remained below 2%. It has been observed with the data that the organs adjacent to the target organ, the nasopharynx, absorb photon doses close to the nasopharynx or even more. With the data obtained by simulation, the organs outside the target mass were found to be very low compared to the photon doses, and it was listed in Table 2.

Table 2. Doses and percentages received by organs at the end of treatment.

Energy for carbon(MeV)	Energy for photon(MeV)	Carbon DoseActor (Gy)	Percentiles		Photon DoseActor (Gy)		Percentiles
160 MeV	12 MeV	Nazofarengal	12.8	%20	Nazofarengal	6.75	%15
		Brain	0.2335	%0.36	Brain	16.4915	%36.65
		Thyroid	0.1192	%0.19	Thyroid	11,90	%26.45
140 MeV	10 MeV	Nazofarengal	12.8	%20	Nazofarengal	6.75	%15
		Brain	0.0510	%0.08	Brain	2.3908	%5.31
		Thyroid	0.0149	%0.02	Thyroid	2.8663	%6.36
120 MeV	9 MeV	Nazofarengal	12.8	%20	Nazofarengal	6.75	%15
		Brain	0.0730	%0.11	Brain	7.4250	%16.5
		Thyroid	0.0125	%0.02	Thyroid	0.0131	%0.03
110 MeV	8 MeV	Nazofarengal	12.8	%20	Nazofarengal	6.75	%15
		Brain	0.2581	%0.40	Brain	0.4342	%0.96
		Thyroid	0.1532	%0.23	Thyroid	9.3685	%20.81
100 MeV	7 MeV	Nazofarengal	12.8	%20	Nazofarengal	6.75	%15
		Brain	0.2564	%0.40	Brain	31.1093	%69.13
		Thyroid	0.0216	%0.03	Thyroid	0.2879	%0.64

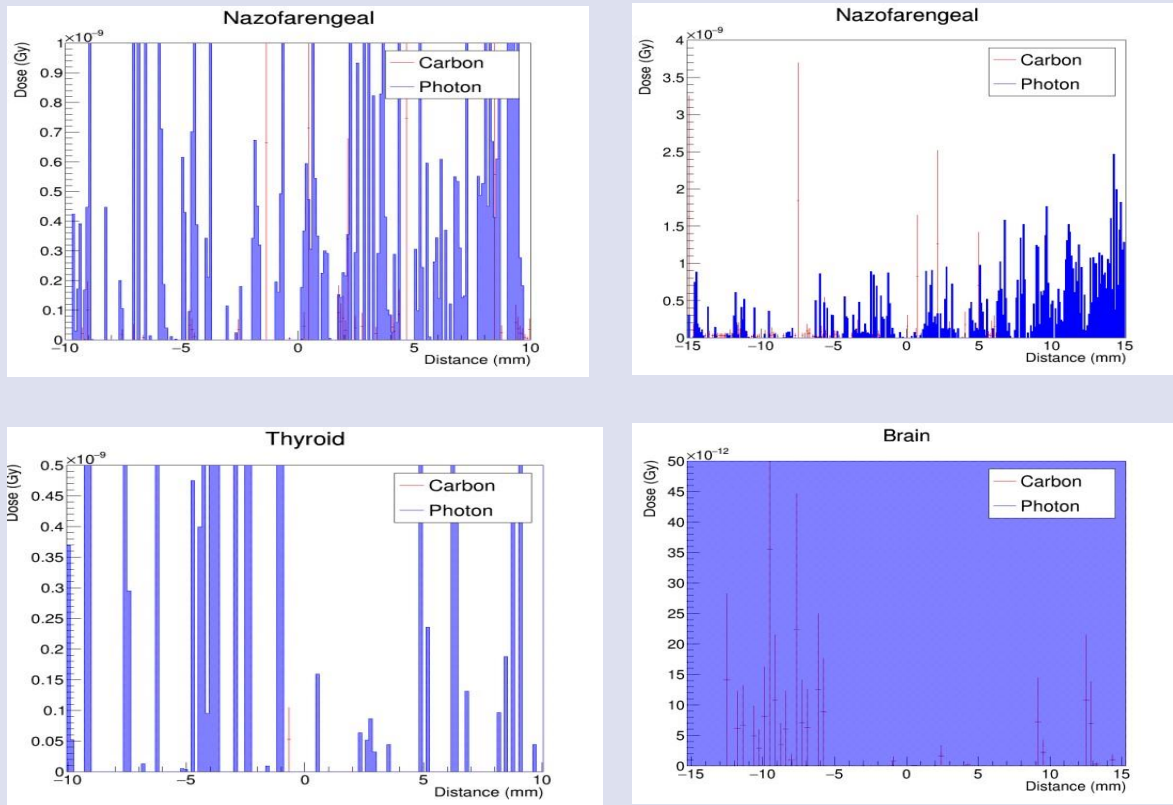


Figure 3. 2D dose distribution plots absorbed in the nasopharynx, thyroid, and brain phantom with applied particle filter. Photon rays with blue color spread over a wider area, therefore a wider area is exposed to the dose. The carbon rays shown with red color spread in a smaller area and create a more dose effect on the target. It is seen that photon rays cause more dose units on both the target audience and critical organs than carbon rays.

During the simulations, insignificant amounts of secondary particles are observed. While the observed types were only the electrons, positrons and gammas for photon irradiations, a wider spectrum of secondary particle types was observed for carbon irradiations including carbon-12(¹²C) ion, protons, electrons, gamma, alphas, ...etc. In order to perform a fair comparison in Table-1, we have applied a particle filter excluding all secondary particles. However, that limitation caused a

decrease in the total dose for carbon irradiation by the factor 2 approximately.

First results revealed that carbon and photon irradiations have quite separate characteristics due to their different nuclear substructure and interactions. In our simulations, that resulted as : *i.* wider dispersion, *ii.* rather randomized penetration features, *iii.* less dose deliverance for photons through out all the tissues in comparison with carbon-ion irradiation as summarized in Table 3.

Table 3. Statistical outputs from photon and carbon simulations of Figure 4 for 10M hit data.

Statistical Parameters	Carbon	Photon
Mean x	1.152	37.8
Mean y	1.6	7.23
Std. Deviation for x (σ_x)	0.5282	27.68
Std. Deviation for y (σ_y)	2.022	14.25
Skewness x	11.71	-1.416
Skewness y	-0.004	-0.5

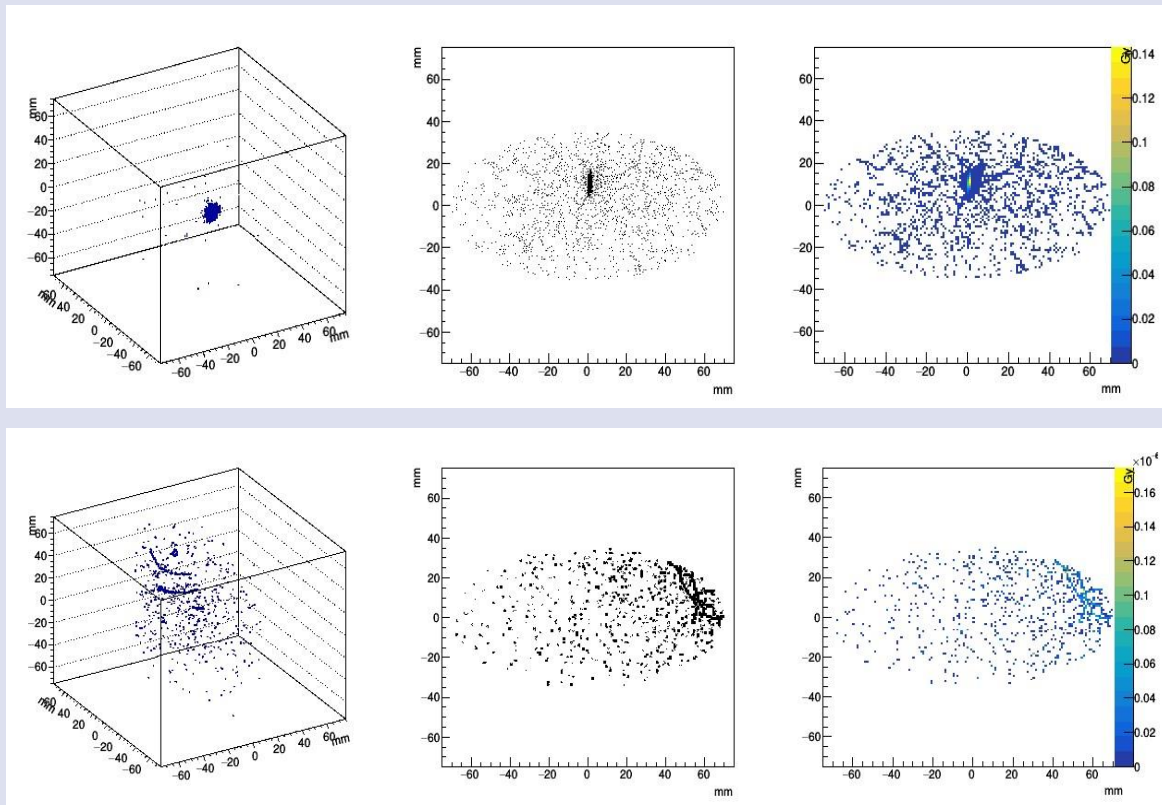


Figure 4. 3D dose distributions of carbon-ion (up) and photon (down) beams absorbed in the brain phantom with 1500 events and more than 10M hits.

Analysis

We applied χ^2 -method on dose values as a statistical method in which goodness or inconsistencies between datasets are generally sought. Considering null hypothesis

(H0) is "no significant dose difference between Carbon and Photon irradiations"(whereas alternate hypothesis is just the opposite),one can see that the total χ^2 values at the order of $\sim 10^{-7}$ - 10^{-9} corresponds to acceptance region of H0.

Table 4. χ^2 data.

Simulation No.	Nazofarengeal	Brain	Thyroid	Total
1	2.66e-08	4.15e-08	10.03e-08	1.38e-07
2	1.43e-07	2.99e-09	3.89e-09	1.49e-07
3	1.59e-09	3.07e-07	3.72e-10	3.09e-07
4	8.44e-09	2.18e-09	7.04e-08	8.10e-08
5	4.89e-08	4.18e-08	3.01e-10	9.10e-08
Total	2.28e-07	3.95e-07	1.45e-07	

However, one can realise from Table 3 that statistical dispersions based on the standart deviation of photon irradiations are huge by the factor of 55 and 7 of carbon standart deviations for x and y directions, respectively. Also, photon irradiation tends to give negative skewness for each directions. Inconsistent mean values of photon case reveals that the targeting of those particles are just failing due to their natural structure that can penetrate deeply in almost all of the tissues.

Conclusion

Based on our analysis, one can conclude carbon ion radiotherapy is a promising treatment technique that can provide additional benefit to treat cancers that are difficult to treat with traditional methods, with the success achieved in studies on cancer patients in carbon radiotherapy centers in Germany and Japan recently for the treatment of tumors [9,10,11]. Carbon ion radiotherapy has the lowest level of toxicity compared to photon radiotherapy. It has a biological and physical

superiority with its high degree of local control and a high degree of general controls. In photon radiotherapy, healthy tissues behind or in front of the targeted tumor are exposed to an overdose. Carbon ions, on the other hand, leave a significant part of their energy at the Bragg peak, and healthy tissues are exposed to the minimum dose due to the low energy accumulated in the entryway before and after the Bragg peak. Therefore, dose adjustment has a great importance in the quality of treatment. Therefore, carbon ion radiotherapy is a more advantageous, safe and effective treatment method. Comprehensive, prospective studies and long-term patient follow-up after treatment are needed to better define the role of CIRT.

Conflicts of interest

The authors declare that they have no conflict of interest.

References

- [1] Yaprak G., Evaluation of radiological and biochemical methods in the late term toxicity of carotic artery, thyroid gland and temporal lob after radiotherapy in patients with nasopharyngeal cancer, master thesis, Ministry of Health-Dr. Lutfi Kırdar Kartal Training and Research Hospital, Radiology Oncology Department, (2007).
- [2] Mohamad O., Sishc B.J., Saha J., Pompos A., Rahimi A., Story M.D., Davis A., Kim D.W.N., Carbon Ion Radiotherapy: A Review of Clinical Experiences and Preclinical, with an Emphasis on DNA Damage/Repair, DNA Repair Pathways in Cancer, 9 (6) (2017) 66.
- [3] Kim J., Park J.M., Wu H.G., Carbon Ion Therapy: A Review of an Advanced Technology, *Progress in Medical Physics*, 31 (3) (2020) 71-80.
- [4] Andreo P., Monte Carlo simulations in radiotherapy dosimetry, *Radiation Oncology*, 13 (2018) 121.
- [5] Arce P., Bolst D., Bordage M.C., Brown J.M.C., Cirrone P., Cortés-Giraldo M.A., Cutajar D., Cuttone G., Desorgher L., Dondero P., Dotti A., Faddegon B., Fedon C., Guatelli S., Incerti S., Ivanchenko V., Konstantinov D., Kyriakou I., Latyshev G., Le A., Mancini-Terracciano C., Maire M., Mantero A., Novak M., Omachi C., Pandola L., Perales A., Perrot Y., Petringa G., Quesada J.M., Ramos-Méndez J., Romano F., Rosenfeld A.B., Sarmiento L.G., Sakata D., Sasaki T., Sechopoulos I., Simpson E.C., Toshito T., Wright D.H., Report on G4-Med, a Geant4 benchmarking system for medical physics applications developed by the Geant4 Medical Simulation Benchmarking Group, *Medical Physics*, 48 (1) (2021) 19-56.
- [6] Amako K, On behalf of the Geant4 Collaboration, *Nuclear Instruments and Methods in Physics Research*, 453 (2000) 455-460.
- [7] Karaca M., Chemoradiotherapy in nasopharyngeal cancer, master thesis, Ankara university, School of Medicine Department of Radiation Oncology, (2008).
- [8] GATE Documentation, OpenGATE Collaboration, Available at: <https://readthedocs.org/projects/gate-demo/downloads/pdf/readthedocs/> Retrieved april 19, 2022.
- [9] Mizoe J., Hasegawa A., Jingu K., Takagi R., Bessyo H., Morikawa T., Tonoki M., Tsuji H., Kamada T., Tsujii H., Okamoto Y., Organizing Committee for the Working Group for Head Neck Cancer, Results of carbon ion radiotherapy for head and neck cancer, *Gynecologic Oncology Reports*, 103 (1) (2012) 32-37.
- [10] Malouff T.D., Mahaian A., Krishnan S., Beltran C., Seneviratne D.S., Trifiletti D.M., Carbon Ion Therapy: A Modern Review of an Emerging Technology, *Frontiers in Oncology*, 10 (82) (2020).
- [11] Ebner D.K., Kamada T., The Emerging Role of Carbon-Ion Radiotherapy, *Frontiers in Oncology*, 6 (140) (2016).

Effects of Deuteron and Alpha Optical Model Potentials on the Production Cross-Section Calculations of Some Radiobromine Isotopes

Mert Şekerci^{1,a,*}, Abdullah Kaplan^{1,b}

¹ Department of Physics, Süleyman Demirel University, Isparta, Türkiye

*Corresponding author

Research Article

History

Received: 26/09/2022

Accepted: 28/11/2022

Copyright




©2022 Faculty of Science,
Sivas Cumhuriyet University

ABSTRACT

The extensive use of radioisotopes in diverse fields, particularly in medical studies for diagnosis and treatment, is one of the outcomes of evolving technology and improved scientific research. Among the various radioisotopes used for medical purposes, an example that can be highlighted considering their properties and utilization possibilities is radiobromine isotopes. It is obvious that both experimental and theoretical studies make significant contributions to the literature on medically relevant radioisotopes. The cross-section, which is the data connected with the occurrence of a reaction, is one of the theoretical metrics that may provide information to researchers. The framework of this study was constructed by taking into account the importance of radiobromine isotopes in medical applications as well as the effects of some parameters that might have an impact on their production cross-section calculations. In this context, the impact of five deuteron and eight alpha optical model potentials, which are available in the 1.95 version of the TALYS code, on the production cross-section calculations of ⁷⁵⁻⁷⁷Br radioisotopes through some (d,x) and (α,x) reactions have been studied. The obtained calculation results were compared visually and numerically with the experimental data available in the literature for each reaction, and the outputs were interpreted.

Keywords: Alpha optical model potential, Cross-section, Deuteron optical model potential, Radiobromine, TALYS

 mertsekerci@sdu.edu.tr

 <https://orcid.org/0000-0003-0870-0506>

 abdullahkaplan@sdu.edu.tr

 <https://orcid.org/0000-0003-2990-0187>

Introduction

The studies that contribute the most to the literature in basic sciences, engineering, medicine and many other fields may seem like experimental studies. However; with a deeper analysis, it can be easily understood that the studies that contribute to the literature are not only experimental studies. It should be considered normal that studies with results that can be integrated into industrial applications in general and people's daily lives in particular attract more attention and that such studies can take place more easily in the literature. The reason for this could be given as the fact that the results of such studies can be used more quickly and are useful in achieving outcomes that can benefit huge groups of people. Nevertheless, the idea that this situation can only be achieved through experimental studies is not entirely correct. Experimental studies are mostly dependent on many parameters such as advanced technological infrastructure, availability of trained people and workforce, large and comfortable financial budgets and effective time management. Furthermore, all of these elements should function in unison. For this reason, it is possible to encounter many problems during the planning and implementation of an experimental study and analyzing the results and converting them into outputs. In such cases, it is extremely important for researchers to obtain information about the studies they plan to carry out. This is valid in all branches of science, albeit to varying degrees. For this reason, theoretical studies are as

important as experimental studies and contribute to the literature. In this context, as in many research areas, theoretical studies carried out according to the content of the planned research are accepted in the literature in studies related to radioisotopes, which are the subject of this study.

Radioisotopes are actively used in a very wide area of modern human life. For example, some of the industrial applications include Carbon-14 used for age determination of carbon-containing structures, Americium-241 used in smoke detectors, Cobalt-60 used in gamma sterilization and industrial radiography, Iridium-192 used in the determination of defects in metal components by gamma radiography, Selenium-75 used in gamma radiography and non-destructive testing and many more [1]. Apart from these radioisotopes, which can be shown as examples in the industrial field, many radioisotopes are used for diagnosis and treatment in many medical applications, considering their characteristics and benefits [2]. In this context, it was necessary to use not only reactors but also accelerators in order to provide supply-demand balance for radioisotopes, which are increasingly used in the medical field. As a result, the production of radioisotopes in accelerators, which are used for diagnostic purposes such as imaging and clinical purposes such as treatment, could be achieved by bombardment of charged particles. From this point of view, it is extremely possible to come across

studies in the literature that experimentally examine the production routes of radioisotopes used in the medical field. On the other hand, there are also theoretical studies investigating the effects of many models and parameters in the calculation of various values such as cross-section, particle emission spectrum, activity and yield in many reactions, including the production routes of various radioisotopes [3-9].

It is a well-known fact that many computable values are extremely important in the theoretical analysis of a reaction. Some values can be measured both experimentally and theoretically. The cross-section, which is defined as a value of the scale of the realization of a reaction, is also a quantity that can be obtained both experimentally and theoretically [10]. Cross-section data is extremely valuable to study the behavior of the reaction in regions outside of the feasible experimental energy range, or the target-incoming particle relationship, to study many special cases. In this context, the improvement of the models on which the calculations are based by comparing the cross-section values obtained with the theoretical calculations with the experimental data, or the investigation of the effects of various parameters on these calculations are seen as very valuable studies. There are many models and parameters that are known to have an impact on cross-section calculations. Level density models, gamma strength functions, deuteron and alpha optical model potentials can be given as examples. Studies examining the use of these models and parameters independently or in combination to produce results that are more compatible with experimental data also contribute to the literature [11-20]. The motivation of this study was created in this conjuncture. In this direction, it is aimed to examine the effects of the deuteron and alpha optical model potentials in the production cross-section calculations of $^{75-77}\text{Br}$ radioisotopes, which are known to be used in the medical field, with some (d,x) and (α ,x) reactions. The results of the calculations for the reactions examined in this study were compared with the experimental data available in the literature and the outcomes were interpreted. While trying to make a visual comparison of the naked eye with the graphics in which the current experimental data and the calculation results are presented together, statistical parameters are used to make quantitative comparisons at the same time.

Materials and Methods

This section will give information regarding the chosen material and the method employed within the context of the primary motivation for this study. This chapter can be divided into two sections in this sense. The first section will attempt to explain why certain radiobromine isotopes are selected. Following that, the models utilized in the calculations, the calculating tools, and how the results are assessed will be discussed.

Some of the many radioisotopes used in medical studies belong to bromine. Bromine, with atomic number

35 and symbolized by Br, is the third lightest halogen. Bromine, which was introduced to the literature in 1825 and 1826 by two independent researchers, occurs in nature as bromide salts or organobromine compounds [21, 22]. Bromine has two stable isotopes, ^{79}Br and ^{81}Br , with abundances of 51 % and 49 %, respectively. Apart from these, it has 32 known radioisotopes, the most stable being ^{77}Br [23]. Among all known radioisotopes, the most preferred ones in medical applications are $^{75-77}\text{Br}$ radioisotopes. The decay modes of ^{75}Br are known as approximately 73 % positron emission (β^+) and approximately 27 % electron capture (EC). ^{75}Br , with a half-life of approximately 96.7 minutes, can form particles with a maximum energy of 2.008 MeV and an average of 0.719 MeV with positron emission. The half-life of ^{76}Br is about 16.2 hours, and its decay modes are positron capture and electron capture at approximately 55 % and 45 %, respectively. In case of decay by positron capture from these possibilities, it can form positrons with an average energy of 1.180 MeV, and the energy of these particles can go up to a maximum of 3.941 MeV. Another radioisotope examined in this study is ^{77}Br , which has a much longer half-life, 57.036 hours, than the other two. On the other hand, ^{77}Br is the radioisotope with the lowest decay rate by positron emission, 0.74 %, and the highest decay rate by electron capture, 99.26 %, among the $^{75-77}\text{Br}$ radioisotopes. The average and highest positron emission values of ^{77}Br are 0.152 MeV and 0.343 MeV, respectively [24]. The use of $^{75-77}\text{Br}$ radioisotopes in medical applications has been accepted in the literature as a result of their characteristic properties and many related parameters. $^{75,76}\text{Br}$ radioisotopes are generally used for Positron Emission Tomography (PET) purposes, as they have a higher rate of positron emission decay and the positrons produced in decay are at moderate energies, while ^{77}Br is mostly used for Auger therapy as an advantage of its high rate of electron capture decay [25].

$^{75-77}\text{Br}$ radioisotopes were planned to be selected within the scope of this study, considering their usability in medical applications and the benefits they provide. The literature has been searched for the experimental studies that cover the production routes of these radioisotopes. As a result, the desire to investigate the implications of theoretical models by performing production cross-section calculations in various reactions where deuterons or alphas were selected as the incident particle was developed. In this context, it is aimed to obtain the production cross-section calculations with deuteron and alpha optical model potentials in accordance with the examined reaction and to interpret the results by comparing them with the experimental data available in the literature. The cross-section value, as explained in the previous section, is a value that can be obtained experimentally and can be calculated with theoretical models under the influence of various parameters. The TALYS [26] code v1.95 was used to investigate the effects of deuteron and alpha optical model potentials on the generation cross-section calculations in accordance with the (d,x) and (α ,x) reactions examined in this study. Since

cross-section calculations require multistage and complex operations, codes such as TALYS have always been needed. In this context, although many codes such as CEM95, ALICE-91, ALICE/ASH, PCROSS and EMPIRE have been developed, it can be understood even with a quick and superficial examination that TALYS is the most preferred code in the literature. The reason for this can be shown as the code's accessibility, ease of use, comprehensive user guide and options that it provides to users, allowing advanced calculation and examination processes compared to other alternatives. In addition, numerous studies examining the effects of various models and parameters on the theoretical acquisition of different values, especially the cross-section, with the mentioned code can be easily seen in the literature, as shown in the citations given earlier in the text. Considering all these, it was decided to use the TALYS code version 1.95 in this study.

The mentioned code accepts the pre-equilibrium reaction mechanism as the default for the incoming particle energies above the last discrete level energy of the target nucleus, among the equilibrium and pre-equilibrium reaction mechanism options in cross-section calculations. In addition, the two-component exciton model is also active in calculations by default and utilized for the calculations that performed within the scope of this study. All details are defined with keywords in the input file of the code. It is possible to activate/deactivate the equilibrium or pre-equilibrium reaction mechanism by the user, or it is possible to select the desired one among four different pre-equilibrium reaction mechanisms. The default model uses the energy dependent matrix element and the exciton model using numerical transition ratios. As a result of the inclusion of different parameters into the input file of the code by the user, it is possible to examine their effects on the calculations. The parameters that constitute the motivation of this study are related to the optical model. The concept of level density model is also refers to another very important factor for similar investigations. In this study, the Constant temperature+Fermi gas model (CTFGM), which was also assigned as the default one within the utilized code, was accepted in all calculations. Turning back to the optical model, the basic assumption underlying the optical model is that the sophisticated interaction between the incoming particle and the nucleus can be represented by a complex mean field potential. This complex mean field potential divides the reaction flow into two parts, which are grouped into the part covering the elastic scattering pattern and all the remaining inelastic channels. The reaction cross-section values calculated with optical models are also very important for semi-classical pre-equilibrium models, and therefore, the examination of optical models is a contribution to the literature [26]. There are different number of deuteron and alpha optical model potential options that can be utilized in the calculations performed via the TALYS v1.95 code. All deuteron and alpha optical model potential options are

shown in Tables 1 and 2, respectively, with their names and abbreviations used in this study.

Table 1. The names and abbreviations of the deuteron optical model potentials

The name of the deuteron optical model potential	Abbreviation used in this study
Normal Deuteron Potential	DOMP1
Deuteron potential of [27]	DOMP2
Deuteron potential of [28]	DOMP3
Deuteron potential of [29]	DOMP4
Deuteron potential of [30]	DOMP5

Table 2. The names and abbreviations of the alpha optical model potentials

The name of the alpha optical model potential	Abbreviation used in this study
Normal Alpha Potential	AOMP1
Alpha potential of [31]	AOMP2
Table 1 of [32]	AOMP3
Table 2 of [32]	AOMP4
Dispersive model of [32]	AOMP5
Avriganu et al. [33]	AOMP6
Nolte et al. [34]	AOMP7
Avriganu et al. [35]	AOMP8

The impacts of the deuteron optical model potentials provided in Table 1 in reactions $^{nat}\text{Se}(d,x)^{75}\text{Br}$, $^{nat}\text{Se}(d,x)^{76}\text{Br}$ and $^{nat}\text{Se}(d,x)^{77}\text{Br}$, as well as the effects of the alpha optical model potentials shown in Table 2 in reactions $^{74}\text{Se}(\alpha,x)^{75}\text{Br}$, $^{74}\text{Se}(\alpha,x)^{76}\text{Br}$, $^{76}\text{Se}(\alpha,x)^{77}\text{Br}$ and $^{77}\text{Se}(\alpha,x)^{77}\text{Br}$, were explored in this work. Calculations were made by using only one deuteron or alpha optical model potential in the calculation at a time, depending on the type of particle involved for each reaction. After the calculations were completed with the appropriate optical models (deuteron or alpha) for each reaction, the results obtained were graphed together with the experimental data so that they could be analyzed visually. In addition, some statistical parameters have been calculated so that quantitative analyzes can be made with numerical values, going beyond just making visual interpretations with the naked eye. The equations that were employed in these computations in where F , D , R and K represents the mean standardized deviation, the mean relative deviation, the mean ratio and the mean square logarithmic deviation, respectively, are listed below [36].

$$F = \left[\frac{1}{N} \sum_{i=1}^N \left[\frac{\sigma_i^{cal} - \sigma_i^{exp}}{\Delta\sigma_i^{exp}} \right]^2 \right]^{1/2}$$

$$D = \left[\frac{1}{N} \sum_{i=1}^N \left| \frac{\sigma_i^{cal} - \sigma_i^{exp}}{\sigma_i^{exp}} \right| \right]$$

$$R = \left[\frac{1}{N} \sum_{i=1}^N \frac{\sigma_i^{cal}}{\sigma_i^{exp}} \right]$$

$$K = 10 \left[\frac{1}{N} \sum_{i=1}^N \left[\log(\sigma_i^{exp}) - (\sigma_i^{cal}) \right]^2 \right]^{1/2}$$

In the equations given for F, D, R and K, σ_i^{exp} and σ_i^{cal} express the experimental and calculated cross-section values,

respectively, while $\Delta\sigma_i^{exp}$ expresses the instability value of each experimental cross-section value, in other words, the amount of error.

Results and Discussion

Within the scope of this study, which was clearly explained in the previous sections, cross-section calculations were completed by triggering the possible deuteron and alpha optical model potentials in the calculations performed by utilizing the TALYS code version 1.95. Obtained calculation results and experimental data are illustrated in Figures 1-7. In addition, the values of the statistical parameters calculated in order to perform a numerical analysis between the experimental data and the calculation results are shown in Tables 3 and 4.

For the reactions of $^{nat}\text{Se}(d,x)^{75}\text{Br}$, $^{nat}\text{Se}(d,x)^{76}\text{Br}$ and $^{nat}\text{Se}(d,x)^{77}\text{Br}$, the experimental data obtained from the study of Tárkányi et al. [37] available in the literature and from EXFOR [38, 39] were used. As can be seen from the results graphed in Figures 1-3, the theoretical calculations for all three reactions were generally able to generate geometric structures similar to those of the experimental data.

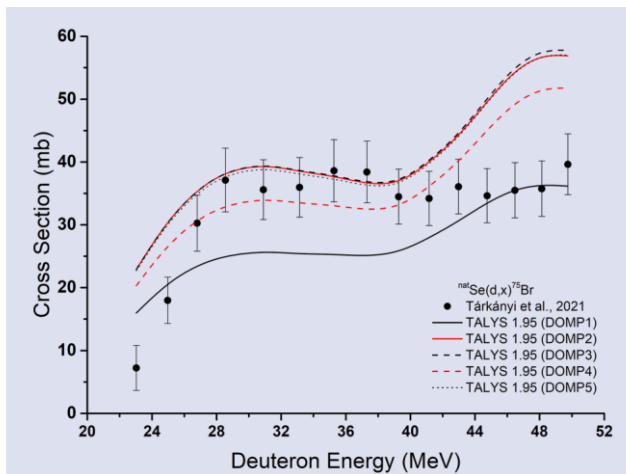


Figure 1. Experimental data along with the calculations results for $^{nat}\text{Se}(d,x)^{75}\text{Br}$ reaction

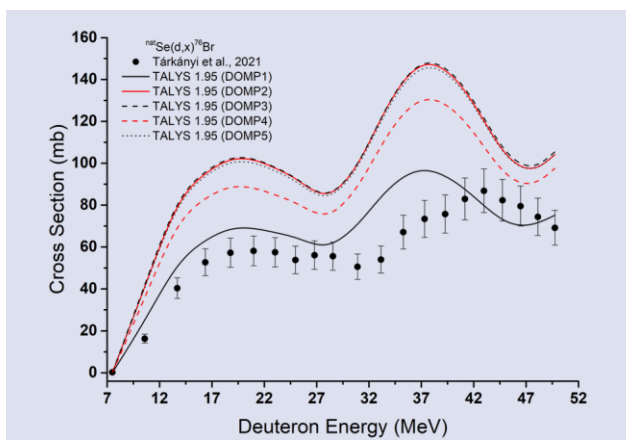


Figure 2. Experimental data along with the calculations results for $^{nat}\text{Se}(d,x)^{76}\text{Br}$ reaction

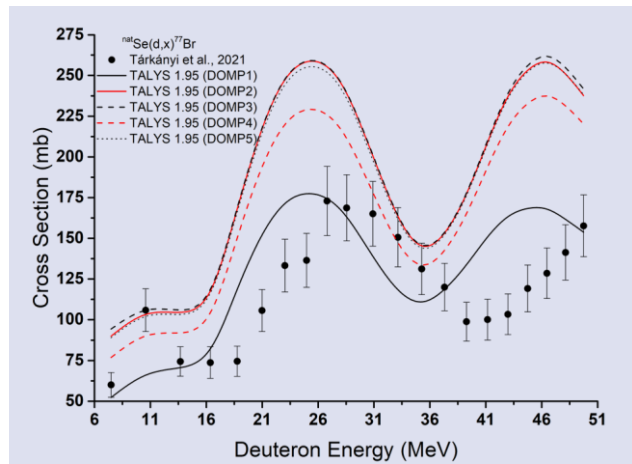


Figure 3. Experimental data along with the calculations results for $^{nat}\text{Se}(d,x)^{77}\text{Br}$ reaction

There have been observations of results that are not expected to be absolutely and exactly the same as experimental data. Furthermore, the calculation results of the models represented by DOMP2, DOMP3, and DOMP5 in all three reactions were produced in such a way that they were exceptionally close and consistent with one another. The values of the statistical parameters shown in Table 3 also help us understand the circumstance.

Using the DOMP2, DOMP3 and DOMP5 models, higher cross-section values were obtained in the $^{nat}\text{Se}(d,x)^{76}\text{Br}$ and $^{nat}\text{Se}(d,x)^{77}\text{Br}$ reactions than almost all of the experimental data, and in the $^{nat}\text{Se}(d,x)^{75}\text{Br}$ reaction than most of the experimental data. When the values of the F , D , R and K parameters are considered together, the deuteron optical model, which provides the most compatible results with the experimental data for the $^{nat}\text{Se}(d,x)^{75}\text{Br}$ and $^{nat}\text{Se}(d,x)^{77}\text{Br}$ reactions, is referred as DOMP1. For the $^{nat}\text{Se}(d,x)^{76}\text{Br}$ reaction, the F , D and R values highlight DOMP1, while the K value suggests that DOMP4 is the model that produces the most consistent results with the experimental data. Components used in the calculation of statistical parameters and sequence of operations can be cited as the reason for this difference. In addition, the logarithmic operation in the K value can be shown as an important factor for this difference.

Levkovski [40]'s experimental data were used in the $^{74}\text{Se}(\alpha,x)^{75}\text{Br}$, $^{74}\text{Se}(\alpha,x)^{76}\text{Br}$, $^{76}\text{Se}(\alpha,x)^{77}\text{Br}$ and $^{77}\text{Se}(\alpha,x)^{77}\text{Br}$ reactions in which the effects of alpha optical model parameters were investigated. Obtained calculation results and experimental data are shown together in Figures 4-7.

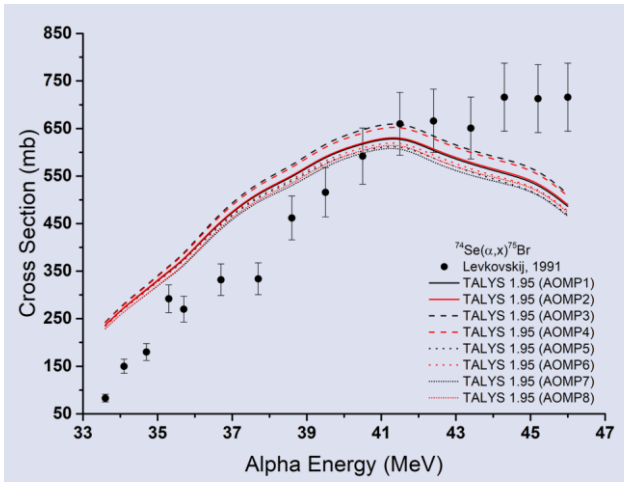


Figure 4. Experimental data along with the calculations results for $^{74}\text{Se}(\alpha,x)^{75}\text{Br}$ reaction

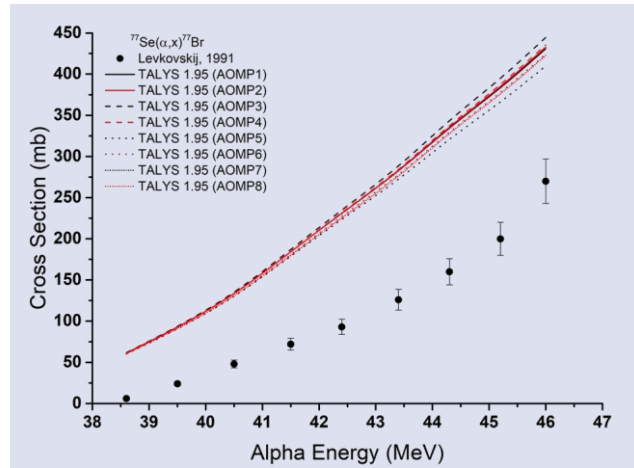


Figure 7. Experimental data along with the calculations results for $^{77}\text{Se}(\alpha,x)^{77}\text{Br}$ reaction

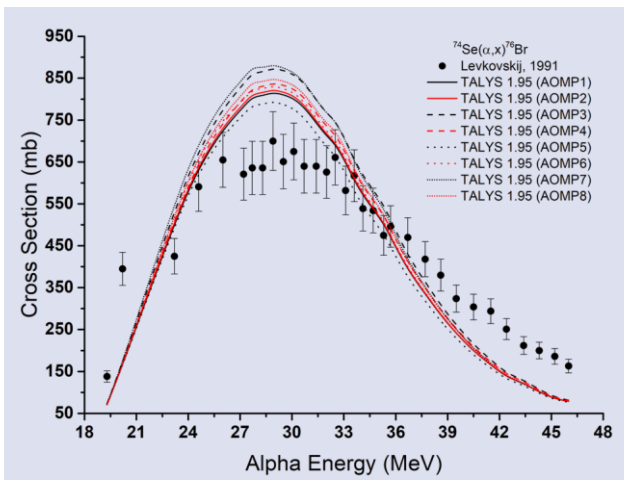


Figure 5. Experimental data along with the calculations results for $^{74}\text{Se}(\alpha,x)^{76}\text{Br}$ reaction

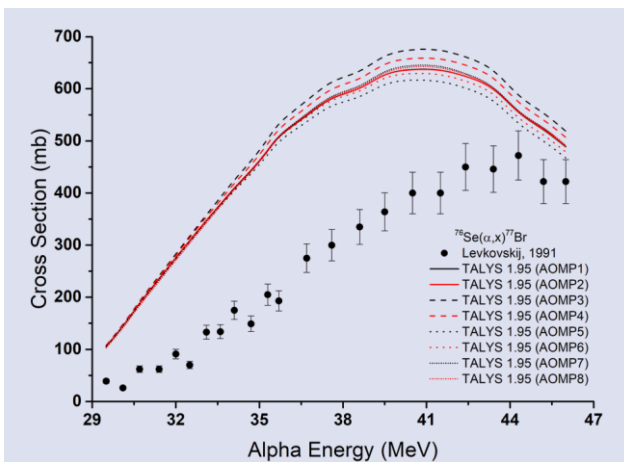


Figure 6. Experimental data along with the calculations results for $^{76}\text{Se}(\alpha,x)^{77}\text{Br}$ reaction

The values of the statistical parameters for the alpha optical model potentials were determined in the same way as they were for the deuteron optical model potentials, and the results are shown in Table 4.

Table 3. The values of the statistical parameters calculated for deuteron optical model potentials

Reaction	Statistical parameters	DOMP1	DOMP2	DOMP3	DOMP4	DOMP5
$\text{natSe}(d,x)^{75}\text{Br}$	F	1.767	2.662	2.729	1.992	2.632
	D	0.260	0.386	0.392	0.300	0.378
	R	0.924	1.376	1.383	1.224	1.366
	K	1.389	1.491	1.496	1.401	1.485
$\text{natSe}(d,x)^{76}\text{Br}$	F	2.342	6.614	6.728	5.044	6.463
	D	0.256	0.758	0.772	0.573	0.742
	R	1.127	1.664	1.678	1.479	1.648
	K	2.965	2.924	2.902	2.877	2.918
$\text{natSe}(d,x)^{77}\text{Br}$	F	2.561	6.268	6.376	5.064	6.168
	D	0.248	0.650	0.664	0.506	0.636
	R	1.136	1.650	1.664	1.490	1.636
	K	1.312	1.705	1.718	1.567	1.693

Table 4. The values of the statistical parameters calculated for alpha optical model potentials

Reaction	Statistical parameters	AOMP1	AOMP2	AOMP3	AOMP4	AOMP5	AOMP6	AOMP7	AOMP8
$^{74}\text{Se}(\alpha,x)^{75}\text{Br}$	F	5.872	5.908	6.203	6.140	5.829	5.797	5.573	5.568
	D	0.394	0.396	0.414	0.409	0.394	0.391	0.376	0.375
	R	1.263	1.269	1.315	1.305	1.244	1.250	1.221	1.229
	K	1.490	1.492	1.509	1.505	1.493	1.488	1.476	1.473
$^{74}\text{Se}(\alpha,x)^{76}\text{Br}$	F	2.952	2.961	3.079	2.953	2.991	3.013	3.227	3.062
	D	0.244	0.247	0.273	0.251	0.240	0.254	0.287	0.264
	R	0.917	0.923	0.984	0.946	0.885	0.931	0.977	0.951
	K	1.466	1.463	1.449	1.450	1.487	1.469	1.480	1.470
$^{76}\text{Se}(\alpha,x)^{77}\text{Br}$	F	17.647	17.668	18.408	18.127	17.460	17.398	17.510	17.224
	D	1.402	1.404	1.493	1.457	1.367	1.378	1.398	1.379
	R	2.402	2.404	2.493	2.457	2.367	2.378	2.398	2.379
	K	2.437	2.439	2.517	2.485	2.410	2.417	2.433	2.414
$^{77}\text{Se}(\alpha,x)^{77}\text{Br}$	F	34.083	33.991	34.463	34.074	33.145	33.350	33.315	33.198
	D	2.296	2.294	2.343	2.3041	2.202	2.239	2.230	2.236
	R	3.296	3.294	3.343	3.304	3.202	3.239	3.230	3.236
	K	3.136	3.136	3.179	3.144	3.054	3.089	3.080	3.087

It can be seen from Figure 4 that the results obtained using alpha optical model potentials in the $^{74}\text{Se}(\alpha,x)^{75}\text{Br}$ reaction and the experimental data are relatively similar. The alpha optical model potential, which produces the computational results most compatible with the experimental data for this reaction, is pointed as AOMP8 by the *F*, *D*, and *K* values, while the *R* value suggests AOMP7. We are now in the part where we will examine the results related to the $^{74}\text{Se}(\alpha,x)^{76}\text{Br}$ reaction. In this reaction, where the calculation results and the experimental data are shown in Figure 5, it can be seen that the calculation results differ from each other at the top of the hump structure to such an extent that they can be noticed even with the naked eye, but they produce results that are very close to each other in other regions. Higher values of cross-section were obtained than experimental data in the energy range of roughly 24-36 MeV, and this condition changed when the calculation

results dropped below the experimental values after approximately 36 MeV. In the $^{74}\text{Se}(\alpha,x)^{76}\text{Br}$ reaction, *D* and *R* values highlight AOMP5, *F* value indicates AOMP1, and *K* value indicates AOMP3. This disparity may have happened because the cross-section value at each energy point has a distinct level of experimental error, while the statistical parameters look at the full energy range.

Table 5. The arithmetic averages of the statistical parameters of the deuteron optical model potentials

Statistical parameters	DOMP1	DOMP2	DOMP3	DOMP4	DOMP5
F	2.223	5.182	5.277	4.033	5.088
D	0.255	0.598	0.609	0.460	0.585
R	1.062	1.564	1.575	1.397	1.550
K	1.889	2.040	2.039	1.948	2.032

Table 6. The arithmetic averages of the statistical parameters of the alpha optical model potentials

Statistical parameters	AOMP1	AOMP2	AOMP3	AOMP4	AOMP5	AOMP6	AOMP7	AOMP8
F	15.138	15.132	15.538	15.324	14.856	14.890	14.906	14.763
D	1.084	1.085	1.131	1.105	1.051	1.066	1.073	1.063
R	1.969	1.972	2.034	2.003	1.925	1.950	1.957	1.949
K	2.132	2.132	2.163	2.146	2.111	2.116	2.117	2.111

Another radiobromine isotope examined in the study is ^{77}Br , and two reactions were investigated for the production of this radioisotope with alpha-input particles, $^{76}\text{Se}(\alpha,x)^{77}\text{Br}$ and $^{77}\text{Se}(\alpha,x)^{77}\text{Br}$. In both of these reactions, the experimental data of Levkovski [40] and the calculation results were visualized together and the graphs obtained are shown in Figures 6 and 7. As can be clearly seen from these figures, triggering of alpha optical model potentials in both reactions caused higher cross-section values to be calculated than the experimental data at all energy values. As the energy value increased along the x-axis, the distance between the cross-section results obtained via the alpha optical model potentials are widened. In the $^{76}\text{Se}(\alpha,x)^{77}\text{Br}$ reaction, the *F* value suggests that if AOMP8 is used, more consistent results can be obtained with the experimental data, while the *D*,

R and *K* values show that such situation can be achieved by using AOMP5. On the other hand, all statistical parameters for the $^{77}\text{Se}(\alpha,x)^{77}\text{Br}$ reaction point to the same alpha optical model potential, AOMP5.

Conclusion

It is a well-known fact that the cross-section value is valuable in terms of the contributions it provides to researchers in cases where experimental studies cannot be performed. From this point of view, the selection of models and appropriate parameters that can produce results that are more compatible with the experimental data is extremely critical. The results of this study, which was designed by considering the importance of radiobromine isotopes, that have a wide range of use in

motivation and health applications, can be summarized as follows.

- It has been demonstrated that activating the deuteron and alpha optical model potentials in cross-section calculations alters the calculation results.

- The cross-section values produced in this work employing deuteron and alpha optical model potentials contributed to the literature.

- Specific to the reactions studied, multiple statistical parameters were used to determine the option that produced more consistent results with the experimental data among all deuteron and alpha optical model potentials included in the calculations. As a result, it was seen that all statistical parameters in $^{nat}\text{Se}(d,x)^{75}\text{Br}$, $^{nat}\text{Se}(d,x)^{77}\text{Br}$ and $^{77}\text{Se}(\alpha,x)^{77}\text{Br}$ reactions point to the same optical model potential. The value of one statistical parameter in each of these three reactions, K in reaction $^{nat}\text{Se}(d,x)^{76}\text{Br}$, R in reaction $^{74}\text{Se}(\alpha,x)^{75}\text{Br}$, and F in reaction $^{76}\text{Se}(\alpha,x)^{77}\text{Br}$, highlighted a different optical model potential from the others. While D and R values imply the same optical model potential in reaction $^{74}\text{Se}(\alpha,x)^{76}\text{Br}$, triggering various optical model potentials in the computations yields findings that are more congruent with the experimental data with respect to F and K values.

- The arithmetic averages of the statistical parameters of the deuteron optical model potentials are provided in Table 5. According to these values, in the reactions where the effects of the deuteron optical model potentials were examined, all statistical parameters (F , D , R and K) showed DOMP1 as the option that provided more consistent results with the experimental data compared to the other options.

- A situation similar to that in Table 5 is presented in Table 6 for alpha optical model potentials. When the results here are examined, the model that produces more compatible results compared to the experimental data and other alpha optical model potentials is AOMP8 according to the F and K parameters, while it is AOMP5 according to the D and R parameters.

When the findings obtained with this study are evaluated as a whole, it is understood once again that the effects of different parameters on the cross-section calculations cannot be ignored. In this context, it is a foregone conclusion that the use of advanced theoretical models in many evaluations, such as production cross-section calculations of radioisotopes, which are used in many aspects of our lives, particularly in industry and health, and provide numerous benefits, will provide significant contributions to researchers in cases where experimental studies are not doable. This and related studies are supposed to be carried out in order to improve/develop the model and parameters, to utilize them independently/together, to be chosen in line with the examined reaction, and to add to the literature by attempting numerous reactions.

Conflicts of interest

There are no conflicts of interest in this work.

References

- [1] World Nuclear Association. Radioisotopes in Industry. Available at: <https://www.world-nuclear.org/information-library/non-power-nuclear-applications/radioisotopes-research/radioisotopes-in-industry.aspx>. Retrieved March 26, 2022.
- [2] Das T., Pillai M.R.A., Options to Meet the Future Global Demand of Radionuclides for Radionuclide Therapy, *Nucl. Med. Biol.*, 40 (1) (2013) 23-32.
- [3] Akkoyun S., Kaya H., Estimations of Cross-Sections for Photonuclear Reaction on Calcium Isotopes by Artificial Neural Network, *Sakarya University Journal of Science*, 24 (5) (2020) 1115-1120.
- [4] Özdoğan H., Şekerci M., Kaplan A., An Investigation on the Effects of Some Theoretical Models in the Cross-Section Calculations of $^{50,52,53,54}\text{Cr}(\alpha,x)$ Reactions, *Phys. At. Nucl.*, 83 (6) (2020) 820-827.
- [5] Şekerci M., Özdoğan H., Kaplan A., An Investigation of Effects of Level Density Models and Gamma Ray Strength Functions on Cross-Section Calculations for the Production of ^{90}Y , ^{153}Sm , ^{169}Er , ^{177}Lu and ^{186}Re Therapeutic Radioisotopes via (n,g) Reactions, *Radiochim. Acta*, 108 (1) (2020) 11-17.
- [6] Şekerci M., Theoretical Cross-Section Calculations for the (α,n) and ($\alpha,2n$) Reactions on ^{46}Ti , ^{50}Cr , ^{54}Fe , and ^{93}Nb Isotopes, *Mosc. Univ. Phys. Bull.*, 75 (2) (2020) 123-132.
- [7] Akkoyun S., Bayram T., Production Cross-Section of ^{51}Cr Radioisotope Using Artificial Neural Networks, *Turkish Journal of Science and Health*, 2 (1) (2021) 133-138.
- [8] Özdoğan H., Üncü Y.A., Karaman O., Şekerci M., Kaplan A., Estimations of Giant Dipole Resonance Parameters Using Artificial Neural Network, *Appl. Radiat. Isot.*, 169, (2021) 109581.
- [9] Yiğit M., Study of Cross Sections for (n,p) Reactions on Hf, Ta and W Isotopes, *Appl. Radiat. Isot.*, 174, (2021) 109779.
- [10] Stöcklin G., Qaim S.M., Rösch F., The Impact of Radioactivity on Medicine Metallic, *Radiochim. Acta*, 70/71 (1995) 249-272.
- [11] Kaplan A, Sarpün İ.H., Aydın A., Tel E., Çapalı V., Özdoğan H., ($\gamma,2n$) Reaction Cross-Section Calculations of Several Even-Even Lanthanide Nuclei Using Different Level Density Models, *Phys. At. Nucl.*, 78 (2015) 53-64.
- [12] Özdoğan H., Şekerci M., Kaplan A., Investigation of Gamma Strength Functions and Level Density Models Effects on Photon Induced Reaction Cross-Section Calculations for the Fusion Structural Materials $^{46,50}\text{Ti}$, ^{51}V , ^{58}Ni and ^{63}Cu . *Appl. Radiat. Isot.*, 143 (2019) 6-10.
- [13] Şekerci M., An Investigation of the Effects of Level Density Models and Alpha Optical Model Potentials on the Cross-Section Calculations for the Production of the Radionuclides ^{62}Cu , ^{67}Ga , ^{86}Y and ^{89}Zr via Some Alpha Induced Reactions, *Radiochim. Acta*, 108 (6) (2019) 459-467.
- [14] Şekerci M., Özdoğan H., Kaplan A., Investigation on the Different Production Routes of ^{67}Ga Radioisotope by Using Different Level Density Models, *Mosc. Univ. Phys. Bull.*, 74 (2019) 277-281.
- [15] Özdoğan H., Üncü Y.A., Şekerci M., Kaplan A., Estimations of Level Density Parameters by Using Artificial Neural Network for Phenomenological Level Density Models, *Appl. Radiat. Isot.*, 169 (2021) 109583.

- [16] Gülümser T., Kaplan A., A Theoretical Study on the Production Cross-Section Calculations for ^{24}Na Medical Isotope, *Erzincan Üniversitesi Fen Bilimleri Enstitüsü Dergisi*, 14 (2) (2021) 802-813.
- [17] Sarpün İ.H., Özdoğan H., Taşdöven K., Yalim H.A., Kaplan A., Theoretical Photoneutron Cross-Section Calculations on Osmium Isotopes by Talys And Empire Codes, *Mod. Phys. Lett. A.*, 34 (26) (2019) 1950210.
- [18] Şekerci M., Özdoğan H., Kaplan A., Level Density Model Effects on the Production Cross-Section Calculations of Some Medical Isotopes via (α, xn) Reactions where $x=1-3$, *Mod. Phys. Lett. A.*, 35 (24) (2020) 2050202.
- [19] Özdoğan H., Şekerci M., Kaplan A., Photo-Neutron Cross-Section Calculations of $^{54,56}\text{Fe}$, $^{90,91,92,94}\text{Zr}$, ^{93}Nb and ^{107}Ag Isotopes with Newly Obtained Giant Dipole Resonance Parameters, *Appl. Radiat. Isot.*, 165 (2020) 109356.
- [20] Özdoğan H., Estimation of (n,p) Reaction Cross Sections at 14.5 ± 0.5 MeV Neutron Energy by Using Artificial Neural Network, *Appl. Radiat. Isot.*, 170 (2021) 109584.
- [21] Weeks M.E., The discovery of the elements. XVII. The halogen family, *J. Chem. Educ.*, 9 (11) (1932) 1915.
- [22] Greenwood N.N., Earnshaw A., Chemistry of the Elements. 2nd ed. United Kingdom: Oxford, (1997) 1-1364.
- [23] Lide, D.R. (ed)., CRC Handbook of Chemistry and Physics. 85th ed. Florida, (2004) 1-2712.
- [24] Rowland D.J., McCarthy T.J., Welch M.J., Radiobromine for Imaging and Therapy. In: Welch M.J., Redvanly C.S., (Eds). Handbook of Radiopharmaceuticals: Radiochemistry and Applications. John Wiley & Sons (2002) 441-465.
- [25] Wilbur D.S., Adam M.J., Radiobromine and Radioiodine for Medical Applications, *Radiochim. Acta*, 107 (9-11) (2019) 1033-1063.
- [26] Koning A., Hilaire S., Goriely S., TALYS-1.95 A Nuclear Reaction Program, User Manual. 1st ed. NRG, The Netherlands (2019).
- [27] Daehnick W.W., Childs J.D., Vrcelj Z., Global Optical Model Potential for Elastic Deuteron Scattering from 12 to 90 MeV, *Phys. Rev. C.*, 21 (1980) 2253-2274.
- [28] Bojowald J., Machner H., Nann H., Oelert W., Rogge M., Turek P., Elastic Deuteron Scattering and Optical Model Parameters at Energies up to 100 MeV, *Phys. Rev. C.*, 38 (1988) 1153-1163.
- [29] Han Y., Shi Y., Shen Q., Deuteron Global Optical Model Potential for Energies up to 200 MeV, *Phys. Rev. C.*, 74 (2006) 044615.
- [30] An H., Cai C., Global Deuteron Optical Model Potential for the Energy Range up to 183 MeV, *Phys. Rev. C.*, 73 (2006) 054605.
- [31] McFadden L., Satchler G.R., Optical-Model Analysis of the Scattering of 24.7 MeV Alpha Particles, *Nucl. Phys.*, 84 (1966) 177-200.
- [32] Demetriou P., Grama C., Goriely S., Improved Global α -optical Model Potentials at Low Energies, *Nucl. Phys. A.*, 707 (2002) 253-276.
- [33] Avrigeanu V., Avrigeanu M., Măniulescu C., Further Explorations of the α -particle Optical Model Potential at Low Energies for the Mass Range $A=45-209$, *Phys. Rev. C.*, 90 (2014) 044612.
- [34] Nolte M., Machner H., Bojowald J., Global Optical Potential for α particles with Energies Above 80 MeV, *Phys. Rev. C.*, 36 (1987) 1312.
- [35] Avrigeanu V., Hodgson P.E., Avrigeanu M., Global Optical Potentials for Emitted Alpha Particles, *Phys. Rev. C.*, 49 (1994) 2136.
- [36] Alabyad M., Mohamed G.Y., Hassan H.E., Takács S., Ditrói F., Experimental Measurements and Theoretical Calculations for Proton, Deuteron and α -Particle Induced Nuclear Reactions on Calcium: Special Relevance to the Production of $^{43,44}\text{Sc}$, *J. Radioanal. Nucl. Chem.*, 316 (1) (2018) 119-128.
- [37] Tárkányi F., Takács S., Ditrói F., Szűcs Z., Brezovcsik K., Hermanne A., Ignatyuk A.V., Investigation of Cross Sections of Deuteron Induced Nuclear Reactions on Selenium up to 50 MeV, *Eur. Phys. J. A*, 57 (4) (2021) 117.
- [38] Otuka N., Dupont E., Semkova V., Pritychenko B., Blokhin A.I., Aikawa M., Babykina S., Bossant M., Chen G., Dunaeva S., Forrest R.A., Fukahori T., Furutachi N., Ganesan S., Ge Z., Gritsai O.O., Herman M., Hlavač S., Katō K., Lalremruata B., Lee Y.O., Makinaga A., Matsumoto K., Mikhaylyukova M., Pikulina G., Pronyaev V.G., Saxena A., Schwerer O., Simakov S.P., Soppera N., Suzuki R., Takács S., Tao X., Taova S., Tárkányi F., Varlamov V.V., Wang J., Yang S.C., Zerkin V., Zhuang Y., Towards a More Complete and Accurate Experimental Nuclear Reaction Data Library (EXFOR): International Collaboration Between Nuclear Reaction Data Centres (NRDC), *Nucl. Data Sheets*, 120 (2014) 272-276.
- [39] Zerkin V.V., Pritychenko B., The experimental nuclear reaction data (EXFOR): Extended Computer Database and Web Retrieval System, *Nucl. Instrum. Methods. Phys. Res. A*, 888 (2018) 31-43.
- [40] Levkovski V.N., Cross-Section of Medium Mass Nuclide Activation ($A=40-100$) by Medium Energy Protons and Alpha Particles ($E=10-50$ MeV), Inter-Vesi, Moscow, USSR (1991).

Searching for New Supernova Remnant Candidates from the VTSS Survey

Elif Beklen^{1,a,*}¹ Department of Physics, Faculty of Arts and Sciences, Süleyman Demirel University, Isparta, Türkiye

*Corresponding author

Research Article

History

Received: 13/10/2022

Accepted: 07/12/2022

Copyright

©2022 Faculty of Science,
Sivas Cumhuriyet Universityelifbeklen@gmail.com<https://orcid.org/0000-0002-4807-2180>

ABSTRACT

The Virginia Tech Spectral Line Survey (VTSS) Galactic Plane Hydrogen-Alpha Survey has the strong ability to search and discover many different types of objects that cannot be identified clearly on red plates and by other Multi-Wavelength Sky Surveys. Here we make a visual search from the VTSS fields with the supportive surveys of Southern Hydrogen-Alpha Sky Survey Atlas (SHASSA) and MDW Hydrogen-Alpha Sky Survey (MDWS) fields, in the Galactic latitude of $|b|$ between -17° and 7° for several new optical emission nebulae. Seven candidates were chosen as most likely supernova remnant candidates by their physical shapes and the three of all having $[SII]/H\alpha$ ratio larger than 0.4, found with T100 photometric observations, are considered to be supernova remnant candidates. Comprehensive optical imaging and spectroscopic observations with multi-wavelength observations will help us to identify the types of all these galactic candidates, more precisely.

Keywords: Surveys, ISM: supernova remnants, Optical

Introduction

Supernova remnants (SNRs) are important objects to understand the evolution of the interstellar medium (ISM) and galaxies. To better understand our galaxy, all of the studies including detecting individual SNRs with an accurate number of Galactic total SNRs become important. There is an apparent divergence between the number of observed and expected Galactic SNRs based on supernovae rates. Currently, there are nearly 300 Galactic SNRs with the most majority discovered through radio observations and some of in X-ray observations [1-4].

Even though less than half of Galactic SNRs show any appreciable optical emission, optical studies of SNRs are useful and become important for dynamical properties in all remnants, and for the kinematics of ejecta in the youngest remnants. For some remnants, a remnant's optical emission can also help to define its overall size and morphology. This is especially true for some radio weak emission or radio-quiet SNRs exhibiting significant optical emission [5-11]. About 40% of the detected Galactic SNRs show associated X-ray emission with a smaller percentage (~30%) showing some coincident optical emission [12]. Although discoveries of Galactic remnants in the optical are less according to others, several [13-15] have recently been made through deep $H\alpha$ surveys such as the $H\alpha$ emission Virginia Tech Spectral Line Survey (VTSS) of the Galactic Plane [16, 17] (e.g. the optical discovery of G159.6+7.3 [14]), the Southern Hydrogen-Alpha Sky Survey Atlas (SHASSA) [18], MDW Hydrogen-Alpha Survey (MDWS) and the Isaac Newton Telescope Photometric Hydrogen Survey [19, 20].

The imaging filters flux ratio of $[SII(6717, 6731)]/H(6563) \geq 0.4$ (firstly proposed by Mathewson and Clarke 1973 [21]) has been using as a well-known and

successful observational criterion to differentiate SNRs from other type of optical emission nebulae in both Galactic and extragalactic searches [11, 22-26]. Mainly, the general idea is expecting SNRs to give higher values of $[SII]$ than HII regions since behind the shock front the collisionally excited gives strong $[SII]$ emission, while in HII regions sulphur is mostly in the form of S^{++} .

The goal of this work is to discover new supernova remnant candidates through $H\alpha$ survey by visual selection of the size or shapes similar to the detected supernova remnants appearance observed through the same survey. The emission fields can also include HII-regions, all of which can be the same in appearance. So, we report a search for large and mid-size possible Galactic SNR candidates through its $H\alpha$ optical emission by using archival VTSS Survey images with the help of SHASSA and MDWS Surveys, and the latest SNR and HII-region catalogs.

Surveys

The VTSS (<http://www1.phys.vt.edu/~halphat/#Images>) covers a wide region around the northern Galactic plane ($15^\circ < l < 230^\circ$, $|b| \leq 30^\circ$), north of $\delta > -15^\circ$, and gain importance in the study of Galactic supernova remnants, HII regions, and many different $H\alpha$ emission sources. 107 fields have been released on the VTSS Web site. The VTSS survey used a fast short-focus lens of f/1.2 camera lens with a 58-mm focal length, together with a 512 x 512 CCD array that projected to 96 arcsec/pixel on the sky. Its $H\alpha$ filter had a FWHM of 17.5 \AA , transmitting mainly the $H\alpha$ line.

Other H α imaging surveys, SHASSA and MDWS are used to search the emission structures that the zone covered by the VTSS survey images. SHASSA is an imaging survey covering 21000deg² of the southern and equatorial sky undertaken with the aim of detecting H α emission from the ionized interstellar medium. The survey consists of 2168 images covering 542 fields south of +16° declination, between Galactic longitudes of 195° and 45° at the mid-plane (GMR01). The SHASSA survey used a fast short-focus lens of f/1.6 camera lens with a focal length of 52 mm, together with 1024 x 1024 CCD array that projected to 48 arcsec/pixel on the sky. Its H α filter had a FWHM of 32 Å ([27], [28]). For both VTSS and SHASSA fields, the continuum-subtracted (generated by subtracting each continuum image from the corresponding H α image) and then smoothed images (for SHASSA survey; saved as SHASSA_CC) are used. Even though to have lower angular resolution both surveys are very deep and are a useful tools to search for any extended large high-latitude nebulae emission. These surveys become a key tool for searching possible SNRs that may have been missed in previous searches.

Another survey used during this search is the MDWS (<https://www.mdwskysurvey.org>) with its wide field-of-view (FoV) of approximately 3°.5 x 3°.5 with a pixel size of 3".17 and relatively low-resolution images, it reveals deeper, more complex and quite extensive optical filaments and structures visible in higher resolution images. This survey consists of a 130 mm telescope at the New Mexico Skies Observatory, with an FLI ProLine 16803 CCD and a 3 nm filter centered on H α [11]. There are 2771 fields under the MDWS website and the exposure times used for the observation of each field was 12x1200 s.

Observations and Data Analysis

The optical imaging observations for some of these emission fields were performed with the

1-meter Turkish Telescope T100, located in TÜBITAK National Observatory of Turkey's (TUG) (<https://tug.tubitak.gov.tr/tr/teleskoplar/t100-odak-duzlemi-aletleri>). We get high-quality photometry by using a cryo-cooler SI 1100 CCD with 4096 x 4096 pixels, with an effective field of view (FoV) of 21'.5 x 21'.5. We used narrow passband interference filters (FWHM = 80 Å) ($\lambda = 6563 \text{ Å}$) H α , (FWHM = 54 Å) ($\lambda = 6728 \text{ Å}$) [SII] and Bessel R filter as continuum filter to remove starlight background from the narrow passband filters images of these regions. The exposure times were 900 s for each narrow band filter with 2 x 200 s for the continuum band filter.

T100 images were reduced by using the reduction photometry pipelines in astropy. Both the bias and flat-field frames for each image were also obtained and during the reduction, the cosmic hits were also removed by using a median-averaged process during the bias-subtraction and flat-fielding of the images. During the observations, we use the Digitized Sky Survey (DSS1 or DSS2) (The STScI Digitized Sky Survey; https://archive.stsci.edu/cgi-bin/dss_form) images as the confirmation of the selected positions of the approximate central coordinates of each candidate.

Methods, Results and Discussion

We will discuss our work done by a visual search conducted of all VTSS fields plus the surveys of SHASSA and MDWS fields that are currently available online. All of the surveys contain wide-field and small-scale H α emission structures, and among these structures, a significant number of supernova remnants will be discovered. These Galactic H α Surveys have high promise to increase our knowledge of optical supernova remnants and their physical properties. In this work, the VTSS Survey images were primarily scanned and visual search was done individually on each field. The selection criteria on the appropriate field images were choosing the field either consisting of previously detected supernova remnants and HII-regions or fully undetected emission structures.

The Orion 08 first and second regions, respectively Ori08(A) and Ori08(B) (see the left and right side of the first row in Figure 1, and for the coordinates see Table 1), are the two selected emission candidates under the Ori08 field in the VTSS Survey. These regions are also observed with the continuum-subtracted SHASSA survey and both survey images are confirming each other. These regions are scanned with their close environments by using the WISE Catalog of Galactic HII-Regions (<http://astro.phys.wvu.edu/wise/>) (version 2.4, [29]) and it was seen that the wide-field Orion region does not include any detected HII regions. Also, the wide-field Orion region was also scanned according to the Green 2019 catalog to explore any detected and known supernova remnants. As a result, there are no identified SNRs in this region. Another SNR and HII-free region located in the Monoceros-Mon07 field in the archive VTSS survey is named Mon07(A) (the image on the right side of the second row in Figure 1). The emission is in partial shape, maybe a part of the composite structure detectable explicitly in another band. This structure can also be observed with the SHASSA survey, and both VTSS and SHASSA images are matching well with each other.

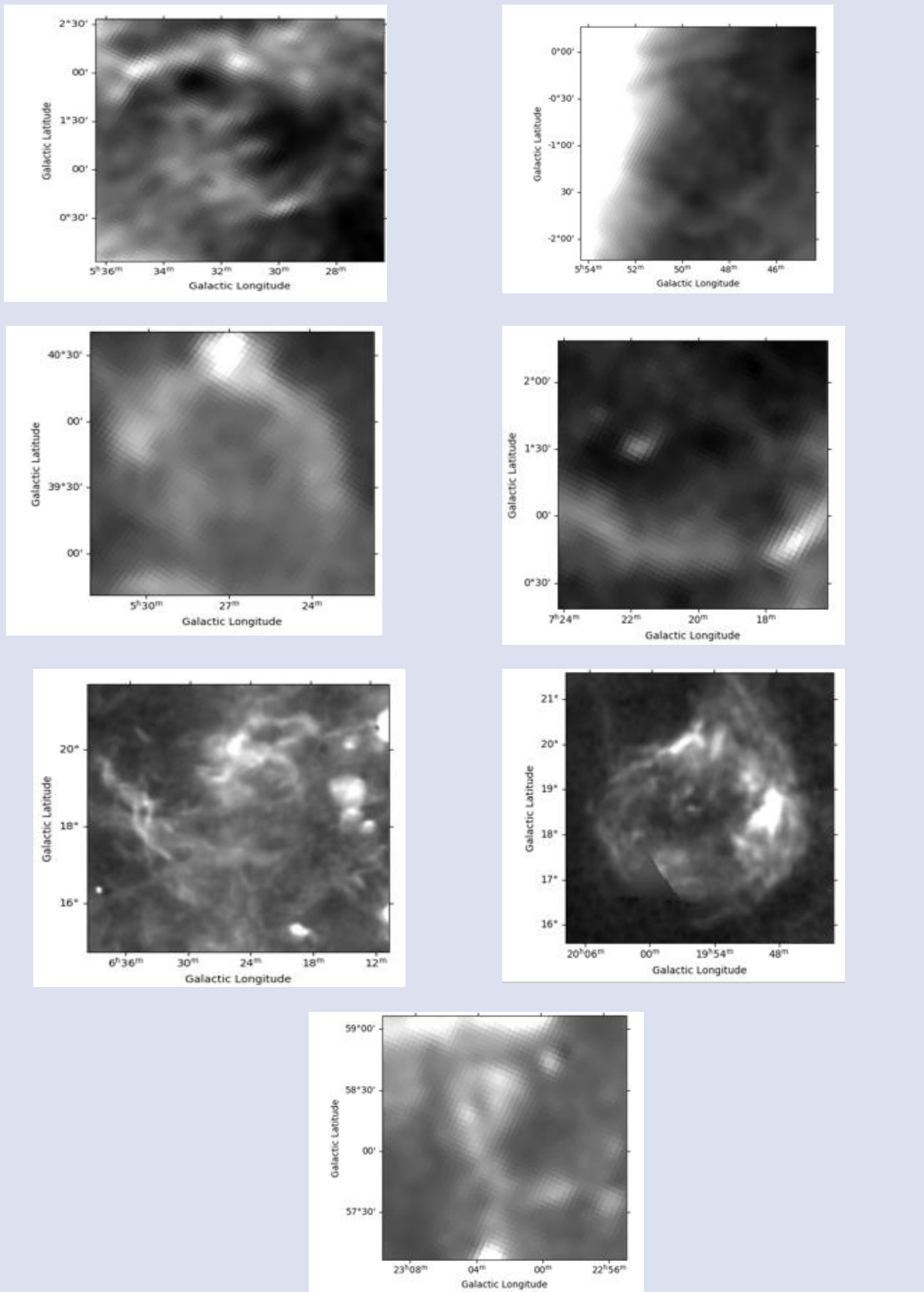


Figure 1. H α image of optical emission nebulae from the VTSS Survey of the Galactic Plane. North is up, east to the left with (J2000.0) coordinates and the occupied area of the regions are shown in Table 1.

Table 1. Central coordinates of the selected emission nebulae fields with their surrounding areas. The last column shows the used surveys for confirming the same structural regions. In each survey, the structures can be visually identified with the same dimensions, clearly

Region Name	R.A. (J2000.0)	Dec. (J2000.0)	Candidate Dimension (Degree °)	Used Surveys
Ori08(A)	05:31:37	+01:24:56	2.5	VTSS, SHASSA, MDWS
Ori08(B)	05:48:58	-01:03:06	2.5	VTSS, SHASSA, MDWS
Aur05(A)	05:26:57	+39:38:02	1.0	VTSS, MDWS
Mon07(B)	06:27:19	+18:29:10	2.5	MDWS
Mon07(A)	07:20:10	+01:18:30	1.0	VTSS, SHASSA
Sge01(A)	19:55:23	+18:37:09	2.5	VTSS
Cep00(A)	23:02:19	+58:07:32	0.8	VTSS

The other four candidates are all located in crowded regions in a sense of previously detected SNRs and HII-regions with well-known locations and sizes. The Mon07(B) (the left image on the third row in Figure 1 with a radius of approximately 2.5°) is visually first noticed in the MDW survey since it is not clearly visible in the

wide-field Mon07 VTSS survey image. There are no detected SNRs in the wide-field region with a size of approximately 7° whereas some labeled HII-regions are taken from WISE-HII region catalog (red circles in the right side of the first row in Figure 2; the candidate is shown with clay circle).

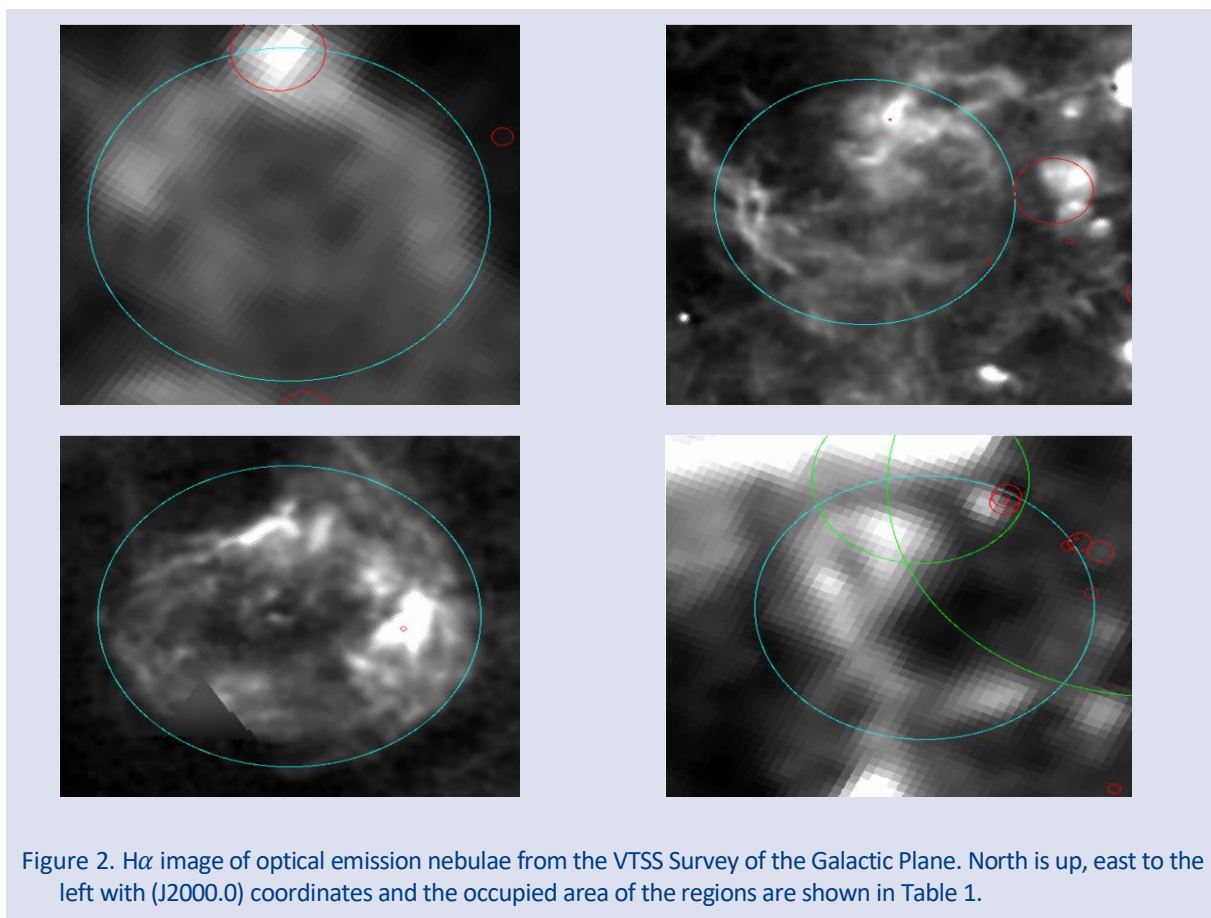


Figure 2. $H\alpha$ image of optical emission nebulae from the VTSS Survey of the Galactic Plane. North is up, east to the left with (J2000.0) coordinates and the occupied area of the regions are shown in Table 1.

For the Auriga-Aur05 field under the sky survey, in the emission region named Aur05(A) (the left image on the second row in Figure 1) there is one large HII-region at the top of and two smaller HII-regions close to our candidate emission (red circles and clay circle in the left side of the first row in Figure 2). There are no known SNR candidates close to the candidate whereas in the large-field of Aur05 region of $\sim 10^\circ$ there are five known SNRs from the Green SNR catalog (SNR G166.0+04.3, SNR G166.3+02.5, etc., ~ 2 degree far away from the selected clay circle). The Sge01(A) (the right image on the third row in Figure 1) is a wide-field emission region including only one detected small (radius of 0.04°) HII-region defined in the WISE-HII catalog (red circle in the left side

of the second row of Figure 2 with the clay circle for the emission field). Neither inside of the region nor close to the region there is no detected supernova remnant published under the Green 2019 catalog. In the region of our last emission candidate of Cep00(A) field (see the image in the fourth row in Figure 1) there are few HII-regions (red circles in the right image of the second row of Figure 2) with a smaller radius, are located both on the edge and outer side of the emission candidate (clay circle). There are detected SNRs very close to the field (ex. CTB 109 SNR) (green circles) and even the extension of the detected SNRs flow into the selected emission region. Currently, the main structure area still remains an unidentified type.

Finally, the standard identification technique for identifying the type of emission nebulae optically gives the flux ratio of $[SII]/H\alpha \geq 0.4$. During this work, the reduction of the optical imaging data is done for only three out of seven nebulae (name of Cep00(A), Sge01(A), and Aur05(A)). For the reduction analysis of each candidate, the structures are divided into several regions; four regions over Cep00(A), two regions over both Sge01(A) and Aur05(A) (see the central coordinates of regions in Table 2). Each

regions are shown with boxes of $21'.5 \times 21'.5$, same as of T100 field-of-view (FoV) (see the continuum-subtracted optical images of these regions, Aur05(A);Figure 3, Sge01(A);Figure 4 and Cep00(A);Figure 5). Since the identification technique applied to imaging for the three emission fields is satisfied the criterion $[SII]/H\alpha \geq 0.4$, it becomes easier to mark these complicated emission fields as SNR candidates.

Table 2. Journal of T100 optical imaging observations for the three emission nebulae divided into several regions are shown with the boxes of size in $21'.5 \times 21'.5$. The central coordinates of each region are shown with J2000 coordinates.

Regions Name	R.A. (J2000.0)	Dec. (J2000.0)
Cep00(A) region1	23:04:34.20	+58:20:33
Cep00(A) region2	23:03:49.89	+57:57:44
Cep00(A) region3	23:00:29.28	+57:39:43
Cep00(A) region4	23:02:26.38	+58:28:15
Sge01(A) region1	19:46:05.09	+17:56:17
Sge01(A) region2	20:02:50.49	+17:41:25
Aur05(A) region1	05:25:00.14	+40:08:18
Aur05(A) region2	05:29:51.82	+39:56:26

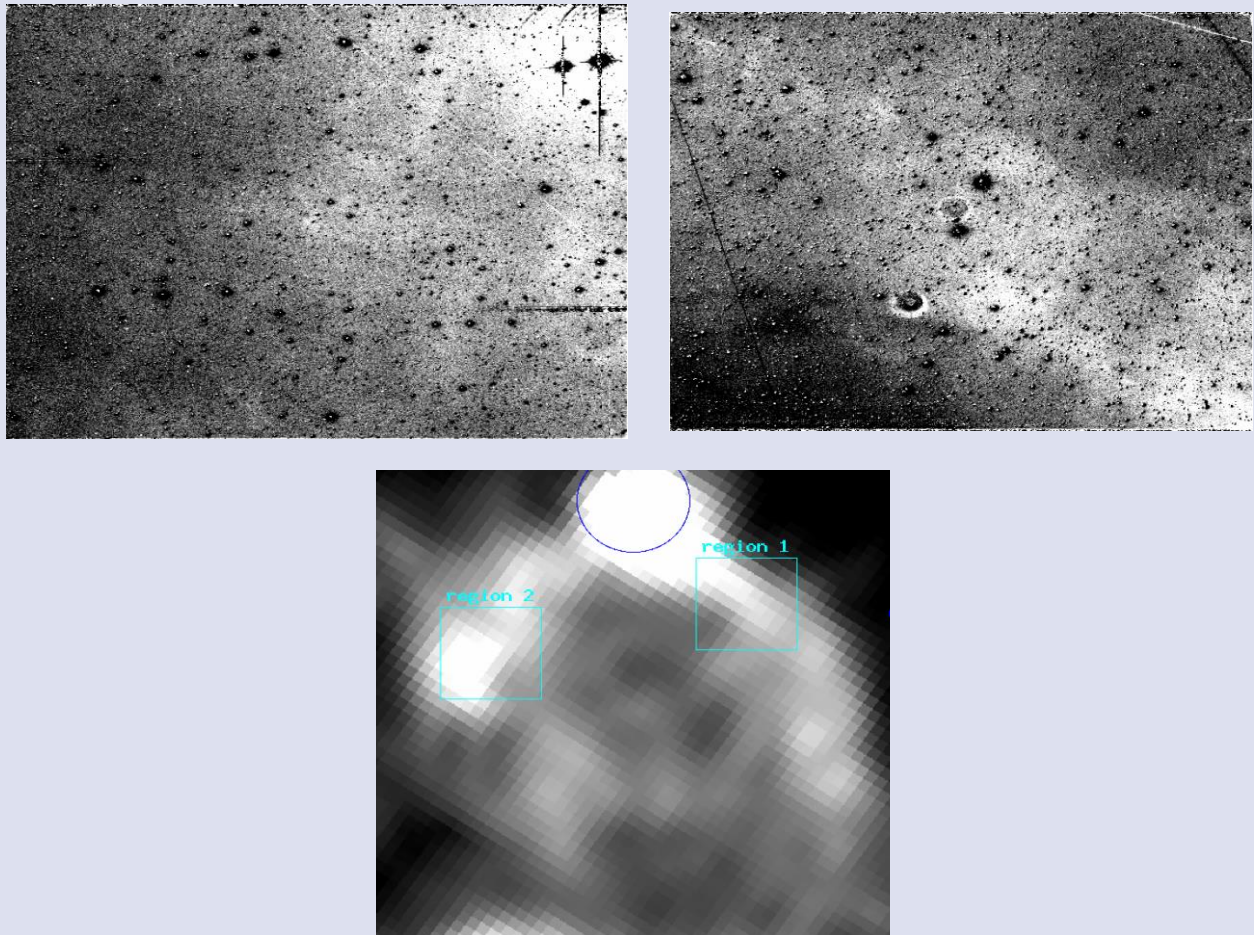


Figure 3. $H\alpha$ image of the selected emission nebula in Aur05(A) field. North is up; east is to the left for the VTSS image. Approximate central coordinate of the $1.0''$ -structure is $\alpha(J2000) = 05h26m53s.0$, $\delta(J2000) = +39^\circ 41' 23''$. The two regions selected over the structure (detected HII-region shown with blue circle) are located in the $H\alpha$ image. The continuum-subtracted images, observed with T100 observatory, used to determine the ratio of $[SII]/H\alpha$ images are shown in the upper row, respectively, the image of region 2 (left side) and region 1 (right side).

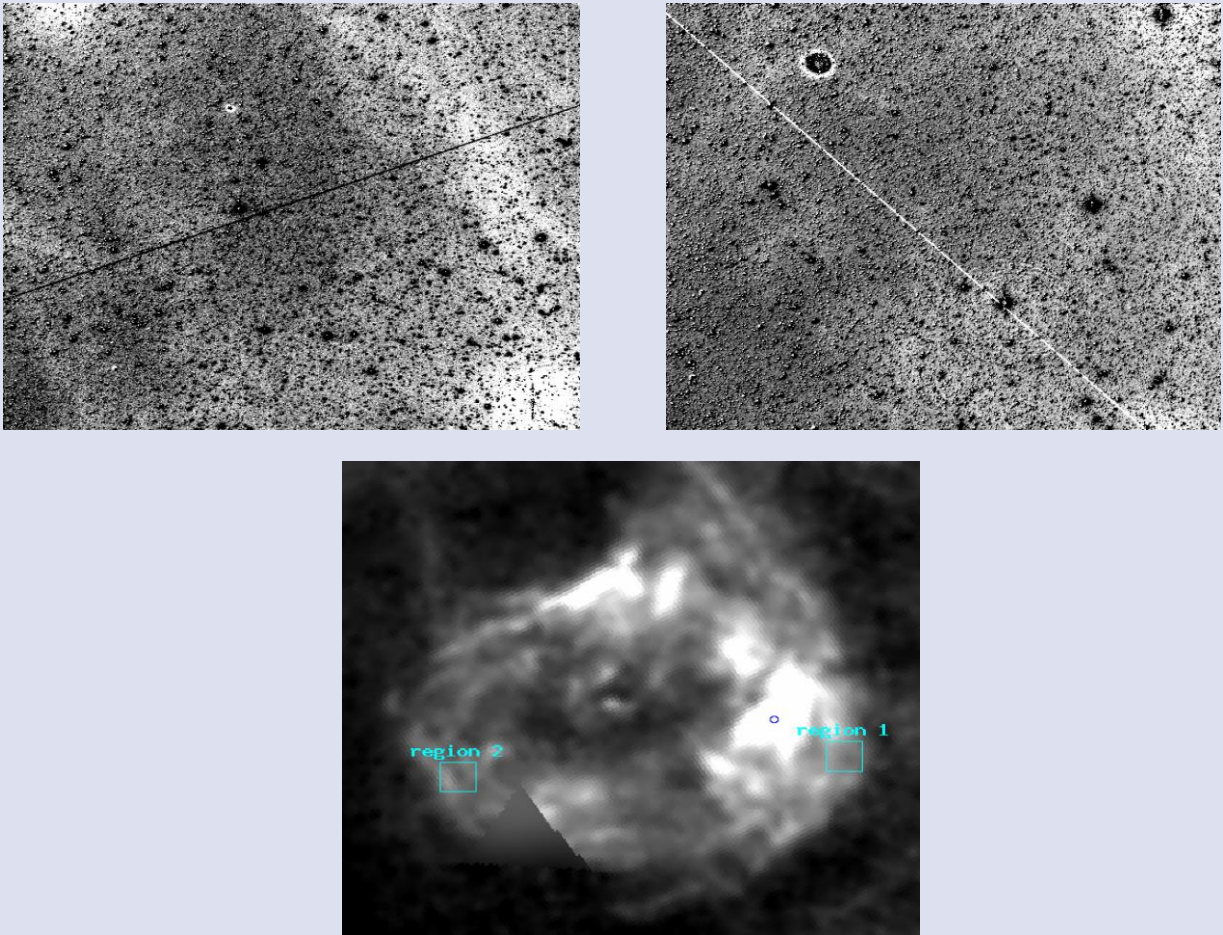


Figure 4. $H\alpha$ VTSS image of emission nebula in Sge01(A) field. North is up; east is to the left for both VTSS survey image. Approximate central coordinate of the 2.5° -structure image is $\alpha(J2000) = 19^h55^m23^s.0$, $\delta(J2000) = +18^\circ 37' 09''$. The two regions selected over the structure (detected HII-region shown with blue circle) are located in the $H\alpha$ image. The continuum-subtracted images, observed with T100 observatory, used to determine the ratio of $[SII]/H\alpha$ images are shown in the upper row, respectively, the image of region 2 (left side) and region 1 (right side).

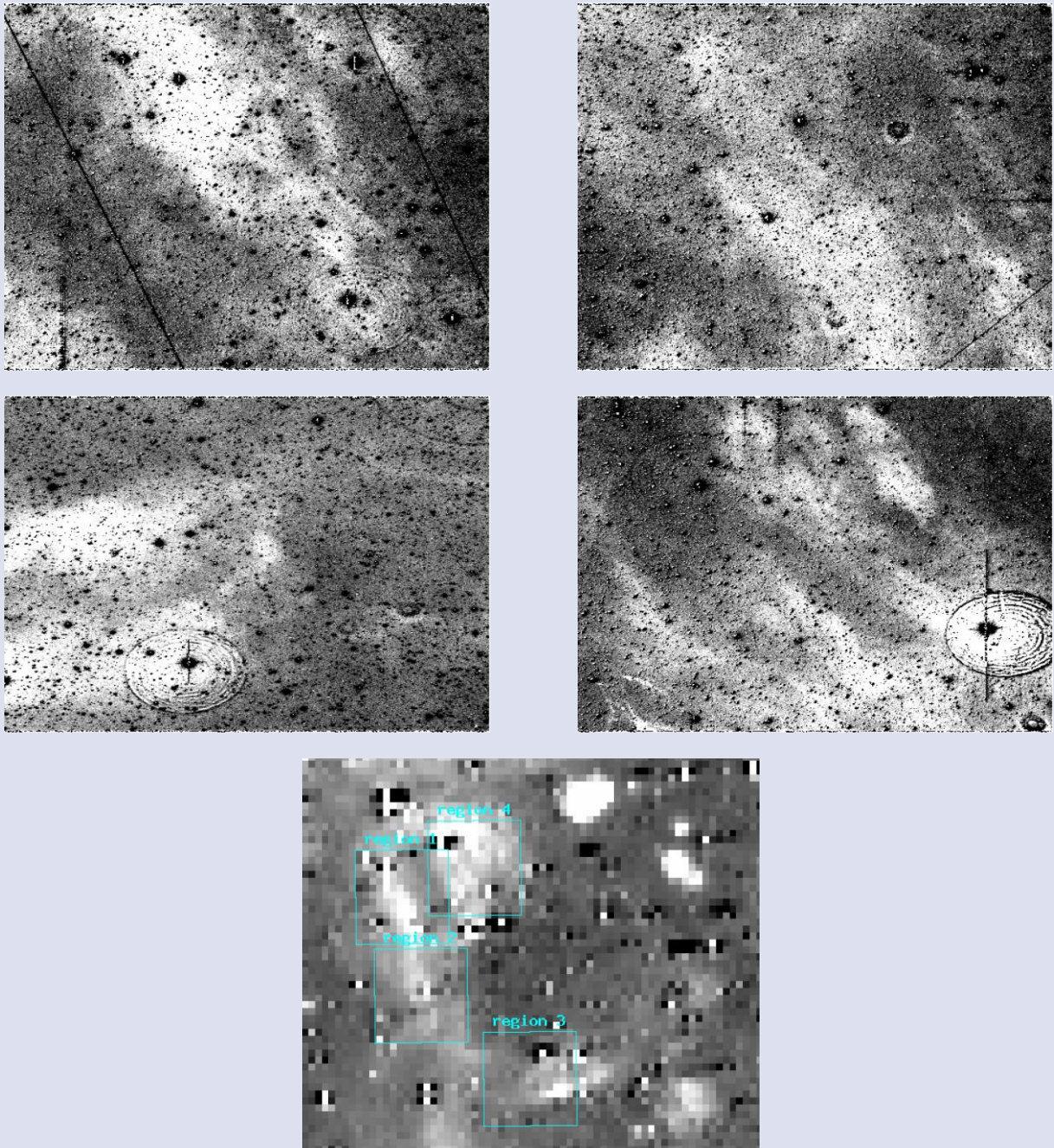


Figure 5. $H\alpha$ VTSS image of emission nebula in Cep00(A) field. North is up; east is to the left for both the below VTSS survey image. Approximate central coordinate of the 1.0° -structure image is $\alpha(J2000) = 23h02m19s.0$, $\delta(J2000) = +58^\circ 07' 32''$. The four regions selected over the structure are located in the $H\alpha$ image. The continuum-subtracted images, observed with T100 observatory, used to determine the ratio of $[SII]/H\alpha$ images are shown in the upper two rows, respectively, the image of region 1 (upper left side), region 2 (upper right side), region 3 (middle left side) and region 4 (middle right side).

The identification technique results having values larger than 0.4 for the three of all give a possibility for the other four nebulae about being a strong SNR candidate even though we have no imaging information currently. These all candidates are in SNR- and HII-rich regions although there are no previously detected or identified emission structures within the specific areas around the given central coordinates, by using any known catalogs.

This situation puts these candidates on top of the new observation list prepared for possible SNR candidates.

In future work, the missing optical imaging for some of the fields and the detailed optical spectroscopic of all fields should be completed. Besides the optical work, complementary search in the radio and X-ray will allow us to fully understand the physical properties of these supernova remnants with their contribution to the environment ISM and our own galaxy.

Acknowledgements

I would like to thank TÜBİTAK National Observatory for a partial support in using T100 telescope with project number 18AT100-1309. Also, I would like to thank the Virginia Tech Spectral-Line Survey (VTSS), which is supported by the National Science Foundation. This work made use of Astropy (<http://www.astropy.org>) a community-developed core Python package and an ecosystem of tools and resources for astronomy [30,31]. I thank the referee for comments and a careful reading that helped to improve the clarity of the paper.

Conflicts of interest

There are no conflicts of interest in this work.

References

- [1] Green D.A., A revised catalogue of 294 Galactic supernova remnants, *J. Astrophys. Astr.*, 40 (4) (2019) 36-48.
- [2] Downes D., New Radio Results on Supernova Remnants, *AJ*, 76 (1971) 305-316.
- [3] Chevalier R.A., The interaction of supernovae with the interstellar medium, *ARAA*, 15 (1977) 175-196.
- [4] Kopsacheili M., Zezas A., Leonidaki I., A diagnostic tool for the identification of supernova remnants, *MNRAS*, 491 (2020) 889-902.
- [5] Boumis P., Xilouris E. M., Alikakos J., Christopoulou, P. E., Mavromatakis F., Katsiyannis A. C., Goudis C. D., Discovery of optical emission from the supernova remnant G 32.8-0.1 (Kes 78), *A&A*, 499 (3) (2009) 789-797.
- [6] Stupar, M., Parker Q. A., Optical detection and spectroscopic confirmation of supernova remnant G213.0-0.6 (now redesignated as G213.3-0.4), *MNRAS*, 419 (2) (2012) 1413-1420.
- [7] Neustadt J. M. M., Fesen R. A., Black C. S., Detection of optical emission associated with the Galactic SNR G64.5+0.9, *MNRAS*, 469 (2017) 516-520.
- [8] Stupar M., Parker Q. A., Frew D. J., Confirmation of G6.31+0.54 as a part of a Galactic supernova remnant, *MNRAS*, 479 (2018) 4432-4439.
- [9] How T. G., Fesen R. A., Neustadt J. M. M., Black C. S., Outter, N., Optical emission associated with the Galactic supernova remnant G179.0+2.6, *MNRAS*, 478 (2) (2018) 1987-1993.
- [10] Fesen R. A., Neustadt J. M. M., How T. G., Black C. S., Detection of extensive optical emission from the extremely radio faint Galactic supernova remnant G182.4+4.3, *MNRAS*, 486 (4) (2019) 4701- 4709.
- [11] Fesen R.A., Weil K. E., Raymond J.C., Huet L., Rusterholz M., Di Cicco D., Mittelman D., Walker S., Drechsler M. and Faworski S., G107.0+9.0: a new large optically bright, radio, and X-Ray faint galactic supernova remnant in Cepheus, *MNRAS*, 498 (4) (2020) 5194–5206.
- [12] Fesen R.A., Neustadt J.M.M., Black C.S. and Koepfel A.H.D., Discovery of an Apparent High Latitude Galactic Supernova Remnant, *AJ*, 812 (1) (2015) 37-48.
- [13] Stupar M., Parker Q. A., Filipovic M. D., Newly confirmed and candidate Galactic SNRs uncovered from the AAO/UKST H α survey, *MNRAS*, 390 (3) (2008) 1037-1054.
- [14] Fesen R. A., Milisavljevic D., Optical Discovery of an Apparent Galactic Supernova Remnant G159.6+7.3, *AJ*, 140 (5) (2010) 1163-1167.
- [15] Sabin L., Parker Q. A., Contreras M. E., Olguín L., Frew D. J., Stupar M., Vázquez R., Wright N. J., Corradi R. L. M., Morris R. A. H., New Galactic supernova remnants discovered with IPHAS, *MNRAS*, 431 (1) (2013) 279-291.
- [16] Dennison B., Simonetti J. H., Topasna G. A., An imaging survey of northern galactic H α emission with arcminute resolution, *PASA*, 15 (1) (1998) 147-148.
- [17] Finkbeiner D.P., A Full-Sky H α Template for Microwave Foreground Prediction, *ApJS*, 146 (2) (2003) 407-415.
- [18] Gaustad J. E., McCullough P. R., Rosing W., and Buren D. Van, A Robotic Wide-Angle H α Survey of the Southern Sky, *PASP*, 113 (789) (2001) 1326–1348.
- [19] Drew J.E., Greimel R., Irwin M.J., et al., The INT Photometric H α Survey of the Northern Galactic Plane (IPHAS), *MNRAS*, 362 (3) (2005) 753-776.
- [20] González-Solares E.A., Walton N.A., Greimel R., et al., Initial data release from the INT Photometric H α Survey of the Northern Galactic Plane (IPHAS), *MNRAS*, 388 (1) (2008) 89-104.
- [21] Mathewson, D. S., Clarke, J. N., Supernova Remnants in the Magellanic Clouds, *AJ*, 182 (1973) 697-698.
- [22] Blair W. P., Kirshner R. P., Chevalier R. A., Supernova remnants in M31, *ApJ*, 247 (1981) 879-893.
- [23] Dopita M.A., Benvenuti P., Dodorico S., Binette L., Radiative shock-wave theory. I. Chemical abundance diagnostics and galactic abundance gradients, *ApJ*, 276 (1984) 653-666.
- [24] Fesen R. A., Blair W. P., Kirshner R. P., Optical emission-line properties of evolved galactic supernova remnants, *AJ*, 292 (1985) 29-48.
- [25] Leonidaki I., Boumis P., Zezas A., A multiwavelength study of supernova remnants in six nearby galaxies - II. New optically selected supernova remnants, *MNRAS*, 429 (1) (2013) 189-220.
- [26] Long K. S., Galactic and Extragalactic Samples of Supernova Remnants: How They Are Identified and What They Tell Us, in Alsabti A. W., Murdin P., eds, *Handbook of Supernovae, Springer International Publishing AG*, (2017) 2005-2040.
- [27] https://doi.org/10.1007/978-3-319-21846-5_90
- [28] Frew D.J., Bojicic I.S., Parker Q.A., A catalogue of integrated H α fluxes for 1258 Galactic planetary nebulae, *MNRAS*, 431 (1) (2013) 2–26.
- [29] Dharmawardena T. E., Barlow M. J., Drew J. E., Seales A., Sale S. E., Jones D., Mampaso A., Parker Q. A., Sabin L., Wesson R., H α fluxes and extinction distances for planetary nebulae in the IPHAS survey of the northern galactic plane, *MNRAS*, 501 (4) (2021) 6156–6167.

- [30] Anderson L.D., Bania T.M., Balser D. S., Cunningham V., Wenger T. V., Johnstone B.M., and Armentrout W.P., The WISE Catalog of Galactic H II Regions, *ApJS*, 212 (1) (2014) 1–18.
- [31] The Astropy Collaboration, Astropy: A community-developed core Python package and an ecosystem of tools and resources for astronomy, *AA*, 558 (2013) A33.
- [32] The Astropy Collaboration, Astropy: A community-developed core Python package and an ecosystem of tools and resources for astronomy, *AJ*, 156 (2018) 123.

Testing Complete Spatial Randomness on Linear Networks: Leon County Traffic Accident Example

İdris Demirsoy^{1,a,*}

¹ Department of Computer Engineering, Faculty of Engineering, Uşak University, Uşak, Türkiye.

*Corresponding author

Research Article

History

Received: 24/05/2022

Accepted: 01/09/2022

Copyright



©2022 Faculty of Science,
Sivas Cumhuriyet University

^a ıdrisdemirsoy1@gmail.com

^{id} <https://orcid.org/0000-0002-3321-4748>

ABSTRACT

A relatively new sub-area within this is the statistical analysis of point processes on linear networks, that is, processes of events occurring randomly in space but with locations constrained to lie on a linear network. For example, traffic accidents occur at random locations constrained to lie on a network of streets. In this case, the network is idealized as a network of line segments in the plane or three-dimensional space. The development of statistical techniques for the analysis of point processes on linear networks is still in its infancy. Many standard statistical techniques for analyzing point processes cannot be directly applied to data arising from linear networks and require suitable modification. Test of Complete Spatial Randomness (CSR) for point processes on the plane based on quadrat counts or nearest neighbors cannot be applied to point processes on linear networks. This paper defines a Voronoi tessellation of the linear network which uses the shortest path distance along the network instead of Euclidean distance, and then develops a chi-square test of CSR for linear networks based on the event counts in the tiles of this tessellation. This test is applied to data on traffic accidents in Leon County, Florida, USA.

Keywords: Spatial statistics, Point pattern, Complete spatial randomness, Linear network.

Introduction

Point processes are used as models for “events” or “points” occurring randomly in some space. As defined in [1] a point process X on \mathbb{R}^d is a random countable subset of a region $S \subseteq \mathbb{R}^d$, and a realization of such a process is a point pattern $x = \{x_1, \dots, x_n\}$ of $n \geq 0$ points contained in S . For any set x , let $n(x)$ denote the cardinality of x . Point processes X used in applications are usually assumed to be simple and locally finite. In a simple point process, no two points coincide, that is, no two “events” occur in the same position in \mathbb{R}^d . A locally finite point process X has only finitely many points in any bounded set. Stated more precisely, all realizations x are locally finite subsets of S , meaning that $n(x_A) < \infty$ for all bounded sets $A \subseteq S$ where $x_A = x \cap A$ is the restriction of the realization x to A .

The terms “point pattern” and “point process” are used interchangeably in most sources [2]. The purpose of a point process is to serve as a model for the pattern of “things” and their distributions. The things have locations in one, two, or three-dimensional spaces. Examples of things are tree locations in a forest, cancer cells in a tissue, bird migration routes, and tornado paths. The things are constructed using points and marks. Points are the locations of things, and marks are additional information associated with the points [2]. The general theory of point processes has been developed for arbitrary dimensions.

The methods suggested for determining randomness can be roughly separated into two types, which are referred to as quadrant methods and distance approaches, respectively [3]. The article [4] has investigated the efficacy of randomness

tests, in particular tests based on nearest-neighbor distance, inter-point distances, and estimators of moment measures. In addition to using distances and quadrants, alternative approaches have also been developed in several studies. The author of article [5] proposed assessing spatial randomness using angles between vectors connecting each sample location to its nearest neighbors. Additionally, [6] also mentioned a way of defining spatial patterns in which sample points travel in a regular arrangement that resembles a hexagonal lattice. However, none of the tests were developed for the test of Complete Spatial Randomness (CSR) on linear networks. The only method developed for the linear network was proposed by [7], which is a distance-based approach for testing CSR on a linear network, however, she advises conditioning on the positions of two arbitrary points to get the cumulative distribution function (CDF) of inter-event distance for complete spatial random (CSR) point pattern on the $m \times n$ grid network. Finally, to test two CSR test methods she suggested are based on inter-event distance and nearest-neighbor distance, respectively are based on Monte Carlo simulations. The method is based on simulation and depends on writing the CDF of the function which is not always straightforward to write CDF of a function. In this paper, we first define linear networks and spatial point process on linear networks, then we review complete spatial randomness on both planar space and linear networks then we define a Voronoi tessellation of the linear network which uses the shortest path distance along the network instead of Euclidean distance, and finally, we developed a chi-square test of CSR for linear networks based

on the event counts in the tiles of this tessellation. This test is applied to data on traffic accidents in Leon County, Florida, USA.

Spatial Point Processes on Linear Networks

Although spatial point processes on the line and plane have been studied since at least the 1950s, work on spatial point processes on linear networks is a recent development. There are important differences between the analysis of point processes on Euclidean spaces (e.g., the line or plane) and point processes on a linear network. For example, the Euclidean distance metric figures prominently in the development of point processes on the plane but may be an insufficient or misleading distance metric for spatial point patterns on linear networks, such as those arising in the study of the locations of traffic accidents, crime on sidewalks, road-kill, the population distribution of dendrites, or the heterogeneity of tree species along a river. For point processes on a linear network, it is usually more appropriate to define the distance between two points on the linear network to be the length of the shortest path between these two points traveling along the linear network. Another important difference between point processes on the plane and on a linear network is illustrated in Figure 1. When one looks at Figure 1(a), one may not think the points are randomly distributed, but Figure 1(b) clearly shows that the points are randomly distributed [8] on a linear network. The notions of “randomness” or “uniformity” are very different on the plane and on a linear network.

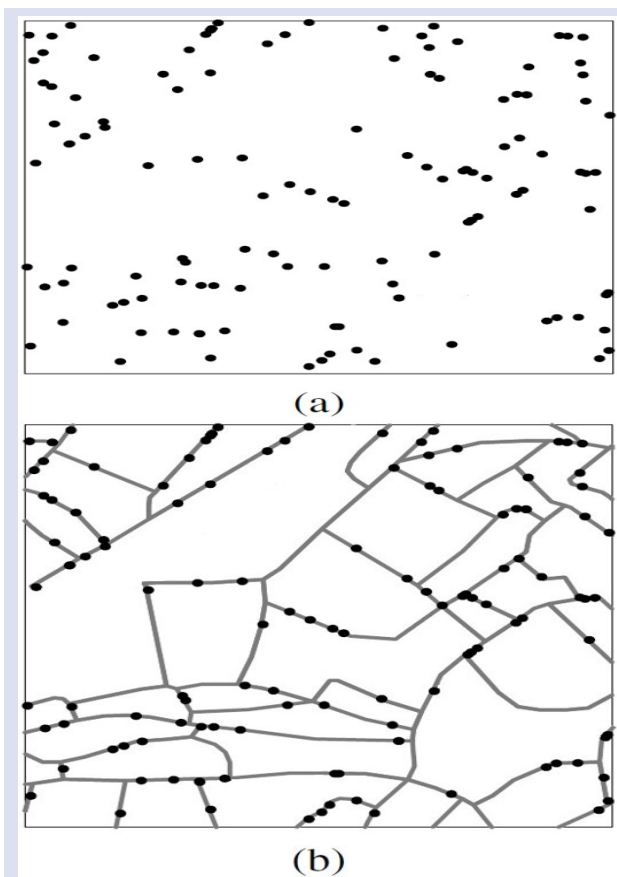


Figure 1: Points on a planar and linear network (Note: (a) and (b) are the same data points)

Definitions Relating to Linear Networks

The line segment l on the plane with endpoints $u, v \in \mathbb{R}^2, u \neq v$, can be written in any of the following ways: $l = l_{u,v} = [u, v] = \{tu + (1 - t)v : 0 \leq t \leq 1\}$

The length of this segment can be written as

$$|l| = |l_{u,v}| = \|u - v\|,$$

where $\|\cdot\|$ is the usual Euclidean norm in \mathbb{R}^2 which for

$$z = (z_1, z_2) \text{ is defined by } \|z\| = \sqrt{z_1^2 + z_2^2}, [9,10].$$

A linear network L is a combination of line segments (edges) l_i :

$$L = \bigcup_{i=1}^n l_i$$

The total length of the linear network L is defined by

$$|L| = \sum_{i=1}^n |l_i|$$

According to [8], the endpoints of segments are called nodes or vertices, and the degree of a node u , written as $d(u)$, is the number of segments that are connected to the node. When $d(u) = 1$, then u is called a *terminal* node [11].

A *path* between u and v in a linear network L is a sequence x_0, x_1, \dots, x_m of points in L such that $x_0 = u, x_m = v$, and $[x_i, x_{i+1}] \subset L$ for each $i = 0, \dots, m - 1$. This path is denoted by $P(u, x_1, \dots, x_{m-1}, v)$. The *length of a path* $P(u, x_1, \dots, x_{m-1}, v)$ on L is defined to be

$$\|u - x_1\| + \|x_1 - x_2\| + \dots + \|x_{m-1} - v\|.$$

The *shortest-path distance* between two points u and v in a linear network L is the length of the shortest path in L between u and v ; this distance is denoted by $d_L(u, v)$.

[9] notes that a point process X on a linear network L is a special case of a point process on a planar space. We assume that X is simple, meaning that it does not have any coincident points. Each realization of X is a finite set $x = \{x_1, \dots, x_n\}$ of distinct points $x_i \in L$, where $n \geq 0$ is (typically) random and not fixed in advance.

When analyzing point patterns on the plane (e.g., the locations of crimes, stores, tree species, etc.), the ordinary Euclidean distance is usually the most appropriate measure of the distance between events. However, when it is known that the events of interest occur on a street network, this is often not a proper choice. In many cities' streets are arranged (at least roughly) in a rectangular grid and the Euclidean distance can sometimes differ substantially from the true street distance (the shortest-path distance along the network) as is illustrated in Figure 2(a). For this reason (as noted by [7]) some researchers began using the “grid distance” (also known as the taxi-cab distance or the L_1 distance) in their analyses, such as the crime pattern along network analysis in [8]. For two points with x - y coordinates (x_1, y_1) and (x_2, y_2) , the grid distance

between them is $|x_1 - x_2| + |y_1 - y_2|$. The grid distance between two points P_1 and P_2 is illustrated in Figure 2(b); it is computed as the summation of the horizontal length x and the vertical length h . However, [12] observe that grid distance is not ideal for two reasons: first, not every city uses grid roads, and many cities are using a circle-radial system. Second, even when a city uses a grid-style network, using grid distance to compute true street distance can be inaccurate. For example, in Figure 2(c), the grid distance between P_1 and P_2 is $x + h$ but the shortest-path distance between P_1 and P_2 is substantially greater than this. Therefore, neither Euclidean distance nor grid distance is an appropriate distance metric to use while analyzing events on a linear network. The shortest-path distance or true street distance is the proper distance [12].

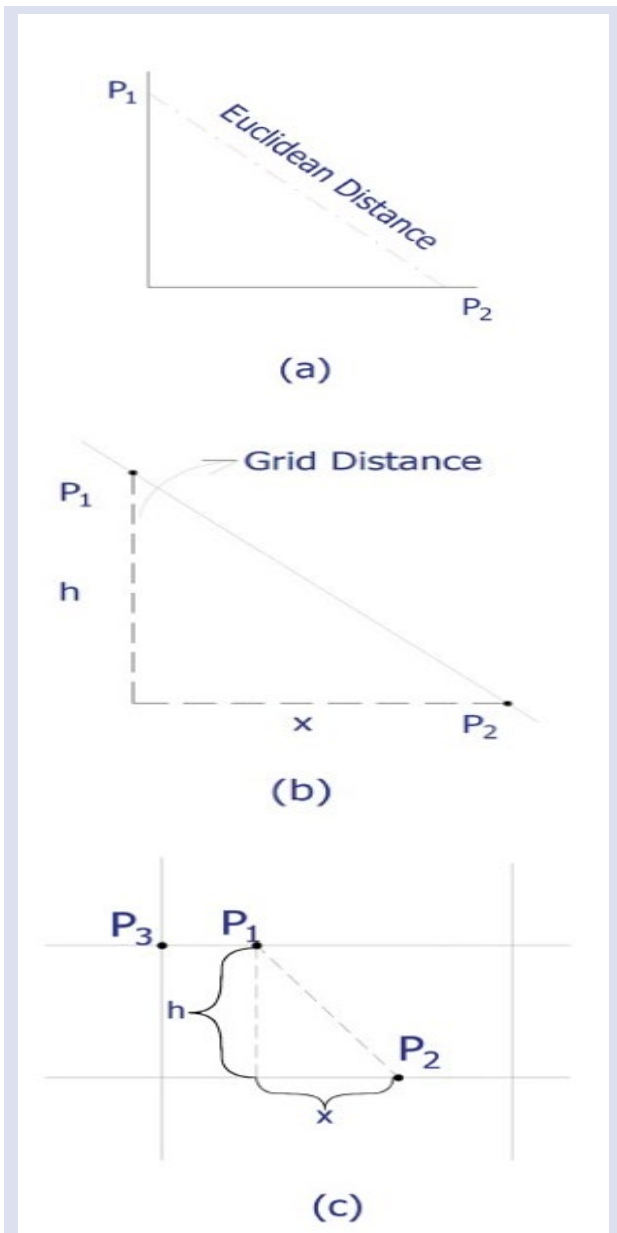


Figure 2: (a) Situation in which Euclidean distance differs greatly from shortest-path distance. (b) Illustration of grid distance between P_1 and P_2 . (c) The situation in which grid distance differs greatly from shortest-path distance. (Note: Solid lines are streets.)

Complete Spatial Randomness

Point pattern analysis differs from other spatial processes in that the number of events and their locations occur randomly. Point pattern analysis has been studied since the early 1920s in the fields of ecology and forestry. The simplest point patterns are those which exhibit *Complete Spatial Randomness* (CSR), which is (roughly speaking) the absence of structure [14]. Mathematically, CSR is equivalent to a point process being a *homogeneous Poisson process*. Checking for CSR is of paramount importance for point pattern analysis. The lack of sufficient evidence for rejecting CSR implies that events can be modeled with a uniform distribution and hence there is no spatial dependence. Therefore, there is no further reason to carry out a spatial analysis because there will be no or limited gain. Secondly, CSR analysis carries a fundamental role in exploring and learning about the data [15].

Many methods have been developed for testing CSR for point patterns in the plane, for example, the quadrat method is commonly used (although [14] notes that this method is not powerful enough to catch characteristics of the pattern on multiple scales). However, CSR on a linear network has not been widely studied. In this paper, we will explore the use of the Voronoi diagram to test CSR on a linear network.

Complete Spatial Randomness on R^2

CSR is synonymous with a homogeneous Poisson process. For such a process, the points (events) which occur in any bounded region $B \subset R^2$ are uniformly distributed over this region and are independent and do not interact with each other. Let $N(B)$ denote the number of events of the process in B . Given that $N(B) = n$, the ordered n -tuple of events $(u_1, u_2, \dots, u_n) \in B_n$ satisfies

$$P(u_1 \in A_1, \dots, u_n \in A_n) = \prod_{i=1}^n \left(\frac{|A_i|}{|B|} \right), \quad A_1, \dots, A_n \subset B,$$

where $|A| \equiv \int_A du$. This implies the events have the same probability to occur anywhere within B with no interaction between them, either repulsively or attractively.

It is difficult to identify whether points are distributed randomly through visual methods. Figure 3 shows three-point patterns, each containing 39 points in the same study area but generated by different methods. For example, Figure 3(c) shows 39 points created by a CSR process. Intuition can be misleading. People frequently do not expect a homogeneous Poisson process to display the apparent clustering and gaps observed in Figure 3(c); they expect the Poisson process to look more like Figure 3(c) which in fact is a process exhibiting fairly strong repulsion between the points leading to the more regular spacing between them. Formal statistical methods are needed to test for complete spatial randomness on R^2 . Some commonly used tests are based on quadrat analysis, the nearest neighbor distance, and the K function.

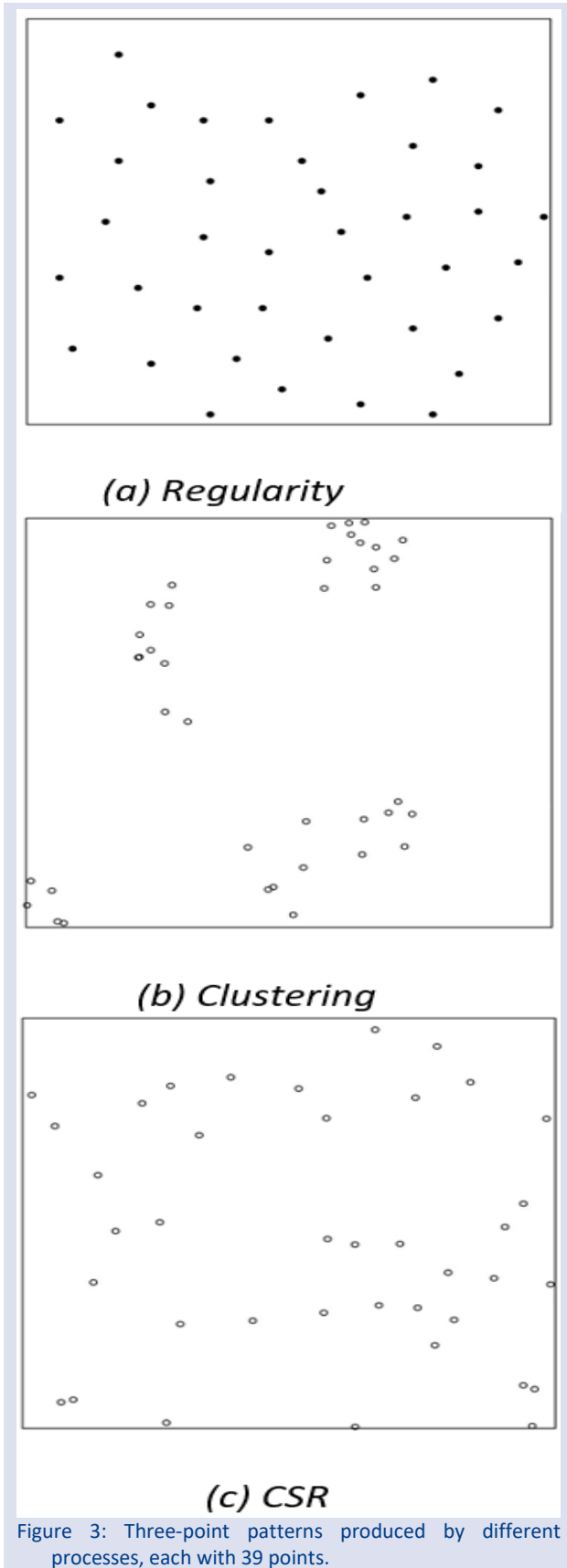


Figure 3: Three-point patterns produced by different processes, each with 39 points.

The current focus is on quadrat analysis because quadrat analysis and a test for CSR based on Voronoi diagrams will be compared in the next subsection. Details about the nearest neighbor distance and K function

methods can be found in many books, including [16], [14], and [15]).

Quadrat Analysis

Quadrats are defined as unions of *regular* sub-regions [17]. The name quadrat comes from dividing the study area in R^2 into small sub-regions of equal areas, preferably square or rectangular, and counting the number of events in each sub-region. The intensity of events in each quadrat is the ratio of the number of events it contains to the area.

Two main assumptions about quadrat methods are:

1. The study area is represented by the Euclidean space.
2. The events in the study area are homogeneous, which implies that the probability of a random event happening in any part of the study area is constant despite the location of the event.

Testing the randomness assumes the event counts in each quadrat follow a Poisson distribution. If there are n quadrats with equal areas having events counts x_1, x_2, \dots, x_n , the test statistics will be

$$X^2 = \frac{(n - 1)S_x^2}{\bar{x}} = \frac{\sum_{i=1}^n (x_i - \bar{x})^2}{\bar{x}}, \tag{1}$$

where, \bar{x} is the mean of observed counts and S_x^2 is the variance of observed counts. Under the null hypothesis of CSR, the statistic X^2 has approximately a chi-square distribution with $n - 1$ degrees of freedom so long as \bar{x} is not too small.

When χ^2 is too big, it is a sign of clustering. When χ^2 is too small, it may indicate regularity. In [16], the *index of dispersion* is computed by $\frac{S_x^2}{\bar{x}}$, and $\frac{S_x^2}{\bar{x}} - 1$ is defined as the *index of cluster size*(ICS). Based on the expected value of ICS one can conclude whether or not the events follow CSR;

$$\begin{cases} E(ICS) > 0, & \text{Clustered} \\ E(ICS) = 0, & \text{CSR} \\ E(ICS) < 0, & \text{Regularity} \end{cases}$$

One drawback of this method is choosing the optimal number of quadrats. There is no agreed-upon number or a mechanism to check. Therefore, it is possible that some quadrat areas are too small or too big, and some quadrats might even be empty which will affect the number of observed events. That would make the interpretation difficult or misleading. Another weakness is that quadrat analysis is not actually a *measure of pattern* analysis because the test statistics in Equation (1), do not include the location or distance between points. Even though they are in the same quadrat, how many of the points are in particular quadrats is the only interest.

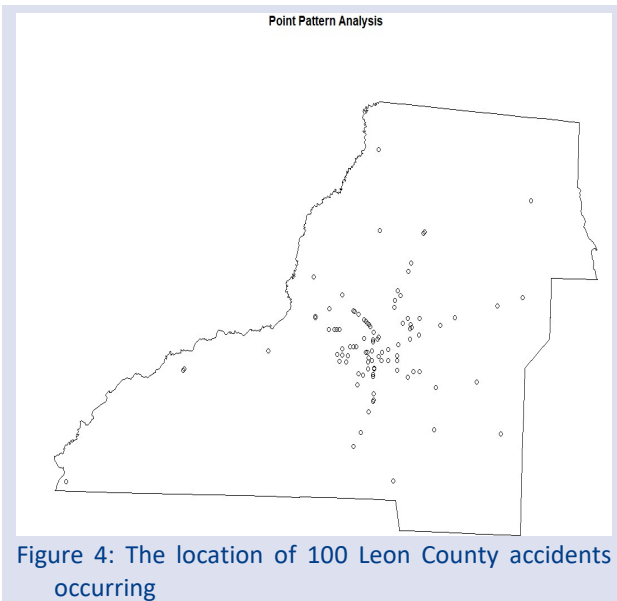


Figure 4: The location of 100 Leon County accidents occurring

For illustration, Figure 4 shows 100 traffic accidents sampled in Leon County, Florida, between January 1, 2008, and December 31, 2013. A quadrat analysis with 3x3 and 6x7 quadrats was executed. Figure 5 shows an example of a quadrat analysis using a 3x3 quadrat setup. In each quadrat, the values represent *observed*, *expected*, and *residuals*. Where $residual_i = (O_i - E_i) / \sqrt{E_i}$. As seen in the 3x3 square quadrat analysis, the quadrat size affects the observed and expected counts and the residuals, which affects the test statistics.

$$\chi^2 = \sum_{i=1}^n \frac{(O_i - E_i)^2}{E_i} \quad (2)$$

Figure 6 shows a 6x7 quadrat analysis for the same study area with the same number of events. Increasing the number of quadrats can create smaller, possibly empty quadrats (right bottom of Figure 6) that will affect the test statistics.

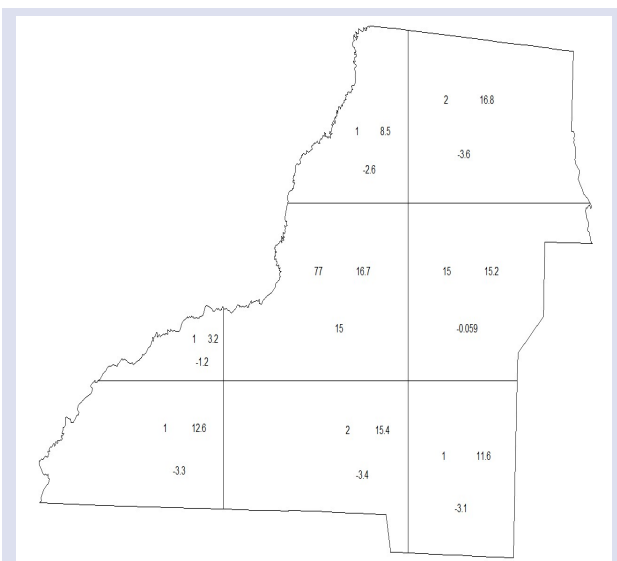


Figure 5: Quadrat analysis: equal-distance 3x3 square quadrats (Note: In each box, the top left is the number of observed points, the top right is the number of expected points and the bottom is the residual)

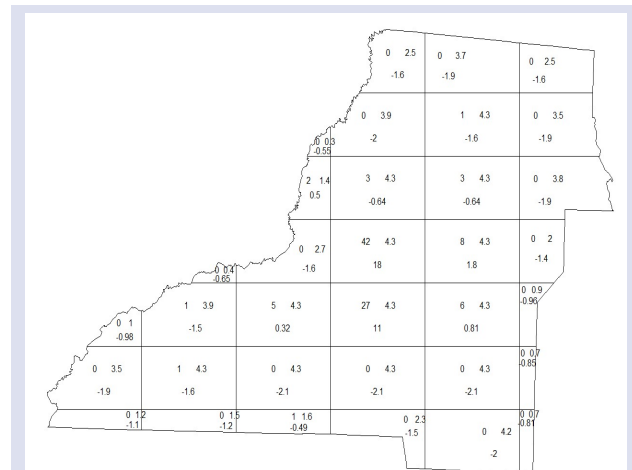


Figure 6: Quadrat analysis: equal-distance 6x7 square quadrats (In each box, the top left number is the observed value, the right top is the number of expected value and the bottom number is residual)

Voronoi tessellation

An alternative method for testing CSR on planar spaces is Voronoi tessellation, also known as Voronoi diagrams or Dirichlet tessellation.

Suppose n distinct points z_1, z_2, \dots, z_n (with $n \geq 2$) are chosen in planar space. The Voronoi tessellation determined by these points (which are called *generator* or *seed* points) is a subdivision of the planar space into n regions (known as *tiles*, *cells*, or *polygons*) denoted $\Phi(z_1), \Phi(z_2), \dots, \Phi(z_n)$. Each of these tiles surrounds one of the generator points. The tile $\Phi(z_i)$ consists of all points in the space that are closer to z_i than to any of the other generators $z_j, j \neq i$. That is,

$$\Phi(z_i) = \{z | d_E(z, z_i) \leq d_E(z, z_j), j = 1, \dots, n\} \quad (3)$$

where $d_E(z, z_i) = \|z - z_i\|$ is the Euclidean distance in R^2 between z and z_i . (For information on Dirichlet tessellations see [18] and [19].)

Complete spatial randomness on linear networks

One of the assumptions for quadrat analysis is the study area is represented by Euclidean space. Some cases show this assumption holds, especially on planar space examples, but some cases show this assumption does not hold such as street crimes, store locations, or traffic accidents. These events are observed along a linear network.

In Figure 8, a linear network is divided into 4x3 quadrats, and the two events z_1 and z_2 are in the same quadrat. The shortest-path distance between these two events could be far because there may or may not be a direct connection between them. Therefore, even if these events are in the same quadrats, they may not be close. [12] noted that one needs to update these assumptions based on the problem;

1. The study area is represented by a linear network.
2. The events on the network are homogeneous, which implies the probability of a random event happening on any segment is constant despite the location of the segment.

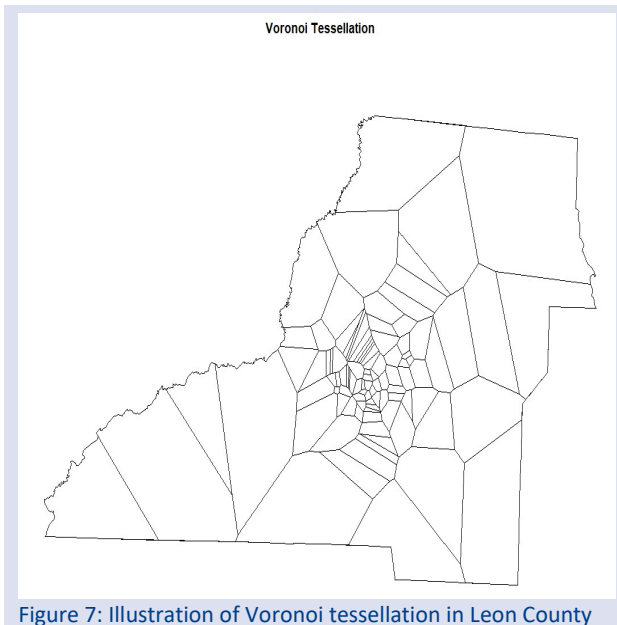


Figure 7: Illustration of Voronoi tessellation in Leon County

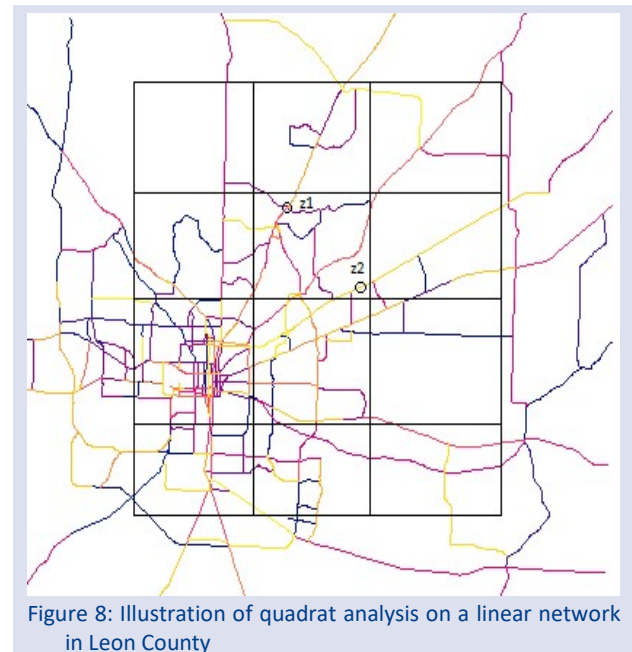


Figure 8: Illustration of quadrat analysis on a linear network in Leon County

In Figure 8, a linear network is divided into 4x3 quadrats, and the two events z_1 and z_2 are in the same quadrat. The shortest-path distance between these two events could be far because there may or may not be a direct connection between them. Therefore, even if these events are in the same quadrats, they may not be close. [12] noted that one needs to update these assumptions based on the problem;

1. The study area is represented by a linear network.
2. The events on the network are homogeneous, which implies the probability of a random event happening on any segment is constant despite the location of the segment.

[17] notes that there have been some attempts to use quadrat analysis on a linear network such as a river network, or on a road network to identify zones with high concentrations of traffic accidents, but [17] uses a heuristic approach. Creating quadrats on a linear network is not as straightforward as in planar space. Therefore, this paper proposes to use Voronoi tessellation on a linear network to test complete spatial randomness.

In Equation (3), [8] showed how to create Voronoi tessellation on planar networks using the Euclidean distance between two events. Therefore,

Equation (3) is updated with the shortest path between z and z_i in Equation (4) for Network Voronoi diagram;

$$\Phi(z_i) = \{z | d_L(z, z_i) \leq d_L(z, z_j)\}, j = 1, \dots, n \quad (4)$$

Voronoi tessellation sets are shown as $\Phi(\mathbf{Z}) = \{\Phi(z_1), \dots, \Phi(z_n)\}$. The configuration of the Voronoi tessellation is determined by the number and location of the generator points and the particular distance metric which is used [9]. Various numbers of tiles have been tried and finally, 15 tiles have been used.

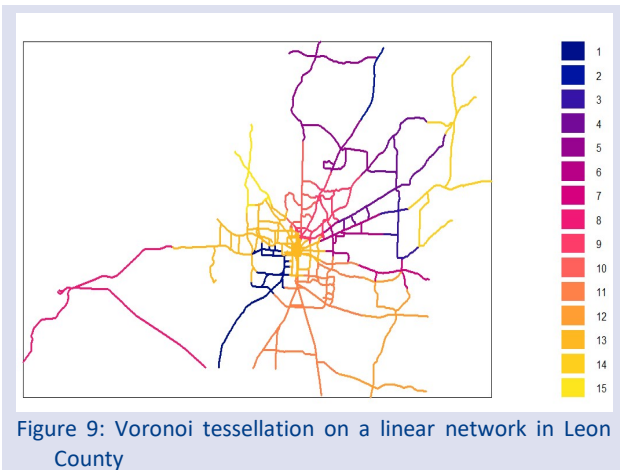
There is no a straightforward method to decide the number of tiles. In Figure 9, using Voronoi tessellation, Leon County's Road network is divided into 15 tiles.

Data Analysis

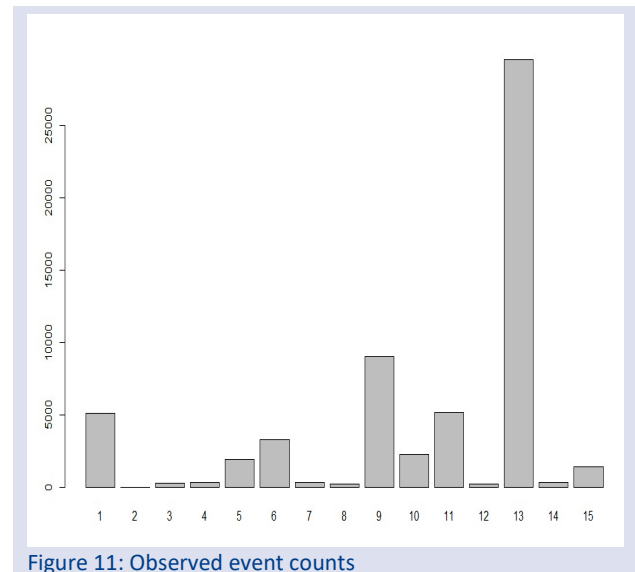
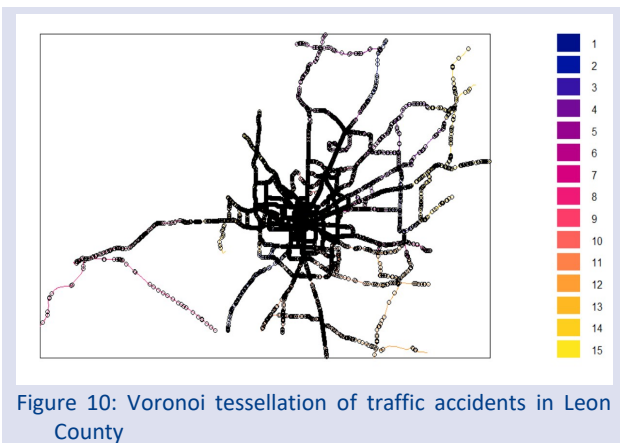
There are two parts to this section. The first one is about how to obtain a linear network and the second part is about where to get the accident data. Road information of Leon County is downloaded from the Florida Department of Transportation (FDOT)'s website. More detail on how Leon County linear network was created is explained in [20]. The data set, which totals 59,773 accident records, consists of accidents occurring from 2013 through 2019 and was provided by the GeoPlan Center affiliated with the Department of Urban & Regional Planning at the University of Florida.

The programming languages used in this paper are R 4.02 and ArcMap [21, 22]. ArcMap has been used to read and manipulate shapefiles that contains road information from Leon County. It is the first step which is creating the linear network. R programming has been used for creating Voronoi tessellation on the linear network and analyzing it, mainly the package *spatstat* has been used [23].

The locations of reported traffic accidents between January 2013 and December 2019 are placed on this tessellation, and the number of accidents in each tile is counted. Figure 10 shows these events. A histogram in Figure 11 shows the number of events in each tile, and tile 13 has the most events. Afterward, the observed number of events in each tile is counted, and a histogram is created for this tessellation.



To get the expected number of points in each tile, the total length of each tile is computed and shown in Table 2's first row. Afterward, the homogeneous intensity is assumed and λ_0 is estimated as the total number of points over the total length of the linear network



($\lambda_0=0.07585275$). Finally, the expected value in each tile is computed as λ_0 times the total length in each tile which is shown in the second row of Table 2.

$$\chi^2 = \sum_{i=1}^n \frac{(O_i - E_i)^2}{E_i} \tag{5}$$

Table 1: Observed counts of events in Leon County

Tile	1	2	3	4	5	6	7	8	9	10	11	12	13	14	15
Observed	5126	42	280	373	1939	3308	336	254	9069	2301	5197	221	29528	348	1448

Table 2: Total length and expected points in each tile in Leon County

Tile	1	2	3	4	5	6	7	8	9	10	11	12	13	14	15
Length	46113.4	10135.48	18208.63	46408.23	63609.3	32589	16190.31	56148.9	57209.4	28667.7	114416.5	52673.3	166410	56182.2	23011.64
Expected	3497.83	768.8	1381.17	3520.19	4824.94	2471.96	1228.08	4259.05	4339.49	2174.52	8678.81	3995.41	12622.66	4261.57	1745.5

The null hypothesis is whether these events follow complete spatial randomness. To test this hypothesis, Equation (5) is used to compute the χ^2 test statistic as 47969.96. There are 15 tiles and one unknown parameter to estimate. The degree of freedom for the χ^2 test employed is 14. Therefore, the 0.05 critical value of χ^2 distribution is $X_{14}^2 = 23.69$. The p-value for this test is computed as $P(X^2 > 47969.96) = 0$. The null hypothesis is rejected. This suggests that these events do not follow complete spatial randomness.

linear network (where M is the total number of events we have in our data) and for each repetition count the number of events in each tile. Averaging the event counts in each tile over sufficiently many repetitions leads to estimates of E_i which may be used in equation (5) to compute χ^2 . Applying this procedure to our data (which has $M = 59770$ events on the network in Figure 9) and using 10000 repetitions leads to the estimates of E_i given in Table 3. Using these values in equation (5) produces the test statistic $\chi^2 = 47967.39$, which is very close to the earlier value and leads to the same conclusion.

In situations where the total length of each tile is difficult to compute, an approach to get the expected number of points is to use Monte Carlo Approximation. To create a long-run average for each tile to approximate the "expected" counts, n number of uniformly random points repeatedly generate M random uniform points on the

Ten thousand simulations are executed for randomly generated 59770 uniform events on the linear network and the expected average number of points in each tile are shown in Table 3.

Table 3: Average expected counts of events in Leon County

Tile	1	2	3	4	5	6	7	8	9	10	11	12	13	14	15
Expected	3497.25	769.11	1381.5	3519.6	4825.29	2471.78	1227.95	4259.59	4340.39	2174.26	8678.78	3995.66	12622.75	4260.67	1745.41

Equation (5) computes χ^2 test statistic as 47967.39. There are 15 tiles and one unknown parameter to estimate. The degree of freedom for the χ^2 test employed is 14. Therefore, the critical value of χ^2 distribution is $\chi^2 = 23.69$. Under a significance level of 0.05, the p-value for this test is computed as $P(\chi^2 > 47967.39) = 0$. The null hypothesis is rejected. This suggests that these events do not follow complete spatial randomness.

Conclusion

Spatial point processes are everywhere from gold mines to tree species and from river streams to road maps. Therefore, testing the randomness of events in these study areas is the first natural step. Quadrat analysis, the nearest neighbor distance, and the K function are common methods to test complete spatial randomness on plane spaces. However, when the study area is a linear network such as a fault line, river stream, and road map, Quadrat analysis is misleading. Therefore, in this paper, Voronoi tessellation is used for testing complete spatial randomness on a linear network.

The proposed method is an upgrade to the quadrat analysis. The road map of Leon County, Florida, USA, has been used for a real data analysis purpose. As in quadrat analysis, a weakness of this approach is that there is not an optimal number of tiles. However, we have seen applied from 5 to 20 tiles and see no significant difference. Hence, 15 tiles have been used in this analysis, with the critical value of χ^2 distribution is $\chi^2 = 23.69$ obtained. Based on a significance level of 0.05, the p-value for this test is computed as $P(\chi^2 > 47967.39) = 0$. It has been observed that there is no spatial randomness and can be further investigation of analysis of the data. The purpose of the paper is to find a quick randomness test on linear networks and the Voronoi tessellation is an easy and quick approach to test complete spatial randomness on linear networks.

Conflict of interest

There are no conflicts of interest in this work.

References

- [1] Moller J., Waagepetersen R. P., Statistical Inference and Simulation for Spatial Point Processes, Chapman and Hall/CRC, (2004).
- [2] Illian J., Penttinen A., Stoyan H., Stoyan D., Statistical Analysis and Modelling of Spatial Point Patterns, John Wiley & Sons, (2008).
- [3] Diggle P. J., Besag J., Gleaves J. T., Statistical Analysis of Spatial Point Patterns by Means of Distance Methods, *Biometrics*, (1976) 659-667.
- [4] Ripley Brian D., Tests of 'randomness' for Spatial Point Patterns, *Journal of the Royal Statistical Society: Series B (Methodological)*, 41(3) (1979) 368-374.
- [5] Assuncao R., Testing Spatial Randomness by Means of Angles, *Biometrics*, (1994) 531-537.
- [6] Perry J. N., Spatial Analysis by Distance Indices, *Journal of Animal Ecology*, (1995) 303-314.
- [7] Chang X., Test of Complete Spatial Randomness on Networks, Master Thesis, University of Minnesota, (2016).
- [8] Okabe A., Sugihara K., Spatial Analysis Along Networks: Statistical and Computational Methods, John Wiley & Sons, (2012).
- [9] Ang Q. W., Baddeley A., and Nair G., Geometrically Corrected Second Order Analysis of Events on A Linear Network, With Applications to Ecology And Criminology, *Scandinavian Journal of Statistics*, 39(4) (2012) 591-617.
- [10] Moradi M. M., Cronie O., Rubak E., Lachieze-Rey R., Mateu J., and Baddeley A., Resample-Smoothing of Voronoi Intensity Estimators, *Statistics and Computing*, 29(5) (2019) 995-1010.
- [11] McSwiggan G., Baddeley A., and Nair G., Kernel Density Estimation on A Linear Network, *Scandinavian Journal of Statistics*, 44(2) (2017) 324-345.
- [12] Lu Y., and Chen X., On the False Alarm of Planar K-Function When Analyzing Urban Crime Distributed Along Streets, *Social Science Research*, 36(2) (2007) 611-632.
- [13] Kent J., Leitner M., and Curtis A., Evaluating the Usefulness of Functional Distance Measures When Calibrating Journey-To-Crime Distance Decay Functions, *Computers, Environment and Urban Systems*, 30(2) (2006) 181-200.
- [14] Cressie N., Statistics for Spatial Data, Terra Nova, (1992).
- [15] Diggle P. J., Statistical Analysis of Spatial and Spatio-Temporal Point Patterns, Chapman and Hall/CRC, (2013).
- [16] Bailey T. C., and Gatrell A. C., Interactive Spatial Data Analysis, Volume 413, Longman Scientific & Technical Essex, (1995).
- [17] Shiode S., Analysis of a Distribution of Point Events Using the Network-Based Quadrat Method, *Geographical Analysis*, 40(4) (2008) 380-400.
- [18] Okabe A., Boots B., Sugihara K., and Chiu S. N., Spatial Tessellations: Concepts and Applications of Voronoi Diagrams, Series in Probability and Statistics. John Wiley and Sons, Inc., 2nd ed., (2000).
- [19] Chiu S., Spatial Point Pattern Analysis by Using Voronoi Diagrams and Delaunay Tessellations—A Comparative Study. *Biometrical Journal: Journal of Mathematical Methods in Biosciences*, 45(3) (2003) 367-376.
- [20] Demirsoy I., Estimating the Intensity of Point Processes on Linear Networks, PhD thesis, Florida State University, 2020.
- [21] R Core Team. R: A Language and Environment for Statistical Computing, *R Foundation for Statistical Computing*, Vienna, Austria, (2020).
- [22] Esri Redlands. ArcGIS Desktop: Release 10, Environmental Systems Research Institute, CA (2011).
- [23] Baddeley Adrian, and Rolf Turner, Spatstat: An R Package for Analyzing Spatial Point Patterns, *Journal of Statistical Software*, 12 (2005) 1-42.

AUTHOR GUIDELINES

Thank you for choosing to submit your paper to Cumhuriyet Science Journal. The following instructions will ensure we have everything required so your paper can move through pre-evaluating, peer review, production and publication smoothly. Please take the time to read and follow them as closely as possible, as doing so will ensure your paper matches the journal's requirements.

Submission

Cumhuriyet Science Journal is an international, peer-reviewed, free of charge journal covering the full scope of both natural and engineering sciences. Manuscripts should be submitted by one of the authors of the manuscript as online submission after registration to the Cumhuriyet Sciences Journal. Microsoft Word (.doc, .docx, .rtf), files can be submitted. There is no page limit. If there is a problem while uploading the files of manuscript, please try to reduce their file size, especially manuscripts including embedded figures. Submissions by anyone other than one of the authors will not be accepted. The submitting author takes responsibility for the paper during submission and peer review. If for some technical reason submission through the online submission system is not possible, the author can contact csj@cumhuriyet.edu.tr for support.

Submission or processing charges

Cumhuriyet Science Journal does not charge any article submission, processing charges, and printing charge from the authors.

Terms of Submission

Papers must be submitted on the understanding that they have not been published elsewhere (except in the form of an abstract or as part of a published lecture, review, or thesis) and are not currently under consideration by another journal. The submitting author is responsible for ensuring that the article's publication has been approved by all the other coauthors. It is also the authors' responsibility to ensure that the articles emanating from a particular institution are submitted with the approval of the necessary institution. Only an acknowledgment from the editorial office officially establishes the date of receipt. Further correspondence and proofs will be sent to the author(s) before publication unless otherwise indicated. It is a condition of submission of a paper that the corresponding author permit editing of the paper for readability. All enquiries concerning the publication of accepted papers should be addressed to csj@cumhuriyet.edu.tr. Please note that Cumhuriyet Science Journal uses iThenticate software to screen papers for unoriginal material. By submitting your paper to Cumhuriyet Science Journal are agreeing to any necessary originality checks your paper may have to undergo during the peer review and production processes. Upon receiving a new manuscript, the Editorial office conducts initial pre-refereeing checks to ensure the article is legible, complete, correctly formatted, original, within the scope of the journal in question, in the style of a scientific article and written in clear English. Any article that has problems with any of the journal criteria may be rejected at this stage.

Peer Review

This journal operates a single blind review process. All contributions will be initially assessed by the editor for suitability for the journal. Papers deemed suitable are then typically sent to a minimum of two independent expert reviewer to assess the scientific quality of the paper. The author is required to upload the revised article to the system within 15 days by making the corrections suggested by the referee. The article will be rejected if there are no fixes in it. The Editor is responsible for the final decision regarding acceptance or rejection of articles. The Editor's decision is final

Title and Authorship Information

The following information should be included

Paper title

Full author names

Full institutional mailing addresses

Corresponding address

Email address

Abstract

The manuscript should contain an abstract. The researchers who are native speakers of Turkish have to add Turkish title and abstract as well. The abstract should be self-contained and citation-free and should be 250-300 words.

Keywords

Keywords of the scientific articles should be selected from the web address of www.bilimadresleri.com

Introduction

This section should be succinct, with no subheadings.

Materials and Methods

This part should contain sufficient detail so that all procedures can be repeated. It can be divided into subsections if required.

Conflicts of interest

Sample sentence if there is no conflict of interest: The authors stated that did not have conflict of interests.

Acknowledgements

Sample sentences for acknowledgements: The work was supported by grants from CUBAP (T-1111). We would like to acknowledge Prof. Mehmet Sözer, MD, for his precious technical and editorial assistance. We would like to thank

References

References to cited literature should be identified by number in the text in square brackets and grouped at the end of the paper in numerical order of appearance. Each reference must be cited in the text. Always give inclusive page numbers for references to journal articles and a page range or chapter number for books. References should be styled and punctuated according to the following examples

- [1] Karaca E., Ulusoy S., Morgül Ü., Ulusoy H.I., Development of Analytical Method for Sensitive Determination of Streptozotocin based on Solid Phase Extraction, Cumhuriyet Sci. J., 41 (4) (2020) 826-831. (sample reference for journals)
- [2] Keskin B., Ozkan A.S., Inverse Spectral Problems for Dirac Operator with Eigenvalue Dependent Boundary and Jump Conditions, Acta Math. Hungar., 130 (2011) 150-159(sample reference for journals)
- [3] Mazur M.T., Kurman R.J., Dysfunctional Uterine Bleeding. In: Mazur M.T., Kurman R.J., (Eds). Diagnosis of endometrial biopsies and curettings, A practical approach. 2nd ed. Berlin: Springer, (2005) 100-120. (sample reference for book chapters)
- [4] Mazur M.T., Kurman R.J.,Diagnosis of endometrial biopsies and curettings, A practical approach. 2nd ed. Berlin, (2005) 100-120. (sample reference for book)
- [5] National Cancer Institute, Surveillance Epidemiology and End Results. Cancer of the Corpus and Uterus, NOS. Available at: http://seer.cancer.gov/statfacts/html/corp.html?statfacts_page=corp. Retrieved March 2, 2008. (sample reference for websites)
- [6] Surname N., Title of thesis, PD or master thesis, Name of university, name of institue, year. (sample reference for thesis)
- [7] Surname N., Title of fulltext conference paper, name of conference, city, year, pages. (sample reference for Abstratcs in conferences are not accepted as a valid reference except full text)

Preparation of Figures

Each figure can be integrated in the paper body or separately uploaded and should be cited in a consecutive order. Figure widths can be 4-6 inch as 300 dpi. The labels of the figures should be clear and informative. The name and the subtitles of the figures must be 9-point font.

Preparation of Tables

Tables should be cited consecutively in the text. Every table must have a descriptive title and if numerical measurements are given, the units should be included in the column heading. Tables should be simple with simple borders and text written as left text. The name and the subtitle of the tables must be 9-point font

Proofs

Corrected proofs must be returned to the publisher within 2 weeks of receipt. The publisher will do everything possible to ensure prompt publication. It will therefore be appreciated if the manuscripts and figures conform from the outset to the style of the journal.

Copyright

Open Access authors retain the copyrights of their papers, and all open access articles are distributed under the terms of the Creative Commons Attribution license, which permits unrestricted use, distribution and reproduction in any medium, provided that the original work is properly cited.

The use of general descriptive names, trade names, trademarks, and so forth in this publication, even if not specifically identified, does not imply that these names are not protected by the relevant laws and regulations.

While the advice and information in this journal are believed to be true and accurate on the date of its going to press, neither the authors, the editors, nor the publisher can accept any legal responsibility for any errors or omissions that may be made. The publisher makes no warranty, express or implied, with respect to the material contained herein.

Ethical Guidelines

New methods and ethically relevant aspects must be described in detail, bearing in mind the following:

Human Experiments. All work must be conducted in accordance with the Declaration of Helsinki (1964). Papers describing experimental work on human subjects who carry a risk of harm must include:

A statement that the experiment was conducted with the understanding and the consent of the human subject.

A statement that the responsible Ethical Committee has approved the experiments.

Animal Experiments. Papers describing experiments on living animals should provide:

A full description of any anaesthetic and surgical procedure used.

Evidence that all possible steps were taken to avoid animal suffering at each stage of the experiment. Papers describing experiments on isolated tissues must indicate precisely how the donor tissues were obtained.

Submission Preparation Checklist

As part of the submission process, authors are required to check off their submission's compliance with all of the following items, and submissions may be rejected that do not adhere to these guidelines.

The submission has not been previously published, nor is it before another journal for consideration (or an explanation has been provided in Comments to the Editor).

The submission file is in Microsoft Word document file (Times New Roman) format.

Where available, URLs for the references have been provided.

The text is single-spaced; uses a 11-point font; employs italics, rather than underlining (except with URL addresses); and all illustrations, figures, and tables are placed within the text at the appropriate points, rather than at the end.

The text adheres to the stylistic and bibliographic requirements outlined in the Author Guidelines, which is found in About the Journal.

If submitting to a peer-reviewed section of the journal, the instructions in Ensuring a Double-Blind Review have been followed.